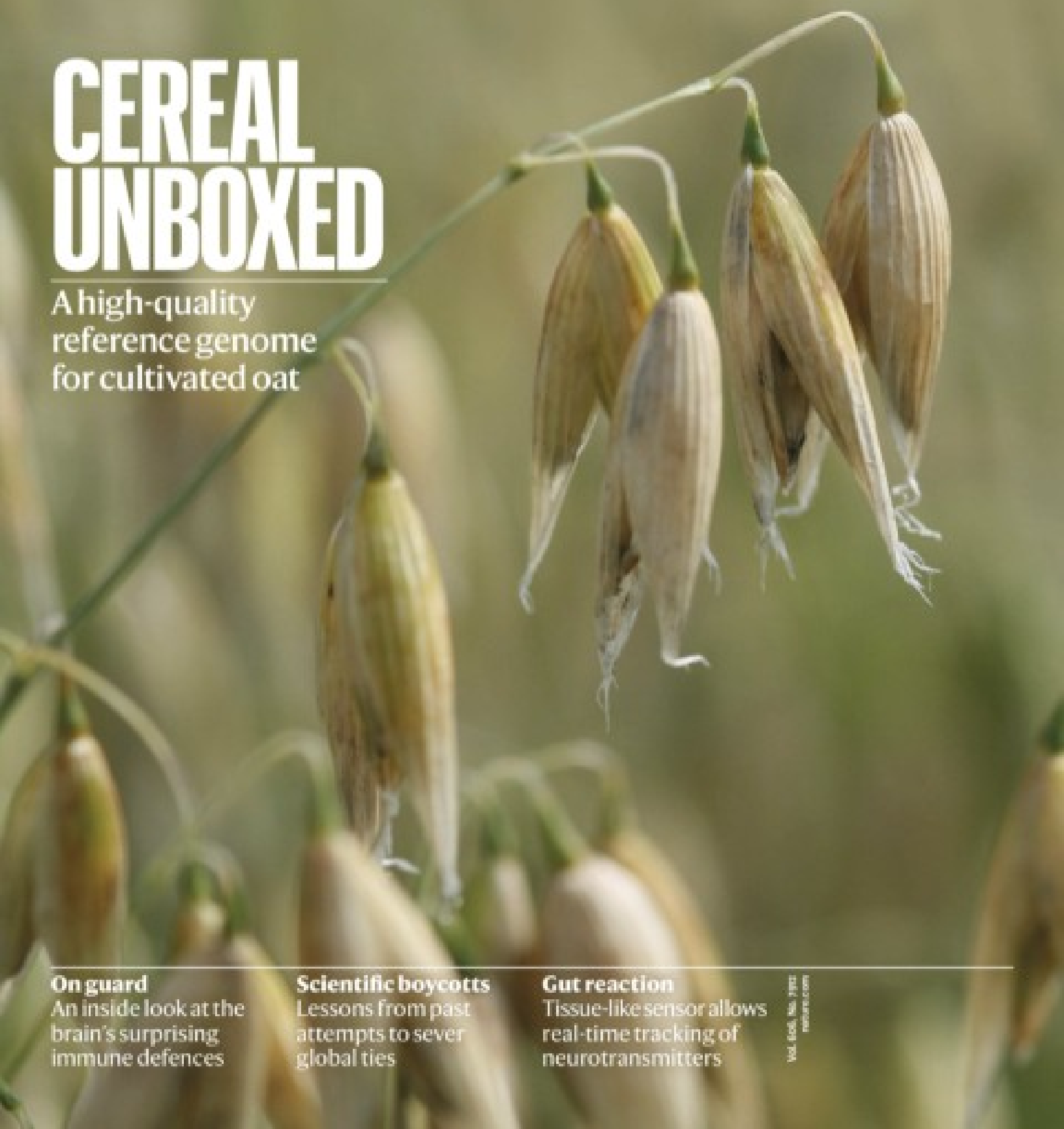


nature

CEREAL UNBOXED

A high-quality
reference genome
for cultivated oat



On guard
An inside look at the
brain's surprising
immune defences

Scientific boycotts
Lessons from past
attempts to sever
global ties

Gut reaction
Tissue-like sensor allows
real-time tracking of
neurotransmitters

Nature.2022.06.04

[Sat, 04 Jun 2022]

- [This Week](#)
- [News in Focus](#)
- [Books & Arts](#)
- [Opinion](#)
- [Work](#)
- [Research](#)

This Week

- **Nature addresses helicopter research and ethics dumping**

[30 May 2022]

Editorial • New framework aims to improve inclusion and ethics in global research collaborations amid wider efforts to end exploitative practices.

- **Fix the process that led to Alzheimer's drug fiasco**

[31 May 2022]

World View • Reforms to accelerated approval should focus on securing reliable information in the present and clinical evidence for the future.

| [Next section](#) | [Main menu](#) |

Nature addresses helicopter research and ethics dumping
[Download PDF](#)

- EDITORIAL
- 30 May 2022

***Nature* addresses helicopter research and ethics dumping**

New framework aims to improve inclusion and ethics in global research collaborations amid wider efforts to end exploitative practices.



Research on ecologically valuable mangroves is one of many fields where not enough local and regional experts are included. Credit: DEA/V. Giannella/Getty

Exploitative research practices, sadly, come in all shapes and sizes. ‘Helicopter research’ occurs when researchers from high-income settings, or who are otherwise privileged, conduct studies in lower-income settings or with groups who are historically marginalized, with little or no involvement from those communities or local researchers in the conceptualization, design, conduct or publication of the research. ‘Ethics dumping’ occurs when similarly privileged researchers export unethical or unpalatable experiments and studies to lower-income or less-privileged settings with different ethical standards or less oversight.

Such behaviours are wrong. They are also bad for research, which is denied crucial expertise and context. But for centuries, exploitative practices were, unfortunately, simply how researchers from around the world conducted studies in the global south. And even as the south’s capacity to do its own research has grown, elements of these practices continue.

That is why Nature Portfolio is introducing a new approach to improving inclusion and ethics in its journals (including *Nature* and all Nature Portfolio journals). The move comes as other journals grapple with similar issues and as the seventh [World Conference on Research Integrity](#), held in Cape Town, South Africa, prepares to publish a statement urging action on them.

There are plenty of examples of the persistent imbalance in research across multiple fields. One analysis¹ of a sample of studies conducted in Africa on a range of infectious diseases found that less than half had an African first or last author. Another report² showed that two-thirds of high-impact geoscience articles on Africa had no African authors.

Even in development research, for which the focus is overwhelmingly on challenges facing the global south, [authors from the global north wrote nearly three-quarters of papers](#) published in the world’s top 20 development journals between 1990 and 2019³.

In 2018, [researchers in Africa published guidelines](#) on how samples and data from the global south can be guarded from exploitation. But changing centuries of bad practice requires a joint effort across the research ecosystem.

Nature's latest steps to improve inclusion and ethics are guided by the [Global Code of Conduct for Research in Resource-Poor Settings](#), developed by TRUST — a European Union-funded project on research ethics — and by the [San Code of Research Ethics, developed by the San Indigenous people in southern Africa](#).

In [the new guidance](#), *Nature* will be encouraging its journals' authors, editors and reviewers to consider the Global Code when developing, conducting, reviewing and communicating research. We also want to create opportunities for authors to be transparent about inclusion and ethics. So we are urging them, through *Nature*'s editorial-policy checklist, to provide an optional disclosure statement on inclusion and ethics that can be shared with reviewers and published in the final paper. Editors can, at their discretion, ask authors to provide a statement.

To guide authors in writing such a statement — and to help minimize the possibility of helicopter science and ethics dumping — we have developed questions drawn from key aspects of the Global Code. These include: did the research design and execution include local scientists? Is the research locally relevant? Are there plans to share the benefits of the research? Where legislation on animal welfare or environmental protection was less stringent in the local setting than where the researchers were based, was the study undertaken to the higher standards?

We are encouraging authors to cite relevant local and regional research, to improve the quality of their citations and [to promote citational justice](#). A study⁴ published on 30 May finds that scientific papers from researchers in a few countries, including the United States, China and the United Kingdom, are more likely to be cited than those on similar subjects from researchers elsewhere.

Nature's new approach also aims to ensure that peer review includes representation from relevant regions and communities.

We don't yet have all the answers, and there are nuances that we will need to grapple with. For example, it might be important to seek out local contributors when researchers are using publicly available or secondary data

that they were not involved in gathering⁵, to add important cultural context or an appreciation of local impacts.

Nature is not alone in tackling these issues. Last year, the open-access publisher PLOS announced a policy intended to combat helicopter research, and a group of researchers — including the editors of the journals *Anesthesia* and *BMJ Global Health* — proposed⁶ that journals ask authors of studies conducted in low- and middle-income countries to supply statements describing how equity was promoted in their work. The statement from this year's World Conference on Research Integrity is expected to call out inequity and unfair practices in research collaborations as a matter of research integrity.

The time is now for all stakeholders — funders, institutions, publishers and researchers — to consider how we can work together to dismantle systemic legacies of exclusion.

Nature **606**, 7 (2022)

doi: <https://doi.org/10.1038/d41586-022-01423-6>

References

1. Mbaye, R. *et al.* *BMJ Glob. Health* **4**, e1001855 (2019).
2. North, M. A., Hastie, W. W. & Hoyer, L. *Earth Sci. Rev.* **208**, 103262 (2020).
3. Amarante, V. *et al.* *Appl. Econ. Lett.* <https://doi.org/10.1080/13504851.2021.1965528> (2021).
4. Gomez, C. J., Herman, A. C. & Parigi, P. *Nature Hum. Behav.* <https://doi.org/10.1038/s41562-022-01351-5> (2022).
5. *Lancet Glob. Health* **6**, E593 (2018).
6. Morton, B. *et al.* *Anesthesia* **77**, 264–276 (2022).

This article was downloaded by **calibre** from <https://www.nature.com/articles/d41586-022-01423-6>

| [Section menu](#) | [Main menu](#) |

Fix the process that led to Alzheimer's drug fiasco
[Download PDF](#)

- WORLD VIEW
- 31 May 2022

Fix the process that led to Alzheimer's drug fiasco



Reforms to accelerated approval should focus on securing reliable information in the present and clinical evidence for the future.

- [Jason Karlawish](#) 0

The morning of 7 June 2021 was a shock. The US Food and Drug Administration (FDA) approved aducanumab, the first treatment targeting β -amyloid, a protein associated with Alzheimer's disease.

Although some celebrated the approval of the first Alzheimer's drug in nearly 20 years, many were aghast at the lack of demonstrated efficacy: ten members of a panel of experts assembled by the FDA had voted against

approving it, with the one remaining member voting ‘uncertain’. Three quit in protest when the drug was approved.

I’m among many Alzheimer’s specialists who agree with the FDA’s statistical reviewers and advisory committee that the late-stage clinical trials were contradictory and incomplete. The reasonable next step was another trial, not approval. A well-intended policy to speed drugs to market has gone awry. One year on, it’s past time to fix it.

Both the FDA and the US House of Representatives have launched efforts to reform the accelerated-approval process, mostly focused on empowering the FDA to rescind approval after a drug is authorized. That’s essential, but in my opinion, the key is to ensure that assessment is transparent and that companies are committed to assessing actual clinical benefit. The FDA must be more careful and forthcoming about the information it collects and the decisions it makes.

The accelerated-approval programme fast-tracks medicines for serious, life-threatening diseases that lack effective treatments. Instead of relying on evidence that a drug extends lives or reduces disease symptoms, US regulators base accelerated approval on a ‘surrogate’ marker — such as tumour shrinkage — that is thought to be ‘reasonably likely’ to indicate clinical benefit. The advisory panel that recommended against approving aducanumab was not consulted (or even notified) about the agency using accelerated approval or whether β-amyloid was an appropriate surrogate, although FDA officials had discussed using this strategy with Biogen, the drug company in Cambridge, Massachusetts, that is developing the drug. What is more, the initial ‘label’ the FDA wrote to advise physicians on prescribing aducanumab was broader than how the drug had been tested. It did not specify that patients should be assessed for disease stage or evidence of amyloid.

One-third of people who take aducanumab experience swelling and bleeding in the brain, which can be fatal. The FDA is supposed to consider patient input on how they feel unproven benefits stack up against potential risks. The FDA approval came shortly after a ‘listening session’ with patients and caregivers, for which no public report exists. It was organized by the Alzheimer’s Association, a non-profit organization in Chicago,

Illinois, which has received funds from Biogen and other companies developing similar treatments. (US government inquiries are under way to consider whether there were improprieties in interactions between Biogen and the FDA; both organizations say the process followed was appropriate. It is not unusual for patient-advocacy groups to receive funds from drug companies working on relevant diseases.)

Launched in the 1990s to speed HIV drugs that reduced viral load to market, accelerated approval's use — and scepticism about it — is growing. From 2005 to 2010, there were about five such approvals per year. In 2020, a dozen new drugs were approved this way. A 2019 assessment found that, of 93 accelerated approvals for cancer treatments from 1992 to 2017, only 19 led to improved overall survival ([B. Gyawali et al. *JAMA Intern Med.* 179, 906–913; 2019](#)). In 2020, the FDA ignored advisers when it approved a drug for Duchenne muscular dystrophy. Companies can charge upwards of US\$100,000 a year for drugs without showing whether patients receiving them will live longer.

Under standard approval, the FDA determines whether a drug is safe and effective. The premise of accelerated approval is quite different. Patients accept uncertainty about whether a drug works to get faster access. (In other countries, such access is patient-by-patient; ‘compassionate use’ regulations allow clinicians to make the case for individual prescriptions). Accelerated approval balances incomplete information with innovation that could serve unmet medical needs. In negotiating this balance, the FDA must avoid being co-opted to serve commercial interests and unwarranted enthusiasm for accruing approvals.

To minimize that risk, the FDA should recast itself as the guardian of information by providing more transparency about its decision-making and ensuring drug companies produce information about clinical benefit. Announcements and labels of drugs receiving accelerated approval should lead with a plain statement that clinical benefit is not proven. (The label of aducanumab states: “Continued approval for this indication may be contingent upon verification of clinical benefit in confirmatory trial(s).”) But drug companies have little incentive to complete those confirmatory trials.

The FDA needs to be open with its advisory committees about plans for accelerated approval, and to thoroughly explain any decisions that go against recommendations by advisory committees. The process shouldn't be a backup for the failure to gain a supportive vote on standard approval. All accelerated approvals must be accompanied by a plan for a confirmatory trial that will assess whether the change in the surrogate marker translates into clinical value. That is how we can better ensure that treatments will lead to a longer or more fulfilling life.

Nature **606**, 9 (2022)

doi: <https://doi.org/10.1038/d41586-022-01507-3>

This article was downloaded by **calibre** from <https://www.nature.com/articles/d41586-022-01507-3>

| [Section menu](#) | [Main menu](#) |

News in Focus

- **Gene-edited tomatoes, South Asian heatwave and Australian election** [01 June 2022]
News Round-Up • The latest science news, in brief.
- **Monkeypox goes global: why scientists are on alert** [20 May 2022]
News • Scientists are trying to understand why the virus, a less-lethal relative of smallpox, has cropped up in so many populations around the world.
- **'Mind blowing' ancient settlements uncovered in the Amazon** [25 May 2022]
News • The urban centres are the first to be discovered in the region, challenging archaeological dogma.
- **Why unprecedented bird flu outbreaks sweeping the world are concerning scientists** [26 May 2022]
News • Mass infections in wild birds pose a significant risk to vulnerable species, are hard to contain and increase the opportunity for the virus to spill over into people.
- **COVID delays are frustrating the world's plans to save biodiversity** [20 May 2022]
News • Scientists hope an ambitious agreement to arrest species extinction will be finalized in China later this year, but the country's pandemic response puts that in doubt.
- **Frustration builds over lengthy delay in revamping Mexico's science law** [20 May 2022]
News • Mexican researchers fear that a polarizing bill could ruin the chances of overhauling the nation's science system.
- **Guardians of the brain: how a special immune system protects our grey matter** [01 June 2022]
News Feature • The nervous and immune systems are tightly intertwined. Deciphering their chatter might help address many brain disorders and diseases.

Gene-edited tomatoes, South Asian heatwave and Australian election
[Download PDF](#)

- NEWS ROUND-UP
- 01 June 2022

Gene-edited tomatoes, South Asian heatwave and Australian election

The latest science news, in brief.



In India, 70% of the country has been affected by this year's record-breaking heatwave. Credit: Debarchan Chatterjee/NurPhoto/Getty

Climate change made South Asian heatwave 30 times more likely

Human-induced climate change [made the deadly heatwave that gripped India and Pakistan in March and April 30 times more likely](#), according to a rapid analysis of the event (see go.nature.com/3nzwag). Temperatures began rising earlier than usual in March, shattering records and claiming at least 90 lives. The prolonged heat has yet to subside.

“High temperatures are common in India and Pakistan, but what made this unusual was that it started so early and lasted so long,” said co-author Krishna AchutaRao, a climate scientist at the Indian Institute of Technology in New Delhi, in a press release. “We know this will happen more often as temperatures rise and we need to be better prepared for it,” AchutaRao said.

In India, March’s temperatures were consistently 3–8 °C above average, reaching highs of 44 °C — the highest they’ve been since records began 122 years ago. Pakistan reported temperatures that exceeded 49 °C in some regions. The heatwave was coupled with below-average rainfall. Pakistan received 62% less rainfall than usual, and India 71% less. Although the lack of rain added to heating from the land’s surface, it also reduced the humidity of the heatwave.

To characterize the extreme heatwave and quantify the role of climate change, a global team of researchers from the World Weather Attribution (WWA) initiative looked at the average daily maximum temperatures across northwestern India and southeastern Pakistan between March and April. They then compared the possibility of such an event occurring in today’s climate compared with that in pre-industrial times, using a combination of climate models and observation data going back to 1979 in Pakistan and 1951 in India.

The team found that climate change increased the probability of the heatwave occurring to once in every 100 years; the odds of such an event would have been once in every 3,000 years in pre-industrial times, says Zeke Hausfather, a climate scientist and researcher at Berkeley Earth, a non-profit organization in California that focuses on climate change and analysis of global temperatures. The researchers also show that the event was around 1 °C warmer than it would have been in a pre-industrial climate.



Tomatoes naturally produce a precursor to vitamin D. Shutting down a pathway that converts it to other chemicals causes the precursor to accumulate. Credit: Getty

Gene-edited tomatoes could be vitamin D source

Gene-edited tomato plants that [produce a precursor to vitamin D](#) could one day provide an animal-free source of the crucial nutrient.

When the gene-edited plants are exposed to ultraviolet light in the laboratory, some of the precursor, called provitamin D₃, is converted to vitamin D₃. But it is not known how the tomatoes will fare when grown outside.

To engineer them, researchers took advantage of a feature of plants in the Solanaceae family. Some plants naturally produce forms of vitamin D, which is often later converted into chemicals that regulate the plants'

growth. Blocking the conversion pathway can cause the vitamin D precursor to accumulate, but also leads to stunted plants. However, solanaceous plants such as tomatoes (*Solanum lycopersicum*) also have a biochemical pathway that converts provitamin D₃ into defensive compounds. Shutting down that pathway, the team found, led to an accumulation of the precursor without affecting the plants' growth in the laboratory ([J. Li et al. *Nature Plants* https://doi.org/hv7f; 2022](https://doi.org/hv7f)).

If the tomatoes perform well in field studies, they could eventually join a limited list of nutritionally enhanced crops that are available to consumers.



Australia's new Prime Minister Anthony Albanese (centre) has promised to end the country's climate wars. Credit: Brent Lewin/Bloomberg/Getty

Australians vote for stronger climate action

Action on global warming was a key election issue for Australian voters, who on 21 May [ousted the incumbent Liberal–National coalition](#) in favour of the centre-left Labor Party.

Researchers in Australia are cautiously optimistic that the new government will take stronger action than its predecessor to reduce greenhouse-gas emissions.

As *Nature* went to press, the Labor Party, led by new Prime Minister Anthony Albanese, had won 77 seats, enough to form a majority government. Fourteen seats had also been won by the Greens and independent candidates, many of whom promised to do more about global warming than the former government.

Albanese has promised to end “the climate wars” that have plagued the nation’s politics for more than a decade. Labor has committed to reducing emissions by 43% of 2005 levels by 2030 and to boosting the share of electricity produced from renewable sources to 82% by 2030, up from 31% in 2021. The Liberal Party had committed only to reducing emissions by 26–28% of 2005 levels in the same period.

The result is “huge” for those pushing for more ambitious climate action, says Jody Webster, a marine geoscientist at the University of Sydney.

Nature **606**, 13 (2022)

doi: <https://doi.org/10.1038/d41586-022-01509-1>

This article was downloaded by **calibre** from <https://www.nature.com/articles/d41586-022-01509-1>

Monkeypox goes global: why scientists are on alert

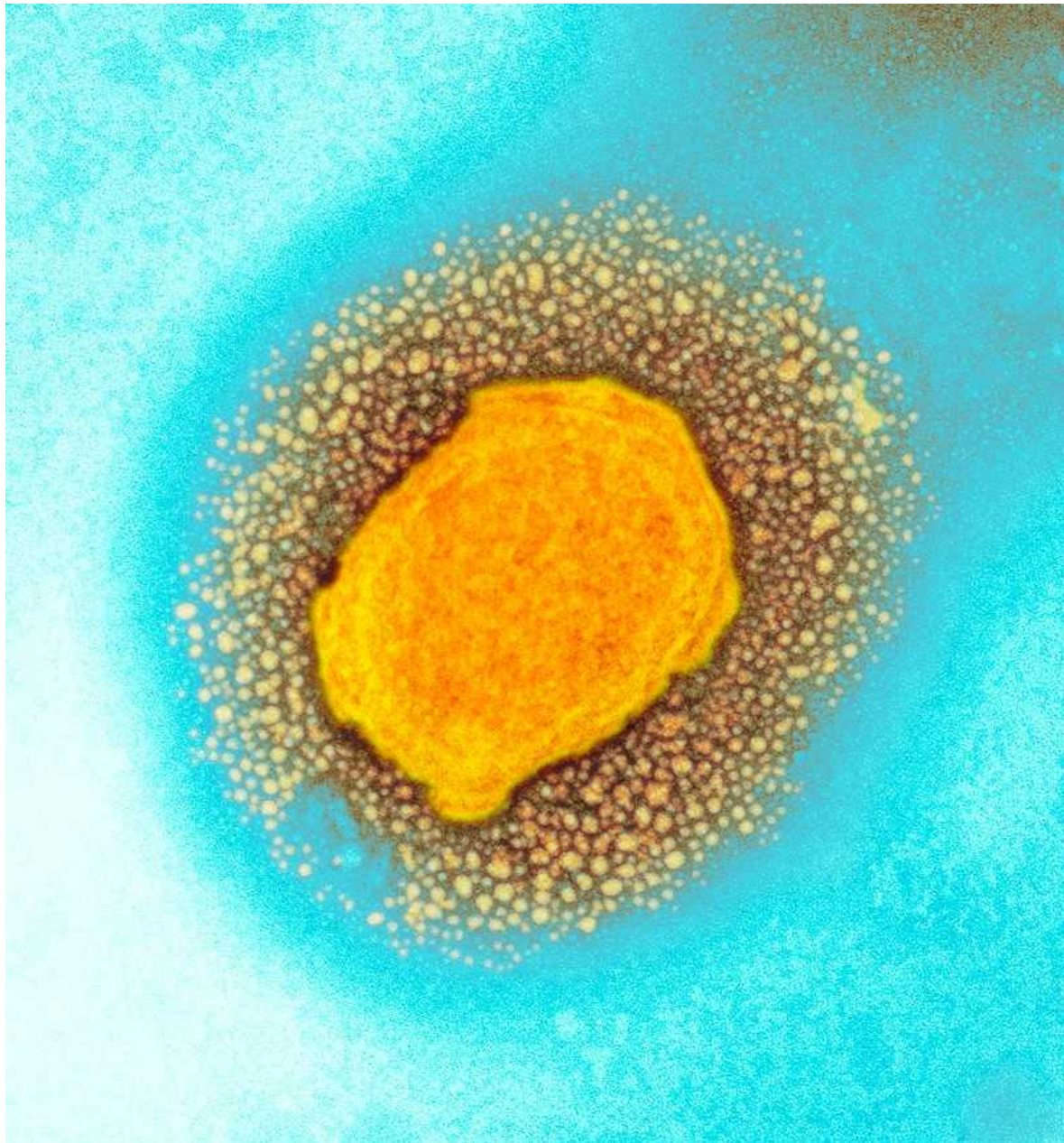
[Download PDF](#)

- NEWS
- 20 May 2022

Monkeypox goes global: why scientists are on alert

Scientists are trying to understand why the virus, a less-lethal relative of smallpox, has cropped up in so many populations around the world.

- [Max Kozlov](#)



The monkeypox virus (shown here in a coloured transmission electron micrograph) is closely related to the smallpox virus. Credit: UK Health Security Agency/Science Photo Library

More than 120 confirmed or suspected cases of monkeypox, a rare viral disease seldom detected outside Africa, [have been reported](#) in at least 11 non-African countries in the past week. The emergence of the virus in separate populations around the world, in locations where it doesn't usually appear has alarmed scientists — and sent them racing for answers.

“It’s eye-opening to see this kind of spread,” says Anne Rimoin, an epidemiologist at the University of California, Los Angeles, who has studied monkeypox in the Democratic Republic of the Congo for more than a decade.

The virus is called monkeypox because researchers first detected it in laboratory monkeys in 1958, but it is thought to transmit to people from wild animals such as rodents or from other infected people. In an average year, a few thousand cases occur in Africa, typically in the western and central parts of the continent. But cases outside Africa have previously been limited to a handful that were associated with travel to Africa or with the importation of infected animals. The number of cases detected outside of Africa in the past week alone — which is almost certain to increase — has already surpassed the total number detected outside the continent since 1970, when the virus was first found to cause disease in humans. This rapid spread is what has scientists on high alert.

But monkeypox is no SARS-CoV-2, the coronavirus responsible for the COVID-19 pandemic, says Jay Hooper, a virologist at the US Army Medical Research Institute of Infectious Diseases in Fort Detrick, Maryland. It doesn’t transmit from person to person as readily, and because it is related to the smallpox virus, there are already treatments and vaccines on hand for curbing its spread. So although scientists are concerned — because any new viral behaviour is worrying — they are not panicked.

Unlike SARS-CoV-2, which spreads through tiny air-borne droplets called aerosols, monkeypox is thought to spread from close contact with bodily fluids, such as saliva from coughing. That means a person with monkeypox is likely to infect far fewer close contacts than someone with SARS-CoV-2, Hooper says. Both viruses can cause flu-like symptoms, but monkeypox also triggers enlarged lymph nodes and, eventually, distinctive fluid-filled lesions on the face, hands and feet. Most people recover from monkeypox in a few weeks without treatment.

On 19 May, researchers in Portugal [uploaded the first draft genome](#) of the monkeypox virus that was detected there, but Gustavo Palacios, a virologist at the Icahn School of Medicine at Mount Sinai in New York City,

emphasizes that it's still a very early draft, and more work needs to be done before any definitive conclusions can be drawn.

What researchers can tell from this preliminary genetic data is that the strain of the monkeypox virus found in Portugal is related to a viral strain predominantly found in West Africa. This strain causes milder disease and has a lower death rate — about 1% in poor rural populations — compared with the one that circulates in Central Africa. But exactly how much the strain causing the current outbreaks differs from the one in West Africa — and whether the cases popping up in various countries are linked to one another — remains unknown.

Answers to those questions could help researchers to determine whether the sudden uptick in cases stems from a mutation that allows monkeypox to transmit more readily than it did in the past, and whether each of the outbreaks traces back to a single origin, says Raina MacIntyre, an infectious-diseases epidemiologist at the University of New South Wales in Sydney, Australia. Unlike SARS-CoV-2, a rapidly evolving RNA virus whose variants have regularly eluded immunity from vaccines and prior infection, monkeypox is caused by a relatively large DNA virus. DNA viruses are better at detecting and repairing mutations than RNA viruses, which means it's unlikely that the monkeypox virus has suddenly mutated to become adept at human-to-human transmission, MacIntyre says.

‘Deeply concerning’

Still, for monkeypox to be detected in people with no apparent connection to one another suggests that the virus might have been spreading silently — a fact that Andrea McCollum, an epidemiologist who heads the poxvirus team at the US Centers for Disease Control and Prevention in Atlanta, Georgia, calls “deeply concerning”.

Unlike SARS-CoV-2, which can spread without causing symptoms, monkeypox does not usually go unnoticed when it infects a person, in part because of the skin lesions it causes. If monkeypox could spread asymptotically, it would be especially troubling, because it would make the virus harder to track, McCollum says.

Another puzzle is why almost all of the case clusters include men aged 20–50, many of whom are men who have sex with men (MSM). Although monkeypox isn't known to be sexually transmitted, sexual activity certainly constitutes close contact, Rimoin says. The most likely explanation for this unexpected pattern of transmission, MacIntyre says, is that the virus was coincidentally introduced into an MSM community, and has continued circulating there. Scientists will have a better idea of the origin of the outbreaks and the risk factors for infection once an epidemiological investigation — which can take weeks and involves rigorous contact tracing — is complete.

Containment strategies

Scientists have been keeping an eye on monkeypox ever since an eradication campaign for smallpox, a closely related virus, wound down in the 1970s. Once smallpox was no longer a threat thanks to worldwide vaccinations, public-health officials stopped recommending smallpox inoculation — which also kept monkeypox at bay. With each year that has passed since smallpox's eradication, the population with weakened or no immunity to these viruses has grown, MacIntyre says.

There have been a few monkeypox outbreaks since then. The Democratic Republic of the Congo, for example, has been grappling with the virus for decades, and Nigeria has been experiencing a large outbreak, with over 500 suspected and more than 200 confirmed cases, since 2017, when the country reported its first case in some 40 years. The United States also reported an outbreak in 2003, when a shipment of rodents from Ghana spread the virus to pet prairie dogs in Illinois and [infected more than 70 people](#).

Public-health authorities are not powerless against monkeypox. As a precaution against bioterrorism, countries such as the United States maintain a supply of smallpox vaccines, as well as an antiviral treatment thought to be highly effective against the virus. However, the therapies probably wouldn't be deployed on a large scale to tackle monkeypox, McCollum says. Health-care workers would probably instead use a method called 'ring vaccination' to contain the spread of the virus: this would vaccinate the close contacts of

people who have been infected with monkeypox to cut off any routes of transmission.

On the basis of the data that she has seen so far, McCollum thinks the current outbreaks probably won't necessitate containment strategies beyond ring vaccination. "Even in areas where monkeypox occurs every day," she says, "it's still a relatively rare infection."

Nature **606**, 15-16 (2022)

doi: <https://doi.org/10.1038/d41586-022-01421-8>

This article was downloaded by **calibre** from <https://www.nature.com/articles/d41586-022-01421-8>

| [Section menu](#) | [Main menu](#) |

‘Mind blowing’ ancient settlements uncovered in the Amazon
[Download PDF](#)

- NEWS
- 25 May 2022
- Correction [26 May 2022](#)

‘Mind blowing’ ancient settlements uncovered in the Amazon

The urban centres are the first to be discovered in the region, challenging archaeological dogma.

- [Freda Kreier](#)



Researchers uncovered ancient urban centres on forested mounds in the Bolivian Amazon Basin. Credit: Roland Seitre/Nature Picture Library

Mysterious mounds in the southwest corner of the Amazon Basin were once the site of ancient urban settlements, scientists have discovered. Using a remote-sensing technology to map the terrain from the air, they found that, starting about 1,500 years ago, ancient Amazonians built and lived in densely populated centres, featuring 22-metre-tall earthen pyramids, that were encircled by kilometres of elevated roadways.

The complexity of these settlements is “mind blowing”, says team member Heiko Prümers, an archaeologist at the German Archaeological Institute headquartered in Berlin.

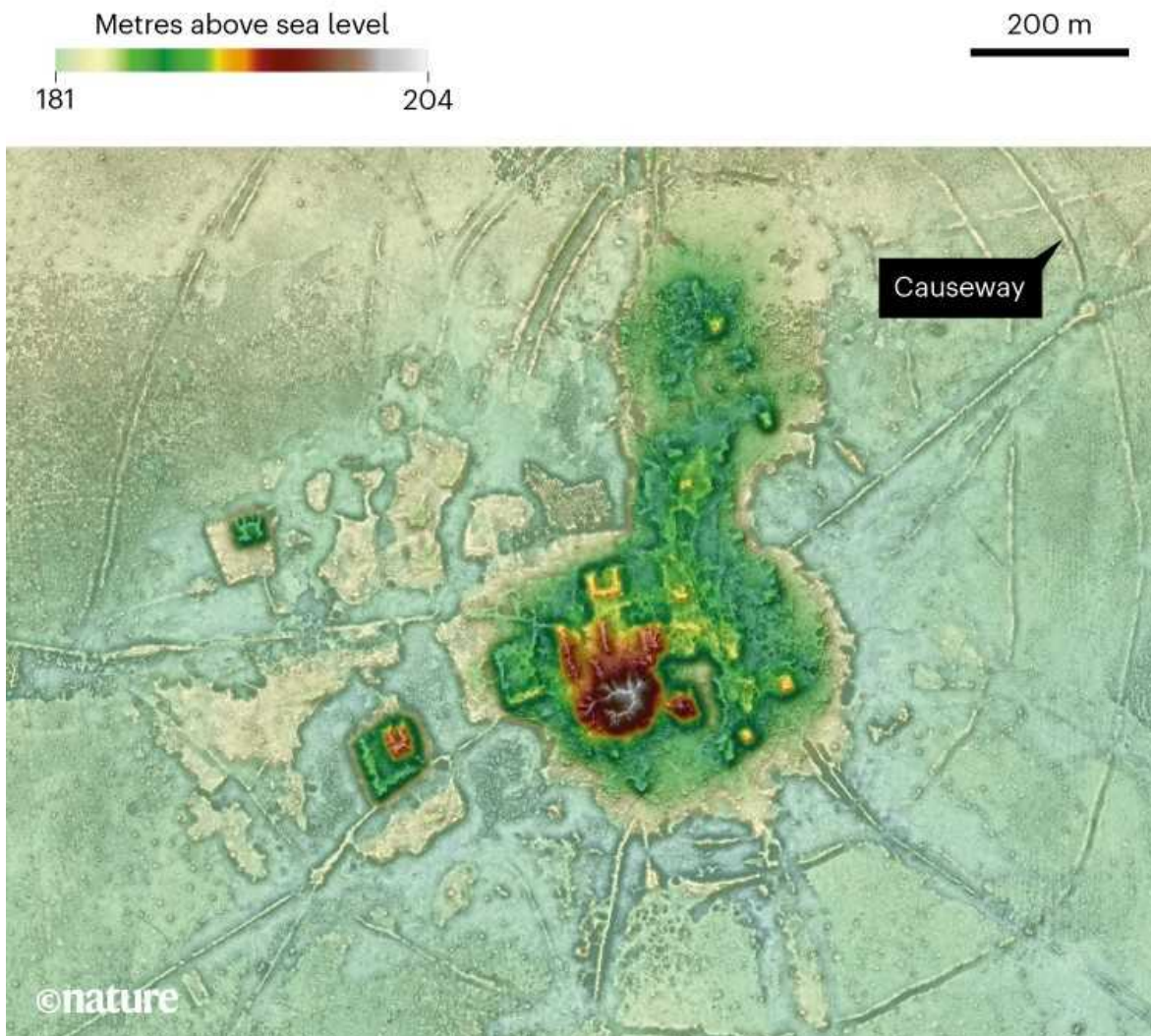
“This is the first clear evidence that there were urban societies in this part of the Amazon Basin,” says Jonas Gregorio de Souza, an archaeologist at the Pompeu Fabra University in Barcelona, Spain. The study adds to a [growing body of research](#) indicating that the Amazon — long thought to have been pristine wilderness before the arrival of Europeans — was home to advanced societies well before that. The discovery was published on 25 May in *Nature*¹.

A shift in thinking

Humans have lived in the Amazon Basin — a vast river-drainage system roughly the size of the continental United States — for around 10,000 years. Researchers thought that before the arrival of Europeans in the sixteenth century, all Amazonians lived in small, nomadic tribes that had little impact on the world around them. And although early European visitors described a landscape filled with towns and villages, later explorers were unable to find these sites.

THE SETTLEMENT BENEATH

Dense vegetation hid this ancient urban centre from view. Researchers unveiled it using a remote-sensing technique called lidar. The site in Bolivia, called Cotoca, had earthen pyramids (largest shown in red), terraces and elevated roads (causeways), and was occupied by the Casarabe culture between AD 500 and 1400.



Source: Ref. 1

By the twentieth century, archaeologists had yet to confirm the rumours, and argued that the Amazon's nutrient-poor soil was unable to support large-scale agriculture, and that it would have prevented tropical civilizations — similar to those found in central America and southeast Asia — from arising in the Amazon. By the 2000s, however, archaeological opinion was beginning to shift. Some researchers suggested² that unusually high

concentrations of domesticated plants, along with patches of unusually nutrient-rich soil that could have been created by people, might indicate that ancient Amazonians had indeed shaped their environment.

The hypothesis gained steam when, in 2018, archaeologists reported³ hundreds of large, geometric mounds that had been uncovered because of deforestation in the southern Amazon rainforest. These structures hinted at ancient organized societies capable of thriving in one location for years — but direct evidence of settlements was lacking.

In 1999, Prümers began studying a set of mounds in the Bolivian part of the Amazon Basin, outside the thick rainforest. There, a multitude of tree-covered mounds rise above a lowland area that floods during the rainy season.

Previous digs had revealed that these ‘forest islands’ contained traces of human habitation, including the remains of the mysterious Casarabe culture, which appeared around ad 500. During one excavation, Prümers and his colleagues realized that they had found what looked like a wall, indicating that a permanent settlement had once occupied the area. The researchers also found graves, platforms and other indications of a complex society. But dense vegetation made it difficult for them to use conventional methods to survey the site.

What lies beneath

By the 2010s, a technique called lidar — a remote-sensing technology that uses lasers to generate a 3D image of the ground below — had come into vogue with archaeologists. In 2012, a lidar survey of a valley in Honduras helped lead to the rediscovery of an ancient pre-Columbian city rumoured to exist in the area. The jungle had completely overtaken the settlement since it was abandoned in the fifteenth century, making it all but impossible to see from the air without lidar.

Prümers and his colleagues took advantage of lidar in 2019, when they flew a helicopter equipped with the technology over six areas near sites confirmed to have been occupied by the Casarabe people. The team got

more than it bargained for, with lidar revealing the size and shape of 26 settlements, including 11 the researchers hadn't been looking for — a monumental task that would have taken 400 years to survey by conventional means, Prümers says.

Two of the urban centres each covered an area of more than 100 hectares — three times the size of Vatican City. The lidar images revealed walled compounds with broad terraces rising 6 metres above the ground. Conical pyramids made of earth towered above one end of the terraces (see ‘The settlement beneath’). People probably lived in the areas around the terraces and travelled along the causeways that connected the sites to one another.

“We have this image of Amazonia as a green desert,” Prümers says. But given that civilizations rose and thrived in other tropical areas, he notes, “Why shouldn’t something like that exist here?”

Mysteries remain

Why these settlements were abandoned after 900 years is still a mystery. Radiocarbon dating has revealed that the Casarabe disappeared around 1400.

Prümers points out that lidar images revealed reservoirs in the settlements, perhaps indicating that this part of the world wasn't always wet — an environmental shift that might have driven people away. However, consistent pollen records reveal⁴ that maize (corn) was grown in the area continuously for thousands of years, indicating sustainable agricultural practices.

At the very least, the discovery of long-lost Amazonian societies “changes the general perspective people have of Amazonian archaeology”, says Eduardo Neves, an archaeologist at the University of São Paulo in Brazil. Present-day logging and farming in the Amazon Basin are almost certainly destroying important archaeological sites that have yet to be discovered, he says, but a growing interest in Amazonian archaeology could lead to the protection of vulnerable places.

These discoveries also counter the narrative that Indigenous peoples were passive inhabitants of the Amazon Basin before the arrival of Europeans. “The people who lived there changed the landscape forever,” Neves says.

Nature **606**, 16–17 (2022)

doi: <https://doi.org/10.1038/d41586-022-01458-9>

Updates & Corrections

- **Correction 26 May 2022:** An earlier version of this story said that there are hundreds of tree-covered mounds rising above a lowland area in the Bolivian Amazon. Some estimates suggest there are many more than that.

References

1. Prümers, H., Betancourt, C. J., Iriarte, J., Robinson, M. & Schaich, M. *Nature* <https://doi.org/10.1038/s41586-022-04780-4> (2022).
2. Neves, E. G. & Heckenberger, M. J. *Annu. Rev. Anthropol.* **48**, 371–388 (2019).
3. de Souza, J. G. *et al.* *Nature Commun.* **9**, 1125 (2018).
4. Carson, J. F. *et al.* *Holocene* **25**, 1285–1300 (2015).

This article was downloaded by **calibre** from <https://www.nature.com/articles/d41586-022-01458-9>

Why unprecedeted bird flu outbreaks sweeping the world are concerning scientists

[Download PDF](#)

- NEWS
- 26 May 2022

Why unprecedeted bird flu outbreaks sweeping the world are concerning scientists

Mass infections in wild birds pose a significant risk to vulnerable species, are hard to contain and increase the opportunity for the virus to spill over into people.

- [Brittney J. Miller](#)



Cranes are among the species dying from avian influenza. Credit: Heidi Levine/SIPA/Shutterstock

A highly infectious and deadly strain of avian influenza virus has infected tens of millions of poultry birds across Europe, Asia, Africa and North America. But scientists are particularly concerned about the unprecedented spread in wild birds — outbreaks pose a significant risk to vulnerable species, are hard to contain and increase the opportunity for the virus to spill over into people.

Since October, the H5N1 strain has caused nearly 3,000 outbreaks in poultry in dozens of countries. More than 77 million birds have been culled to curb the spread of the virus, which almost always causes severe disease or death in chickens. Another 400,000 non-poultry birds, such as wild birds, have also died in 2,600 outbreaks — twice the number reported during the last major wave, in 2016–17.

Researchers say that the virus seems to be spreading in wild birds more easily than ever before, making outbreaks particularly hard to contain. Wild birds help to transport the virus around the world, with their migration

patterns determining when and where it will spread next. Regions in Asia and Europe will probably continue to see large outbreaks, and infections could creep into currently unaffected continents such as South America and Australia.

Although people can catch the virus, infections are uncommon. Only two cases have been reported since October, one each in the United Kingdom and the United States. But scientists are concerned that the high levels of virus circulating in bird populations mean that there are more opportunities for spillover into people. Avian influenza viruses change slowly over time, but the right mutation could make them more transmissible in people and other species, says Ian Barr, deputy director of the World Health Organization (WHO)-collaborating influenza centre at the Doherty Institute in Melbourne, Australia. “These viruses are like ticking time bombs,” he says. “Occasional infections are not an issue — it’s the gradual gaining of function of these viruses” that is the real concern, he says.

Virus origin

The highly pathogenic H5N1 strain emerged in commercial geese in Asia in around 1996, and spread in poultry throughout Europe and Africa in the early 2000s. By 2005, the strain was causing mass deaths in wild birds, first in East Asia and then in Europe. Since then, the strain has repeatedly infected wild birds in many parts of the world, says Andy Ramey, a research wildlife geneticist at the US Geological Survey Alaska Science Center in Anchorage. Through repeated spillovers, Ramey says, H5N1 seems to have become more adapted to wild birds. It’s “now become an emerging wildlife disease”, he says.

In 2014, a new highly pathogenic H5 lineage — called 2.3.4.4 — emerged and started infecting wild birds without always killing them. This created opportunities for the virus to spread to North America for the first time. The lineage has since dominated outbreaks around the world, including the current ones.

The virus affects some wild bird species more severely than others. For instance, some infected mallard ducks (*Anas platyrhynchos*) show no signs

of disease, whereas the virus killed roughly 10% of the breeding population of barnacle geese (*Branta leucopsis*) in the Norwegian archipelago of Svalbard late last year and hundreds of Dalmatian pelicans (*Pelecanus crispus*) in Greece earlier this year. Wildlife researchers are trying to understand why the virus affects species differently. They are particularly concerned about the virus's impact on vulnerable bird species with smaller populations or restricted geographic ranges, and species that are particularly susceptible to infection, such as whooping cranes (*Grus americana*) and emperor geese (*Anser canagicus*), Ramey says.

Ramey adds that only a fraction of cases in wild birds are diagnosed and reported. More monitoring could unveil the true magnitude of wild bird mortality, he says.

Controlling the spread

Better monitoring of infected wild birds could also help to alert poultry facilities to the risk of future outbreaks — although regions with large poultry or migratory bird populations are at high risk of further outbreaks no matter how good their surveillance is, says Keith Hamilton, head of the department for preparedness and resilience at the World Organisation for Animal Health.

Tracking disease in wild birds is resource-intensive and challenging owing to the sheer size of their populations, Hamilton says. He suggests targeted surveillance in areas more likely to encounter the virus, such as popular flyways or breeding grounds.

An effective vaccine for poultry could help to stem the spread, along with decreases in the number of birds in production facilities, says Michelle Wille, a wild-bird virologist at the University of Sydney in Australia. The poultry industry can also continue to improve biosecurity by restricting entry to facilities, protecting their water sources and decreasing contact between poultry and wild birds.

Although poultry populations can be culled to stop the spread of highly pathogenic avian influenza, researchers emphasize that wild birds should not

be harmed to mitigate outbreaks. Killing wild birds to prevent further infections would not work because of the huge size and vast ranges of their populations, says Lina Awada, a veterinary epidemiologist at the World Organisation for Animal Health. It could even make the situation worse, because it would disrupt wild-bird movements and behaviours, helping the virus spread further, she says.

“The same way we shouldn’t be shooting bats because of coronavirus, the solution to this is not trying to kill wild birds,” Wille says.

Researchers say that what is needed is a holistic approach that considers how avian influenza spreads through wild birds, poultry and people. Collaboration between public-health researchers and animal-health groups is vital for picking up spillover events into people. “If we control this in poultry, we control this in humans, and it’s likely that we control this in wild birds, as well,” Wille says.

Nature **606**, 18-19 (2022)

doi: <https://doi.org/10.1038/d41586-022-01338-2>

This article was downloaded by **calibre** from <https://www.nature.com/articles/d41586-022-01338-2>

COVID delays are frustrating the world's plans to save biodiversity
[Download PDF](#)

- NEWS
- 20 May 2022

COVID delays are frustrating the world's plans to save biodiversity

Scientists hope an ambitious agreement to arrest species extinction will be finalized in China later this year, but the country's pandemic response puts that in doubt.

- [Smriti Mallapaty](#)



Young caimans captured in Brazil. Illegal hunting is a major threat to biodiversity.Credit: Collart Hervé/Sygma via Getty

Researchers are increasingly concerned that the world is running two years behind schedule to finalize a new global framework on biodiversity conservation. They say the delay to the agreement, which aims to halt the alarming rate of species extinctions and protect vulnerable ecosystems, has consequences for countries' abilities to meet ambitious targets to protect biodiversity over the next decade.

Representatives from almost 200 member states of the United Nations' Convention on Biological Diversity (CBD) were [set to meet](#) in Kunming, China, in October 2020, to finalize a draft agreement. It includes 21 conservation targets, such as protecting 30% of the world's land and seas. But the meeting, called the 15th Conference of the Parties, was cancelled because of the COVID-19 pandemic and has been postponed several times since.

The conference is tentatively rescheduled for late August or early September, but China — which as the conference president is also the host — hasn't confirmed the date. And now the country's strict COVID-19 lockdown in Shanghai and rising cases of the virus in Beijing have put that meeting in doubt, too.

Researchers say the delay in finalizing the agreement is stalling conservation work, especially in countries that rely on funds committed by wealthier nations to achieve the targets. The almost two-year hold-up means that countries will have less time to meet the agreement's 2030 deadline. "We now have eight years to do more, whilst many countries are facing a recession and trying to prioritize economic recovery," says Alice Hughes, a conservation biologist at the University of Hong Kong. "The longer we wait, the more diversity is lost."

A [2019 report](#) estimated that roughly one million species of plants and animals face extinction, many within decades. In the past 2 years alone, the International Union for Conservation of Nature's Red List has classified more than 100 species as extinct, including the large sloth lemur (*Palaeopropithecus ingens*), the Guam flying fox (*Pteropus tokudae*) and the

Yunnan lake newt (*Cynops wolterstorffi*). Sparse monitoring means that the true scale of species and habitat loss is unknown, says Hughes.

On top of that, tropical forests, especially in Brazil, are disappearing fast, environmental safeguards have been relaxed in some regions, and researchers have documented escalated poaching of plants driven by unemployment during the pandemic. “Every year we continue to lose biodiversity at an unprecedented and unacceptable rate, undermining nature and human well-being,” says Robert Watson, a retired environmental scientist formerly at the University of East Anglia in Norwich, UK.

Releasing funds

The importance of a global agreement on biodiversity cannot be overstated, says Aban Marker Kabraji, an adviser to the United Nations on biodiversity and climate change. These agreements spur action — for example, governments might hold off on updating or developing their national strategies until after they are settled. “It is extremely important that these meetings take place in the cycle in which they’re planned,” says Kabraji.

Global agreements also lead to the release of funds earmarked to help countries to meet their biodiversity goals, such as through the Global Environment Facility, says Hughes. At a preparatory meeting in October 2021, Chinese President Xi Jinping committed 1.5 billion yuan (US\$223 million) towards a Kunming Biodiversity Fund to support developing countries in protecting their biodiversity, but details about those funds have yet to be released.

Funding delays will be felt especially in “countries which have the highest levels of biodiversity and the fewest resources to actually conserve it”, says Kabraji.

Meeting uncertain

The CBD secretariat in Montreal, Canada, has said that the Kunming conference will take place in the third quarter of 2022, but it is waiting for China to confirm dates. David Ainsworth, information officer for the

secretariat, says preparations for the meeting are under way, including plans for meeting participants to be isolated from local residents, similar to the process for the Winter Olympics in Beijing in February. There are provisions for the event to be held in another location if a host has to back out, but Ainsworth says there are no official plans to do that yet. Conference officials, including representatives from China, were due to meet on 19 May to discuss the date and location of the summit, he says.

A decision to relocate the meeting would require China's approval, which it is unlikely to give, say researchers. But sticking to having the meeting in Kunming could delay it further, owing to China's strict lockdowns that have brought cities to a standstill. Several major sports events scheduled for later this year, including the Asian Games in Hangzhou, have already been postponed. The meeting will probably be pushed to after September or even next year, says Ma Keping, an ecologist at the Chinese Academy of Sciences Institute of Botany in Beijing.

Some researchers say that the world should wait for China to host the meeting — whenever that will be — and that its leadership is important for the success of negotiations. “The Chinese government has worked very hard to prepare such a meeting,” says Ma. “It should happen in China.”

Others think that it is more important that the meeting happens this year — whether in China or not. Facilities to host such a meeting exist in Rome, Nairobi and Montreal. “Any of these places would be preferable to indefinite further delays,” says Hughes.

“A further delay sends a problematic signal that habitat loss and species extinction can somehow wait,” says Li Shuo, a policy adviser at Greenpeace China in Beijing.

Regardless of when and where the meeting happens, researchers say what's most important is that the world agrees to ambitious biodiversity goals and delivers on them. The two-year delay has given countries more time to develop the draft framework, but countries have yet to agree to [many of the terms](#), or to figure out how to finance and monitor the work. There are “significant disagreements still on just about every aspect of every target”, says Anne Larigauderie, executive secretary of the Intergovernmental

Science-Policy Platform on Biodiversity and Ecosystem Services in Bonn, Germany. Nations will meet again only once more — in Nairobi, Kenya, in June — before the agreement is expected to be finalized at the summit in Kunming.

Nature **606**, 19-20 (2022)

doi: <https://doi.org/10.1038/d41586-022-01384-w>

This article was downloaded by **calibre** from <https://www.nature.com/articles/d41586-022-01384-w>

| [Section menu](#) | [Main menu](#) |

Frustration builds over lengthy delay in revamping Mexico's science law
[Download PDF](#)

- NEWS
- 20 May 2022

Friction builds over lengthy delay in revamping Mexico's science law

Mexican researchers fear that a polarizing bill could ruin the chances of overhauling the nation's science system.

- [Emiliano Rodríguez Mega](#)



Mexican President Andrés Manuel López Obrador, who took office in 2018, has been at odds with scientists. Credit: Daniel Becerril/Reuters/Alamy

It has been almost a year and a half since Mexico's Congress missed its deadline to approve a bill that would drastically overhaul how science and technology are governed. Worried about the lack of progress since then, researchers fear that political wrangling and a lack of consensus might waste a prime opportunity to boost Mexican science.

A constitutional amendment compelled Congress to pass the legislation by 15 December 2020. But the deadline came and went without lawmakers even discussing the various proposals on the table, or whether to merge them. One proposal that has yet to make its way to Congress, but that was [made available for public comment in March](#), has drawn the ire of some researchers. They say that this bill, developed by the country's science agency, the National Council of Science and Technology (Conacyt), ignores the community's wishes and concentrates decision-making power at Conacyt.

“What they are trying to do is to impose a single vision,” says Carlos Arámburo, a neurobiologist at the National Autonomous University of Mexico (UNAM) in Querétaro. He participated in a series of meetings with Conacyt to express worries about the proposal, but says that the agency did not address many of the community's concerns and suggestions. Conacyt officials did not respond to *Nature*'s queries about criticisms of the proposal.

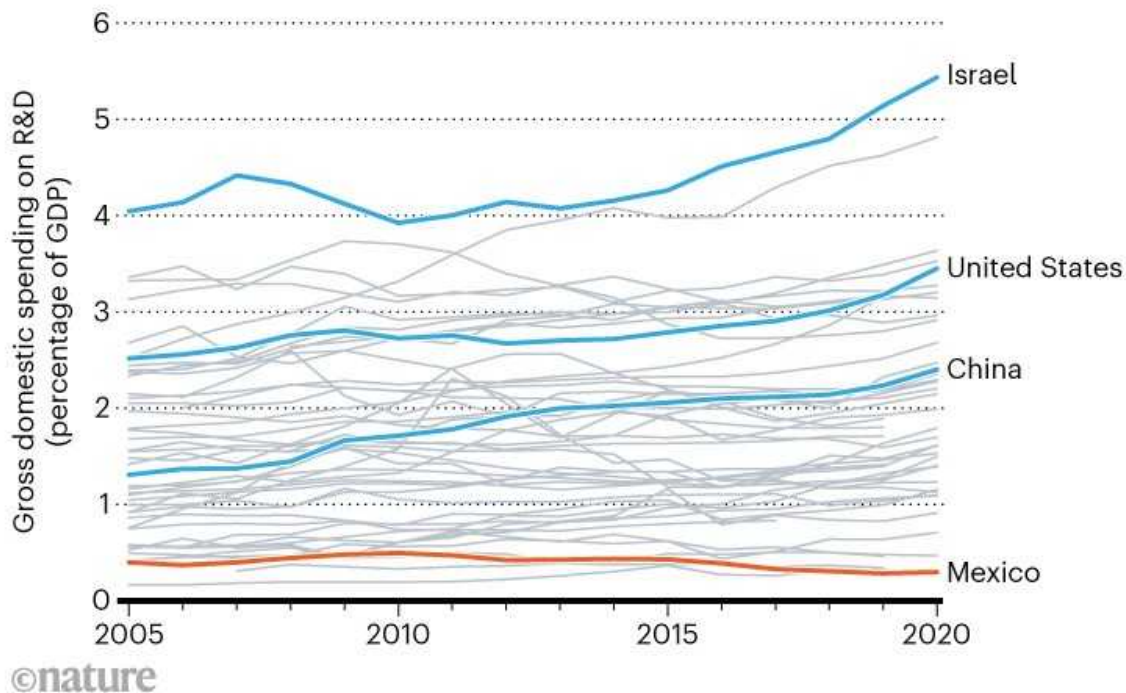
The wait for a new science law adds to tensions between researchers and Mexico's left-wing president, Andrés Manuel López Obrador, who took office in late 2018. His austerity measures and pledges to fight corruption in Mexico have led to [debilitating budget cuts](#) for science, as well as [accusations of organized crime against scientists](#). Under his government, scientists have sharply criticized Conacyt for irregular management of funds, [unjustified dismissals](#) of early-career researchers from the agency and what they see as disdain for private academic institutions. Conacyt [has denied some of these allegations](#).

Many researchers think that if a bill is passed, it will be Conacyt's version that will win the day. And it has its supporters.

“It seems quite reasonable to me,” says Edmundo Gutiérrez Domínguez, a physicist at the National Institute of Astrophysics, Optics and Electronics in Puebla — one of 27 public research centres across Mexico that are coordinated by Conacyt. The bill promises to regulate not only science, technology and innovation, but also the humanities — an area that some feel has been neglected by previous administrations. If approved, it would ensure that science and technology are reoriented to “solve the great problems of the country”, says Gutiérrez Domínguez, who was appointed director of his institute in 2019 by the head of Conacyt, María Elena Álvarez-Buylla Roces.

UNMET PROMISE

Since 2002, Mexico’s science law has required it to invest no less than 1% of the country’s gross domestic product (GDP) in research and development (R&D). The goal has never been met. Among the members of the Organisation for Economic Co-operation and Development, Mexico is currently investing one of the smallest amounts in R&D.



Source: Main Science and Technology Indicators/OECD

Other scientists are not so hopeful. “On the one hand, you see this speech of good intentions embodied in the law,” says Judith Zubieta, a science-policy researcher at UNAM in Mexico City. “On the other, you’re seeing concrete

actions that completely contradict what the pretty words say.” For instance, Mexico’s current science law states that national spending on research and technology should not be less than 1% of the country’s gross domestic product. Conacyt’s proposal says only that the nation will provide “sufficient, timely and adequate” funds.

Although Mexico has never hit the 1% spending goal — the closest it has come was in 2010, when it invested nearly 0.5%, according to the Organisation for Economic Co-operation and Development (see ‘Unmet promise’) — having a mandate is better than leaving the goal open to interpretation, says Carlos Iván Moreno, a public-policy researcher at the University of Guadalajara in Mexico.

A prime opportunity

Mexico’s current science and technology law was enacted in 2002, after intense lobbying by the research community.

Although the law had its strong points, it didn’t succeed in making science a priority in Mexico. In May 2019, an opportunity to improve the law arose when legislators modified the country’s constitution to include the right of its people to “enjoy the benefits” of science and technological innovation. The amendment required that Congress issue a general science law no later than 2020. Anyone could submit a proposal, and López Obrador asked Conacyt to draft the government’s.

So far, four proposals have been drafted. Aside from Conacyt, they have come from a group of academics and a network of state science councils. More are expected from opposition lawmakers.

However, some of them “have [little] possibility of moving forward”, says Alma Cristal Hernández, president of the Mexican Association for the Advancement of Science in Mexico City. Conacyt’s version looks like the strongest contender, because López Obrador’s party and its allies hold a majority in Congress.

But not much has happened so far. Legislators have “unfinished business” with the new law, says Alfonso Cruz Ocampo, the technical secretary of the

Science, Technology and Innovation Commission of Mexico's Chamber of Deputies, the lower house of its Congress. The commission will help to review the various proposals that have been put forward. "We will seek to integrate the virtues of each of them," he says.

The COVID-19 pandemic, a disgruntled research community and, most of all, political polarization have also contributed to the extreme delay, Moreno says. "The preliminary draft presented by Conacyt has been rejected in the main academic and institutional circles," he explains. "There is no consensus."

Helpful or harmful?

Conacyt's leadership says its law will bring about positive change for science in Mexico. In an opinion piece [published in the newspaper *La Jornada*](#) last year, Álvarez-Buylla Roces wrote that, if approved, the legislation would "promote the advancement of knowledge" and the development of the country's own technologies to ensure "the well-being of the Mexican people".

But other provisions in Conacyt's proposal have not quelled fears of bias against some scientific institutions in Mexico.

For example, the law would provide tax exemptions for universities and research centres when they purchase supplies, equipment and material — but only from state-owned suppliers. A letter written by Coparmex, an independent employers' union that represents more than 36,000 companies in Mexico, calls this part of Conacyt's bill "discriminatory".

The government's proposal also guarantees universal access to scholarships for students, as well as economic stimuli for researchers, but only as long as they study or work at public universities or institutions. "It's deeply exclusionary," says Romeo Saldaña Vázquez, an ecologist at the private Ibero-American University in Puebla. The measure means he would lose the extra stipend of 20,000 pesos (about US\$1,000) he receives each month from the National System of Researchers, a programme managed by

Conacyt that rewards scientists for their productivity. “I would no longer have an incentive to do research,” he says.

Most worrying, other critics say, is that the draft would give Conacyt power over most science-based policies in Mexico. The document implies the elimination of at least nine advisory bodies — some of which were created as a result of the current science law — that represent the country’s academic and scientific community. “I would see it as the return of a very centralized policy, a centralized vision of science,” similar to that in the 1970s, when all science-policy decisions fell on Conacyt’s shoulders, says Rosalba Medina Rivera, president of the National Network of State Councils and Organizations of Science and Technology in San Luis Potosí, which submitted its own law proposal to the Senate.

Gutiérrez Domínguez sees it differently. “It seems to me to be a policy that retakes control of science” by the Mexican government, he says, adding that the law would allow the participation of different sectors of society, including the academic community.

The myriad of concerns has led some to ask: does Mexico even need a new science law?

“That’s a very important question,” says Alma Maldonado, a higher-education researcher at the Center for Research and Advanced Studies in Mexico City. “There is a battle, a political and ideological dispute, over a law that could be beneficial — but could also do a lot of harm.”

The science commissions of the Senate and Chamber of Deputies are set to meet in mid-May to explore a way forward. If everything goes to plan, Cruz Ocampo says, the legislators will evaluate the available proposals and then craft a single document that will “substantially benefit” the humanities, science, technology and innovation in Mexico.

Nature **606**, 20-21 (2022)

doi: <https://doi.org/10.1038/d41586-022-01408-5>

Disclosure: While getting his undergraduate degree, Emiliano Rodríguez Mega, the reporter of this story, co-authored a paper in 2015 with María Elena Álvarez-Buylla Roces, the current head of Conacyt.

This article was downloaded by **calibre** from <https://www.nature.com/articles/d41586-022-01408-5>

| [Section menu](#) | [Main menu](#) |

Guardians of the brain: how a special immune system protects our grey matter

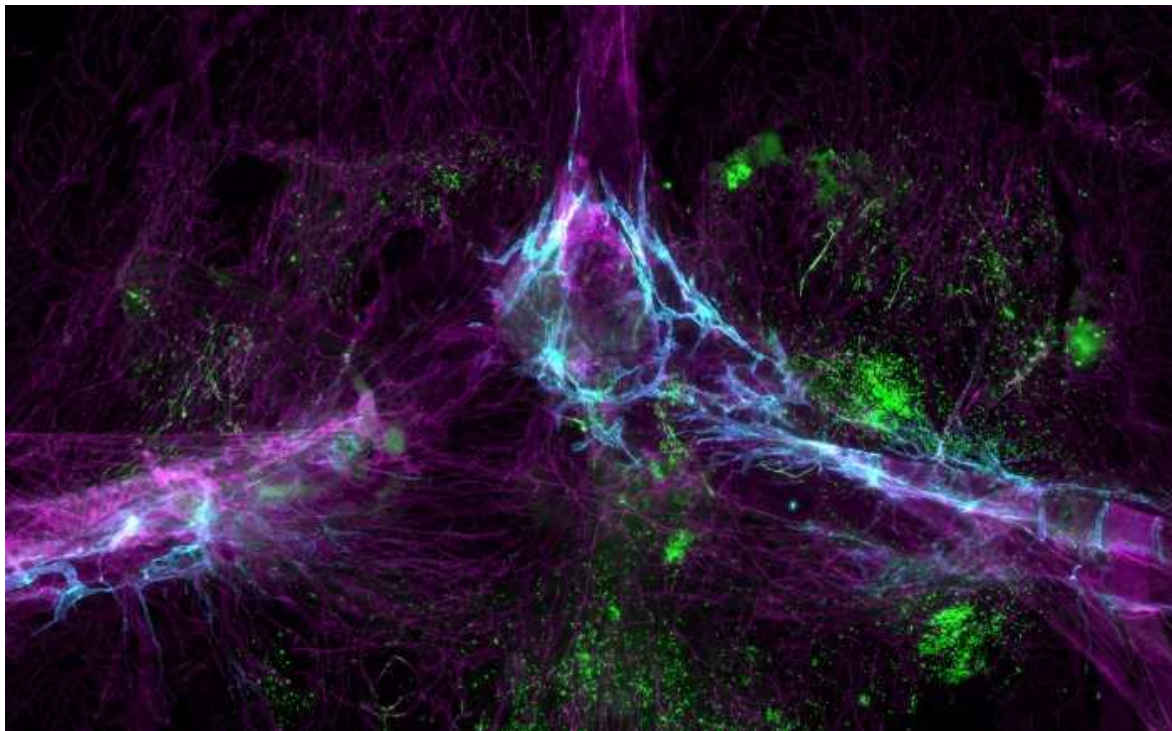
[Download PDF](#)

- NEWS FEATURE
- 01 June 2022

Guardians of the brain: how a special immune system protects our grey matter

The nervous and immune systems are tightly intertwined. Deciphering their chatter might help address many brain disorders and diseases.

- [Diana Kwon](#) ⁰



The brain's immune system includes a network of transport vessels (blue) and its own immune cells made in the bone marrow (green). Credit: Siling Du, Kipnis lab, Washington University in St. Louis

The brain is the body's sovereign, and receives protection in keeping with its high status. Its cells are long-lived and shelter inside a fearsome fortification called the blood–brain barrier. For a long time, scientists thought that the brain was completely cut off from the chaos of the rest of the body — especially its eager defence system, a mass of immune cells that battle infections and whose actions could threaten a ruler caught in the crossfire.

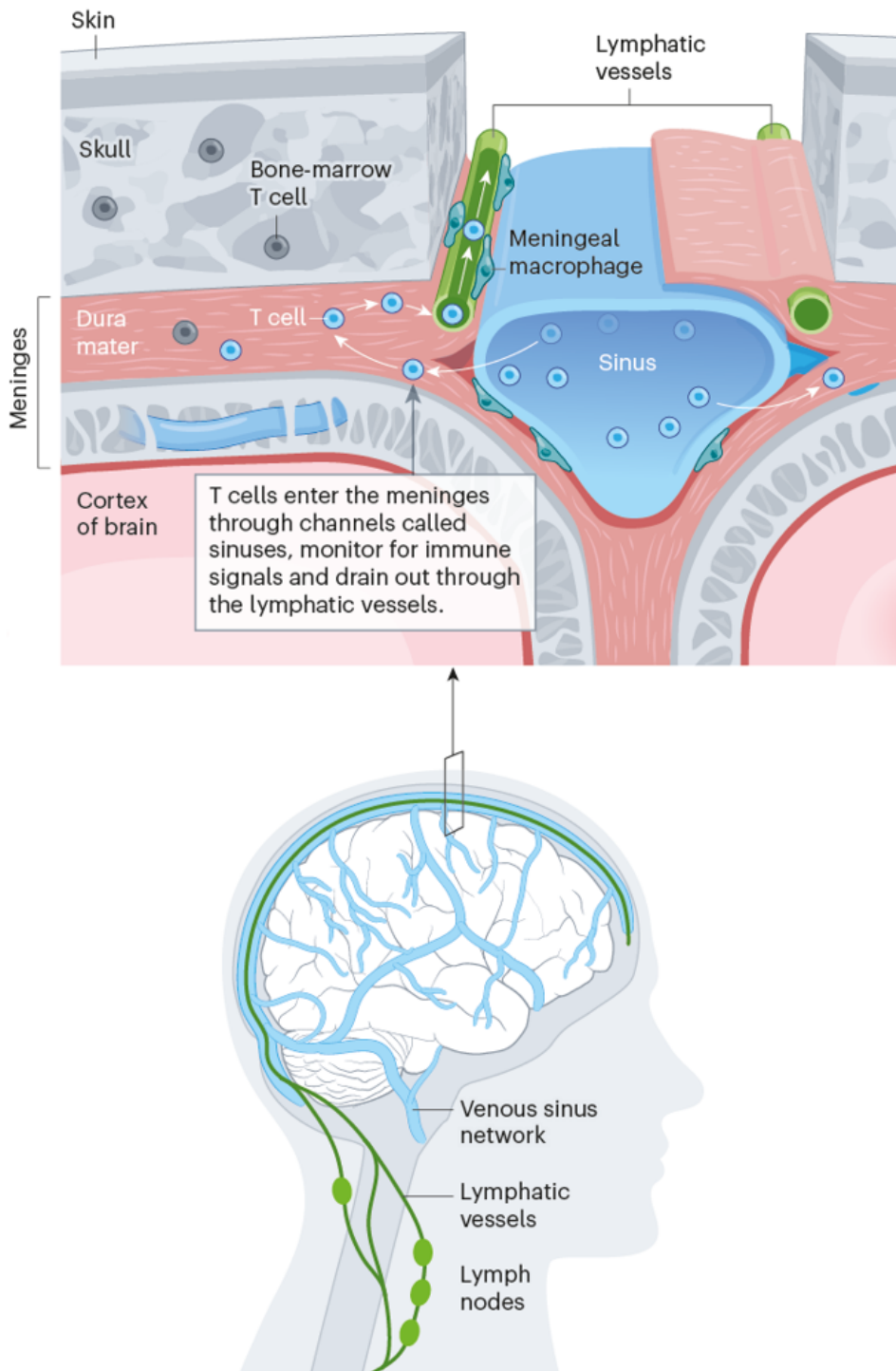
In the past decade, however, scientists have discovered that the job of protecting the brain isn't as straightforward as they thought. They've learnt that its fortifications have gateways and gaps, and that its borders are bustling with active immune cells.

A large body of evidence now shows that the brain and the immune system are tightly intertwined. Scientists already knew that the brain had its own resident immune cells, called microglia; recent discoveries are painting more-detailed pictures of their functions and revealing the characteristics of the other immune warriors housed in the regions around the brain. Some of these cells come from elsewhere in the body; others are produced locally, in the bone marrow of the skull. By studying these immune cells and mapping out how they interact with the brain, researchers are discovering that they play an important part in both healthy and diseased or damaged brains. Interest in the field has exploded: there were fewer than 2,000 papers per year on the subject in 2010, swelling to more than 10,000 per year in 2021, and researchers have made several major findings in the past few years.

No longer do scientists consider the brain to be a special, sealed-off zone. "This whole idea of immune privilege is quite outdated now," says Kiavash Movahedi, a neuroimmunologist at the Free University of Brussels (VUB). Although the brain is still seen as immunologically unique — its barriers prevent immune cells from coming and going at will — it's clear that the brain and immune system constantly interact, he adds (see 'The brain's immune defences').

THE BRAIN'S IMMUNE DEFENCES

Long thought to be cut off from the body's immune system, the brain is now known to host its own immune cells while allowing others to circulate through its fluid-filled borders, the meninges. Cell types include microglia inside the brain and T cells and macrophages at the edges. Together, these help the healthy brain to function and defend it from disease.



Credit: Nik Spencer/*Nature*

This shift in attitude is widespread in the community, says Leonardo Tonelli, chief of the neuroendocrinology and neuroimmunology programme at the US National Institute of Mental Health in Bethesda, Maryland. In his experience, almost every neuroscientist who reviews grant proposals for the agency accepts the connection, he says, although many still need to catch up with the latest discoveries in neuroimmunology, which have started to reveal the underlying mechanisms.

The rush to understand how the brain and immune system knit together has prompted a wealth of questions, says Tony Wyss-Coray, a neuroimmunologist at Stanford University in California. “How important is this in normal brain function or disease? That is a very hard question to answer.”

Privileged space

More than two decades ago, when neuroimmunologist Michal Schwartz had just set up her laboratory at the Weizmann Institute of Science in Rehovot, Israel, she couldn’t stop asking herself an unpopular question: could it really be true that the brain is completely cut off from immune protection? “It was completely axiomatic that the brain cannot tolerate any immune activity — everyone thought that if you have any immune activation, this was a sign of pathology,” she says. “But it didn’t make sense that tissue that is so indispensable, like the brain, cannot enjoy the benefit of being assisted by the immune system.”

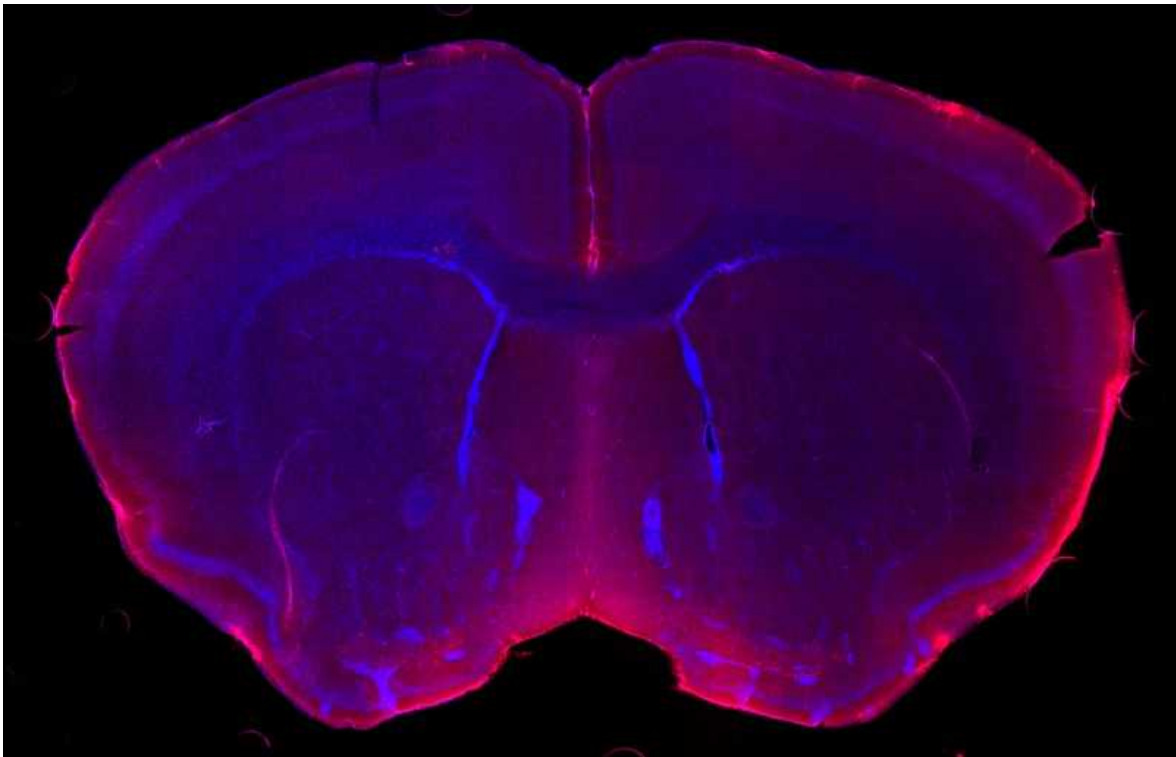
The idea that the brain was off limits to the immune system took root decades earlier. In the 1920s, the Japanese scientist Y. Shirai reported¹ that when tumour cells were implanted in a rat’s body, the immune response destroyed them, but when placed in the brain, they survived — indicating a feeble or absent immune response. Similar findings followed in the 1940s.

Most scientists also thought that the brain lacked a system for ferrying immune molecules in and out — the lymphatic drainage system that exists elsewhere in the body — even though such a system was first described in

the brain more than two centuries ago². The prevailing view, then, was that the brain and the immune system lived largely separate lives. The two were thought to collide only under hostile circumstances: when immune cells went rogue, attacking the body's own cells in diseases such as multiple sclerosis.

So when, in the late 1990s, Schwartz and her team reported³ that after an acute injury to the central nervous system, two types of immune cells, macrophages and T cells, protected neurons from damage and supported their recovery, many scientists were sceptical. "Everyone told me, you're absolutely wrong," Schwartz recalls.

Since those early experiments, Schwartz's team and others have amassed a large body of evidence showing that immune cells do, indeed, have a significant role in the brain, even in the absence of autoimmune disease. Researchers have shown, for example, that in mice engineered to lack an immune system, neurodegenerative diseases such as motor neuron disease (amyotrophic lateral sclerosis) and Alzheimer's disease seemed to progress more rapidly⁴, whereas restoring the immune system slowed their progression. Scientists have also revealed a potential role for microglia in Alzheimer's disease.



Cerebrospinal fluid (coloured red) seeps into the brain tissue (blue) through tiny gaps in the blood vessels that run through the brain's protective layers. Credit: Antoine Drieu, Kipnis lab, Washington University in St. Louis

More recently, scientists have shown that immune cells at the brain's edges are active in neurodegenerative diseases. After examining the cerebrospinal fluid of people with Alzheimer's, Wyss-Coray and his colleagues found evidence of a rise in numbers of T cells in the brain's fluid-filled borders⁵. The expansion of these immune-cell populations suggests that they might have a role in the disease, Wyss-Coray says.

But whether immune cells hurt or help the brain is an open question. In their studies of Alzheimer's and other neurodegenerative disorders, Wyss-Coray and his colleagues suggest that the immune system could be damaging neurons by releasing molecules that boost inflammation and trigger cell death. Others have suggested that T cells and other immune cells could instead be protective. For example, Schwartz's group has reported⁶ that in mouse models of Alzheimer's, boosting the immune response leads to a clearance of amyloid plaques — a pathological hallmark of the disease — and improves cognitive performance.

Busy borders

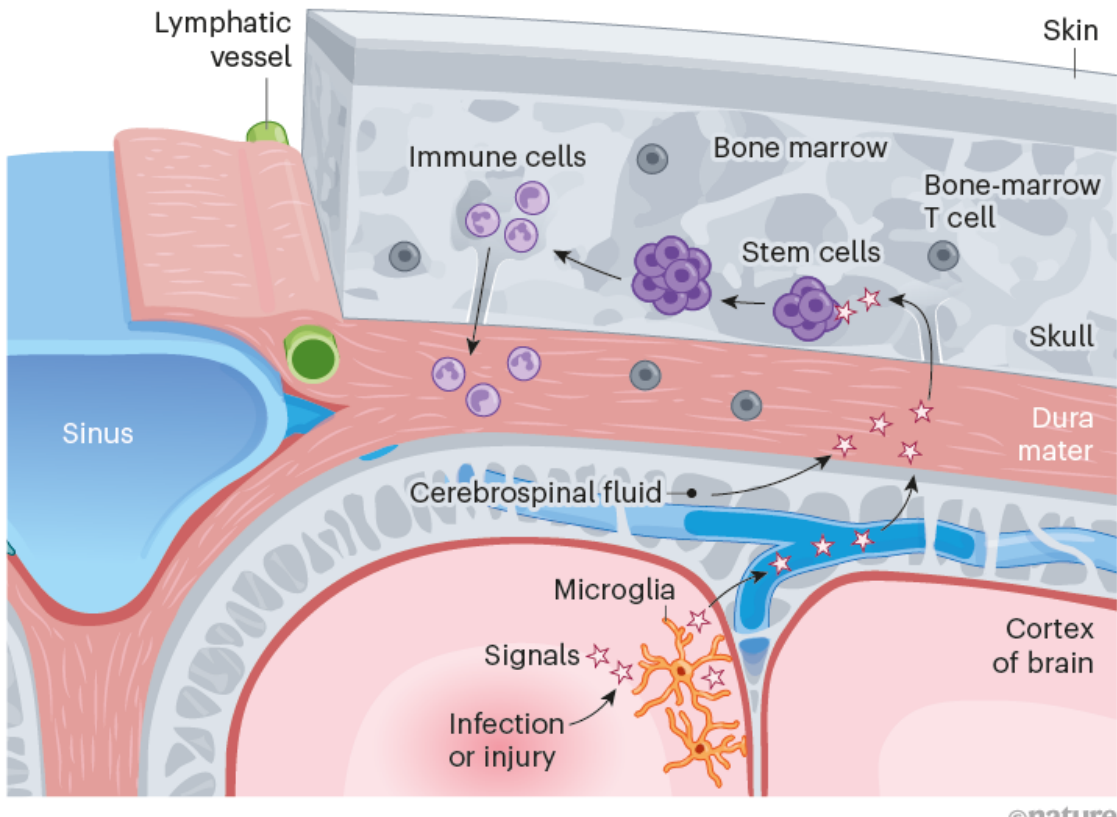
It's now becoming clear that the brain's margins are immunologically diverse: almost any type of immune cell in the body can also be found in the area surrounding the brain. The meninges — the fluid-filled membranes that wrap the brain — are an “immunological wonderland”, says Movahedi, whose work focuses on macrophages in the brain's borders. “There's so much happening out there.”

Some residents are exclusive to the frontiers. In 2021, Jonathan Kipnis, a neuroimmunologist at Washington University in St. Louis, Missouri, and his colleagues reported⁷ that there is a local source of immune cells: the bone marrow of the skull.

When they explored how the bone marrow mobilizes these cells, Kipnis and his colleagues demonstrated⁸ that, in response to an injury to the central nervous system or in the presence of a pathogen, signals carried in the cerebrospinal fluid were delivered to the skull bone marrow, prompting it to produce and release these cells (see ‘Private protectors’).

PRIVATE PROTECTORS

Brain immune cells are produced by stem cells in the bone marrow, in response to signals from the cerebrospinal fluid indicating infection or injury in the brain tissue.



©nature

Credit: Nik Spencer/*Nature*

What role these locally produced immune cells have remains to be seen, but Kipnis's group thinks that they might have a gentler role than immune cells from elsewhere in the body, regulating the immune response rather than being primed to fight. Kipnis says that this distinction, if true, has implications for treatment. In diseases such as multiple sclerosis, he says, symptoms could perhaps be improved by preventing immune cells from other parts of the body from coming in. By contrast, with a brain tumour, he adds, "you want the fighters".

His team has also detected a network of channels that snake and branch over the surface of the brain, and which swarm with immune cells, forming the brain's own lymphatic system². These vessels, which sit in the outermost

part of the meninges, give immune cells a vantage point near the brain from where they can monitor any signs of infection or injury.

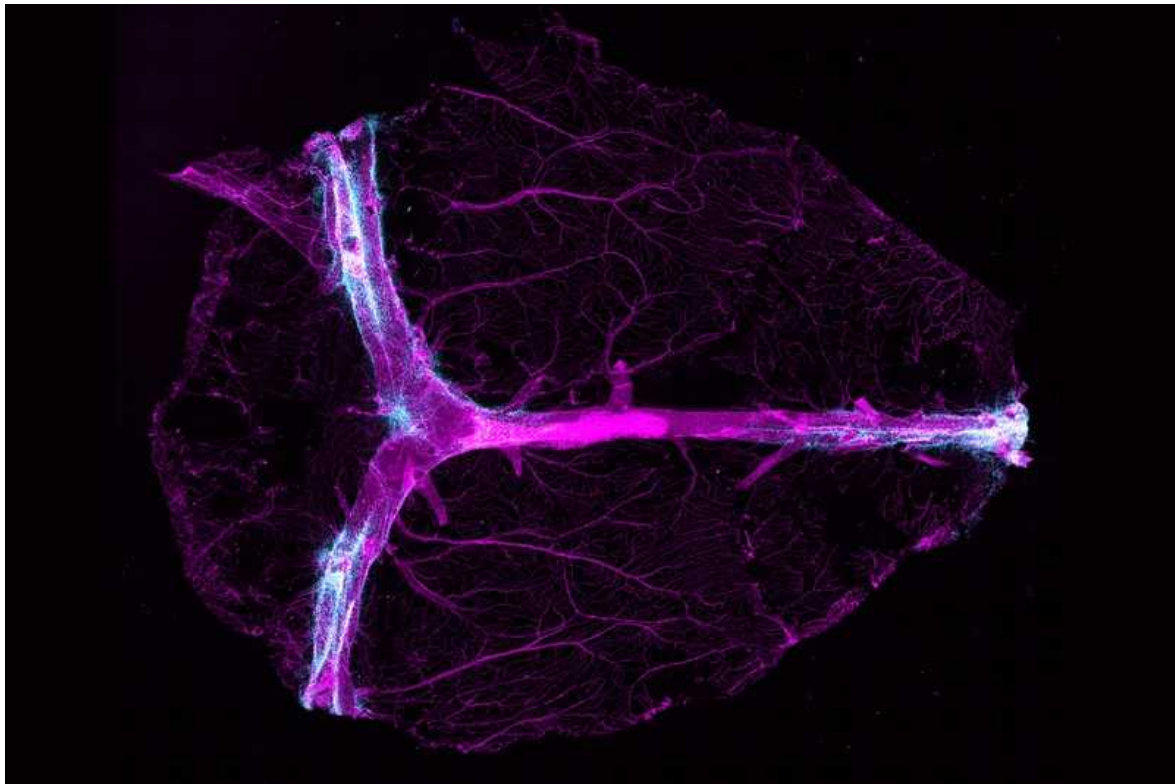
In sickness and in health

As evidence builds for the involvement of immune cells during brain injury and disease, researchers have been exploring their function in healthy brains. “I think the most exciting part of neuroimmunology is that it’s relevant to so many different disorders and conditions and to normal physiology,” says Beth Stevens, a neuroscientist at Boston Children’s Hospital in Massachusetts.

Many groups, including Stevens’s, have found microglia to be important to the brain’s development. These cells are involved in pruning neuronal connections, and studies suggest that problems in the pruning process might contribute to neurodevelopmental conditions.

Border immune cells, too, have been shown to be essential in healthy brains. Kipnis, Schwartz and their colleagues, for example, have shown that mice that lack some of these cells display problems in learning and social behaviour¹⁰. Others reported¹¹ in 2020 that mice that develop without a specific population of T cells in both the brain and the rest of the body have defective microglia. Their microglia struggle to prune neuronal connections during development, leading to excessive numbers of synapses and abnormal behaviour. The authors propose that during this crucial period, T cells migrate into the brain and help microglia to mature.

One big mystery is how exactly immune cells — particularly those around the borders — talk to the brain. Although there is some evidence that they might occasionally cross into the organ, most studies so far suggest that these cells communicate by sending in molecular messengers known as cytokines. These, in turn, influence behaviour.



Signals carried in the cerebrospinal fluid (blue) are presented to immune cells in blood vessels (magenta) in the brain's protective outer layers. Credit: Justin Rustenhoven, Kipnis lab, Washington University in St. Louis

Researchers have been studying how cytokines affect behaviour for decades, finding, for example, that cytokines sent out by immune cells during infection can initiate 'sickness behaviours' such as increased sleep^{[12](#)}. They have also shown in animal models that alterations in cytokines — induced by depleting them throughout the body or knocking out specific cytokine receptors on neurons — can lead to alterations in memory, learning and social behaviours^{[13](#)}. How cytokines travel into the brain and exert their effects remains an area of active study.

Cytokines might also be a link between the immune system and [neurodevelopmental conditions such as autism](#). When Gloria Choi, a neuroimmunologist at the Massachusetts Institute of Technology in Cambridge, and her colleagues boosted cytokine levels in pregnant mice, they saw brain changes and autism-like behaviours in the offspring^{[14](#)}.

Although these insights are tantalizing, much of the work on how immune cells, especially those in the borders, operate in the brain is still in its infancy. “We are very far away from understanding what’s happening in healthy brains,” Kipnis says.

A two-way street

Communication between the immune system and the brain also seems to go in the other direction: the brain can direct the immune system.

Some of these insights are decades old. In the 1970s, scientists conditioned rats to become immunosuppressed when they tasted saccharin, an artificial sweetener, by pairing it with an immunosuppressive drug for several days¹⁵.

In more recent work, Asya Rolls, a neuroimmunologist at Technion — Israel Institute of Technology in Haifa, and her team explored the link between emotion, immunity and cancer in mice. They reported¹⁶ in 2018 that activating neurons in the ventral tegmental area, a brain region involved in positive emotions and motivation, boosted the immune response and, in turn, slowed tumour growth.

Then, in 2021, her group pinpointed neurons in the insular cortex — a part of the brain involved in processing emotion and bodily sensations, among other things — that were active during inflammation in the colon, a condition also known as colitis.

By activating these neurons artificially, the researchers were able to reawaken the intestinal immune response¹⁷. Just as Pavlov’s dogs learnt to associate the sound of a bell with food, causing the animals to salivate any time they heard the noise, these rodents’ neurons had captured a ‘memory’ of the immunological response that could be rebooted. “This showed that there is very intense crosstalk between neurons and immune cells,” says Movahedi, who wasn’t involved with this work.

Rolls suspects that organisms evolved such immunological ‘memories’ because they are advantageous, gearing up the immune system in situations when the body might meet pathogens. She adds that in certain cases, they

can instead be maladaptive — when the body anticipates an infection and mounts an unnecessary immune response, causing collateral damage. This pathway might help to explain how psychological states can influence the immune response, providing a potential mechanism for many psychosomatic disorders, according to Rolls.

It could also inspire therapies. Rolls and her team found that blocking the activity of those inflammation-associated neurons lessened inflammation in mice with colitis. Her group hopes to translate these findings to humans, and is examining whether inhibiting activity using non-invasive brain stimulation can help to alleviate symptoms in people with Crohn's disease and psoriasis — disorders that are mediated by the immune system. This work is in the early phases, Rolls says, “but it'll be really cool if it works”.

Other groups are exploring how the brain controls the immune system. Choi's team is tracing out the specific neurons and circuits that modulate the immune response. One day, she hopes to be able to generate a comprehensive map of the interactions between the brain and immune system, outlining the cells, circuits and molecular messengers responsible for the communication in both directions — and connecting those to behavioural or physiological readouts.

One of the biggest challenges now is to tease apart which populations of cells are involved in these myriad functions. To tackle it, some researchers have been probing how these cells differ at the molecular level, by sequencing genes in single cells. This has revealed a subset of microglia associated with neurodegenerative disease, for example. Understanding how these microglia function differently from their healthy counterparts will be useful in developing treatments, Stevens says. They could also be used as markers to track the progression of a disease or the efficacy of therapies, she adds.

Researchers have already begun using these insights into the immune ecosystem in and around the brain. Schwartz's team, for example, is rejuvenating the immune system in the hope of fighting Alzheimer's disease. This work has opened up new avenues for therapeutics, particularly for neurodegenerative conditions, Schwartz says. “It's an exciting time in the history of brain research.”

Nature **606**, 22–24 (2022)

doi: <https://doi.org/10.1038/d41586-022-01502-8>

References

1. Shirai, Y. *Jap. Med. World* **1**, 14–15 (1921).
2. Mascagni, P. *Vasorum Lymphaticorum Corporis Humani Historia et Ichnographia* (Pazzini Carli, 1787).
3. Moalem, G. *et al.* *Nature Med.* **5**, 49–55 (1999).
4. Beers, D. R., Henkel, J. S., Zhao, W., Wang, J. & Appel, S. H. *Proc. Natl Acad. Sci. USA* **105**, 15558–15563 (2008).
5. Gate, D. *et al.* *Nature* **577**, 399–404 (2020).
6. Baruch, K. *et al.* *Nature Med.* **22**, 135–137 (2016).
7. Cugurra, A. *et al.* *Science* **373**, eabf7844 (2021).
8. Mazzitelli, J. A. *et al.* *Nature Neurosci.* **25**, 555–560 (2022).
9. Louveau, A. *et al.* *Nature* **523**, 337–341 (2015).
10. Filiano, A. J. *et al.* *Nature* **535**, 425–429 (2016).
11. Pasciuto, E. *et al.* *Cell* **182**, 625–640 (2020).
12. Krueger, J. M., Walter, J., Dinarello, C. A., Wolff, S. M. & Chedid, L. *Am. J. Physiol.* **246**, R994–R999 (1984).
13. Salvador, A. F., de Lima, K. A. & Kipnis, J. *Nature Rev. Immunol.* **21**, 526–541 (2021).
14. Choi, G. B. *et al.* *Science* **351**, 933–939 (2016).
15. Ader, R. & Cohen, N. *Psychosom. Med.* **37**, 333–340 (1975).

16. Ben-Shaanan, T. L. *et al.* *Nature Commun.* **9**, 2723 (2018).

17. Koren, T. *et al.* *Cell* **184**, 5902–5915 (2021).

This article was downloaded by **calibre** from <https://www.nature.com/articles/d41586-022-01502-8>

| [Section menu](#) | [Main menu](#) |

Books & Arts

- **Chronic pain — why science has scant succour for one in five people** [31 May 2022]

Book Review • A physician calls on the medical system to contextualize and personalize the treatment of pain.

- **Animal power, and how to perpetuate wonder: Books in brief** [13 May 2022]

Book Review • Andrew Robinson reviews five of the week's best science picks.

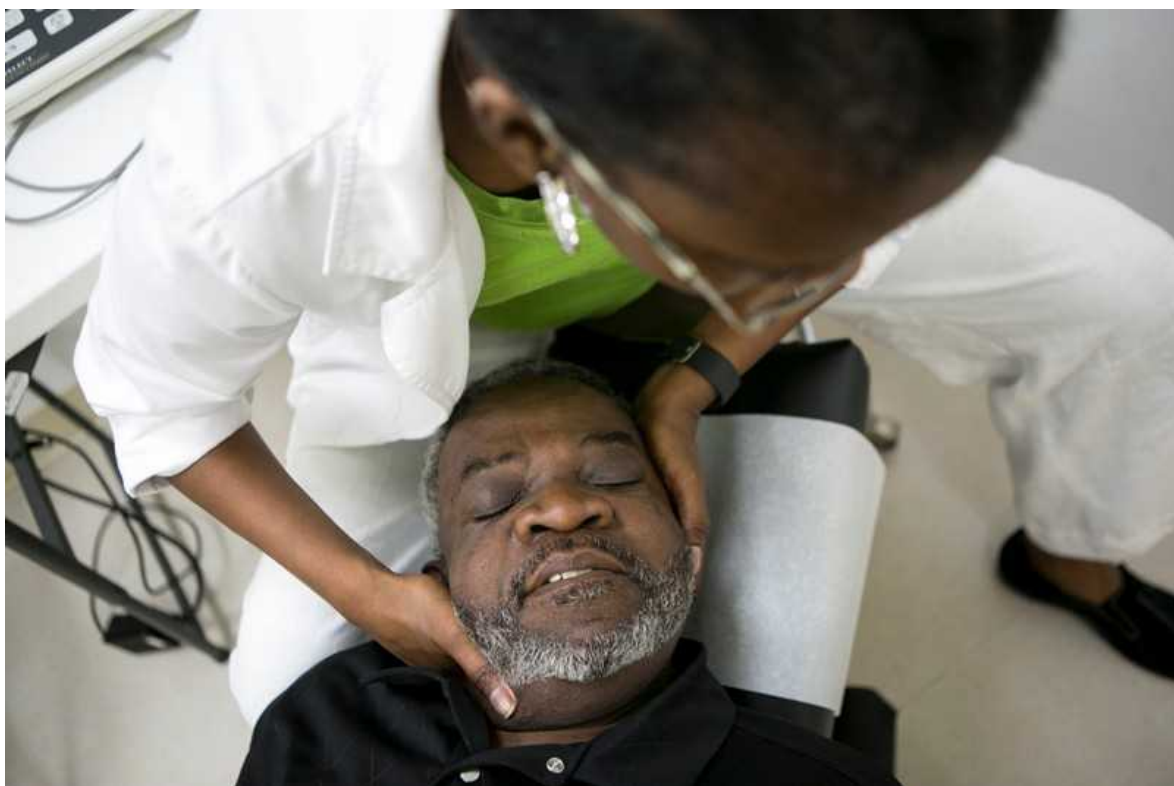
Chronic pain — why science has scant succour for one in five people
[Download PDF](#)

- BOOK REVIEW
- 31 May 2022

Chronic pain — why science has scant succour for one in five people

A physician calls on the medical system to contextualize and personalize the treatment of pain.

- [Anna Nowogrodzki](#)



Chiropractor Toya Burton treats Alabama man Robert Prince.Credit: Ilana Panich-Linsman/New York Times/Redux/eyevine

The Song of our Scars: The Untold Story of Pain Haider Warraich Basic (2022)

As a medical student in Pakistan, Haider Warraich loved to go to the gym. One day, while bench pressing, he dropped a 90-kilogram weight on himself. His back injury ended his plans to become a surgeon and almost dashed his hopes of being a physician. But it gave him something unusual in common with his patients: an insider's view of a life lived in chronic pain.

In *The Song of our Scars*, Warraich draws on personal and professional experiences to explore acute pain, chronic pain and the US medical system's dismal failures to address them effectively. Acute pain is caused by a specific injury, illness or other trauma. When pain persists after the underlying cause has healed, or for more than 12 weeks, it's chronic pain.

Warraich, now a doctor at Brigham and Women's Hospital in Boston, Massachusetts, offers a fascinating tour of the biology and neuroscience of pain. He delves into the US opioid-use epidemic, and asks how treatment is affected by systemic racial and gender biases. He blasts the US medical system for lacking empathy and time to devote to patients, as well as for being too siloed, insufficiently committed to social justice and too swayed by pharmaceutical marketing. His case is made more urgent by chronic pain's links with long COVID: around 30% of people with the condition in an Italian study reported chronic muscle or bone pain ([F. Ursini et al. RMD Open 7, e001735; 2021](#)). Yet his conclusion feels rushed.

One of Warraich's central criticisms is that the medical system has flattened pain, erasing its context and emotional dimensions and collapsing its diversity into numbers on a ten-point scale. The common usage, he explains, encompasses nociception, pain and suffering. Nociception is sensory information — for example, the feeling of the sharp end of a pin pressing into your finger. Pain happens when nociception is processed in the brain and labelled as negative or unpleasant. Suffering results when mental or emotional distress is added — when the pain makes you feel worried, out of control or bad about yourself. So pain is created by the brain and the environment working together. Or acute pain is.

Chronic pain is a different beast, Warraich contends. It is a top-down process in which the brain can tell the body to feel pain without any input from the senses or environment. Chronic and acute pain “light up two separate, non-overlapping circuits in the brain”, he writes.

One in five people worldwide has chronic pain, yet doctors don’t know how to treat it effectively, and patients are used to being dismissed and disappointed. “We basically treat chronic pain the way we used to treat tuberculosis before we discovered what caused it,” neuroscientist Clifford Woolf tells Warraich.

Chronic pain might be a memory of pain. Memory usually helps us to survive by avoiding painful stimuli in future. But neuroscientist Vania Apkarian suggests that chronic pain could be a memory gone haywire, inducing pain without stimulus. Other research examined PKMzeta, a protein that helps to solidify memories in humans. When researchers blocked it in mice, the animals stopped displaying behaviours associated with chronic pain.

Warraich explores biases including the ugly colonial history of opioids, and the racist notion that Black people have thicker skin than white people (a survey shows that this idea persisted very recently; [K. M. Hoffman et al. Proc. Natl Acad. Sci. USA 113, 4296–4301; 2016](#)). He reports the finding that physicians are five times less likely to prescribe opioids to Black children with acute appendicitis than to white children with the condition. A section on gender explores the history of pain management during childbirth, including the misogynist and white-supremacist origins of the natural-childbirth movement, and a rousing endorsement of the epidural. In general, women (including trans women taking oestrogen) experience more pain than men, and are more sensitive to it. Even female rodents tend to experience more pain than male ones.

Empathy and acceptance

Warraich eventually comes to the origins and current state of the US opioid epidemic. He gives an overview of how the Sackler family ran Purdue

Pharma, which made opioids including OxyContin and generated huge wealth by expanding the range of conditions for which they were prescribed.

An extensive body of research shows that opioids don't work for chronic pain, except in the case of cancer, Warraich writes. He breezes through ketamine and cannabis in three pages, and concludes that no drugs are effective at treating chronic pain. It is really all in our heads, he contends — but not dismissively. The only treatments that do work, he says, tackle the mental dimension: providers' empathy, hypnotherapy, the placebo effect, exercise, and acceptance and commitment therapy. The latter is a practical form of cognitive behavioural therapy that involves accepting difficult feelings, with empathy for oneself.

This conclusion seems overly rosy. Exercise is "entirely safe" for people with chronic pain, Warraich writes — it brought him relief, although it was excruciating at first. But exercise is not like a pill. A person has to find the right kind, which might take trial and error, along with guidance from the right physical therapist or trainer, which costs money and time and requires access. It's going to take a lot to roll that out to one-fifth of the world's population. I yearned to hear about the daily lives of people with diverse types of chronic pain who have used the approaches Warraich lauds.

Pain resists easy categorization. It has a vast array of causes, in a vast array of bodies and minds. The assurance that whole categories of treatments will or won't work for everyone is puzzling for a book that calls on the medical system to treat pain in a more contextualized and personalized way.

Nature **606**, 25-26 (2022)

doi: <https://doi.org/10.1038/d41586-022-01510-8>

This article was downloaded by **calibre** from <https://www.nature.com/articles/d41586-022-01510-8>

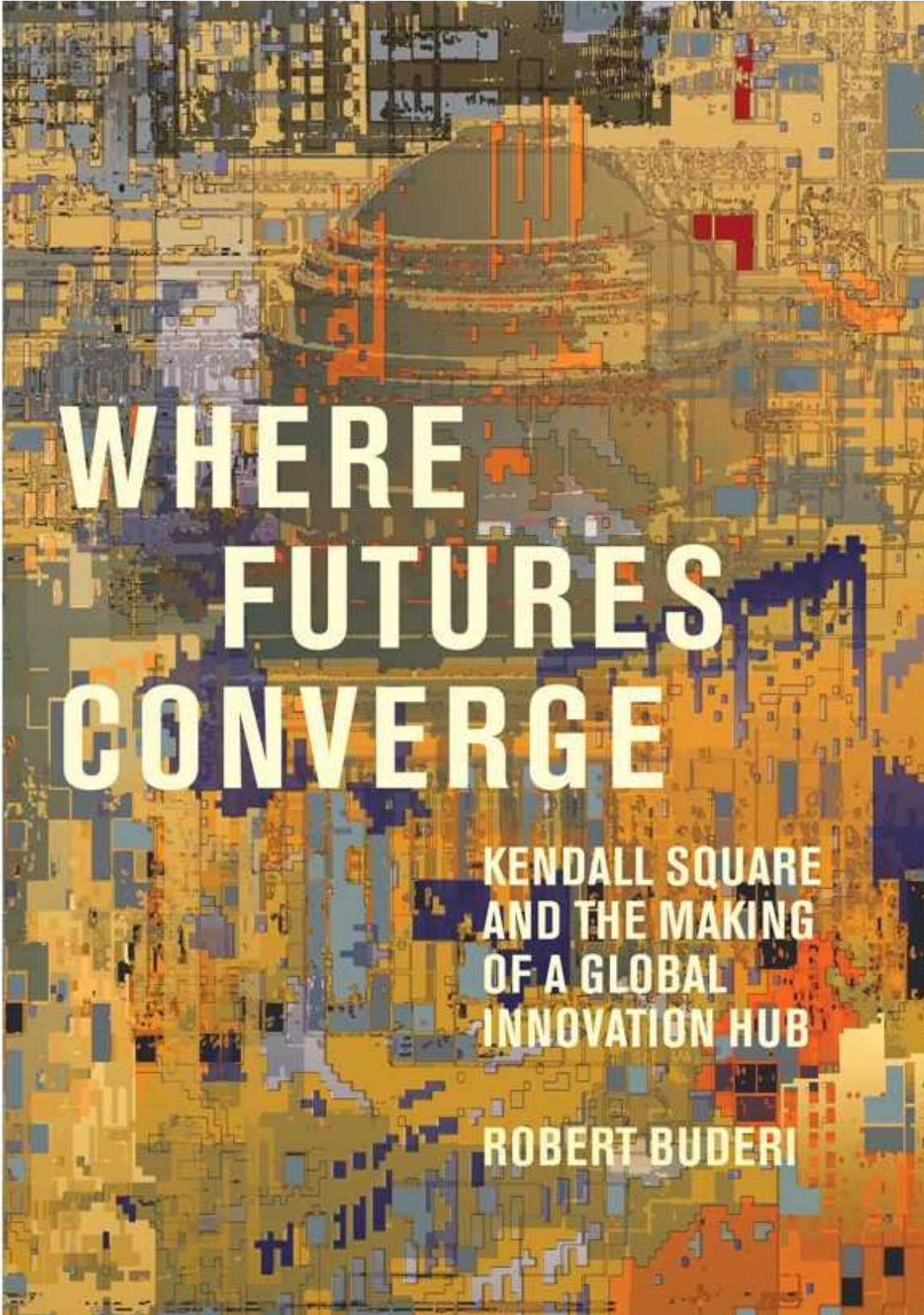
Animal power, and how to perpetuate wonder: Books in brief
[Download PDF](#)

- BOOK REVIEW
- 13 May 2022

Animal power, and how to perpetuate wonder: Books in brief

Andrew Robinson reviews five of the week's best science picks.

- [Andrew Robinson](#) 0



WHERE FUTURES CONVERGE

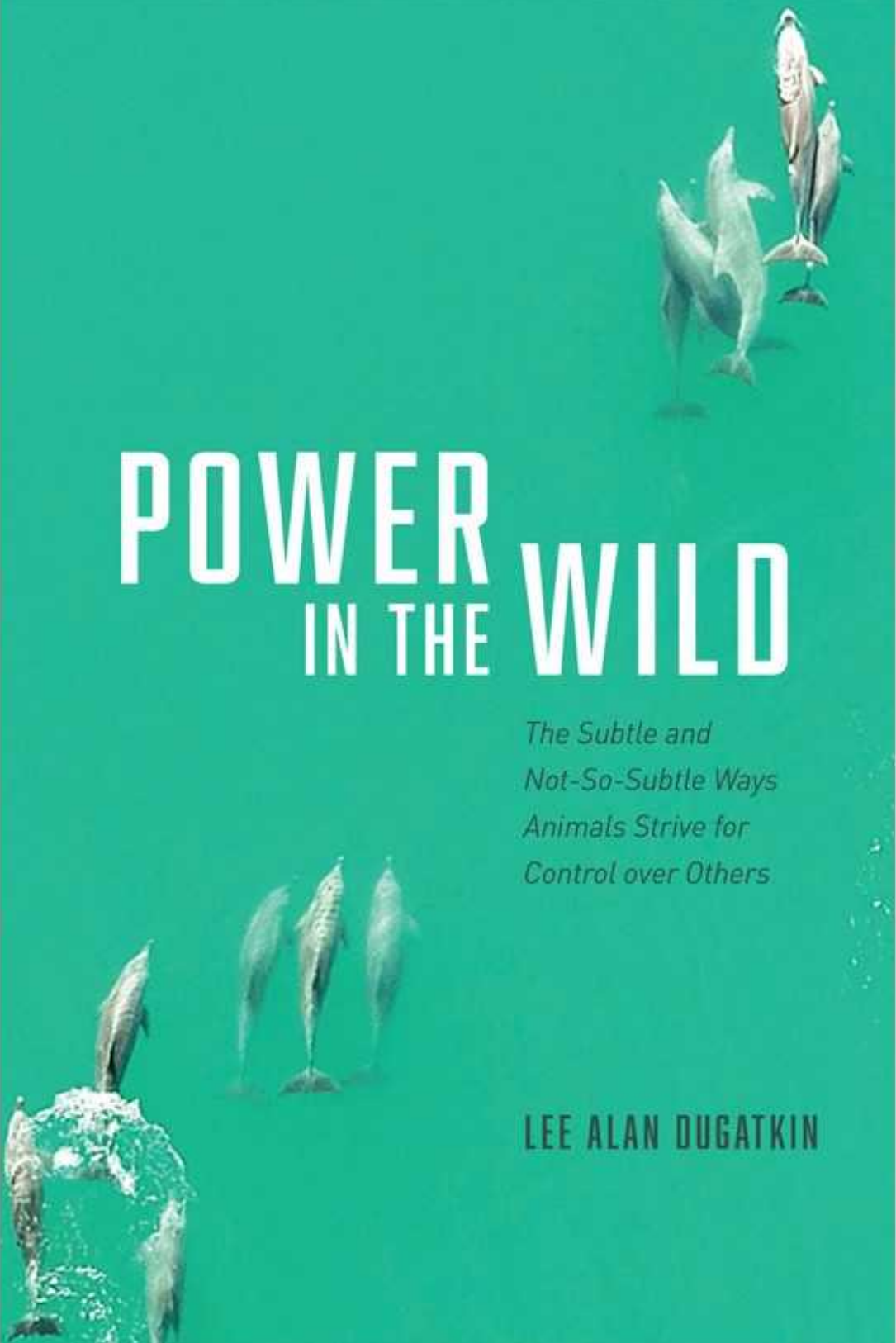
KENDALL SQUARE
AND THE MAKING
OF A GLOBAL
INNOVATION HUB

ROBERT BUDERI

Where Futures Converge

Robert Buderi *MIT Press* (2022)

Kendall Square in Cambridge, Massachusetts, has been dubbed “the most innovative square mile on earth”. Neighbouring the Massachusetts Institute of Technology, it is a centre for life-sciences companies, tech firms and start-ups, from Moderna to IBM. One building with a history including the first long-distance telephone call now houses almost 70 biomedical start-ups. Entrepreneur and Kendall Square inhabitant Robert Buderi considers the area’s past, present and future by interviewing local notables.



POWER IN THE WILD

*The Subtle and
Not-So-Subtle Ways
Animals Strive for
Control over Others*

LEE ALAN DUGATKIN

Power in the Wild

Lee Alan Dugatkin *Univ. Chicago Press* (2022)

While visiting a wolf research park in Austria, animal behaviourist Lee Dugatkin was startled to see one male sitting on top of another, clamping its snout in its jaws. The park's director assured him there was no harm involved, only a display of power. This theme defines Dugatkin's engaging book, which is based on the work of many scientists with a huge range of animals from around the world, including baboons, dolphins, mongooses and ravens. "Power pervades every aspect of the social lives of animals," he says.

MORTEN H. CHRISTIANSEN

NICK CHATER

THE LANGUAGE GAME



HOW IMPROVISATION CREATED
LANGUAGE AND CHANGED
THE WORLD

The Language Game

Morten H. Christiansen & Nick Chater *Basic* (2022)

Charles Darwin noted in 1871: “The survival and preservation of certain favoured words in the struggle for existence is natural selection.” But he did not claim that humans evolved a specific biological capacity for language, say cognitive scientists Morten Christiansen and Nick Chater in their study spanning continents and millennia. They argue that language speaking has no genetic basis. Languages evolve too quickly for genes (or computers) to keep up — through cultural evolution, as speakers play verbal charades.

"Frank Keil is among the deepest thinkers about thought, and here he explores the wondrous urge that drives our lifelong quest to understand the world."
—STEVEN PINKER, author of *Rationality*

Frank C. Keil

W O N D E R

Childhood
and the Lifelong Love
of Science

Wonder

Frank C. Keil *MIT Press* (2022)

Psychologist Frank Keil opens with his children asking about small fossils found near their house. “We are intrinsically driven to wonder about the world and to address those wonders.” How to perpetuate wonder — and respect for science — in adulthood is the heart of his appealing book. He recalls anthropologist Margaret Mead’s observation in Papua New Guinea: children explained how a roped canoe had drifted away overnight because its rocking loosened the knot; adults invoked moral and supernatural causes.

THE
INVISIBLE SIEGE

THE RISE OF
CORONAVIRUSES

and the
SEARCH FOR A CURE

DAN WERB



The Invisible Siege

Dan Werb *Crown* (2022)

To blame a Chinese laboratory leak for SARS-CoV-2 is like blaming a fire department for blazes caused by climate change, remarks epidemiologist Dan Werb. The real reason has to be the accelerating emergence of human pathogens because of the globalized world's drive for expansion. Coronavirus specialist Ralph Baric, the focus of Werb's well-informed, powerfully written study of the pandemic, agrees, despite his personal reservations about China's refusal to share more data.

Nature **606**, 26 (2022)

doi: <https://doi.org/10.1038/d41586-022-01292-z>

This article was downloaded by **calibre** from <https://www.nature.com/articles/d41586-022-01292-z>

| [Section menu](#) | [Main menu](#) |

Opinion

- **[A century of science boycotts](#)** [25 May 2022]
Comment • Researchers have severed global ties before — what happened?
- **[Fifty years after UN environment summit, researchers renew call for action](#)** [01 June 2022]
Correspondence •

A century of science boycotts

[Download PDF](#)

- COMMENT
- 25 May 2022

A century of science boycotts

Researchers have severed global ties before — what happened?

- [Michael D. Gordin](#) 0



Albert Einstein was exempted from a 1919–26 boycott of German scientists because of his pacifist views. Credit: Scherl/Süddeutsche Zeitung

Photo/Alamy

The orders came from Moscow, and took the world by surprise. Governments elsewhere had not expected a militarized invasion on this scale, reasoning that it would be logistically almost impossible to occupy the territory, and that the local resistance would be prolonged and potentially ruinous to the invading forces. Nonetheless, many nations quickly responded with sanctions and trade embargoes. The United Nations General Assembly overwhelmingly condemned the aggressor and demanded immediate withdrawal of all troops.

Meanwhile, the Kremlin responded fiercely to outbursts of domestic opposition. Although some grumbling against the leadership in Moscow had been indulged in the preceding decade, in recent years, the state's tolerance had largely vanished. The few protests were quashed with arrests. The highest-profile critic of the regime was apprehended and sentenced, sparking even more international condemnation.

Then came calls for boycotts to supplement the sanctions, including from the scientific community, which felt especially betrayed by the regime's arrest of their champion. Decrying the invasion and the internal exile of dissident physicist Andrei Sakharov — winner of the 1975 Nobel Peace Prize for his courageous opposition to the nuclear arms race and human-rights abuses — 65 nations boycotted the 1980 Summer Olympics in Moscow.

The parallels between the aggression of the Soviet Union against Afghanistan in December 1979 and against Ukraine in 2022 are mostly superficial. The Soviet Union was not the same thing as the Russian Federation is today, in terms of population, geography, ideology or military capability. Opposition leader and anti-corruption activist Alexey Navalny, who was sentenced by a Russian court in March to nine years in prison for fraud and contempt, is not an avatar of Sakharov. And Russian President Vladimir Putin is not Soviet leader Leonid Brezhnev.



Physicist Andrei Sakharov was internally exiled in 1980 for opposing the Soviet–Afghan war. Credit: AP/Shutterstock

Yet the demands for sanctions from the international community and for boycotts by the scientific community — among others — resonate strongly. [Ukrainian scientists have asked international journal editors to refuse to publish studies by former colleagues from the Russian Federation.](#) Many research organizations have suspended collaborations with Russian state universities, professional societies and the Russian Academy of Sciences in Moscow. Grants have been suspended. Talks cancelled. Sometimes these are straightforward expressions of moral revulsion against the Kremlin's violence; sometimes they represent efforts to protect Russian colleagues who could be punished for having transnational connections^{[1,2](#)}. Condemnation has also hit researchers of Russian origin outside the nation's borders. This is a cruel irony, given how many had themselves been refugees from that previous regime when it attacked Afghanistan, or had fled the economic chaos that followed the Soviet Union's dissolution.

The practical efficacy of sanctions depends on how they fit the economic realities. Forswearing imports of Russian pineapples or smartphones will not leave a dent. The equivalent is true for a boycott severing science ties. The international organization of science has been overhauled several times since the first major attempt at a scientific boycott during and after the First World War. Yet every effort to sanction Moscow — 2022 and 1980 are not the only instances — has failed. Why? Because they have not adequately recognized how the Soviet Union and post-Soviet Russia fit into the global knowledge infrastructure.

The first boycott

Although the practice of punishing perceived wrongdoing by withholding trade or succour has been around since time immemorial, the practice received its enduring label only in 1880. The overbearing land agent for Lord Erne in County Mayo, Ireland, was so shunned by the local community that workers had to be imported from distant counties and guarded to reap the harvest. With that pyrrhic victory, on 1 December 1880, Charles Boycott left Ireland³. Those outraged by the impunity of the powerful have never forgotten him, and the *fin de siècle* was studded with boycotts of one sort or another. The world of science soon joined in.

Before scientific boycotts were repeatedly targeted at Moscow, they focused on Berlin. The most significant — so much so that its legacy still colours, often unconsciously, all later discussions of the practice — was that imposed in 1919 by Belgian, French, British and US scientists on the vanquished powers of the Great War. Or, rather, it was imposed on the successor states of the vanquished: the democratic republic of Weimar Germany and the new states of Austria and Hungary.

Many specific transgressions were invoked to justify punishing all scientists from the losing nations. The most frequently cited incitement was the notorious Manifesto of the Ninety-Three, a proclamation officially entitled *To the Cultured World* that was signed by a host of literary and philosophical luminaries and released on 4 October 1914. The document's goal was to defend the honour of the German nation against allegations of atrocities committed by German troops during the invasion of Belgium. It was the list

of prominent signatories that stuck in the craw of the later boycotting scientists. Among the names were Adolf von Baeyer, Paul Ehrlich, Fritz Haber, Felix Klein, Walther Nernst, Wilhelm Ostwald, Max Planck and Wilhelm Röntgen⁴.

These scientists, willing to politicize the disinterested quest for knowledge, were repaid in their own coin. After the war, all scientists in the defeated countries — not just these signatories — were excluded from conferences or scientific meetings, denied space in journals of the boycotting powers and barred from the new administrative structures of international science that were being rebuilt on the ashes of pre-war transnational organizations. The boycott was planned to last until 1931.

It had one exception. It did not apply to Albert Einstein, who was distinguished as one of four signatories to an anti-war counter-manifesto, *To the Europeans*, penned by Einstein's Berlin colleague and like-minded pacifist, the physiologist Georg Nicolai. Bans on German nationals notwithstanding, Einstein was feted in 1919 on the announcement of the successful results of a British expedition to test the general theory of relativity during a solar eclipse. He travelled to the boycotting United States in 1921 and France in 1922. Einstein made his own exceptions in turn: he entertained invitations that were specifically to him, but refused to go to any international meeting, such as the Solvay conferences in physics in 1921 and 1924, because those denied access to Germans. He thought the boycott was a terrible thing for science⁵.

So did those countries that had remained politically neutral during the conflict, such as the Netherlands and Denmark. Their scientists argued that the blanket condemnation was senseless and ineffective. Ironically, the strictures granted sites such as physicist Niels Bohr's institute in Copenhagen an outsized importance as places where boycotters and boycottees could fraternize. What, argued these scientists, was being punished, and what was the policy change that would lead to the lifting of the boycott?

The boycott was thus incomplete and toothless, in that the Austrian and German scientific communities were vibrant and diverse enough to function reasonably well without intercourse with the shunning nations. The only

thing that was hurt was science and common sense, argued neutral scientists, and they lobbied hard for the League of Nations to admit the now-democratic Germany to its ranks, signalling an end to the scientific freeze. The boycott ended five years earlier than intended, in 1926. Among other things, Einstein attended the Solvay conference the following year.

Calls for boycotts returned in 1933. With the appointment of Adolf Hitler as Chancellor of Germany in January that year, and his complete seizure of power a few months later, a Civil Service Law fired most Jewish people, including scientists, from their university positions.

This time, Einstein was on the side of the boycotters. He openly resigned from his position at the Prussian Academy of Sciences in Berlin in March 1933, frustrating the state's attempts to publicly fire him, and refused to publish in German journals. As he wrote to his exiled colleague Cornelius Lanczos from Princeton University in New Jersey in 1935: "The German intellectuals have as a whole behaved disgracefully concerning all the abominable injustices and have richly deserved to be boycotted."⁶ Likewise, physicist Percy Bridgman at Harvard University in Cambridge, Massachusetts, announced in 1939 that he would no longer share any information with former colleagues in "totalitarian states", meaning Germany⁷. Hitler's regime, for its part, boycotted this very journal when it persisted in calling attention to Nazi crimes.

The Second World War soon cut off connections between Germany and its antagonists, but on the grounds of military secrecy rather than morality. After the war, scientists among the Allied nations led the efforts to fold former belligerents back in.



In response to the invasion of Ukraine, Europe's particle-physics laboratory CERN in Geneva, Switzerland, has halted new collaborations with Russia and its institutions until further notice. Credit: olrat/Alamy

Top tactic

The boycott remained a favoured tactic, despite the fact that it had not demonstrably accomplished any change in behaviour in its previous deployments. Certainly, there were cold-war proponents among the scientists who wanted to boycott the Soviet Union to protest against the subjugation of Eastern Europe. But how could they? For the first decade after the end of the Second World War there were so few scientific contacts between the Soviet Union and capitalist nations that there was not really anything to boycott. Thus, the Berlin Blockade of 1948–49 and the suppression of the Hungarian Revolution in 1956 were greeted only with private indignation by scientists.

Within a decade of the death of Soviet leader Joseph Stalin in 1953, boycotting once again became thinkable, as Soviet and especially US scientists began a concerted campaign to integrate the former into emergent

global scientific networks. The Lacy–Zarubin Agreement of 1958 initiated exchanges between the United States and Soviet Union across many artistic and scientific fields as a step to relieve tensions. Such exchanges were accelerated with the deepening of détente in the early 1970s. US President Richard Nixon and his secretary of state Henry Kissinger cared about arms control and geopolitical leverage, not scientific communication. But their efforts in the former brought improvements in the latter, including a series of exchanges between the US National Academy of Sciences and the Soviet Academy of Sciences⁸. Amid this general trend of rapprochement, the worldwide criticism of the Soviet-led invasion of Czechoslovakia in 1968 produced only faint calls for a boycott.

The post-Afghanistan boycott was triggered precisely because those efforts at integration were seen as valuable, something the Soviet leadership might be loath to lose. It did not change the Soviet deployment, however, which lasted until 1989. Even before then, Soviet leader Mikhail Gorbachev's wave of glasnost and perestroika reforms in the preceding few years had catalysed an even more vigorous effort at integrating Soviet scientists into global science. A similar push happened after 1991 with post-Soviet scientists (including Russians, who numerically dominated this group).

The resulting financial and intellectual investment was the very opposite of a boycott. Philanthropic funding came from financier George Soros's International Science Foundation in Moscow and New York City and the MacArthur Foundation in Chicago, Illinois; US state support through the Civilian Research and Development Foundation in Arlington, Virginia; and multilateral collaboration under the auspices of the International Science and Technology Center in Moscow and its Kyiv equivalent, the Science & Technology Center in Ukraine, among others. The investments forged new links between the scientific communities in the various successor states of the former Soviet Union and international science⁹.

The catch? All of this effort was being expended on a rapidly shrinking scientific community in these former socialist countries. Across the region, the scientific workforce dropped by at least 50%, in part because of emigration (the notorious ‘brain drain’), but mostly because of the lack of funding for science and better opportunities for stable employment in the private sector. Even after the economic crisis of the 1990s and after the

governments of Putin and Dmitry Medvedev increased budgetary allotments, the scale of investment and the corresponding uptake by scientists remained meagre¹⁰. What remained was more connected to global science, but it was a shadow of the Soviet scale.

Boycotts today

What does this history mean for the question of scientific boycotts against Russia today? The answer depends entirely on what a boycott is for.

If a boycott is intended to cripple the scientific enterprise of a nation or region, the history of both the anti-German and anti-Soviet boycotts show that when a country has a sizeable and dynamic scientific community (or sphere of influence), then detachment from global science is not especially impactful, at least in the short term. In recent years, China's scientific community boasts something of this quality.

If a nation has a smaller scientific community that cannot survive on its own, however, then sustained boycotts can indeed be damaging. An arguable exception to the record of failure was the academic boycott of South Africa, launched in the 1960s with the support of the African National Congress. It was initiated to oppose the country's system of apartheid, and was terminated in 1990 with the end of that system. Although never total, that boycott took its toll because it severed necessary connections to the transnational system of scientific exchange. South Africa's scientific community was not large or diverse enough to subsist autonomously¹¹. (This example has motivated calls by some to boycott Israel's scientific community.)

For the past two decades, Russian science has been much more connected to global networks than since the Bolshevik Revolution cut Tsarist links to Europe, and much smaller than the Soviet sector had been. So the damage to Russian science, even from the limited steps already taken, could be severe.

Could a boycott, as has been claimed for South Africa, help to produce a change of mindset in the regime? To be effective in this way, the political leadership has to care about scientists and science. And Russia does not

seem to care. Witness the limited investments in research in the past decade, the chasing after status and rankings rather than improving fundamentals, the lacklustre response to COVID-19, and the designation of various scientific collaborations and non-profit organizations (such as the MacArthur Foundation) as “foreign agents” and kicking them off Russian soil¹². All of these signs of government apathy towards science were visible for years before the current invasion of Ukraine triggered international outrage.

Ending the limited scientific linkages that have survived the recent decades of neglect can function as a statement of moral revulsion — which was how the academic boycott against South Africa started. If that is the primary goal, it should be embraced as such by boycott advocates. But despite the laudable hopes of its advocates, a scientific boycott is as unlikely to change the course of the present war as that which greeted Russia’s invasion of Afghanistan.

Nature **606**, 27-29 (2022)

doi: <https://doi.org/10.1038/d41586-022-01475-8>

References

1. Brainard, J. *Science* <https://doi.org/10.1126/science.adb1981> (2022).
2. Burke, M. ‘Invasion of Ukraine Begins Cascade of Decoupling from Russian Science’ *Chemistry World* (22 March 2022).
3. Le Grys Norgate, G. In *Dictionary of National Biography* (1st suppl.) Vol. I, 243–244 (Smith, Elder, 1901).
4. von Ungern-Sternberg, J. & von Ungern-Sternberg, W. *Der Aufruf “An die Kulturwelt!”: Das Manifest der 93 und die Anfänge der Kriegspropaganda im ersten Weltkrieg* (Franz Steiner, 1996).
5. Stanley, M. *Einstein’s War: How Relativity Triumphed Amid the Vicious Nationalism of World War I* (Dutton, 2019).

6. A. Einstein to C. Lanczos, 11 September 1935, 15-246, Albert Einstein Duplicate Archive, Princeton University Library, Rare Books and Special Collections, Box 18, Folder: “C. Lanczos, 1919–1940.”
7. Bridgman, P. W. *Science* **89**, 179 (1939).
8. Graham, L. R. *Science* **202**, 383–390 (1978).
9. Sher, G. S. *From Pugwash to Putin: A Critical History of US–Soviet Scientific Cooperation* (Indiana Univ. Press, 2019).
10. Graham, L. & Dezhina, I. *Science in the New Russia: Crisis, Aid, Reform* (Indiana Univ. Press, 2008).
11. Haricombe, L. J. & Lancaster, F. W. *Out in the Cold: Academic Boycotts and the Isolation of South Africa* (Information Resources Press, 1995).
12. Tavernise, S. ‘MacArthur Foundation to Close Offices in Russia’ *The New York Times* (22 July 2015).

This article was downloaded by **calibre** from <https://www.nature.com/articles/d41586-022-01475-8>

Fifty years after UN environment summit, researchers renew call for action
[Download PDF](#)

- CORRESPONDENCE
- 01 June 2022

Fifty years after UN environment summit, researchers renew call for action

- [Maria Ivanova](#) ⁰ &
- [Sharachchandra Lele](#) ¹

On the eve of the 1972 United Nations Conference on the Human Environment in Stockholm, a group of 2,200 scientists signed a letter — now known as the Monton Message — to their (then) 3.5 billion neighbours on Earth. In one of the earliest examples of researchers collectively calling for societal change, they sounded the alarm on the ongoing environmental crisis, the nuclear arms race and the possibility of the extinction of life on Earth. As the Stockholm+50 summit gets under way this week — the UN conference's 50th anniversary — the International Science Council, Future Earth and the Stockholm Environment Institute have convened an expert group of natural scientists, social scientists, engineers and humanities scholars to modernize and extend that historical call. Writing as co-chairs of that group, we invite readers to sign our open letter at <https://science4stockholm50.world>.

After 50 years, environmental action seems like one step forward and two back. The world now produces more food than ever before, yet many still go hungry. We continue to subsidize and invest in fossil fuels, even though renewable energy is increasingly cost-effective. Governments subsidize private cars instead of building public transport systems. We extract

resources where the price is lowest, often with disregard for local rights and values.

These and other contradictions are rooted mainly in mismatches around values, world views and institutions. Our individualistic, materialistic, exploitative short-term thinking has led us to lose sight of the global public good. The focus on economic growth is detracting from human well-being and destroying our shared resources. The belief that we can bend all nature to our will through the unrestricted use of new technologies is an illusion.

Economic, political and social institutions are failing us. Financial power is concentrated in the hands of a few and legitimizes the relentless pursuit of profits, manipulation of citizens as consumers and valuation of nature for short-term economic gain. Racism and patriarchy continue to legitimize the deprivation of and environmental impacts on people of colour, women and Indigenous communities. Those most responsible for the crisis are the ones who suffer the least.

The worst fears of the Merton Message have not been realized, but we are getting closer to the brink (see [M. Ivanova *Nature* 590, 365; 2021](#)). Action is needed to create a safer and better future. The priority is to redefine our normative goals. Personal well-being needs to focus on physical and mental health, community and peace. Goals for societal well-being should include a sustainable future, justice and respect for all humans and the protection and conservation of all species. The privileged must recognize their responsibilities: those who consume too much must scale back and make space for those who are disenfranchised and disempowered.

Collective action is crucial. We must shift to an economy of cooperation and sharing, instead of competition, accumulation and planned obsolescence. Democracy and participatory governance should be strengthened and reinforced. Compassion and collaboration in our families, communities and nations are paramount.

A small but important first step is to meet current international commitments to reduce pollution, improve conservation and tackle climate change. Naming and acclaiming countries, companies or citizen groups that deliver on pledges will inspire action, as will honouring the UN

Environment Programme (see [*Nature* 591, 8; 2021](#)) and ensuring that the United Nations receives the best scientific advice (see [*Nature* 600, 189–190; 2021](#)).

The scientific, engineering and scholarly community must deepen its engagement with these issues, building bridges that span disciplines, geography and income discrepancies, and ensuring that technological innovation is socially responsible. Together with our teaching, research and technological skills, we can help to secure sustainability, justice and dignity for all.

We must become good ancestors and better neighbours.

Nature 606, 30 (2022)

doi: <https://doi.org/10.1038/d41586-022-01511-7>

This article was downloaded by **calibre** from <https://www.nature.com/articles/d41586-022-01511-7>

| [Section menu](#) | [Main menu](#) |

Work

- **[Has the ‘great resignation’ hit academia?](#)** [31 May 2022]
Career Feature • A wave of departures, many of them by mid-career scientists, calls attention to widespread discontent in universities.
- **[How engineers and drug developers are working to change childhood cancer’s deadly calculus](#)** [30 May 2022]
Technology Feature • A non-profit organization merges engineering and biology to accelerate drug development for childhood cancers.
- **[A down-to-earth approach to climate change](#)** [31 May 2022]
Where I Work • Asmeret Asefaw Berhe researches how physical changes to soil affect how much carbon is released into the atmosphere.

Has the ‘great resignation’ hit academia?

[Download PDF](#)

- CAREER FEATURE
- 31 May 2022

Has the ‘great resignation’ hit academia?

A wave of departures, many of them by mid-career scientists, calls attention to widespread discontent in universities.

- [Virginia Gewin](#) ⁰

[Find a new job](#)



Many mid-career scientists are leaving academia for greener pastures in industry.Credit: Adapted from Getty

On 4 March, Christopher Jackson tweeted that he was leaving the University of Manchester, UK, to work at Jacobs, a scientific-consulting firm with headquarters in Dallas, Texas. Jackson, a prominent geoscientist, is part of a growing wave of researchers using the #leavingacademia hashtag when announcing their resignations from higher education. Like many, his discontent festered in part owing to increasing teaching demands and pressure to win grants amid lip-service-level support during the COVID-19 pandemic.

He is one of many academics who say the pandemic sparked a widespread re-evaluation of scientists' careers and lifestyles. "Universities, spun up to full speed, expected the same and more" from struggling staff members, he says, who are now reassessing where their values lie. The demands add to long-standing discontent among early-career researchers, who must work longer and harder to successfully compete for a declining number of tenure-track or permanent posts at universities. And Jackson had another reason. He received what was, in his opinion, a racially insensitive e-mail that constituted harassment and alluded to using social media to police staff opinions, which, he says, was the last straw. Jackson filed a formal complaint and the University of Manchester responded: "The investigation has now concluded. We have made Professor Jackson aware of its findings as well as the recommendations and actions we will be taking forward as an institution."

The level of unhappiness among academics was reflected in *Nature*'s 2021 annual careers survey. Mid-career researchers were consistently more dissatisfied than were either early- or late-career academics (see 'Mid-career malcontent'). In the United Kingdom, pension cuts have [worsened ongoing university-faculty strikes](#). Now, researchers in secure, long-term posts are quitting. "For mid-career individuals, it says something much more significant if they have got a mortgage, car and kids — and still are leaving," Jackson adds.

Mid-career malcontent

Nature's 2021 salary and satisfaction survey offered a snapshot of the working conditions and quality of life of researchers around the world. The survey drew responses from more than 1,200 researchers who identified as mid-career, a stage of scientific life that comes with particular challenges and uncertainties. Taken together, the results help to explain why many mid-career researchers are rethinking their paths.

Thirty-seven per cent of mid-career researchers were dissatisfied with their current position, a degree of dissatisfaction that set them apart from both early- (32%) and late-career (32%) researchers.

For mid-career scientists, uncertainty about the future looms larger: nearly one-quarter (24%) said they were extremely dissatisfied with their opportunities for career advancement. By comparison, 17% of early-career and 19% of late-career researchers had that level of doubt.

Mid-career researchers often face duties and administrative tasks that go beyond the lab. In the survey, 34% of researchers at the mid-career stage said they were unhappy with the amount of time they have for research. Twenty-one per cent of early-career researchers and 28% of late-career researchers echoed that complaint.

Forty-one per cent of mid-career researchers — compared with 32% of early-career scientists — reported that organizational politics or bureaucracy frequently or always frustrated their efforts to do a good job. — **Research by Chris Woolston.**

Karen Kelsky has watched conditions in academia deteriorate in the 12 years since the cultural anthropologist left her post at the University of Illinois at Urbana-Champaign to become a career coach. Grievances include a lack of support, increased workloads, micromanagement, increasing right-wing hostility towards academics and salaries that have not kept up with cost of living, says Kelsky, who is based in Eugene, Oregon, and wrote the 2015 academic-career guide *The Professor is In*. The pandemic set the stage for a mass exodus. “COVID-19 is the straw that broke the camels’ backs,” she says.

In early 2021, Kelsky, seeing a dramatic shift in discontent, started The Professor is Out, a private Facebook group for higher-education professionals to share advice and support for those who are leaving academia. It has grown to more than 20,000 members in the past year. “What’s wild is how many of them are tenured,” she says. “The overwhelming narrative is that people are happier once they leave academia.”



Christopher Jackson now works in scientific consulting after an academic career that spanned almost two decades. Credit: Thomas Angus, Imperial College London

Higher education has not escaped the ‘great resignation’ — the international wave of worker resignations that began in 2021, including a record 47 million US residents and 2 million UK adults, largely because of the consequences of the COVID-19 pandemic and stagnant wages. *Nature* spoke to more than a dozen scientists leaving academia, who describe toxic work environments, bullying and a lack of regard for their safety and well-being as factors in their decisions. A 2018 study predicted that higher education would lose half to two-thirds of its academic workforce to retirement, career

burnout or job dissatisfaction within five years ([T. Heffernan & A. Heffernan Prof. Dev. Educ. 45, 102–113; 2018](#)). Established researchers might have the privilege to leave willingly, but many are unsure how their skills will translate to other sectors. Others who face systemic racism and sexism are finding themselves forced out, partly owing to structural biases. Their exits threaten progress on diversity, equity and inclusivity in the academic workforce.

Reasons for leaving

On 31 March, Caspar Addyman, a developmental psychologist who studies babies' emotions at Goldsmiths, University of London, announced his resignation, effective in June, on Twitter. His resignation letter cites, what was in his opinion, faculty frustration with university mismanagement, which has culminated in "a massive vote of no confidence [in senior administrators], countless individual appeals and testimonies and unprecedented local strikes". But it was the 38% cut to his pension that finally pushed him to leave.

"I could imagine spending the rest of my life figuring out why babies were happy, but after seven years, it became too hard to imagine doing this grind forever," he says, referring to increasing administrative responsibilities and what he describes as an ever more regimented approach to teaching. Although being an academic felt like his identity, Addyman didn't consider moving to a different institution. "Why stay in this world if it's just going to be a slightly different version?" he asks.

Facing a hostile funding environment and rising costs, Goldsmiths has announced 20 staff cuts so far. A Goldsmiths spokesperson says: "We recognize how deeply upsetting and painful this period of change has been, and continues to be, for our community as we make some difficult decisions to ensure Goldsmiths has a sustainable future. We will continue to support and advise all those affected with comprehensive careers support."

Similar workforce reductions have occurred in Australia, a country hard-hit by the loss of revenue from fees for international students, who could not enter the country owing to COVID-19 restrictions. By May 2021, one in five

academic jobs in Australia had been cut. “Now, we’re seeing a lot of people look for work elsewhere, or retire if they can afford it,” says Lara McKenzie, an anthropologist who studies academic-workforce trends at the University of Western Australia in Perth. Those who remain lose trusted colleagues and don’t want to take on the massive workloads left behind, she adds.



Faced with a large pension cut, Caspar Addyman resigned from his academic post without a clear plan. Credit: Kerry Harrison

Naomi Tyrrell, a social-research consultant based in Barnstaple, UK, set up a Facebook support group in 2020 called AltAc Careers UK to help people transition out of academia. Before COVID-19, she says, the most visible exoduses were from biosciences, computing and medical sciences — disciplines with obvious research opportunities in the private sector. “That’s changing a bit. [Being overworked] is a key factor right now” for those in all disciplines who are planning to leave, she says. The shift towards the for-profit model of UK university management has also frustrated people. As student enrolment increases, so do precarious contract-based positions — as well as complaints from staff about being taken for granted. “I hear things

like, ‘Nobody said thank you or asked if I was OK or how the university could support me,’” she says.

Jess Leveto, a sociologist at Kent State University in Ohio, hears similar grievances — particularly from academic mothers — in the United States. “For a long time, people invested in the ideal-worker mentality of ‘I’m going to produce as much as I can and show them I’m a good employee but the care wasn’t reciprocated,’ ” she says.

Leveto has surveyed roughly 1,000 US university faculty members over the past two years to monitor how the pandemic affected career outlooks, but has not yet published the results. In 2021, she says, respondents were angry and frustrated because they felt universities were too eager to put them back into classrooms amid pandemic safety concerns.

Leveto started a Facebook group called PhD Mamas in 2015 as a support system for academic mothers. It had fewer than 1,500 members, for years. Now, it has roughly 12,000 — and a dedicated subgroup of more than 300 mothers exploring how to leave academia. [Mothers in academia have had a stressful time](#): bogged down by childcare demands during the pandemic, many women’s careers suffered much more than men’s ([M. I. Cardell *et al.* Ann. Am. Thorac. Soc. 17, 1366–1370; 2020](#)).

Stacy, a psychology researcher at a US west-coast university who requested anonymity because she’s interviewing for industry jobs, tears up when explaining how she knew she wouldn’t become a full professor: “My productivity tanked trying to take care of a one-year-old during the early stages of the pandemic and quarantine, with no meaningful structural supports to offset the challenges.” She requested — but did not receive — a reduced teaching load, reduced time on university committees, teaching assistance and research support in the form of tuition breaks for graduate students.

In January 2022, she started sending out applications for industry positions that pay double her current salary. In some fields, such as hers, undergraduates and graduate students often receive no stipends. “My research happens because of free labour,” Stacy says, and she no longer wants to enable these conditions for the next generation of researchers.

Avoiding complicity in the inequities of academic training is contributing to mid-career researchers' resignations, says Meredith Gibson, interim chief-executive of the Association of Women in Science, a Washington DC-based advocacy organization. She and Kelsky anticipate the wave of resignations will continue. "There are people who will take roughly 18 months to lay the groundwork to pivot," Gibson says. "I don't think it's over."

Pushed out by systemic bias

Women of colour interviewed by *Nature*, in particular, describe how systemic inequality leaves them struggling to attain job security. Mary, a cancer biologist at a high-profile private university in the northeastern United States, has fretted for months over her pending grant application at the US National Cancer Institute (NCI). If she doesn't secure a major grant this year, she will have to leave her position.

Mary, who has asked for anonymity to protect her job prospects, blames structural bias and a lack of resources for holding her research back. In November 2008, she was hired for a chemical-engineering position at a public university in the southern United States; the role was created with funding available specifically for a qualified candidate from an under-represented background. But she was hired at the last minute who started alongside five others in the department, and she felt she was given inadequate lab space and no access to the equipment and mentoring she needed to secure NCI funding and tenure.



Nazzy Pakpour left academia for industry after being offered tenure but not a promotion. Credit: Ashley Villanueva

Although she didn't get the job security or the pay increase that comes with tenure, her research record was good enough to get her to her current, more prestigious institution — although she has been stuck at the same pay rate for more than ten years.

It's hard for Mary to accept that her academic career could soon be over. "This is a sad realization for someone like me. My mom doesn't have a formal education, my father died in a homeless shelter," she says. "I've beaten so many odds, but I can't beat this odd."

Nazzy Pakpour, a biologist who is a queer Iranian-American mother, resigned from her position at California State University, East Bay (CSUEB) in Hayward after she was offered tenure — but not a promotion — last October. The committee found that her portfolio of achievements met the criteria for her to get tenure, but denied her promotion to associate professor and a rise in pay owing to a lack of research productivity. "It all seemed very arbitrary and personal to me," says Pakpour, who studies parasitic infections.

“If you hire someone, invest this much time and energy, then why be punitive? If someone is underperforming, clearly communicate that in the five prior reviews,” she says, referring to the lack of feedback before she was up for promotion.

She says her university had written guidelines for tenure and promotion evaluations, but her department had not. Departments without explicit written criteria leave the door open for implicit biases against women and people of colour to tank their chances of promotion, she says. CSUEB’s biology-department chair, Brian Perry, confirms that Pakpour was given a written ‘faculty development plan’ outlining expectations when she was hired in 2015 — but noted that the department does not have its own written guidelines for promotion.

Since February, Pakpour has been a senior scientist at a biotechnology company in Davis, California. Her salary is higher, she works 40 hours a week, instead of 80, and she feels supported. “Knowing your worth is really important,” she says.

Post-exodus workforce

Will staff cuts and widespread resignations hamper faculty recruitment efforts? Some institutions are working hard to prevent that. In 2018, Barbara Boyan, dean of the college of engineering at Virginia Commonwealth University (VCU) in Richmond, and Susan Kornstein, executive director of the VCU Institute for Women’s Health, won a US National Science Foundation ADVANCE grant to increase recruitment, retention and advancement of diverse science-faculty members who are women. VCU Engineering did not lose any female faculty members because of the pandemic, says Boyan, who credits the grant — worth US\$3 million over five years — with preventing the loss of women.



Postdoctoral neuroscientist Sarah Tashjian keeps tabs on academic job market trends on social media. Credit: V. Urfalian

In 2021, two of three tenured women of colour have achieved the title of full professor at the engineering school — in part owing to nudging from Boyan. “Somebody has to tell them, ‘You are ready,’” she says. Kornstein adds that having so few professors from minority ethnic groups to mentor through advancement is “why recruitment and retention initiatives are so important”.

McKenzie, who studies the Australian workforce, wonders how these dynamics will shape academia for budding researchers. Will institutions bring in more junior people and replace longer-term contracts with shorter ones, she asks, thereby increasing instability?

Sarah Tashjian — a postdoctoral neuroscience researcher at California Institute of Technology in Pasadena, who is the first in her family to attend university — is watching current events play out on social media. She thinks the tenure denials in the past year will change academia by accelerating loss

of talent at early-career levels. Gibson anticipates that the academic job market is in for a rocky stretch — in part because the current wave of departing academics is happening amid a larger cultural shift, she says. “It’s [now] surprising to think you’d go into a tenure-track position and be somewhere for your whole career,” Gibson says.

Tashjian laments how career goal posts keep shifting. “When I started in 2015, ten first-author papers would write your ticket anywhere,” she says. “I have 29 publications and 16 of them are first-author.” But she’s unsure whether it’s enough to secure a tenure-track position. She’s giving herself three years on the academic job market before she’ll change her tack and look for industry positions. “[My team] studies motivation and irrational decision-making,” she notes. “At a certain point, it doesn’t make sense to continue what we call ‘costly persistence’.”

Nature **606**, 211-213 (2022)

doi: <https://doi.org/10.1038/d41586-022-01512-6>

This article was downloaded by **calibre** from <https://www.nature.com/articles/d41586-022-01512-6>

| [Section menu](#) | [Main menu](#) |

How engineers and drug developers are working to change childhood cancer's deadly calculus

[Download PDF](#)

- TECHNOLOGY FEATURE
- 30 May 2022

How engineers and drug developers are working to change childhood cancer's deadly calculus

A non-profit organization merges engineering and biology to accelerate drug development for childhood cancers.

- [Esther Landhuis](#) ⁰



Biologists and engineers worked together to create an inexpensive quail-egg platform to quickly test large numbers of drugs in living tissue. Credit: Erika Ellis

In a single motion, a sliding blade slices the bottoms off six speckled quail eggs, and their yolks plop into a six-well dish.

Quail eggs aren't common in research, and most biomedical scientists have never seen this guillotine-like device. But at the biotechnology laboratory of the Children's Cancer Therapy Development Institute (cc-TDI), just outside Portland, Oregon, these eggs are helping researchers to quickly prioritize drug candidates for long, costly mouse studies. Last December, cc-TDI published a description of this platform¹ in *Scientific Reports* — just one example of how the non-profit organization is breaking norms in cancer research as one of the only freestanding research labs focused on developing drugs for paediatric cancer.

Each year, some 400,000 children and adolescents around the world develop cancer. In the United States, cancer kills around 1,800 young people annually, more than all other diseases combined. Yet, since 1978, fewer than a dozen drugs developed specifically for childhood cancers have earned US Food and Drug Administration approval. (On average, 12 drugs for adult cancers reach the market every year.)

It's a cruel economic conundrum: despite their huge collective impact, individual childhood cancers are rare, and few companies are willing to invest the millions of dollars required to develop a drug with a tiny market. "How on Earth are you going to make money treating 300 kids a year with rhabdomyosarcoma?" asks Charles Keller, scientific director and founder of cc-TDI, referencing a rare type of cancer that forms in muscle and other soft tissues and that affects mostly children.

A physician-researcher with a background in biomedical engineering, Keller launched cc-TDI in 2015 to change that calculus. Partnering with biotech and pharmaceutical companies to vet experimental therapies for clinical testing, the institute has already helped to move a pair of drug candidates into nationwide phase I trials, including one for diffuse intrinsic pontine

glioma, a lethal brain tumour for which the survival rate and treatment options have not improved in several decades.

Flexible funding

Federal grants don't typically fund drug-validation and preclinical-development studies, so researchers aren't financially incentivized to complete them. A new mechanism, a promising drug target, perhaps a candidate drug — those are the kinds of project that tend to attract government investments.



Charles Keller (left) and Noah Berlow work together at cc-TDI. Credit: Erika Ellis

cc-TDI runs on a lean US\$2.5-million budget — of which just \$350,000 is supplied by grants from the US National Institutes of Health (NIH). The bulk comes from foundations, families and philanthropy. “It takes just as

much work to steward a relationship of trust with a donor as it does to write an NIH grant,” Keller says. One young woman raised more than \$980,000 for cc-TDI before dying of rhabdomyosarcoma in March, a month shy of her 21st birthday. A Portland-area philanthropist gave \$270,000.

Philanthropy and private donations can fund high-impact preclinical research that would struggle to attract federal dollars. With funding from multiple foundations, for instance, cc-TDI laid the groundwork for repurposing a class of antibiotic compounds called fluoroquinolones to prevent relapses in Ewing sarcoma, a rare cancer for which two drugs have failed clinical trials. Fluoroquinolones could enter clinical trials once cc-TDI secures funding to identify promising compounds and test them in more cell and animal models.

An engineer’s perspective

For tools to get the job done, the institute turns to engineers. Noah Berlow came on board in 2015 after obtaining an electrical engineering PhD at Texas Tech University in Lubbock. In his research, Berlow used applied maths and artificial intelligence to find cancer therapies, as part of a collaboration between Keller, then at the Oregon Health & Science University in Portland, and Ranadip Pal, an electrical engineer and Berlow’s thesis adviser at Texas Tech.

At cc-TDI, engineers and biologists work together to analyse drug-testing results alongside DNA- and RNA-sequencing data of tumours — resulting in massive data sets. Berlow says the engineer’s role is to help make sense of them. When intriguing features in the data emerge, biologists can work out what they mean. Although engineers rely on biologists’ expertise to contextualize what might appear as a smattering of stray data points, an engineer’s scant biomedical knowledge — and their fresh perspective — can prove advantageous.

“When you start making assumptions that you know how things work, cancer has a way of turning that on its head,” Berlow says.



Researchers examine quail-egg membranes (right) underneath the microscope.Credit: Erika Ellis

Berlow co-developed an automated screening tool that ranks by diagnosis likelihood all the possible cancers a person could have. This helps pathologists to decide quickly which confirmatory tests to conduct, and could prove especially useful in rural areas and developing countries that lack pathologists². Trained on 424 tissue slides of sarcoma tumours, the model is more than 88% effective at detecting all tested sarcoma subtypes.

Another engineer, Samuel Rasmussen, joined cc-TDI fresh out of university, where he studied mechanical engineering. Rasmussen put himself through Portland State University in Oregon by working nights at a local distribution warehouse of the farm-equipment manufacturer John Deere. He was part of a team of undergraduates doing a senior research project in early 2016 under Keller's supervision. Their charge: create a device to crack eggs without breaking the yolk.

The team's design didn't work, but Rasmussen kept tinkering. Experimenting over a mixing bowl at the student union, he determined that

removing the bottom of the egg with a knife could release the yolk unscathed. Within days, Rasmussen created a working prototype. Keller offered him a summer internship — and, six months later, hired him full time.

Rasmussen was first author of the *Scientific Reports* paper¹, in which he and colleagues placed drug-treated tumour cells onto shell-free quail embryos growing in lab dishes, providing a quick and inexpensive way to screen drugs on living tissue. Data from an 11-day quail-egg assay, which uses up to 200 eggs per screening at around 35 cents an egg, agreed with mouse data, even when results from mouse and lab-dish experiments differed, Keller says. That suggests the quail-egg system could be used to reliably select candidates for testing in studies using mice implanted with human tumours. Those mouse studies take ten or more weeks and cost tens of thousands of US dollars.

Because mouse studies “are really expensive and time-consuming”, says Maya Ridinger, a biologist at Cardiff Oncology, a biotech firm based in San Diego, California, scientists can investigate only a limited number of compounds, doses and models. Cardiff Oncology is working with cc-TDI to test onvansertib, a drug designed to treat a childhood liver cancer called hepatoblastoma. “I think the quail-egg system is a great opportunity,” says Ridinger.

Mission minded

Rasmussen’s work was funded by a John Deere dealership owner who gave money to cc-TDI after losing a niece to childhood cancer. The John Deere link was coincidental, but Keller has a knack for rallying diverse people to a singular mission — getting drugs into paediatric-cancer trials. In addition to nurturing connections with families and funders, Keller maintains close ties with pharmaceutical collaborators and groups that run clinical trials, to focus cc-TDI’s preclinical work on what is potentially translatable. “You probably can’t overstate that, because we’ve been curing cancer in mice for many years,” says Douglas Hawkins, a paediatric haematologist-oncologist at Seattle Children’s in Washington. Hawkins, who chairs the Children’s Oncology Group, a federally funded clinical-trial network that is conducting

one of the cc-TDI trials, adds: “Trying to take whatever we’ve learnt in the lab and apply it to humans, that’s been one of the harder things.”

Since 2004, the US National Cancer Institute has funded a preclinical research programme to evaluate compounds — mostly pharmaceutical drugs previously developed for adult cancers — for inclusion in paediatric cancer trials. For the five-year funding cycle that began in July 2021, the Pediatric Preclinical In Vivo Testing Consortium (PIVOT) provided \$5 million per year to a coordinating centre and seven research teams to test specific compounds in models in the lab. Among more than 140 drugs studied by the programme, only a few have proceeded to clinical testing, says paediatric oncologist and PIVOT director Malcolm Smith.



Samuel Rasmussen (right) was hired at cc-TDI after creating a working prototype of the quail-egg device as an undergraduate.Credit: Erika Ellis

At cc-TDI, Keller aims to beat those odds by focusing on team diversity and his belief that a great scientist can come from anywhere.

Andy Woods, for example, is a former tile contractor who left his business and moved his family to Oregon in 2017 to work at cc-TDI as a senior research associate. In October 2021, he published a paper³ on his daughter's kidney cancer, Wilms' tumour, describing how he and his colleagues used genomics to identify drug candidates for a subtype of the disease that responds poorly to standard therapies.

Another recent addition to cc-TDI is Tim Brown, a former vice-president of biotech company Genentech, based in South San Francisco, California. In 2015, Brown's 20-year-old son died from Duchenne muscular dystrophy. Brown connected with Keller through a cc-TDI research assistant who was part of the team that helped his son, then an undergraduate at the University of Portland, with eating, dressing and daily tasks as his disease progressed. Brown began volunteering at cc-TDI last October to honour his son's memory by applying his supply-chain and manufacturing expertise to projects such as automating the quail-egg assay.

The multidisciplinary team and culture of innovation were a big draw, Brown says. "There's really good connection between us folks who have a few years of experience in different industries, and these young scientists."

By casting a wide net, the institute "was, and always is, an experiment", Keller says. Its junior board of directors, which helps to plan local events and fundraising efforts, is open to young people aged 7 to 17. It has former vice-presidents of the semiconductor manufacturer Intel on its board of directors. And it hosts annual summer 'nanocourses', weeklong crash courses in the basics of childhood cancers, drug development and clinical trials, to train members of the public to liaise between cancer researchers and the community. "This is a grass-roots cause," Keller concludes, "where a few people who care a lot about a rare condition come together because they're driven by the mission."

Nature **606**, 214-215 (2022)

doi: <https://doi.org/10.1038/d41586-022-01513-5>

References

1. Rasmussen, S. V. *Sci. Rep.* **11**, 23302 (2021).
 2. Frankel, A. O. *et al. Mod. Pathol.* <https://doi.org/10.1038/s41379-022-01075-x> (2022).
 3. Woods, A. D. *et al. Pediatr. Blood Cancer* **69**, e29401 (2022).
-

This article was downloaded by **calibre** from <https://www.nature.com/articles/d41586-022-01513-5>

| [Section menu](#) | [Main menu](#) |

A down-to-earth approach to climate change

[Download PDF](#)

- WHERE I WORK
- 31 May 2022
- Clarification [31 May 2022](#)

A down-to-earth approach to climate change

Asmeret Asefaw Berhe researches how physical changes to soil affect how much carbon is released into the atmosphere.

- [Virginia Gewin](#) ⁰



Asmeret Asefaw Berhe is a biogeochemist at the University of California, Merced, and director of the US Department of Energy Office of Science. Credit: T.A. Ghezzehei for *Nature*

Humans are, of course, reliant on soil for food. But what many might not realize is that soil's rich biodiversity helps to regulate the composition of Earth's atmosphere by recycling and storing nutrients, such as carbon.

Growing up in Eritrea, my scientific training focused on the soil of east Africa — home to the earliest land cultivators, but now suffering from deforestation and desertification. I studied how carbon is lost through soil disturbance and degradation.

I've been in California since 2000, and in my work as a biogeochemist I study how physical changes to soil — from erosion, fire or changing climatic conditions — affect carbon dynamics, and how Earth helps to balance carbon levels.

I'm interested in how some soils hold on to organic carbon for hundreds, even thousands, of years without degrading — and how that stability controls the amount of carbon emitted to the atmosphere. My team at the University of California, Merced, has found that more than 70% of soil carbon in some temperate regions can be stored long-term at depths of up to 10 metres; this keeps it out of the atmosphere, where it can accelerate climate change.

To get such insights, we have to dig pits or collect samples to understand what happens deep underground. In this image, I'm on my belly (after a recent foot injury) examining clods at Merced Vernal Pools and Grassland Reserve soil pit, where I teach students how to describe soils in terms of their colour, clay content and ability to form stable clumps.

Earth and soil science is an area that desperately needs more diversity in its participants. My goal as professor and associate dean for graduate education is to create a welcoming environment that will attract under-represented groups. If we continue to exclude scholars from minoritized communities, we're not just hurting them, we're hurting the science needed to help us adapt to climate change.

Nature **606**, 218 (2022)

doi: <https://doi.org/10.1038/d41586-022-01500-w>

Updates & Corrections

- **Clarification 31 May 2022:** An earlier version of this story mistakenly referred to Asmeret Asefaw Berhe as Asmeret Berhe.

This article was downloaded by **calibre** from <https://www.nature.com/articles/d41586-022-01500-w>

| [Section menu](#) | [Main menu](#) |

Research

- **[Probing CP symmetry and weak phases with entangled double-strange baryons](#)** [01 June 2022]
Article • Using spin-entangled baryon–antibaryon pairs, the BESIII Collaboration reports on high-precision measurements of potential charge conjugation and parity (CP)-symmetry-violating effects in hadrons.
- **[Quantum computational advantage with a programmable photonic processor](#)** [01 June 2022]
Article • Gaussian boson sampling is performed on 216 squeezed modes entangled with three-dimensional connectivity⁵, using Borealis, registering events with up to 219 photons and a mean photon number of 125.
- **[The mosaic oat genome gives insights into a uniquely healthy cereal crop](#)** [18 May 2022]
Article • Assembly of the hexaploid oat genome and its diploid and tetraploid relatives clarifies the evolutionary history of oat and allows mapping of genes for agronomic traits.
- **[Neuropathic pain caused by miswiring and abnormal end organ targeting](#)** [25 May 2022]
Article • Longitudinal imaging of nerve fibres in mice reveals that reinnervation after nerve injury can lead to neuropathic pain, which is mediated through aberrant patterns of reinnervation in denervated areas by nociceptors.
- **[Gene regulation by gonadal hormone receptors underlies brain sex differences](#)** [04 May 2022]
Article • A study maps neuronal genomic targets of oestrogen receptor- α and shows how they coordinate brain sexual differentiation, concluding that the genome remains responsive to hormonal changes after structural dimorphisms have been established.
- **[Developmental dynamics of two bipotent thymic epithelial progenitor types](#)** [25 May 2022]
Article • Two populations of thymic progenitors are identified, an early bipotent progenitor type biased towards cortical epithelium and a postnatal bipotent progenitor type biased towards medullary epithelium.
- **[Fundamental immune–oncogenicity trade-offs define driver mutation fitness](#)** [11 May 2022]

Article • A mathematical framework to estimate the fitness of cancer driver mutations by integrating mutational bias, oncogenicity and immunogenicity finds fundamental trade-offs in cancer evolution.

- **MCM complexes are barriers that restrict cohesin-mediated loop extrusion** [18 May 2022]

Article • Single-nucleus Hi-C of embryos, polymer simulations and single-molecule imaging collectively reveal that MCM complexes influence genome folding and gene expression by impeding DNA loop extrusion.

[Download PDF](#)

- Article
- Open Access
- [Published: 01 June 2022](#)

Probing CP symmetry and weak phases with entangled double-strange baryons

- [The BESIII Collaboration](#)

Nature volume **606**, pages 64–69 (2022)

- 814 Accesses
- 59 Altmetric
- [Metrics details](#)

Subjects

- [Experimental nuclear physics](#)
- [Experimental particle physics](#)

Abstract

Though immensely successful, the standard model of particle physics does not offer any explanation as to why our Universe contains so much more matter than antimatter. A key to a dynamically generated matter–antimatter asymmetry is the existence of processes that violate the combined charge conjugation and parity (CP) symmetry¹. As such, precision tests of CP

symmetry may be used to search for physics beyond the standard model. However, hadrons decay through an interplay of strong and weak processes, quantified in terms of relative phases between the amplitudes. Although previous experiments constructed CP observables that depend on both strong and weak phases, we present an approach where sequential two-body decays of entangled multi-strange baryon–antibaryon pairs provide a separation between these phases. Our method, exploiting spin entanglement between the double-strange Ξ^- baryon and its antiparticle² $(\bar{\Xi}^+)$, has enabled a direct determination of the weak-phase difference, $(\zeta_P - \zeta_S) = (1.2 \pm 3.4 \pm 0.8) \times 10^{-2}$ rad. Furthermore, three independent CP observables can be constructed from our measured parameters. The precision in the estimated parameters for a given data sample size is several orders of magnitude greater than achieved with previous methods³. Finally, we provide an independent measurement of the recently debated Λ decay parameter α_Λ (refs. ^{4,5}). The $(\Lambda \bar{\Lambda})$ asymmetry is in agreement with and compatible in precision to the most precise previous measurement⁴.

Main

Small violations of CP symmetry are predicted by the standard model^{6,7} and are a well established phenomenon in weak decays of mesons. However, the mechanisms of the standard model are too specific to yield effects of a size that can explain the observed matter–antimatter asymmetry of the Universe^{8,9}. Therefore, CP tests can be considered a promising area to search for physics beyond the standard model^{10,11}. So far, no CP-violating effects beyond the standard model have been observed in the baryon sector¹².

In general, CP symmetry is tested by comparing the decay patterns of a particle to those of its antiparticle. Many CP-symmetry tests in hadron decays rely on strong interactions of the final particles to reveal the signal. This strategy is applied in the determination of the ratio ε'/ε , quantifying the difference between the two-pion decay rates of the two weak eigenstates of neutral kaons. The ε'/ε measurement constitutes the only observation of direct CP violation for light strange hadrons^{13,14} and provides the most

stringent test of contributions beyond the standard model in strange quark systems¹⁵. This strategy, however, comes at a price: it is difficult to disentangle, in a model-independent way, the contributions from weak interactions or processes beyond the standard model from those of strong processes. Approaches that do not rely on strong interactions require that the kaon decay into four final-state particles¹⁶.

Baryons provide additional information through spin measurements. Known examples involving three-body decays are spin correlations and polarization in nuclear and neutron β decays¹⁷. Sequential two-body decays of entangled multi-strange baryon–antibaryon pairs provide another, hitherto unexplored, diagnostic tool to separate the strong and the weak phases.

In this work we explore spin correlations in weak two-body decays of spin- $\frac{1}{2}$ baryons. The spin direction of the parent baryon manifests itself in the momentum direction of the daughter particle, enabling straightforward experimental access to the spin properties. Spin- $\frac{1}{2}$ baryon decays are described by a parity-conserving (P-wave) and a parity-violating (S-wave) amplitude, quantified in terms of the decay parameters α_Y , β_Y and γ_Y (ref. [18](#)). The Y refers to the decaying parent hyperon (for example, Λ or Ξ^-). These parameters are constrained by the relation $\sqrt{(\alpha_Y^2 + \beta_Y^2 + \gamma_Y^2)} = 1$. By defining the parameter ϕ_Y according to

$$\begin{aligned} \beta_Y &= \sqrt{1 - \alpha_Y^2} \sin \phi_Y, \\ \gamma_Y &= \sqrt{1 - \alpha_Y^2} \cos \phi_Y, \end{aligned} \quad (1)$$

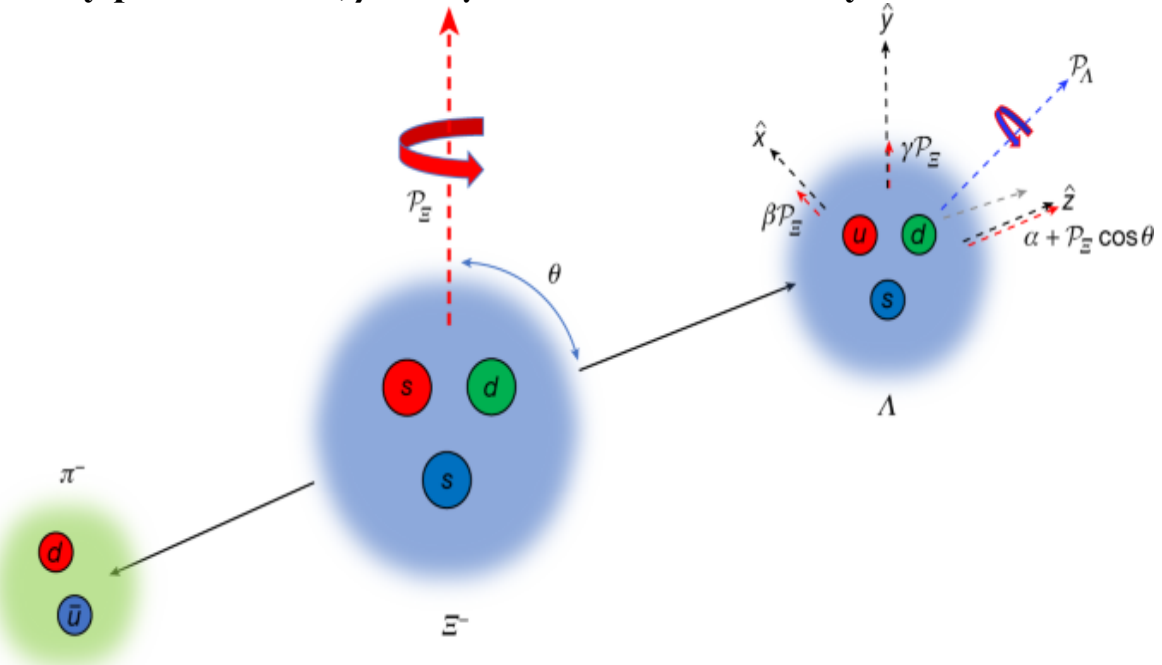
the decay is completely described by two independent parameters α_Y and ϕ_Y . In the standard experimental approach^{[3,4,19,20,21](#)}, the initial baryon is produced in a well defined spin polarized state, which allows access to the decay parameters through the angular distribution of the final-state particles. For sequentially decaying baryons, for example, the decay of the double-strange Ξ^- baryon into $\Lambda\pi^-$, two effects are possible: 1) a polarized Ξ^- transfers its polarization \mathbf{P}_{Ξ^-} to the daughter Λ ; 2) a longitudinal component of the daughter Λ polarization is induced by the Ξ^- decay, even if the Ξ^-

polarization has no component in this direction. In a reference system with the $(\hat{\bf z})$ axis along the Λ momentum in the Ξ^- rest frame and the $(\hat{\bf y})$ axis along $(\{\bf P\})_{\perp} \varXi$ times $(\hat{\bf z})$, the Λ polarization vector is given by¹⁸

$$\begin{aligned}
 & \$\$ \begin{array}{c} \{\bf c\} \{\{\bf P\}\}_{\perp} \varLambda \cdot \\
 \hat{\bf z} = \frac{\alpha}{\sqrt{1-\alpha^2}} + (\{\bf P\}_{\perp} \varLambda) \cdot \hat{\bf z} \\
 \hat{\bf z} \{1+\alpha\}_{\perp} \varLambda \{\bf P\}_{\perp} \varLambda \cdot \hat{\bf z} \\
 \hat{\bf z} \{1+\alpha\}_{\perp} \varLambda \sqrt{1-\alpha^2} \frac{\sin \phi}{\sqrt{1-\alpha^2}} \hat{\bf z} \\
 \{1+\alpha\}_{\perp} \varLambda \hat{\bf z} + \cos \phi \hat{\bf z} \hat{\bf z} \\
 \hat{\bf z} \end{array} \$\$ \\
 (2)
 \end{aligned}$$

as illustrated in Fig. 1. This means that the longitudinal ($(\hat{\bf z})$) component depends on α_{Ξ} , and the transversal components are rotated by the angle ϕ_{Ξ} with respect to the Ξ^- polarization.

Fig. 1: Illustration of the polarization vectors of Ξ^- and Λ in relation to the decay parameters α , β and γ of the $\Xi^- \rightarrow \Lambda \pi^-$ decay.



The Λ polarization $\langle \{\mathbf{P}\} \rangle_{\Lambda}^{\{-\}}$ has a component in the longitudinal as well as the transverse direction, where the former (\hat{z}) is defined by the Λ momentum. The longitudinal component depends on the Λ emission angle and arises from the transferred Ξ^- polarization $\langle \{\mathbf{P}\} \rangle_{\Xi}^{\{-\}}$ combined with the decay parameter α . The remaining Ξ^- polarization is transferred to the transverse components according to $\langle \beta \rangle_{\varXi} \langle \mathbf{P} \rangle_{\varXi}^{\{-\}} (\hat{x})$ and $\langle \gamma \rangle_{\varXi} \langle \mathbf{P} \rangle_{\varXi}^{\{-\}} (\hat{y})$. Quarks: d , down; s , strange; u , up; \bar{u} , antiup.

The decay parameter α_{Ξ} appears explicitly in the angular distribution of the direct decay $\Xi^- \rightarrow \Lambda \pi^-$, whereas the sequential decay distribution of the daughter Λ depends on both α_{Λ} and ϕ_{Ξ} . CP symmetry implies that the baryon decay parameters α and ϕ equal those of the antibaryon $\bar{\alpha}$ and $\bar{\phi}$ but with opposite sign. Hence, CP violation can be quantified in terms of the observables

$$\begin{aligned} \langle A \rangle_{\rm CP}^Y &= \frac{\alpha_Y + \bar{\alpha}_Y}{\alpha_Y - \bar{\alpha}_Y}, \\ \langle \rm CP \rangle &= \frac{\phi_Y + \bar{\phi}_Y}{2}. \end{aligned} \quad (3)$$

CP violation can only be observed if there is interference between CP-even and CP-odd terms in the decay amplitude. Because the decay amplitude for $\Xi^- \rightarrow \Lambda \pi^-$ consists of both a P-wave and an S-wave part, the leading-order contribution to the CP asymmetry, $\langle A \rangle_{\rm CP}^Y$, can be written as

$$\langle A \rangle_{\rm CP}^Y \approx -\tan(\delta_P - \delta_S) \tan(\xi_P - \xi_S), \quad (4)$$

where $\tan(\delta_P - \delta_S) = \beta/\alpha$ denotes the strong-phase difference of the final-state interaction between the Λ and π^- from the Ξ^- decay. CP-violating effects would manifest themselves in a nonzero weak-phase difference $\xi_P - \xi_S$ (refs. 22,23,24), an observable that is complementary to the kaon decay parameter ε'

(refs. [13,14,25](#)) because the latter only involves an S-wave. The strong-phase difference can be extracted from the ϕ_{Ξ} parameter, and is found to be small^{[3,26](#)}: (-0.037 ± 0.014) . Hence, CP-violating signals in $\langle A_{CP} \rangle$ are strongly suppressed and difficult to interpret in terms of the weak-phase difference.

An independent CP-symmetry test in $\Xi^- \rightarrow \Lambda \pi^-$ is provided by determining the value of $\Delta\phi_{CP}$. At leading order, this observable is related directly to the weak-phase difference:

$$\frac{\langle \xi_P - \xi_S \rangle}{\langle \alpha \rangle} = \frac{\beta + \bar{\beta}}{\alpha - \bar{\alpha}} \approx \frac{\sqrt{1 - \langle \alpha \rangle^2}}{\langle \alpha \rangle} \Delta\phi_{CP}, \quad (5)$$

where $\langle \alpha \rangle = (\alpha - \bar{\alpha})/2$, and can be measured even if $\delta_P = \delta_S$. The absence of a strong suppression factor therefore improves the sensitivity to CP-violation effects by an order of magnitude with respect to that of the $\langle A_{CP} \rangle$ observable^{[22,23](#)}. To measure $\Delta\phi_{CP}$ using the standard polarimeter technique from refs. [21,28](#) requires beams of polarized Ξ^- and $\langle \bar{\Xi} \rangle$. In such experiments the precision is limited by the magnitude of the polarization and the accuracy of the polarization determination, which in turn is sensitive to asymmetries in the production mechanisms^{[27](#)}. In fact, no experiment with a polarized $\langle \bar{\Xi} \rangle$ has been performed, and the polarization of the Ξ^- beams were below 5% (ref. [3](#)). Here we present an alternative approach, in which the baryon–antibaryon pair is produced in a spin-entangled CP eigenstate and all decay sequences are analysed simultaneously.

To the best of our knowledge, no direct measurements of any of the asymmetries defined in equation (3) have been performed for the Ξ^- baryon. The HyperCP experiment^{[28](#)}, designed for the purpose of CP tests in baryon decays, used samples of around 10^7 – 10^8 Ξ^- and $\langle \bar{\Xi} \rangle$ events to determine the products $\alpha_{\Xi}\alpha_A$ and $\langle \bar{\alpha} \rangle \langle \bar{\Xi} \rangle$. From these measurements, the sum $\langle \bar{\alpha} \rangle \langle \Lambda \rangle$.

$(\{A\}_{\{\rm CP\}})^{\{\Lambda\}} + \{A\}_{\{\rm CP\}}^{\{\Xi\}}$) was estimated to be $(0.0 \pm 5.5 \pm 4.4) \times 10^{-4}$, where the first uncertainty is statistical and the second systematic. In addition to the aforementioned problem of the smallness of ϕ_{Ξ} , which limits the sensitivity of $(\{A\}_{\{\rm CP\}})^{\{\Xi\}}$ to CP violation, an observable defined as the sum of asymmetries comes with other drawbacks: if $(\{A\}_{\{\rm CP\}})^{\{\Lambda\}}$ and $(\{A\}_{\{\rm CP\}})^{\{\Xi\}}$ have opposite signs, the sum could be consistent with zero even in the presence of CP-violating effects. A precise interpretation therefore requires an independent measurement of $(\{A\}_{\{\rm CP\}})^{\{\Lambda\}}$ with matching precision. The most precise result so far is a recent BESIII measurement⁴ where $(\{A\}_{\{\rm CP\}})^{\{\Lambda\}}$ was found to be $(-6 \pm 12 \pm 7) \times 10^{-3}$. Furthermore, ref.⁴ revealed a 17% disagreement with previous measurements on the α_A parameter²⁶, a result that rapidly gained some support from a re-analysis of CLAS data⁵. Although the CLAS result is in better agreement with BESIII than with the Particle Data Group value from 2018 and earlier, there is a discrepancy between the CLAS and BESIII results that needs to be understood. This is particularly important because many physics quantities from various fields depend on the parameter α_A . Examples include baryon spectroscopy, heavy-ion physics and hyperon-related studies at the Large Hadron Collider^{29,30,31,32,33,34}.

In this work we apply a newly designed method^{2,35} to study entangled, sequentially decaying baryon–antibaryon pairs in the process $e^+ e^- \rightarrow J/\psi \rightarrow \bar{\Lambda} \Lambda \pi^+ \pi^-$. This approach enables a direct measurement of all weak decay parameters of the $\Xi^- \rightarrow \Lambda \pi^-$, $\Lambda \rightarrow p \pi^-$ decay, and the corresponding parameters of the $\bar{\Lambda} \Lambda$. The production and multi-step decays can be described by nine kinematic variables, here expressed as the helicity angles $\{\boldsymbol{\xi}\} = (\theta, \theta_{\bar{\Lambda}}, \varphi_{\bar{\Lambda}}, \theta_{\Lambda}, \varphi_{\Lambda}, \theta_p, \varphi_p, \theta_{\bar{p}}, \varphi_{\bar{p}})$. The first, θ , is the Ξ^- scattering angle with respect to the e^+ beam in the centre-of-momentum system of the reaction. The angles θ_A and φ_A ($\theta_{\bar{\Lambda}}$, $\varphi_{\bar{\Lambda}}$) are defined by the Λ ($\bar{\Lambda}$) direction in a reference system denoted $\{\boldsymbol{\xi}\}$

$\{\mathcal{R}\}_{\bar{X}_i} (\{\mathcal{R}\}_{\bar{X}_i})$ ($\{\mathcal{R}\}_{\bar{X}_i}$) where Ξ^- ($\{\bar{X}_i\}^+$) is at rest and where the \hat{z} axis points in the direction of the Ξ^- ($\{\bar{X}_i\}^+$) in the centre-of-momentum system. The \hat{y} axis is normal to the production plane. The angles θ_p and φ_p ($\{\theta\}_{\bar{p}}$ and $\{\varphi\}_{\bar{p}}$) give the direction of the proton (antiproton) in the Λ ($\{\bar{\Lambda}\}$) rest system, denoted $\{\mathcal{R}\}_{\bar{\Lambda}}$ ($\{\mathcal{R}\}_{\bar{\Lambda}}$), with the \hat{z} axis pointing in the direction of the Λ ($\{\bar{\Lambda}\}$) in the $\{\mathcal{R}\}_{\bar{X}_i}$ ($\{\mathcal{R}\}_{\bar{X}_i}$) system and the \hat{y} axis normal to the plane spanned by the direction of the Ξ^- ($\{\bar{X}_i\}^+$) and the direction of the Λ ($\{\bar{\Lambda}\}$). The structure of the nine-dimensional angular distribution is determined by eight global (that is, independent of the Ξ^- scattering angle) parameters $\{\boldsymbol{\omega}\} = (\alpha_{\psi}, \varDelta\Phi, \alpha_{\mu}, \alpha_{\nu}, \phi_{\mu}, \phi_{\nu}, \alpha_{\lambda}, \alpha_{\bar{\lambda}})$, and can be written in a modular form as³⁵:

$$\begin{aligned}
& \$\{\mathcal{W}\}(\{\boldsymbol{\omega}\}; \{\boldsymbol{\xi}\}) = \mathop{\sum}_{\{\mu, \nu=0\}^3} \{C\}_{\{\mu, \nu\}} \\
& \quad \mathop{\sum}_{\{\mu', \nu'=0\}^3} \{a\}_{\{\mu, \nu\}} \{a\}_{\{\mu', \nu'\}} \{a\}_{\{\mu', \nu'\}} \{a\}_{\{\mu, \nu\}} \\
& \quad \{a\}_{\{\mu, \nu\}} \{a\}_{\{\mu', \nu'\}} \{a\}_{\{\mu', \nu'\}} \{a\}_{\{\mu, \nu\}}. \\
(6)
\end{aligned}$$

Here $C_{\mu\nu}(\theta; \alpha_{\psi}, \Delta\Phi)$ is a 4×4 spin density matrix, defined in the aforementioned reference systems $\{\mathcal{R}\}_{\bar{X}_i}$ and $\{\mathcal{R}\}_{\bar{\Lambda}}$, describing the spin configuration of the entangled hyperon–antihyperon pair. The parameters α_{ψ} and $\Delta\Phi$ are related to two production amplitudes, where α_{ψ} parameterizes the Ξ^- angular distribution. The $\Delta\Phi$ is the relative phase between the two production amplitudes (in the so-called helicity representation)³⁶ and governs the polarization P_y of the produced Ξ^- and $\{\bar{X}_i\}^+$ as well as their spin correlations C_{ij} . The matrix elements are related to $P_y = P_y(\theta)$ and $C_{ij} = C_{ij}(\theta)$ in the following way:

$$\begin{aligned}
\$ \{C\}_{\mu\nu} = & (1 + \{\alpha\}_{\psi} \cos^2 \theta) \begin{array}{c} \text{cccc} \\ 1 & 0 & P_y & 0 \\ 0 & 0 & C_{xx} & 0 \\ 0 & 0 & C_{xz} & -P_y \\ 0 & 0 & C_{yy} & 0 \\ 0 & 0 & -C_{xz} & 0 \\ 0 & 0 & C_{zz} \end{array} \end{aligned}$$

(7)

The matrices $\langle\langle a\rangle_\mu \nu\rangle^Y\rangle$ in equation (6) represent the propagation of the spin density matrices in the sequential decays. The elements of these 4×4 matrices are parameterized in terms of the weak decay parameters α_Y and ϕ_Y as well as the helicity angles: $\langle\langle a\rangle_\mu \nu\rangle^Y\rangle$ in reference system $\langle\langle \mathcal{R}_X \rangle\rangle$, $\langle\langle a\rangle_\mu \nu\rangle^Y\rangle$ in system $\langle\langle \mathcal{R}_\Lambda \rangle\rangle$, and $\langle\langle a\rangle_\mu \nu\rangle^Y\rangle$ in system $\langle\langle \mathcal{R}_\Xi \rangle\rangle$. The full expressions of $C_{\mu\nu}$ and $\langle\langle a\rangle_\mu \nu\rangle^Y\rangle$ are given in ref. [35](#).

We have carried out our analysis on a data sample of $(1.3106 \pm 0.0070) \times 10^9$ J/ψ events collected in electron–positron annihilations with the multi-purpose BESIII detector^{[37](#)}. The J/ψ resonance decays into the $\langle\langle \bar{\chi}_i \rangle\rangle$ final state with a branching fraction^{[26](#)} of $(9.7 \pm 0.8) \times 10^{-4}$. Our method requires exclusively reconstructed $\langle\langle \bar{\chi}_i \rangle\rangle$ to $\langle\langle \bar{\Lambda} \rangle\rangle$ events. The final-state particles are measured in the main drift chamber, where a superconducting solenoid provides a magnetic field allowing momentum determination with an accuracy of 0.5% at $1.0 \text{ GeV}/c$. The $\Lambda (\langle\langle \bar{\Lambda} \rangle\rangle)$ candidates are identified by combining $p\pi^- (\langle\langle \bar{p} \rangle\rangle)$ pairs and the $\Xi^- (\langle\langle \bar{\Xi} \rangle\rangle)$ candidates by subsequently combining $\Lambda\pi^- (\langle\langle \bar{\Lambda} \rangle\rangle)$ pairs. Because it was found that the long-lived Ξ^- and $\langle\langle \bar{\Xi} \rangle\rangle$ can only be reconstructed with sufficient quality if they fulfil $|\cos\theta| < 0.84$, only

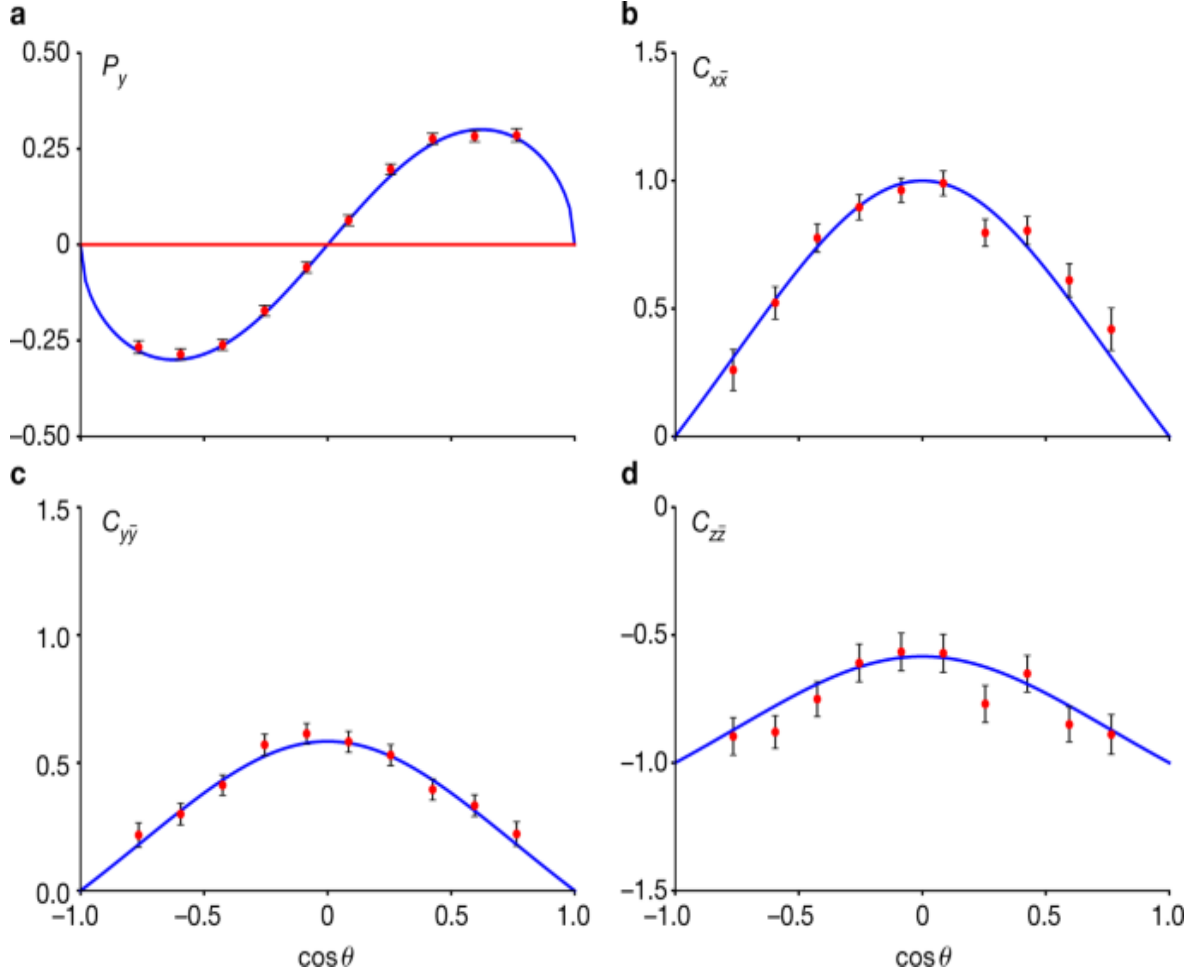
Ξ^- and $(\{\bar{X}_i\})^{(+})$ reconstructed within this range were considered. After applying all selection criteria, $73,244 (\{\bar{\text{var}}X_i\}^{-})$ $(\bar{\text{var}}X_i)^{(+})$ event candidates remain in the sample. The number of background events in the signal is estimated to be 199 ± 17 . More details of the analysis are given in Methods.

For each event, the complete set of the kinematic variables ξ is calculated from the intermediate and final-state particle momenta. The physical parameters in ω are then determined from ξ by an unbinned maximum log-likelihood fit where the multidimensional reconstruction efficiency is taken into account. The details of the maximum log-likelihood fit procedure and the systematic uncertainties are described in Methods.

The results of the fit, that is, the weak decay parameters $\Xi^- \rightarrow \Lambda\pi^-$ and $(\{\bar{\text{var}}X_i\}^{(+})$ to $\bar{\text{var}}\Lambda(\{\pi\}^{(+})$, as well as the production-related parameters α_ψ and $\Delta\Phi$, are summarized in Table 1. To illustrate the fit quality, the diagonal spin correlations and the polarization defined in equation (7) are shown in Fig. 2. The upper-left panel of Fig. 2 shows that the Ξ^- baryon is polarized with respect to the normal of the production plane. The maximum polarization is approximately 30%, as shown in the figure. The data points are determined by independent fits for each $\cos\theta$ bin, without any assumptions on the $\cos\theta$ dependence of $C_{\mu\nu}$. The red curves represent the angular dependence obtained with the parameters α_ψ and $\Delta\Phi$ determined from the global maximum log-likelihood fit. The independently determined data points agree well with the globally fitted curves.

Table 1 Summary of results

Fig. 2: Polarization in and spin correlations of the $(e^+e^-)\rightarrow(\bar{\text{var}}X_i)^{-}\{\bar{\text{var}}X_i\}^{(+})$ reaction.



a, Polarization in the $e^+e^- \rightarrow \Xi^- \bar{\Xi}^0$ reaction. **b–d**, Spin correlations of the $e^+e^- \rightarrow \Xi^- \bar{\Xi}^0$ reaction. The coordinate systems $(\mathcal{R}_\Xi, \mathcal{X}_\Xi)$ and $(\mathcal{R}_{\bar{\Xi}}, \bar{\mathcal{X}}_{\bar{\Xi}})$ of the Ξ^- and $(\bar{\Xi}^0)^+$, respectively, are described in the text. The data points are determined independently in each bin of the Ξ^- cosine scattering angle in the e^+e^- centre-of-momentum system. The blue curves represent the expected angular dependence obtained with the production parameters α_ψ and $\Delta\Phi$ from the global maximum log-likelihood fit. The error bars indicate the statistical uncertainties.

The extracted values of α_{Ξ} , ϕ_{Ξ} , α_A and Λ and their correlations allow for three independent CP symmetry tests. The asymmetry $A_{CP}(\Xi^-)$ is measured for the first time and found to

be $(6 \pm 13 \pm 6) \times 10^{-3}$, where the first uncertainty is statistical and the second systematic. The corresponding standard model (SM) prediction²⁴ is $\langle A \rangle_{\{\rm CP\}, \{\rm SM\}}^{\{\Xi\}} = (-0.6 \pm 1.6) \times 10^{-3}$.

The result for the decay parameter $\langle |\bar{\phi}| \rangle_{\{\Xi\}}$ is, to our knowledge, the first measurement of its kind for a weakly decaying antibaryon. By combining this parameter with the corresponding ϕ_{Ξ} measurement, the CP asymmetry $\langle \varDelta \phi \rangle_{\{\rm CP\}}^{\{\Xi\}}$ can be determined, and is found to be $(-5 \pm 14 \pm 3) \times 10^{-3}$ rad. Because this result is consistent with zero, we can improve our knowledge of the value of ϕ_{Ξ} by assuming CP symmetry and then calculating the mean value of ϕ_{Ξ} and $\langle |\bar{\phi}| \rangle_{\{\varDelta \phi\}}$. This procedure yields $\langle \phi_{\Xi} \rangle = 0.016 \pm 0.014 \pm 0.007$ rad, which differs from the HyperCP measurement, $\phi_{\Xi, \text{HyperCP}} = -0.042 \pm 0.011 \pm 0.011$ rad, by 2.6 standard deviations³. It is noteworthy that our method yields a precision in $\langle \phi_{\Xi} \rangle$ that is similar to that of the HyperCP result, despite the three-orders-of-magnitude larger data sample of the latter measurement. This demonstrates the intrinsically high sensitivity that can be achieved with entangled baryon–antibaryon pairs.

The measurement of $\langle \phi_{\Xi} \rangle$, together with the mean value $\langle \alpha_{\Xi} \rangle = -0.373 \pm 0.005 \pm 0.002$, enables a direct determination of the strong-phase difference, which is found to be $(\delta_P - \delta_S) = (-4.0 \pm 3.3 \pm 1.7) \times 10^{-2}$ rad. This is consistent with the standard model predictions obtained in the framework of heavy-baryon chiral perturbation theory²⁴ of $(1.9 \pm 4.9) \times 10^{-2}$ rad but in disagreement with the value $(10.2 \pm 3.9) \times 10^{-2}$ rad that one obtains from the HyperCP ϕ_{Ξ} measurement³ by using $\alpha_{\Xi} = -0.376$ from this work. Because the $(\delta_P - \delta_S)$ value obtained in our analysis is consistent with zero, a calculation of the weak-phase difference from equation (4) is unfeasible. Instead, we apply equation (5), which yields $(\xi_P - \xi_S) = (1.2 \pm 3.4 \pm 0.8) \times 10^{-2}$ rad. This is one of the most precise tests of the CP symmetry for strange baryons and the first direct measurement of the weak-phase difference for any baryon. The corresponding standard model prediction²⁴ is $(\xi_P - \xi_S)_{\text{SM}} = (1.8 \pm 1.5) \times 10^{-4}$ rad.

Sequential Ξ^- decays also provide an independent measurement of the Λ decay parameters α_Λ and $\langle \bar{\alpha} \rangle_{\bar{\Lambda}}$. Being the lightest baryon with strangeness, Λ appear in the decay chain of many other baryons (Σ^0 , Ξ^0 , Ξ^- , Ω , Λ_c and so on) decay with appreciable fractions into final states containing Λ . The measurements of spin observables^{38,39,40} and decay parameters of heavier baryons^{41,42} therefore implicitly depend on α_Λ . Furthermore, because decaying Λ and $\bar{\Lambda}$ beams are used for producing polarized proton and antiproton beams⁴³, all physics from such experiments rely on a correct determination of α_Λ . The value of $\alpha_\Lambda = 0.757 \pm 0.011 \pm 0.008$ measured in this analysis is in excellent agreement with that obtained from the $\langle J/\psi \rightarrow \bar{\Lambda} \bar{\Lambda} \rangle$ analysis of BESIII⁴, although it disagrees with the result from the re-analysis of CLAS data⁵. The precision of our measurement is similar to that of the $\langle J/\psi \rightarrow \bar{\Lambda} \bar{\Lambda} \rangle$ study⁴, despite being based on a data sample that was six times smaller. The larger sensitivity is primarily explained by the fact that α_Λ in equation (6) appears in a product with the polarization, which is much larger in the case of Λ baryons from Ξ^- decays compared to those directly produced in $\langle J/\psi \rightarrow \bar{\Lambda} \bar{\Lambda} \rangle$. Furthermore, the multi-step process enhances the angular correlations between the baryons and antibaryons to such an extent that α_Ξ and α_Λ can be measured with the same precision even if the $\langle \bar{\chi}^- \bar{\chi}^+ \rangle$ pair is produced unpolarized².

To summarize, this Article presents a very sensitive test of CP symmetry. This test provides a hunting ground for physics beyond the standard model in strange hadrons that is complementary to ε'/ε measurements in kaon decays⁴⁴. The contributions to ε and ε' , from hyperon decays on the one hand and kaon decays on the other, are described by different combinations of quark operators. In addition, hyperons provide information on the spin structure of the operators that is not possible to obtain from kaon decays. When applied to future measurements with larger datasets at BESIII⁴⁵, the upcoming PANDA experiment at FAIR⁴⁶ and the proposed Super-Charm Tau Factory projects in China and Russia^{47,48}, our method has potential to reach the required precision for CP-violating signals, provided such effects exist.

Methods

Monte Carlo simulation

For the selection and optimization of the final event sample, estimation of background sources as well as normalization for the fit method, Monte Carlo simulations have been used. The simulation of the BESIII detector is implemented in the simulation software GEANT4^{50,51}. GEANT4 takes into account the propagation of the particles in the magnetic field and particle interactions with the detector material. The simulation output is digitized, converting energy loss to pulse heights and points in space to channels. In this way the Monte Carlo digitized data have the same format as the experimental data. The production of the J/ψ is simulated by the Monte Carlo event generator KKMC⁵². Particle decays are simulated using the package BesEvtGen^{53,54,55}, where the properties of mass, branching ratios and decay lengths come from the world-averaged values²⁶. We find that although the mass of the Λ in our data agrees with the established value, that of the Ξ is 95 keV/ c^2 above the central value of the world average²⁶, $m_{\Xi,\text{PDG}} = 1,321.71 \pm 0.07 \text{ MeV}/c^2$ (PDG, Particle Data Group). Hence, we have adjusted the input mass value in the simulation accordingly⁵⁵.

The signal channels used for optimization and consistency checks are implemented with the helicity formalism and with parameter values in close proximity to the results presented in Table 1.

Selection criteria

The data were accumulated during two run periods, in 2009 and 2012, where the later set is approximately five times larger than the earlier. For the analysis all charged final-state particles have to be reconstructed. The main drift chamber of the BESIII experimental set-up is used for reconstructing the charged-particle tracks. At least three positively and three negatively charged tracks are required, each track fulfilling the condition that $|\cos\theta_{\text{LAB}}| < 0.93$, where θ_{LAB} is the polar angle with respect to the positron beam direction. The momentum distributions of protons and pions from the signal process are well separated and do not overlap, as shown in Extended Data

Fig. 1. Therefore a simple momentum criterion suffices for particle identification: $p_{\text{pr}} > 0.32 \text{ GeV}/c$ and $p_\pi < 0.30 \text{ GeV}/c$ for protons and pions, respectively. The probability of misidentifying a proton (antiproton) for a π^+ (π^-) is 0.17% (0.18%). Only events with at least one proton, one antiproton, two negatively and two positively charged pions are saved for further analysis. Each Ξ decay chain is reconstructed separately, and is here described for the sequence $\Xi^- \rightarrow \Lambda\pi^- \rightarrow p\pi^-\pi^-$. To find the correct Ξ^- and Λ particles all proton and π^- candidates are combined together. The Λ and Ξ^- particles are reconstructed through vertex fits by first combining the $(p\{\pi\}_{i}^{-})$ pair to form a Λ and then the $(\varLambda\{\pi\}_{j}^{-})$ ($i \neq j$) pair to form a Ξ^- . The fits take into account the nonzero flight paths of the hyperons, which can give rise to different production and decay points. All vertex fits must converge and the combination that minimizes $((m_{p\pi\pi} - m_{\Xi})^2 + (m_{p\pi} - m_{\Lambda})^2)^{1/2}$, where m_{Ξ} and m_{Λ} are the nominal masses and $m_{p\pi\pi}$ ($m_{p\pi}$) is the mass of the candidate Ξ (Λ), is retained for further analysis. The same procedure is performed for the (\bar{X}_i) decay chain. For each decay chain the probability that the pions from the $\Xi \rightarrow \Lambda\pi$ and $\Lambda \rightarrow p\pi$ decays are wrongly assigned is found to be 0.51% and 0.49% for π^+ and π^- , respectively, which is negligible for the analysis. The $(m_{\Lambda}\{\pi\}^{-})$ versus $(m_{\bar{X}_i}\{\pi\}^{+})$ scatter plot is shown in Extended Data Fig. 2. A four-constraint kinematic fit requiring energy and momentum conservation (4C) is imposed on the $(e^+e^- \rightarrow J/\psi \rightarrow \bar{X}_i \pi^+ \bar{X}_i \pi^-)$ system, and only events where $(\chi_4 \{C\})^2 < 100$ are retained for further analysis. The kinematic fit is effective for removing the background processes $(e^+e^- \rightarrow J/\psi \rightarrow \gamma\eta \rightarrow \gamma\eta \pi^+\pi^-)$ and $(e^+e^- \rightarrow J/\psi \rightarrow \bar{X}_i(1530)\pi^+\pi^-)$ (and its charge conjugate), which have the same charged final-state topology as the signal channel, but contain extra neutral particles.

The invariant masses of the $p\pi^-$ and $(\bar{X}_i\{\pi\}^+)$ pairs are also required to fulfil $|m_{p\pi} - m_{\Lambda,\text{peak}}| < 11.5 \text{ MeV}/c^2$, where $m_{\Lambda,\text{peak}}$ is the peak position of the Λ mass distribution. A similar mass window criterion, optimized to remove the broad resonance $(\varSigma(1385))$

$\{\bar{\text{varSigma}}\}^{(+)}(1385)\}$ background contribution, is imposed on the Ξ particle, $|m_{\Lambda\pi} - m_{\Xi,\text{peak}}| < 11.0 \text{ MeV}/c^2$.

The decay length is defined as the distance between the point of origin and the decay position of the decaying Λ or Ξ particle. If the hyperon momentum points oppositely to the direction from the collision to the decay point, then the decay length becomes negative in the vertex-fit algorithm. These events are removed from the sample.

Differences between experimental data and Monte Carlo simulations are observed for large polar angles. This discrepancy induces a systematic bias on the parameter values. This bias can, however, be reduced to a negligible level by requiring $|\cos\theta| < 0.84$. The Ξ scattering angle θ is defined in the main text.

After applying all aforementioned selection criteria, $73,244 \langle |\text{varXi}|^{-} \rangle \langle |\bar{\text{varXi}}|^{(+)} \rangle$ candidates remain in the final sample. This is shown in Extended Data Fig. 3. The number of remaining background events are estimated to be 199 ± 17 . The background contribution has a marginal effect on the results at this precision and is therefore neglected.

Definition of the helicity systems

In the $\langle e^+ e^- \rangle \langle \bar{\text{varXi}} \rangle \langle |\bar{\text{varXi}}|^{(+)} \rangle$, $\Xi^- \rightarrow \Lambda\pi^-$, $\Lambda \rightarrow p\pi^-$, $\langle |\bar{\text{varXi}}|^{(+)} \rangle \langle \bar{\text{varLambda}} \rangle \langle |\pi|^{(+)} \rangle$, $\langle |\bar{\text{varLambda}}| \rangle \langle p \rangle \langle |\pi|^{(+)} \rangle$ process, the ‘master coordinate system’, denoted $\langle \mathcal{R} \rangle$, is defined in the e^+e^- centre-of-momentum system. In this system, we define the unit vector $\langle \hat{\bf z} \rangle$ in the direction of the positron momentum. The coordinate system $\langle \mathcal{R} \rangle \langle \Xi \rangle$ is then defined in the rest frame of the Ξ^- baryon, with the z axis along the unit vector $\langle \hat{\bf z} \rangle \langle \Xi \rangle$ defined by the direction of the Ξ^- momentum in the $\langle \mathcal{R} \rangle$ system. A Cartesian coordinate system with $\langle \hat{\bf x} \rangle \langle \Xi \rangle$ and $\langle \hat{\bf y} \rangle \langle \Xi \rangle$ unit vectors is defined as

$$\langle \hat{\bf x} \rangle \langle \Xi \rangle = \frac{\langle \hat{\bf z} \rangle \langle \Xi \rangle}{\langle \hat{\bf z} \rangle \langle \Xi \rangle} \times \langle \hat{\bf z} \rangle \langle \Xi \rangle \langle \hat{\bf z} \rangle \langle \Xi \rangle + \frac{\langle \hat{\bf z} \rangle \langle \Xi \rangle}{\langle \hat{\bf z} \rangle \langle \Xi \rangle} \times \langle \hat{\bf z} \rangle \langle \Xi \rangle \langle \hat{\bf z} \rangle \langle \Xi \rangle$$

$$\frac{\hat{z} \times \hat{y} - \hat{y} \times \hat{z}}{\|\hat{z}\| \|\hat{y}\|}. \quad (8)$$

The helicity system $\{\mathcal{R}\}_{\bar{X}_i}$ is defined in the same way in the $\{\bar{X}_i\}^+$ rest frame, and because $\{\hat{z}\}_{\bar{X}_i} = -\{\hat{z}\}_{\bar{X}_i}$, the axes $\{\hat{x}\}_{\bar{X}_i} = \{\hat{x}\}_{\bar{X}_i}$ and $\{\hat{y}\}_{\bar{X}_i} = -\{\hat{y}\}_{\bar{X}_i}$. The system $\{\mathcal{R}\}_{\Lambda}$ is defined in the rest frame of the Λ , with the $\{\hat{z}\}_{\Lambda}$ pointing in the direction of the Λ momentum in the $\{\mathcal{R}\}_{\bar{X}_i}$ system. A new Cartesian coordinate system is then defined by the unit vectors $\{\hat{x}\}_{\Lambda}$ and $\{\hat{y}\}_{\Lambda}$

$$\begin{aligned}
 & \frac{\hat{\Lambda}_z}{\varXi} = \frac{\hat{\Lambda}_y}{\varXi} \times \frac{\hat{\Lambda}_z}{\varXi} + \frac{\hat{\Lambda}_x}{\varXi} \times \frac{\hat{\Lambda}_z}{\varXi} \\
 & \frac{\hat{\Lambda}_y}{\varXi} = \frac{\hat{\Lambda}_x}{\varXi} \times \frac{\hat{\Lambda}_y}{\varXi} + \frac{\hat{\Lambda}_z}{\varXi} \times \frac{\hat{\Lambda}_y}{\varXi} \\
 & \frac{\hat{\Lambda}_x}{\varXi} = \frac{\hat{\Lambda}_y}{\varXi} \times \frac{\hat{\Lambda}_x}{\varXi} + \frac{\hat{\Lambda}_z}{\varXi} \times \frac{\hat{\Lambda}_x}{\varXi}
 \end{aligned}
 \quad (9)$$

In the same way, the system $\{\{\mathcal{R}\}_\bar{\Lambda}\}$ can be derived, and hence there is a unique definition of the orientations of the coordinate systems $\{\{\mathcal{R}\}_\Xi\}$, $\{\{\mathcal{R}\}_\bar{X}\}$, $\{\{\mathcal{R}\}_\Lambda\}$ and $\{\{\mathcal{R}\}_\bar{\Lambda}\}$ used in the analysis.

The maximum log-likelihood fit procedure

The global fit is performed on the data through the joint angular distribution. For N events the likelihood function is given by

```
 $$\begin{array}{c} \mathcal{L} (\{\boldsymbol{x}_i\})_1, \\ \{\boldsymbol{x}_i\}_2, \ldots, \{\boldsymbol{x}_i\}_N; \\ \boldsymbol{\omega} ) = \mathop{\mathrm{prod}} \limits_{i=1}^N
```

$$\begin{aligned} & \{\mathbf{P}\}(\{\boldsymbol{\xi}_i\}; \{\boldsymbol{\omega}\}) \\ &= \text{mathop}\{\prod\limits_{i=1}^N \frac{\mathbf{W}}{\{\boldsymbol{\xi}_i\}; \{\boldsymbol{\omega}\}}\} \text{varepsilon} \\ & (\{\boldsymbol{\xi}_i\}) \{ \mathbf{N} \} (\{\boldsymbol{\omega}\}), \end{aligned} \quad (10)$$

where $\varepsilon(\xi)$ is the efficiency, $\{\mathbf{W}\}(\{\boldsymbol{\xi}_i\}; \{\boldsymbol{\omega}\})$ is the weight as specified in equation (6), and the normalization factor $\{\mathbf{N}\}(\{\boldsymbol{\omega}\}) = \int \mathbf{W}(\{\boldsymbol{\xi}_i\}; \{\boldsymbol{\omega}\}) \text{varepsilon}(\{\boldsymbol{\xi}_i\}) \text{d}\{\boldsymbol{\xi}_i\}$. The normalization factor is approximated as $\{\mathbf{N}\}(\{\boldsymbol{\omega}\}) \approx \frac{1}{M} \sum_{j=1}^M \{\mathbf{W}\}(\{\boldsymbol{\xi}_j\}; \{\boldsymbol{\omega}\})$, using M Monte Carlo events ξ_j generated uniformly over phase space, propagated through the detector and reconstructed in the same way as data. M is chosen to be much larger than the number of events in data N ; our results exploit a simulation sample where $M/N \approx 35$. By taking the natural logarithm of the joint probability density, the efficiency function can be separated and removed as it only affects the overall log-likelihood normalization and is not dependent on the parameters in ω . To determine the parameters, the Minuit package from the CERN library is used⁵⁶. The minimized function is given by $S = -\ln(\{\mathcal{L}\})$. The operational conditions were slightly different for the 2009 and 2012 datasets, most notably in the nominal value of the magnetic field. For this reason, the likelihoods are constructed separately for the two different run periods.

The results of the simultaneous fit are shown in Table 1. Those results that depend on combinations of decay parameters account for the correlations between the parameters. The correlation coefficients between the decay parameters are given in Extended Data Table 1. Assuming that CP symmetry is conserved we find $\langle \alpha_A \rangle = 0.760 \pm 0.006 \pm 0.003$ and $\langle \alpha_E \rangle = -0.373 \pm 0.005 \pm 0.002$, where the latter result is in disagreement with the current standard value²⁶ $\alpha_E = -0.401 \pm 0.010$. The parameter α_E has previously only been measured indirectly via the product $\alpha_E \alpha_A$ and the assumed value of α_A . The current standard value of $\alpha_A = 0.732 \pm 0.014$ is an average based on the

two incompatible results of BESIII and the re-analysed CLAS data^{4,5}, and in disagreement with the value found in this analysis. By contrast, our measured value for the product $\langle \alpha_{\Xi} \rangle \langle \alpha_{\Lambda} \rangle = -0.284 \pm 0.004 \pm 0.002$ is compatible with the world average²⁶ $\alpha_{\Xi} \alpha_{\Lambda} = -0.294 \pm 0.005$.

Systematic uncertainties

The systematic uncertainties are assigned by performing studies related to the kinematic fit, the Λ and Ξ mass window requirements, the Λ and Ξ decay length selection, and a combined test on the $\langle \varXi \rangle \langle \bar{\varXi} \rangle$ fit reconstruction with the p, π main drift chamber track reconstruction efficiency. Searches of systematic effects are tested by varying the criteria above and below the main selection. For each test, i , the parameter values are re-obtained, $\omega_{sys,i}$ and the changes evaluated compared to the central values, $\Delta_i = |\omega - \omega_{sys,i}|$. Also calculated are the uncorrelated uncertainties $\langle \sigma_{uc,i} \rangle = \sqrt{\langle \sigma_{\omega}^2 \rangle - \langle \sigma_{\omega,sys,i}^2 \rangle}$, where σ_{ω} and $\sigma_{\omega,sys,i}$ correspond to the fit uncertainties of the main and systematic test results, respectively. If the ratio $\Delta_i / \sigma_{uc,i}$ shows a trending behaviour and larger than two this is attributed to a systematic effect^{57,58}. For each systematic effect the corresponding uncertainty is evaluated. The assigned systematic uncertainties are given in Extended Data Tables 2–4, where the individual systematic uncertainties are summed in quadrature.

1. 1.

Estimator. To test if the method produces systematically biased results, a large Monte Carlo data sample is produced with production and decay distributions corresponding to those of the fit results to the data sample (~ 10 times the experimental data). The simulated data are divided into subsamples with equal number of events as the experimental sample, and run through the fit procedure. The obtained fit parameters and uncertainties are found to be consistent within one standard deviation of the generated parameter values and hence no bias is detected.

2. 2.

Kinematic fit. The systematic differences from the kinematic fit are tested by varying the kinematic fit χ^2 value from 40 to 200, with an increment of 20 in each step. Significant effects are seen for the parameters $\Delta\Phi$, ϕ and $\langle|\bar{\chi}|_{\rm rm{4C}}\rangle^2$ when $\langle|\bar{\chi}|_{\rm rm{4C}}\rangle^2 > 100$. For $\langle|\bar{\chi}|_{\rm rm{4C}}\rangle^2 < 100$ systematic deviations occur for α_{Ξ} and $\langle|\bar{\alpha}_{\Lambda}\rangle_{\Lambda}\rangle$. The difference in track resolution between data and Monte Carlo is the probable cause for these changes in the parameter values. The systematic uncertainty is assigned to be the average difference of the main result to a lower and upper limit, determined to be at $\langle|\bar{\chi}|_{\rm rm{4C}}\rangle^2=60$ and 200, respectively.

3. 3.

Λ and Ξ mass window selection. Possible systematic effects due to the $\langle|\bar{\chi}|_{\rm varLambda}\rangle_{\rm varLambda}$, $\langle|\bar{\chi}|_{\rm varLambda}\rangle$, Ξ^- and $\langle|\bar{\chi}|_{\rm varXi}\rangle$ mass windows are investigated by varying the selection criteria between 2 and 30 MeV/ c^2 and 2 and 20 MeV/ c^2 for the $\langle|\bar{\chi}|_{\rm varLambda}\rangle$ and $\langle|\bar{\chi}|_{\rm varXi}\rangle$ candidates, respectively. For the Λ selection systematic deviations are seen for decreasing mass windows. The uncertainty is assigned to be the difference of the nominal result to the result when 95% of the events are included, at $|m_{p\pi} - m_{\Lambda,\text{peak}}| < 6.9$ MeV/ c^2 . For the Ξ^- and $\langle|\bar{\chi}|_{\rm varXi}\rangle$ mass windows, significant effects are seen for the parameters $\alpha_{J/\psi}$, α_{Λ} and ϕ_{Ξ} . The systematic uncertainties for these parameters are assigned to be the difference of the main result and the results obtained one standard deviation lower than the main selection window, estimated from the $m_{\Lambda\pi}$ line shape uncertainty.

4. 4.

Λ and Ξ decay length. Possible systematic effects related to the Λ and Ξ lifetimes are studied by varying the decay length selection criteria for the Λ and Ξ candidates. For Ξ no strong trending behaviours are seen, but for Λ a dependence is seen for the asymmetry parameters α_{Λ} and $\langle|\bar{\chi}|_{\rm rm{4C}}\rangle^2$.

$(\bar{\alpha}_\Lambda - \bar{\alpha}_\Xi)$, which is accounted for in the final systematic uncertainty.

5. 5.

The combined efficiency of \varXi reconstruction and p, π^- tracking. For the study of systematic effects related to the tracking and the Λ and Ξ reconstruction it is assumed that the combined efficiency for proton, antiproton and π^\pm depends only on the polar angle $\cos\theta_{\text{LAB}}$ and the transverse momentum, p_T . To study the tracking efficiency the fitted probability density function is modified by allowing for arbitrary efficiency corrections as a function of $\cos\theta_{\text{LAB}}$ and p_T for each particle type in an iterative procedure. The correction procedure is repeated until the maximum log-likelihood is stable within $\ln(2)$ between two successive iterations. The difference between the fit results with and without the tracking correction is assigned as the systematic uncertainty.

6. 6.

The $\cos\theta$ scattering angle. From comparing data to Monte Carlo simulation a discrepancy is seen for charged tracks with polar angles $|\cos\theta_{\text{LAB}}| > 0.84$. The discrepancy is also seen to have a notable effect on some of the decay parameters. The effect can be isolated by removing only the events where $|\cos\theta| > 0.84$. Although the observed data–simulation differences are removed by requiring that $|\cos\theta| < 0.84$, residual systematic effects are observed for $\langle\alpha_\Xi\rangle$ and $\langle\alpha_\Xi\rangle\langle\alpha_\Lambda\rangle$, which are included in the systematic uncertainty.

7. 7.

Dataset consistency. When comparing the statistically independent results of the 2009 and 2012 datasets, all parameters are found to agree within two standard deviations. As there is no evidence of systematic bias, no uncertainty is assigned associated with possible dataset differences.

Data availability

The data points displayed in the plots within this paper are available on request to besiii-publications@ihep.ac.cn.

Code availability

All algorithms used for data analysis and simulation are archived by the authors and are available on request to besiii-publications@ihep.ac.cn.

References

1. Sakharov, A. D. Violation of CP invariance, C asymmetry, and baryon asymmetry of the universe. *Zh. Eksp. Teor. Fiz. Pisma* **5**, 32–35 (1967).
2. Adlarson, P. & Kupsc, A. CP symmetry tests in the cascade–anticascade decay of charmonium. *Phys. Rev. D* **100**, 114005 (2019).
3. HyperCP Collaboration. New measurement of $\Xi^- \rightarrow \Lambda\pi^-$ decay parameters. *Phys. Rev. Lett.* **93**, 011802 (2004).
4. The BESIII Collaboration. Polarization and entanglement in baryon–antibaryon pair production in electron–positron annihilation. *Nat. Phys.* **15**, 631–634 (2019).
5. Ireland, D. G. et al. Kaon photoproduction and the Λ decay parameter α_- . *Phys. Rev. Lett.* **123**, 182301 (2019).
6. Cabibbo, N. Unitary symmetry and leptonic decays. *Phys. Rev. Lett.* **10**, 531–533 (1963).
7. Kobayashi, M. & Maskawa, T. CP-violation in the renormalizable theory of weak interaction. *Prog. Theor. Phys.* **49**, 652–657 (1973).
8. Bernreuther, W. CP violation and baryogenesis. *Lect. Notes Phys.* **591**, 237–293 (2002).

9. Canetti, L., Drewes, M. & Shaposhnikov, M. Matter and antimatter in the Universe. *New J. Phys.* **14**, 095012 (2012).
10. Bigi, I. I. & Sanda A. I. *CP Violation* (Cambridge Univ. Press, 2009).
11. Bediaga, I. & Göbel, C. Direct CP violation in beauty and charm hadron decays. *Prog. Part. Nucl. Phys.* **114**, 103808 (2020).
12. Particle Data Group. Review of particle physics: 13. CP violation in the quark sector. *Phys. Rev. D* **98**, 030001 (2018).
13. KTeV Collaboration. . Observation of direct CP violation in $K_{S,L} \rightarrow \pi\pi$ decays. *Phys. Rev. Lett.* **83**, 22–27 (1999).
14. NA48 Collaboration. A new measurement of direct CP violation in two pion decays of the neutral kaon. *Phys. Lett. B* **465**, 335–348 (1999).
15. Buras, A. *Gauge Theory of Weak Decays: the Standard Model and the Expedition to New Physics Summits* Ch. 10 (Cambridge Univ. Press, 2020).
16. Sehgal, L. M. & Wanninger, M. CP violation in the decay $K_L \rightarrow \pi^+\pi^-e^+e^-$. *Phys. Rev. D* **46**, 1035–1041 (1992). erratum 46, 5209-5210 (1992).
17. González-Alonso, M., Naviliat-Cuncic, O. & Severijns, N. New physics searches in nuclear and neutron β decay. *Prog. Part. Nucl. Phys.* **104**, 165–223 (2019).
18. Lee, T. & Yang, C. N. General partial wave analysis of the decay of a hyperon of spin 1/2. *Phys. Rev.* **108**, 1645–1647 (1957).
19. Cronin, J. W. & Overseth, O. E. Measurement of the decay parameters of the Λ^0 particle. *Phys. Rev.* **129**, 1795–1807 (1963).
20. Dauber, P. M., Berge, J. P., Hubbard, J. R., Merrill, D. W. & Muller, R. A. Production and decay of cascade hyperons. *Phys. Rev.* **179**, 1262–1285 (1969).

21. Fermilab E756 Collaboration. Search for direct CP violation in nonleptonic decays of charged Ξ and Λ hyperons. *Phys. Rev. Lett.* **85**, 4860–4863 (2000).
22. Donoghue, J. F. & Pakvasa, S. Signals of CP nonconservation in hyperon decay. *Phys. Rev. Lett.* **55**, 162–165 (1985).
23. Donoghue, J. F., He, X. G. & Pakvasa, S. Hyperon decays and CP nonconservation. *Phys. Rev. D* **34**, 833–842 (1986).
24. Tandean, J. & Valencia, G. CP violation in hyperon nonleptonic decays within the standard model. *Phys. Rev. D* **67**, 056001 (2003).
25. Christenson, J. H., Cronin, J. W., Fitch, V. L. & Turlay, R. Evidence for the 2π decay of the K_2^0 meson. *Phys. Rev. Lett.* **13**, 138–140 (1964).
26. Particle Data Group. Review of particle physics. *Prog. Theor. Exp. Phys.* **2020**, 083C01 (2020).
27. Sozzi, M. *Discrete Symmetries and CP Violation: From Experiment to Theory* (Oxford Univ. Press, 2008).
28. HyperCP Collaboration. Search for CP violation in charged- Ξ and Λ hyperon decays. *Phys. Rev. Lett.* **93**, 262001 (2004).
29. Klempert, E., Bradamante, F., Martin, A. & Richard, J. F. Antinucleon nucleon interaction at low energy: scattering and protonium. *Phys. Rept.* **368**, 119–316 (2002).
30. ATLAS Collaboration. Measurement of the transverse polarization of Λ and $\bar{\Lambda}$ hyperons produced in proton-proton collisions at $\sqrt{s} = 7$ TeV using the ATLAS detector. *Phys. Rev. D* **91**, 032004 (2015).
31. CLAS Collaboration. Photoproduction of Λ and Σ^0 hyperons using linearly polarized photons. *Phys. Rev. C* **93**, 065201 (2016).
32. The STAR Collaboration. Global Λ hyperon polarization in nuclear collisions. *Nature* **548**, 62–65 (2017).

33. HyperCP Collaboration. Observation of parity violation in the $\Omega^- \rightarrow \Lambda K^-$ decay. *Phys. Lett. B* **617**, 11–17 (2005).
34. HyperCP Collaboration. Measurement of the α asymmetry parameter for the $\Omega^- \rightarrow \Lambda K^-$ decay. *Phys. Rev. D* **71**, 051102 (2005).
35. Perotti, E., Fäldt, G., Kupsc, A., Leupold, S. & Song, J. J. Polarization observables in e^+e^- annihilation to a baryon–antibaryon pair. *Phys. Rev. D* **99**, 056008 (2019).
36. Fäldt, G. & Kupsc, A. Hadronic structure functions in the $e^+e^- \rightarrow \bar{\Lambda}\Lambda$ reaction. *Phys. Lett. B* **772**, 16–20 (2017).
37. Ablikim, M. et al. Design and construction of the BESIII detector. *Nucl. Instrum. Meth. A* **614**, 345–399 (2010).
38. STAR Collaboration. Polarization of $\Lambda(\bar{\Lambda})$ hyperons along the beam direction in Au + Au collisions at $\sqrt{s_{NN}} = 200$ GeV. *Phys. Rev. Lett.* **123**, 132301 (2019).
39. Becattini, F. & Lisa, M. Polarization and vorticity in the quark gluon plasma. *Annu. Rev. Nucl. Part. Sci.* **70**, 395–423 (2020).
40. BESIII Collaboration. Complete measurement of the Λ electromagnetic form factors. *Phys. Rev. Lett.* **123**, 122003 (2019).
41. Blake, T., Meinel, S. & van Dyk, D. Bayesian analysis of $b \rightarrow s\mu^+\mu^-$ Wilson coefficients using the full angular distribution of $\Lambda_b \rightarrow \Lambda(\rightarrow p\pi^-)\mu^+\mu^-$ decays. *Phys. Rev. D* **101**, 035023 (2020).
42. Han, T. Z., Ping, R. G. & Luo, T. Polarization in $\Lambda_c \rightarrow c\Lambda$ decays. *Chin. Phys. C* **44**, 013002 (2020).
43. Nurushev, S., Rzaev, R., Sakharov, V., Solovyanov V. & Vasilyev, A. Polarized proton beam at IHEP. In *High-Energy Physics With Polarized Beams And Polarized Targets* (eds Joseph, C. & Soffer, J.) 501–502 (Springer, 1981).

44. Tandean, J. New physics and CP violation in hyperon nonleptonic decays. *Phys. Rev. D* **69**, 076008 (2004).
45. Ablikim, M. et al. Future physics programme of BESIII. *Chin. Phys. C* **44**, 040001 (2020).
46. PANDA Collaboration. The potential of and studies with PANDA at FAIR. *Eur. Phys. J. A* **70**, 395–423 (2009).
47. Bondar, A. E. et al. Project of a super charm-tau factory at the Budker Institute of Nuclear Physics in Novosibirsk. *Yad. Fiz.* **76**, 1132–1145 (2013).
48. Shi, X. D., Zhou, X. R., Qin, X. S. & Peng, H. P. A fast simulation package for STCF detector. *J. Instrum.* **16**, P03029 (2021).
49. BESIII Collaboration. Study of ψ decays to the $\bar{\chi}_1^0 \chi_1^0$ and $\bar{\chi}_1^0 \chi_2^0$ final states. *Phys. Rev. D* **93**, 072003 (2016).
50. GEANT4 Collaboration. GEANT4—a simulation toolkit. *Nucl. Instrum. Meth. A* **506**, 250–303 (2003).
51. Allison, J. et al. Geant4 developments and applications. *IEEE Trans. Nucl. Sci.* **53**, 270–278 (2006).
52. Jadach, S., Ward, B. & Włodarczyk, Z. The precision Monte Carlo event generator KK for two fermion final states in e^+e^- collisions. *Comput. Phys. Commun.* **130**, 260–325 (2000).
53. Lange, D. The EvtGen particle decay simulation package. *Nucl. Instrum. Meth. A* **462**, 152–155 (2001).
54. Ping, R.-G. Event generators at BESIII. *Chin. Phys. C* **32**, 599–602 (2008).
55. Chen, J. C., Huang, G. S., Qi, X. R., Zhang, D. H. & Zhu, Y. S. Event generator for J/ψ and $\psi(2S)$ decay. *Phys. Rev. D* **62**, 034003 (2000).

56. James, F. & Roos, M. Minuit – a system for function minimization and analysis of the parameter errors and correlations. *Comput. Phys. Commun.* **10**, 343–367 (1975).
57. Barlow, R. Systematic errors: facts and fictions. Preprint at <https://arxiv.org/abs/hep-ex/0207026> (2002).
58. Wanke, R. in *Data Analysis in High Energy Physics: A Practical Guide to Statistical Methods* (eds Behnke, O. et al.) 263–296 (Wiley, 2013).

Acknowledgements

The BESIII collaboration thanks the staff of BEPCII and the IHEP Computing Centre for their strong support. This work is supported in part by the National Key Research and Development Program of China under contract nos 2020YFA0406300 and 2020YFA0406400; the National Natural Science Foundation of China (NSFC) under contract nos 11625523, 11635010, 11735014, 11822506, 11835012, 11905236, 11935015, 11935016, 11935018, 12075107 and 11961141012; the Chinese Academy of Sciences (CAS) Large-Scale Scientific Facility Program; Joint Large-Scale Scientific Facility Funds of the NSFC and CAS under contract nos U1732263 and U1832207; the CAS Key Research Program of Frontier Sciences under contract nos QYZDJ-SSW-SLH003 and QYZDJ-SSW-SLH040; the 100 Talents Program of CAS; the CAS President’s International Fellowship Initiative (PIFI) programme; INPAC and Shanghai Key Laboratory for Particle Physics and Cosmology; the Shanghai Pujiang Program (20PJ1401700); the ERC under contract no. 758462; the European Union Horizon 2020 research and innovation programme under Marie Skłodowska-Curie grant agreement no. 894790; the German Research Foundation (DFG) under contract nos 443159800, Collaborative Research Center (CRC) 1044, FOR 2359, GRK 214; the Istituto Nazionale di Fisica Nucleare, Italy; the Ministry of Development of Turkey under contract no. DPT2006K-120470; the National Science and Technology fund; the Olle Engkvist Foundation under contract no. 200-0605; STFC (United Kingdom); The Knut and Alice Wallenberg Foundation (Sweden) under contract no. 2016.0157; The Royal Society, UK under contract nos DH140054 and DH160214; the Swedish Research Council; the US Department of Energy

under contract nos DE-FG02-05ER41374 and DE-SC-0012069; and the National Science Centre (Poland) under contract no. 2019/35/O/ST2/02907.

Funding

Open access funding provided by Uppsala University.

Author information

Author notes

1. M. N. Achasov, N. Yu. Muchnoi & I. B. Nikolaev

Present address: Novosibirsk State University, Novosibirsk, Russia

2. Y. Ban, Y. Gao, Z. Huang, Y. J. Mao, Y. X. Song, D. Y. Wang, M. Z. Wang, X. Wang, X. H. Xie, X. Q. Yuan & Y. Zheng

Present address: State Key Laboratory of Nuclear Physics and Technology, Peking University, Beijing, People's Republic of China

3. G. Chelkov & A. Zhemchugov

Present address: Moscow Institute of Physics and Technology, Moscow, Russia

4. Z. J. Chen, X. Sun, J. S. Yu, Y. Zeng & Shulei Zhang

Present address: School of Physics and Electronics, Hunan University, Changsha, People's Republic of China

5. Y. P. Guo, H. J. Li, M. H. Liu, T. Luo, X. Pan, X. L. Wang, X. Wu, H. Xiao, F. Yan, L. Yan, Yi Zhang & W. J. Zhu

Present address: Key Laboratory of Nuclear Physics and Ion-beam Application (MOE), Fudan University, Shanghai, People's Republic of China

6. Y. P. Guo, H. J. Li, M. H. Liu, T. Luo, X. Pan, X. L. Wang, X. Wu, H. Xiao, F. Yan, L. Yan, Yi Zhang & W. J. Zhu

Present address: Institute of Modern Physics, Fudan University,
Shanghai, People's Republic of China

7. M. Himmelreich, S. Nakhoul, F. Nerling & K. Peters

Present address: Goethe University Frankfurt, Frankfurt am Main,
Germany

8. J. F. Hu

Present address: Guangdong Provincial Key Laboratory of Nuclear
Science, South China Normal University, Guangzhou, People's
Republic of China

9. J. F. Hu

Present address: Institute of Quantum Matter, South China Normal
University, Guangzhou, People's Republic of China

10. S. Janchiv

Present address: Institute of Physics and Technology, Ulaanbaatar,
Mongolia

11. S. Nisar

Present address: Department of Physics, Harvard University,
Cambridge, MA, USA

12. A. Sarantsev

Present address: NRC "Kurchatov Institute", PNPI, Gatchina, Russia

13. H. J. Yang

Present address: Key Laboratory for Particle Physics, Astrophysics and Cosmology (MOE), Shanghai, People's Republic of China

14. H. J. Yang

Present address: Shanghai Key Laboratory for Particle Physics and Cosmology, Shanghai, People's Republic of China

15. H. J. Yang

Present address: Institute of Nuclear and Particle Physics, Shanghai Jiao Tong University, Shanghai, People's Republic of China

Authors and Affiliations

1. Institute of High Energy Physics, Beijing, People's Republic of China

M. Ablikim, X. Cai, G. F. Cao, N. Cao, J. F. Chang, W. L. Chang, G. Chen, H. S. Chen, M. L. Chen, Y. B. Chen, H. L. Dai, X. C. Dai, Z. Y. Deng, J. Dong, L. Y. Dong, M. Y. Dong, J. Fang, S. S. Fang, Y. Fang, C. D. Fu, W. X. Gong, M. H. Gu, C. Y. Guan, K. L. He, Y. K. Heng, Z. L. Hou, H. M. Hu, T. Hu, Y. Hu, Y. P. Huang, Q. Ji, X. B. Ji, X. L. Ji, X. S. Jiang, B. C. Ke, R. Kiuchi, M. G. Kurth, F. Li, G. Li, H. B. Li, Ke Li, L. K. Li, W. D. Li, W. G. Li, Xiaoyu Li, H. Liang, L. Z. Liao, B. J. Liu, C. X. Liu, Fang Liu, H. M. Liu, Huanhuan Liu, J. Y. Liu, K. Liu, P. L. Liu, T. Liu, Z. A. Liu, X. C. Lou, J. D. Lu, J. G. Lu, X. L. Lu, Y. Lu, Y. P. Lu, X. L. Luo, H. L. Ma, M. M. Ma, Q. M. Ma, R. Q. Ma, X. X. Ma, X. Y. Ma, Z. P. Mao, X. H. Mo, Z. Ning, Q. Ouyang, A. Pathak, R. G. Ping, S. Qian, Z. H. Qin, J. F. Qiu, G. Rong, X. Y. Shen, R. S. Shi, X. Shi, W. M. Song, G. X. Sun, H. K. Sun, S. S. Sun, T. Sun, Y. Z. Sun, Z. T. Sun, G. Y. Tang, B. Wang, H. P. Wang, K. Wang, L. L. Wang, Meng Wang, Y. F. Wang, Y. Q. Wang, Z. Wang, Z. Y. Wang, Zongyuan Wang, S. P. Wen, J. F. Wu, L. H. Wu, L. J. Wu, Z. Wu, S. Y. Xiao, Y. G. Xie, T. Y. Xing, G. F. Xu, W. Xu, H. X. Yang, Yifan Yang, M. Ye, J. H. Yin, B. X. Yu, G. Yu, C. Z. Yuan, Y. Yuan, B. X. Zhang, H. Y. Zhang, J. W. Zhang, J. Y. Zhang, J. Z. Zhang, Jianyu Zhang, Jiawei Zhang, Y. H. Zhang, Yao Zhang, G. Zhao, J. Y. Zhao, J. Z. Zhao, Ling Zhao, Q. Zhao, Y. B. Zhao, J. P.

Zheng, L. P. Zhou, Q. Zhou, A. N. Zhu, K. Zhu, K. J. Zhu, Z. A. Zhu, B. S. Zou & J. H. Zou

2. G.I. Budker Institute of Nuclear Physics SB RAS (BINP), Novosibirsk, Russia

M. N. Achasov, N. Yu. Muchnoi & I. B. Nikolaev

3. Uppsala University, Uppsala, Sweden

P. Adlarson, J. Biernat, J. Hansson, W. Ikegami Andersson, T. Johansson, A. Kupsc, K. Schönnig, V. Thoren & M. Wolke

4. Helmholtz Institute Mainz, Mainz, Germany

S. Ahmed, A. Dbeysi, P. Larin, F. E. Maas & Ch. Rosner

5. Ruhr-University Bochum, Bochum, Germany

M. Albrecht, R. E. de Boer, F. Feldbauer, M. Fritsch, F. H. Heinsius, T. Held, T. Holtmann, S. Jaeger, I. K. Keshk, B. Kopf, M. Kuemmel, M. Kuessner, J. Q. Li, S. Maldaner, M. Pelizaeus, C. Schnier, U. Wiedner & L. Wollenberg

6. Johannes Gutenberg University of Mainz, Mainz, Germany

R. Aliberti, N. Berger, A. Denig, W. Gradl, N. Hüskens, C. H. Heinz, P. Kiese, H. Leithoff, M. Lellmann, T. Lenz, C. F. Redmer, Y. Schelhaas & P. Weidenkaff

7. University of Turin, Turin, Italy

A. Amoroso, F. Bianchi, A. Bortone, M. Destefanis, F. De Mori, M. Greco, L. Lavezzi, M. Maggiora, S. Marcello, S. Sosio & S. Spataro

8. INFN, Turin, Italy

A. Amoroso, F. Bianchi, A. Bortone, W. S. Cheng, F. Cossio, M. Destefanis, F. De Mori, L. Fava, M. Greco, L. Lavezzi, S. Lusso, M.

Maggiora, S. Marcello, A. Rivetti, M. Rolo, S. Sosio & S. Spataro

9. Liaoning Normal University, Dalian, People's Republic of China

M. R. An, W. Y. Han, C. H. Li, C. X. Yue, J. Zhao & X. Y. Zhou

10. University of Science and Technology of China, Hefei, People's Republic of China

Q. An, C. Q. Feng, Y. Gao, G. S. Huang, M. Irshad, Z. H. Lei, Cheng Li, H. Li, X. H. Li, H. Liang, D. Liu, J. B. Liu, L. Liu, S. B. Liu, W. M. Liu, H. P. Peng, V. Prasad, H. Qi, H. S. Sang, X. Y. Shan, M. Shao, H. C. Shi, X. D. Shi, Y. J. Sun, Y. K. Sun, Y. X. Tan, J. X. Teng, W. P. Wang, Y. Wang, L. Xia, W. B. Yan, H. Zhang, Y. T. Zhang, Yan Zhang, Lei Zhao, Z. G. Zhao, X. R. Zhou & Y. C. Zhu

11. State Key Laboratory of Particle Detection and Electronics, Hefei, People's Republic of China

Q. An, X. Cai, J. F. Chang, M. L. Chen, Y. B. Chen, H. L. Dai, J. Dong, M. Y. Dong, J. Fang, C. Q. Feng, Y. Gao, W. X. Gong, M. H. Gu, Y. K. Heng, T. Hu, G. S. Huang, M. Irshad, X. L. Ji, X. S. Jiang, Z. H. Lei, Cheng Li, F. Li, H. Li, X. H. Li, H. Liang, D. Liu, J. B. Liu, L. Liu, S. B. Liu, W. M. Liu, Z. A. Liu, X. C. Lou, J. G. Lu, Y. P. Lu, X. L. Luo, X. Y. Ma, X. H. Mo, Z. Ning, Q. Ouyang, H. P. Peng, V. Prasad, H. Qi, S. Qian, Z. H. Qin, X. Y. Shan, M. Shao, H. C. Shi, X. Shi, X. D. Shi, Y. J. Sun, Y. K. Sun, Y. X. Tan, J. X. Teng, K. Wang, W. P. Wang, Y. Wang, Y. F. Wang, Z. Wang, Z. Wu, L. Xia, Y. G. Xie, W. B. Yan, M. Ye, B. X. Yu, H. Y. Zhang, J. W. Zhang, Y. H. Zhang, Y. T. Zhang, Yan Zhang, J. Z. Zhao, Lei Zhao, Y. B. Zhao, Z. G. Zhao, J. P. Zheng, X. R. Zhou, K. J. Zhu & Y. C. Zhu

12. University of Jinan, Jinan, People's Republic of China

X. H. Bai, Y. Jin & Z. X. Meng

13. Southeast University, Nanjing, People's Republic of China

Y. Bai

14. Joint Institute for Nuclear Research, Dubna, Russia

O. Bakina, I. Boyko, G. Chelkov, D. Dedovich, I. Denysenko, A. Guskov, Y. Nefedov, A. Sarantsev & A. Zhemchugov

15. INFN Laboratori Nazionali di Frascati, Frascati, Italy

R. Baldini Ferroli, M. Bertani, A. Calcaterra, G. Felici & P. Patteri

16. INFN Sezione di Ferrara, Ferrara, Italy

I. Balossino, D. Bettoni, G. Cibinetto, R. Farinelli, I. Garzia, G. Mezzadri & M. Scodello

17. Peking University, Beijing, People's Republic of China

Y. Ban, Y. Gao, Z. Huang, Y. J. Mao, Y. X. Song, D. Y. Wang, M. Z. Wang, X. Wang, X. H. Xie, X. Q. Yuan & Y. Zheng

18. Institute of Physics and Technology, Ulaanbaatar, Mongolia

K. Begzsuren & S. Janchiv

19. University of Muenster, Muenster, Germany

J. Bloms, A. Khoukaz, M. Rump & F. Weidner

20. Carnegie Mellon University, Pittsburgh, PA, USA

R. A. Briere

21. Wuhan University, Wuhan, People's Republic of China

H. Cai, X. Dong, Y. L. Fan, P. T. Ge, Q. Liu, K. X. Su, L. Sun, Y. H. Tan, W. H. Wang, Z. Y. Zhang & X. Zhou

22. University of Chinese Academy of Sciences, Beijing, People's Republic of China

G. F. Cao, N. Cao, W. L. Chang, H. S. Chen, X. C. Dai, L. Y. Dong, M. Y. Dong, S. S. Fang, C. Y. Guan, K. L. He, Y. K. Heng, Y. R. Hou, H. M. Hu, T. Hu, X. B. Ji, X. S. Jiang, M. G. Kurth, H. B. Li, W. D. Li, Xiaoyu Li, H. Liang, L. Z. Liao, H. M. Liu, J. Y. Liu, Q. Liu, T. Liu, Z. A. Liu, X. C. Lou, J. D. Lu, X. R. Lyu, M. M. Ma, R. Q. Ma, R. T. Ma, X. X. Ma, X. H. Mo, S. L. Olsen, Q. Ouyang, R. G. Ping, W. B. Qian, C. F. Qiao, G. Rong, X. Y. Shen, R. S. Shi, S. S. Sun, T. Sun, H. P. Wang, Meng Wang, Y. F. Wang, Ziyi Wang, Zongyuan Wang, J. F. Wu, L. J. Wu, T. Y. Xing, W. Xu, Y. C. Xu, S. L. Yang, Yifan Yang, B. X. Yu, G. Yu, C. Z. Yuan, J. W. Zhang, J. Z. Zhang, Jianyu Zhang, Jiawei Zhang, J. Y. Zhao, Y. H. Zheng, L. P. Zhou, Q. Zhou, X. K. Zhou, A. N. Zhu, K. J. Zhu & Z. A. Zhu

23. Istinye University, Sariyer, Turkey

S. A. Cetin & O. B. Kolcu

24. Central China Normal University, Wuhan, People's Republic of China

D. Y. Chen, Y. G. Gao, Feng Liu, Ke Liu, Y. J. Mo, Y. H. Xie & Z. H. Zhang

25. Nanjing University, Nanjing, People's Republic of China

S. J. Chen, L. M. Gu, S. Jin, T. J. Min, M. Qi, C. W. Wang, Lei Zhang & S. F. Zhang

26. Institute of Modern Physics, Lanzhou, People's Republic of China

X. R. Chen, Y. T. Liang, K. H. Qi, Y. T. Tian, Zhi Yang & Y. X. Zhao

27. Hunan University, Changsha, People's Republic of China

Z. J. Chen, X. Sun, J. S. Yu, Y. Zeng & Shulei Zhang

28. Nankai University, Tianjin, People's Republic of China

X. F. Cui, C. Dong, Y. B. Liu, S. Q. Qu, P. X. Shen, C. X. Yu, M. G. Zhao, J. Zhu & W. J. Zhu

29. Liaoning University, Shenyang, People's Republic of China

Y. Ding, L. Gong, X. S. Kang, K. Y. Liu & F. C. Ma

30. Zhengzhou University, Zhengzhou, People's Republic of China

S. X. Du, D. M. Li, W. C. Yan & S. J. Zhao

31. University of Eastern Piedmont, Alessandria, Italy

L. Fava

32. Sun Yat-Sen University, Guangzhou, People's Republic of China

J. H. Feng, C. Geng, J. S. Li, Z. Y. Li, C. X. Lin, F. X. Lu, P. W. Luo, Z. Qian, J. Tang, W. Wang, Y. Wang, Z. Y. You, Z. Y. Yuan, H. H. Zhang, L. Q. Zhang & S. Zhang

33. University of South China, Hengyang, People's Republic of China

Y. Gao, L. Q. Huang, J. L. Liu, T. Yu, B. Zheng & C. Zhong

34. University of Ferrara, Ferrara, Italy

I. Garzia & M. Scodeggio

35. University of Manchester, Manchester, UK

E. M. Gersabeck, J. J. Lane, Y. Pan & D. J. White

36. University of Oxford, Oxford, UK

A. Gilman, S. Malde, G. Wilkinson & Y. Zhang

37. GSI Helmholtzcentre for Heavy Ion Research GmbH, Darmstadt, Germany

K. Goetzen, M. Himmelreich, R. Kliemt, S. Nakhoul, F. Nerling & K. Peters

38. Beihang University, Beijing, People's Republic of China
S. Gu, T. Y. Qi & L. Yuan
39. Guangxi University, Nanning, People's Republic of China
Y. T. Gu & H. B. Liu
40. Indiana University, Bloomington, IN, USA
A. Q. Guo, N. Hüskens, W. Imoehl & R. E. Mitchell
41. Nanjing Normal University, Nanjing, People's Republic of China
L. B. Guo, C. L. Luo, J. L. Ping, W. Y. Sun, Z. J. Xiao, J. Q. Zhang & B. Zhong
42. Shandong Normal University, Jinan, People's Republic of China
R. P. Guo
43. Fudan University, Shanghai, People's Republic of China
Y. P. Guo, H. J. Li, M. H. Liu, T. Luo, X. Pan, T. Y. Qi, X. P. Qin, C. P. Shen, X. L. Wang, X. Wu, H. Xiao, F. Yan, L. Yan, Yi Zhang & W. J. Zhu
44. Shandong University, Jinan, People's Republic of China
T. T. Han, X. T. Huang, Y. Y. Ji, H. B. Jiang, J. B. Jiao, J. L. Li, X. L. Li, Z. Q. Liu, L. L. Ma, X. S. Qin, J. J. Song, F. F. Sui, M. Wang & X. Y. Zhang
45. Henan Normal University, Xinxiang, People's Republic of China
X. Q. Hao, Q. P. Ji, H. J. Li, F. X. Lu, J. F. Sun & Guangyi Zhang
46. University of Hawaii, Honolulu, HI, USA
F. A. Harris

47. Suranaree University of Technology, Nakhon Ratchasima, Thailand
C. Herold
48. South China Normal University, Guangzhou, People's Republic of China
J. F. Hu
49. University of the Punjab, Lahore, Pakistan
T. Hussain, Q. A. Malik, K. H. Rashid & A. A. Zafar
50. Huangshan College, Huangshan, People's Republic of China
Z. Jiao & H. J. Lu
51. University of Groningen, Groningen, The Netherlands
N. Kalantar-Nayestanaki, R. Kappert, M. Kavatsyuk, J. G. Messchendorp & V. Rodin
52. Shanxi Normal University, Linfen, People's Republic of China
B. C. Ke, H. Li, L. Yang & J. J. Zhang
53. II. Physikalisches Institut, Justus-Liebig-Universität Giessen, Giessen, Germany
L. Koch, W. Kühn & J. S. Lange
54. Indian Institute of Technology Madras, Chennai, India
A. Lavania, J. Libby & K. Ravindran
55. Qufu Normal University, Qufu, People's Republic of China
C. Li

56. Beijing Institute of Petrochemical Technology, Beijing, People's Republic of China

Lei Li

57. Lanzhou University, Lanzhou, People's Republic of China

P. R. Li, X. Liu, Y. Liu, H. J. Wang, X. F. Wang & Y. Y. Wang

58. Tsinghua University, Beijing, People's Republic of China

S. Y. Li, H. R. Qi & L. M. Zhang

59. Jilin University, Changchun, People's Republic of China

H. Liang, W. M. Song, W. Y. Sun & H. H. Zhang

60. Sichuan University, Chengdu, People's Republic of China

Y. F. Liang & C. J. Tang

61. Guangxi Normal University, Guilin, People's Republic of China

G. R. Liao, L. Q. Qin, D. H. Wei & Y. X. Yang

62. Shanxi University, Taiyuan, People's Republic of China

F. H. Liu

63. Henan University of Science and Technology, Luoyang, People's Republic of China

Huihui Liu

64. Soochow University, Suzhou, People's Republic of China

Shuai Liu, D. C. Shan, J. F. Shangguan, P. P. Su, X. P. Xu & Xu Yan

65. Zhejiang University, Hangzhou, People's Republic of China

M. X. Luo

66. INFN Sezione di Perugia, Perugia, Italy

A. Mangoni & S. Pacetti

67. University of Minnesota, Minneapolis, MN, USA

H. Muramatsu & R. Poling

68. COMSATS University Islamabad, Lahore, Pakistan

S. Nisar

69. University of Perugia, Perugia, Italy

S. Pacetti

70. Hunan Normal University, Changsha, People's Republic of China

W. Shan

71. Near East University, North Cyprus, Mersin, Turkey

I. Uman

72. North China Electric Power University, Beijing, People's Republic of China

Y. D. Wang & X. D. Zhang

73. Hangzhou Normal University, Hangzhou, People's Republic of China

Q. J. Xu

74. Shanghai Jiao Tong University, Shanghai, People's Republic of China

H. J. Yang

75. China Center of Advanced Science and Technology, Beijing, People's Republic of China

M. H. Ye

76. Xinyang Normal University, Xinyang, People's Republic of China

J. L. Zhang & T. J. Zhu

77. University of Science and Technology Liaoning, Anshan, People's Republic of China

S. H. Zhu

Consortia

The BESIII Collaboration

- , M. Ablikim
- , M. N. Achasov
- , P. Adlarson
- , S. Ahmed
- , M. Albrecht
- , R. Aliberti
- , A. Amoroso
- , M. R. An
- , Q. An
- , X. H. Bai
- , Y. Bai
- , O. Bakina
- , R. Baldini Ferroli
- , I. Balossino
- , Y. Ban
- , K. Begzsuren
- , N. Berger
- , M. Bertani
- , D. Bettoni
- , F. Bianchi

- , J. Biernat
- , J. Bloms
- , A. Bortone
- , I. Boyko
- , R. A. Briere
- , H. Cai
- , X. Cai
- , A. Calcaterra
- , G. F. Cao
- , N. Cao
- , S. A. Cetin
- , J. F. Chang
- , W. L. Chang
- , G. Chelkov
- , D. Y. Chen
- , G. Chen
- , H. S. Chen
- , M. L. Chen
- , S. J. Chen
- , X. R. Chen
- , Y. B. Chen
- , Z. J. Chen
- , W. S. Cheng
- , G. Cibinetto
- , F. Cossio
- , X. F. Cui
- , H. L. Dai
- , X. C. Dai
- , A. Dbeysi
- , R. E. de Boer
- , D. Dedovich
- , Z. Y. Deng
- , A. Denig
- , I. Denysenko
- , M. Destefanis
- , F. De Mori
- , Y. Ding

- , C. Dong
- , J. Dong
- , L. Y. Dong
- , M. Y. Dong
- , X. Dong
- , S. X. Du
- , Y. L. Fan
- , J. Fang
- , S. S. Fang
- , Y. Fang
- , R. Farinelli
- , L. Fava
- , F. Feldbauer
- , G. Felici
- , C. Q. Feng
- , J. H. Feng
- , M. Fritsch
- , C. D. Fu
- , Y. Gao
- , Y. Gao
- , Y. Gao
- , Y. G. Gao
- , I. Garzia
- , P. T. Ge
- , C. Geng
- , E. M. Gersabeck
- , A. Gilman
- , K. Goetzen
- , L. Gong
- , W. X. Gong
- , W. Gradl
- , M. Greco
- , L. M. Gu
- , M. H. Gu
- , S. Gu
- , Y. T. Gu
- , C. Y. Guan

- , A. Q. Guo
- , L. B. Guo
- , R. P. Guo
- , Y. P. Guo
- , A. Guskov
- , T. T. Han
- , W. Y. Han
- , J. Hansson
- , X. Q. Hao
- , F. A. Harris
- , N. Hüskens
- , K. L. He
- , F. H. Heinsius
- , C. H. Heinz
- , T. Held
- , Y. K. Heng
- , C. Herold
- , M. Himmelreich
- , T. Holtmann
- , Y. R. Hou
- , Z. L. Hou
- , H. M. Hu
- , J. F. Hu
- , T. Hu
- , Y. Hu
- , G. S. Huang
- , L. Q. Huang
- , X. T. Huang
- , Y. P. Huang
- , Z. Huang
- , T. Hussain
- , W. Ikegami Andersson
- , W. Imoehl
- , M. Irshad
- , S. Jaeger
- , S. Janchiv
- , Q. Ji

- , Q. P. Ji
- , X. B. Ji
- , X. L. Ji
- , Y. Y. Ji
- , H. B. Jiang
- , X. S. Jiang
- , J. B. Jiao
- , Z. Jiao
- , S. Jin
- , Y. Jin
- , T. Johansson
- , N. Kalantar-Nayestanaki
- , X. S. Kang
- , R. Kappert
- , M. Kavatsyuk
- , B. C. Ke
- , I. K. Keshk
- , A. Khoukaz
- , P. Kiese
- , R. Kiuchi
- , R. Kliemt
- , L. Koch
- , O. B. Kolcu
- , B. Kopf
- , M. Kuemmel
- , M. Kuessner
- , A. Kupsc
- , M. G. Kurth
- , W. Kühn
- , J. J. Lane
- , J. S. Lange
- , P. Larin
- , A. Lavania
- , L. Lavezzi
- , Z. H. Lei
- , H. Leithoff
- , M. Lellmann

- , T. Lenz
- , C. Li
- , C. H. Li
- , Cheng Li
- , D. M. Li
- , F. Li
- , G. Li
- , H. Li
- , H. Li
- , H. B. Li
- , H. J. Li
- , H. J. Li
- , J. L. Li
- , J. Q. Li
- , J. S. Li
- , Ke Li
- , L. K. Li
- , Lei Li
- , P. R. Li
- , S. Y. Li
- , W. D. Li
- , W. G. Li
- , X. H. Li
- , X. L. Li
- , Xiaoyu Li
- , Z. Y. Li
- , H. Liang
- , H. Liang
- , H. Liang
- , Y. F. Liang
- , Y. T. Liang
- , G. R. Liao
- , L. Z. Liao
- , J. Libby
- , C. X. Lin
- , B. J. Liu
- , C. X. Liu

- , D. Liu
- , F. H. Liu
- , Fang Liu
- , Feng Liu
- , H. B. Liu
- , H. M. Liu
- , Huanhuan Liu
- , Huihui Liu
- , J. B. Liu
- , J. L. Liu
- , J. Y. Liu
- , K. Liu
- , K. Y. Liu
- , Ke Liu
- , L. Liu
- , M. H. Liu
- , P. L. Liu
- , Q. Liu
- , Q. Liu
- , S. B. Liu
- , Shuai Liu
- , T. Liu
- , W. M. Liu
- , X. Liu
- , Y. Liu
- , Y. B. Liu
- , Z. A. Liu
- , Z. Q. Liu
- , X. C. Lou
- , F. X. Lu
- , F. X. Lu
- , H. J. Lu
- , J. D. Lu
- , J. G. Lu
- , X. L. Lu
- , Y. Lu
- , Y. P. Lu

- , C. L. Luo
- , M. X. Luo
- , P. W. Luo
- , T. Luo
- , X. L. Luo
- , S. Lusso
- , X. R. Lyu
- , F. C. Ma
- , H. L. Ma
- , L. L. Ma
- , M. M. Ma
- , Q. M. Ma
- , R. Q. Ma
- , R. T. Ma
- , X. X. Ma
- , X. Y. Ma
- , F. E. Maas
- , M. Maggiora
- , S. Maldaner
- , S. Malde
- , Q. A. Malik
- , A. Mangoni
- , Y. J. Mao
- , Z. P. Mao
- , S. Marcello
- , Z. X. Meng
- , J. G. Messchendorp
- , G. Mezzadri
- , T. J. Min
- , R. E. Mitchell
- , X. H. Mo
- , Y. J. Mo
- , N. Yu. Muchnoi
- , H. Muramatsu
- , S. Nakhoul
- , Y. Nefedov
- , F. Nerling

- , I. B. Nikolaev
- , Z. Ning
- , S. Nisar
- , S. L. Olsen
- , Q. Ouyang
- , S. Pacetti
- , X. Pan
- , Y. Pan
- , A. Pathak
- , P. Patteri
- , M. Pelizaeus
- , H. P. Peng
- , K. Peters
- , J. L. Ping
- , R. G. Ping
- , R. Poling
- , V. Prasad
- , H. Qi
- , H. R. Qi
- , K. H. Qi
- , M. Qi
- , T. Y. Qi
- , T. Y. Qi
- , S. Qian
- , W. B. Qian
- , Z. Qian
- , C. F. Qiao
- , L. Q. Qin
- , X. P. Qin
- , X. S. Qin
- , Z. H. Qin
- , J. F. Qiu
- , S. Q. Qu
- , K. H. Rashid
- , K. Ravindran
- , C. F. Redmer
- , A. Rivetti

- , V. Rodin
- , M. Rolo
- , G. Rong
- , Ch. Rosner
- , M. Rump
- , H. S. Sang
- , A. Sarantsev
- , Y. Schelhaas
- , C. Schnier
- , K. Schönning
- , M. Scodeggio
- , D. C. Shan
- , W. Shan
- , X. Y. Shan
- , J. F. Shangguan
- , M. Shao
- , C. P. Shen
- , P. X. Shen
- , X. Y. Shen
- , H. C. Shi
- , R. S. Shi
- , X. Shi
- , X. D. Shi
- , J. J. Song
- , W. M. Song
- , Y. X. Song
- , S. Sosio
- , S. Spataro
- , K. X. Su
- , P. P. Su
- , F. F. Sui
- , G. X. Sun
- , H. K. Sun
- , J. F. Sun
- , L. Sun
- , S. S. Sun
- , T. Sun

- , W. Y. Sun
- , W. Y. Sun
- , X. Sun
- , Y. J. Sun
- , Y. K. Sun
- , Y. Z. Sun
- , Z. T. Sun
- , Y. H. Tan
- , Y. X. Tan
- , C. J. Tang
- , G. Y. Tang
- , J. Tang
- , J. X. Teng
- , V. Thoren
- , Y. T. Tian
- , I. Uman
- , B. Wang
- , C. W. Wang
- , D. Y. Wang
- , H. J. Wang
- , H. P. Wang
- , K. Wang
- , L. L. Wang
- , M. Wang
- , M. Z. Wang
- , Meng Wang
- , W. Wang
- , W. H. Wang
- , W. P. Wang
- , X. Wang
- , X. F. Wang
- , X. L. Wang
- , Y. Wang
- , Y. Wang
- , Y. D. Wang
- , Y. F. Wang
- , Y. Q. Wang

- , Y. Y. Wang
- , Z. Wang
- , Z. Y. Wang
- , Ziyi Wang
- , Zongyuan Wang
- , D. H. Wei
- , P. Weidenkaff
- , F. Weidner
- , S. P. Wen
- , D. J. White
- , U. Wiedner
- , G. Wilkinson
- , M. Wolke
- , L. Wollenberg
- , J. F. Wu
- , L. H. Wu
- , L. J. Wu
- , X. Wu
- , Z. Wu
- , L. Xia
- , H. Xiao
- , S. Y. Xiao
- , Z. J. Xiao
- , X. H. Xie
- , Y. G. Xie
- , Y. H. Xie
- , T. Y. Xing
- , G. F. Xu
- , Q. J. Xu
- , W. Xu
- , X. P. Xu
- , Y. C. Xu
- , F. Yan
- , L. Yan
- , W. B. Yan
- , W. C. Yan
- , Xu Yan

- , H. J. Yang
- , H. X. Yang
- , L. Yang
- , S. L. Yang
- , Y. X. Yang
- , Yifan Yang
- , Zhi Yang
- , M. Ye
- , M. H. Ye
- , J. H. Yin
- , Z. Y. You
- , B. X. Yu
- , C. X. Yu
- , G. Yu
- , J. S. Yu
- , T. Yu
- , C. Z. Yuan
- , L. Yuan
- , X. Q. Yuan
- , Y. Yuan
- , Z. Y. Yuan
- , C. X. Yue
- , A. A. Zafar
- , Y. Zeng
- , B. X. Zhang
- , Guangyi Zhang
- , H. Zhang
- , H. H. Zhang
- , H. H. Zhang
- , H. Y. Zhang
- , J. J. Zhang
- , J. L. Zhang
- , J. Q. Zhang
- , J. W. Zhang
- , J. Y. Zhang
- , J. Z. Zhang
- , Jianyu Zhang

- , Jiawei Zhang
- , L. M. Zhang
- , L. Q. Zhang
- , Lei Zhang
- , S. Zhang
- , S. F. Zhang
- , Shulei Zhang
- , X. D. Zhang
- , X. Y. Zhang
- , Y. Zhang
- , Y. H. Zhang
- , Y. T. Zhang
- , Yan Zhang
- , Yao Zhang
- , Yi Zhang
- , Z. H. Zhang
- , Z. Y. Zhang
- , G. Zhao
- , J. Zhao
- , J. Y. Zhao
- , J. Z. Zhao
- , Lei Zhao
- , Ling Zhao
- , M. G. Zhao
- , Q. Zhao
- , S. J. Zhao
- , Y. B. Zhao
- , Y. X. Zhao
- , Z. G. Zhao
- , A. Zhemchugov
- , B. Zheng
- , J. P. Zheng
- , Y. Zheng
- , Y. H. Zheng
- , B. Zhong
- , C. Zhong
- , L. P. Zhou

- , Q. Zhou
- , X. Zhou
- , X. K. Zhou
- , X. R. Zhou
- , X. Y. Zhou
- , A. N. Zhu
- , J. Zhu
- , K. Zhu
- , K. J. Zhu
- , S. H. Zhu
- , T. J. Zhu
- , W. J. Zhu
- , W. J. Zhu
- , Y. C. Zhu
- , Z. A. Zhu
- , B. S. Zou
- & J. H. Zou

Contributions

All authors have contributed to the publication, being variously involved in the design and the construction of the detectors, in writing software, calibrating sub-systems, operating the detectors and acquiring data and finally analysing the processed data.

Ethics declarations

Competing interests

The authors declare no competing interests.

Peer review

Peer review information

Nature thanks Yasmine Amhis, Sandrine Emery-Schrenk and the other, anonymous, reviewer(s) for their contribution to the peer review of this work. [Peer reviewer reports](#) are available.

Additional information

Publisher's note Springer Nature remains neutral with regard to jurisdictional claims in published maps and institutional affiliations.

Extended data figures and tables

[Extended Data Fig. 1 Final-state particle momenta of pions and protons for the decay process \$\langle J/\psi \rightarrow \bar{\chi}_i \rangle^{\{-\}} \cdot \langle \bar{\chi}_i \rangle^{\{+\}} \rightarrow \bar{\Lambda} \langle \pi \rangle^{\{-\}} \bar{\Lambda} \langle \pi \rangle^{\{+\}} \cdot \langle \pi \rangle^{\{-\}} \langle p \rangle \langle \pi \rangle^{\{+\}} \langle \pi \rangle^{\{+\}} \rangle\$](#)

The non-overlapping momentum ranges of the protons and pions allow for a straightforward assignment of particle species. The blue boxes and the red solid line denote the experimental and simulated data, respectively.

[Extended Data Fig. 2 Invariant mass distributions of the \$\Xi^-\$ and \$\langle \bar{\Lambda} \boldsymbol{\chi}_i \rangle^{\{+\}}\$ signal candidates.](#)

Distribution of the invariant masses $\langle m \rangle_{\langle \bar{\Lambda} \rangle \langle \pi \rangle^{\{-\}}} \rangle$ versus $\langle m \rangle_{\langle \bar{\Lambda} \rangle \langle \pi \rangle^{\{+\}}} \rangle$. The $\langle \langle \chi_i \rangle^{\{-\}} \rangle \langle \bar{\chi}_i \rangle^{\{+\}} \rangle$ candidates appear as an enhancement around $\langle m \rangle_{\langle \bar{\Lambda} \rangle \langle \pi \rangle^{\{-\}}} = \langle m \rangle_{\langle \bar{\Lambda} \rangle \langle \pi \rangle^{\{+\}}} = 1.32 \text{ GeV}/c^2$. The structure at $\langle m \rangle_{\langle \bar{\Lambda} \rangle \langle \pi \rangle^{\{+\}}} = 1.39 \text{ GeV}/c^2$ is from the reaction $\langle J/\psi \rightarrow \bar{\sigma}(1385) \rangle^{\{-\}} \langle \bar{\sigma}(1385) \rangle^{\{+\}}$.

[Extended Data Fig. 3 Invariant mass distribution of the \$\Xi^-\$ signal candidates before the final selection criterion.](#)

The $\Lambda\pi^-$ distribution, in log scale, for the BESIII data sample before the $\Lambda\pi^-$ mass window has been applied. The final requirement selects the events between the two lines. The total number of events in the distribution is 76,523.

Extended Data Table 1 Correlation coefficients for the production and asymmetry decay parameters

Extended Data Table 2 Contributing systematic uncertainties, and the sum in quadrature

Extended Data Table 3 Contributing systematic uncertainties to CP tests, and the sum in quadrature

Extended Data Table 4 Contributing systematic uncertainties to average values of decay parameters, and the sum in quadrature

Supplementary information

Peer Review File

Rights and permissions

Open Access This article is licensed under a Creative Commons Attribution 4.0 International License, which permits use, sharing, adaptation, distribution and reproduction in any medium or format, as long as you give appropriate credit to the original author(s) and the source, provide a link to the Creative Commons license, and indicate if changes were made. The images or other third party material in this article are included in the article's Creative Commons license, unless indicated otherwise in a credit line to the material. If material is not included in the article's Creative Commons license and your intended use is not permitted by statutory regulation or exceeds the permitted use, you will need to obtain permission directly from the copyright holder. To view a copy of this license, visit <http://creativecommons.org/licenses/by/4.0/>.

Reprints and Permissions

About this article

Cite this article

The BESIII Collaboration. Probing CP symmetry and weak phases with entangled double-strange baryons. *Nature* **606**, 64–69 (2022).

<https://doi.org/10.1038/s41586-022-04624-1>

- Received: 20 May 2021
- Accepted: 08 March 2022
- Published: 01 June 2022
- Issue Date: 02 June 2022
- DOI: <https://doi.org/10.1038/s41586-022-04624-1>

Share this article

Anyone you share the following link with will be able to read this content:

[Get shareable link](#)

Sorry, a shareable link is not currently available for this article.

[Copy to clipboard](#)

Provided by the Springer Nature SharedIt content-sharing initiative

This article was downloaded by **calibre** from <https://www.nature.com/articles/s41586-022-04624-1>

[Download PDF](#)

- Article
- Open Access
- [Published: 01 June 2022](#)

Quantum computational advantage with a programmable photonic processor

- [Lars S. Madsen](#)¹ na1,
- [Fabian Laudenbach](#)¹ na1,
- [Mohsen Falamarzi Askarani](#)¹ na1,
- [Fabien Rortais](#)¹,
- [Trevor Vincent](#)¹,
- [Jacob F. F. Bulmer](#) [ORCID: orcid.org/0000-0002-2633-9569](#)¹,
- [Filippo M. Miatto](#) [ORCID: orcid.org/0000-0002-6684-8341](#)¹,
- [Leonhard Neuhaus](#)¹,
- [Lukas G. Helt](#) [ORCID: orcid.org/0000-0003-0346-2342](#)¹,
- [Matthew J. Collins](#) [ORCID: orcid.org/0000-0003-3969-5797](#)¹,
- [Adriana E. Lita](#)²,
- [Thomas Gerrits](#)²,
- [Sae Woo Nam](#)²,
- [Varun D. Vaidya](#)¹,
- [Matteo Menotti](#)¹,
- [Ish Dhand](#)¹,
- [Zachary Vernon](#) [ORCID: orcid.org/0000-0003-3268-6986](#)¹,
- [Nicolás Quesada](#) ¹ &
- [Jonathan Lavoie](#) [ORCID: orcid.org/0000-0002-5208-6729](#)¹

Nature volume **606**, pages 75–81 (2022)

- 9839 Accesses
- 805 Altmetric
- [Metrics details](#)

Subjects

- [Information theory and computation](#)
- [Quantum information](#)
- [Quantum optics](#)
- [Quantum simulation](#)
- [Single photons and quantum effects](#)

Abstract

A quantum computer attains computational advantage when outperforming the best classical computers running the best-known algorithms on well-defined tasks. No photonic machine offering programmability over all its quantum gates has demonstrated quantum computational advantage:

previous machines^{1,2} were largely restricted to static gate sequences. Earlier photonic demonstrations were also vulnerable to spoofing³, in which classical heuristics produce samples, without direct simulation, lying closer to the ideal distribution than do samples from the quantum hardware.

Here we report quantum computational advantage using Borealis, a photonic processor offering dynamic programmability on all gates implemented. We carry out Gaussian boson sampling⁴ (GBS) on 216 squeezed modes entangled with three-dimensional connectivity⁵, using a time-multiplexed and photon-number-resolving architecture. On average, it would take more than 9,000 years for the best available algorithms and supercomputers to produce, using exact methods, a single sample from the programmed distribution, whereas Borealis requires only 36 μs. This runtime advantage is over 50 million times as extreme as that reported from earlier photonic machines. Ours constitutes a very large GBS experiment, registering events with up to 219 photons and a mean photon number of 125. This work is a critical milestone on the path to a practical quantum computer, validating key technological features of photonics as a platform for this goal.

Main

Only a handful of experiments have used quantum devices to carry out computational tasks that are outside the reach of present-day classical computers^{1,2,6,7}. In all of these, the computational task involved sampling from probability distributions that are widely believed to be exponentially hard to simulate using classical computation. One such demonstration relied on a 53-qubit programmable superconducting processor⁶, whereas another used a non-programmable photonic platform implementing Gaussian boson sampling (GBS) with 50 squeezed states fed into a static random 100-mode interferometer¹. Both were shortly followed by larger versions, respectively enjoying more qubits^{7,8} and increased control over brightness and a limited set of circuit parameters². In these examples, comparison of the duration of the quantum sampling experiment to the estimated runtime and scaling of the best-known classical algorithms placed their respective platforms within the regime of quantum computational advantage.

The superconducting quantum supremacy demonstrations serve as crucial milestones on the path to full-scale quantum computation. On the other hand, the choice of technologies used in the photonic machines^{1,2}, and their consequential lack of programmability and scalability, places them outside any current proposed roadmap for fault-tolerant photonic quantum computing^{9,10,11} or any GBS application^{12,13,14,15,16,17,18}. A demonstration of photonic quantum computational advantage incorporating hardware capabilities required for the platform to progress along the road to fault-tolerance is still lacking.

In photonics, time-domain multiplexing offers a comparatively hardware-efficient¹⁹ path for building fault-tolerant quantum computers, but also near-term subuniversal machines showing quantum computational advantage. By encoding quantum information in sequential pulses of light—effectively multiplexing a small number of optical channels to process information on a large number of modes²⁰—large and highly entangled states can be processed with a relatively small number of optical components. This decouples the required component count and physical extent of the machine from the size of the quantum circuit being executed; provided device

imperfections can be maintained sufficiently small, this decoupling represents a substantial advantage for scaling. Moreover, the relatively modest number of optical pathways and control components avoids many of the challenges of traditional, planar two-dimensional implementations of optical interferometers, which suffer from high complexity and burdensome parallel control requirements, especially when long-range connectivity is desired. Although attractive for scaling, hardware efficiency must not come at the cost of unacceptably large errors. Implementations of time-domain multiplexing must therefore be tested in demanding contexts to validate their promise for building practically useful quantum computers.

Using time-domain multiplexing, large one- and two-dimensional cluster states have been deterministically generated^{21,22,23} with programmable linear operations implemented by projective measurements^{24,25}, whereas similar operations have been implemented in ref. ²⁶ using a single loop with reconfigurable phase. These demonstrations leverage low-loss optical fibre for delay lines, which allows photonic quantum information to be effectively buffered. Although groundbreaking, these demonstrations have remained well outside the domain of quantum computational advantage, as they lacked non-Gaussian elements and were unable to synthesize states of sufficient complexity to evade efficient classical simulation²⁷. The demonstration of a set of hardware capabilities needed for universal fault-tolerant quantum computing, in the demanding context of quantum computational advantage, would serve as a validating signal that the corresponding technologies are advancing as needed. Yet no such demonstration is available for time-domain multiplexing.

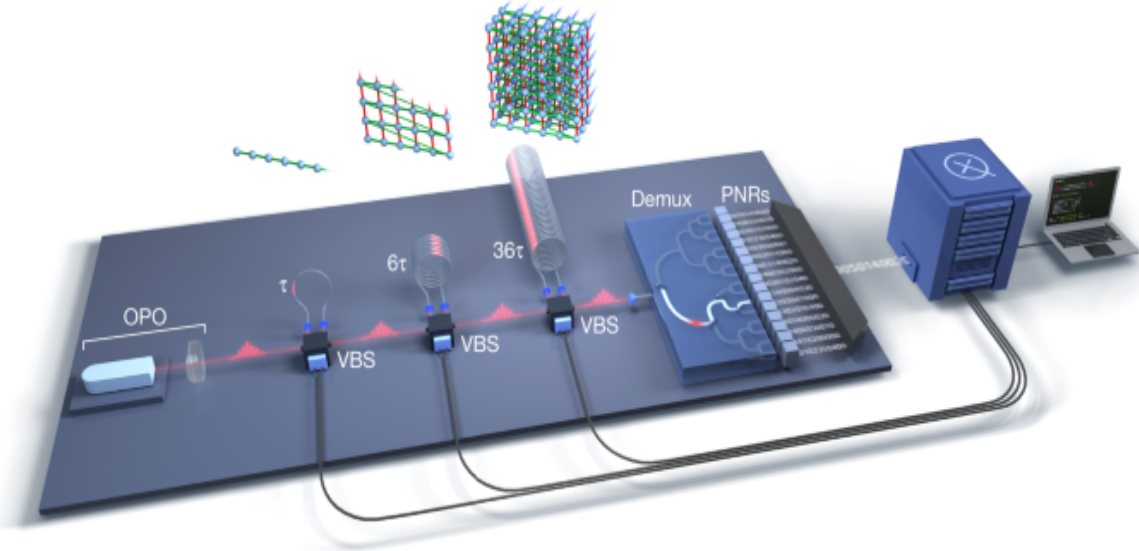
In this work, we solve technological hurdles associated with time-domain multiplexing, fast electro-optical switching, high-speed photon-number-resolving detection technology and non-classical light generation, to build a scalable and programmable Gaussian boson sampler, which we name Borealis. These features allow us to synthesize a 216-mode state with a three-dimensional entanglement topology. This is particularly notable because three-dimensional cluster states are sufficient for measurement-based fault-tolerant quantum computing^{28,29}; although the states we synthesize are themselves not cluster states, the device can be readily programmed to generate cluster states by selecting appropriate phase and

beam-splitting ratios at the loops. Borealis uses 216 independent quantum systems to achieve quantum computational advantage, placing it well beyond the capabilities of current state-of-the-art classical simulation algorithms³⁰. Our use of photon-number-resolving detectors unlocks access to sampling events with much larger total photon number, a regime inaccessible to earlier experiments that used traditional threshold detectors. In the same vein, our use of time-domain multiplexing allows us access to more squeezed modes without increasing the physical extent or complexity of the system. In addition, its output cannot be efficiently spoofed in cross-entropy benchmarks using a generalization of the most recent polynomial-time algorithms³. We leave as an open question to the community whether better polynomial-time algorithms for spoofing can be developed.

Experiment

The optical circuit we implement, depicted in Fig. 1, is fully programmable, provides long-range coupling between different modes and allows all such couplings to be dynamically programmed. It implements linear-optical transformations on a train of input squeezed-light pulses, using a sequence of three variable beamsplitters (VBSs) and phase-stabilized fibre loops that act as effective buffer memory for light, allowing interference between modes that are either temporally adjacent, or separated by six or 36 time bins. This system synthesizes a programmable multimode entangled Gaussian state in a 6 MHz pulse train, which is then partially demultiplexed to 16 output channels and sampled from using photon-number-resolving detectors.

Fig. 1: High-dimensional GBS from a fully programmable photonic processor.



A periodic pulse train of single-mode squeezed states from a pulsed OPO enters a sequence of three dynamically programmable loop-based interferometers. Each loop contains a VBS, including a programmable phase shifter, and an optical fibre delay line. At the output of the interferometer, the Gaussian state is sent to a 1-to-16 binary switch tree (demux), which partially demultiplexes the output before readout by PNRs. The resulting detected sequence of 216 photon numbers, in approximately 36 μ s, comprises one sample. The fibre delays and accompanying beamsplitters and phase shifters implement gates between both temporally adjacent and distant modes, enabling high-dimensional connectivity in the quantum circuit. Above each loop stage is depicted a lattice representation of the multipartite entangled Gaussian state being progressively synthesized. The first stage (τ) effects two-mode programmable gates (green edges) between nearest-neighbour modes in one dimension, whereas the second (6τ) and third (36τ) mediate couplings between modes separated by six and 36 time bins in the second and third dimensions (red and blue edges, respectively). Each run of the device involves the specification of 1,296 real parameters, corresponding to the sequence of settings for all VBS units.

Unlike some quantum algorithms whose correct functioning on a quantum computer can be readily verified using a classical computer, it remains an open question how to verify that a GBS device is operating correctly. In what follows, we present evidence that our machine is operating correctly, that is, it samples from the GBS distribution specified by the device transfer

matrix T and vector of squeezing parameters \mathbf{r} , which together define the ground truth of the experiment. In previous experiments^{1,2} the results were benchmarked against a ground truth obtained from tomographic measurements of a static interferometer, whereas for Borealis, the ground truth is obtained from the quantum program specified by the user, that is the squeezing parameters and phases sent to the VBS components in the device.

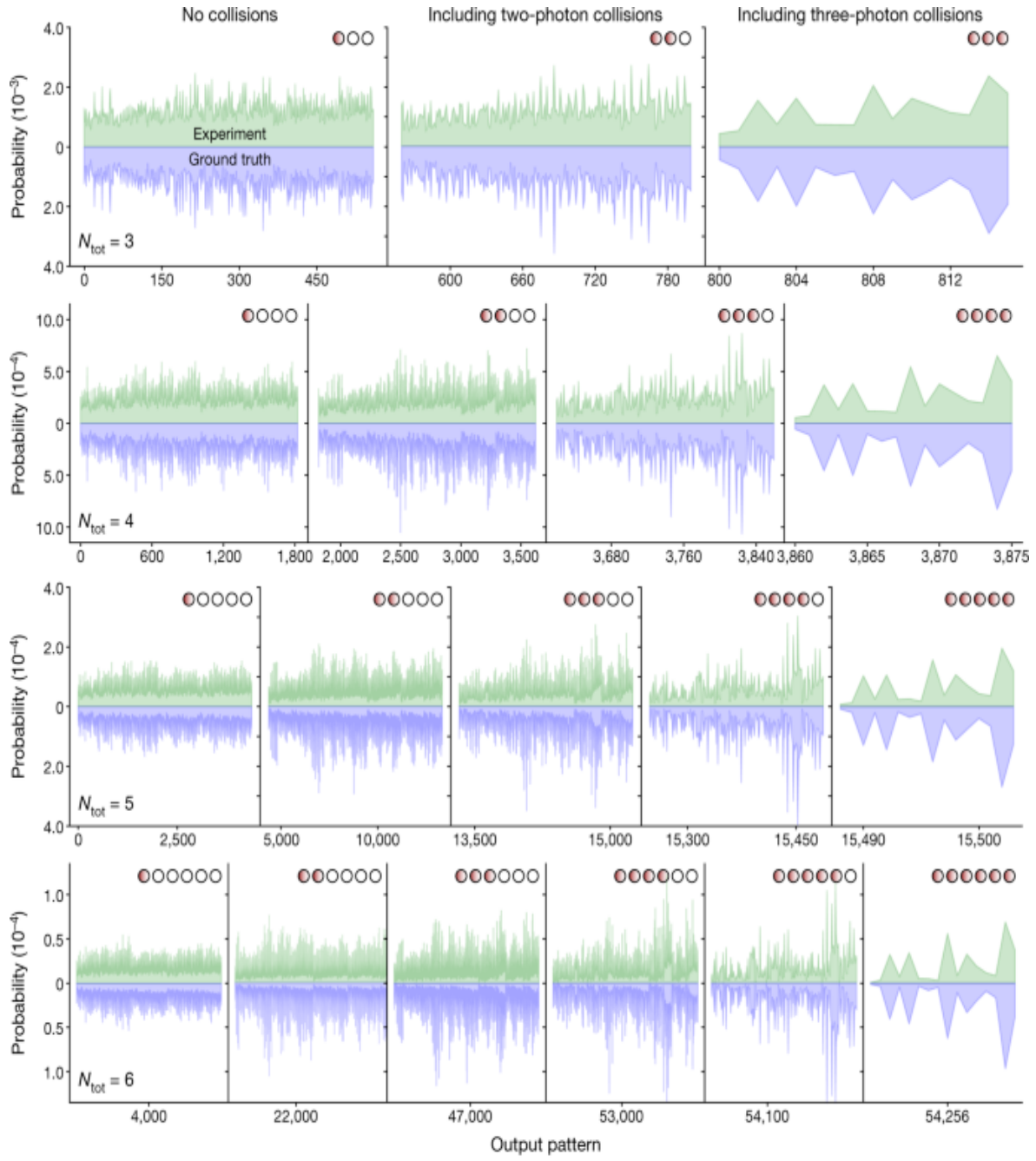
The transfer matrix is obtained by combining the three layers of VBSs acting over the different modes, together with common (to all modes) losses due to propagation and the finite escape efficiency of the source, as well as imperfect transmittance through the demultiplexing and detection systems; it corresponds classically (quantum mechanically) to the linear transformation connecting input and output electric fields (annihilation operators).

As noted in refs. ^{5,31}, if one were to target a universal and programmable interferometer, with depth equal to the number of modes, that covers densely the set of unitary matrices, the exponential accumulation of loss would prohibit showing a quantum advantage. There are then two ways around this no-go result: one can either give up programmability and build an ultralow loss fixed static interferometer, as implemented in refs. ^{1,2}, or give up universality while maintaining a high degree of multimode entanglement using long-ranged gates.

We first consider the regime of few modes and low photon number, in which it is possible to collect enough samples to estimate outcome probabilities, and also calculate these from the experimentally characterized lossy transmission matrix T and the experimentally obtained squeezing parameters \mathbf{r} programmed into the device. In Fig. 2 we show the probabilities inferred from the random samples collected in the experiment and compare them against the probabilities for different samples S obtained from simulations, under the ground truth assumption. We cover the output pattern of all possible permutations $\langle\langle\begin{array}{c}N+M-1\\ N\end{array}\rangle\rangle$, in which N is the number of photons, from 3 to 6, and $M=16$ is the number of modes. To quantify the performance of Borealis we calculate the fidelity (F) and total variation distance (TVD) of the 3, 4, 5 and 6 total photon-number probabilities relative to the ground truth. For a particular total photon number, fidelity and TVD are, respectively, defined as $\langle F = \sum_i p_i \sqrt{q_i} \rangle$ (also known as the Bhattacharyya coefficient)

and $\text{rm}\{\text{TVD}\} = \sum_i |p_i - q_i|/2$. Parameters p_i and q_i represent the theoretical and experimental probability of the i th output pattern, respectively, and are normalized by the probability of the respective total photon number. For the total photon-number sectors considered we find fidelities in excess of 99% and TVDs below or equal to 6.5%, thus showing that our machine is reasonably close to the ground truth in the low- N regime addressed by these data. Note that, because we are calculating all the possible probabilities with N photons, estimating outcome probabilities from the experimentally characterized transmission matrix would require us to obtain orders of magnitude more samples, beyond our current processing abilities. This limitation will lead to TVD growing as N increases and, beside the impractical computational cost, is the reason that data past $N > 6$ were left for subsequent benchmarks.

Fig. 2: Experimental validation of the GBS device.



N	F	TVD
3	0.999(11)	0.039(1)
4	0.998(6)	0.047(1)
5	0.998(3)	0.054(1)
6	0.997(2)	0.065(1)

Each panel compares experimentally obtained sample probabilities, against those calculated from the ground truth (r, T), for up to six-photon events in a 16-mode state. A total of 84.1×10^6 samples were collected and divided

according to their total photon number N and further split according to the collision pattern, from no collision (no more than one photon detected per PNR) to collisions of different densities (more than one photon per PNR). The overall fidelity (F) and TVD to simulations for each photon-number event is shown below. Further analysis of TVD for classical adversaries in the 16-mode GBS instance can be found in the [Supplementary Information](#).

In an intermediate mode- and photon-number regime, we calculate the cross entropy of the samples generated by the experiment for each total photon-number sector for a high-dimensional GBS instance with $M=216$ computational modes and total mean photon number $\langle\bar{N}\rangle=21.120\pm 0.006$. For a set of K samples $\{\{S_i\}\}_{i=1}^K$, each having a total of N photons, the cross-entropy benchmark under the ground truth given by (\mathbf{r}, T) is

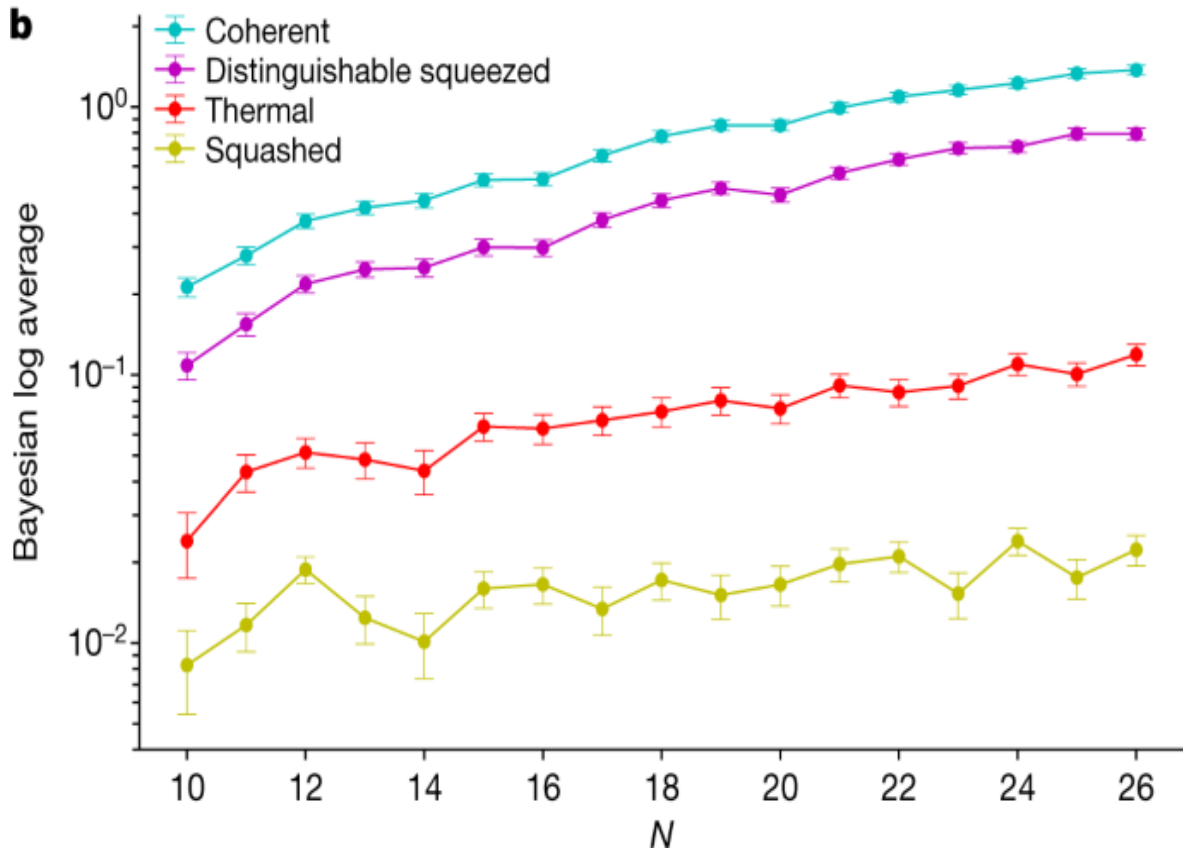
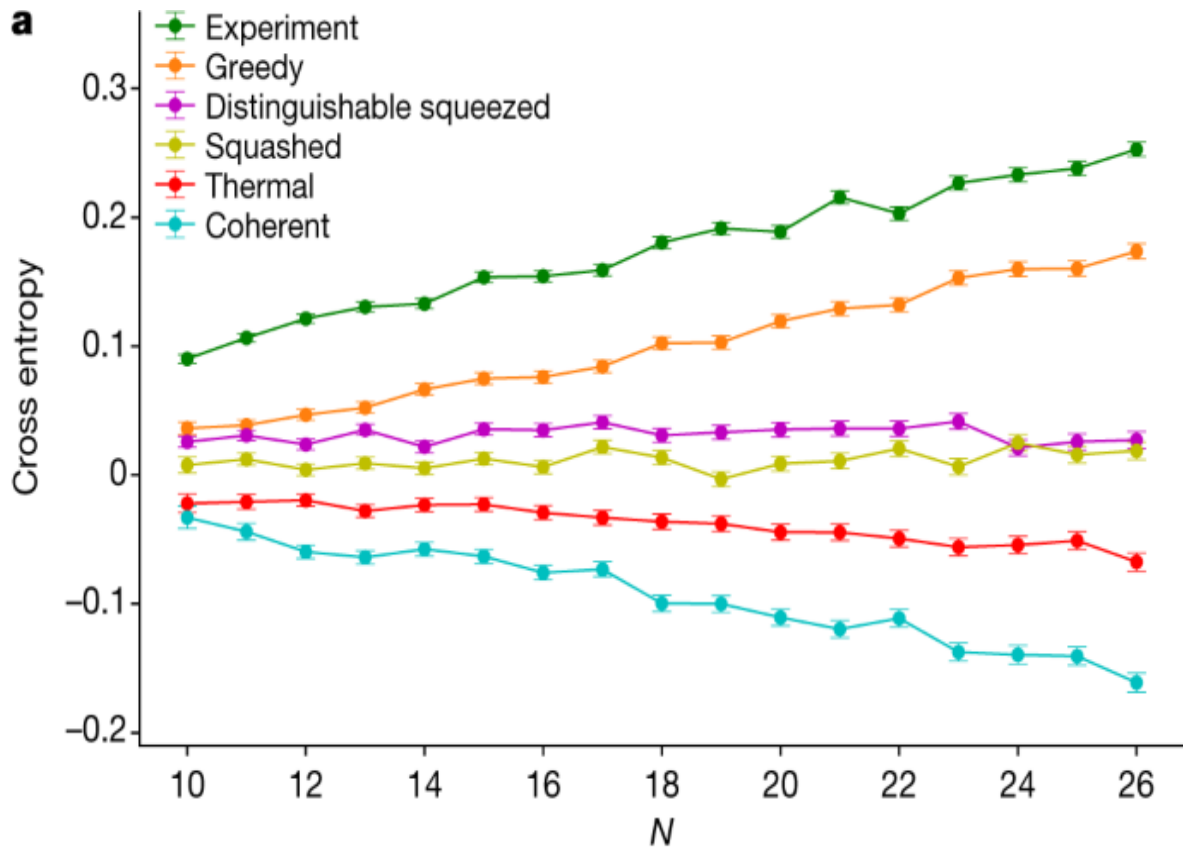
$$\text{XE} = -\frac{1}{K} \sum_{i=1}^K \ln \left(\frac{\Pr(S_i)}{\Pr^{(0)}(S_i)} \right) \quad (1)$$

where $\Pr^{(0)}(N) = \Pr(N)/(N!)$ is a normalization constant determined by the total number of ways in which N photons can be placed in M modes and $\Pr^{(0)}(N)$ is the probability of obtaining a total of N photons under the ground truth assumption.

We then compare the average score (Fig. [3a](#)) of the 10^6 samples, divided in 10,000 samples per total photon number N , generated by our machine in the cross entropy against classical adversarial spoofers that try to mimic the ground truth distribution (\mathbf{r}, T) . These adversaries are constructed with the extra constraint that they must have the same first-order (mean) photon-number cumulants as the ground truth distribution. The five adversaries considered send (1) squashed, (2) thermal, (3) coherent and (4) distinguishable squeezed light into the interferometer specified by T , or (5) use a greedy algorithm to mimic the one- and two-mode marginal distributions of the ground truth, as was used in ref. [3](#) to spoof earlier large GBS experiments^{[1,2](#)}. Squashed states (1) are the classical-Gaussian states with the highest fidelity to lossy-squeezed states^{[31](#)}, that is they are optimal

within the family of Gaussian states that are classical, and thus provide a more powerful adversary than thermal, coherent or distinguishable squeezed states, which were the only adversaries considered in previous photonic quantum computational advantage claims^{1,2}. In all cases, the samples from Borealis perform significantly better than any adversary at having a high cross entropy with respect to the ground truth; equivalently, none of the adversaries are successful spoofers in this benchmark. In particular, the best-performing adversary—the greedy sampler—remains significantly below the experiment in cross-entropy, and shows no trend towards outperforming the experiment for larger N . Given the supercomputing resources and time needed to estimate all scores for $N=26$ (22 h), we can extrapolate this time and estimate that it would take roughly 20 days to benchmark our data for $N=30$. For this reason, and the lack of evidence that the scores may change in favour of any alternative to the ground truth, we are confident that the studied range of $N=[10,26]$ is sufficient to rule out all classical spoofers considered, even in the regime in which it is unfeasible to perform these benchmarks.

Fig. 3: Benchmarks against the ground truth.



a, Cross-entropy benchmark against the ground truth. Experimental samples from a high-dimensional GBS instance of 216 modes, averaging $\langle \bar{N} \rangle = 21.120 \pm 0.006$ photons per sample, are bundled according to their total photon number N , from 10 to 26. Each point (score) corresponds to an average (equation (1)) over 10,000 samples per N . Genuine samples from the quantum hardware score higher than all classical spoofers, validating the high device fidelity with the ground truth. Error bars are standard errors of the mean. **b**, Bayesian log average score against the ground truth. Experimental samples from a 72-mode GBS instance and $\langle \bar{N} \rangle = 22.416 \pm 0.006$ photon number per sample. Each score is averaged over 2,000 samples with N from 10 to 26. Error bars are standard errors of the mean. All scores are above zero, including error bar, indicating that the samples generated by Borealis are closer to the ground truth than from the adversarial distribution corresponding to squashed, thermal, coherent and distinguishable squeezed spoofers.

Next, we consider another test—a Bayesian method similar to that used in other GBS demonstrations^{1,2}. For each subset of samples generated in the experiment with a given total photon number N , we calculate the ratio of the probability that a sample S could have come from the lossy ground truth specified by T and \mathbf{r} to the probability that S came from any of the alternative spoofing hypotheses (1)–(4). For a particular sample S_i and a particular adversary I this ratio is given by

$$\begin{aligned} \text{\$}\{\text{R}\}^{\wedge\{0\}}(\{S\}_{\text{i}}) &= \frac{\{\{\text{rm}\{\text{Pr}\}\}\}^{\wedge\{0\}}(\{S\}_{\text{i}}|N)}{\{\{\text{rm}\{\text{Pr}\}\}\}^{\wedge\{I\}}(\{S\}_{\text{i}}|N)} = \frac{\{\{\text{rm}\{\text{Pr}\}\}\}^{\wedge\{0\}}(\{S\}_{\text{i}})}{\{\{\text{rm}\{\text{Pr}\}\}\}^{\wedge\{I\}}(N)} \cdot \frac{\{\{\text{rm}\{\text{Pr}\}\}\}^{\wedge\{I\}}(\{S\}_{\text{i}})}{\{\{\text{rm}\{\text{Pr}\}\}\}^{\wedge\{0\}}(N)}. \\ (2) \end{aligned}$$

which allows us to form the Bayesian log average

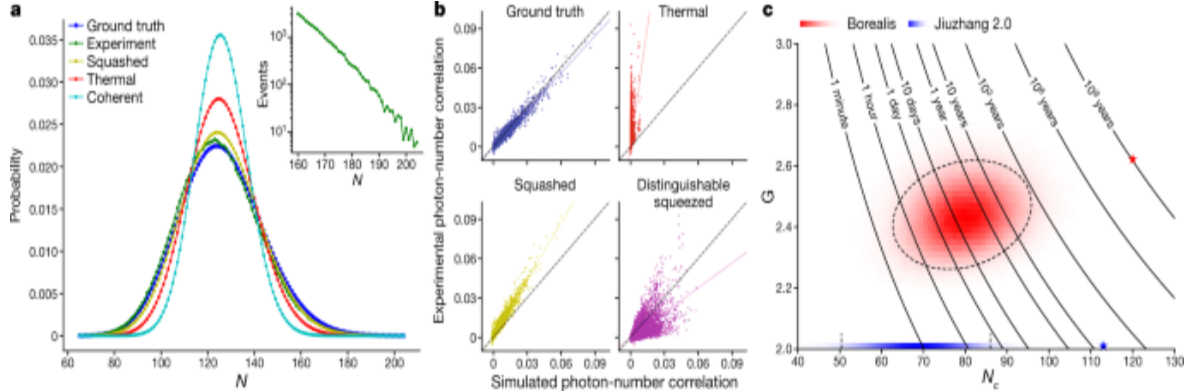
$$\frac{1}{K} \sum_{i=1}^K \ln R^{S_i}(3)$$

If $\Delta \{H\}_{0|I} > 0$ we conclude that the samples generated by Borealis are more likely to have come from the ground truth than from the adversarial distribution corresponding to the first four spoofers (1)–(4); the

greedy adversary (5) can generate samples mimicking the ground truth but there is no known expression or algorithm to obtain the ‘greedy probability distribution’, thus we cannot use it to generate a Bayesian score. One can see in Fig. 3b that the Bayesian log average is strictly above zero for all remaining adversaries.

Finally, we consider the regime of many modes and large photon number, in which calculating the probability of even a single event using a classical computer is unfeasible. In this regime we consider the first- and second-order cumulants of the photon-number distributions of 216 modes and 10^6 samples against the lossy ground truth and the different spoofer distributions. Note that these samples are generated from the same family of unitaries as the samples generated in the intermediate regime, we only change the brightness of the squeezed input light. In Fig. 4a we plot the total photon-number probability distributions measured in the experiment, and calculated from the ground truth and different spoofers. By construction, the samples generated from each classical adversary have the same first-order cumulants (mode photon-number means) as the ground truth and thus they also have the same total mean photon number centred at $\langle \bar{N} \rangle = 125$. Deliberately matching the first moments exactly to the ground truth ensures that we give our adversaries fair conditions to spoof our experiment. However, their second-order cumulants, defined between mode i and mode j as $\langle C_{ij} \rangle = \langle n_i n_j \rangle - \langle n_i \rangle \langle n_j \rangle$ with n_i the photon number in mode i , are different. We calculate the distribution of all C_{ij} obtained experimentally and compare the result with those obtained from theoretical predictions and different adversaries, as shown in Fig. 4b. These cumulants can be calculated efficiently. Overall, it is clear that the statistics of experimental samples diverge from the adversarial hypotheses considered and agree with the ground truth of our device (as seen in the top left panel of Fig. 4b) where they cluster around the identity line at 45° .

Fig. 4: Quantum computational advantage.



a, Measured photon statistics of 10^6 samples of a high-dimensional Gaussian state compared with those generated numerically from different hypotheses. The inset shows the same distribution in a log scale having significant support past 160 photons, up to 219. **b**, Scatter plot of two-mode cumulants C_{ij} for all the pairs of modes comparing experimentally obtained ones versus the ones predicted by four different hypotheses. A perfect hypothesis fit (shown in plot) would correspond to the experimentally obtained cumulants lying on a straight line at 45° (shown in plot). Note that the ground truth is the only one that explains the cumulants well. Moreover, to make a fair comparison all the hypothesis have exactly the same first-order cumulants (mean photon in each mode). **c**, Distribution of classical simulation times for each sample from this experiment, shown as Borealis in red and for Jiuzhang 2.0 in blue². For each sample of both experiments, we calculate the pair (N_c, G) and then construct a frequency histogram populating this two-dimensional space. Note that because the samples from Jiuzhang 2.0 are all threshold samples they have $G = 2$, whereas samples from Borealis, having collisions and being photon-number resolved, have $G \geq 2$. Having plotted the density of samples for each experiment in (N_c, G) space, we indicate with a star the sample with the highest complexity in each experiment. For each experiment, the starred sample is at the very end of the distribution and occurs very rarely; for Jiuzhang 2.0 this falls within the line $G = 2$. Finally, we overlay lines of equal simulation time as given by equation (4) as a function of N_c and G . To guide the eye we also show boundaries delineating two standard deviations in plotted distributions (dashed lines).

Unlike earlier experiments^{1,2} in which more than half of the input ports of the interferometer are empty, in this current work every input port of the

time-domain interferometer is populated with a squeezed state. This property indicates that the third- and fourth-order photon-number cumulants with no modes repeated are extremely small ($\approx 10^{-6}$) in our ground truth. The greedy spoofe we implemented using first- and second-order cumulant information automatically produces third-order cumulants on the order of 10^{-5} , and thus no extra gain can be attained by using a greedy algorithm with third-order correlations, as they are well explained using only single-mode and pairwise correlations. Note that the difference between the ground truth cumulants and the ones from the greedy samples are more than accounted for by finite size statistics.

For Gaussian states undergoing only common loss (including the special case of lossless GBS), it is straightforward to show that the third-order photon-number cumulants involving any three distinct modes are all strictly zero. Thus, the fact that significant third- and fourth-order cumulants are observed in refs. [1,2](#) is simply a reflection of the fact that most of their inputs are vacuum and that their experiment lacks photon-number resolution. The latter observation could in principle be exploited by a classical adversary to speed up the simulation of GBS with mostly vacuum inputs because strategies exist to speed up the simulation of GBS when the number of input squeezed states is fixed and is a small fraction of the total number of photons observed. These strategies used the fact that hafnians of low-rank matrices [32,33](#) can be calculated faster than hafnians of full rank matrices of equal size. For our system, the matrices needed for simulation are all full rank as every input is illuminated with squeezed light.

Finally, note that in Fig. [4b](#), we do not compare against the cumulants of the greedy sampler. These are, by construction, very close to the ground truth (see details in [Supplementary Information](#)). But for the brightnesses for which one calculates cross entropy, they do not perform as well as the samples from our machine.

In the experimental distribution of the total photon number in Fig. [4a](#), the outcome with the highest probability is $N = 124.35 \pm 0.02$ and the distribution has significant support past 160 photons as shown in the inset. The best-known algorithm to simulate GBS^{[30,34](#)} scales with the total number of modes and the time it takes to calculate a probability amplitude of a pure-

state GBS instance. Thus we can estimate the time it would take to simulate a particular sample $S = (n_1, \dots, n_m)$ in Fugaku, the current most powerful supercomputer in the world³⁵, to be

$$\text{\$}\$\{\text{\rm time}\}(\{N\}_{c},G)=\frac{1}{2}\{c\}_{\{\text{\rm Fugaku}\}}M\{N\}_{c}^3\{G\}^{\{N\}_{c}/2},\$\$ \quad (4)$$

where the collision parameter is $\langle G \rangle = (\prod_{i=1}^M (n_i + 1))^{1/N_c}$, n_i is the number of photons in the i th mode and N_c is the number of non-zero detector outcomes. We estimate $c_{\text{Fugaku}} = c_{\text{Niagara}}/122.8$ from the LINPACK benchmark (a measure of a computer's floating-point rate of execution) ratio of floating operations per second measured on Fugaku and Niagara⁵ found $c_{\text{Niagara}} = 5.42 \times 10^{-15}$ s from which we get $c_{\text{Fugaku}} = 4.41 \times 10^{-17}$ s. Finally, we take $M = 216$ for both our system and the experiment in ref. ². This assumption slightly overestimates the time it takes a supercomputer to simulate the experiment of ref. ², as it has two-thirds the number of modes of the largest Borealis instance we consider but simplifies the analysis.

Equation (4) captures the collision-free complexity of the hafnian of an $N \times N$ matrix of $\langle O(N)_c^3 \rangle$ because in that case $G = 2$. For the purposes of sampling, a threshold detection event that in an experiment can be caused by one or many photons, can always be assumed to have been caused by a single photon, thus threshold samples have the same complexity as in the formula above with $G = 2$ (ref. ³⁰), which is quadratically faster than the estimates in refs. ^{1,2,36}. One could hope that tensor networks techniques³⁷ could speed up the simulation of a circuit such as the one we consider here, but this possibility is ruled out in ref. ⁵ where it is shown that, even when giving tensor network algorithms effectively infinite memory, they require significantly more time than hafnian based methods to calculate probability amplitudes.

On the basis of these assumptions we estimate that, on average, it would take Fugaku 9,000 years to generate one sample, or 9 billion years for the million samples we collected from Borealis. Using the same assumptions,

we estimate that Fugaku would require 1.5 h, on average, to generate one sample from the experiment in ref. 2, or 8,500 years for the 50 million generated in their experiment. In Fig. 4c, we plot the distribution of classical runtimes of Fukagu for each sample drawn in the experiment, and show the sample with the largest runtime as a star. For comparison, we also compare to the highest brightness experiment from Jiuzhang 2.0 (ref. 2). The regime we explore in our experiment is seven orders of magnitude harder to simulate than previous experiments and, moreover, we believe it cannot be spoofed by current state-of-the-art greedy algorithms or classical-Gaussian states in cross entropy.

Discussion and outlook

We have successfully demonstrated quantum computational advantage in GBS using a photonic time-multiplexed machine. Unlike previous photonic devices used for such demonstrations, Borealis offers dynamic programmability over all gates used, shows true photon-number-resolved detection and requires a much more modest number of optical components and paths. Among all photonic demonstrations of quantum computational advantage—photonic or otherwise—our machine uses the largest number of independent quantum systems: 216 squeezed modes injected into a 216-mode interferometer having three-dimensional connectivity, with up to 219 detected photons. Our demonstration is also more resistant to classical spoofing attacks than all previous photonic demonstrations, enabled by the high photon numbers and photon-number resolution implemented in the experiment.

The programmability and stability of our machine enables its deployment for remote access by users wishing to encode their own gate sequences in the device. Indeed, the machine can be accessed by such users without any knowledge of the underlying hardware, a key property for exploring its use at addressing problems on structured, rather than randomized data. Furthermore, besides demonstrating variable beam-splitting and switching (both in the loops and demultiplexing system), the successful use in our machine of several phase-stabilized fibre loops to act as effective buffer memory for quantum modes is a strong statement on the viability of this technique, which is a requirement in many proposed architectures for fault-

tolerant photonic quantum computers^{9,10,11,38}. Our demonstration thus marks a significant advance in photonic technology for quantum computing.

Methods

Optical circuit

The input of the interferometer is provided by a single optical parametric oscillator (OPO), emitting pulsed single-mode squeezed states at a 6 MHz rate that are then sent to three concatenated, programmable, loop-based interferometers. Each loop contains a VBS, including a programmable phase shifter, and an optical fibre delay line acting as a buffer memory for light, and allows for the interference of modes that are temporally adjacent ($\tau = (6 \text{ MHz})^{-1}$), or separated by six or 36 time bins (6τ or 36τ) in the first, second and third loop, respectively. Optical delays provide a compact and elegant method to mediate short- and long-range couplings between modes. The high-dimensional Gaussian state generated for this experiment can be visualized, as depicted above the three loops in Fig. 1, using a three-dimensional lattice representation. Given a lattice of size $a = 6$, where a is the number of modes separating two interacting pulses in the second loop, one can form a cubic lattice by injecting $M = a^3 = 216$ squeezed-light pulses into the interferometer.

Owing to the use of a single time-multiplexed squeezed-light source, all temporal modes are, to very good approximation, indistinguishable in all degrees of freedom except time signature, and passively phased locked with respect to each other; the squeezer is driven by pump pulses engineered to generate nearly single-temporal-mode squeezed-light pulses on a 6 MHz clock. Spatial overlap is ensured by using single-mode fibre coupling at the entrance and exit of each loop delay, and samples are collected using an array of photon-number resolving (PNR) detectors based on superconducting transition-edge sensors (TES) with 95% detection efficiency^{39,40}. These samples consist of 216 (integer) photon-number measurement outcomes for as many modes. To bridge the gap between the 6 MHz clock, chosen to maintain manageable fibre loop lengths, and the slower relaxation time of the TES detectors, a 1-to-16 binary-tree switching

network was used to partially demultiplex the pulse train after the loops and before the detectors.

Experimental challenges

Despite the simple conceptual design of Borealis (Fig. 1), building a machine capable of delivering quantum computational advantage in a programmable fashion using photonics, in a large photon-number regime, required solving considerable technological hurdles that were previously outstanding. These include: (1) lack of PNR-compatible single-mode squeezed-light sources and non-invasive phase stabilization techniques requiring bright laser beams, (2) slow PNR reset times that would necessitate unfeasibly long fibre loops and (3) lack of sufficiently fast and low-loss electro-optic modulators (EOMs) preventing programmability. Our solutions to these challenges for this work are, respectively, (1) the design of a bright and tunable source of single-mode squeezed states and phase stabilization techniques (OPO and interferometer) using locking schemes compatible with PNR detectors, (2) active demultiplexing to increase the effective rate of PNR acquisition by a factor of 60, compared to previous systems⁴⁰, by constructing a low-loss 1-to-16 binary switch tree and developing new photon-number extraction techniques and (3) the use of new, efficient and fast customized EOMs (QUBIG GmbH) that enable arbitrary dynamic programming of photonic gates with low loss and high speeds. The success of this experiment also relies on a robust calibration routine, accurately extracting all experimental parameters contained in the transfer matrix T and the squeezing parameters r that define each GBS instance. We describe each of these advances in the following sections. Other details pertinent to the apparatus can be found in the [Supplementary Information](#).

With further fabrication and device optimization, the raw operational speed of PNR detectors can be increased, eliminating the need for the demultiplexer (demux) and associated losses (roughly 15%). Improvements to the filter stack (20% loss) would also considerably increase performance. Several paths thus exist to even further increase the robustness of our machine against hypothetical improved classical adversaries. In addition, in trial runs we have extended the number of accessible modes to 288

(see [Supplementary Information](#)) without any changes to the physical architecture, and expect further scalability in this number to be readily achievable by improving the long-time stabilization of the device. Such scaling will place the device even further ahead of the regime of classical simulability and potential vulnerability to spoofing.

For applications requiring a universal interferometer, a recirculation loop long enough to accommodate all 216 modes could be implemented⁴¹, replacing any two of the three existing loops. The remaining existing loop would be nested in the larger 216-mode loop, allowing repeated application of the remaining VBS to all 216 modes, albeit at the cost of higher losses.

Pulsed squeezed-light source

The main laser is an ultralow phase noise fibre laser with a sub-100 Hz linewidth centred at 1,550 nm, branched out into different paths. To prepare the pump, in one path pulses are carved using a 4 GHz lithium niobate electro-optic intensity modulator. It is then amplified and upconverted to 775 nm using a fibre-coupled MgO:LN ridge waveguide. The resulting pump is a 6 MHz stream of 3-ns-duration rectangular pulses with an average power of 3.7 mW. Squeezed-light pulses are generated in a doubly resonant, phase-stabilized hemilithic cavity⁴² comprising a 10-mm-long plano-convex potassium titanyl phosphate crystal with its temperature stabilized at 32.90 °C using a Peltier element, for optimal Type-0 phase matching ([Supplementary Information](#)). All spectral side bands of the OPO cavity, around the degenerate frequency band, are suppressed by more than 25 dB using a pair of fibre Bragg gratings (0.04 nm bandwidth at 0.5 dB), one in reflection and the other in transmission (more details in [Supplementary Information](#)).

Programmable photonic processor

A train of single-mode squeezed vacuum pulses is emitted by the OPO, coupled into a single-mode fibre and directed towards the programmable photonic processor consisting of three loop-based interferometers in series, as shown in Fig. 1. Each loop (\ell=0,1,2) is characterized by a VBS with transfer matrix

$$\begin{aligned}
\$B\{S\}^{\{\ell\}}(\{\alpha_k, \varphi_k\}) = & (\begin{array}{cc} \\
e^{i\varphi_k}, \cos \alpha_k & i\sqrt{\eta_\ell} \\
e^{i\mu_\ell}, \sin \alpha_k & i e^{i\varphi_k} \sin \alpha_k \\
e^{i\mu_\ell}, \cos \alpha_k & \end{array}) \\
(5)
\end{aligned}$$

where each phase $\phi_k = [-\pi/2, \pi/2]$ and $\alpha_k = [0, \pi/2]$ can be programmed independently, $\langle \{\mu_\ell\} \rangle$ is a phase offset associated with each loop and $\langle \{\eta_\ell\} \rangle$ is the energy transmittance coefficient associated with one complete circulation in loop $\langle \{\ell\} \rangle$. The time delay experienced in the first loop is $\tau = 1/(6 \text{ MHz})$, equals the delay between two consecutive squeezed-light pulses, whereas the second and third loops have 6τ and 36τ time delay, respectively. The transmittance t_k of a VBS with parameter α_k is given by $t_k = \cos^2 \alpha_k$. For $t_k = 1$ all the incoming light is directed into the fibre delay, whereas the light entering the VBS from the fibre delay is fully coupled out. The output of the last loop is coupled into a single-mode fibre and directed towards the final sampling stage of the experiment.

All three loops are independently phase stabilized using a counter-propagating laser beam, piezo transducers and lock-in techniques. To avoid stray light from reflections of this beam towards the detectors, we alternate between measurement ($65 \mu\text{s}$) and phase stabilization of the loops ($35 \mu\text{s}$), leading to a sampling rate of 10 kHz . The estimated phase noise (standard deviation from the mean) inside the interferometer is $0.02, 0.03$ and 0.15 rad for the first, second and third loops, respectively, as measured with classical pulses. We carefully reduced mode mismatch throughout the entire interferometer: spatial overlap is ensured using single-mode fibres, with coupling efficiencies $>97\%$, and the length of each loop delay is carefully adjusted to have $>80\%$ classical visibility between 250-ps -long classical pulses, which gives $>99\%$ temporal overlap for the squeezed states.

Connectivity

The programmable time-domain multiplexed architecture implemented here and introduced in ref. [5](#) generates sufficiently connected transmission

matrices (in which two-thirds of the entries of the matrix are non-zero) to furnish a high level of entanglement between the modes (we estimate the log negativity between modes $0 \dots i-1$ and $i \dots 216$ for the ground truth to be on average 5.96 for $\{i \in \{36, 72, 108, 144, 180\}\}$), while keeping losses sufficiently low (with transmission above 33%). This is not the case for other architectures in which one either has to give up programmability^{1,2} or suffer steep losses that, in the asymptotic limit of many modes, render the sampling task roughly simulable as the loss scales exponentially with the system size³¹. In a universal programmable interferometer each mode passes through several lossy components (with transmission η_{unit}) proportional to the number of modes. For the interferometers considered here, each mode sees a fixed number (six) of beamsplitters in which the loss is dominated by the transmission of the largest loop. If the shortest loop, which accommodates only one mode, has transmission η_{unit} then the largest loss is given by $(\eta_{\text{unit}})^{36}$, which should be contrasted with $(\eta_{\text{unit}})^{216}$ for a universal interferometer. Whereas we sacrifice some connectivity, the many-mode entanglement predicted in our ground truth (logarithmic negativity⁴³ of 6.08 when splitting the modes of the ground truth between the first and last 108) is comparable to the one found in Gaussian state prepared using a random Haar-interferometer with a comparable net transmission and brightness (for which the logarithmic negativity across the same bipartition is 15.22). For the largest experiment considered below, the net transmittance is around 33%. As discussed in the [Methods](#), combined with the high brightness of our source averaging $r \sim 1.1$, places our experiment well beyond any attempt at a now-known polynomial-time approximate classical simulation³¹.

Sampling of high-dimensional GBS instances

All temporal modes of our synthesized high-dimensional Gaussian states are sampled using superconducting TES allowing photon-number resolution up to 13 photons per detector in our data. Relaxation time of our TES, back to baseline following illumination, is of the order of 10 to 20 μs corresponding to 50–100 kHz (ref. ⁴⁰), and depends on the expected photon number. At this speed, the length of the shortest loop delay would be 2 km, leading to excessive losses and more challenging phase stabilization in our system. Thus our pulse train and thus processing speed of 6 MHz, chosen to maintain

manageable loop lengths, is too fast for a reliable photon-number extraction. To bridge the gap between the typical PNR speed and our processing speed, we use a demultiplexing device allowing to speed up by effectively $16\times$, and to develop a postprocessing scheme, described below, for ‘tail-subtraction’ enabling operation of each PNR at 375 kHz.

The role of the demux, depicted as a binary tree in Fig. 1, is to reroute squeezed-light pulse modes from the incoming train into 16 separate and independent spatial modes, each containing a fibre-coupled PNR-TES detector. There are 15 low-loss resonant EOMs grouped in four different layers. EOMs in each layer have a preset frequency: one at 3 MHz, two at 1.5 MHz, four at 750 kHz and eight at 375 kHz. Each EOM is sandwiched between two polarizing beamsplitter and a quarter-waveplate at 45° in front. The modulators are driven by a standalone unit, generating several phase-locked sine wave signals temporally synchronized with the input train. The switching extinction ratio is measured to be above 200:1 for all modulators.

Several methods have been demonstrated to extract photon numbers from a PNR’s output voltage waveform, each with their own advantages^{44,45,46,47}. Here we use a modified version of the method presented in ref. 47. First, each detector is calibrated using well separated pulses of squeezed light with a high mean photon number around $\langle n \rangle \approx 1$ and 500×10^3 repetitions. This gives enough high photon-number events to ensure that at least the 0 to 11 photon clusters can be identified using the area method. From each cluster, the mean shape of the waveforms is defined. To extract the photon-number arrays from experiment, the mean square distance between each waveform and the mean shape is estimated. The photon number is then assigned to the closest cluster. Because we operate the individual PNRs at 375 kHz, faster than the relaxation time (back to baseline following illumination), the tail of each pulse still persists when the next pulse arrives at the same PNR. To avoid these tails reducing photon-number extraction fidelity in a pulse, the mean shape for the identified previous photon number is subtracted. See [Supplementary Information](#) for details.

Estimation of the ground truth parameters

Given that all the squeezed states come from the same squeezer and the programmability of our system, we can parametrize and characterize the loss budget of our system using a very small set of parameters. The first set of parameters correspond to the relative efficiencies of the 16 different demux-detector channels, $\eta_{\text{demux},i}$ for $(i \in \{0,1,\dots,15\})$. The second parameter is simply the common transmittance η_C . Finally, we have the transmittance associated with a round-trip through each loop η_k for $(k \in \{0,1,2\})$.

To characterize the first two parameter sets, namely the demux and common loss, we set all the loops to a ‘bar’ state ($\alpha_k = \pi/2$), preventing any light from entering the delays. As the input energy is the same, we can simply estimate the ratio of the transmittance of the different demux-detector channels as $\langle \eta_{\text{demux}} \rangle_i / \langle \eta_{\text{demux}} \rangle_j = \langle \bar{n}_i \rangle / \langle \bar{n}_j \rangle$ where $\langle \bar{n}_j \rangle$ is the mean photon number measured in the detector j . Without loss of generality, we can take the largest of the $\eta_{\text{demux},i}$ to be equal to one and assign any absolute loss from this and any other channel into the common loss η_C . To determine the common loss, we use the noise reduction factor (NRF), defined as^{48,49}

$$\text{NRF} = \frac{\langle (\Delta n)^2 \rangle}{\langle n_i \rangle + \langle n_j \rangle}, \quad (6)$$

where n_i and n_j are the photon-number random variables measured in mode i and j , and we write variances as $\langle (\Delta X)^2 \rangle = \langle X^2 \rangle - \langle X \rangle^2$.

If losses can be considered as uniform, which is an excellent approximation if we use only the loop with the shortest delay, it is straightforward to show that the NRF of a two-mode squeezed vacuum gives directly the loss seen by the two modes as $\text{NRF}_{\text{TMSV}} = 1 - \eta$. To prepare the two-mode squeezed vacuum we set our VBS matrix to be proportional to $\begin{bmatrix} 1 & i \\ i & 1 \end{bmatrix}$ when the two single-mode squeezed pulses meet at the beamsplitter. To this end, we use the following sequence [$t_0 = 0$, $t_1 = 1/2$, $t_2 = 0$], where, recall, we write $t_i = \cos^2 \alpha_i$ to indicate the transmittance of a

particular loop time bin i . We can now scan the controllable phase of the VBS, ϕ_k , and determine where the minimum occurs $\langle\langle\{\varphi\}$
 $\}_{k}^{\wedge}\{\{\rm{min}\}\}\rangle=\{\mu\}_0\backslash,\{\rm{mod}\}\backslash,\pi\rangle)$, and at the same time provide the relative offset in the first loop and the net transmittance of the setup. This observation can be used to obtain the phase offset of any other loop round-trip. Although in the current version of our system these are set by the locking system, they can in principle also be made programmable. The transmittance $\eta = 1 - \text{NRF}_{\text{TMSV}} = \eta_C \times \eta_0 \times \eta_{\text{demux}}$ is the product of the common transmittance η_C , the round-trip in the first loop η_0 and the average transmittance associated with two demux-detector channels used to detect the two halves of the two-mode squeezed vacuum $\langle\langle\{\eta\}$
 $\}_{\{\{\rm{demux}\}\}}=\frac{1}{2}\langle\langle\{\eta\}_{\{\{\rm{demux}\},i\}}+\langle\langle\{\eta\}_{\{\{\rm{demux}\},j\}}\rangle\rangle$). From this relation, we can find

$$\$\$\langle\langle\{\eta\}_C=\frac{1-\langle\langle\{\rm{NRF}\}\rangle\rangle_{\{\{\rm{TMSV}\}\}}}{\langle\langle\{\eta\}_0\}\times\langle\langle\{\eta\}_{\{\{\rm{demux}\}\}}\rangle\rangle}.\$\$$$

(7)

This calibration depends on knowing the value of the round-trip transmittance factor associated with the first loop. To estimate the round-trip transmittance of a particular loop $\langle\langle\{\ell\}\rangle\rangle$, we bypass the other loop delays and compare the amount of light detected when light undergoes a round-trip through a particular loop, relative to when all the round-trip channels are closed, that is, all loops in a ‘bar’ state. We obtain $\langle\langle\{\eta\}_{\{\{\ell\}\}}\rangle\rangle$, which we can then plug in equation (7) to complete the calibration sequence.

Finally, having characterized the loss budget in the experiment, we can obtain the brightness and squeezing parameters at the source by measuring photon numbers when all the loops are closed and then dividing by the net transmittance. For any of the three regimes considered in the main text the standard deviation of the estimated squeezing parameters and mean photon numbers is below 1% of the respective means.

From the same data acquired above for a pair of modes, we calculate the unheralded second-order correlation

$$\$\$\langle\langle\{g\}^{(2)}\rangle\rangle=\frac{\langle\langle\{n\}_i^2\rangle\rangle-\langle\langle\{n\}_i\rangle\rangle^2}{\langle\langle\{n\}_i\rangle\rangle^2}\$\$$$

(8)

for each pair of temporal modes. When we attain the minimum NRF at $\phi_k = \mu_0$, that is, when we prepare two-mode squeezed vacuum, it is easy to see that⁵⁰

$$\text{g}^{(2)} = 1 + \frac{1}{K}, \quad (9)$$

where K is the so-called Schmidt number of the source. This quantifies the amount of spectral mixedness in the generated squeezed light. An ideal squeezed vacuum light source would yield $g^{(2)} = 2$. We report $K = 1.12$ for $g^{(2)} = 1.89$ for the dataset used in the large mode and photon-number regime.

Theory sections

Transfer matrix, T

The loop-based interferometer, as well as any other interferometer, can be described by a transfer matrix T that uniquely specifies the transformation effected on the input light. For our GBS implementation, this interferometer is obtained by combining three layers of phase gates and beamsplitters (two-mode gates), interfering modes that are contiguous, or separated by six or 36 time bins, which we write as

$$T = \sqrt{\eta_C} T_{\rm demux} \left[\prod_{d=0}^{D-1} \prod_{i=0}^{M-a^d} B_{i,i+a^d} \right] \quad (10)$$

where in our case $D = 3$ gives the number of loops, while $\{a\}^d \in \{0, 1, 2\}$ gives $\{d\} \in \{1, 6, 36\}$ with $a = 6$ gives the number of modes that each loop can hold. $B_{i,i+a^d}$ is a $M \times M$ transfer matrix that acts like the VBS in the subspace of modes i and $j = i + a^d$ and like the identity elsewhere.

In the last equation, η_C is the common transmittance throughout the interferometer associated with the escape efficiency of the squeezer cavity and the propagation loss in common elements. T_{demux} is a diagonal matrix that contains the square roots of the energy transmittance into which any of the modes are rerouted for measurement using the demux. Because the demux has 16 channels, it holds that $\sqrt{\{\{T\}_{\{\text{rm}\{\text{demux}\}}}\}}_{\{i,i\}} = \sqrt{\{\{T\}_{\{\text{rm}\{\text{demux}\}}}\}}_{\{i+16,i+16\}}$. Finally, we set the phases of the VBS to be uniformly distributed in the range $[-\pi/2, \pi/2]$ and the transmittances to be uniformly in the range [0.45, 0.55]. This range highlights the programmability of the device while also generating high degrees of entanglement that are typically achieved when the transmittance is half.

In the idealized limit of a lossless interferometer, the matrix representing it is unitary, otherwise the matrix T is subunitary (meaning its singular values are bounded by 1). The matrix T together with the input squeezing parameters r defines a GBS instance. Squeezed states interfered in an interferometer (lossy or lossless) always lead to a Gaussian state, that is, one that has a Gaussian Wigner function. Moreover, loss is never able to map a non-classical state (having noise in a quadrature below the vacuum level) to a classical state. Thus there exists a finite separation in Hilbert space between lossy-squeezed states and classical states. To gauge this separation, and how it influences sampling, we use the results from ref. [31](#) to show in the section ‘Regimes of classical simulability’ that the probability distribution associated with the ground truth programmed into the device cannot be well-approximated by any classical-Gaussian state.

Similar to previous GBS experiments in which the ground truth to which a quantum computer is compared contains imperfections due to loss, we also benchmark our machine against the operation of a lossy unitary. In this more realistic scenario in which losses are included, the state generated at the output cannot be described by a state vector and thus one cannot assign probability amplitudes to an event. In this case, probabilities are calculated from the density matrix of the Gaussian state using the standard Born rule and then the probability of an N photon event is proportional to the hafnian of a $2N \times 2N$ matrix.

Regimes of classical simulability

As a necessary but not sufficient test for beyond-classical capabilities of our machine, we consider the GBS test introduced in ref. [31](#). This test states that a noisy GBS device can be classically efficiently simulated up to error ϵ if the following condition is satisfied:

$$\text{\$}\$\text{\text{sec}}\{\text{\rm h}\}\left(\frac{1}{2}, \max[0, \text{\rm ln}]\right) > \epsilon^{-\frac{1}{2}} \cdot \frac{q_D}{M} \cdot \eta^{1-2r+1-\eta} \quad (11)$$

Here q_D is the dark count probability of the detectors, η is the overall transmittance of the interferometer, r is the squeezing parameter of the M input squeezed states (assumed to be identical) and ϵ is a bound in the TVD of the photon-number probability distributions of GBS instance and the classical adversary. For our experiment, we estimate an average transmittance of $\eta = \text{Tr}(TT^\dagger)/M = 0.32$, $q_D = 10^{-3}$, an average squeezing parameter of $r = 1.10$ and M is the total number of modes. With these parameters we find that the inequality above has no solution for $\epsilon \in [0, 1]$, meaning that our machine passes this non-classicality test.

Greedy adversarial spoofer

The greedy adversarial spoofer tries to mimic the low order correlations of the distribution and takes as input the k order, $(k \in \{1, 2\})$, marginal distributions and optimizes a set of samples (represented as an array of size $M \times K$) so as to minimize the distance between the marginals associated with this array and the ones associated with the ground truth. In a recent preprint Villalonga et al. [3](#) argue that, using a greedy algorithm such as the one just described, they can obtain a better score at the cross-entropy benchmark against the ground truth of the experiment in refs. [1, 2](#) than the samples generated in the same experiment. We generalized the greedy algorithm introduced by Villalonga et al. [3](#) to work with photon-number-resolved samples and find that it is unable to spoof the samples generated by our machine at the cross-entropy benchmark that we use for scoring the different

adversaries. Details of the algorithm are provided in the [Supplementary Information](#).

Data availability

The datasets generated and analysed for this study are available from this link: <https://github.com/XanaduAI/xanadu-qca-data>.

References

1. Zhong, H.-S. et al. Quantum computational advantage using photons. *Science* **370**, 1460–1463 (2020).
2. Zhong, H.-S. et al. Phase-programmable Gaussian boson sampling using stimulated squeezed light. *Phys. Rev. Lett.* **127**, 180502 (2021).
3. Villalonga, B. et al. Efficient approximation of experimental Gaussian boson sampling. Preprint at <https://arxiv.org/abs/2109.11525> (2021).
4. Hamilton, C. S. et al. Gaussian boson sampling. *Phys. Rev. Lett.* **119**, 170501 (2017).
5. Deshpande, A. et al. Quantum computational advantage via high-dimensional gaussian boson sampling. *Sci. Adv.* **8**, eabi7894 (2022).
6. Arute, F. et al. Quantum supremacy using a programmable superconducting processor. *Nature* **574**, 505–510 (2019).
7. Wu, Y. et al. Strong quantum computational advantage using a superconducting quantum processor. *Phys. Rev. Lett.* **127**, 180501 (2021).
8. Zhu, Q. et al. Quantum computational advantage via 60-qubit 24-cycle random circuit sampling. *Sci. Bull.* **67**, 240–245 (2022).
9. Bourassa, J. E. et al. Blueprint for a scalable photonic fault-tolerant quantum computer. *Quantum* **5**, 392 (2021).

10. Bartolucci, S. et al. Fusion-based quantum computation. Preprint at <https://arxiv.org/abs/2101.09310> (2021).
11. Larsen, M. V., Chamberland, C., Noh, K., Neergaard-Nielsen, J. S. & Andersen, U. L. Fault-tolerant continuous-variable measurement-based quantum computation architecture. *PRX Quantum* **2**, 030325 (2021).
12. Bromley, T. R. et al. Applications of near-term photonic quantum computers: software and algorithms. *Quantum Sci. Technol.* **5**, 034010 (2020).
13. Huh, J., Guerreschi, G. G., Peropadre, B., McClean, J. R. & Aspuru-Guzik, A. Boson sampling for molecular vibronic spectra. *Nat. Photonics* **9**, 615–620 (2015).
14. Arrazola, J. M. & Bromley, T. R. Using Gaussian boson sampling to find dense subgraphs. *Phys. Rev. Lett.* **121**, 030503 (2018).
15. Banchi, L., Fingerhuth, M., Babej, T., Ing, C. & Arrazola, J. M. Molecular docking with Gaussian boson sampling. *Sci. Adv.* **6**, eaax1950 (2020).
16. Jahangiri, S., Arrazola, J. M., Quesada, N. & Killoran, N. Point processes with Gaussian boson sampling. *Phys. Rev. E* **101**, 022134 (2020).
17. Jahangiri, S., Arrazola, J. M., Quesada, N. & Delgado, A. Quantum algorithm for simulating molecular vibrational excitations. *Phys. Chem. Chem. Phys.* **22**, 25528–25537 (2020).
18. Banchi, L., Quesada, N. & Arrazola, J. M. Training Gaussian boson sampling distributions. *Phys. Rev. A* **102**, 012417 (2020).
19. Takeda, S. & Furusawa, A. Toward large-scale fault-tolerant universal photonic quantum computing. *APL Photonics* **4**, 060902 (2019).
20. Motes, K. R., Gilchrist, A., Dowling, J. P. & Rohde, P. P. Scalable boson sampling with time-bin encoding using a loop-based architecture. *Phys. Rev. Lett.* **113**, 120501 (2014).

21. Yoshikawa, J.-i et al. Invited article: generation of one-million-mode continuous-variable cluster state by unlimited time-domain multiplexing. *APL Photonics* **1**, 060801 (2016).
22. Larsen, M. V., Guo, X., Breum, C. R., Neergaard-Nielsen, J. S. & Andersen, U. L. Deterministic generation of a two-dimensional cluster state. *Science* **366**, 369–372 (2019).
23. Asavanant, W. et al. Generation of time-domain-multiplexed two-dimensional cluster state. *Science* **366**, 373–376 (2019).
24. Asavanant, W. et al. Time-domain-multiplexed measurement-based quantum operations with 25-MHz clock frequency. *Phys. Rev. Appl.* **16**, 034005 (2021).
25. Larsen, M. V., Guo, X., Breum, C. R., Neergaard-Nielsen, J. S. & Andersen, U. L. Deterministic multi-mode gates on a scalable photonic quantum computing platform. *Nat. Phys.* **17**, 1018–1023 (2021).
26. Enomoto, Y., Yonezu, K., Mitsuhashi, Y., Takase, K. & Takeda, S. Programmable and sequential Gaussian gates in a loop-based single-mode photonic quantum processor. *Sci. Adv.* **7**, eabj6624 (2021).
27. Bartlett, S. D., Sanders, B. C., Braunstein, S. L. & Nemoto, K. Efficient classical simulation of continuous variable quantum information processes. *Phys. Rev. Lett.* **88**, 097904 (2002).
28. Raussendorf, R., Harrington, J. & Goyal, K. A fault-tolerant one-way quantum computer. *Ann. Phys.* **321**, 2242–2270 (2006).
29. Raussendorf, R., Harrington, J. & Goyal, K. Topological fault-tolerance in cluster state quantum computation. *New J. Phys.* **9**, 199 (2007).
30. Bulmer, J. F. et al. The boundary for quantum advantage in Gaussian boson sampling. *Sci. Adv.* **8**, eabl9236 (2021).
31. Qi, H., Brod, D. J., Quesada, N. & García-Patrón, R. Regimes of classical simulability for noisy Gaussian boson sampling. *Phys. Rev. Lett.* **124**, 100502 (2020).

32. Björklund, A., Gupt, B. & Quesada, N. A faster Hafnian formula for complex matrices and its benchmarking on a supercomputer. *J. Exp. Algor.* **24**, 11 (2019).
33. Gupt, B., Izaac, J. & Quesada, N. The walrus: a library for the calculation of Hafnians, hermite polynomials and Gaussian boson sampling. *J. Open Source Softw.* **4**, 1705 (2019).
34. Quesada, N. et al. Quadratic speed-up for simulating gaussian boson sampling. *PRX Quantum* **3**, 010306 (2022).
35. 56th edition of the top 500 *Top 500 the List*
<https://www.top500.org/lists/top500/2020/11/> (2020).
36. Li, Y. et al. Benchmarking 50-photon Gaussian boson sampling on the sunway taihulight. *IEEE Trans. Parallel Distrib. Syst.* **33**, 1357–1372 (2021).
37. Gray, J. & Kourtis, S. Hyper-optimized tensor network contraction. *Quantum* **5**, 410 (2021).
38. Rohde, P. P. Simple scheme for universal linear-optics quantum computing with constant experimental complexity using fiber loops. *Phys. Rev. A* **91**, 012306 (2015).
39. Lita, A. E., Miller, A. J. & Nam, S. W. Counting near-infrared single-photons with 95% efficiency. *Opt. Express* **16**, 3032–3040 (2008).
40. Arrazola, J. M. et al. Quantum circuits with many photons on a programmable nanophotonic chip. *Nature* **591**, 54–60 (2021).
41. Qi, H., Helt, L. G., Su, D., Vernon, Z. & Brádler, K. Linear multiport photonic interferometers: loss analysis of temporally-encoded architectures. Preprint at <https://arxiv.org/abs/1812.07015> (2018).
42. Mehmet, M. et al. Squeezed light at 1550 nm with a quantum noise reduction of 12.3 dB. *Opt. Express* **19**, 25763–25772 (2011).

43. Weedbrook, C. et al. Gaussian quantum information. *Rev. Mod. Phys.* **84**, 621 (2012).
44. Figueira-Feliciano, E. et al. Optimal filter analysis of energy-dependent pulse shapes and its application to tes detectors. *Nucl. Instrum. Methods Phys. Res., Sect. A* **444**, 453–456 (2000).
45. Humphreys, P. C. et al. Tomography of photon-number resolving continuous-output detectors. *New J. Phys.* **17**, 103044 (2015).
46. Morais, L. A. et al. Precisely determining photon-number in real-time. Preprint at <https://arxiv.org/abs/2012.10158> (2020).
47. Levine, Z. H. et al. Algorithm for finding clusters with a known distribution and its application to photon-number resolution using a superconducting transition-edge sensor. *J. Opt. Soc. Am. B* **29**, 2066–2073 (2012).
48. Harder, G. et al. Single-mode parametric-down-conversion states with 50 photons as a source for mesoscopic quantum optics. *Phys. Rev. Lett.* **116**, 143601 (2016).
49. Aytür, O. & Kumar, P. Pulsed twin beams of light. *Phys. Rev. Lett.* **65**, 1551 (1990).
50. Christ, A., Laiho, K., Eckstein, A., Cassemiro, K. N. & Silberhorn, C. Probing multimode squeezing with correlation functions. *New J. Phys.* **13**, 033027 (2011).

Acknowledgements

We thank J. M. Arrazola and M. V. Larsen for providing feedback on the manuscript, S. Fayer and D. Phillips for assistance with the PNR detectors, M. Seymour and J. Hundal for assistance with data acquisition code, D.H. Mahler for helpful discussions, K. Brádler for guidance and A. Fumagalli for assistance with software. N.Q. thanks H. Qi, A. Deshpande, A. Mehta, B. Fefferman, S. S. Nezhadi and B. A. Bell for discussions. We thank SOSCIP for their computational resources and financial support. We acknowledge the

computational resources and support from SciNet. SciNet is supported by: the Canada Foundation for Innovation; the Government of Ontario; Ontario Research Fund: Research Excellence and the University of Toronto. SOSCIP is supported by the Federal Economic Development Agency of Southern Ontario, IBM Canada Ltd and Ontario academic member institutions. Certain commercial equipment, instruments or materials are identified in this paper to foster understanding. Such identification does not imply recommendation or endorsement by the National Institute of Standards and Technology, nor does it imply that the materials or equipment identified are necessarily the best available for the purpose.

Author information

Author notes

1. These authors contributed equally: L. S. Madsen, F. Laudenbach, M. F. Askarani

Authors and Affiliations

1. Xanadu, Toronto, ON, Canada

Lars S. Madsen, Fabian Laudenbach, Mohsen Falamarzi.
Askarani, Fabien Rortais, Trevor Vincent, Jacob F. F. Bulmer, Filippo
M. Miatto, Leonhard Neuhaus, Lukas G. Helt, Matthew J.
Collins, Varun D. Vaidya, Matteo Menotti, Ish Dhand, Zachary
Vernon, Nicolás Quesada & Jonathan Lavoie

2. National Institute of Standards and Technology, Boulder, CO, USA

Adriana E. Lita, Thomas Gerrits & Sae Woo Nam

Contributions

L.S.M., M.F.A. and J.L. designed and built the experiment. F.L. developed the software stack for programmable hardware and data analysis with L.G.H. and L.N. F.R., M.J.C., T.G., A.E.L. and S.W.N. developed and built

the PNR detector system. T.V. carried out high-performance computations and generated plots for the manuscript. J.F.F.B., I.D. and N.Q. provided guidance on theory, approach and benchmarking. F.M.M. implemented the greedy sampler algorithm. V.D.V. and M.M. designed and simulated the squeezed-light source. N.Q. and J.L. led the project, and cowrote the manuscript with Z.V., with input from all authors.

Corresponding authors

Correspondence to [Nicolás Quesada](#) or [Jonathan Lavoie](#).

Ethics declarations

Competing interests

The authors declare no competing interests.

Peer review

Peer review information

Nature thanks Sergio Boixo and the other, anonymous, reviewer(s) for their contribution to the peer review of this work.

Additional information

Publisher's note Springer Nature remains neutral with regard to jurisdictional claims in published maps and institutional affiliations.

Supplementary information

[Supplementary Information.](#)

Rights and permissions

Open Access This article is licensed under a Creative Commons Attribution 4.0 International License, which permits use, sharing, adaptation, distribution and reproduction in any medium or format, as long as you give appropriate credit to the original author(s) and the source, provide a link to the Creative Commons license, and indicate if changes were made. The images or other third party material in this article are included in the article's Creative Commons license, unless indicated otherwise in a credit line to the material. If material is not included in the article's Creative Commons license and your intended use is not permitted by statutory regulation or exceeds the permitted use, you will need to obtain permission directly from the copyright holder. To view a copy of this license, visit <http://creativecommons.org/licenses/by/4.0/>.

Reprints and Permissions

About this article

Cite this article

Madsen, L.S., Laudenbach, F., Askarani, M.F. *et al.* Quantum computational advantage with a programmable photonic processor. *Nature* **606**, 75–81 (2022). <https://doi.org/10.1038/s41586-022-04725-x>

- Received: 12 November 2021
- Accepted: 05 April 2022
- Published: 01 June 2022
- Issue Date: 02 June 2022
- DOI: <https://doi.org/10.1038/s41586-022-04725-x>

Share this article

Anyone you share the following link with will be able to read this content:

[Get shareable link](#)

Sorry, a shareable link is not currently available for this article.

[Copy to clipboard](#)

Provided by the Springer Nature SharedIt content-sharing initiative

Loops simplify a set-up to boost quantum computational advantage

- Daniel Jost Brod

Nature News & Views 01 Jun 2022

This article was downloaded by **calibre** from <https://www.nature.com/articles/s41586-022-04725-x>

| [Section menu](#) | [Main menu](#) |

[Download PDF](#)

- Article
- Open Access
- [Published: 18 May 2022](#)

The mosaic oat genome gives insights into a uniquely healthy cereal crop

- [Nadia Kamal¹](#)^{na1},
- [Nikos Tsardakas Renhuldt](#) [ORCID: orcid.org/0000-0001-7216-5320²](#)^{na1},
- [Johan Bentzer²](#),
- [Heidrun Gundlach](#) [ORCID: orcid.org/0000-0002-6757-0943¹](#),
- [Georg Haberer](#) [ORCID: orcid.org/0000-0002-6612-6939¹](#),
- [Angéla Juhász³](#),
- [Thomas Lux](#) [ORCID: orcid.org/0000-0002-5543-1911¹](#),
- [Utpal Bose^{3,4}](#),
- [Jason A. Tye-Din](#) [ORCID: orcid.org/0000-0001-7687-9654^{5,6}](#),
- [Daniel Lang](#) [ORCID: orcid.org/0000-0002-2166-0716¹](#)^{nAff20},
- [Nico van Gessel](#) [ORCID: orcid.org/0000-0002-0606-246X⁷](#),
- [Ralf Reski](#) [ORCID: orcid.org/0000-0002-5496-6711⁷](#),
- [Yong-Bi Fu⁸](#),
- [Peter Spégel](#) [ORCID: orcid.org/0000-0002-6092-2387⁹](#),
- [Alf Ceplitis¹⁰](#),
- [Axel Himmelbach¹¹](#),
- [Amanda J. Waters¹²](#),
- [Wubishet A. Bekele¹³](#),
- [Michelle L. Colgrave^{3,4}](#),
- [Mats Hansson](#) [ORCID: orcid.org/0000-0002-0168-9968¹⁴](#),

- [Nils Stein](#) [ORCID: orcid.org/0000-0003-3011-8731^{11,15}](#),
- [Klaus F. X. Mayer](#) [ORCID: orcid.org/0000-0001-6484-1077^{1,16}](#),
- [Eric N. Jellen](#) [ORCID: orcid.org/0000-0002-7906-4845¹⁷](#),
- [Peter J. Maughan](#) [ORCID: orcid.org/0000-0003-3714-3411¹⁷](#),
- [Nicholas A. Tinker](#) [ORCID: orcid.org/0000-0002-2452-4779¹³](#),
- [Martin Mascher](#) [ORCID: orcid.org/0000-0001-6373-6013^{11,18}](#),
- [Olof Olsson¹⁹](#),
- [Manuel Spannagl](#) [ORCID: orcid.org/0000-0003-0701-7035¹](#) &
- [Nick Sirijovski](#) [ORCID: orcid.org/0000-0002-6191-3845^{2,19}](#) nAff21

Nature volume **606**, pages 113–119 (2022)

- 11k Accesses
- 2 Citations
- 359 Altmetric
- [Metrics details](#)

Subjects

- [Agricultural genetics](#)
- [Evolutionary genetics](#)
- [Genomics](#)
- [Plant breeding](#)
- [Polyploidy in plants](#)

Abstract

Cultivated oat (*Avena sativa* L.) is an allohexaploid (AACCDD, $2n = 6x = 42$) thought to have been domesticated more than 3,000 years ago while growing as a weed in wheat, emmer and barley fields in Anatolia^{1,2}. Oat has a low carbon footprint, substantial health benefits and the potential to replace animal-based food products. However, the lack of a fully annotated reference genome has hampered efforts to deconvolute its complex evolutionary history and functional gene dynamics. Here we present a high-

quality reference genome of *A. sativa* and close relatives of its diploid (*Avena longiglumis*, AA, $2n = 14$) and tetraploid (*Avena insularis*, CCDD, $2n = 4x = 28$) progenitors. We reveal the mosaic structure of the oat genome, trace large-scale genomic reorganizations in the polyploidization history of oat and illustrate a breeding barrier associated with the genome architecture of oat. We showcase detailed analyses of gene families implicated in human health and nutrition, which adds to the evidence supporting oat safety in gluten-free diets, and we perform mapping-by-sequencing of an agronomic trait related to water-use efficiency. This resource for the *Avena* genus will help to leverage knowledge from other cereal genomes, improve understanding of basic oat biology and accelerate genomics-assisted breeding and reanalysis of quantitative trait studies.

Main

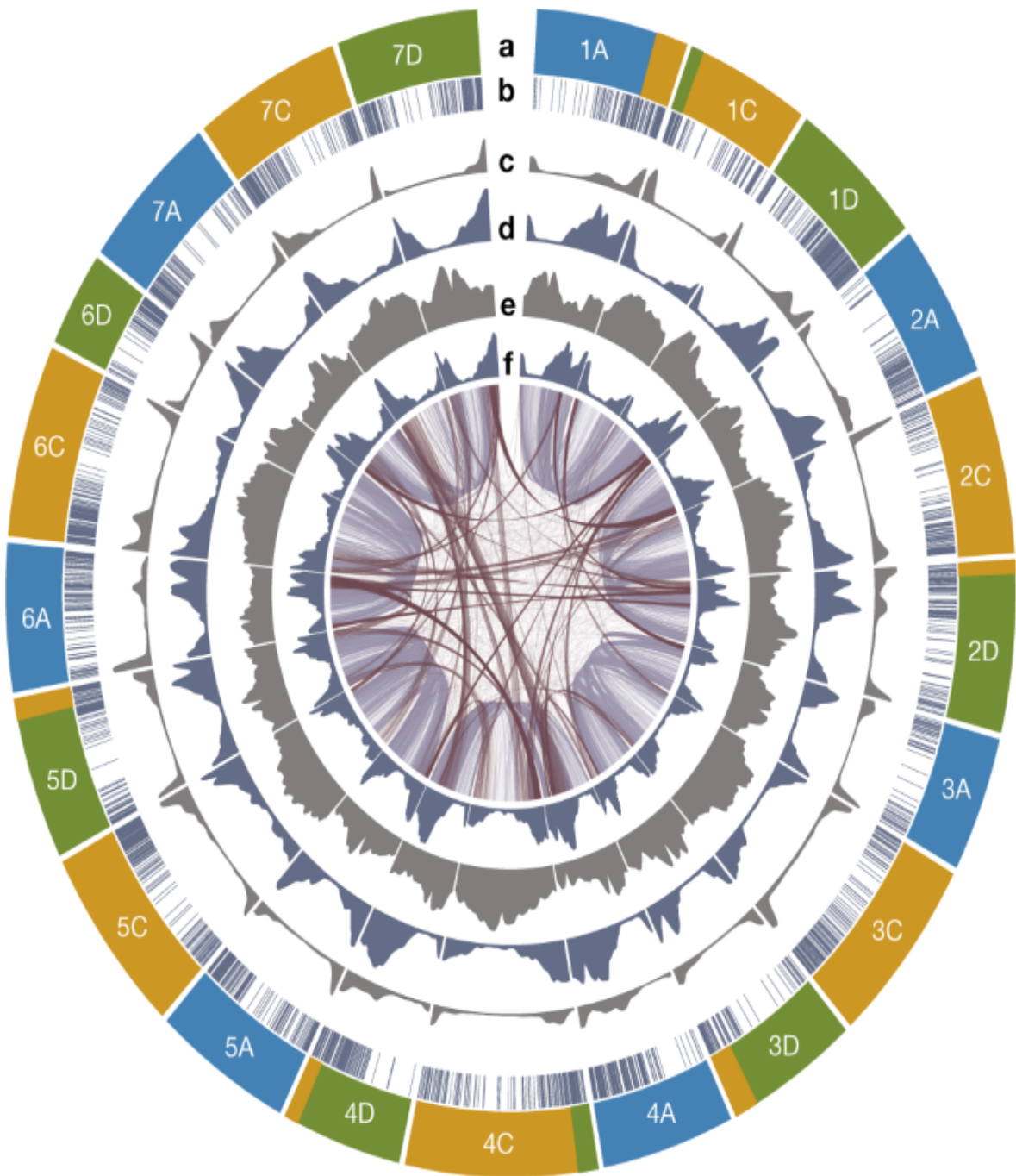
Oat is a member of Poaceae, an economically important grass family that includes wheat, rice, barley, common millet, maize, sorghum and sugarcane. *Avena* species exist in nature as diploids, tetraploids and hexaploids and exhibit the greatest genetic diversity around the Mediterranean, Middle East, Canary Islands and Himalayas. Currently, oat is a global crop with production ranking seventh among cereals (<http://www.fao.org/faostat/en/>, accessed May 2021). Compared with that of other cereals, oat cultivation requires fewer treatments with insecticides, fungicides or fertilizers. Whole-grain oats are a healthy source of antioxidants, polyunsaturated fatty acids, proteins and dietary fibre such as β -glucan, which is important in post-meal glycaemic responses and for preventing cardiovascular disease^{3,4,5}. Cereals such as wheat, barley and rye store high amounts of gluten proteins in their grain; by contrast, oat and rice store globular proteins in their grain.

Genome assembly and composition

We produced a chromosome-scale reference sequence of oat cv. ‘Sang’ comprising 21 pseudochromosomes (Fig. 1, Extended Data Fig. 1a and Supplementary Table 1), with a BUSCO (v5.1.2; ref. ⁶) score of 98.7% (Extended Data Fig. 2a), following the short-read strategy used for wheat⁷, barley⁸ and rye⁹. Inspection of Hi-C contact matrices (Supplementary Fig. 1)

and the consensus genetic map¹⁰ (Supplementary Fig. [2a](#)) and their comparison with the independent assembly (long-read) of hexaploid oat OT3098 (ref. [11](#); version 2; Supplementary Table [2](#)) verified the integrity of the assembly (Extended Data Fig. [2b](#) and Supplementary Fig. [2](#)). We also assembled pseudochromosomes of the diploid *Avena longiglumis* and tetraploid *Avena insularis*, which are presumed A and CD subgenome progenitors of *Avena sativa*¹² (Extended Data Figs. [1a](#) and [2a](#) and Supplementary Figs. [3](#) and [4](#)). Phylogenomic analyses (Supplementary Fig. [5](#)) used to assign *A. sativa* chromosomes to subgenomes showed that gene order is conserved in the proximal chromosomal regions. The 21 *A. sativa* chromosomes, named 1A–7D following the subgenome assignments of ref. [13](#), were oriented to preserve the orientations of core regions across homoeologues and possibly between *Avena* and Triticeae. Alignments to barley (Extended Data Fig. [1b](#)), *Avena eriantha*¹⁴ (Supplementary Fig. [6](#)), *A. longiglumis* (Supplementary Fig. [7a](#)) and *A. insularis* (Supplementary Fig. [7b](#)) confirmed the validity of this revised nomenclature, which is accepted by the International Oat Nomenclature Committee¹⁵.

Fig. 1: Structural and functional landscape of the 21 oat pseudochromosomes.



a–f, The tracks from the outer circles towards the centre of the diagram display the chromosome name and subgenome origin (A, blue; C, gold; D, green) with major translocations (a); anchored oat genetic markers⁵¹ (b); distribution of recombination rates (c); density and genomic distribution of high-confidence genes (d); age distribution of long terminal repeat retrotransposons (e); and median gene expression in 1-Mb windows (f). Inner connections show the best bidirectional BLAST hits between genes on

homoeologous chromosomes (grey) and between genes on non-homoeologous chromosomes (dark red). Figure generated with Circa (<http://omgenomics.com/circa>).

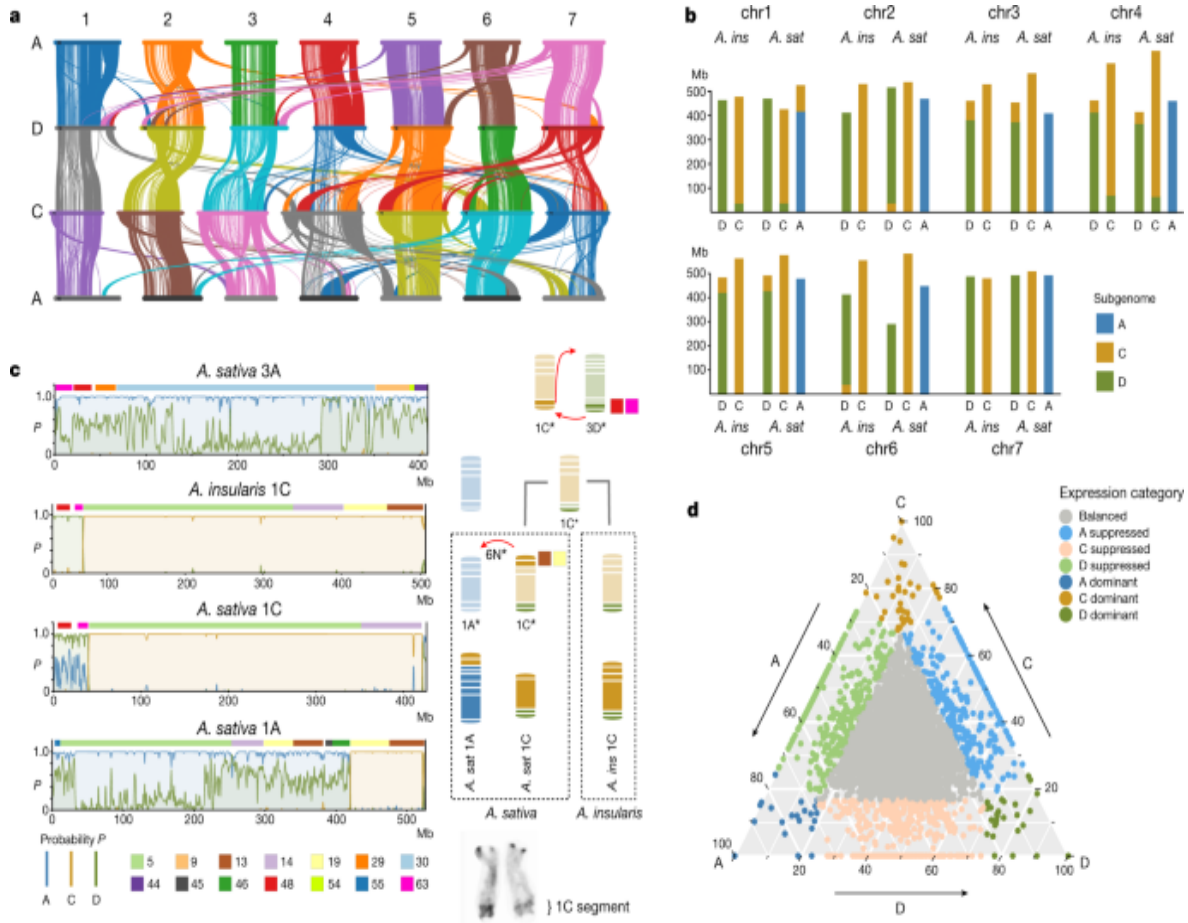
We predicted gene models in the oat genome using an automated annotation pipeline¹⁶, assisted by RNA-sequencing (RNA-seq) and Iso-seq transcriptome data, protein homology and ab initio prediction. This yielded 80,608 high-confidence protein-coding loci (98.5% BUSCO; Extended Data Fig. 2c and Supplementary Table 3), 83.5% of which showed evidence of transcription in at least one condition. Another 71,727 low-confidence protein-coding loci primarily represent gene fragments, pseudogenes and gene models with weak support. The overall amount and composition of transposable elements is very similar between the Sang and OT3098 assemblies (Supplementary Tables 4 and 5 and Supplementary Fig. 8). Transposable elements accounted for 64% of the oat genome sequence. The size difference of about 1 Gb observed between the C and A or D subgenome probably reflects higher transposon activity in the diploid ancestor of the C subgenome, as evidenced by a 1.3-fold increase in the number of full-length long terminal repeat retrotransposons, an enrichment in specific transposable element-related Pfam domains and Csubgenome specific transposon families, higher repetitivity, more tandem repeats and higher numbers of transposable element and low-confidence genes (Extended Data Fig. 1c). Several tandem repeat subfamilies were unequally distributed across the subgenomes, highlighting potentially rearranged genomic regions (Extended Data Fig. 1d). However, limitations of the short-read assembly arising from lower contiguity (Supplementary Table 1) were apparent in the overall reduced representation of tandem repeats and ribosomal DNA loci (Supplementary Tables 4 and 6) as well as in regions of reduced gene density mainly in centromeric and pericentromeric regions and unplaced genes (Supplementary Fig. 9, Supplementary Table 7 and [Supplementary Methods](#)).

Mosaic chromosome architecture of oat

The overall structure of the oat genome is similar to that of Triticeae genomes, although frequent genomic rearrangements in oat have resulted in a mosaic-like genome architecture. In many oat chromosomes, gene and

recombination density is not a monotonic function of distance from the centromere (Extended Data Fig. 3), as is mostly observed in the Triticeae¹⁷. Examination of whole-genome alignments, subgenome-specific k -mers and orthologous and homoeologous genes clustering as synteny blocks in genomic neighbourhoods in four *Avena* species (Extended Data Figs. 1d and 4) revealed numerous large-scale genomic rearrangements affecting the order of these blocks within and between subgenomes (Fig. 2a). We detected seven large-scale genomic rearrangements in *A. sativa* and traced them back to eight translocation events between the A, C and D subgenomes (Fig. 2b, c, Extended Data Figs. 4a and 5a, Supplementary Fig. 10 and Supplementary Table 8), spanning 4.3% of the genome and approximately 7.9% of the high-confidence genes. Two of the translocation events were specific to *A. sativa*. Unlike those in wheat⁷, the oat subgenomes exhibit unbalanced gene counts; specifically, the C subgenome appears to have 12% fewer genes than the A or D subgenome (Extended Data Fig. 2d and Supplementary Table 9). Analysis of orthologous gene groups (Supplementary Table 10 and Supplementary Figs. 11 and 12) showed that unbalanced gene families were associated with significant spatial clustering (Supplementary Fig. 13) in genomic rearrangements. Ancestral state reconstruction of the oat chromosomes revealed a loss of at least 226 Mb of gene-rich regions from the C subgenome to the A and D subgenomes (Supplementary Table 9). This implies that the translocations fully account for the lower gene count in the C subgenome and not gene loss or subfractionation after formation of the hexaploid.

Fig. 2: Genome organization, rearrangement and subgenome interplay in oat.



a, Overview of syntenic blocks across the three subgenomes⁵². **b**, Predicted borders of the seven major inter-subgenomic translocations in hexaploid oat *A. sativa* (*A. sat*) and its closest tetraploid ancestor, *A. insularis* (*A. ins*). Blue, gold and green colours represent the A-, C- and D-subgenomic regions, respectively. **c**, Reconstruction of translocations in *A. sativa* and *A. insularis* using subgenome-specific *k*-mers and syntenic blocks and orthoblocks. Left side, probabilities of the A-, C- and D-subgenome classification by *k*-mers for chromosome 1C of *A. insularis* and chromosomes 3A, 1C and 1A of *A. sativa*. The boxes above each plot show the order and identity of colour-coded blocks of the respective orthologous homoeologous genes according to the colour bar at the bottom left. Right side, illustration of two translocation events deduced from the information at left: translocation of blocks 48 and 63 from chromosome 3D to 1C, which is shared by *A. sativa* and *A. insularis* and occurred in their tetraploid ancestor, and the transfer of blocks 13 and 19 from chromosome 1C to 1A in *A. sativa*, resulting in a duplication pattern of these blocks. The ancestral

location of blocks 48 and 63 on chr3 is supported by chr3A of *A. sativa* (top left); chr3C of *A. sativa*, *A. insularis* and *A. eriantha*; and chr3A of *A. longiglumis*. Bottom right, the 1C segment of chr1A in *A. sativa* is cytologically highlighted. Asterisks refer to the ancestral state of chromosomes. **d**, Ternary plot of the relative expression levels of 7,726 ancestral triads (23,178 genes) in hexaploid oat in a combined analysis of all transcriptome samples. Each dot represents a gene triad with an A, C and D coordinate. Subgenome-dominant categories are defined by triads in vertices, whereas suppressed categories are associated with triads near edges and between vertices. Grey dots in the centre indicate balanced triads.

Previous molecular marker studies using oat mapping and breeding populations have provided independent evidence for frequent translocations among oat subgenomes^{18,19}. Using the oat genome to reanalyse the data (Extended Data Fig. 6), we observed inter-chromosomal pseudo-linkage in a population that segregates for the 1C translocation on 1A. Such pseudo-linkage has been implicated in the propensity for cold hardiness to remain associated with non-carriers of this translocation²⁰. An accompanying study²¹ details similar associated opportunities and barriers in genomic breeding strategies. The mosaic nature of the oat genome may be associated with the apparent lack of an orthologue of *TaZIP4-B2* (located within the *Ph1* locus), which in bread wheat stabilizes the genome structure during meiosis and suppresses crossovers between homoeologues^{22,23,24} (Extended Data Fig. 5b and Supplementary Figs. 14 and 15). In contrast to wheat²⁵, interploidy crosses and alien introgressions have been extremely challenging in *Avena*²⁶, suggesting that incompatible genome architecture is an additional barrier preventing genetic gains in oat.

Oat subgenome expression is balanced

After polyploidization, sub- and neofunctionalization and gene loss modify the gene content in the new species^{27,28}. Systematic differences in subgenome/homoeologue gene expression (homoeologue expression bias²⁹) may also be prevalent. In fact, quantitative variation for many agronomic traits may reflect genetic interactions between homoeologues such as functional redundancy (buffering) or dominant phenotypes attributed to one

homoeologue³⁰. To investigate homoeologue expression bias in hexaploid oat, we defined 7,726 homoeologous gene triads with a 1:1:1 correspondence across the three oat subgenomes (Supplementary Table 11), referred to as ancestral triads. Average expression values across transcriptome samples from six tissues showed that C-subgenome genes were slightly less expressed (32.32%) than those in the D (33.53%) and A (33.76%) subgenomes (Kruskal–Wallis, $P = 0.054$). We considered six homoeologous expression categories³¹ and found that most ancestral triads (84.1%) showed balanced expression, 3.4% showed single-homoeologue dominance and 12.6% showed single-homoeologue suppression. The relative contributions of the different categories (Extended Data Fig. 7a) indicated no major overall bias for one of the subgenomes (Fig. 2d). A co-expression network approach revealed that genes from the C subgenome were found in divergent expression modules more frequently than their A- and D-subgenome homoeologues (χ^2 test, $P = 2.085 \times 10^{-6}$; Extended Data Fig. 7b and Supplementary Table 12).

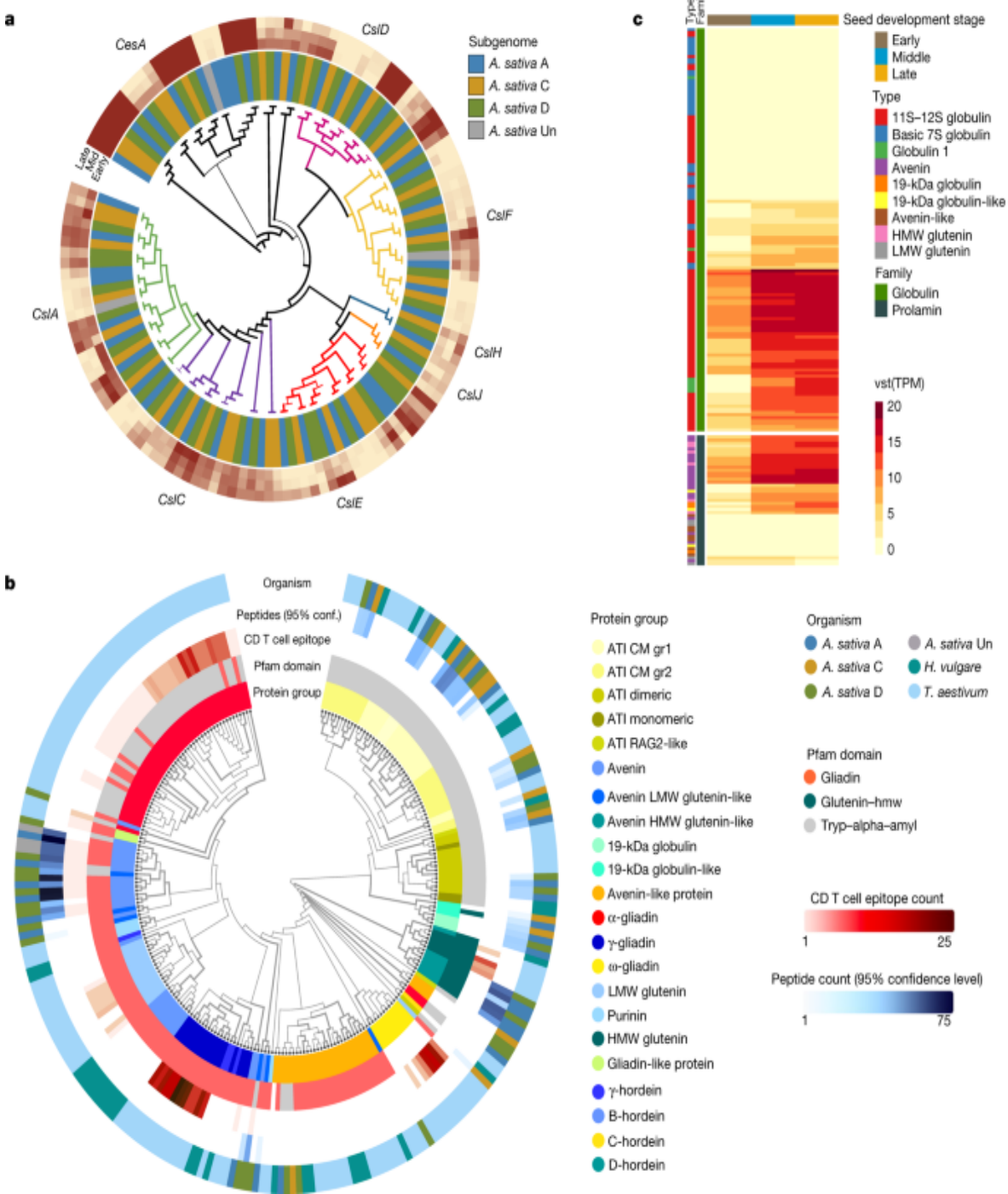
In another 1,508 triad gene clusters containing at least one member positioned in a translocated region (relocated triads; Supplementary Table 13), the overall expression patterns were similar to those of the ancestral triads (Extended Data Fig. 7c). The C-suppressed category was slightly larger (5.1%) in the ancestral triads compared with the A-suppressed (3.5%) or D-suppressed (4.1%) triads, but the subgenome suppression patterns were reversed (4.5% A, 4.2% C and 5.2% D) in the relocated triads (χ^2 test, $P = 0.019$; Extended Data Fig. 7c). Our results indicate that translocations and rearrangements in the oat genome may affect global and homoeologous gene expression patterns. Understanding how homoeologues interact to influence gene expression and identifying functional single-copy genes showing non-balanced expression will inform crop improvement in oats.

Soluble fibre-related gene families

Mixed-linkage β -glucans are soluble fibres present at high levels in oat endosperm cell walls (3.8–6.1 g per 100 g dry weight) that reduce blood cholesterol and post-meal glycaemic responses^{3,4}. The cellulose synthase-like gene *CslF6* is central for β -glucan biosynthesis in cereals^{32,33}. We catalogued the cellulose synthase (GT2) and callose synthase (GT48)

families of glycosyltransferases to identify the genetic foundation underlying oat β -glucan biosynthesis. The hexaploid oat genome encodes 134 members of the cellulose synthase gene superfamily (Fig. 3a), representing the cellulose synthase (*CesA*) subfamily (Supplementary Fig. 16) and seven cellulose synthase-like subfamilies, including *CslA*, *CslC*, *CslD*, *CslE*, *CslF*, *CslH* and *CslJ*. The *GT48* family comprised 28 members (Supplementary Fig. 17). Genes within the *CesA* and *CslF* subfamilies were most highly expressed over multiple stages of seed development (Fig. 3a and Supplementary Fig. 18). Investigation of differentially expressed genes between stages indicated specific roles for particular subfamilies such as *CslE* and *CslF* (including the C-subgenome copy of *CslF6*), which were upregulated in late stages of seed development (Supplementary Fig. 19), as shown in barley³⁴. Compared with other grasses, the oat cellulose synthase superfamily showed no significant expansions apart from duplication events in the *CesA*, *CslC*, *CslE* and *CslJ* subfamilies (Supplementary Fig. 20 and Extended Data Fig. 8). These findings suggest that the high content and quality of β -glucan in oat are not driven by major differences in the copy number of cellulose synthase superfamily genes relative to other grasses but rather by allelic variation and transcription factors, as previously reported³⁴.

Fig. 3: Analysis of cellulose synthase and seed storage protein gene families in *A. sativa*.



a, Phylogeny of the cellulose synthase protein superfamily in *A. sativa* highlighting the eight subfamilies. Outer tracks represent the variance stabilizing-transformed transcripts per million (TPM) values determined for early, middle and late seed-development stages. The TPM level correlates with the intensity of burgundy colouring; the branch thickness corresponds to the bootstrap values and increases with higher bootstrap. **b**, Schematic

representation and phylogeny of cereal storage proteins. The protein types used for the analysis were: wheat gliadins, glutenins, avenin-like proteins and ATIs⁷; barley hordeins, avenin-like proteins and ATIs⁵³; and oat avenins, HMW glutenins, avenin-like proteins and ATIs identified in this study. Pfam domains and the identified protein groups are highlighted in separate layers. Epitopes used for the analysis included coeliac disease (CD)-associated T cell epitopes⁴⁷. The numbers of T cell epitopes are labelled in the red colour scale. The number of peptides identified at the 95% confidence level are labelled in the blue colour scale; the branch thickness corresponds to bootstrap values and increases with higher bootstrap. LMW, low molecular weight. **c**, Expression of oat prolamin and globulin genes in three stages of seed development. The variance stabilizing transformed (vst) TPM levels correlate with the intensity of yellow to red colouring.

Oat storage proteins and human health

Oat globulins constitute 75–80% of grain protein content, with prolamins (avenins) accounting for approximately 10–15%. Prolamin superfamily members trigger coeliac disease, food allergies and baker's asthma³⁵. We identified genes encoding 25 avenins, 6 high-molecular-weight glutenins (HMW-GS) and 61 genes representing α -amylase/trypsin inhibitors (ATIs) and other prolamin superfamily members related to protein accumulation and immunogenicity (Supplementary Table 14). Hexaploid oat has avenin loci on chromosomes 1D, 3D and 7A; seed storage globulin loci (135 genes) on chromosomes 1A, 1D, 3D, 7A, 4A and 4D; and no storage protein loci mapping to the C subgenome (Fig. 3b and Supplementary Table 14).

Unlike that of wheat, the oat genome harboured no α - or ω -gliadin genes, and the identified avenins co-clustered with γ -gliadins, low-molecular-weight glutenins and B-hordeins (Fig. 3b). We detected four complete, highly conserved oat HMW-GS gene models as two distinct loci on 1A and one locus pair on 1D, with no HMW-GS genes mapping to 1C. We identified a prolamin type, the 19-kDa globulin-like proteins, with an unknown function that is distinct from the avenins yet shares sequence similarity with HMW-GS and 19-kDa globulins (Fig. 3b). The predicted oat HMW-GS and avenins were highly conserved in their Pfam domains (Fig. 3b) and cysteine

patterns (Extended Data Fig. 9). Glutamine- and proline-rich repetitive peptides were fewer in these oat proteins, making them shorter than those in wheat or barley (Extended Data Fig. 9).

We detected transcripts for most of the avenin genes, which showed gene expression patterns that aligned with their wheat orthologues, with increased transcript levels from the middle phase of seed development³⁶ (Fig. 3c), and protein levels by using liquid chromatography with tandem mass spectrometry (Fig. 3b). We identified inactive genes and pseudogenes among avenin-encoding genes (Fig. 3b,c and Supplementary Table 14) in a similar proportion as in wheat γ -gliadins^{37,38}. This indicates a lower level of gene expansion and pseudogenization compared with the highly immunogenic wheat α -gliadin genes³⁹. Moreover, the expression of 11S globulin genes initiated early in seed development and was higher than that of the avenin genes (Fig. 3c). Discovery proteomics detected thirty-six distinct 11S globulins, five globulin-1 proteins and two 7S globulins, with an average of 83% protein sequence coverage at a 1% false discovery rate.

The oat avenins and globulins showed opposite trends compared with their wheat orthologues in gene copy number, protein length and enrichment in glutamine and asparagine residues that serve as a nitrogen storage sink (Extended Data Fig. 10a). Together with pronounced differences in transcription factor-binding sites specific to the nitrate response (Extended Data Fig. 10b and Supplementary Table 15), this may contribute to the primary role of oat globulins in nitrogen storage. These results confirm that the genomic organization, sequence characteristics and expression patterns of oat storage proteins share more similarities with rice and dicotyledonous plants than with wheat and other gluten-rich cereals^{40,41}.

We mapped previously reported coeliac disease-associated T cell epitopes to the predicted oat avenin proteins and compared them with the T cell epitope patterns of wheat and barley prolamins⁴². The results showed that only a subset of encoded avenin proteins contain coeliac disease-associated immune-reactive regions compared with the high prevalence found in wheat or barley (Fig. 3b). Taken together, the low copy number of genes encoding coeliac disease epitopes, low frequency of detected T cell epitopes in the protein sequence, low occurrence of other highly immunogenic proteins,

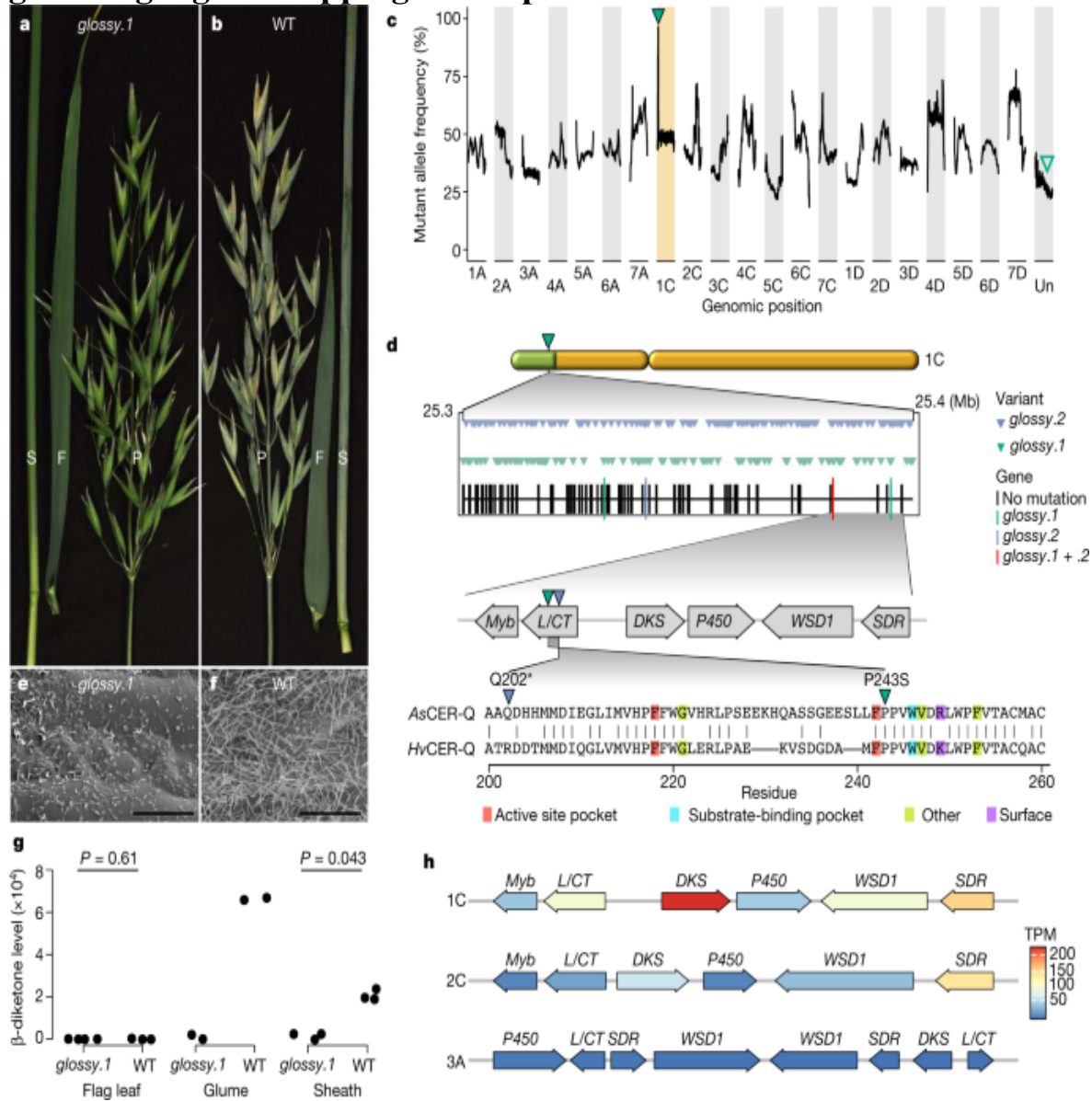
proportion of avenins within total oat protein and relative immunogenicity of avenin epitopes⁴³ all support the inclusion of oats in gluten-free diets³⁵.

Single-gene mapping of a wax mutant

To demonstrate how an annotated reference genome enables greater use of resources such as TILLING populations^{44,45}, we mapped the causal mutation in the epicuticular wax mutant *glossy.1* (Fig. 4a, b). Epicuticular waxes have a role in biotic and abiotic stress resistance^{46,47} and provide an important target for oat breeding. We identified homozygous polymorphisms unique to the mutant, which mapped to chromosome 1C (Fig. 4c and Supplementary Fig. 21), and identified a single gene annotated as an α/β-hydrolase (*AVESA.00010b.r2.UnGI403470*) as a likely candidate that is orthologous to barley *Cer-q* (*HORVU.MOREX.r3.2HG0097460*) (Supplementary Fig. 22). An independent mutant line (*glossy.2*) exhibited the same glossy phenotype (Fig. 4d, Supplementary Fig. 23 and Supplementary Table 16). Barley *Cer-q* mutants⁴⁸ are deficient in the same β-diketone (hentriacontane-14,16-dione) and wax tubules that are absent in the *glossy* mutants (Fig. 4e–g and Supplementary Figs. 24–26). The scaffold containing the candidate gene was localized to the region of chromosome 1C (Fig. 4c and Supplementary Table 17). The presumed *glossy.1* mutation introduced a P243S substitution in the encoded protein adjacent to a deleterious F219L substitution known to inactivate barley CER-Q⁴⁹ (Fig. 4d and Supplementary Fig. 27). We identified gene clusters on oat chromosomes 1C, 2C and 3A and in wild *Avena* species (Supplementary Figs. 22 and 28–33) that are homologous to the barley *Cer-cqu* cluster^{49,50}. We also noted genes encoding proteins with similarity to *Arabidopsis* wax ester synthase/diacylglycerol acyltransferase 1 (*WSD1*), a Myb-domain transcription factor and a short-chain dehydrogenase/reductase (*SDR*) protein near the *Cer-cqu* homologues in the *Avena* genomes. All genes from the 1C cluster except *SDR* were expressed at levels 3–6 times higher than those of the 3A cluster, with very low expression from 2C cluster genes and with no differential expression between the *glossy* and glaucous glume tissue (two-sided Wald test, null hypothesis logarithmic fold change = 0, adjusted $P < 0.01$; Fig. 4h and Supplementary Fig. 34). Together, these results suggest that *AVESA.00010b.r2.UnGI403470* is the oat *Cer-q* gene. The reference

genome thus facilitated a major advance in understanding β -diketone biosynthesis in oat and can help breeders manipulate tissue-specific epicuticular wax composition in future oat cultivars adapted for hotter climates.

Fig. 4: Single-gene mapping of an epicuticular wax mutant.



a, b, Epicuticular wax phenotypes of the *glossy.1* mutant (**a**) and the glaucous parental cultivar (**b**) at the early grain filling stage. S, sheath; F, flag leaf; P, panicle. **c**, Sliding window of allele frequency for variants unique to *glossy.1*. A window of 100 variants (total allelic depth ≥ 30) was used. Green triangle, chromosomal region shared by the *glossy.1* pool;

empty triangle, location of the contig with the candidate gene in the assembly. Hi-C data anchor the contig to the 1C peak. **d**, Mapping of the *glossy.1* locus. Top, genes and variants (total allelic depth ≥ 30) at the 1C peak. Middle, the candidate gene (Gene-ID: *AVESA.00010b.r2.UnGI403470*) encoding a lipase/carboxyltransferase (L/CT), indicated by the red vertical bar, is located in the putative biosynthetic gene cluster orthologous to the barley *Cer-cqu* cluster. The genes encoding diketone synthase (DKS) and L/CT are orthologous to the barley *Cer-c* and *Cer-q* genes, respectively (Supplementary Figs. 22 and 28). Green triangle, *glossy.1* mutation; blue triangle, *glossy.2* mutation. Bottom, alignment of *HvCER-Q* and *AsCER-Q*. Known deleterious single-amino acid substitutions from barley⁴⁹ are indicated. **e, f**, Scanning electron micrographs of the glume cuticle surface in *glossy.1* (**e**) and the glaucous parental cultivar (**f**) at $\times 4,000$ magnification; scale bars, 10 μm . **g**, Hentriacontane-14,16-dione is the major metabolite not detected in *glossy.1* (two-sided Welch *t*-test, *P* values adjusted using Benjamini–Hochberg procedure; glaucous flag leaf, $n = 4$; *glossy* flag leaf, $n = 3$; sheath, $n = 3$; glume, $n = 2$). **h**, Homoeologous gene clusters on chromosomes 1C, 3A and 2C. Genes are coloured according to the mean TPM value (four biological replicates) in glaucous glumes. *Myb*, Myb factor; *P450*, cytochrome P450; *WSD1*, wax ester synthase/diacylglycerol acyltransferase 1; *SDR*, short-chain dehydrogenase/reductase.

Discussion

In summary, this fully annotated hexaploid oat reference genome lays the foundation for advances in oat breeding and basic oat biology and for the ongoing pan-genome project. With the chromosome rearrangements in a typical spring oat cultivar now delineated, breeders and researchers will have access to a resource equal in calibre to Triticeae genomes, which may help them to overcome the breeding barriers and segregation anomalies described in numerous mapping studies. Using the reference genome to map genes associated with agronomic and human nutrition-related traits is a viable approach for precisely adapting oat varieties. Known quantitative trait loci can be anchored to the Sang reference, and the transcriptome co-expression networks can be leveraged to identify candidate genes in the vicinity of specific quantitative trait loci. Modern breeding strategies such as

genome editing and gene pyramiding can now more easily be applied in oat to develop varieties that meet the increasing global demand for oat-derived products. Our proteogenomic investigation of oat storage proteins confirms qualitative and quantitative differences in the expression of proteins compared with the more abundant and immunogenic sequences in wheat, barley and rye, which supports the safety of oats in gluten-free diets. The detailed genome annotation and case studies presented here provide examples of the myriad possibilities for the discovery and exploitation of functional genetic mechanisms in oat.

Reporting summary

Further information on research design is available in the [Nature Research Reporting Summary](#) linked to this paper.

Data availability

The raw sequence data used for de novo whole-genome assembly are available from the European Nucleotide Archive (ENA) under accession number [PRJEB44810](#) (*A. sativa* cv. Sang) and from the Sequence Read Archive under accession numbers [PRJNA727490](#) (*A. insularis* BYU209) and [PRJNA726919](#) (*A. longiglumis* CN58138). Chromosome conformation capture (Hi-C) sequencing data are available from ENA under accession numbers [PRJEB43668](#) (*A. sativa* cv. Sang), [PRJEB43670](#) (*A. insularis* BYU209) and [PRJEB43669](#) (*A. longiglumis* CN58138). Chromosome-scale sequence assemblies (pseudomolecules) are available from ENA under accession numbers [PRJEB44810](#) (*A. sativa* cv. Sang), [PRJEB45088](#) (*A. insularis* BYU209) and [PRJEB45087](#) (*A. longiglumis* CN58138). The raw RNA-seq and genome-sequencing data generated in this study are available under ENA accession number [PRJEB46365](#). Pseudomolecules, annotation data and analysis results are available at the Plant Genomics and Phenomics Research Data Repository at <https://doi.org/10.5447/ipk/2022/2>. The DOI was registered using e! DAL (<https://edal.ipk-gatersleben.de/>).

Pseudomolecules, annotation data and associated analyses for *A. sativa* cv. Sang, *A. longiglumis* and *A. insularis* are also available from GrainGenes⁵⁴: Sang genome browser, <https://wheat.pw.usda.gov/jb/?data=ggds/oat-sang>; Sang data download, <https://wheat.pw.usda.gov/GG3/content/avena-sang->

[download](#); *A. longiglumis* genome browser, <https://wheat.pw.usda.gov/jb/?data=/ggds/oat-longiglumis>; *A. longiglumis* data download, <https://wheat.pw.usda.gov/GG3/content/avena-longiglumis-download>; *A. insularis* genome browser, <https://wheat.pw.usda.gov/jb/?data=/ggds/oat-insularis>; *A. insularis* data download, <https://wheat.pw.usda.gov/GG3/content/avena-insularis-download>. The mass spectrometry proteomics data and ProteinPilot search result files have been deposited to MassIVE (<https://massive.ucsd.edu>) under accession number [MSV000088727](#). The publicly available OT3098 oat genome data were generated by PepsiCo and Corteva Agriscience. This dataset (annotation version 2) has been obtained and is available from GrainGenes at <https://wheat.pw.usda.gov/GG3/content/pepsico-ot3098-hexaploid-oat-version-2-genome-assembly-release-collaboration-graingenes>. Databases used in this study included PTREP release 19, Uniref download 2019-09-03, Pfam download 2019-09-03, Swiss-Prot, TAIR, TrEMBL, REdat_9.9_Poaceae section of the PGSB transposon library, Immune Epitope Database and Analysis Resource (<https://www.iedb.org>), PLACE and PlantCare promoter motif databases and pfam2GO.

Code availability

All relevant code developed in this study was deposited in the GitHub node at <https://github.com/PGSB-HMGU/oatkmers>.

References

1. Vavilov, N. I. in *Origin and Geography of Cultivated Plants* (ed. Dorofeyev, V. F.) 22–135 (Cambridge Univ. Press, 1992).
2. Malzew, A. I. *Wild and Cultivated Oats, Sectio Euavena Griseb.* (Publ. of the All-Union Inst. of Appl. Botany and New Cultures under the Council of People's Commissars of the USSR, 1930).
3. EFSA Panel on Dietetic Products, Nutrition and Allergies (NDA). Scientific opinion on the substantiation of a health claim related to oat β-glucan and lowering blood cholesterol and reduced risk of (coronary)

heart disease pursuant to Article 14 of Regulation (EC) no. 1924/2006. *EFSA J.* <https://doi.org/10.2903/j.efsa.2010.1885> (2010).

4. EFSA Panel on Dietetic Products, Nutrition and Allergies (NDA). Scientific opinion on the substantiation of health claims related to β -glucans from oats and barley and maintenance of normal blood LDL-cholesterol concentrations (ID 1236, 1299), increase in satiety leading to a reduction in energy intake (ID 851, 852), reduction of post-prandial glycaemic responses (ID 821, 824), and ‘digestive function’ (ID 850) pursuant to Article 13(1) of Regulation (EC) no. 1924/2006. *EFSA J.* <https://doi.org/10.2903/j.efsa.2011.2207> (2011).
5. Mathews, R., Kamil, A. & Chu, Y. Global review of heart health claims for oat β -glucan products. *Nutr. Rev.* **78**, 78–97 (2020).
6. Manni, M., Berkeley, M. R., Seppey, M. & Zdobnov, E. M. BUSCO: assessing genomic data quality and beyond. *Curr. Protoc.* **1**, e323 (2021).
7. International Wheat Genome Sequencing Consortium (IWGSC). et al. Shifting the limits in wheat research and breeding using a fully annotated reference genome. *Science* **361**, eaar7191 (2018).
8. Monat, C. et al. TRITEX: chromosome-scale sequence assembly of Triticeae genomes with open-source tools. *Genome Biol.* **20**, 284 (2019).
9. Rabanus-Wallace, M. T. et al. Chromosome-scale genome assembly provides insights into rye biology, evolution and agronomic potential. *Nat. Genet.* **53**, 564–573 (2021).
10. Bekele, W. A., Wight, C. P., Chao, S., Howarth, C. J. & Tinker, N. A. Haplotype-based genotyping-by-sequencing in oat genome research. *Plant Biotechnol. J.* **16**, 1452–1463 (2018).
11. GrainGenes: a database for Triticeae and *Avena*, *Avena sativa*, OT3098 v2, PepsiCo, <https://wheat.pw.usda.gov/jb?data=ggds/oat-ot3098v2-pepsico> (accessed 15 January 2022).

12. Ladizinsky, G. A new species of *Avena* from Sicily, possibly the tetraploid progenitor of hexaploid oats. *Genet. Resour. Crop Evol.* **45**, 263–269 (1998).
13. Sanz, M. J. et al. A new chromosome nomenclature system for oat (*Avena sativa* L. and *A. byzantina* C. Koch) based on FISH analysis of monosomic lines. *Theor. Appl. Genet.* **121**, 1541–1552 (2010).
14. Maughan, P. J. et al. Genomic insights from the first chromosome-scale assemblies of oat (*Avena* spp.) diploid species. *BMC Biol.* **17**, 92 (2019).
15. Nomenclature Database, National Oat Conference Newsletter, <https://oatnews.org/nomenclature> (accessed 8 March 2021).
16. Mascher, M. et al. Long-read sequence assembly: a technical evaluation in barley. *Plant Cell* **33**, 1888–1906 (2021).
17. Mascher, M. et al. A chromosome conformation capture ordered sequence of the barley genome. *Nature* **544**, 427–433 (2017).
18. Chaffin, A. S. et al. A consensus map in cultivated hexaploid oat reveals conserved grass synteny with substantial subgenome rearrangement. *Plant Genome* <https://doi.org/10.3835/plantgenome2015.10.0102> (2016).
19. Yan, H. et al. High-density marker profiling confirms ancestral genomes of *Avena* species and identifies D-genome chromosomes of hexaploid oat. *Theor. Appl. Genet.* **129**, 2133–2149 (2016).
20. Santos, A. G., Livingston, D. P., Jellen, E. N., Wooten, D. R. & Murphy, J. P. A cytological marker associated with winterhardiness in oat. *Crop Sci.* **46**, 203–208 (2006).
21. Tinker, N. A. et al. Genome analysis in *Avena sativa* reveals hidden breeding barriers and opportunities for oat improvement. *Commun. Biol.* <https://doi.org/10.1038/s42003-022-03256-5> (2022).

22. Alabdullah, A. K., Moore, G. & Martín, A. C. A duplicated copy of the meiotic gene *ZIP4* preserves up to 50% pollen viability and grain number in polyploid wheat. *Biology* **10**, 290 (2021).
23. Griffiths, S. et al. Molecular characterization of *Ph1* as a major chromosome pairing locus in polyploid wheat. *Nature* **439**, 749–752 (2006).
24. Rey, M.-D. et al. Exploiting the *ZIP4* homologue within the wheat *Ph1* locus has identified two lines exhibiting homoeologous crossover in wheat–wild relative hybrids. *Mol. Breed.* **37**, 95 (2017).
25. Moskal, K., Kowalik, S., Podyma, W., Łapiński, B. & Boczkowska, M. The pros and cons of rye chromatin introgression into wheat genome. *Agronomy* **11**, 456 (2021).
26. Dilkova, M., Jellen, E. N. & Forsberg, R. A. C-banded karyotypes and meiotic abnormalities in germplasm derived from interploidy crosses in *Avena*. *Euphytica* **111**, 175–184 (2000).
27. Otto, S. P. The evolutionary consequences of polyploidy. *Cell* **131**, 452–462 (2007).
28. Jiao, Y. & Paterson, A. H. Polyploidy-associated genome modifications during land plant evolution. *Philos. Trans. R. Soc. Lond. B* **369**, 20130355 (2014).
29. Grover, C. E. et al. Homoeolog expression bias and expression level dominance in allopolyploids. *New Phytol.* **196**, 966–971 (2012).
30. van de Peer, Y., Mizrahi, E. & Marchal, K. The evolutionary significance of polyploidy. *Nat. Rev. Genet.* **18**, 411–424 (2017).
31. Ramírez-González, R. H. et al. The transcriptional landscape of polyploid wheat. *Science* **361**, eaar6089 (2018).
32. Garcia-Gimenez, G. et al. Targeted mutation of barley (1,3;1,4)- β -glucan synthases reveals complex relationships between the storage and cell wall polysaccharide content. *Plant J.* **104**, 1009–1022 (2020).

33. Nemeth, C. et al. Down-regulation of the *CSLF6* gene results in decreased (1,3;1,4)- β -d-glucan in endosperm of wheat. *Plant Physiol.* **152**, 1209–1218 (2010).
34. Wong, S. C. et al. Differential expression of the *HvCslF6* gene late in grain development may explain quantitative differences in (1,3;1,4)- β -glucan concentration in barley. *Mol. Breed.* **35**, 20 (2015).
35. Pinto-Sánchez, M. I. et al. Safety of adding oats to a gluten-free diet for patients with celiac disease: systematic review and meta-analysis of clinical and observational studies. *Gastroenterology* **153**, 395–409 (2017).
36. Vinje, M. A., Walling, J. G., Henson, C. A. & Duke, S. H. Comparative gene expression analysis of the β -amylase and hordein gene families in the developing barley grain. *Gene* **693**, 127–136 (2019).
37. Juhász, A. et al. Genome mapping of seed-borne allergens and immunoresponsive proteins in wheat. *Sci. Adv.* **4**, eaar8602 (2018).
38. Zhang, Y. et al. Genome-, transcriptome- and proteome-wide analyses of the gliadin gene families in *Triticum urartu*. *PLoS ONE* **10**, e0131559 (2015).
39. Huo, N. et al. Dynamic evolution of α -gliadin prolamin gene family in homeologous genomes of hexaploid wheat. *Sci. Rep.* **8**, 5181 (2018).
40. Shewry, P. R. & Halford, N. G. Cereal seed storage proteins: structures, properties and role in grain utilization. *J. Exp. Bot.* **53**, 947–958 (2002).
41. Black, M. & Derek Bewley, J. *Seed Technology and Its Biological Basis* (CRC Press, 2000).
42. Sollid, L. M. et al. Update 2020: nomenclature and listing of celiac disease-relevant gluten epitopes recognized by CD4 $^{+}$ T cells. *Immunogenetics* **72**, 85–88 (2020).
43. Hardy, M. Y. et al. Ingestion of oats and barley in patients with celiac disease mobilizes cross-reactive T cells activated by avenin peptides

- and immuno-dominant hordein peptides. *J. Autoimmun.* **56**, 56–65 (2015).
44. Adamski, N. M. et al. A roadmap for gene functional characterisation in crops with large genomes: lessons from polyploid wheat. *eLife* **9**, e55646 (2020).
 45. Chawade, A. et al. Development and characterization of an oat TILLING-population and identification of mutations in lignin and β -glucan biosynthesis genes. *BMC Plant Biol.* **10**, 86 (2010).
 46. von Wettstein-Knowles, P. Ecophysiology with barley *eceriferum* (*cer*) mutants: the effects of humidity and wax crystal structure on yield and vegetative parameters. *Ann. Bot.* **126**, 301–313 (2020).
 47. Wang, X., Kong, L., Zhi, P. & Chang, C. Update on cuticular wax biosynthesis and its roles in plant disease resistance. *Int. J. Mol. Sci.* **21**, 5514 (2020).
 48. von Wettstein-Knowles, P. The polyketide components of waxes and the *Cer-cqu* gene cluster encoding a novel polyketide synthase, the β -diketone synthase, DKS. *Plants* **6**, 28 (2017).
 49. Schneider, L. M. et al. The *Cer-cqu* gene cluster determines three key players in a β -diketone synthase polyketide pathway synthesizing aliphatics in epicuticular waxes. *J. Exp. Bot.* **67**, 2715–2730 (2016).
 50. Hen-Avivi, S. et al. A metabolic gene cluster in the wheat *W1* and the barley *Cer-cqu* loci determines β -diketone biosynthesis and glaucousness. *Plant Cell* **28**, 1440–1460 (2016).
 51. Tinker, N. A. et al. A SNP genotyping array for hexaploid oat. *Plant Genome* **7**, 1–8 (2014).
 52. Bandi, V. & Gutwin, C. Interactive exploration of genomic conservation. In *Proceedings of the 46th Graphics Interface Conference 2020 (GI'20)* <https://synvisio.github.io> (2020).

53. Mascher, M. et al. Pseudomolecules and annotation of the third version of the reference genome sequence assembly of barley cv. Morex [Morex V3]. *e!DAL Plant Genomics and Phenomics Research Data Repository (PGP)* <https://doi.org/10.5447/ipk/2021/3> (accessed 3 December 2020).
54. Blake, V. C. et al. GrainGenes: centralized small grain resources and digital platform for geneticists and breeders. *Database* **2019**, baz065 (2019).

Acknowledgements

We are grateful for funding from Stiftelsen för Strategisk Forskning (SSF) (ScanOats: IRC15-0068) and the members of the ScanOats Industrial Research Center: Lund University; the Research Institute of Sweden (RISE); the Swedish University of Agricultural Sciences (SLU, Alnarp); Lantämmen ek för; Oatly AB; and Swedish Oat Fiber AB. We thank the Lantmännen Research Foundation for supporting the raw data collection for the Sang reference genome and mutated oat lines (2016H033, 2018F005). The pre-sequencing phase of the Sang genome project was supported by the Swedish Farmers Supply and Crop Marketing Co-operative (grant no. O-14-20-177). Funding was also provided by the German Federal Ministry of Education and Research (De.NBI, FKZ 031A536), German Federal Ministry of Food and Agriculture (FUGE, FKZ 28AIN02D20), Agriculture and Agri-Food Canada and Genome Quebec (Targeted and Useful Genomics for Barley and Oat), Australian Research Council Centre of Excellence for Innovations in Peptide and Protein Science (CE200100012), National Health and Medical Research Council (investigator grant APP1176553) and Coeliac Australia (G1005443). The authors acknowledge support from the National Genomics Infrastructure funded by the Science for Life Laboratory, the Knut and Alice Wallenberg Foundation and the Swedish Research Council. The SNIC/Uppsala Multidisciplinary Center for Advanced Computational Science provided assistance with massively parallel sequencing and access to the UPPMAX computational infrastructure. We acknowledge V. Llaca and K. Fengler for sequencing and assembly of OT3098 v2 and D. Eickholt for OT3098 project support. We thank D. Ahren for supervision of N.T.R., and bioinformatics guidance to J.B. and N. Sirijovski. We thank L. Sjögren

for isolating Sang genomic DNA for shotgun and massively parallel libraries, O. Van Aken and E. Darwish for contributing RNA-seq data used in the atlas, and A. Hansson for support during the initial planning phase of the Sang project. We are grateful to M. Knauf and I. Walde for assistance with Hi-C library preparation and sequencing; A. Fiebig for support in sequence data submission; E. Wilcox for support and expertise with PacBio sequencing; the staff at the Centre d'expertise et de services (Genome Quebec); A. Itaya and C. Wight for biological materials and sample preparation; S. Stockwell for proteomics sample preparation; O. Gustafsson for assistance with scanning electron microscopy; and R. Öste, K. E. Andersson and L. Bülow for major contributions to the SFF ScanOats grant application. We thank the GrainGenes database (<https://wheat.pw.usda.gov>) for providing a long-term home for the datasets, genome browsers and BLAST functionality for the oat genomes. The opinions in this study are those of the authors and do not necessarily represent the opinions or policies of PepsiCo, Inc.

Funding

Open access funding provided by Lund University.

Author information

Author notes

1. Daniel Lang

Present address: Department of Microbial Genomics and Bioforensics, Bundeswehr Institute of Microbiology, Munich, Germany

2. Nick Sirijovski

Present address: Food Science Organisation, Oatly AB, Lund, Sweden

3. These authors contributed equally: Nadia Kamal, Nikos Tsardakas Renhultt

Authors and Affiliations

1. Plant Genome and Systems Biology, German Research Center for Environmental Health, Helmholtz Zentrum München, Neuherberg, Germany

Nadia Kamal, Heidrun Gundlach, Georg Haberer, Thomas Lux, Daniel Lang, Klaus F. X. Mayer & Manuel Spannagl

2. ScanOats Industrial Research Centre, Department of Chemistry, Division of Pure and Applied Biochemistry, Lund University, Lund, Sweden

Nikos Tsardakas Renhuldt, Johan Bentzer & Nick Sirijovski

3. Australian Research Council Centre of Excellence for Innovations in Peptide and Protein Science, School of Science, Edith Cowan University, Joondalup, Western Australia, Australia

Angéla Juhász, Utpal Bose & Michelle L. Colgrave

4. Agriculture and Food, Commonwealth Scientific and Industrial Research Organisation, St Lucia, Queensland, Australia

Utpal Bose & Michelle L. Colgrave

5. Immunology Division, Walter and Eliza Hall Institute of Medical Research, Parkville, Victoria, Australia

Jason A. Tye-Din

6. Department of Gastroenterology, Royal Melbourne Hospital, Parkville, Victoria, Australia

Jason A. Tye-Din

7. Plant Biotechnology, Faculty of Biology, University of Freiburg, Freiburg, Germany

Nico van Gessel & Ralf Reski

8. Plant Gene Resources of Canada, Agriculture and Agri-Food Canada,
Saskatoon, Saskatchewan, Canada

Yong-Bi Fu

9. Department of Chemistry, Centre for Analysis and Synthesis, Lund
University, Lund, Sweden

Peter Spégel

10. Plant Breeding, Lantmännen, Svalöv, Sweden

Alf Ceplitis

11. Leibniz Institute of Plant Genetics and Crop Plant Research (IPK),
Seeland, Germany

Axel Himmelbach, Nils Stein & Martin Mascher

12. Research and Development Division, PepsiCo, St Paul, MN, USA

Amanda J. Waters

13. Ottawa Research and Development Centre, Agriculture and Agri-Food
Canada, Ottawa, Ontario, Canada

Wubishet A. Bekele & Nicholas A. Tinker

14. Molecular Cell Biology, Department of Biology, Lund University,
Lund, Sweden

Mats Hansson

15. Department of Crop Sciences, Center of Integrated Breeding Research
(CiBreed), Georg-August-University, Göttingen, Germany

Nils Stein

16. School of Life Sciences Weihenstephan, Technical University of Munich, Freising, Germany

Klaus F. X. Mayer

17. Department of Plant and Wildlife Sciences, Brigham Young University, Provo, UT, USA

Eric N. Jellen & Peter J. Maughan

18. German Centre for Integrative Biodiversity Research (iDiv), Halle-Jena-Leipzig, Leipzig, Germany

Martin Mascher

19. CropTailor AB, Department of Chemistry, Division of Pure and Applied Biochemistry, Lund University, Lund, Sweden

Olof Olsson & Nick Sirijovski

Contributions

O.O. conceived the Sang genome study and secured funding. N. Sirijovski and M.S. conceived and coordinated the study. N. Sirijovski performed molecular biology and coordinated sequencing and assembly for Sang. N.A.T., W.A.B., E.N.J., P.J.M. and Y.-B.F. contributed *A. insularis* and *A. longiglumis* assemblies. A.H. and N. Stein prepared Hi-C libraries and performed sequencing. M.M. performed pseudomolecule assemblies. M.M. and H.G. determined chromosome nomenclature. N. Sirijovski prepared RNA for atlas samples presented in this work. A.C. contributed sequence data: RNA-seq, hexaploid markers and pedigree background. A.J.W. contributed Iso-seq data and was principal investigator of the OT3098 genome project. M.S. and K.F.X.M. supervised annotation, with assistance from N.K., N.T.R. and T.L. N.T.R. performed confidence classification. TE and repeat analyses were performed by H.G. Ontology annotations were provided by D.L., N.V.G. and R.R. J.B. was responsible for data management and submission, with assistance from T.L. N. Sirijovski performed experiments with mutants with support from M.H. and P.S. for

profiling of wax metabolites. N.T.R. performed variant calling and single-gene mapping. N.K. conducted expression analysis with assistance from J.B. N.A.T. and W.A.B. performed molecular marker and recombination landscape analysis. E.N.J. contributed cytogenetic data. N.K., N.T.R. and A.J. performed gene family analysis and manual annotations. G.H. and H.G. analysed genome structure, organization and translocations. A.J. and M.L.C. supervised proteomics: U.B. performed proteomic data acquisition; A.J., U.B. and M.L.C. conducted proteomic data analysis; A.J. performed storage protein analysis; J.A.T.-D. performed storage protein data interpretation. M.S. and N. Sirijovski drafted the manuscript with input from N.K., N.T.R., J.B., M.M., A.J., U.B., J.A.T.-D., M.L.C., H.G., G.H. and N.A.T. All co-authors contributed to and edited the final version.

Corresponding authors

Correspondence to [Manuel Spannagl](#) or [Nick Sirijovski](#).

Ethics declarations

Competing interests

N. Sirijovski was an employee of CropTailor AB, a commercial enterprise, and became employed by Oatly AB during manuscript revision. O.O. is an employee of CropTailor AB. A.C. is an employee at Lantmännen. A.J.W. is an employee of PepsiCo, Inc. These authors are not expected to benefit financially from publication of these results. All other authors declare no competing interests.

Peer review

Peer review information

Nature thanks John Lovell for their contribution to the peer review of this work.

Additional information

Publisher's note Springer Nature remains neutral with regard to jurisdictional claims in published maps and institutional affiliations.

Extended data figures and tables

Extended Data Fig. 1 Assembly of three *Avena* species and chromosome organisation of hexaploid oat.

a, Summary of assembly statistics of the hexaploid *A. sativa* cv. Sang, diploid *A. longiglumis* CN58138 and tetraploid *A. insularis* BYU209 genomes. **b**, Gene-based collinearity of oat (*A. sativa*) to barley (*H. vulgare*). Each data point is an aligned gene. Genes in core regions are shown in red. The phylogenetically informed nomenclature is used on the bottom x-axis. The top axis shows the chromosome names according to Bekele et al. (2018)¹⁰, (Mrg groups) and according to Sanz et al. (2010)¹³, respectively. Centromere positions in oat and barley are indicated by red triangles (x axis) and red diamonds (y axis). **c**, Subgenome composition of hexaploid oat cv. Sang. Subgenome-specific features related to independent transposon histories in the diploid ancestors. The upper part shows the x-fold increase compared to the lowest of the three values across subgenomes A–C. The lower part summarises differences in genome size and gene number between the extant hexaploid and the ancestral state predating the seven translocations between the tetraploid and hexaploid subgenomes. **d**, Tandem repeat families in hexaploid oat cv. Sang specific to either the C or the A/D diploid ancestor or enriched in the extant A subgenome (from top to bottom).

Extended Data Fig. 2 Validation and statistics of *A. sativa* cv. Sang assembly and gene annotation.

a, BUSCO (lineage poales_odb10, created 2020-08-05) scores of the genome assemblies of *A. sativa* cv. Sang, *A. insularis* and *A. longiglumis* as well as the diploid progenitors *A. eriantha* and *A. atlantica* as a comparison. **b**, Colinearity plot of the pseudomolecules of *A. sativa* cv. Sang (short read assembly, y-axis) and OT3098 (long read assembly, x-axis). **c**, BUSCO (lineage poales_odb10, created 2020-08-05) scores for the oat reference

gene annotation v1.1 in comparison to the results of recent gene predictions for maize, rice and bread wheat. **d**, *Top*: overview of the number of predicted genes (HC - high confidence; LC - low confidence) for the three oat subgenomes and unplaced/unknown scaffolds. *Bottom*: total number of basepairs assembled for the respective three subgenomes and the number of basepairs in unplaced scaffolds.

Extended Data Fig. 3 Chromosome architecture of hexaploid oat.

Distribution of main features along the 21 Sang chromosomes. Track 1 displays synteny blocks based on the chromosome pattern of gene clusters with exactly three members. Track 2 denotes the sub genome assignment. The background of the bottom part consists of a stacked bar chart for the major genome components. The lines in the front show smoothed chromosomal distributions for mean 20-mer frequency, average recombination rate (cM/Mb) and gene density (#/Mb), each scaled min to max per chromosome. The population-level analysis of crossover frequency is explored in (N.T., W.B. et al. [21](#)). Therein we focus on average recombination rates that may result from global chromosome restructuring within *Avena*. Of particular interest are the long stretches of increased recombination on the long arms of chromosomes 4A and 4D. These regions coincide with stretches of high gene density and reduced transposon frequency. Other regions containing multiple ancestral telomeric regions showed corresponding multiple peaks of gene density and recombination. Also of interest is a region of suppressed recombination on chromosome 7D which is speculated to result from intraspecific rearrangements on this chromosome that impede meiotic pairing and crossovers.

Extended Data Fig. 4 Mosaic composition of hexaploid oat chromosomes.

a, Subgenome-specific kmers and synteny blocks in *A. sativa*. Probabilities of A- (blue), C- (yellow) and D- (green) subgenome classification by subgenomic-kmers are shown. Top row in each subplot displays identified synteny shown in alternative colours to emphasise block borders. From top to bottom, chromosomes 1 to 7 for subgenomes A (left column), C (mid

column) and D (right column), Y-axis: kmer-probability, x-axis: chromosomal position in Mb. **b**, Ancestral subgenome origin. In the extant Sang genome seven peripheral regions ranging from 40 Mb to 106 Mb differ in their subgenome signature from their current location. Five of these regions are of C genome origin: chr1A (106 Mb), chr2D (40Mb), chr3D (79 Mb), chr4D (46 Mb), chr5D (62 Mb). Two regions on the extant C subgenome are of D genome origin: chr1C (40 Mb) and chr4C (67 Mb). All in all, the transfers between subgenomes add up to 441 Mb, with a net loss in the C subgenome of 226 Mb. The upper tracks display homoeologous syntenic blocks within the Sang genome based on the chromosome pattern of gene clusters with exactly three members. The pattern A1-A1-D1 corresponds for example to a cluster with two members from chr1A and one member from chr1D. The core denotes all seven symmetric cluster patterns from A1-D1-C1 up to A7_D7_C7 with one member on each homoeolog chromosome (equivalent to the red dots in Extended Data Fig. [1b](#)).

Extended Data Fig. 5 Genome rearrangements in oat.

a, Translocation history in *A. insularis* and *A. sativa* cv. Sang. Top panel displays likely ancestral syntenic blocks for *Avena* chromosomes 1, 2, 3 and 6, for chromosomes 4, 5 and 7 we only provide ancestral states in the A-, D- and C-lineages separately. From top to bottom, subsequent panels show chromosomes and translocation operations for the initial tetraploid (directly after the hybridization of the diploid ancestors), the ancestral tetraploid after translocations, translocation events occurring after the split of *A. insularis* and oat, and the extant states. Genomic positions for each inter-subgenomic translocation in the extant tetra- and hexaploid are provided in Supplementary Table [8](#). A-, C- and D-subgenomic blocks are coloured in blue, yellow and green, respectively. Blocks contributing to translocations are accented in the mid panels by darker colours. Circled numbers represent translocation events: (1) represents two non-reciprocal translocations between the ancestral 1C and 3D chromosomes, (2) to (5) are additional translocations shared by *A. sativa* and *A. insularis*, while (6) and (7) are translocation differentiating extant oat and *A. insularis*. Asterisks refer to the ancestral state of chromosomes. **b**, Schematic representation of syntetic genomic regions between bread wheat (chromosome 5B harbouring *TaZIP4*-

B2) and oat (chromosomes 5A, 5C, 5D). At the syntenic position, a *TaZIP4-B2* ortholog is absent in the oat genome.

Extended Data Fig. 6 An example of a hidden breeding barrier in *Avena sativa* revealed by recombination matrices in two oat populations.

Average pairwise recombination frequencies (r) among chromosomes 1A, 1C and 1D were computed in 16 Mbp windows at 1 Mbp increments for two RIL populations and are visualised as blended colours of yellow ($r = 0$) to cyan ($r = 0.25$) to burgundy ($r = 0.5$). Blocks of yellow along the diagonal dashed lines indicate recombination suppression within a chromosome. Blocks of yellow off the diagonal represent pseudo-linkage between chromosomes. **a**, recombination in the population ‘Goslin’ x ‘HiFi’, where Goslin carries a 1C-A translocation (like Sang) and HiFi is a non-carrier. The result is that a large proportion of 1C shows pseudo linkage to the part of 1A where the translocation is present (large yellow rectangle in the intersection of 1A and 1C). **b**, both parents of the population (‘TX07CS-1948’ x ‘Hidalgo’) carry the same translocation as Sang thus no pseudo linkage is observed. The 1C-1A translocation is associated with adaptation-related traits²⁰, with pseudo linkage limiting the possibility of recombining different traits affected by genes in the translocated region in crosses between translocated and non-translocated germplasm.

Extended Data Fig. 7 Gene expression analysis in the hexaploid oat genome.

a, Box plots representation of the relative contribution of each subgenome based on triad assignment to the seven categories defined, balanced n = 6,308, A-suppressed n = 263, C-suppressed n = 378, D-suppressed n = 303, A-dominant n = 83, C-dominant n = 98, D-dominant n = 74, n=number of triads. Values from the first to third quartiles are shown within the boxplots boxes (inter-quartile range) with the median represented by the middle line. The upper and lower whiskers extend from the edge to the largest and smallest value of the edge but no further than $1.5 \times$ the inter-quartile range, the data beyond the end of the whiskers are outliers plotted individually. **b**, Heatmap representation of WGCNA modules showing the relation between

the expected representation of each subgenome in the module based on the overall number of genes per subgenome and the observed one. > 1: higher than expected, < 1 lower than expected. 1 = as expected. **c**, Gene expression patterns in ancestral triads versus triads with genes positioned in translocated regions across all samples (upper two panels) and in seed tissue (lower two panels).

Extended Data Fig. 8 Phylogeny of the CesA-subfamily of cellulose synthase genes and the Cellulose synthase-like subfamilies.

CslA, C, D, E, F, H, and J in 11 different species including oat. Tree branches for different subfamilies are shown in different colours. Branch thickness corresponds to bootstrap values and increases with higher bootstrap.

Extended Data Fig. 9 Comparative analysis of coeliac disease and allergy related epitopes in oat, wheat and barley.

a, Protein sequence alignment of avenins with γ -gliadins, B-hordeins, and LMW glutenins shows the conserved position of cysteine residues (black bars) and differences in the T cell epitope prevalence and variability. Blue bars represent T cell epitopes characteristic at γ -gliadins, green bars indicate epitopes characteristic at LMW glutenins, pink bars show positions of avenin-specific epitopes. Colour code on the left side indicates the species: oat (highlighted in pale yellow); wheat (highlighted in pale blue); and barley (highlighted in jagged ice). **b**, Sequence alignment of HMW glutenins show the conserved position of cysteine residues in the N- and C-terminal regions in oat and wheat HMW glutenins and barley D-hordein and shows the complete absence of coeliac disease (highlighted in red) and wheat allergy-related epitopes (shown as blue bars) in the sequences.

Extended Data Fig. 10 Comparative analysis of nitrogen storing capacity and transcription factor binding site motifs.

a, Size distribution of prolamin and globulin protein sequences in amino acid residues (aa) identified in the genomes of hexaploid oat cultivar Sang, the IWGSC v1 wheat reference genome, *Oryza sativa* Japonica IRGSP-1.0 rice genome and soybean reference genome, *Glycine max* v2.1 in relation to their nitrogen storing capacity, measured as a sum of asparagine and glutamine content in their sequence. **b**, Comparison of nitrogen-responsive transcription factor binding site patterns in oat, wheat and rice prolamins and oat, wheat, rice and soybean globulins. Consensus motifs identified in the 0 to -500 region and the related transcription factor families are labelled in each column; total numbers of detected motifs normalised by the number of gene models are indicated in each row.

Supplementary information

Supplementary Information

This file contains Supplementary Figs. 1–36, Supplementary Tables 1, 4–6, 8–10 and 21, Supplementary Methods and Supplementary References. The display items include 36 figures and 8 tables that support the validity of the genome assemblies, genome organization, chromosome rearrangement, gene families and expression analyses and single-gene mapping of the oat mutant.

Reporting Summary

Supplementary Tables

This file contains Supplementary Tables 2, 3, 7, 11–20 and 22, which support the genome annotation, ancestral and relocated triads, asymmetric modules, storage proteins and associated transcription factor-binding sites, single-gene mapping, assembly statistics of ancestral *Avena* genomes, metadata for datasets and samples and accession IDs used in the gene family analyses.

Rights and permissions

Open Access This article is licensed under a Creative Commons Attribution 4.0 International License, which permits use, sharing, adaptation, distribution and reproduction in any medium or format, as long as you give appropriate credit to the original author(s) and the source, provide a link to the Creative Commons license, and indicate if changes were made. The images or other third party material in this article are included in the article's Creative Commons license, unless indicated otherwise in a credit line to the material. If material is not included in the article's Creative Commons license and your intended use is not permitted by statutory regulation or exceeds the permitted use, you will need to obtain permission directly from the copyright holder. To view a copy of this license, visit <http://creativecommons.org/licenses/by/4.0/>.

Reprints and Permissions

About this article

Cite this article

Kamal, N., Tsardakas Renhuldt, N., Bentzer, J. *et al.* The mosaic oat genome gives insights into a uniquely healthy cereal crop. *Nature* **606**, 113–119 (2022). <https://doi.org/10.1038/s41586-022-04732-y>

- Received: 28 July 2021
- Accepted: 06 April 2022
- Published: 18 May 2022
- Issue Date: 02 June 2022
- DOI: <https://doi.org/10.1038/s41586-022-04732-y>

Share this article

Anyone you share the following link with will be able to read this content:

[Get shareable link](#)

Sorry, a shareable link is not currently available for this article.

[Copy to clipboard](#)

Provided by the Springer Nature SharedIt content-sharing initiative

Further reading

- [**Oat genome — sequence of a superfood**](#)

- Simon G. Krattinger
- Beat Keller

Nature Plants (2022)

- [**Genome analysis in *Avena sativa* reveals hidden breeding barriers and opportunities for oat improvement**](#)

- Nicholas A. Tinker
- Charlene P. Wight
- Martin Mascher

Communications Biology (2022)

[**Genome analysis in *Avena sativa* reveals hidden breeding barriers and opportunities for oat improvement**](#)

- Nicholas A. Tinker
- Charlene P. Wight
- Martin Mascher

Communications Biology Article Open Access 18 May 2022

[**Oat genome — sequence of a superfood**](#)

- Simon G. Krattinger
- Beat Keller

Nature Plants News & Views 26 May 2022

This article was downloaded by **calibre** from <https://www.nature.com/articles/s41586-022-04732-y>.

| [Section menu](#) | [Main menu](#) |

[Download PDF](#)

- Article
- Open Access
- [Published: 25 May 2022](#)

Neuropathic pain caused by miswiring and abnormal end organ targeting

- [Vijayan Gangadharan](#) ORCID: [orcid.org/0000-0002-2385-045X^{1,2}](https://orcid.org/0000-0002-2385-045X),
- [Hongwei Zheng](#) ORCID: [orcid.org/0000-0001-6657-9105³](https://orcid.org/0000-0001-6657-9105),
- [Francisco J. Taberner](#)^{1,4},
- [Jonathan Landry](#) ORCID: [orcid.org/0000-0003-2262-9099⁵](https://orcid.org/0000-0003-2262-9099),
- [Timo A. Nees](#)¹,
- [Jelena Pistolic](#)⁵,
- [Nitin Agarwal](#)¹,
- [Deepitha Männich](#) ORCID: [orcid.org/0000-0002-8990-3518¹](https://orcid.org/0000-0002-8990-3518),
- [Vladimir Benes](#) ORCID: [orcid.org/0000-0002-0352-2547⁵](https://orcid.org/0000-0002-0352-2547),
- [Moritz Helmstaedter](#) ORCID: [orcid.org/0000-0001-7973-0767²](https://orcid.org/0000-0001-7973-0767),
- [Björn Ommer](#)⁶,
- [Stefan G. Lechner](#) ORCID: [orcid.org/0000-0001-9402-9127¹](https://orcid.org/0000-0001-9402-9127),
- [Thomas Kuner](#)³ &
- [Rohini Kuner](#) ORCID: [orcid.org/0000-0002-3333-9129¹](https://orcid.org/0000-0002-3333-9129)

Nature volume **606**, pages 137–145 (2022)

- 8661 Accesses
- 1 Citations
- 104 Altmetric

- [Metrics details](#)

Subjects

- [Chronic pain](#)
- [Somatic system](#)

Abstract

Nerve injury leads to chronic pain and exaggerated sensitivity to gentle touch (allodynia) as well as a loss of sensation in the areas in which injured and non-injured nerves come together^{1,2,3}. The mechanisms that disambiguate these mixed and paradoxical symptoms are unknown. Here we longitudinally and non-invasively imaged genetically labelled populations of fibres that sense noxious stimuli (nociceptors) and gentle touch (low-threshold afferents) peripherally in the skin for longer than 10 months after nerve injury, while simultaneously tracking pain-related behaviour in the same mice. Fully denervated areas of skin initially lost sensation, gradually recovered normal sensitivity and developed marked allodynia and aversion to gentle touch several months after injury. This reinnervation-induced neuropathic pain involved nociceptors that sprouted into denervated territories precisely reproducing the initial pattern of innervation, were guided by blood vessels and showed irregular terminal connectivity in the skin and lowered activation thresholds mimicking low-threshold afferents. By contrast, low-threshold afferents—which normally mediate touch sensation as well as allodynia in intact nerve territories after injury^{4,5,6,7}—did not reinnervate, leading to an aberrant innervation of tactile end organs such as Meissner corpuscles with nociceptors alone. Genetic ablation of nociceptors fully abrogated reinnervation allodynia. Our results thus reveal the emergence of a form of chronic neuropathic pain that is driven by structural plasticity, abnormal terminal connectivity and malfunction of nociceptors during reinnervation, and provide a mechanistic framework for the paradoxical sensory manifestations that are observed clinically and can impose a heavy burden on patients.

Main

Recent years have witnessed major breakthroughs in our understanding of central-nervous-system-based mechanisms of neuropathic pain, with key contributions attributed to spinal glial activation^{8,9,10,11} and the cellular circuitry and signalling that mediate the disinhibition of nociception by light touch^{7,12,13,14,15}. Whether peripheral nerve alterations are causally linked to the maintenance of chronic neuropathic pain or only required as an initial trigger for central plasticity processes remains unclear^{3,16}. Chronic pain has seldom been studied in association with nerve regeneration after injury.

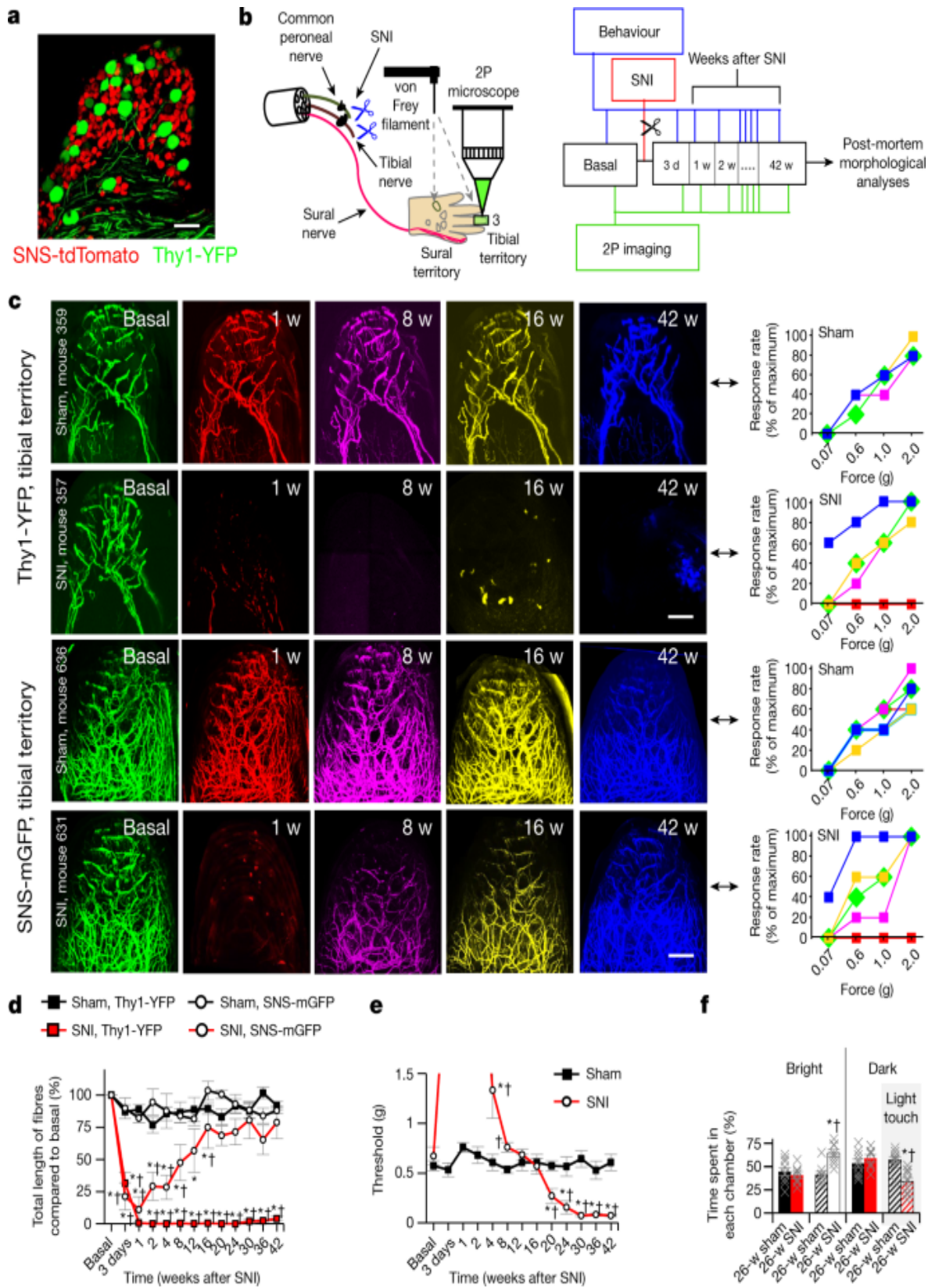
After physical trauma, damaged peripheral nerve fibres have a limited capacity to gradually regenerate in permissive environments^{17,18,19,20}. If regeneration is hindered by physical obstacles or a non-conducive local environment, neighbouring undamaged nerve fibres can invade denervated regions through collateral sprouting^{17,18,19,20}. However, whether this leads to the recovery of normal sensation and disappearance of pain²¹, or to the exacerbation of neuropathic pain through hyper-innervation²² or miswiring of collaterals¹⁸, is controversial and unresolved. Unequivocally disambiguating the role of peripheral nerve regeneration in neuropathic pain has been hindered so far by the correlative and population-based nature of post-mortem tissue analyses in preclinical and clinical studies, which do not take into account the dynamic nature of changes, inter-individual variability of innervation patterns and connectivity with terminal end organs; these studies also lack causal analyses, thus failing to establish whether peripheral reorganization is a cause or a consequence of neuropathic pain.

In vivo imaging of sensory innervation

In this study, we now disambiguate the role of peripheral regeneration in chronic pain by overcoming these multiple caveats through longitudinal imaging of specific, defined subsets of sensory afferents. We dynamically visualized in living mice the degeneration, regeneration, collateral sprouting and end organ connectivity of peripheral tactile fibres and nociceptors in the skin before and for 10 months to a year after nerve injury, and combined this with coordinated behavioural assessments of sensory function. Using multiphoton excitation fluorescence imaging, which permits studying deep-seated structures in a minimally invasive manner²³, we tracked pain-sensing high-threshold unmyelinated or thinly myelinated C and A- δ nociceptive

fibres²⁴ in mice expressing fluorescent reporters using the SNS-Cre transgene, which uses promoter elements of the mouse Nav1.8-encoding *Scn10a* gene²⁵, and visualized touch-sensitive low-threshold mechanosensory afferents of A β neurons⁷ (A β -LTMRs) using a strain of Thy1-YFP mice. In double transgenic SNS-tdTomato:Thy1-YFP mice, a mostly non-overlapping expression of tdTomato and YFP was found (Fig. 1a), with only 2.6% of YFP-positive neurons expressing tdTomato and only 0.4% of tdTomato-positive neurons expressing YFP (Extended Data Fig. 1, Supplementary Note 1), thereby demonstrating a clean segregation of non-nociceptive and nociceptive neurons. For imaging of the distal skin trajectories and the extremely fine, free nerve endings of nociceptors, we expressed a myristolated membrane-bound form of enhanced green fluorescent protein (mGFP) instead of tdTomato (SNS-mGFP mice; Supplementary Note 1). We were able to repetitively visualize labelled fibres with high fidelity and quantify structural changes in the living mouse stably over several months (Supplementary Video 1). We established an in-house imaging and analytical pipeline of mathematical algorithms and machine learning approaches for thresholding, image processing, segmentation, registration, quantitative analysis and visualization of the complex four-dimensional datasets (Supplementary Figs. 1–7, Supplementary Note 2). Because mixed injuries with damaged and undamaged nerves particularly frequently lead to neuropathic pain², we used the spared nerve injury (SNI) model of neuropathic pain²⁶ (Fig. 1b). This model allows us to study both damaged and undamaged nerve territories in a segregated manner within an individual animal by focusing on the following regions on the hind paw glabrous surface: (1) injured or denervated territory, which is normally innervated by the tibial and common peroneal nerves that are lesioned and ligated in SNI (for example, digit 3 shown in Fig. 1b), thereby simulating hindrance of normal regeneration; and (2) non-injured territory innervated largely by the sural nerve (lateral edge of digit 5 of the mouse hind paw in Fig. 1b), which is physically intact after SNI, develops exquisite mechanical hypersensitivity²⁶ (Extended Data Fig. 2a, b) and has been the subject of most studies on neuropathic pain using this model. We longitudinally intercalated nerve fibre imaging with behavioural analyses at the tibial-innervated digit (Fig. 1b).

Fig. 1: Emergence of chronic neuropathic pain and allodynia after a period of complete loss of sensation as nociceptors repopulate denervated territories whereas tactile fibres do not regenerate.



a, Confocal image of DRGs, showing the segregation of YFP-expressing touch-sensitive neurons (A β -LTMRs; Thy1-YFP transgene) and tdTomato-expressing pain-sensing neurons (nociceptors; SNS-Cre transgene) ($n = 5$). Scale bar, 100 μm . **b**, Experimental scheme of non-invasive two photon imaging longitudinally over 42 weeks and concurrent behavioural analyses in the SNI model, which involves ligation and cutting of the tibial and common peroneal branches while leaving the sural branch intact. 2P, two-photon; d, days; w, weeks; bold number 3 indicates digit 3. **c**, Examples of imaging in individual Thy1-YFP mice and SNS-mGFP mice with concurrent analysis of mechanical sensitivity (von Frey force in grams) at the imaged digit 3 (middle end phalanx) longitudinally over 42 weeks after sham or SNI surgery; matching time points are indicated by using the same false colours in imaging (left) and behaviour (right). Scale bars, 200 μm . **d**, Quantitative summary of total length of YFP-positive A β -LTMRs (square symbols; $n = 4$ and 4 for sham and SNI, respectively; $F_{(1,12)} = 8,614.43, P = 1.63 \times 10^{-18}$) and mGFP-positive nociceptors (circular symbols; $n = 4$ and 6 for sham and SNI, respectively; $F_{(1,12)} = 9.153, P = 0.016$; two-way repeated measures ANOVA with Bonferroni multiple comparison) in the tibial innervation territory. **e**, Summary of changes in withdrawal thresholds to von Frey force in tibial territory digit ($n = 9$ per group; after 20 weeks: $F_{(1,4)} = 43.33, P = 0.00223$. * $P < 0.05$ compared to baseline, † $P < 0.05$ compared to control group (sham); two-way repeated measures ANOVA with Bonferroni multiple comparison). **f**, Aversion to light touch in the previously insensitive tibial territory in the PEAP; the dark chamber was associated with mechanical stimulation ($n = 9$ for sham and $n = 7$ for SNI in no stimulation group, and $n = 9$ for sham and $n = 10$ for SNI in mechanical stimulation group; $F_{(3,31)} = 8.794, P = 0.000228$. * $P < 0.05$ as compared to without mechanical stimulation, † $P < 0.05$ as compared to sham group; one-way repeated measures ANOVA with Bonferroni comparison). Data are mean \pm s.e.m.

[Source data](#)

Reinnervation and emergence of pain

Figure 1c shows time series of maximum intensity projections of three-dimensional (3D) imaging stacks acquired *in vivo* from the middle end phalanx (tibial innervated digit) of individual Thy1-YFP and SNS-mGFP mice with corresponding stimulus–response curves to graded mechanical stimuli applied to the same area in the same mice (shown on the right of each row, curves colour-coded to the time of imaging). As expected, within three days to a week after SNI injury, the denervated tibial territory was entirely insensitive to mechanical stimulation at non-noxious (0.07–0.6 g) and noxious (1.0–2.0 g) intensities as both A β -LTMRs and nociceptive afferents were lost in Thy1-YFP and SNS-mGFP mice (red-coloured images and behaviour curves in Fig. 1c, Extended Data Fig. 3). Over time, the insensitive tibial territory gradually reacquired responsivity, first to noxious intensities (around 8 weeks after SNI; magenta-coloured curves) and thereafter also to non-noxious mechanical stimulation (by 16 weeks; yellow-coloured curves) as the mice concurrently showed a progressive re-innervation with nociceptive fibres, whereas A β fibres were still conspicuously missing in the tibial territory (Fig. 1c, Extended Data Fig. 2b). Notably, starting from week 20 after SNI, both SNS-mGFP and Thy1-YFP mice showed marked hyperalgesia as well as allodynia to mechanical stimuli in the previously insensitive regions of the tibial territory; this was still apparent when the experiment was terminated at week 42 after SNI (blue-coloured curves in Fig. 1c, Extended Data Figs. 2b, 3). Concurrently with this switch from recovery of normal sensitivity to marked hyperalgesia and allodynia as of 20 weeks after SNI, nociceptors were seen to have re-established a dense network, whereas reinnervation with tactile afferents was not detectable in the tibial territory at all (blue-coloured images in Fig. 1c). Supplementary Videos 2–5 (sham groups: 2 and 4; SNI groups: 3 and 5) show examples depicting 3D views of afferent type-specific denervation and reinnervation (or lack thereof) in the tibial territory of Thy1-YFP and SNS-mGFP mice at baseline and 42 weeks after SNI. Mice of both sexes showed similar changes.

Quantitative analyses of total fibre length, representing the cumulative length of the fibres that could be unequivocally traced in the imaged 3D volume common to all imaging sessions (typically 600 $\mu\text{m} \times 600 \mu\text{m} \times 450 \mu\text{m}$; $X \times Y \times Z$) in the digit, and behavioural analyses in large cohorts of SNS-mGFP and Thy1-YFP mice confirmed that the maximum observed recovery of nociceptor density (Fig. 1d) is reached just before the time point

of functional manifestation of mechanical allodynia (marked drop in threshold of eliciting a withdrawal response in Fig. 1e). By contrast, A β -LTMRs failed to emerge in all mice by the end of the experiment at 42 weeks after SNI (Fig. 1d, Extended Data Fig. 3). This mechanical hypersensitivity could not be accounted for by hyper-reflexia and was associated with aversion, as shown by behaviour in the voluntary place escape–avoidance paradigm (PEAP) (Extended Data Fig. 2c). At 24 weeks after SNI, mice showed avoidance of a dark chamber in which they received 0.16 g stimulation in the tibial nerve territory and showed preference for a bright chamber that they would have normally shunned (Fig. 1f, Extended Data Fig. 2d). Sham-treated mice did not develop avoidance, thereby showing that this stimulus is only aversive to SNI mice when applied to the tibial territory (Fig. 1f, Extended Data Fig. 2d). Significant cold allodynia was also observed in the tibial territory, although to a lesser extent than in the sural territory (Extended Data Fig. 2e). Together, this progressive shift from a lack of sensation to exaggerated nociceptive sensitivity, allodynia and aversion in a denervated region unmasks an emergence of late-onset, chronic neuropathic pain. Whereas most neuropathic pain studies have addressed pain in uninjured domains when nerves undergo partial or mixed injury, our findings now reveal pain that develops through regeneration of fibres into the denervated component of mixed injuries. Notably, these are clinically particularly frequently associated with neuropathic pain and a high burden of suffering for patients^{2,27}. We therefore refer to this phenomenon as reinnervation-induced neuropathic pain and show that it is associated with the re-emergence of nociceptors, but not A β -LTMRs.

In particular because these implications differ strongly from the prevailing view of the paramount importance of A β -LTMRs in neuropathic allodynia that is studied in the uninjured domains^{4,5,6,7}, we included several control experiments. First, photo damage to afferents was ruled out by the observed stability of innervation patterns of both nociceptive and non-nociceptive fibres over several months in sham-operated mice (Fig. 1c, d, Supplementary Videos 2, 4). Second, post-mortem immunohistochemical analyses with endogenous marker proteins for sensory afferents confirmed the loss of NF200-expressing large-diameter fibres and the recovery of CGRP-expressing nociceptors (Extended Data Fig. 4), thus ruling out potential caveats through pathophysiological alterations in the expression of

the transgenic fluorescent reporters. Third, when SNI mice that showed reinnervation with mGFP-positive nociceptors at 42 weeks after SNI were subjected to severance and ligation of the sural nerve, all mGFP fluorescence was lost from the tibial territory (Extended Data Fig. 5), thus demonstrating that fibres invading the tibial territory in conjunction with the emergence of neuropathic pain are nociceptors sprouting as collaterals from the neighbouring, intact sural nerve.

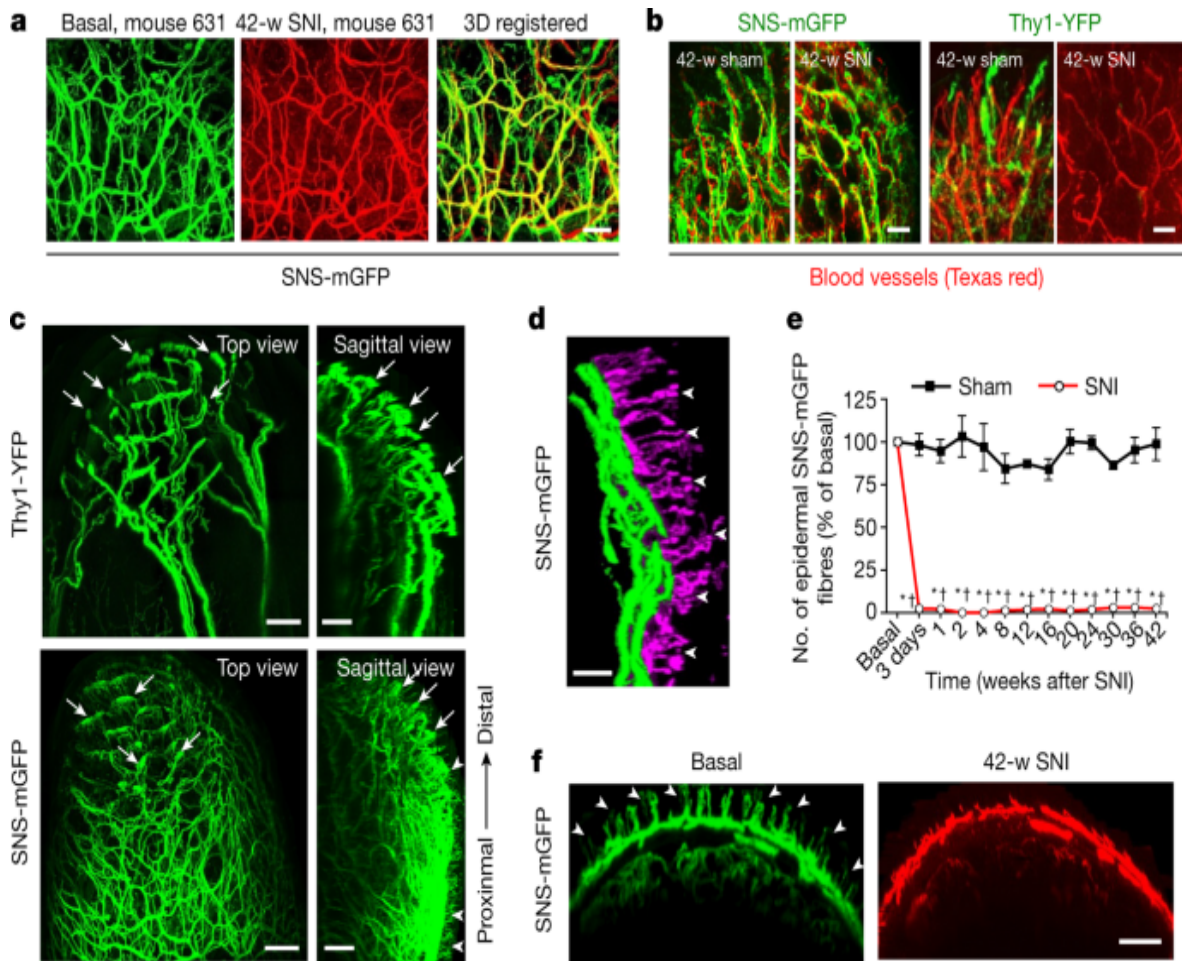
Differences in fibre trajectories

We next sought to address the question of why sural nociceptors enter the denervated tibial territory but A β -LTMRs cannot. Previous studies suggest that unmyelinated nerve fibres have an overall higher regenerative capacity than thickly myelinated fibres. This can be attributed (1) to differences in the types of axon itself; for example, a study in *Drosophila* implicates Piezo—an ion channel essential for mechanotransduction that is expressed in A β LTMRs more prominently than in nociceptors—as an inhibitor of axonal regeneration²⁸; or (2) to the different types of Schwann cells that support axonal growth and regenerative growth by forming conduits. Chronic denervation has been linked to a decreased capacity of myelinating Schwann cells to support regenerating axons^{19,29,30} and a maintenance of expression of markers of immature states—for example, the p75 neurotrophic receptor—specifically in Remak Schwann cells that ensheathe smaller unmyelinated axons (such as nociceptors), which may thereby facilitate regenerative support²⁰. In terms of collateral sprouting, recapitulating growth trajectories and distal connectivity is critical for achieving functional recovery. In this regard, we made two observations. First, we noted that the 3D architecture of nociceptor innervation of tibial nerve nociceptors under baseline conditions could be nearly perfectly registered with that of sural nerve nociceptors that have invaded the tibial territory at 42 weeks after SNI (Fig. 2a, Supplementary Video 5), showing that unrelated nociceptors from a different nerve are capable of exactly retracing the trajectories of the original nociceptors during collateral sprouting. In a second set of experiments, by acutely labelling blood vessels in the paw at 42 weeks after SNI through intravenous injection of high-molecular-weight dextran labelled with Texas red, we observed that the small distal branches of the collaterally sprouting mGFP-labelled nociceptors were intertwined with small blood vessels (Fig.

[2b](#)). By contrast, Thy1-YFP-labelled A β fibres showed trajectories that were distinct from blood vessel patterning in control mice and were absent from the tibial territory while intact blood vessels were detected (Fig. [2b](#)).

Because nociceptors in control mice without SNI were also observed to be in contact with blood vessels, and because blood vessels were not lost when mice underwent SNI, this suggests that nociceptors that are collaterally invading denervated areas can use small blood vessels as scaffolds to recreate the original patterning of trajectories in their distal projection zones. Structural neurovascular interactions represent an emerging field in developmental sciences, wherein nerve-derived cues—such as VEGF—are suggested to guide blood vessels over early embryonic life^{[31](#)}. Our observations now reveal that morphological trajectories of blood vessels and regenerating small-diameter nerves are replicated in the context of adult regeneration, and implicate blood vessels in providing a scaffold for collaterally sprouting nociceptors in denervated tissue.

Fig. 2: During the emergence of reinnervation-induced neuropathic pain, collaterally sprouting nociceptors of sural origin precisely replicate the original trajectories of tibial nociceptors along blood vessels but do not invade the epidermis.



a, Comparison of the original innervation with tibial nociceptors (green) and invading sural nociceptors (false coloured in red) at 42 weeks after nerve injury; representative images of mouse 631, out of 6 similar results from experiments in 6 mice. Scale bar, 50 µm. **b**, Dual-colour multiphoton imaging of Texas-red-dextran-labelled blood vessels with YFP-positive A β fibres (right) and GFP-labelled nociceptors (left) in the tibial territory. Scale bars, 25 µm. Representative images, out of 6 similar results from experiments in 3 sham and 3 SNI mice. **c**, Processed 3D stacks of in vivo multiphoton images showing complete innervation pattern of a single hind paw digit by YFP-positive A β -LTMRs and mGFP-expressing nociceptors; arrows indicate specialized endings with Meissner-corpuscle-like morphology and arrowheads indicate intra-epidermal free endings ($n = 4$). Scale bars, 100 µm. **d**, Segmentation of intra-epidermal free endings (false coloured in purple; arrowheads) of nociceptors from their afferent branches (green) ($n = 4$). Scale bar, 25 µm. **e**, **f**, Quantitative summary (e) and typical example (f) demonstrating the lack of epidermal invasion (arrowheads in f) over time after SNI. Sham mice (black squares) show stable innervation levels (~100% of basal), while SNI mice (red circles) show a significant decrease in innervation levels immediately after SNI and remain significantly lower than sham mice for the duration of the experiment (3 weeks).

of collaterally sprouting sural nociceptors in the tibial territory, expressed as a percentage fraction of baseline values ($n = 4$ and 4 for sham and SNI, respectively; groups $F_{(1,12)} = 1,429.65$, $P = 7.53 \times 10^{-14}$; two-way repeated measures ANOVA with Bonferroni multiple comparison). * $P < 0.05$, as compared to basal values; † $P < 0.05$, as compared to sham group. Data are mean \pm s.e.m. Scale bar, 100 μm .

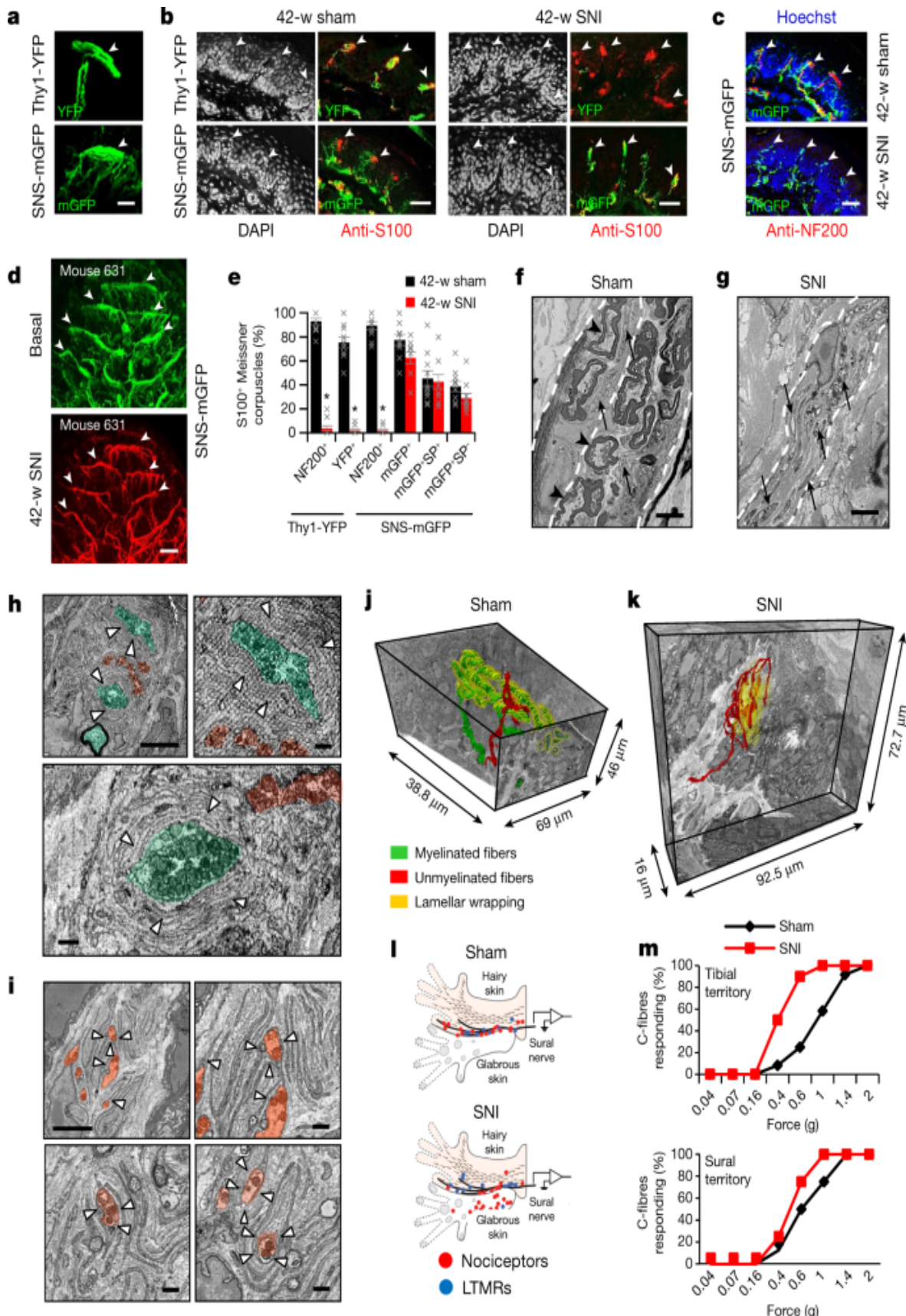
Source data

Aberrations in terminal connectivity

We next investigated why collateral sprouting of nociceptors into the denervated territory results in allodynia rather than the simple restoration of normal nociception. Ultimately, connectivity to end organs that transduce diverse types of external sensory stimuli onto distinct types of nerve fibres in the skin is key to functional selectivity and discernment between pain and touch, and there has been a lot of interest and progress in this regard³². Indeed, we found marked defects in the terminal connectivity and function of collaterally sprouting nociceptors that can account for the switch from normal nociception to allodynia. In SNS-mGFP mice, the intricate meshwork of mGFP-labelled, mostly thin fibres terminated in tiny free nerve endings in the epidermis of the skin that are characteristic to nociceptors (Fig. 2c, Supplementary Video 6), which we could segment out in the epidermis using a custom-developed algorithm (Fig. 2d; see Extended Data Fig. 6, Supplementary Note 2 for details). In contrast to the rich innervation of the epidermis by intra-epidermal free nerve endings under baseline conditions (Fig. 2c, d), collaterally sprouting nociceptors did not enter the epidermis of the tibial territory and were restricted at the basal membrane separating the dermis from the epidermis all the way up to the termination of the experiment at 42 weeks after SNI (quantitative summary in Fig. 2e and examples in Fig. 2f). That this is not an artefact of transgenic reporter expression was confirmed by immunostaining for native markers of nociceptors, such as CGRP, in the same tissue (Extended Data Fig. 4b). Thus, reinnervation-induced neuropathic allodynia was associated with an invasion of nociceptors in denervated areas that paradoxically lacked intra-epidermal free nerve endings, thereby reproducing a hallmark feature of several types of highly painful human C-fibre neuropathies³.

Another notable observation came with respect to afferent terminations on Meissner corpuscles, which transduce touch. As expected, thick, YFP-labelled A β afferents were found to end in oval-shaped terminations in the glabrous skin that are characteristic of Meissner corpuscles (Figs. 2c, 3a, Supplementary Videos 6, 7), which was confirmed by labelling for S100—the protein that labels the glial sheath of Meissner corpuscles (Fig. 3b). However, several mGFP-labelled nociceptive fibres were also found to terminate at the border between the epidermis and the dermis (Figs. 2c, 3a) and directly apposed S100-expressing Meissner corpuscles (Fig. 3b). In contrast to A β fibres, which innervate the Meissner corpuscles by coiling within the S100-expressing glial sheath, our imaging experiments showed that nociceptors form a sparse transverse meshwork of endings that colocalize with glial cells of Meissner corpuscles (Fig. 3a, Extended Data Fig. 7; see Supplementary Video 7 for a 3D view). For decades, the largest body of literature on Meissner corpuscles referred to their exclusive innervation by myelinated, low-threshold tactile afferents^{7,33}, which were recently reported to segregate into two phylogenetically distinct populations of A β neurons³⁴. However, a handful of reports have described the ‘intracorpuscular’ location of small-diameter unmyelinated fibres in human skin^{35,36,37} and in New World monkeys³⁸ and rodents³⁹; these fibres have not received attention and their functional importance is completely unknown so far.

Fig. 3: Nociceptors pathologically switch to a tactile low-threshold fibre phenotype after collateral sprouting into denervated skin.



a–d, High-magnification *in vivo* multiphoton images (**a**, **d**) and confocal images (**b**, **c**) of YFP-positive A β -LTMR fibres (expressing NF200 in **c**; $n = 4$) and mGFP-expressing nociceptors (bottom) at Meissner-like structures (arrowheads; expressing S100; $n = 4$) and nociceptor free endings in the tibial territory of control mice and after SNI (**b–d**). Scale bars, 25 μm (**a**); 50 μm (**b**, **c**); 100 μm (**d**). **e**, Quantitative overview of sensory afferent terminations at S100-expressing Meissner corpuscles in the tibial territory at 42 weeks after SNI or sham ($n = 10$ per group; for groups $F_{(1,5)} = 225.321$, $P = 2.37 \times 10^{-5}$; two-way ANOVA with Bonferroni multiple comparison). SP, substance P. **f–k**, Ultrastructural high-resolution 3D analyses in the tibial territory 24–28 weeks after SNI (**g**, **i**, **k**) or in control mice (**f**, **h**, **j**) showing dermal nerves (**f**, **g**) and Meissner corpuscles (**h–k**). Images show myelinated axons (black arrowheads) and their terminations (false coloured in green) or unmyelinated axons (black arrows) and their terminations (false coloured in red) and glial cell lamellae (white arrowheads) in Meissner corpuscles ($n = 3$ SNI and 3 control mice). Scale bars, 5 μm (**f**, **g**, **h** (top left), **i** (top left); 1 μm (**h** (top right and bottom), **i** (top right and bottom)). **j**, **k**, Full 3D reconstruction of Meissner innervation showing terminations of unmyelinated fibres (false coloured in red), myelinated fibres (false coloured in green) and glial cell lamellar wrapping (false coloured in yellow) in control (<https://wklink.org/8342>) and SNI (<https://wklink.org/8231>) mice. **l**, Electrophysiological single-fibre recordings demonstrating receptive fields of C-fibres (red dots) and A β -LTMRs (blue dots) in the sural nerve after stimulation of the tibial territory ($n = 12$ fibres each from 3 sham and 3 SNI mice). **m**, Single-fibre recordings showing C-fibre recruitment by tactile stimuli in denervated tibial territory, but not in the intact sural territory ($n = 8$ fibres each from 6 control and 5 SNI mice). P values derived from chi square analysis for tibial territory ($P = 1.25 \times 10^{-6}$) and for sural territory ($P = 0.1255$). Data are mean \pm s.e.m.

Source data

Of note, in the denervated tibial territory at 42 weeks after SNI, Meissner corpuscles showed a loss of connectivity with A β -LTMRs, which was confirmed by loss of labelling with the native LTMR marker, NF200 (Fig. [3c](#), Extended Data Fig. [8a](#)). In contrast to the control situation, Meissner zones were now observed to be solely associated with nociceptive fibre

terminals, as seen with mGFP-labelled terminations (note high-fidelity spatial recovery of original pattern with collaterally sprouting nociceptors in Fig. 3d, Supplementary Video 5) and with the native labelling of nociceptors with CGRP (Extended Data Fig. 8b). Quantitative analyses confirmed a marked loss of Meissner innervation by NF200-expressing fibres (Fig. 3e), and showed peptidergic and non-peptidergic nociceptors in apposition to S100-positive Meissner corpuscles (Fig. 3e, Extended Data Fig. 8c). To address the question of whether this reflects aberrant connectivity in the end organ, we performed serial block-face scanning electron microscopy to generate high-resolution representations of terminal connectivity within the tibial territory at 24 weeks after SNI. In contrast to control mice, myelinated fibres were conspicuously absent in the dermis of SNI mice, and unmyelinated axons comprised the only nerves present post-innervation (Fig. 3f,g), thus further validating our light microscopy findings. In Meissner corpuscles of control mice, the terminals of myelinated afferents were surrounded by concentric patterning of the glial cell lamellae that are critical for sensing mechanical pressure³⁴, and terminals of unmyelinated C-fibres were found at the outer edges of these lamellar cushions (Fig. 3h). By contrast, in the tibial territory after SNI, collaterally sprouted unmyelinated afferents showed multiple terminations dispersed in between loosely patterned lamellae and made close contacts with lamellae, with some occupying the centre of lamellar cushions (Fig. 3i)—a position only taken by A β fibre terminations in control mice (Fig. 3h). This finding was further validated by full 3D high-resolution reconstructions of Meissner corpuscles from control and SNI mice (images shown in Fig. 3j,k, respectively; 3D views shown in Supplementary Videos 8, 9, respectively): in control mice, myelinated afferents showed a classical patterning of winding throughout the Meissner corpuscles and were fully covered by glial cell lamellae, whereas the unmyelinated afferents did not branch extensively inside the Meissner volume and were not surrounded by concentric lamellae. In the tibial territory of SNI mice, in the absence of A β terminations, the collaterally sprouted unmyelinated afferents were observed to invade throughout the volume of the Meissner corpuscles, elaborately meandering in between and being surrounded by glial cell lamellae. This morphological pattern shows abnormalities of end organ connectivity and places unmyelinated afferents, as the only nerve afferent component found inside the Meissner corpuscles,

physically in a position to sense changes induced by the indentation of lamellae after mechanical stimulation.

Unmyelinated C-fibres also include a subpopulation of non-peptidergic C-fibres—namely C-LTMRs—that respond to light touch in a similar manner to A β -LTMRs^{40,41}. We therefore also tested the possibility that C-LTMRs, which typically innervate hair follicles, sprout into the denervated glabrous tibial territory by immunostaining with anti-tyrosine hydroxylase (TH) (but see Supplementary Note 3). However, only 2 of 8 mice tested at 42 weeks after SNI showed the ectopic presence of TH-positive fibres at the dermal–epidermal border (Extended Data Fig. 9, Supplementary Note 3). Our analyses thus do not provide adequate evidence to suggest that C-LTMRs sprout into the sub-epidermal zone in denervated glabrous skin. Because TH also labels adrenergic fibres, this also negates the involvement of sympathetic structural remodelling.

C-fibres switch to tactile responsiveness

We next investigated whether the remodelling of peripheral connectivity leads to functional abnormalities in nociceptors that invade into the denervated tissue. We performed electrophysiological recordings of A β -LTMRs and C-nociceptors at 24 weeks after SNI using the skin–nerve preparation, which was modified to span the glabrous sural as well as tibial territories. In the first set of recordings, only the stimulation of the sural territory evoked responses in sural nerve fibres in sham-treated mice (Fig. 31). By contrast, mice at 24 weeks after SNI exhibited marked responses in sural nerve fibres when the tibial nerve glabrous territory was mechanically stimulated (Fig. 31). These newly acquired tibial territory receptive fields for sural afferents in SNI mice were found only for nociceptors, and not for A β -LTMRs (with only one exception; Fig. 31). These data thus independently and functionally verify our findings that nociceptors—but not A β -LTMR fibres—from the sural nerve repopulate the denervated tibial territory. In a separate set of experiments, we measured the activation thresholds of C-fibres, identified using conduction velocity measurements (Extended Data Figs. 10a,c), and observed that sural nerve C-fibre responses that were mechanically evoked from the tibial territory of SNI mice showed significantly lower thresholds as compared to physiological innervation (that

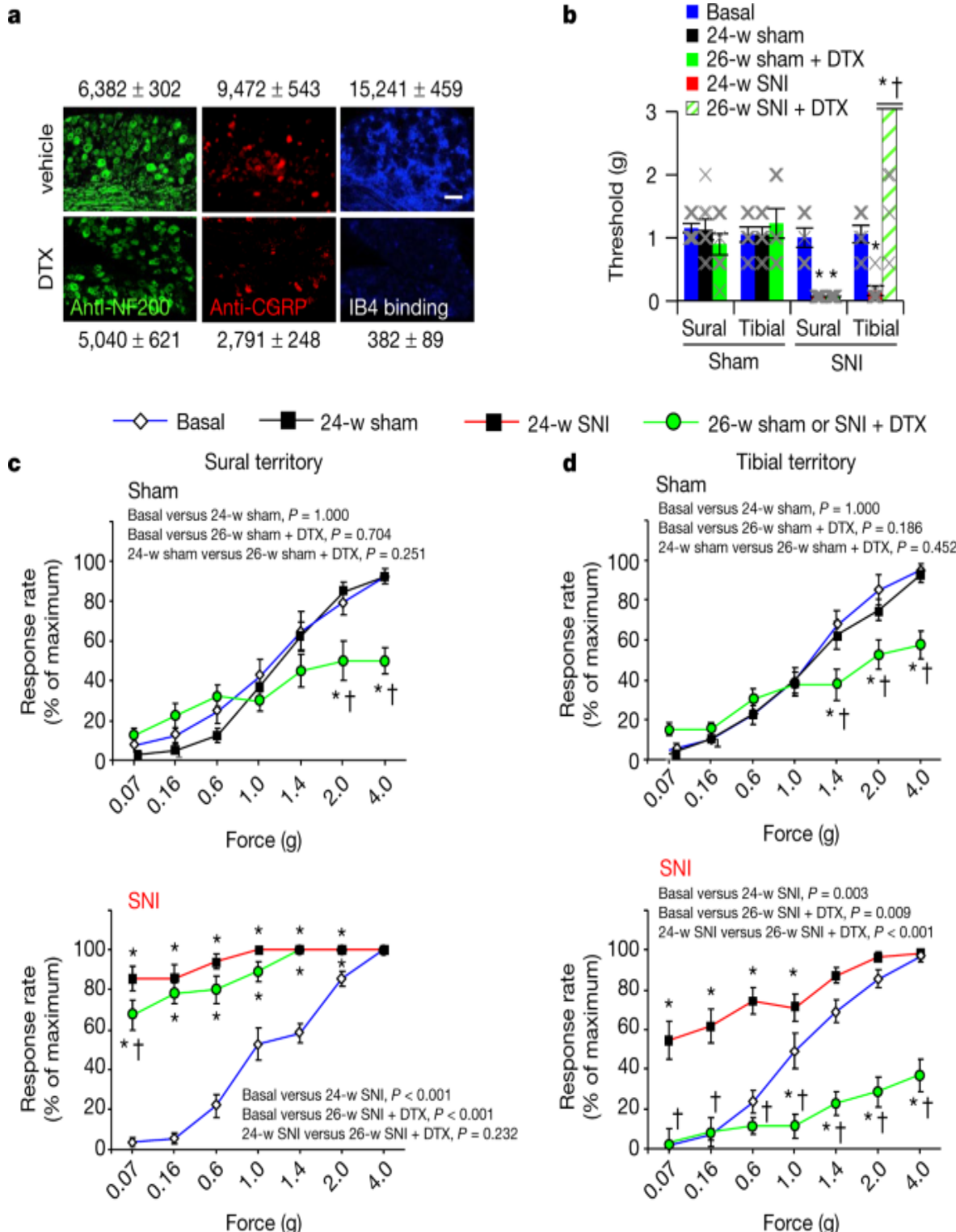
is, tibial nerve C-fibre responses from the tibial territory of control mice) (Fig. 3m, Extended Data Fig. 10b). Mechanical stimulation of the undamaged sural territory evoked C-fibre responses in the sural nerve, with a tendency towards a lowering of the activation threshold after SNI compared to controls, although this tendency was not statistically significant (Fig. 3m, Extended Data Fig. 10d, e). These data reveal that collaterally sprouting nociceptors have altered activation properties such that they respond to innocuous mechanical stimuli like low-threshold afferents do, and suggest that they acquire this property during the reinnervation of the tibial territory.

An inflammatory milieu in the denervated tibial territory and persistent peripheral sensitization could be responsible for changes in nociceptor sensitivity during reinnervation. Several observations speak against this possibility. First, we did not find any remaining accumulation of immune cells, such as macrophages or T cells, in the tibial territory when neuropathic pain was manifested after 24 weeks (Extended Data Fig. 11). Second, pharmacological inhibition of classical sensitization-associated mediators such as prostaglandins, TRPV1 and TRPA1, or sequestration of nerve growth factor (NGF), did not block reinnervation neuropathic allodynia (Extended Data Fig. 12). Third, unbiased gene transcriptional analyses performed on the somata of dorsal root ganglia (DRGs) of collaterally sprouting nociceptors, which were identified through retrograde labelling from the tibial territory at 24 weeks after SNI, did not reveal the regulation of key sensitization-associated genes (see Supplementary Note 4, Extended Data Fig. 13 for details). This suggests that nociceptor sensitization phenomena that are hallmarks of other types of pain, such as acute and chronic inflammatory pain, are not causing the observed change in mechanical thresholds upon reinnervation. Rather, most of the genes that showed altered expression in collaterally sprouting nociceptors over controls were found to be linked to structural changes, such as NGF-dependent neurite outgrowth, axonal pathfinding, neuroprotection and axonal survival (Extended Data Fig. 13, Supplementary Note 4), thus further indicating structural remodelling.

Nociceptors mediate reinnervation pain

Finally, we addressed whether nociceptors are causally responsible for reinnervation-induced neuropathic pain developing in previously denervated and insensitive areas by using diphtheria toxin (DTX)-mediated ablation of nociceptors (Fig. 4a; 98% loss of non-peptidergic nociceptors, 70% loss of peptidergic nociceptors and a statistically non-significant 20% reduction in NF200-expressing neurons after treatment with DTX). Consistent with nociceptor ablation, DTX-treated mice in the absence of nerve injury (sham) showed significantly reduced basal responsiveness to mechanical von Frey stimuli in the nociceptive range (that is, 1.0 g and above; Fig. 4c,d). Measurements of mechanical thresholds after SNI showed that nociceptor ablation reversed mechanical allodynia in the denervated territory of the tibial nerve (Fig. 4b,d), but not in the territory of the uninjured sural nerve (Fig. 4b,c). To rule out that the observed phenotypic differences arise from the ablation of any cells at loci other than DRG neurons in SNS-Cre mice, we directly injected adeno-associated virions expressing caspase-3 in a Cre-dependent manner or EGFP as a control into the L3–L4 DRGs of SNS-Cre mice 24 weeks after SNI. In contrast to EGFP-expressing mice, caspase-3-mediated ablation of nociceptors completely abrogated mechanical hypersensitivity in the tibial territory, but only partially and transiently reduced hypersensitivity in the sural territory (Extended Data Fig. 14). These findings thus conclusively demonstrate that the emergence of reinnervation-induced neuropathic allodynia is mediated by nociceptors. This is in sharp contrast to allodynia reported in uninjured territories, in which loss- or gain-of-function experiments show that A β afferents are both necessary and sufficient to induce mechanical allodynia^{5,6} and allodynia develops even when nociceptors are genetically ablated⁴².

Fig. 4: Genetic ablation experiments reveal a causal role for nociceptors in reinnervation-induced chronic neuropathic allodynia.



a, In mice with DTX-induced ablation of nociceptors (SNS-DTR), examples and quantitative estimate of large-diameter NF200-positive neurons (left; $n = 3$ per group, degrees of freedom (DF) = 2.897, $t = 1.941$, $P = 0.124$),

CGRP-positive peptidergic nociceptors (middle; $n = 3$ per group, DF = 2.802, $t = 11.179$, $P = 0.000365$) and non-peptidergic isolectin B4 (IB4)-binding nociceptors ($n = 3$ per group, DF = 2.149, $t = 31.750$, $P = 5.87 \times 10^{-6}$) after treatment with vehicle or DTX (two-tailed t -test). Numbers of DRG neurons from three mice per treatment are shown. Scale bar, 100 μm . **b–d**, Nociceptor ablation significantly decreases mechanical nociception and reverses reinnervation-induced allodynia in the tibial territory (**b**, **d**), but not allodynia in the intact sural territory (**b**, **c**), as demonstrated by analysis of response thresholds (**b**) and response rates (**c**, **d**) to mechanical stimulation. In **b**, $n = 8$ per group; groups $F_{(3,6)} = 25.234$, $P = 0.000842$; treatment $F_{(2,6)} = 10.001$, $P = 0.0122$; groups \times treatment $F_{(6,56)} = 12.525$, $P = 6.74 \times 10^{-9}$. In **c** (sural territory): $n = 8$ per group; for sham (top part): groups $F_{(2,12)} = 1.798$, $P = 0.202$; for SNI (bottom part): groups $F_{(2,12)} = 93.888$, $P = 4.697 \times 10^{-8}$). In **d** (tibial territory): $n = 8$ per group; for sham (top part): groups $F_{(2,12)} = 2.226$, $P = 0.145$; for SNI (bottom part): groups $F_{(2,12)} = 29.514$, $P = 2.32 \times 10^{-5}$; these P values correspond to group P values (P values shown within the figure refer to comparisons between pairs of treatment group (that is, individual pairs from three different groups)). In all panels, * $P < 0.05$ compared to baseline, † $P < 0.05$ compared to before DTX application, two-way repeated measures ANOVA with Bonferroni multiple comparison in **b**, **c**. Data are mean \pm s.e.m.

[Source data](#)

Together with the current knowledge on neuropathic pain^{5,7,8,13,42}, our findings reveal the existence of two completely different forms and mechanisms of mechanical allodynia after nerve injury, namely: (1) a well-studied, A β -fibre-dependent form with an early onset and chronic nature arising from uninjured nerve territories; and (2) a new form described here, which is found in denervated territories of injured nerves, is nociceptor-dependent, becomes manifest with a late onset during the reinnervation process, and has been consequently overlooked in most preclinical work on neuropathic pain (summarized in Extended Data Fig. 15). These findings thus fill a long-standing gap in the representation of the complex clinical state of neuropathic pain arising from mixed nerve crush injuries that are clinically more frequently associated with chronic neuropathic pain^{2,27}, and

indicate that both forms of allodynia should be investigated in studies of the mechanisms and therapy of pain resulting from nerve injury. Of note, the findings also bridge the fields of regeneration and chronic pain, which are mostly studied independently of each other in mainstream literature, to highlight the importance of structural plasticity and miswiring during reinnervation processes, and thus pave the way for addressing a new direction in neuropathic pain. Our findings inadvertently highlight and help to rationalize observations in a historically important experiment on nerve regeneration and pain in humans⁴³, which involved repeated sensory testing over four years after a self-inflicted experimental nerve injury in a healthy individual. Reporting in 1908, the authors suggested that there are two different types of ‘sensation’—protopathic and epicritic—that recover at different rates after nerve injury; an early recovery of protopathic sensation causes “exquisite pain and hyperesthesia”, whereas normal sensation is restored only after a late recovery of epicritic sensation^{43,44}. Our longitudinal structure–function analyses reveal the cellular identity and ensuing alterations in the terminal connectivity of the underlying classes of afferents and help to establish causality for reinnervation-induced neuropathic pain. One possibility is that this miswiring and abnormal connectivity studied at the peripheral end of sensory neurons ties in functionally with aberrant discharges that have been reported in DRG somata¹, as well as anatomical alterations and misconnectivity that have been proposed to occur at central terminals⁴⁵ after nerve injury.

Our study has also addressed several mechanistic possibilities for the manifestation of reinnervation-induced neuropathic pain. First, the lowered activation thresholds that we observed in collaterally sprouting nociceptors may result from ‘sensitization memory’ or ‘priming’^{46,47}, given their origin in the ‘spared’ sural nerve that is subject to sensitizing influences by the inflamed milieu in the paw after nerve injury despite being morphologically intact. However, at the time of manifestation of reinnervation-induced neuropathic pain, we observed neither overt sensitization in nociceptors in the sural territory nor inflammatory changes in the tibial or sural territory. Moreover, pharmacological studies and gene expression analyses did not support the occurrence of classical peripheral sensitization by molecular mediators. Second, selective sprouting and reinnervation with sub-classes of nociceptors with particular properties supporting neuropathic pain—for

example, the NP1 cluster amongst non-peptidergic nociceptors⁴⁸—is a possibility. However, our gene expression analyses did not reveal any differences in the relative abundance of the various subclasses of nociceptors that innervate the tibial territory between sham and neuropathic mice. Third, our observations on the peripheral terminations of fibres implicate miswiring as a basis for the abnormal functional properties of collaterally sprouting nociceptors. Failure to enter the epidermis may lead to a concentrated localization of sensory transducers and excitatory ion channels at nociceptor endings under the epidermal border instead of being spread over the original thin, long filopodia-like free endings over the epidermis, leading to altered activation profile and dynamics. This irregular patterning of nociceptor terminals is also likely to change their functional connectivity with specialized cutaneous mechanosensitive glial cells at the sub-epidermal border, which are proposed to transmit nociceptive signals⁴⁹. Consistently, ablation of these specialized Schwann cells was recently reported to cause the retraction of epidermal nerve fibres and induce allodynia⁵⁰. Our ultrastructural morphological observations on atypical Meissner connectivity during reinnervation also raise the idea that remodelling of Meissner corpuscles anatomically links light touch to nociceptor activation in neuropathic pain, essentially ‘converting’ nociceptors to low-threshold afferents. Together with recent studies on end organ connectivity and function in the periphery^{7,34,51,52}, our results highlight the emerging concept that sensory specificity is determined by the properties of the specialized sensory ‘organelles’ in the skin, rather than by the nerve fibres themselves. Fourth, given that A β -LTMRs inhibit spinal second-order nociceptive neurons by recruiting interneurons under physiological conditions^{7,12,13,15,53}, a lack of A β input from denervated tissue in the presence of restored nociceptor input would be expected to disinhibit nociceptive transmission, thereby opening the spinal ‘gate’ for pain^{54,55,56}, as well as altering the top-down control of spinal nociception by brain centres⁵⁷. The results of this study, when taken together with current knowledge, particularly support peripheral miswiring and central disinhibition as mechanisms that are likely to underlie the manifestation of reinnervation-induced neuropathic pain; our findings thus meaningfully integrate the hypothesis of peripheral structural remodelling with important concepts with regard to the plasticity of spinal circuits in neuropathic pain. Ultimately, understanding the cellular mechanisms and molecular cues that lead to faulty regeneration or aberrant

rewiring of the different classes of sensory afferents will help to prevent or reverse chronic neuropathic pain after nerve injury.

Methods

Genetically modified mice

Cre reporter mice carrying either mGFP⁵⁸ or tdTomato (Jacksons lab; stock no. 007909) flanked by a transcriptional stop cassette in the Rosa26 locus were crossed with SNS-Cre mice^{25,59}, in which Cre recombinase is transgenically driven by 110-kb promoter elements of the mouse Nav1.8-encoding *Scn10a* gene to obtain SNS-mGFP or SNS-tdTomato mice that express fluorescent marker in peripheral nociceptive sensory neurons. Mice expressing YFP under the control of the Thy1 promoter (Thy1-YFP 16) were obtained from The Jackson Laboratory; stock no. 003709. In these mice, non-nociceptive sensory neurons are labelled. SNS-iDTR mice were obtained by crossing SNS-cre mice with mice carrying simian diphtheria toxin receptor (DTR) flanked by a transcriptional stop cassette in the Rosa26 locus⁶⁰. For ablating nociceptors, SNS-iDTR mice were injected intraperitoneally (i.p) with 40 µg kg⁻¹ of DTX (Sigma D0564) twice, at an interval of 72 h. After five days, mice were acclimatized to behavioural set-up in sessions over at least two days, and behavioural analyses of baseline nociceptive sensitivity were done from day 8 after the second DTX injection, followed by nerve injury. Mice of all genotypes were backcrossed to the C57bl6 background for more than eight generations before crossing with each other. All of the animal experiments were conducted according to the ethical guidelines of the ‘Protection of Animals Act’ under supervision of the ‘Animal Welfare Officers’ of Heidelberg University and were approved by the local governing body named ‘Regierungspräsidium Karlsruhe: Abteilung 3 - Landwirtschaft, Ländlicher Raum, Veterinär- und Lebensmittelwesen’, Germany (approval numbers: G-206/11 and G-177/17). ARRIVE guidelines were followed. Sample sizes were based on previous experience with G-power analyses. Only adult mice (older than 8 weeks) were used. Mice of both sexes were tested in imaging, behavioural and electrophysiological experiments and in all experiments, mice were

randomized and experimenters were blinded to the identity of the treatment groups.

Pain model and behavioural analyses

SNI

In this pain model, two of the three branches of sciatic nerve, tibial and common peroneal nerve were cut leaving the sural branch intact as described in detail previously²⁶.

von Frey test

Mechanical hyper- or hyposensitivity induced by SNI was measured using von Frey filaments of increasing strength starting from 0.07 g to 4 g, applied to the digits or hind paw region of various skin dermatome (sural and tibial) as described previously²⁶.

PEAP

Mice were placed in a bright–dark chamber set-up with free access to both bright and dark sides. On day 1, mice were allowed to explore freely on both sides for a period of 20 min that allows us to assess their preference towards a particular chamber. Twenty-four hours later, mice were again placed in the same chamber and this time a von Frey filament of 0.16 g strength was applied to the tibial area of the hind paw at an interval of at least 10 s whenever mice entered the dark side. The time spent on either side of the chamber for a total period of 20 min was measured and the decrease in time spent or active escape or avoidance of the chamber in which mechanical stimuli applied directly reflects pain sensitivity. ANY-maze software was used for tracking mice.

Application of pharmacological agents

Mechanical hypersensitivity was tested in mice at 24 weeks after SNI or sham surgery or 24 h after injection of complete Freund's adjuvant (CFA),

before and 30 min after intraplantar application of the following drugs, each in a volume of 20 µl: diclofenac (D6899, Sigma Aldrich; 50 µg), celecoxib (PHR1683, Sigma Aldrich; 150 µg), AMG 9810 (A2731, Sigma Aldrich; 20 µg), AP-18 (A7232, Sigma Aldrich; 4.2 µg) and tanezumab (anti-NGF antibody; TAB-111, CreativeBiolabs; 30 µg).

Intravital two-photon imaging

Mice were anaesthetized by using a narcotic mix consisting of 60 µl medetomidine (1 mg ml⁻¹, Pfizer), 160 µl midazolam (5 mg ml⁻¹, Hameln) and 40 µl fentanyl (0.1 mg ml⁻¹, Janssen) at a dosage of 3.1 µl per g body weight. The entire paw was embedded in 2% low-melting agarose (A6013; Sigma) in a small custom-built well with hind paw skin exposed to a 25× water immersion objective (Nikon MRD77225; numerical aperture of 1.1) of an upright TriM Scope II microscope (LaVision BioTec). A femtosecond pulsed Ti:sapphire laser (Chameleon Ultra II; Coherent) was tuned to 960 nm for multi-photon excitation of mGFP, YFP or Texas red. The laser power was linearly increased from 5% at the surface to 15% at the maximal depth to improve acquisition from deep imaging layers (Imspector software, LaVision BioTec⁶¹). The emitted light was split by a 575-nm dichroic mirror and filtered by a 500–550-nm bandpass filter for the green channel and 585–635-nm bandpass filter for the red channel. To cover the entire end phalanx, four adjacent images were acquired sequentially for each focal plane at 10% overlap. This was repeated for each z-focal plane of the stack, yielding image stacks of 450 µm × 450 µm × 500 µm at a voxel size of 427 nm × 427 nm × 1,000 nm for each of the quadrants. These were then merged into one ‘superstack’ covering a volume of 854 µm × 854 µm × 500 µm (see (i) in ‘Automated workflow for processing of large-scale two-photon imaging data’). Blood vessels were labelled by retro-orbital injection of 50 µl of Texas-red-labelled dextran (D1830; molecular weight, 70,000 D; molecular probes). ImageJ was used for assessing the quality of the images.

Automated workflow for processing of large-scale two-photon imaging data

The vast amount of data (more than 800 3D image stacks corresponding to approximately 35 TB of raw data) necessitated automated image analysis

and use of a high-performance cluster for computation (bwMLS&WISO). Our automated analysis workflow consists of five main steps as described below and further detailed in Supplementary Note 2. Processing and quantitative analysis were performed in a blinded manner.

1. (i)

Stitching of four 16-bit raw image stacks to capture the entire end phalanx in one ‘superstack’. Four individual image stacks, each consisting of 500 frames at 1,050 pixels × 1,050 pixels were stitched together resulting in a superstack of 500 frames at 2,000 pixels × 2,000 pixels. Our workflow first generates maximum intensity projections of neighbouring stacks and then applies the feature detectors SIFT⁶² or SURF⁶³ on the 10% overlap regions in the two MIP images. The stitching algorithm reduces and cleans the noisy influence of the original image boundary to obtain a seamlessly stitched superstack.

2. (ii)

Removal of epidermal autofluorescence to facilitate subsequent steps of automated analysis. Epidermal autofluorescence and skin appendages were removed using a weakly supervised regularization approach developed on discrete graph spaces for perceptual image segmentation through a semi-supervised learning algorithm. Each image in a 3D image stack is segmented according to the parameters and label information derived from 3D space. Gaps in the epidermal signal and hair can be accurately classified and removed. A spectral clustering method is embedded and extended into regularization on discrete graph spaces. In consequence, the spectral graph clustering is optimized and smoothed by integrating top-down and bottom-up processes through semi-supervised learning. Then, a nonlinear diffusion filter is used to maintain semi-supervised learning, labelling and differences between foreground or background regions. Furthermore, the segmentation is penalized and adjusted using labelling prior and optimal window-based affinity functions in a regularization framework on discrete graph spaces. The algorithm is robust in handling images from variable environments.

3. (iii)

Sixteen-bit to eight-bit conversion of superstacks by nonlinear adaptive depth-dependent adjustment on global and local scales. To reduce the size of the superstacks for subsequent processing steps, we devised an approach that converts 16-bit to 8-bit image stacks while optimally maintaining the dynamic range of the signals. First, a global-to-local nonlinear contrast enhancement method was used to improve the global contrast on the basis of the range of intensity and the histogram of each image in a stack. To reflect the increase in laser power with imaging depth, the global-to-local contrast enhancement adjusts the histogram between the top and the bottom layers of the image stack. Second, a depth-adaptive intensity-based image enhancement method was developed for obtaining the final 8-bit enhanced image stacks. The MATLAB function `im2uint8` was used for conversion of image stacks according to the global-to-local adaptive histogram in each image. Finally, to consider image stacks acquired at different time points of our longitudinal experimental design, the conversion takes advantage of normalized criteria including normalized human visual perceptual contrast.

4. (iv)

Automatic rigid and non-rigid four-dimensional registration of stacks acquired at different time points. Superstacks acquired during a time frame of up to one year were aligned using a weakly supervised automated registration algorithm optimized for large-scale datasets. To find the largest similarity (for example, intensity localization and patterns) between two superstacks, we directly extracted representative feature points from the source and target superstacks in 3D space. To achieve this, we extracted 3D point clouds of nerve fibres from original superstacks and estimated the 3D registration parameters from the extracted 3D point clouds on the basis of the iterative closest point algorithm described by the iterative closest point (ICP) function. The 3D registration method seeks to find the best transformation T that relates two entities P and Q whose 3D point clouds are given by R_P and R_Q , respectively. T_P was found such that the objective function $J(R_P,$

R_Q) is minimized, $\langle J(\{R\}_{\{\rm{rm}\{P\}\}}, \{R\}_{\{\rm{rm}\{Q\}\}}) \rangle = \sum_{P \in R_P} \{ \rm{rm}\{P\} \} \cdot \Psi(P)$, where $\Psi: P \rightarrow Q$; for $P \in R_P$, $\Psi(P) \in R_Q$. The transformation T_P is used to optimally align two point clouds. The function $\Psi(P)$ is usually unknown and needs to be computed. When a good initial value is given, the algorithm can achieve global convergence. First, the automatic registration system has been implemented in a stratified 3D model registration framework, which efficiently handles hierarchical pyramid multi-resolution 3D image stacks. The stratified methods for auto-registration involve 3D-to-3D pose correction, 3D-to-3D projection and 3D-to-3D linear and nonlinear registration. Furthermore, we applied the thin-plate-spline (TPS) method⁶⁴ for global registration by jointly warping local feature points onto their global position. By using this technique, the system not only achieves accurate 3D pose normalization, but also becomes reliable and avoids difficulties in the linear transformation of 3D image stack pairs. The approach is efficient and robust especially for large-scale 3D data alignment and even alignment of superstacks with partial similarity (for example, after many nerve fibres got lost after SNI).

5. (v)

Automated neuronal segmentation, tracing and statistical neural network analysis. Quantitative measurements of fibre length of the same phalanx at different time points were made, including the length of total fibres, number of fibre endings, distribution and density of fibre endings. To improve the tracing fidelity and to measure efficiency of structural changes from all nerve fibres in the end phalanx, we developed a 3D tracing algorithm adapted for computing large-scale 3D datasets in a weighted global to local optimization manner. Nerve fibres with discontinuities caused by fluctuations of signal strength, epidermal fibres and neighbouring cells can be identified independently of the autofluorescence background. To determine morphological changes as well as the relationship between structural plasticity of nerves and pain levels over time, we developed algorithms for not only measuring the change of fibres quantitatively, but also localizing these changes in fibre networks so that data-driven and target-oriented structural

plasticity analysis can be achieved. The method includes the following steps: (a) cropping of all superstacks acquired from a mouse at different time steps to the largest common volume to ascertain quantitative comparisons; (b) graph-based analysis of connectivity and fibres (see Supplementary Note 2 for details); (c) accurate 3D registration of nerve fibre changes to localize the changes of fine structures and branching changes; (d) localization and measurement of dynamic changes in the fine structure of filopodia and small branches; (e) identification of dynamic changes in fibre connections (clusters, undirected graph to directed graph); and (f) plasticity analysis of the fibre network.

6. (vi)

Quantitative analysis of structural plasticity in SNS-mGFP and Thy1-YFP mice. In this step, we measured different parameters for thick fibres (A β -fibres) and thin fibres (A β -fibres, C-fibres) as well as fibre endings, Meissner corpuscles and epidermal fibres. In SNS-mGFP mice, we studied intra-epidermal fibres with respect to distribution, density and fine structures (for example, filopodia or small branches) and we analysed deeper fibres forming a network in the dermis. In Thy1-YFP mice, the unstable thin fibres and relatively stable thick fibres were classified into two groups and analysed in regions of interest. Fibre sprouting and regeneration were measured and localized quantitatively in space at different time points. To achieve this, we designed and implemented different analysis approaches specialized for the characteristics of two different types of data. See Supplementary Note 2 for further details.

Immunohistochemistry

Mice were transcardially perfused with 4% PFA (Sigma) and DRGs and hind paw skin were dissected out. Tissue samples were cryo-protected with 30% sucrose overnight before cryo-sectioning. The sections were treated with 50 mM glycine in 0.05 M PBS for 15 min followed by permeabilization with 0.2% Triton-X-100 for 15 min. After blocking for 30 min with 10% normal horse serum in 0.1% PBST, sections were incubated with primary antibody such as rabbit anti-beta-tubulin III (T2200, Sigma; 1:500), anti-NF200 (CH23015, Neuromics; 1:200), anti-CGRP (24112, Immunostar;

1:200), anti-SP (GP14103 Neuromics; 1:200), anti-S100 (Z0311, Dako; 1:200), anti-TH (SO25000, Neuromics; 1:200), anti Gr-1(Mouse Ly-6G/ly-6C, MAB 1037, R&D Systems; 1:500), anti-CD8a (14-0808-82, Thermo Fisher Scientific; 1:200), anti-CD4 (14-9766-82, Thermo Fisher Scientific; 1:100) and biotinylated IB4 (1:200; B-1205, Vector) in blocking solution, overnight at 4 °C. Next day, the sections were washed once with blocking solution and twice with 0.2% PBST for 15 min. Sections were then incubated for 1 h at room temperature with the following corresponding Alexa-conjugated secondary antibodies (1:750; Thermo Fisher Scientific): donkey anti-Rabbit IgG, Alexa 488 conjugated (A32790); donkey anti-rabbit IgG, Alexa 594 conjugated (A32754); donkey anti-rabbit IgG, Alexa 647 conjugated (A32787); donkey anti-rat IgG, Alexa 647 conjugated (A48272); donkey anti-rat IgG, Alexa 594 conjugated (A48271); donkey anti-rat IgG, Alexa 488 conjugated (A48269); goat anti-guinea pig IgG, Alexa 647 conjugated (A-21450). After 3 washes for 15 min each in 0.2% PBST, sections were treated with 10 mM Tris pH 8.0 for 15 min and mounted with Mowiol and stored in the dark at 4 °C. The sections were then imaged with a confocal microscope using Leica Application Suite X (LAS X).

Skin-nerve recordings

Mice were killed by placing them in a CO₂-filled chamber for 2–4 min followed by cervical dislocation. The glabrous and hairy hind paw skin were dissected free in one piece together with the sural nerve or the tibial nerve, respectively, and placed in a heated (32 °C) organ bath chamber that was perfused with synthetic interstitial fluid (SIF buffer) consisting of 108 mM NaCl, 3.5 mM KCl, 0.7 mM MgSO₄, 26 mM NaHCO₃, 1.7 mM Na H₂PO₄, 1.5 mM CaCl₂, 9.5 mM sodium gluconate, 5.5 mM glucose and 7.5 mM sucrose at a pH of 7.4. As hairy and glabrous skin were dissected as one piece, only the skin covering the palm and the back of the paw, but not the skin covering the digits, could be fully preserved during the dissection procedure. The skin was placed with the corium side up in the organ bath and the nerve was placed in an adjacent chamber for fibre teasing and single-unit recording. Single units were isolated with a mechanical search stimulus applied with a glass rod and classified by conduction velocity, von Frey hair thresholds and adaptation properties to suprathreshold stimuli as previously described⁵³. Mechanical ramp-and-hold stimuli were applied

with a cylindrical metal rod (diameter 1 mm) that was driven by a nanomotor (MM2A-LS, Kleindiek Nanotechnik) that was coupled to a force measurement system (FMS-LS, Kleindiek Nanotechnik). The von Frey thresholds of single units were determined by mechanically stimulating the most sensitive spot of the receptive fields with von Frey filaments (Ugo Basile) and the force exerted by the weakest von Frey filament that was sufficient to evoke an action potential was considered as the von Frey threshold. The raw electrophysiological data were amplified with an AC coupled differential amplifier (Neurolog NL104 AC), filtered with a notch filter (Neurolog NL125-6), converted into a digital signal with a PowerLab 4SP (ADIInstruments) and recorded at a sampling frequency of 20 kHz using LabChart 7.1 (ADIInstruments).

DRG cell labelling and RNA sequencing

Mice were injected in the specified nerve territory of digits either with 2 µg of cholera toxin B (CTB) conjugated with Alexa 488/594 (C34775/C34777, Thermo Fisher Scientific) or 40 µg of fast blue (17740-1, Polysciences). L3–L4 DRGs were collected 48 h later and cells were dissociated with collagenase IV (1 mg ml⁻¹, Sigma-Aldrich, C5138) and trypsin (0.5 mg ml⁻¹, Sigma-Aldrich, T1005) for 30 min each at 37 °C, washed, placed on laminin-coated slides and counterstained with Alexa Fluor 568 conjugate (2.5 µg ml⁻¹, Isolectin GS-IB from *Griffonia simplicifolia*, Alexa Fluor 568 conjugate, Invitrogen, I21412) for 10–15 min at room temperature. IB4-positive and IB4-negative cells were identified and manually collected using a fire polished pipette, immediately shock frozen in liquid nitrogen and expelled into PBS with RNase inhibitor (Takara 2313A). Cell lysates were directly processed to reverse transcription using the previously published SmartSeq2 protocol⁶⁵. Libraries were prepared on the basis of the fragmentation protocol described previously⁶⁶. The cDNA was generated using 18 pre-amplification cycles. Libraries were sequenced with an Illumina NextSeq 500.

Sequencing reads were mapped to the GRCm38 mouse reference genome using STAR⁶⁷ (v.2.7.1a) using default parameters and extracting also gene counts (quantMode GeneCounts) based on GRCm38.101 gene annotation. Differential gene expression analysis was performed using DESeq2⁶⁸

(v.1.28.1) and only genes having a false discovery rate (FDR) lower than 10% were considered as significant. Functional enrichment analysis on the significant differentially expressed genes was assessed using the MGSA R package⁶⁹ (v.1.36.0). We used the R package BisqueRNA⁷⁰ to decompose our bulk expression data based on a reference single-cell sequencing dataset⁴⁸.

Three-dimensional electron microscopy imaging

Mice were transcardially perfused using fixative containing 2.5% paraformaldehyde (Sigma), 1.25% glutaraldehyde (Serva) and 2 mM calcium chloride (Sigma) in 80 mM cacodylate buffer adjusted to pH 7.4 with an osmolarity of 700–800 mOsmol l⁻¹. Skin (digit) tissue from the corresponding nerve territory was dissected and postfixed at 4 °C overnight. Samples were then stained using the Hua protocol⁷¹. Sample blocks were infiltrated in Spurr's resin. Three-dimensional electron microscopy imaging was acquired using serial block-face electron microscopy⁷². Serial sectioning was done using a custom-built microtome that was operated by custom-written software⁷³, placed in a scanning electron microscope (FEI, Thermo Fisher Scientific). Electron microscopy images were acquired at a resolution of 11.24 nm × 11.24 nm × 30 nm. The stacks of electron microscopy images were aligned using custom-written software described previously^{73,74} and aligned image stacks were then uploaded in webKnossos⁷⁵ for further analysis and visualization.

Intraganglionic injections

Adeno-associated virions were injected into the DRGs as described previously^{76,77}. In brief, AAV-EF1a-flexed-taCasp3-TEVp or AAV-GFP (approx. 1×10^{13} – 4×10^{13} viral genomes per ml) was mixed with 0.1% fast green to assess the injection efficiency. This mixture was injected unilaterally into L3 and L4 DRG neurons using a glass pipette with a diameter of approximately 25 μm. Mice were allowed to recover for three weeks before behavioural assessment.

Statistical analyses

All data were calculated and are presented as mean \pm s.e.m. A one-way or two-way ANOVA for repeated measures followed by Bonferroni's post-hoc test or Tukey's test was used to determine statistically significant differences for multiple group comparisons. For comparisons involving two groups, a two-tailed *t*-test was used. Chi square analysis was used in electrophysiological analyses of proportion of responding C-fibres. Changes with $P < 0.05$ were considered to be significant. Sigma plot, Microsoft Excel and GraphPad Prism software were used for statistical analyses.

Reporting summary

Further information on research design is available in the [Nature Research Reporting Summary](#) linked to this paper.

Data availability

All of the raw data for behavioural, electrophysiological and immunohistochemical analyses are provided in the source data files and in the figures. RNA sequencing data are available through the European Nucleotide Archive (<https://www.ebi.ac.uk/ena>) under the accession number [PRJEB50184](#). The raw data for multiphoton imaging and electron microscopy analyses will be made available upon request. Source data are available for this paper.

Code availability

Electron microscopy acquisition codes are available at Gitlab (<https://gitlab.mpcdf.mpg.de/connectomics/emacquisitionmacro.git>) and the codes used for analysis of multiphoton imaging data are available at GitHub (https://github.com/zheng-tklab/pns_2photon_longitudinal-3Ddata-analysis).

References

1. Devor, M. in *Wall and Melzack's Textbook of Pain* 5th edn (eds McMahon, S. B. & Koltzenburg, M.) 905–927 (Churchill Livingstone, 2006).

2. Campbell, J. N. & Meyer, R. A. Mechanisms of neuropathic pain. *Neuron* **52**, 77–92 (2006).
3. Finnerup, N. B., Kuner, R. & Jensen, T. S. Neuropathic pain: from mechanisms to treatment. *Physiol. Rev.* **101**, 259–301 (2021).
4. Campbell, J. N., Raja, S. N., Meyer, R. A. & Mackinnon, S. E. Myelinated afferents signal the hyperalgesia associated with nerve injury. *Pain* **32**, 89–94 (1988).
5. Dhandapani, R. et al. Control of mechanical pain hypersensitivity in mice through ligand-targeted photoablation of TrkB-positive sensory neurons. *Nat. Commun.* **9**, 1640 (2018).
6. Tashima, R. et al. Optogenetic activation of non-nociceptive A β fibers induces neuropathic pain-like sensory and emotional behaviors after nerve injury in rats. *eNeuro* **5**, <https://doi.org/10.1523/eneuro.0450-17.2018> (2018).
7. Moehring, F., Halder, P., Seal, R. P. & Stucky, C. L. Uncovering the cells and circuits of touch in normal and pathological settings. *Neuron* **100**, 349–360 (2018).
8. Ji, R.-R. & Strichartz, G. Cell signaling and the genesis of neuropathic pain. *Sci. STKE* **2004**, re14 (2004).
9. Beggs, S., Trang, T. & Salter, M. W. P2X4R $^+$ microglia drive neuropathic pain. *Nat. Neurosci.* **15**, 1068–1073 (2012).
10. Ji, R. R., Donnelly, C. R. & Nedergaard, M. Astrocytes in chronic pain and itch. *Nat. Rev. Neurosci.* **20**, 667–685 (2019).
11. Chen, G., Zhang, Y. Q., Qadri, Y. J., Serhan, C. N. & Ji, R. R. Microglia in pain: detrimental and protective roles in pathogenesis and resolution of pain. *Neuron* **100**, 1292–1311 (2018).
12. Cheng, L. et al. Identification of spinal circuits involved in touch-evoked dynamic mechanical pain. *Nat. Neurosci.* **20**, 804–814 (2017).

13. Peirs, C. et al. Dorsal horn circuits for persistent mechanical pain. *Neuron* **87**, 797–812 (2015).
14. Coull, J. A. et al. BDNF from microglia causes the shift in neuronal anion gradient underlying neuropathic pain. *Nature* **438**, 1017–1021 (2005).
15. Foster, E. et al. Targeted ablation, silencing, and activation establish glycinergic dorsal horn neurons as key components of a spinal gate for pain and itch. *Neuron* **85**, 1289–1304 (2015).
16. Kuner, R. & Flor, H. Structural plasticity and reorganisation in chronic pain. *Nat. Rev. Neurosci.* **18**, 20–30 (2016).
17. Burnett, M. G. & Zager, E. L. Pathophysiology of peripheral nerve injury: a brief review. *Neurosurg. Focus* **16**, E1 (2004).
18. Griffin, J. W., Pan, B., Polley, M. A., Hoffman, P. N. & Farah, M. H. Measuring nerve regeneration in the mouse. *Exp. Neurol.* **223**, 60–71 (2010).
19. Jessen, K. R., Mirsky, R. & Lloyd, A. C. Schwann cells: development and role in nerve repair. *Cold Spring Harb. Perspect. Biol.* **7**, a020487 (2015).
20. Bolívar, S., Navarro, X. & Udina, E. Schwann cell role in selectivity of nerve regeneration. *Cells* **9**, 2131 (2020).
21. Taylor, K. S., Anastakis, D. J. & Davis, K. D. Chronic pain and sensorimotor deficits following peripheral nerve injury. *Pain* **151**, 582–591 (2010).
22. Peleshok, J. C. & Ribeiro-da-Silva, A. Delayed reinnervation by nonpeptidergic nociceptive afferents of the glabrous skin of the rat hindpaw in a neuropathic pain model. *J. Comp. Neurol.* **519**, 49–63 (2011).
23. Kerr, J. N. & Denk, W. Imaging in vivo: watching the brain in action. *Nat. Rev. Neurosci.* **9**, 195–205 (2008).

24. Basbaum, A. I., Bautista, D. M., Scherrer, G. & Julius, D. Cellular and molecular mechanisms of pain. *Cell* **139**, 267–284 (2009).
25. Agarwal, N., Offermanns, S. & Kuner, R. Conditional gene deletion in primary nociceptive neurons of trigeminal ganglia and dorsal root ganglia. *Genesis* **38**, 122–129 (2004).
26. Decosterd, I. & Woolf, C. J. Spared nerve injury: an animal model of persistent peripheral neuropathic pain. *Pain* **87**, 149–158 (2000).
27. Djouhri, L., Fang, X., Koutsikou, S. & Lawson, S. N. Partial nerve injury induces electrophysiological changes in conducting (uninjured) nociceptive and nonnociceptive DRG neurons: possible relationships to aspects of peripheral neuropathic pain and paresthesias. *Pain* **153**, 1824–1836 (2012).
28. Song, Y. et al. The mechanosensitive ion channel piezo inhibits axon regeneration. *Neuron* **102**, 373–389 (2019).
29. Zigmond, R. E. & Echevarria, F. D. Macrophage biology in the peripheral nervous system after injury. *Prog. Neurobiol.* **173**, 102–121 (2019).
30. Monk, K. R., Feltri, M. L. & Taveggia, C. New insights on Schwann cell development. *Glia* **63**, 1376–1393 (2015).
31. Weinstein, B. M. Vessels and nerves: marching to the same tune. *Cell* **120**, 299–302 (2005).
32. Abraira, V. E. & Ginty, D. D. The sensory neurons of touch. *Neuron* **79**, 618–639 (2013).
33. Fleming, M. S. & Luo, W. The anatomy, function, and development of mammalian A β low-threshold mechanoreceptors. *Front. Biol.* **8**, 408–420 (2013).
34. Neubarth, N. L. et al. Meissner corpuscles and their spatially intermingled afferents underlie gentle touch perception. *Science* **368**, eabb2751 (2020).

35. Dogiel, A. S. Die Nervenendigunden in Meissnerschen tasktköperen. *Monthly Int. J. Anat. Physiol.* **9**, 76–85 (1892).
36. Cauna, N. Nerve supply and nerve endings in Meissner's corpuscles. *Am. J. Anat.* **99**, 315–350 (1956).
37. Johansson, O., Fantini, F. & Hu, H. Neuronal structural proteins, transmitters, transmitter enzymes and neuropeptides in human Meissner's corpuscles: a reappraisal using immunohistochemistry. *Arch. Dermatol. Res.* **291**, 419–424 (1999).
38. Paré, M., Elde, R., Mazurkiewicz, J. E., Smith, A. M. & Rice, F. L. The Meissner corpuscle revised: a multiafferented mechanoreceptor with nociceptor immunochemical properties. *J. Neurosci.* **21**, 7236–7246 (2001).
39. Ishida-Yamamoto, A., Senba, E. & Tohyama, M. Calcitonin gene-related peptide- and substance P-immunoreactive nerve fibers in Meissner's corpuscles of rats: an immunohistochemical analysis. *Brain Res.* **453**, 362–366 (1988).
40. Seal, R. P. et al. Injury-induced mechanical hypersensitivity requires C-low threshold mechanoreceptors. *Nature* **462**, 651–655 (2009).
41. Delfini, M.-C. et al. TAFA4, a chemokine-like protein, modulates injury-induced mechanical and chemical pain hypersensitivity in mice. *Cell Rep.* **5**, 378–388 (2013).
42. Abrahamsen, B. et al. The cell and molecular basis of mechanical, cold, and inflammatory pain. *Science* **321**, 702–705 (2008).
43. Rivers, W. H. R. & Head, H. A human experiment in nerve division. *Brain* **31**, 323–450 (1908).
44. Compston, A. A human experiment in nerve division by W. H. R. Rivers MD FRS, Fellow of St John's College, Cambridge and Henry Head MD FRS, Physician to the London Hospital, *Brain* 1908: 31; 323–450. *Brain* **132**, 2903–2905 (2009).

45. Woolf, C. J., Shortland, P. & Coggeshall, R. E. Peripheral nerve injury triggers central sprouting of myelinated afferents. *Nature* **355**, 75–78 (1992).
46. Bogen, O., Alessandri-Haber, N., Chu, C., Gear, R. W. & Levine, J. D. Generation of a pain memory in the primary afferent nociceptor triggered by PKC ϵ activation of CPEB. *J. Neurosci.* **32**, 2018–2026 (2012).
47. Calvo, M., Dawes, J. M. & Bennett, D. L. The role of the immune system in the generation of neuropathic pain. *Lancet Neurol.* **11**, 629–642 (2012).
48. Usoskin, D. et al. Unbiased classification of sensory neuron types by large-scale single-cell RNA sequencing. *Nat. Neurosci.* **18**, 145–153 (2015).
49. Abdo, H. et al. Specialized cutaneous Schwann cells initiate pain sensation. *Science* **365**, 695–699 (2019).
50. Rinwa, P. et al. Demise of nociceptive Schwann cells causes nerve retraction and pain hyperalgesia. *Pain* **162**, 1816–1827 (2021).
51. Maksimovic, S. et al. Epidermal Merkel cells are mechanosensory cells that tune mammalian touch receptors. *Nature* **509**, 617–621 (2014).
52. Woo, S. H. et al. Piezo2 is required for Merkel-cell mechanotransduction. *Nature* **509**, 622–626 (2014).
53. Arcourt, A. et al. Touch receptor-derived sensory information alleviates acute pain signaling and fine-tunes nociceptive reflex coordination. *Neuron* **93**, 179–193 (2017).
54. Melzack, R. & Wall, P. D. Pain mechanisms: a new theory. *Science* **150**, 971–979 (1965).
55. Prescott, S. A., Ma, Q. & De Koninck, Y. Normal and abnormal coding of somatosensory stimuli causing pain. *Nat. Neurosci.* **17**, 183–191 (2014).

56. Duan, B., Cheng, L. & Ma, Q. Spinal circuits transmitting mechanical pain and itch. *Neurosci. Bull.* **34**, 186–193 (2018).
57. Liu, Y. et al. Touch and tactile neuropathic pain sensitivity are set by corticospinal projections. *Nature* **561**, 547–550 (2018).
58. Hippenmeyer, S. et al. A developmental switch in the response of DRG neurons to ETS transcription factor signaling. *PLoS Biol.* **3**, e159 (2005).
59. Gangadharan, V. et al. Peripheral calcium-permeable AMPA receptors regulate chronic inflammatory pain in mice. *J. Clin. Invest.* **121**, 1608–1623 (2011).
60. Buch, T. et al. A Cre-inducible diphtheria toxin receptor mediates cell lineage ablation after toxin administration. *Nat. Methods* **2**, 419–426 (2005).
61. Theer, P. & Denk, W. On the fundamental imaging-depth limit in two-photon microscopy. *J. Opt. Soc. Am. A* **23**, 3139–3149 (2006).
62. Lowe, D. G. Distinctive image features from scale-invariant keypoints. *Int. J. Comput. Vis.* **60**, 91–110 (2004).
63. Bay, H., Tuytelaars, T. & Van Gool, L. SURF: Speeded Up Robust Features. In *Proc. 9th European Conference on Computer Vision* (eds Leonardis, A., Bischof, H. & Pinz, A.) 404–417 (Springer, 2006).
64. Wahba, G. *Spline Models for Observational Data* (Society for Industrial and Applied Mathematics, 1990).
65. Picelli, S. et al. Full-length RNA-seq from single cells using Smart-seq2. *Nat. Protoc.* **9**, 171–181 (2014).
66. Hennig, B. P. et al. Large-scale low-cost NGS library preparation using a robust Tn5 purification and tagmentation protocol. *G3* **8**, 79–89 (2018).

67. Dobin, A. et al. STAR: ultrafast universal RNA-seq aligner. *Bioinformatics* **29**, 15–21 (2013).
68. Love, M. I., Huber, W. & Anders, S. Moderated estimation of fold change and dispersion for RNA-seq data with DESeq2. *Genome Biol.* **15**, 550 (2014).
69. Bauer, S & Gagneur, J. Mgsa: Model-based gene set analysis. R version 1.42.0 <https://github.com/sbal/mgsa-bioc> (2021).
70. Jew, B. et al. Accurate estimation of cell composition in bulk expression through robust integration of single-cell information. *Nat. Commun.* **11**, 1971 (2020).
71. Hua, Y., Laserstein, P. & Helmstaedter, M. Large-volume en-bloc staining for electron microscopy-based connectomics. *Nat. Commun.* **6**, 7923 (2015).
72. Denk., W. & Horstmann, H. Serial block-face scanning electron microscopy to reconstruct three-dimensional tissue nanostructure. *PLoS Biol.* **2**, e329 (2004).
73. Karimi, A., Odenthal, J., Drawitsch, F., Boergens, K. M. & Helmstaedter, M. Cell-type specific innervation of cortical pyramidal cells at their apical dendrites. *eLife* **9**, e46876 (2020).
74. Motta, A. et al. Dense connectomic reconstruction in layer 4 of the somatosensory cortex. *Science* **366**, eaay3134 (2019).
75. Boergens, K. et al. webKnossos: efficient online 3D data annotation for connectomics. *Nat. Methods* **14**, 691–694 (2017).
76. Selvaraj, D. et al. A functional role for VEGFR1 expressed in peripheral sensory neurons in cancer pain. *Cancer Cell* **27**, 780–796 (2015).
77. Schweizerhof, M. et al. Hematopoietic colony-stimulating factors mediate tumor-nerve interactions and bone cancer pain. *Nat. Med.* **15**, 802–807 (2009).

Acknowledgements

We thank S. Arber, A. Basbaum and Y. De Koninck for feedback on the study and the manuscript; S. Arber for the gift of the Tau-loxP-mGFP mice; N. Gehrig, H.-J. Wrede and D. Baumgartl-Ahlert for technical assistance; H. Wissler for his support with visualization of 3D electron microscopy data; and M. Kurejova and M. Seefeld for help with the early stages of setting up multiphoton imaging in mouse paw. The research leading to these results has received funding from the following sources: an ERC Advanced Investigator grant to R.K. (Pain Plasticity 294293); grants from the Deutsche Forschungsgemeinschaft to R.K. (SFB1158, projects B01, B06), to T.K. (SFB1158, project B08), to S.G.L. (SFB1158, project A01) and to V.G. (SFB1158, project A03); a grant to B.O. (project number 371923335); and grant CIDEVENT/2020/052 from Generalitat Valenciana to F.J.T. R.K. is a member of the Molecular Medicine Partnership Unit of the European Molecular Biology Laboratory and Medical Faculty Heidelberg. V.G. and T.A.N. were partially supported by a post-doctoral fellowship and physician scientist fellowship, respectively, from the Medical Faculty Heidelberg. D.M. was partially supported by a post-doctoral fellowship from Excellence Cluster CellNetworks. We acknowledge support from the Interdisciplinary Neurobehavioral Core (INBC) for the behavioural experiments, the data storage service SDS@hd and bwMLS&WISO HPC supported by the state of Baden-Württemberg and the German Research Foundation (DFG) through grants INST 35/1314-1 FUGG and INST 35/1134-1 FUGG, respectively.

Author information

Authors and Affiliations

1. Institute of Pharmacology, Heidelberg University, Heidelberg, Germany

Vijayan Gangadharan, Francisco J. Taberner, Timo A. Nees, Nitin Agarwal, Deepitha Männich, Stefan G. Lechner & Rohini Kuner

2. Max Planck Institute for Brain Research, Frankfurt am Main, Germany

Vijayan Gangadharan & Moritz Helmstaedter

3. Department of Functional Neuroanatomy, Institute for Anatomy and Cell Biology, Heidelberg University, Heidelberg, Germany

Hongwei Zheng & Thomas Kuner

4. Instituto de Neurociencias de Alicante, Universidad Miguel Hernández–CSIC, San Juan de Alicante, Spain

Francisco J. Taberner

5. Genomics Core Facility, European Molecular Biology Laboratory, Heidelberg, Germany

Jonathan Landry, Jelena Pistolic & Vladimir Benes

6. Interdisciplinary Center for Scientific Computing, Heidelberg University, Heidelberg, Germany

Björn Ommer

Contributions

V.G., D.M., T.A.N. and N.A. performed all wet experiments under the supervision of R.K., apart from the establishment of longitudinal multiphoton imaging on mouse paw, which was performed by V.G. under the supervision of T.K., the electrophysiology experiments, which were performed by F.J.T. and S.G.L., and the RNA sequencing analyses, which were performed by J.P. under the supervision of V.B. H.Z. developed mathematical algorithms for image analysis under the supervision of B.O. and T.K. J.L. performed bioinformatics analyses on RNA sequencing. V.G. performed electron microscopy analyses under the supervision of M.H., with conceptual input from T.K. V.G. and R.K. conceptualized the project and T.K. and B.O. provided regular conceptual input. V.G. and H.Z. prepared the figures and videos. R.K. wrote the manuscript and all of the authors provided conceptual input in writing the manuscript and presenting the data. All of the authors read the manuscript in the submitted form.

Corresponding author

Correspondence to [Rohini Kuner](#).

Ethics declarations

Competing interests

The authors declare no competing interests.

Peer review

Peer review information

Nature thanks Clifford Woolf and the other, anonymous, reviewer(s) for their contribution to the peer review of this work. [Peer reviewer reports](#) are available.

Additional information

Publisher's note Springer Nature remains neutral with regard to jurisdictional claims in published maps and institutional affiliations.

Extended data figures and tables

[Extended Data Fig. 1 Comprehensive characterization of the neurochemical identity of fluorescently marked cells in the DRGs of Thy1-YFP mice and SNS-tdTomato mice.](#)

(a) Confocal images of YFP and Tomato expression are shown with immunohistochemical staining of diverse sensory neuron populations. Scale bar = 100 µm. **(b)** Quantitative degree of co-localization with markers of distinct classes of DRG neurons (n = 5 mice/group). **(c)** Quantification of lack of colocalization of Thy1-labelled and tdTomato-labelled neuronal population mice in double-transgenic mice. (n = 5 mice/group). Data shown as mean ± S.E.M.

[Source data](#)

Extended Data Fig. 2 Development of late-onset, chronic neuropathic pain after a period of complete loss of sensitivity in denervated skin of mice with nerve injury, referred to henceforth as reinnervation-induced neuropathic pain.

(**a, b**) In the SNI model, intense mechanical allodynia develops in the territory of the undamaged sural nerve, as previously described, as evidenced by drop in response threshold to application of graded mechanical force via von Frey hairs to the plantar surface of the hind paw. Shown are data from the digit (**a**) and central part of the paw plantar surface (upper panel in **b**) in the sural territory. In **a** N = 9 per group: $F_{(1,12)} = 329.423$, P = 4.31E-10. As expected, mice initially show a complete loss of sensitivity in the territory of the ligated and severed tibial nerve, recover sensitivity around 12 weeks post-SNI and unexpectedly show marked reduction in mechanical response threshold as of 16 weeks post-SNI. In **b** (lower panel), data from the central paw surface in the tibial territory are shown, complementary to data from the corresponding digit shown in main Fig. 1e. N = 9 per group; sural territory: $F_{(1,12)} = 284.970$, P = 9.99E-10; tibial territory after 20 weeks: $F_{(1,4)} = 86.057$, P = 0.00075; In **a, b**, * represents $p < 0.05$ compared to baseline, † $p < 0.05$ compared to control group (sham), two-way repeated measures ANOVA with Bonferroni multiple comparison. Data shown as mean \pm S.E.M. (**c, d**) Passive escape avoidance behaviour after application of 0.16 g von Frey force to the tibial innervation territory (middle digit) either ipsilateral to the nerve injury in the dark chamber at 24 weeks post sham- or SNI surgery. Shown are schematic overview (**c**), one typical example each from SNI and sham mice (**d**), complementary to main Fig. 1f. (**e**) Increased duration of nocifensive responses to acetone, demonstrating significant cold allodynia in undamaged sural territory and the denervated tibial territory after collateral sprouting at 24-26 weeks post-SNI (N = 8 for sham and 14 for SNI; sural territory: $t = 4.27$, df = 20, F = 33.91, P = 0.00037; tibial territory: $t = 2.392$, df = 20, F = 13.91, P = 0.0266; * $p < 0.05$; two-tailed unpaired t test).

[Source data](#)

Extended Data Fig. 3 Alterations in tibial innervation territory (middle digit) after loss of tibial and common peroneal nerves through SNI.

(a) Schematic representation of multiphoton non-invasive imaging in tibial digit (3rd digit) (right panel). At day 3 after SNI, both large diameter sensory fibres (YFP-positive) and nociceptive fibres (mGFP-positive) are fully lost in the respect transgenic mouse lines (left panel) (N = 4). (b) After degeneration of YFP-positive fibres in Thy1-YFP mice, YFP fluorescence is seen in cell-like structures; by 30-36 weeks, there is faint re-emergence of YFP fluorescence in a few medium-diameter nerves although the large fibres ending in Meissner corpuscles are still missing. (N = 4) (c) High magnification view of YFP-expressing cells, which show a stellate morphology resembling dendritic-type immune cells (N = 2); see Supplementary Note 1 for details. (d) YFP-positive cells found in the vicinity of blood vessels labelled via Texas-red-conjugated Dextran (N = 2). Scale bar = 100 µm in a, b, d and 50 µm in c.

Extended Data Fig. 4 Further demonstration of the absence of reinnervation with A β -LTMR and recovery of nociceptor innervation with the emergence of reinnervation-induced neuropathic pain in the tibial territory through co-immunostaining with endogenous marker proteins.

(a, b) Example confocal images represent the skin of the area at the centre of the hind paw in panel a and the digit in the tibial nerve territory in panel b. Both panels show nociceptors expressing mGFP in SNS-mGFP mice that repopulate the tibial innervation territory at the at 42 weeks post-SNI or sham surgery. Large diameter (A β) fibres are identified via immunostaining for Neurofilament 200 (NF200) in panel a and peptidergic nociceptors are identified via immunostaining for the peptidergic nociceptor marker, calcitonin gene related peptide (CGRP) in panel b. Hoechst dye (blue) was used to counterstain nuclei in panel b. In all panels, arrowheads represent intra-epidermal nerve fibres. Taken together, both panels show that collaterally sprouting nociceptors arrive at dermal-epidermal border in SNI mice, despite a loss of NF200-immunoreactive A β fibres; however, they do

not enter the epidermis (arrowheads). These images complement with endogenous markers of sensory afferents the data shown with transgenic fluorescent markers in main Fig. 1d and Fig. 2e, f.

Extended Data Fig. 5 Analysis establishing the sural origin of GFP-expressing fibres that populate the denervated tibial territory after SNI.

Experimental steps are schematically shown on the left and the corresponding multiphoton analyses are shown on the right. (a) Innervation pattern of mGFP-expressing nociceptive nerves in the middle digit (tibial territory) in SNS-mGFP prior to SNI. (b) Sprouted mGFP-positive fibres that repopulate the denervated territory when analysed at 42 weeks post-SNI. (c) Complete loss of GFP-expressing fibres in the same mouse 1 week after transection of the sural nerve at 42 W post-SNI, demonstrating the sural origin of the collaterally sprouted nociceptive fibres in the denervated tibial territory (N = 2). Scale bar = 200 μ m.

Extended Data Fig. 6 Workflow for quantitative analyses of sensory fibres in in vivo multiphoton imaging datasets.

(a) Workflow used for extraction of signals over background in two photon imaging of individual digits in mouse hind paw. Examples show skin afferents of mice with SNS-Cre-derived expression of membrane GFP expression (mGFP) in small-diameter nociceptors. (b) Segmentation of free endings (shown in false colour purple, arrowheads) of mGFP-labelled nociceptors and their delineation from afferent branches (shown in green) in top view and transverse view, which enabled 3D quantitative analyses (N = 4). This figure is complementary to main Fig. 2c, d.

Extended Data Fig. 7 Analysis of precise termination patterns of labelled nociceptors and A β -LTMRs in the hind paw skin of SNS-mGFP and Thy1-YFP mice, respectively.

(a) Schematic representation of parts of the paw digit where sensory fibre terminations were studied. (b) Upper panels show labelling of A β -LTMRs in

Thy1-YFP mice. Shown are DAPI-stained images depicting the dermal invaginations into the epidermis (arrows, left panels), harbouring YFP-expressing large diameter fibres ending in Meissner corpuscles (arrowheads, left panels) in distal regions (i) and YFP-expressing fibres more proximally (ii) in the digits (right panels). Lower panels show terminations of labelled nociceptors in SNS-mGFP mice in form of mesh-like structures surrounding Meissner corpuscles at dermal invaginations in DAPI-stained images distally (i) and epidermal free nerve endings (arrowheads) distally (i) and proximally (ii). (c) Anti-S100 immunohistochemistry to identify Meissner corpuscles (arrows) in paw sections of Thy1-YFP and SNS-mGFP mice ($N = 4$). Arrowheads indicate free nerve endings. Panel c is a more complete representation of main Fig. 3b.

Extended Data Fig. 8 Further demonstration of loss of A β -LTMR terminations and recovery of nociceptor terminations at Meissner corpuscle zones in the tibial territory of mice with SNI through co-immunostaining with endogenous marker proteins.

(a) Confocal analyses showing recovery of collaterally sprouted nociceptor terminations (SNS-mGFP) at Meissner zones, whereas A β -LTMR innervation is lost as seen with native marker protein NF200 in the tibial territory post-SNI. These images correspond to the overlay image shown in main Fig. 3c. (b) Both YFP fluorescence as well as NF200-expressing terminations are lost, whereas collaterally sprouted nociceptors expressing the peptide CGRP are seen in the Meissner zone at the dermis–epidermis border in the tibial territory 42 weeks post-SNI. These examples extend the data shown in main Fig. 3b,e ($N = 4$). (c) Complementary to the quantitative summary shown in main Fig. 3d, this panel shows Meissner corpuscle cells identified via S100-immunoreactivity that are seen in close proximity of collaterally sprouted mGFP-expressing nociceptors in tibial territory of SNI mice (42 weeks) and sham controls, of which some are Substance P-negative (arrowheads) and some are Substance P-positive (arrows) ($N = 4$).

Extended Data Fig. 9 C-LTMRs in denervated tibial territories in mice at 42 weeks after SNI.

Examples of immunostaining for tyrosine hydroxylase (TH), a marker of C-LTMRs, which also stains sympathetic fibres, at 42 weeks after sham (**a**) and SNI (**b, c**) treatment in SNS-mGFP mice. Shown are examples of SNI mice (2 out of 8 mice) which showed ectopic presence of TH-expressing fibres at the dermal border (arrows in b) and SNI mice (6 out of 8 mice) that did not show any differences to sham-treatment (c). Scale bar = 50 μ m.

Extended Data Fig. 10 Electrophysiological single-fibre recordings from skin nerve preparation from sural or tibial nerve with attached paw skin after mechanical stimulation over the sural (intact) and tibial (denervated) territories in mice at 24 weeks after SNI as compared to sham-treated mice.

(**a–c**) C-fibres identified via measurement of conduction velocity (a) and typical examples of evoked C-fibre responses in the tibial (sham) or sural (SNI) nerve after stimulation of the tibial territory (c) are shown. C-fibre response thresholds after stimulation of sural or tibial territories as indicated are shown (b). In panels a and b, N = 12 fibres from 3 sham mice and 12 fibres from 3 SNI mice; Unpaired two-tailed t-test; P = 0.4673, t = 0.74, df = 20, F = 1.37; in panel **a** and P = 0.00147, t = 3.68, df = 20, F = 5.55 in panel **b**. (**d, e**) Conduction velocity (d) and response threshold (e) of evoked C-fibre responses in the sural nerve (sham and SNI) after stimulation of the sural territory. In d and e, N = 8 fibres each from 6 sham and 5 SNI mice. Unpaired two-tailed t-test; P = 0.2362, t = 1.23, df = 14, F = 1.758 in panel **d** and P = 0.1788, t = 1.42, df = 14, F = 2.724 in panel **e**. Data are shown as mean \pm S.E.M. This figure extends the data shown in main Fig. [3l, m](#).

[Source data](#)

Extended Data Fig. 11 Analysis of potential immune cell accumulation in injured and uninjured nerve territories at the time of emergence of reinnervation neuropathic allodynia.

Typical examples (**a, c**) and quantification (**b, d**) demonstrating lack of immune cell infiltration and accumulation in the tibial or sural nerve territories at 24-26 weeks post-SNI, using tissue from hind paw inflamed

with Complete Freund's Adjuvant (CFA) as positive controls. Shown are data with anti-Gr1 immunohistochemistry to identify macrophages (**a**, **b**; arrows in **a**) and anti-CD4/CD8 to identify T-cells (**c**, **d**; arrows in **c**). In both cases, N = 2–3 sections each from the 4 mice for sham-sural, 6 mice for sham-tibial group, 5 mice each from SNI-sural and SNI-tibial groups and 2 mice injected with CFA. ROI: region of interest.

[Source data](#)

Extended Data Fig. 12 Effects of pharmacological inhibition of classical mediators of sensitization on reinnervation neuropathic allodynia.

Mechanical hypersensitivity in the tibial territory 24–26 weeks post-SNI is shown as compared to control (**a**), using mice with CFA-induced paw inflammation as positive controls for mechanisms of peripheral sensitization (**b**). Shown are data with inhibition of prostaglandin synthesis via blockade of both Cox-1 and Cox-2 (Diclofenac), Cox2-selective inhibition (Celecoxib), blockade of TRPV1 or TRPA1 or sequestration of NGF using a neutralizing antibody. In both models, vehicle-treated mice were used as negative controls. Note that blockade of prostaglandin synthesis, TRPA1 inhibition and NGF sequestration led to significant decrease in inflammatory mechanical allodynia, but did not affect reinnervation mechanical allodynia. N = 7 mice for and SNI -vehicle group, 8 mice for Sham-drug group and 6 mice each for CFA–drug and CFA–vehicle groups. For group comparison in panel a, $F_{(3,15)} = 1.608$, $P = 0.223$ (Diclofenac), $F_{(3,15)} = 0.541$, $P = 0.66$ (celecoxib), $F_{(3,15)} = 0.279$, $P = 0.84$ (AMG9810), $F_{(3,15)} = 0.649$, $P = 0.594$ (AP18) and $F_{(3,15)} = 0.121$, $P = 0.947$ (Tanezumab). For group comparison in panel b, $F_{(3,15)} = 29.222$, $P = 1.64E-06$ (Diclofenac), $F_{(3,15)} = 11.842$, $P = 0.000308$ (celecoxib), $F_{(3,15)} = 0.846$, $P = 0.49$ (AMG9810), $F_{(3,15)} = 10.0$, $P = 0.00071$ (AP18) and $F_{(3,15)} = 4.778$, $P = 0.0157$ (Tanezumab). Two-way ANOVA of repeated measures followed by Bonferroni's test for multiple comparisons was performed (* < p 0.05). Data are shown as mean ± S.E.M.

[Source data](#)

Extended Data Fig. 13 Overview of gene expression analyses of DRG neurons innervating the sural territory or collaterally sprouting into the tibial territory at 24 weeks after SNI as compared to control mice.

(a, b) Volcano plots and summary of results (**a**) and putative functions ascribed to regulated genes or their families (**b**) in collaterally sprouting nociceptors in the tibial territory in SNI mice as compared to nociceptors innervating the tibial territory in control mice. Red and blue dots represent upregulated and downregulated genes, respectively. Unlabelled dots represent sequences lacking annotation. **(c)** Relative abundance of sub-populations of nociceptors was not significantly different between collaterally sprouting nociceptors in the tibial territory as compared to nociceptors innervating the tibial territory in control mice. ANOVA of random measures revealed lack of statistical significance. **(d)** Volcano plots and summary of results of genes regulated in nociceptors in the sural nerve territory of SNI mice as compared to control mice. Owing to space limits, not all regulated genes represented by blue and red dots are labelled in panel d. Further details are given in Supplementary Note 4 and sequencing reads are placed on the European Nucleotide Archive (<https://www.ebi.ac.uk/ena>) under the accession number PRJEB50184.

Source data

Extended Data Fig. 14 Effects of caspase-3-mediated nociceptor ablation specifically in L3–L4 DRGs on reinnervation neuropathic allodynia.

Shown is the behavioural effect of adeno-associated virus injection-mediated Cre-dependent caspase-3 expression in L3-L4 DRGs at 24-26 wks post-sham treatment or SNI on withdrawal responses to graded von Frey mechanical stimuli in the latter-most digit (sural territory, panel **a**) ($n = 4$ per group; $F_{(1,6)} = 33.0$, $P = 0.01$) or the middle digit (tibial territory, panel **b**) ($n = 4$ per group; $F_{(1,6)} = 15.0$, $P = 0.030$). Panel **c** represents mechanical sensitivity in mice receiving AAV-GFP (control) ($n = 4$ per group; for tibial, $F_{(1,6)} = 1.417$, $P = 0.312$ and for sural, $F_{(1,6)} = 3.0$, $P = 0.182$) injections. In all

panels, * represents $p < 0.05$ compared to baseline, † $p < 0.05$ compared to control group (sham), two-way repeated measures ANOVA with Bonferroni multiple comparison. Data shown as mean \pm S.E.M.

[Source data](#)

[Extended Data Fig. 15 Schematic model.](#)

The scheme depicts the proposed differential roles of nociceptors and A β -LTMRs in mediating two distinct types of neuropathic allodynia, both of which come about when areas undergoing denervation and intact nerve territories are intermingled, as is clinically the most frequent scenario with nerve trauma-associated neuropathic pain. In the novel reinnervation neuropathic allodynia described in this study, in the absence of A β reinnervation, collaterally sprouting C-fibres show abnormal pattern of connectivity in tactile-sensing Meissner corpuscles.

Supplementary information

[Supplementary Information](#)

This file contains Supplementary Notes 1–4; Supplementary References and legends for Supplementary Videos 1–9

[Reporting Summary](#)

[Peer Review File](#)

[Supplementary Video 1](#)

[Supplementary Video 2](#)

[Supplementary Video 3](#)

[Supplementary Video 4](#)

[Supplementary Video 5](#)

[Supplementary Video 6](#)

[Supplementary Video 7](#)

[Supplementary Video 8](#)

[Supplementary Video 9](#)

Source data

[Source Data Fig. 1](#)

[Source Data Fig. 2](#)

[Source Data Fig. 3](#)

[Source Data Fig. 4](#)

[Source Data Extended Data Fig. 1](#)

[Source Data Extended Data Fig. 2](#)

[Source Data Extended Data Fig. 10](#)

[Source Data Extended Data Fig. 11](#)

[Source Data Extended Data Fig. 12](#)

[Source Data Extended Data Fig. 13](#)

[Source Data Extended Data Fig. 14](#)

Rights and permissions

Open Access This article is licensed under a Creative Commons Attribution 4.0 International License, which permits use, sharing, adaptation, distribution and reproduction in any medium or format, as long as you give appropriate credit to the original author(s) and the source, provide a link to the Creative Commons license, and indicate if changes were made. The images or other third party material in this article are included in the article's Creative Commons license, unless indicated otherwise in a credit line to the material. If material is not included in the article's Creative Commons license and your intended use is not permitted by statutory regulation or exceeds the permitted use, you will need to obtain permission directly from the copyright holder. To view a copy of this license, visit <http://creativecommons.org/licenses/by/4.0/>.

[Reprints and Permissions](#)

About this article

Cite this article

Gangadharan, V., Zheng, H., Taberner, F.J. *et al.* Neuropathic pain caused by miswiring and abnormal end organ targeting. *Nature* **606**, 137–145 (2022).
<https://doi.org/10.1038/s41586-022-04777-z>

- Received: 15 April 2021
- Accepted: 20 April 2022
- Published: 25 May 2022
- Issue Date: 02 June 2022
- DOI: <https://doi.org/10.1038/s41586-022-04777-z>

Share this article

Anyone you share the following link with will be able to read this content:

[Get shareable link](#)

Sorry, a shareable link is not currently available for this article.

[Copy to clipboard](#)

Provided by the Springer Nature SharedIt content-sharing initiative

Further reading

- [**Nerve regrowth can be painful**](#)

- Suna L. Cranfill
- Wenqin Luo

Nature (2022)

[**Nerve regrowth can be painful**](#)

- Suna L. Cranfill
- Wenqin Luo

Nature News & Views 25 May 2022

This article was downloaded by **calibre** from <https://www.nature.com/articles/s41586-022-04777-z>

[Download PDF](#)

- Article
- Open Access
- [Published: 04 May 2022](#)

Gene regulation by gonadal hormone receptors underlies brain sex differences

- [B. Gegenhuber^{1,2}](#),
- [M. V. Wu ORCID: orcid.org/0000-0002-5246-2659¹](#),
- [R. Bronstein¹](#) &
- [J. Tollkuhn ORCID: orcid.org/0000-0001-5991-7620¹](#)

Nature volume **606**, pages 153–159 (2022)

- 21k Accesses
- 2 Citations
- 588 Altmetric
- [Metrics details](#)

Subjects

- [Development of the nervous system](#)
- [Epigenetics in the nervous system](#)
- [Sexual dimorphism](#)
- [Transcriptional regulatory elements](#)

Abstract

Oestradiol establishes neural sex differences in many vertebrates^{1,2,3} and modulates mood, behaviour and energy balance in adulthood^{4,5,6,7,8}. In the canonical pathway, oestradiol exerts its effects through the transcription factor oestrogen receptor- α (ER α)⁹. Although ER α has been extensively characterized in breast cancer, the neuronal targets of ER α , and their involvement in brain sex differences, remain largely unknown. Here we generate a comprehensive map of genomic ER α -binding sites in a sexually dimorphic neural circuit that mediates social behaviours. We conclude that ER α orchestrates sexual differentiation of the mouse brain through two mechanisms: establishing two male-biased neuron types and activating a sustained male-biased gene expression program. Collectively, our findings reveal that sex differences in gene expression are defined by hormonal activation of neuronal steroid receptors. The molecular targets we identify may underlie the effects of oestradiol on brain development, behaviour and disease.

Main

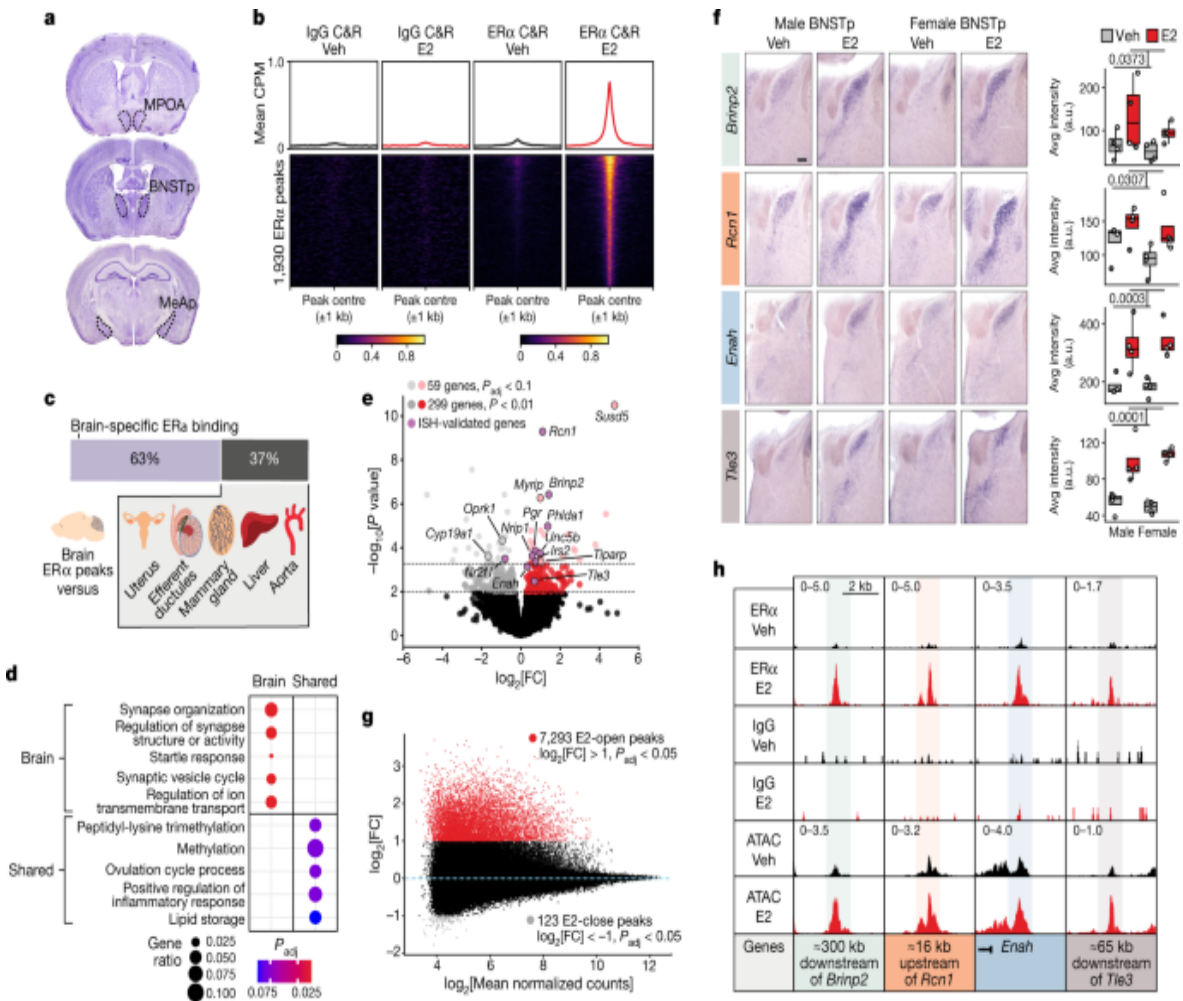
In mammals, gonadal steroid hormones regulate sex differences in neural activity and behaviour. These hormones establish sex-typical neural circuitry during critical periods of development and activate the display of innate social behaviours in adulthood. Among these hormones, oestradiol is the principal regulator of brain sexual differentiation in mice. In males, the testes briefly activate at birth, generating a sharp rise in testosterone that subsides within hours¹⁰. Neural aromatase converts circulating testosterone to 17 β -oestradiol, which acts through ER α in discrete neuronal populations to specify sex differences in cell number and connectivity^{1,3,11}. Despite extensive characterization of the neural circuits controlling sex-typical behaviours^{12,13}, the underlying genomic mechanisms by which steroid hormone receptors act in these circuits remain unknown. Recent advancements in low-input and single-cell chromatin profiling methods have provided transformative insights into how transcription factors (TFs) regulate gene expression in small numbers of cells¹⁴. We set out to use these

methods to discover the neuronal genomic targets of ER α and how they coordinate brain sexual differentiation.

Genomic targets of ER α in the brain

To determine the genomic targets of ER α in the brain, we used an established hormone starvation and replacement paradigm that reproducibly elicits sex-typical behaviours² and replicates the medium conditions required to detect ER α genomic binding in cell lines¹⁵. At 4 h after treatment with oestradiol benzoate (E2) or vehicle control, we profiled ER α binding in three interconnected limbic brain regions in which ER α regulates sex-typical behaviours: the posterior bed nucleus of the stria terminalis (BNSTp), medial pre-optic area and posterior medial amygdala^{11,12,16} (Fig. 1a). We used the low-input TF profiling method CUT&RUN, which we first validated in MCF-7 breast cancer cells by comparing to a previous dataset for chromatin immunoprecipitation with sequencing (ChIP-seq) of ER α (Extended Data Fig. 1). We detected 1,930 E2-induced ER α -bound loci in the brain (Fig. 1b, Extended Data Fig. 2 and Supplementary Table 1). The most enriched TF-binding motif in these peaks was the oestrogen response element (ERE), the canonical binding site of oestrogen receptors (Extended Data Fig. 2c,d). Comparison of these ER α -binding sites to those previously detected in peripheral mouse tissues revealed that most are specific to the brain (Fig. 1c and Extended Data Fig. 2f). Brain-specific ER α binding events were uniquely enriched for synaptic and neurodevelopmental disease Gene Ontology terms, including neurotransmitter receptors, ion channels, neurotrophin receptors and extracellular matrix genes (Fig. 1d, Extended Data Fig. 2h–k and Supplementary Table 1). We also found evidence supporting direct crosstalk between oestradiol and neuroprotection, as ER α directly binds loci for the neurotrophin receptors *Ntrk2* (also known as *TrkB*) and *Ntrk3* (Extended Data Fig. 2k and Supplementary Table 1). Moreover, ER α targets the genes encoding androgen and progesterone receptors (*Ar* and *Pgr*; Supplementary Table 1).

Fig. 1: Genomic targets of ER α in sexually dimorphic neuronal populations.



a, Coronal sections containing sexually dimorphic brain areas used for ER α CUT&RUN. MPOA, medial pre-optic area; BNSTp, posterior bed nucleus of the stria terminalis; MeAp, posterior medial amygdala. **b**, Line plots (top) and heatmaps (bottom) of mean IgG and ER α CUT&RUN (C&R) CPM \pm 1 kb around E2-induced ER α CUT&RUN peaks (DiffBind edgeR, $P_{adj} < 0.1$). The heatmaps are sorted by E2 ER α CUT&RUN signal. Colour scale is counts per million (CPM). Veh, vehicle. **c**, Cross-tissue ER α comparison, showing the proportion of ER α peaks detected specifically in brain. **d**, Top Gene Ontology biological process terms associated with genes nearest to brain-specific or shared (≥ 4 other tissues) ER α CUT&RUN peaks (clusterProfiler, $P_{adj} < 0.1$). The plot shows enrichment of biological processes like Synapse organization, Regulation of synapse structure or activity, Startle response, Synaptic vesicle cycle, Regulation of ion transmembrane transport, Peptidyl-lysine trimethylation, Methylation, Ovulation cycle process, Positive regulation of inflammatory response, and Lipid storage.

e, Combined sex E2 versus vehicle RNA-seq in BNSTp *Esr1*⁺ cells. Scatter plot of $-\log_{10}[P \text{ value}]$ versus $\log_2[\text{FC}]$. Light grey dots represent DESeq2, $P_{adj} < 0.1$; dark grey dots represent DESeq2, $P < 0.01$; purple dots represent ISH-validated genes. Genes shown include *Susd5*, *Rcn1*, *Mmp9*, *Brinp2*, *Oprk1*, *Cyp19at1*, *Nrpf1*, *Linc56*, *Tlarp*, *Grb10*, *Tie2*, *Tie3*, and *Erbb3*.

f, In situ hybridization (ISH) images and box plots of average intensity (a.u.) for *Brinp2*, *Rcn1*, *Erbb3*, and *Tie3* in Male and Female BNSTp under Veh and E2 conditions.

g, Scatter plot of $\log_2[\text{FC}]$ versus $\log_2[\text{Mean normalized counts}]$ for E2-open peaks ($\log_2[\text{FC}] > 1$, $P_{adj} < 0.05$) and E2-close peaks ($\log_2[\text{FC}] < -1$, $P_{adj} < 0.05$).

h, ChIP-seq tracks for ER α Veh, ER α E2, IgG Veh, IgG E2, ATAC Veh, and ATAC E2. Scale bars indicate genomic regions: ≈ 300 kb downstream of *Brinp2*, ≈ 16 kb upstream of *Rcn1*, and ≈ 65 kb downstream of *Tie3*.

negative FC is E2-downregulated. **f**, Images (left panels) and quantitative analysis (right panels) of ISH for select genes induced by E2 in both sexes. Boxplot centre, median; box boundaries, first and third quartiles; whiskers, $1.5 \times \text{IQR}$ from boundaries. Two-way analysis of variance: *Brinp2* $P = 0.0373$, *Rcn1* $P = 0.0307$, *Enah* $P = 0.0003$, *Tle3* $P = 0.0001$; $n = 4$ per condition; scale bar, 200 μm . **g**, MA plot of E2-regulated ATAC-seq peaks in BNSTp *Esr1*⁺ cells; red dots are E2-open peaks (DiffBind edgeR, $\log_2[\text{FC}] > 1$, $P_{\text{adj}} < 0.05$), grey dots are E2-close peaks (DiffBind edgeR, $\log_2[\text{FC}] < -1$, $P_{\text{adj}} < 0.05$). **h**, Example ER α peaks at E2-induced genes. Top left number is the y-axis range in CPM. Shaded band indicates peak region.

Source Data

To determine the effects of ER α binding on gene expression and chromatin state, we focused on a single brain region, the BNSTp, given its central role in the regulation of sex-typical behaviours. The BNSTp receives olfactory input through the accessory olfactory bulb and projects to the medial pre-optic area, medial amygdala, hypothalamus and mesolimbic reward pathway^{11,17}. We used our oestradiol treatment paradigm and performed translating ribosome affinity purification (TRAP), followed by RNA sequencing (RNA-seq), on the BNSTp from *Esr1*^{Cre/+}; *Rpl22*^{HA/+} mice, enabling selective capture of ribosome-bound transcripts from *Esr1*⁺ cells. We identified 358 genes regulated by oestradiol, including genes known to be induced by E2 in breast cancer, such as *Pgr* and *Nrip1* (Fig. 1e and Supplementary Table 2). We then validated several of these E2-regulated genes by in situ hybridization (Fig. 1f, Extended Data Fig. 3 and Extended Data Table 1). Genes that contribute to neuron wiring (*Brinp2*, *Unc5b* and *Enah*) and synaptic plasticity (*Rcn1* and *Irs2*) were robustly induced by oestradiol in the BNSTp, illustrating how oestradiol signalling may sculpt sexual differentiation of BNSTp circuitry.

To identify oestradiol-responsive chromatin regions, which may involve signalling pathways other than direct ER α binding¹⁸, we used our oestradiol treatment paradigm and performed assay for transposase-accessible chromatin with sequencing (ATAC-seq) on BNSTp *Esr1*⁺ cells collected from *Esr1*^{Cre/+}; *Sun1-GFP*^{lx/+} mice. Across sexes, we detected 7,293 chromatin regions that increase accessibility with treatment (E2-open) as

well as 123 regions that decrease accessibility (E2-close; Fig. 1g, Extended Data Fig. 4a–e and Supplementary Table 3). Motif enrichment analysis of these E2-open regions, which occurred primarily at distal enhancer elements (Extended Data Fig. 4c), showed that 89% contain an ERE (Extended Data Fig. 4f), consistent with the observation that nearly all ER α -binding sites overlapped an E2-open region (Extended Data Fig. 4g). These results indicate that direct oestrogen receptor binding, rather than indirect signalling pathways, drives most E2-responsive chromatin regions in the BNSTp¹⁹.

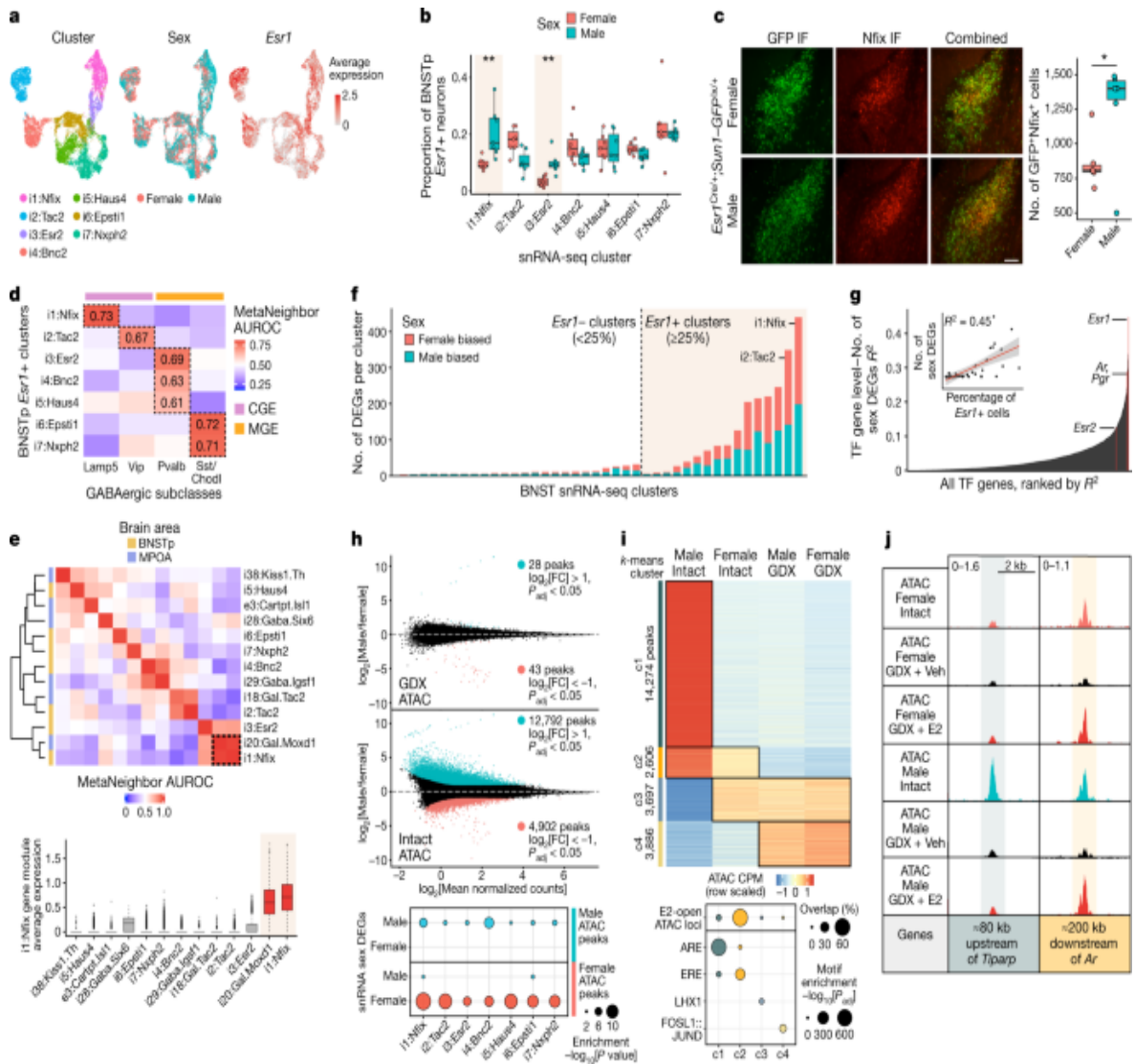
After examining the relationship between oestradiol-regulated chromatin loci and gene expression, we noted that E2-open regions localized at both E2-upregulated and E2-downregulated genes (Extended Data Fig. 5a). E2-open regions at downregulated genes contained EREs yet lacked widespread ER α binding (Extended Data Fig. 5b,c), suggesting that transient ER α recruitment may contribute to gene repression²⁰. E2-upregulated genes with corresponding E2-responsive chromatin loci include *Brinp2*, *Rcn1*, *Enah* and *Tle3* (Fig. 1h); E2-downregulated genes include *Astn2*, a regulator of synaptic trafficking, and *Nr2f1* (Extended Data Figs. 3 and 5d).

Although most oestradiol regulation events were shared between sexes in our treatment paradigm, we noted certain sex-dependent effects. Pairwise comparison by sex revealed nearly 300 differential genes between females and males in our TRAP RNA-seq data (Supplementary Table 2). Moreover, we observed 306 genes with a differential response to oestradiol between sexes (Extended Data Fig. 5e,f and Supplementary Table 2). These sex-dependent, E2-responsive genes lacked enrichment of E2-responsive chromatin regions (Extended Data Fig. 5g), which may indicate further oestradiol regulation at the translational level²¹. Likewise, across ER α CUT&RUN and ATAC-seq modalities, we observed negligible sex differences and sex-dependent, E2-responsive loci (Extended Data Fig. 5h–j and Supplementary Table 3), demonstrating that females and males mount a similar genomic response to exogenous oestradiol on removal of the hormonal milieu.

Sex differences in gene regulation

Across rodents and humans, the BNSTp of males is approximately 1.5–2 times larger than that of females^{22,23}. In mice, this structural dimorphism arises from male-specific neonatal ER α activation, which promotes neuron survival^{24,25}. Although BNSTp *Esr1*⁺ neurons are known to be GABAergic¹⁶, the identity of male-biased GABAergic neuron types remains unclear. To characterize these cells, we reanalysed a single-nucleus RNA-seq (snRNA-seq) dataset collected from the BNST of adult, gonadally intact females and males²⁶. Seven BNSTp *Esr1*⁺ transcriptomic neuron types emerged from this analysis, and two of these marked by *Nfix* (i1:Nfix) and *Esr2* (i3:Esr2) are more abundant in males than in females (Fig. 2a, b and Extended Data Fig. 6a, b). Although a male bias in *Esr2*/ER β -labelled cells is known²⁷, *Nfix* expression has not been described previously in the BNSTp. Immunofluorescent staining confirmed that males have twice as many ER α ⁺*Nfix*⁺ neurons as females (Fig. 2c and Extended Data Fig. 6c).

Fig. 2: Sex differences in cell type abundance and gene regulation in BNSTp *Esr1*⁺ cells.



a, Uniform manifold approximation and projection (UMAP) visualization of BNSTp *Esr1*+ snRNA-seq inhibitory neuron clusters, coloured by identity (left), sex (middle) and *Esr1* expression (right). **b**, Proportion of BNSTp *Esr1*+ nuclei in each BNSTp *Esr1*+ inhibitory neuron cluster per sex. Higher proportions of i1:Nfix ($P_{adj} = 0.002$) and i3:Esr2 ($P_{adj} = 0.002$) neurons are in males than females. Boxplot centre, median; box boundaries, first and third quartiles; whiskers, $1.5 \times$ IQR from boundaries, $n = 7$, $**P_{adj} < 0.01$, one-sided, Wilcoxon rank-sum test, adjusted with the Benjamini–Hochberg procedure. **c**, BNSTp immunofluorescence (IF) staining for GFP (left micrographs) and Nfix (middle micrographs) in P14 female and male *Esr1*^{Cre/+}; *Sun1-GFP*^{lx/+} animals (scale bar, 100 μ m), with combined images (right micrographs) and their quantification (boxplots; right). Boxplot centre,

median; box boundaries, first and third quartiles; whiskers, $1.5 \times \text{IQR}$ from boundaries, $n = 6$, $P = 0.0422$, * $P < 0.05$, two-sided, unpaired t -test. **d**, Heatmap of median MetaNeighbor area under the receiver operating characteristic curve (AUROC) values for BNSTp *Esr1*⁺ clusters and cortical/hippocampal GABAergic neuron subclasses. The colour bar indicates the developmental origin of GABAergic subclasses. CGE, caudal ganglionic eminence; MGE, medial ganglionic eminence. **e**, Top: heatmap of MetaNeighbor AUROC values for BNSTp and MPOA *Esr1*⁺ clusters. Bottom: average expression of i1:Nfix marker genes across BNSTp and MPOA *Esr1*⁺ clusters. Dotted box indicates shared identity of i1:Nfix and i20:Gal.Moxd1 cells. $n = 297$ i20:Gal.Moxd1 cells, 2,459 i1:Nfix cells. Boxplot centre, median; box boundaries, first and third quartiles; whiskers, $1.5 \times \text{IQR}$ from boundaries. **f**, Number of differentially expressed genes (DEGs) between females and males (DESeq2, $P_{\text{adj}} < 0.1$) per BNST neuron snRNA-seq cluster. **g**, R^2 between percentage of TF gene expression and number of sex DEGs per cluster across snRNA-seq clusters. The inset shows correlation for the top-ranked TF gene, *Esr1*. The error band represents the 95% confidence interval. **h**, Differential ATAC sites between gonadectomized (GDX), vehicle-treated females and males (top) and gonadally intact females and males (middle). Blue dots (edgeR, $\log_2[\text{FC}] > 1$, $P_{\text{adj}} < 0.05$), red dots (edgeR, $\log_2[\text{FC}] < -1$, $P_{\text{adj}} < 0.05$). Bottom: enrichment analysis of sex-biased ATAC peaks at sex DEGs. **i**, Top: *k*-means clustering (c1–c4) of differentially accessible ATAC peaks across four conditions (edgeR, $P_{\text{adj}} < 0.01$). Bottom: dotplot showing the percentage of sites per cluster overlapping E2-open ATAC loci and motif enrichment analysis of peaks in each cluster (AME algorithm). ARE, androgen response element. **j**, Example ATAC peaks in *k*-means clusters 1 and 2. Top left number is the y-axis range in CPM. Shaded band indicates peak region.

Source Data

To interpret the functional relevance of BNSTp *Esr1*⁺ neuron types, we compared their gene expression profiles to the mouse cortical and hippocampal single-cell RNA-seq atlas using MetaNeighbor^{28,29}. i1:Nfix neurons uniquely matched the identity of *Lamp5*⁺ neurogliaform interneurons^{30,31} (Fig. 2d and Extended Data Fig. 6d,e) and also shared markers (*Moxd1* and *Cplx3*; Extended Data Fig. 6b,f,g) with a male-biased

neuron type (i20:Gal/Moxd1) in the sexually dimorphic nucleus of the preoptic area (SDN-POA) that is selectively activated during male-typical mating, inter-male aggression and parenting behaviours³². Beyond these two genes, i1:Nfix and i20:Gal/Moxd1 neuron types share a transcriptomic identity, consistent with observed Nfix immunofluorescence in both the BNSTp and SDN-POA (Fig. 2e and Extended Data Fig. 6h). Together, these results define male-biased neurons in the BNSTp and reveal a common *Lamp5*⁺ neurogliaform identity between the BNSTp and SDN-POA.

We next examined sex differences in gene expression and found extensive and robust (false discovery rate < 0.1) sex-biased expression across BNST neuron types (Fig. 2f, Extended Data Fig. 7a–d and Supplementary Table 4). Most sex differences were specific to individual types (for example, *Dlg2*/PSD-93 and *Kctd16* in i1:Nfix neurons), whereas select differences were detected in multiple populations (for example, *Tiparp* and *Socs2*; Extended Data Fig. 7b,c). Relative to all other TF genes in the genome, *Esr1*, along with coexpressed hormone receptors, *Ar* and progesterone receptor (*Pgr*), correlated best with sex-biased gene expression (Fig. 2g and Extended Data Fig. 7e,f), indicating potential regulatory function.

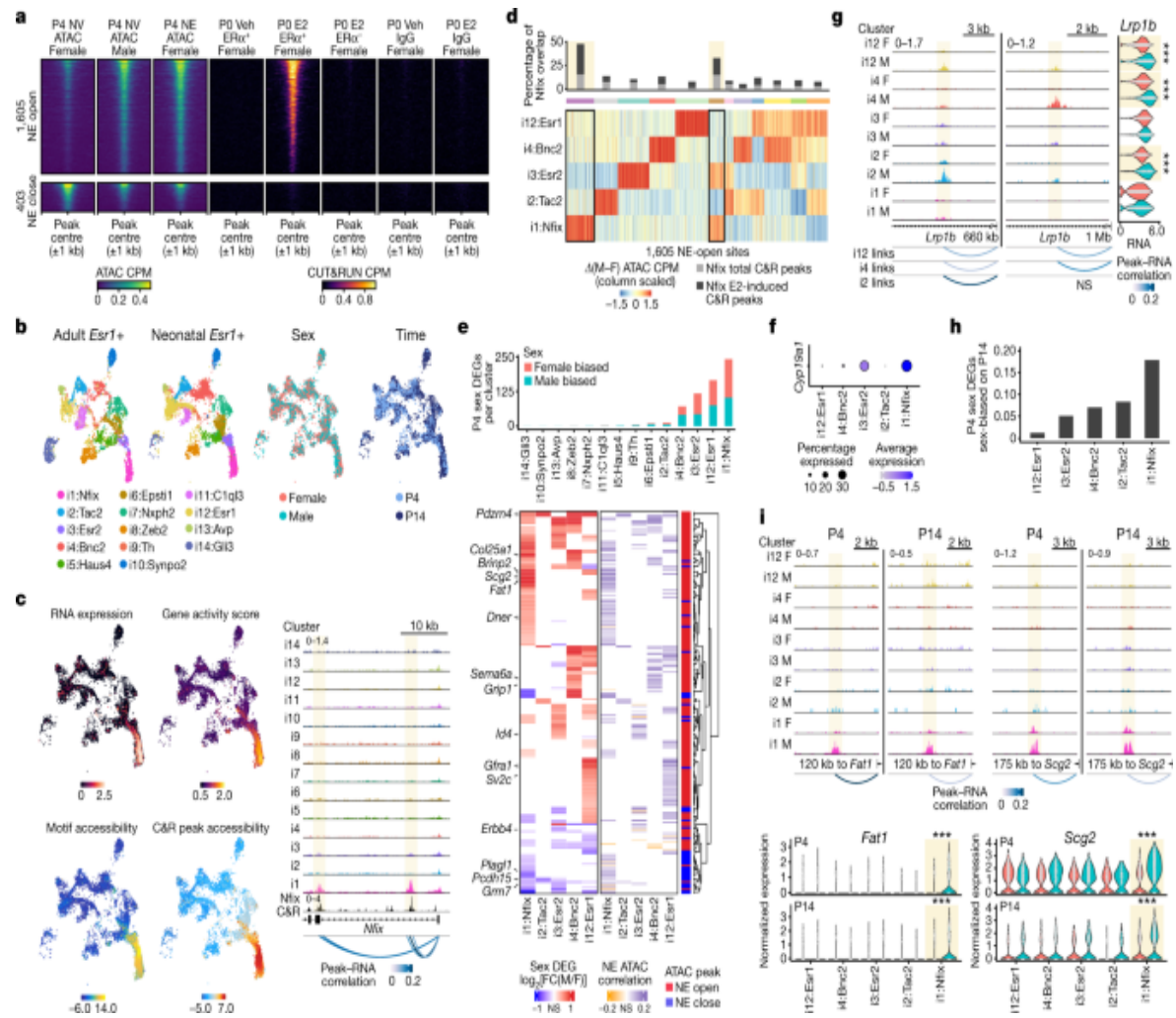
To identify chromatin regions controlling sex differences in BNSTp gene expression, we performed ATAC-seq on BNSTp *Esr1*⁺ cells collected from gonadally intact *Esr1*^{Cre/+}; *Sun1*–GFP^{lx/+} mice. Approximately 18,000 regions differed in accessibility between sexes; moreover, these regions localized at sex-biased genes detected in *Esr1*⁺ neuron types (Fig. 2h, Extended Data Fig. 7g,h and Supplementary Table 5). By contrast, gonadectomy reduced the number of sex-biased regions to 71 (Fig. 2h and Supplementary Table 5). We compared chromatin accessibility across sexes and gonadal hormone status using *k*-means clustering and discovered male-specific, but not female-specific, responses to gonadectomy (Fig. 2i and Extended Data Fig. 7i–k). Notably, chromatin regions that close specifically in males on gonadectomy (cluster 1) primarily contained the androgen response element, whereas regions closing across both sexes (cluster 2) were enriched for the ERE and strongly overlapped E2-open regions (Fig. 2i,j). Thus, in the BNSTp, oestradiol maintains chromatin in an active state across both sexes, whereas testosterone promotes chromatin activation and repression in males. Collectively, these data indicate that gonadal hormone

receptors drive adult sex differences in gene expression, largely as a consequence of acute hormonal state.

ER α drives neonatal chromatin state

Sexual dimorphism in BNSTp wiring emerges throughout a 2-week window following birth, well after neural oestradiol has subsided in males. To determine the genomic targets of the neonatal surge, we performed ATAC-seq on BNSTp *Esrl*⁺ cells at postnatal day 4 (P4), which corresponds to the onset of male-biased BNSTp cell survival and axonogenesis^{33,34}. We detected about 2,000 sex differences in chromatin loci at this time, and nearly all sex differences were dependent on neonatal oestradiol (NE; Fig. 3a, Extended Data Fig. 8a, b and Supplementary Table 6). NE-open regions were similarly induced by oestradiol in our adult dataset (Extended Data Fig. 8c, d). To determine whether ER α drives male-typical chromatin opening, we performed ER α CUT&RUN on *Esrl*⁺ cells from females treated acutely with vehicle or oestradiol on the day of birth. Oestradiol rapidly recruited ER α to NE-open regions (Fig. 3a, Extended Data Fig. 8e–h and Supplementary Table 7). Our results demonstrate that ER α activation controls neonatal sex differences in the chromatin landscape.

Fig. 3: Neonatal ER α genomic binding drives a sustained male-biased gene expression program.



a, Heatmap of P4 BNST *Esr1*+ ATAC, P0 IgG CUT&RUN and P0 ER α CUT&RUN CPM ± 1 kb around 1,605 NE-open and 403 NE-close ATAC peaks (edgeR, $P_{adj} < 0.1$). ER α^+ , Sun1-GFP $^+$ nuclei; ER α^- , Sun1-GFP $^-$ nuclei. **b**, UMAPs of adult (left) and neonatal (middle left) BNST *Esr1*+ snRNA-seq clusters; neonatal snRNA-seq clusters coloured by sex (middle right) and time point (right). **c**, Left: UMAPs of *Nfix* expression (top left), gene activity score (top right), motif chromVAR deviation score (bottom left) and CUT&RUN chromVAR deviation score (bottom right). Right: neonatal single-nucleus ATAC (snATAC) and adult BNSTp *Nfix* CUT&RUN tracks at the *Nfix* locus. Top left number is the y-axis range in CPM. Shaded band indicates peak region. Peak-RNA correlation indicates correlation coefficient for snATAC peaks correlated with *Nfix* expression. **d**, Heatmap of differential snATAC CPM between males (M) and females (F) at 1,605 NE-open sites, scaled across snRNA-seq clusters and grouped using tSNE.

k-means clustering. The barplot indicates the percentage of overlap for each *k*-means cluster with total and E2-induced BNSTp Nfix CUT&RUN peaks. **e**, Top: number of sex DEGs (MAST, $P_{\text{adj}} < 0.05$) in P4 multiome clusters. Bottom: heatmaps indicating RNA $\log_2[\text{FC}]$ of P4 sex DEGs (left) and Pearson's correlation coefficient of NE-open (red) and NE-close (blue) ATAC peaks (right) linked to sex DEGs in each cluster. Genes without significant differential expression or correlation coefficients (not significant (NS)) are shown in white. **f**, *Cyp19a1*/aromatase expression on P4. **g**, Left: NE-open ATAC peaks correlating with *Lrp1b* expression in *Cyp19a1*-clusters, i2:Tac2 and i12:Esr1. Top left number is the y-axis range in CPM. Shaded band indicates peak region. Right, sex difference in *Lrp1b* expression in i2:Tac2 ($n = 260$ female, 153 male, $P_{\text{adj}} = 2.13 \times 10^{-8}$), i4:Bnc2 ($n = 437$ female, 373 male, $P_{\text{adj}} = 5.62 \times 10^{-37}$), i12:Esr1 ($n = 803$ female, 507 male, $P_{\text{adj}} = 1.09 \times 10^{-12}$) cells. *** $P_{\text{adj}} < 0.001$, MAST. **h**, Proportion of P4 sex DEGs detected as sex biased on P14. **i**, Top: i1:Nfix-specific, NE-open ATAC peaks at *Fat1* and *Scg2* loci on P4 and P14. Top left number is the y-axis range in CPM. Shaded band indicates peak region. Bottom: Sex difference in i1:Nfix *Fat1* and *Scg2* expression on P4 (*Fat1*, $P_{\text{adj}} = 1.28 \times 10^{-37}$; *Scg2*, $P_{\text{adj}} = 1.54 \times 10^{-46}$; $n = 887$ female, 676 male) and P14 (*Fat1*, $P_{\text{adj}} = 1.13 \times 10^{-11}$; *Scg2*, $P_{\text{adj}} = 1.52 \times 10^{-5}$; $n = 554$ female, 829 male). *** $P_{\text{adj}} < 0.001$, MAST.

Previous studies have proposed that adult sex differences in behaviour arise from permanent epigenomic modifications induced during the neonatal hormone surge³⁵. Our datasets allowed us to examine whether chromatin regions regulated by neonatal hormone maintain sex-biased accessibility into adulthood. Only a small proportion of NE-regulated regions (about 10%) are maintained as sex biased in gonadally intact adults (Extended Data Fig. 9a), implying substantial reprogramming of sex differences as a result of hormonal production during puberty (Fig. 2h). Notably, although most NE-open loci did not maintain male-biased accessibility after puberty, they still localized at adult male-biased genes and clustered around adult male-biased ATAC peaks (Extended Data Fig. 9b-d). These results suggest that certain male-biased genes undergo sequential regulation by ERα and AR in early life and adulthood, respectively.

Sustained sex-biased gene expression

Our identification of approximately 2,000 chromatin regions controlled by the neonatal hormone surge suggests that ER α drives extensive sex differences in the expression of genes that control brain sexual differentiation. To identify these genes, and assess the longevity of their expression, we performed single-nucleus multiome (RNA and ATAC) sequencing on female and male BNST *Esr1*⁺ cells collected at P4 and P14, after the closure of the neonatal critical period³ (Fig. 3b and Extended Data Fig. 10a,b). We profiled 14,836 cells and found that *Esr1*⁺ neuron identity is largely the same across P4, P14 and adulthood³⁶ (Fig. 3b and Extended Data Fig. 10c–f).

To identify TFs regulating *Esr1*⁺ neuron identity, we ranked TFs on their potential to control chromatin accessibility and their expression specificity across neuron types³⁷ (Extended Data Fig. 10g). This approach uncovered canonical GABAergic identity TF genes a priori, including *Lhx6*, *Prox1* and *Nkx2-1*, as well as regulators *Zfhx3* and *Nr4a2* (Extended Data Fig. 10g). In addition, *Nfix* was predicted to regulate the identity of the male-biased i1:Nfix neuron type (Fig. 3c and Extended Data Fig. 10f,g). Profiling Nfix binding in the adult BNSTp confirmed that the binding sites of this factor, including at the *Nfix* locus itself, are maintained in an active state primarily in i1:Nfix neurons (Fig. 3c, Extended Data Fig. 10h,i and Supplementary Table 8). Further examination of NE-responsive chromatin regions showed that NE-open regions vary as a function of neuron identity, with NE-open regions in i1:Nfix neurons preferentially containing Nfix binding events (Fig. 3d). These data suggest that, in addition to specifying the chromatin landscape, identity TFs may dictate the cellular response to neonatal oestradiol by influencing ER α binding.

Differential expression analysis across *Esr1*⁺ neuron types on P4 identified >400 sex-biased genes (Fig. 3e, Extended Data Fig. 11a and Supplementary Table 9). Performing RNA-seq on BNSTp *Esr1*⁺ cells collected from females treated at birth with vehicle or oestradiol showed that these sex differences largely arise as a consequence of the neonatal surge (Extended Data Fig. 11b–e and Supplementary Table 10). Notably, oestradiol-dependent sex differences in gene expression and chromatin state occurred

in neurons lacking *Cyp19a1*/aromatase expression (Fig. 3e–g), indicative of non-cell-autonomous oestradiol signalling.

To link our chromatin and gene expression data, we constructed a gene regulatory map across *Esr1*⁺ neuron types consisting of sex-biased genes and NE-regulated enhancers with correlated accessibility (Fig. 3e and Extended Data Fig. 11f,g). This map demonstrates both divergent responses across neuron types as well as neuron-type-specific enhancers for common sex-biased targets. Notably, we identified *Arid1b*, an autism spectrum disorder candidate gene, among genes regulated by distinct enhancers across neuron types (Extended Data Fig. 11g). Further examination showed that about 40% of high-confidence (family-wise error rate ≤ 0.05) autism spectrum disorder candidate genes³⁸, including *Grin2b*, *Scn2a1* (also known as *Scn2a*) and *Slc6a1*, contained NE-open chromatin regions and ER α occupancy (Extended Data Fig. 8j and Supplementary Table 6).

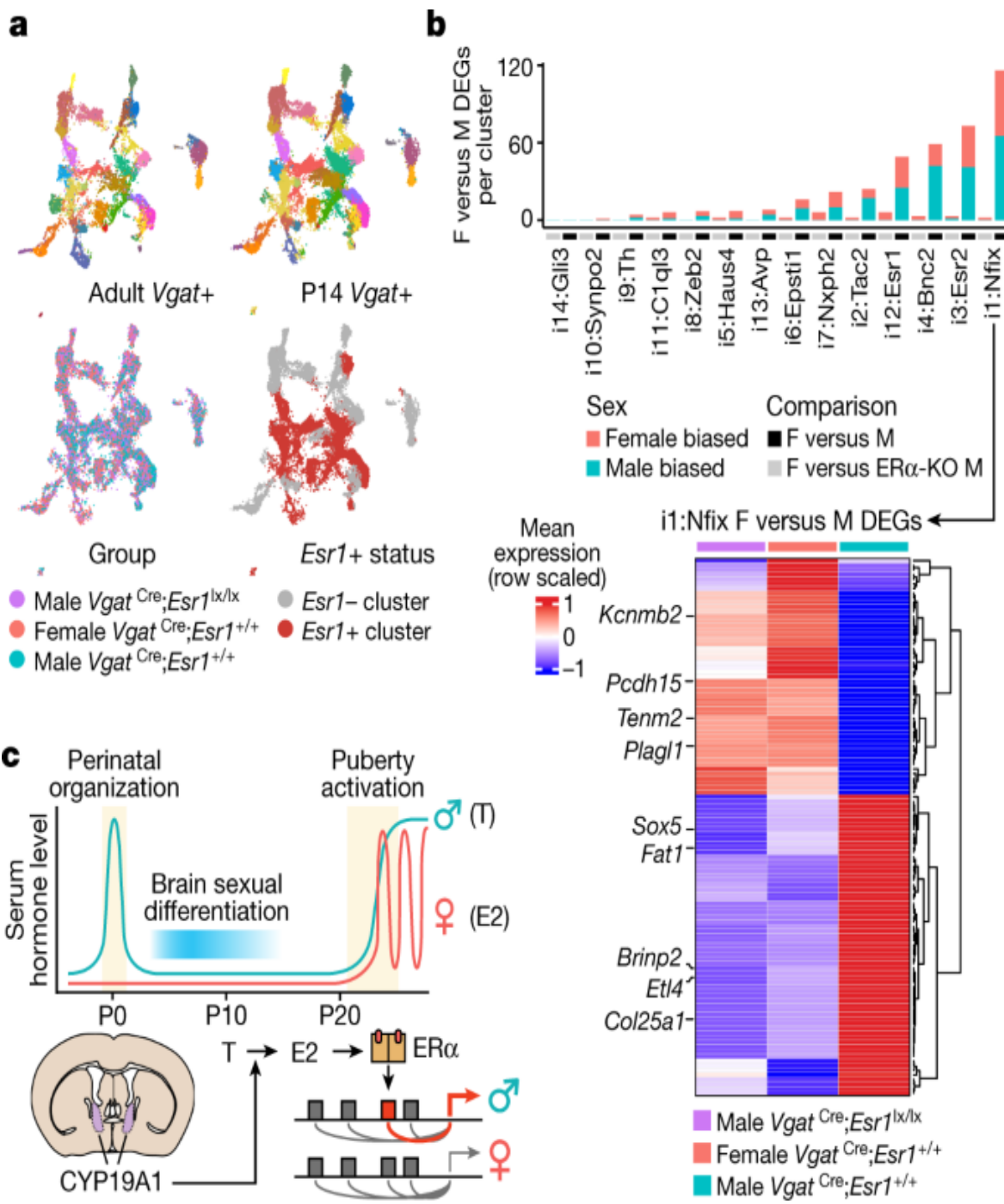
We also examined whether sex-biased genes, and their corresponding enhancers, are sustained across the neonatal critical period by comparing *Esr1*⁺ neurons between P4 and P14. Although the total number of sex-biased genes declined between P4 and P14, a subset persisted as sex biased throughout the neonatal critical window (Fig. 3h and Supplementary Table 10). In i1:Nfix neurons, about 20% of differentially expressed genes on P4 persisted as sex biased on P14. These genes regulate distinct components of neural circuit development, including neurite extension (*Klh1* and *Pak7* (also known as *Pak5*)), axon pathfinding (*Epha3* and *Nell2*), neurotransmission (*Kcnab1* and *Scg2*) and synapse formation (*Illrap* and *Tenm2*; Fig. 3h and Extended Data Fig. 11h). Together, these results show that neonatal ER α activation drives the epigenetic maintenance of a gene expression program that facilitates sexual differentiation of neuronal circuitry.

Sustained sex differences require ER α

The adult display of male mating and territoriality behaviours requires ER α expression in GABAergic neurons¹⁶. To determine whether ER α is also required for sustained sex differences in gene expression, we performed snRNA-seq on 38,962 BNST GABAergic neurons isolated from P14

conditional mutant males lacking ER α ($Vgat^{Cre};Esr1^{\text{lx/lx}};Sunl-GFP^{\text{lx}}$), and littermate control females and males ($Vgat^{Cre};Esr1^{+/+};Sunl-GFP^{\text{lx}}$; Fig. 4a and Extended Data Fig. 12a–d). GABAergic neurons in ER α -mutant males did not deviate from P14 control or adult BNST neuron types (Fig. 4a and Extended Data Fig. 12b), indicating that ER α is dispensable for neuron identity. However, the abundance of male-biased i1:Nfix and i3:Esr2 neurons dropped to female levels in $Vgat^{Cre};Esr1^{\text{lx/lx}}$ males (Fig. 4b and Extended Data Fig. 12d), suggesting that neonatal ER α activation is essential for their male-typical abundance.

Fig. 4: ER α is required for sustained sex differences in gene expression.



a, UMAPs of adult (top left) and P14 (top right) BNST *Vgat*+ snRNA-seq clusters; P14 *Vgat*+ snRNA clusters coloured by group (bottom left) and *Esr1*+ status (bottom right). **b**, Top: number of female versus male sex DEGs (MAST, $P_{adj} < 0.05$) in P14 snRNA clusters (black bar). Number of female versus male sex DEGs detected in female versus male KO comparison (grey bar). Bottom: heatmap of mean expression of i1:Nfix sex

DEGs, scaled across control males, control females and conditional ER α -KO males. **c**, Neonatal ER α activation drives a sustained male-typical gene expression program.

Differential expression analysis between control females and control or conditional ER α -knockout (KO) males in each neuron type established that ER α is required for nearly all sexually dimorphic gene expression, with the exception of those located on the Y chromosome or escaping X inactivation (Fig. 4b, Extended Data Fig. 12e and Supplementary Table 11). Notably, ER α -KO males exhibited feminized expression of sex-biased genes (Fig. 4c and Extended Data Fig. 12f). Together, these findings demonstrate that the neonatal hormone surge drives a sustained male-typical gene expression program through activation of a master regulator TF, ER α (Fig. 4c).

Discussion

Here we identify the genomic targets of ER α in the brain and demonstrate that BNSTp sexual differentiation is defined by both male-biased cell number and gene expression. We find that sexual dimorphism in the BNSTp equates to increased numbers of i1:Nfix and i3:Esr2 neurons in males. The transcriptomic identity of i1:Nfix neurons resembles that of cortical *Lamp5*⁺ neurogliaform interneurons, which provide regional inhibition through synaptic and ambient release of GABA³⁹. As all BNSTp neurons and much of the POA are GABAergic, we predict that higher numbers of i1:Nfix inhibitory neurons enables stronger disinhibition of downstream projection sites. The net result is a gain of responses to social information, leading to male-typical levels of mounting or attacking⁴⁰. Male-biased populations of inhibitory neurons also modulate sex-typical behaviours in *Drosophila*, but they do not rely on gonadal hormones to specify sex-biased enhancers^{41,42,43,44,45}. In vertebrates, hormone receptor signalling may have evolved to coordinate gene regulation throughout a neural circuit as a strategy for controlling context-dependent behavioural states. Moreover, the association between hormone receptor target genes identified here and human neurological and neurodevelopmental conditions may explain the notable sex biases of these diseases.

Our data show that the neonatal hormone surge activates ER α to drive a sustained male-biased gene expression program in the developing brain. We speculate that this program establishes male-typical neuronal connectivity across the neonatal critical period and potentially primes the response to hormone receptor activation at puberty. In the adult brain, gonadectomy ablated sex differences in chromatin accessibility, and under these conditions, *Esr1*⁺ neurons of both sexes exhibited a similar genomic response to exogenous oestradiol. Together, these findings suggest that although sex differences in developmental gonadal hormone signalling establish dimorphisms in BNSTp circuitry, the genome remains responsive to later alterations in the hormonal milieu. Likewise, manipulating hormonal status, circuit function or individual genes consistently demonstrates that both sexes retain the potential to engage in behaviours typical of the opposite sex^{46,47,48,49}. This study implicates puberty as a further critical period for sexual differentiation of gene regulation and provides an archetype for studying hormone receptor action across life stages, brain regions and species.

Methods

Animals

All animals were maintained on a 12-h light/12-h dark cycle and provided food and water ad libitum. All mouse experiments were performed under strict guidelines set forth by the CSHL Institutional Animal Care and Use Committee. All animals were randomly assigned to experimental groups. *Esr1*^{Cre} (ref. 50), *Rpl22*^{HA} (ref. 51), *ROSA26*^{CAG-Sun1-sfGFP-Myc} (ref. 52); abbreviated as *Sun1-GFP*), *Vgat*^{Cre} (ref. 53) and C57Bl6/J wild-type mice were obtained from Jackson Labs. *Esr1*^{lx} mice were received from S. A. Khan⁵⁴. Adult male and female mice were used between 8 and 12 weeks of age. For adult hormone treatment experiments, animals were euthanized for tissue collection 4 h after subcutaneous administration of 5 μ g E2 (Sigma E8515) suspended in corn oil (Sigma C8267) or vehicle 3 weeks post-gonadectomy. For neonatal CUT&RUN, ATAC-seq and RNA-seq experiments, animals were treated with 5 μ g E2 or vehicle on P0 and collected 4 h later (ER α CUT&RUN) or 4 days later (ATAC-seq and nuclear

RNA-seq). For neonatal multiome, snRNA-seq and IF quantification, animals were collected on P4 (multiome) or P14 (multiome, snRNA-seq and IF staining).

Cell lines

Cell lines include mHypoA clu-175 clone (Cedarlane Labs) and MCF-7 (ATCC). Cell lines were not tested for mycoplasma contamination. Cells were maintained in standard DMEM supplemented with 10% FBS and penicillin/streptomycin. Before CUT&RUN, MCF7 cells were grown in phenol-red-free DMEM medium containing 10% charcoal-stripped FBS and penicillin/streptomycin for 48 h and then treated with 20 nM 17- β -oestradiol or vehicle (0.002% ethanol) for 45 min.

Adult RNA-seq and in situ hybridization

Experiments were performed as previously described⁵⁵. Briefly, the BNSTp was microdissected following rapid decapitation of deeply anaesthetized adult *Esr1*^{Cre/+}; *Rpl22*^{HA/+} mice. Tissue homogenization, immunoprecipitation and RNA extraction were performed, and libraries were prepared from four biological replicate samples (each consisting of 8–9 pooled animals) using NuGEN Ovation RNA-Seq kits (7102 and 0344). Multiplexed libraries were sequenced with 76-bp single-end reads on the Illumina NextSeq. Validation by in situ hybridization staining and quantification was performed by an investigator blinded to experimental condition, as previously described^{16,55}. Riboprobe sequences are listed in Extended Data Table 1.

Isolation of nuclei from adult mice for ATAC-seq

Adult *Esr1*^{Cre/+}; *Sun1-GFP*^{lx/+} mice (four pooled per condition) were deeply anaesthetized with ketamine/dexmedetomidine. Sections of 500 μ m spanning the BNSTp were collected in an adult mouse brain matrix (Kent Scientific) on ice. The BNSTp was microdissected and collected in 1 ml of cold supplemented homogenization buffer (250 mM sucrose, 25 mM KCl, 5 mM MgCl₂, 120 mM tricine-KOH, pH 7.8), containing 1 mM dithiothreitol, 0.15 mM spermine, 0.5 mM spermidine and 1× EDTA-free PIC (Sigma

Aldrich 11873580001). The tissue was dounce homogenized 15 times in a 1-ml glass tissue grinder (Wheaton) with a loose pestle. Next, 0.3% IGEPAL CA-630 was added, and the suspension was homogenized five times with a tight pestle. The homogenate was filtered through a 40- μ m strainer and then centrifuged at 500g for 15 min at 4 °C. The pellet was resuspended in 0.5 ml homogenization buffer containing 1 mM dithiothreitol, 0.15 mM spermine, 0.5 mM spermidine and 1× EDTA-free PIC. A total of 30,000 GFP⁺ nuclei were collected into cold ATAC-RSB (10 mM Tris-HCl pH 7.5, 10 mM NaCl, 3 mM MgCl₂) using the Sony SH800S Cell Sorter (purity mode) with a 100- μ m sorting chip. After sorting, 0.1% Tween-20 was added, and the nuclei were centrifuged at 500g for 5 min at 4 °C. The pellet of nuclei was directly resuspended in transposition reaction mix.

ATAC-seq library preparation

Tn5 transposition was performed using the OMNI-ATAC protocol⁵⁶. A 2.5 μ l volume of Tn5 enzyme (Illumina 20034197) was used in the transposition reaction. Libraries were prepared with NEBNext High-Fidelity 2× PCR Master Mix (NEB M0541L), following the standard protocol. After the initial five cycles of amplification, another four cycles were added, on the basis of qPCR optimization. Following amplification, libraries were size selected (0.5 \times –1.8 \times) twice with AMPure XP beads (Beckman Coulter A63880) to remove residual primers and large genomic DNA. Individually barcoded libraries were multiplexed and sequenced with paired-end 76-bp reads on an Illumina NextSeq, using either the Mid or High Output Kit.

Cell line CUT&RUN

To collect cells for CUT&RUN, cells were washed twice with Hank's buffered salt solution (HBSS) and incubated for 5 min with pre-warmed 0.5% trypsin-EDTA (10 \times) at 37 °C/5% CO₂. Trypsin was inactivated with DMEM supplemented with 10% FBS and penicillin/streptomycin (mHypoA cells) or phenol-red-free DMEM supplemented with 10% charcoal-stripped FBS and penicillin/streptomycin (MCF-7 cells). After trypsinizing, cells were centrifuged at 500g in a 15-ml conical tube and resuspended in fresh medium. CUT&RUN was performed as previously described¹⁴, with minor modifications. Cells were washed twice in wash buffer (20 mM HEPES, pH

7.5, 150 mM NaCl, 0.5 mM spermidine, 1× PIC, 0.02% digitonin). Cell concentration was measured on a Countess II FL Automated Cell Counter (Thermo Fisher). A total of 25,000 cells were used per sample. Cells were bound to 20 µl concanavalin A beads (Bangs Laboratories, BP531), washed twice in wash buffer, and incubated overnight with primary antibody (ER α : Santa Cruz sc-8002 or EMD Millipore Sigma 06-935, Nfix: Abcam ab101341) diluted 1:100 in antibody buffer (wash buffer containing 2 mM EDTA). The following day, cells were washed twice in wash buffer, and 700 ng ml $^{-1}$ protein A-MNase (pA-MNase, prepared in-house) was added. After 1 h incubation at 4 °C, cells were washed twice in wash buffer and placed in a metal heat block on ice. pA-MNase digestion was initiated with 2 mM CaCl₂. After 90 min, digestion was stopped by mixing 1:1 with 2× stop buffer (340 mM NaCl, 20 mM EDTA, 4 mM EGTA, 50 µg ml $^{-1}$ RNase A, 50 µg ml $^{-1}$ glycogen, 0.02% digitonin). Digested fragments were released by incubating at 37 °C for 10 min, followed by centrifuging at 16,000g for 5 min at 4 °C. DNA was purified from the supernatant by phenol–chloroform extraction, as previously described¹⁴.

Adult brain CUT&RUN

Nuclei were isolated from microdissected POA, BNSTp and MeAp from gonadectomized C57Bl6/J mice, following anatomic designations⁵⁷ (Fig. 1a), as described previously⁵². Following tissue douncing, brain homogenate was mixed with a 50% OptiPrep solution and underlaid with 4.8 ml of 30% then 40% OptiPrep solutions, in 38.5-ml Ultra-clear tubes (Beckman-Coulter C14292). Ultracentrifugation was performed with a Beckman SW-28 swinging-bucket rotor at 9,200 r.p.m. for 18 min at 4 °C. Following ultracentrifugation, an \approx 1.5-ml suspension of nuclei was collected from the 30/40% OptiPrep interface by direct tube puncture with a 3-ml syringe connected to an 18-gauge needle. Nucleus concentration was measured on a Countess II FL Automated Cell Counter. For ER α CUT&RUN (1:100, EMD Millipore Sigma 06-935), 400,000 nuclei were isolated from BNST, MPOA and MeA of five animals. For Nfix CUT&RUN (1:100, Abcam ab101341), 200,000 nuclei were isolated from BNSTp of five animals. A total of 400,000 cortical nuclei were used for the CUT&RUN IgG control (1:100, Antibodies-Online ABIN101961). Before bead binding, 0.4% IGEPAL CA-630 was added to the nucleus suspension to increase affinity for

concanavalin A magnetic beads. All subsequent steps were performed as described above, with a modified wash buffer (20 mM HEPES, pH 7.5, 150 mM NaCl, 0.1% BSA, 0.5 mM spermidine, 1× PIC).

CUT&RUN library preparation

Cell line CUT&RUN libraries were prepared using the SMARTer ThruPLEX DNA-seq Kit (Takara Bio R400676), with the following PCR conditions: 72 °C for 3 min, 85 °C for 2 min, 98 °C for 2 min, (98 °C for 20 s, 67 °C for 20 s, 72 °C for 30 s) × 4 cycles, (98 °C for 20 s, 72 °C for 15 s) × 14 cycles (MCF7) or 10 cycles (mHypoA). Brain CUT&RUN libraries were prepared using the same kit with 10 PCR cycles. All samples were size selected with AMPure XP beads (0.5×–1.7×) to remove residual adapters and large genomic DNA. Individually barcoded libraries were multiplexed and sequenced with paired-end 76-bp reads on an Illumina NextSeq, using either the Mid or High Output Kit. For the mHypoA experiment, samples were sequenced with paired-end 25-bp reads on an Illumina MiSeq.

Nfix immunofluorescence staining

Brains were dissected from perfused P14 *Esr1*^{Cre/+}; *Sun1*–*GFP*^{lx/+} animals and cryosectioned at 40 µm before immunostaining with primary antibodies to GFP (1:1,000, Aves GFP-1020) and Nfix (1:1,000, Thermo Fisher PA5-30897), and secondary antibodies against chicken (1:300, Jackson Immuno 703-545-155) and rabbit (1:800, Jackson Immuno 711-165-152), as previously described¹⁶. A Zeiss Axioimager M2 System equipped with MBF Neurolucida Software was used to take 20× wide-field image stacks spanning the BNSTp (five sections, both sides). The number of Nfix⁺, GFP⁺ and Nfix⁺GFP⁺ cells was quantified using Fiji/ImageJ from the centre three optical slices by an investigator blinded to condition.

Neonatal bulk ATAC-seq

Female and male *Esr1*^{Cre/+}; *Sun1*–*GFP*^{lx/+} mice were injected subcutaneously with 5 µg E2 or vehicle on P0 and collected on P4 (4–5 animals pooled per condition and per replicate). The BNSTp was microdissected, as described above, and collected in 300 µl of cold,

supplemented homogenization buffer. Nuclei were extracted as described for the adult brain. After filtering through a 40- μ m strainer, the nuclei were diluted 3:1 with 600 μ l of cold, supplemented homogenization buffer and immediately used for sorting. A total of 30,000 GFP $^+$ nuclei were collected into cold ATAC-RSB buffer using the Sony SH800S Cell Sorter (purity mode) with a 100- μ m sorting chip. After sorting, nuclei transposition and library preparation were performed, as described above.

P0 ER α CUT&RUN

Female *Esr1*^{Cre/+}; *Sun1*-GFP $^{lx/+}$ mice were injected subcutaneously with 5 μ g E2 or vehicle on P0 and collected 4 h later (5 animals pooled per condition and per replicate). The BNSTp, MPOA and MeA were microdissected, and nuclei were extracted, as described for the neonatal bulk ATAC-seq experiment. After filtering through a 40- μ m strainer, the nuclei were diluted 3:1 with 600 μ l of cold, supplemented homogenization buffer. A 2 mM concentration of EDTA was added, and the sample was immediately used for sorting. A total of 150,000 GFP $^+$ nuclei were collected into cold CUT&RUN wash buffer using the Sony SH800S Cell Sorter (purity mode) with a 100- μ m sorting chip. GFP $^-$ events were collected into cold CUT&RUN wash buffer, and 150,000 nuclei were subsequently counted on the Countess II FL Automated Cell Counter for ER α - and IgG negative-control CUT&RUN. All subsequent steps were performed as described for the adult brain CUT&RUN experiments. P0 CUT&RUN libraries were prepared with 10 PCR cycles.

Neonatal single-nucleus multiome sequencing

The BNST was microdissected fresh from P4 and P14 female and male *Esr1*^{Cre/+}; *Sun1*-GFP $^{lx/+}$ mice, as described above (4–5 animals pooled per condition). Nuclei were extracted and prepared for sorting, as performed for the neonatal bulk ATAC-seq experiment, with the inclusion of 1 U μ l $^{-1}$ Protector RNase inhibitor (Sigma) in the homogenization buffer. A total of 40,000–50,000 GFP $^+$ nuclei were collected into 1 ml of cold ATAC-RSB buffer, supplemented with 0.1% Tween-20, 0.01% digitonin, 2% sterile-filtered BSA (Sigma A9576) and 1 U μ l $^{-1}$ Protector RNase inhibitor. The

nuclei were centrifuged in a swinging-bucket rotor at 500g for 10 min at 4 °C. About 950 µl of supernatant was carefully removed, and 200 µl 10x Genomics dilute nuclei buffer was added to the side of the tube without disturbing the pellet. The nuclei were centrifuged again at 500g for 10 min at 4 °C. About 240 µl of supernatant was carefully removed, and the nuclei were resuspended in the remaining volume (about 7 µl). Samples were immediately used for the 10x Genomics Single Cell Multiome ATAC + Gene Expression kit (1000285), following the manufacturer's instructions. snRNA-seq and snATAC-seq libraries were sequenced on an Illumina NextSeq, using the High Output kit. Each sample was sequenced to a depth of about 40,000–80,000 mean reads per cell for the snATAC library and about 40,000–50,000 mean reads per cell for the snRNA library.

P14 snRNA-seq

The BNSTp was microdissected from P14 female and male *Vgat*^{Cre}; *Esr1*^{+/+}; *Sun1*–*GFP*^{lx} and male *Vgat*^{Cre}; *Esr1*^{lx/lx}; *Sun1*–*GFP*^{lx} mice. Tissue samples from individual animals were immediately flash frozen in an ethanol dry-ice bath and stored at –80 °C until $n = 3$ animals were collected per group. On the day of the experiment, tissue samples were removed from –80 °C and maintained on dry ice. With the tissue still frozen, cold, supplemented homogenization buffer was added to the tube, and the tissue was immediately transferred to a glass homogenizer and mechanically dounced and filtered, as described for our other neonatal experiments. A total of 80,000–90,000 GFP⁺ nuclei were collected into 100 µl of cold ATAC-RSB buffer, supplemented with 1% sterile-filtered BSA (Sigma A9576), and 1 U µl^{–1} Protector RNase inhibitor, in a 0.5-ml DNA lo-bind tube (Eppendorf) pre-coated with 30% BSA. After collection, nuclei were pelleted with two rounds of gentle centrifugation (200g for 1 min) in a swinging-bucket centrifuge at 4 °C. After the second round, the supernatant was carefully removed, leaving about 40 µl in the tube. The nuclei were gently resuspended in this remaining volume and immediately used for the 10x Genomics Single Cell 3' Gene Expression kit v3 (1000424), following the manufacturer's instructions. Each biological sample was split into two 10× lanes, producing 6 libraries that were pooled and sequenced on an Illumina NextSeq 2000 to a depth of about 45,000–60,000 mean reads per cell.

Neonatal nuclear RNA-seq

Female *Esr1*^{Cre/+}; *Sun1-GFP*^{lx/+} mice were injected subcutaneously with 5 µg E2 or vehicle on P0. Four days later, animals were rapidly decapitated, and 400-µm sections were collected in cold homogenization buffer using a microtome (Thermo Scientific Microm HM 650V). The BNST was microdissected (4 animals pooled per condition) and collected in 1 ml of cold, supplemented homogenization buffer containing 0.4 U ml⁻¹ RNaseOUT (Thermo Fisher, 10777019). Nuclei were isolated as described for neonatal bulk ATAC-seq. A total of 12,000 GFP⁺ nuclei were collected into cold Buffer RLT Plus supplemented 1:100 with β-mercaptoethanol (Qiagen, 74034) using the Sony SH800S Cell Sorter (purity mode) with a 100-µm sorting chip. Nuclei lysates were stored at -80 °C until all replicates were collected. Nuclei samples for all replicates were thawed on ice, and RNA was isolated using the Qiagen RNeasy Plus Micro Kit (74034). Strand-specific RNA-seq libraries were prepared using the Ovation SoLo RNA-seq system (Tecan Genomics, 0501-32), following the manufacturer's guidelines. Individually barcoded libraries were multiplexed and sequenced with single-end 76-bp reads on an Illumina NextSeq, using the Mid Output Kit.

Bioinformatics and data analysis

CUT&RUN data processing

Paired-end reads were trimmed to remove Illumina adapters and low-quality basecalls (cutadapt -q 30)⁵⁸. Trimmed reads were aligned to mm10 using Bowtie2 (ref. ⁵⁹) with the following flags:--dovetail--very-sensitive-local--no-unal--no-mixed--no-discordant--phred33. Duplicate reads were removed using Picard (<http://broadinstitute.github.io/picard/>) MarkDuplicates (REMOVE_DUPLICATES = true). Reads were filtered by mapping quality⁶⁰ (samtools view -q 40) and fragment length⁶¹ (deepTools alignmentSieve --maxFragmentLength 120). Reads aligning to the mitochondrial chromosome and incomplete assemblies were also removed using SAMtools. After filtering, peaks were called on individual replicate BAM files using MACS2 callpeak (--min-length 25 -q 0.01)⁶². To identify

consensus Nfix peaks across samples, MACS2 callpeak was performed on BAM files merged across biological replicates ($n = 2$) and subsequently intersected across treatment and sex. TF peaks that overlapped peaks called in the IgG control were removed using bedtools intersect (-v)⁶³ before downstream analysis.

CUT&RUN data analysis

CUT&RUN differential peak calling was performed with DiffBind v2.10.0(ref. ⁶⁴). A count matrix was created from individual replicate BAM and MACS2 narrowpeak files ($n = 2$ per condition). Consensus peaks were recentred to ± 100 bp around the point of highest read density (summits = 100). Contrasts between sex and treatment were established (categories = c(DBA_TREATMENT, DBA_CONDITION)), and edgeR ⁶⁵ was used for differential peak calling. Differential ER α peaks with $P_{adj} < 0.1$ were used for downstream analysis. For Nfix, differential peaks with a $P_{adj} < 0.1$ and $\text{abs}(\log_2[\text{FC}]) > 1$ were used for downstream analysis. Differential peak calling for the MCF-7 CUT&RUN experiment was performed with DESeq2 ($P_{adj} < 0.1$) in DiffBind. Differential peak calling for the P0 ER α CUT&RUN experiment was performed with DESeq2 ($P_{adj} < 0.01$) in DiffBind. To identify sex-dependent, oestradiol-responsive peaks for adult brain ER α CUT&RUN, the DiffBind consensus peakset count matrix was used as input to edgeR, and an interaction between sex and treatment was tested with glmQLFTest.

Brain E2-induced ER α CUT&RUN peaks were annotated to NCBI RefSeq mm10 genes using ChIPseeker⁶⁶. DeepTools plotHeatmap was used to plot ER α CUT&RUN (Fig. ^{1b}), representing CPM-normalized bigwig files pooled across replicate and sex per condition, at E2-induced ER α peaks. Heatmaps of individual ER α CUT&RUN replicates are shown in Extended Data Fig. ². CUT&RUNTools ⁶⁷ was used to plot ER α CUT&RUN fragment ends surrounding ESR1 motifs (JASPAR MA0112.3) in E2-induced ER α ChIP-seq peaks. BETA (basic mode, -d 500000)⁶⁸ was used to determine whether ER α peaks were significantly overrepresented at E2-regulated RNA-seq genes ($P < 0.01$), as well as sex-dependent E2-regulated genes ($P < 0.01$), compared to non-differential, expressed genes. Motif enrichment

analysis of ER α peaks was performed with AME⁶⁹ using the 2020 JASPAR core non-redundant vertebrate database. Motif enrichment analysis was performed using a control file consisting of shuffled primary sequences that preserves the frequency of k -mers (--control --shuffle--). The following seven ER α ChIP-seq files were lifted over to mm10 using UCSC liftOver and intersected with E2-induced ER α peaks to identify brain-specific and shared (≥ 4 intersections) ER α -binding sites: uterus (intersection of GEO: [GSE36455](#) (uterus 1)⁷⁰ and GEO: [GSE49993](#) (uterus 2)⁷¹), liver (intersection of GEO: [GSE49993](#) (liver 1)⁷¹ and GEO: [GSE52351](#) (liver 2)⁷²), aorta⁷² (GEO: [GSE52351](#)), efferent ductules⁷³ (Supplementary Information) and mammary gland⁷⁴ (GEO: [GSE130032](#)). ClusterProfiler⁷⁵ was used to identify associations between brain-specific and shared ER α peak-annotated genes and Gene Ontology (GO) biological process terms (enrichGO, ont = 'BP', $P_{adj} < 0.1$). For Disease Ontology (DO) and HUGO Gene Nomenclature Committee (HGNC) gene family enrichment, brain-specific ER α peak-associated gene symbols were converted from mouse to human using bioMart⁷⁶ and then analysed with DOSE⁷⁷; enrichDO, $P_{adj} < 0.1$ and enricher ($P_{adj} < 0.1$). Log-odds ESR1 and ESR2 motif scores in brain-specific and shared ER α peaks were calculated with FIMO⁷⁸, using default parameters.

MCF7 ER α CUT&RUN data were compared to MCF7 ER α ChIP-seq data from ref. ⁷⁹ (GEO: [GSE59530](#)). Single-end ChIP-seq fastq files for two vehicle-treated and two 17 β -oestradiol (E2)-treated IP and input samples were accessed from the Sequence Read Archive and processed identically to ER α CUT&RUN data, with the exception of fragment size filtering. Differential ER α ChIP-seq peak calling was performed using DiffBind DESeq2 ($P_{adj} < 0.01$). DeepTools was used to plot CPM-normalized ER α CUT&RUN signal at E2-induced ER α ChIP-seq binding sites. DREME⁸⁰ and AME were used to compare de novo and enriched motifs between E2-induced MCF7 ER α CUT&RUN and ChIP-seq peaks.

Adult RNA-seq data processing and analysis

Reads were adapter trimmed and quality filtered ($q > 30$) (http://hannonlab.cshl.edu/fastx_toolkit/), and then mapped to the mm10

reference genome using STAR⁸¹. The number of reads mapping to the exons of each gene was counted with featureCounts⁸², using the NCBI RefSeq mm10 gene annotation. Differential gene expression analysis was performed using DESeq2 (ref. ⁸³) with the following designs: effect of treatment (design = ~ batch + hormone), effect of sex (design = ~ batch + sex), two-way comparison of treatment and sex (design = ~ batch + hormone_sex), four-way comparison (design = ~ 0 + hormone_sex) and sex–treatment interaction (design = ~ batch + sex + hormone + sex:hormone).

ATAC–seq data processing

ATAC–seq data were processed using the ENCODE ATAC–seq pipeline (<https://github.com/ENCODE-DCC/atac-seq-pipeline>) with default parameters. To generate CPM-normalized bigwig tracks, quality-filtered, Tn5-shifted BAM files were converted to CPM-normalized bigwig files using DeepTools bamCoverage (--binSize 1 --normalizeUsing CPM).

Adult GDX treatment ATAC–seq data analysis

ATAC–seq differential peak calling was performed with DiffBind v2.10.0. A DiffBind dba object was created from individual replicate BAM and MACS2 narrowPeak files ($n = 3$ per condition). A count matrix was created with dba.count, and consensus peaks were recentred to ± 250 bp around the point of highest read density (summits = 250). Contrasts between sex and treatment were established (categories = c(DBA_TREATMENT, DBA_CONDITION)), and edgeR was used for differential peak calling. Differential peaks with an FDR < 0.05 and $\text{abs}(\log_2[\text{FC}]) > 1$ or $\text{abs}(\log_2[\text{FC}]) > 0$ were used for downstream analysis. DeepTools computeMatrix and plotHeatmap were used to plot mean ATAC CPM at E2-open ATAC peaks. To identify sex-dependent, oestradiol-responsive peaks, the DiffBind consensus peakset count matrix was used as input to edgeR, and an interaction between sex and treatment was tested with glmQLFTest. E2-open ATAC peaks and total vehicle or E2 ATAC peaks (intersected across replicate and sex for each treatment condition) were annotated to NCBI RefSeq mm10 genes using Chipseeker. ClusterProfiler was used to calculate the enrichment of GO biological process terms, DO and HGNC

gene family enrichment was performed on E2-open ATAC peak-associated genes, as described above for ER α CUT&RUN analysis. BETA (basic mode, -d 500000)⁶⁸ was used to determine whether E2-open ATAC peaks were significantly overrepresented at E2-regulated RNA-seq genes ($P < 0.01$), as well as sex-dependent E2-regulated genes ($P < 0.01$), compared to non-differential, expressed genes. Motif enrichment analysis of E2-open ATAC peaks was performed with AME, using the 2020 JASPAR core non-redundant vertebrate database. FIMO was used to determine the percentage of E2-open ATAC peaks containing the enriched motifs shown in Extended Data Fig. 4h,i.

Adult gonadally intact ATAC-seq analysis

ATAC-seq differential peak calling and comparison between gonadally intact (abbreviated as intact) and GDX ATAC samples were performed with DiffBind v2.10.0 and edgeR. A DiffBind dba object was created from individual replicate BAM and MACS2 narrowPeak files for the four groups: female intact ($n = 2$), male intact ($n = 2$), female GDX vehicle treated ($n = 3$), male GDX vehicle treated ($n = 3$). A count matrix was created with dba.count, and consensus peaks were recentred to ± 250 bp around the point of highest read density (summits = 250). The consensus peakset count matrix was subsequently used as input to edgeR. Differential peaks ($\text{abs}(\log_2[\text{FC}]) > 1$, $P_{\text{adj}} < 0.05$) were calculated between female intact and male intact and between female GDX vehicle treated and male GDX vehicle -treated groups using glmQLFTest. BETA was used to assess statistical association between gonadally intact, sex-biased ATAC peaks and sex DEGs called in BNSTp *Esr1*+ snRNA-seq clusters (top 500 genes per cluster, ranked by P_{adj}). Sex DEGs ranked by ATAC regulatory potential score⁶⁸, a metric that reflects the number of sex-biased peaks and distance of sex-biased peaks to the TSS, are shown in Extended Data Fig. 7g. HGNC gene family enrichment was performed on sex DEGs, using a background of expressed genes in any of the seven BNSTp *Esr1*+ clusters.

To identify differential peaks across the four conditions, an ANOVA-like design was created in edgeR by specifying multiple coefficients in glmQLFTest (coefficient = 2:4). A matrix of normalized counts in these

differential peaks ($P_{\text{adj}} < 0.01$) was clustered using k -means clustering (kmeans function in R), with $k = 4$ and iter.max = 50. For each k -means cluster, the cluster centroid was computed, and outlier peaks in each cluster were excluded on the basis of having low Pearson's correlation with the cluster centroid ($R < 0.8$). Depth-normalized ATAC CPM values in these peak clusters are shown in Fig. 2i (mean across biological replicates per group) and Extended Data Fig. 7 (individual biological replicates). Peak cluster overlap with E2-open ATAC loci ($\text{abs}(\log_2[\text{FC}]) > 0$, $P_{\text{adj}} < 0.05$) was computed with bedtools intersect (-wa). For each peak cluster, motif enrichment analysis was performed by first generating a background peak list (matching in GC content and accessibility) from the consensus ATAC peak matrix using chromVAR (addGCBias, getBackgroundPeaks)⁸⁴, and then calculating enrichment with AME using the background peak list as the control (--control background peaks). In Fig. 2i, the JASPAR 2020 AR motif (MA0007.3) is labelled as ARE, and the ESR2 motif (MA0258.2) is labelled as ERE.

Adult snRNA-seq and single-cell RNA-seq analysis

Mouse BNST snRNA-seq data containing 76,693 neurons across 7 adult female and 8 adult male biological replicates²⁶ were accessed from GEO: [GSE126836](#) and loaded into a Seurat object⁸⁵. Mouse MPOA single-cell RNA-seq data containing 31,299 cells across 3 adult female and 3 adult male biological replicates³² were accessed from GEO: [GSE113576](#) and loaded into a Seurat object. Cluster identity, replicate and sex were added as metadata features to each Seurat object. Pseudo-bulk RNA-seq analysis was performed to identify sex differences in gene expression in the BNST snRNA-seq dataset. Briefly, the Seurat object was converted to a SingleCellExperiment object (as.SingleCellExperiment). Genes were filtered by expression (genes with >1 count in ≥ 5 nuclei). NCBI-predicted genes were removed. For each cluster, nuclei annotated to the cluster were subsetted from the main Seurat object. Biological replicates containing ≤ 20 nuclei in the subsetted cluster were excluded. Gene counts were summed for each biological replicate in each cluster. Differential gene expression analysis across sex in each cluster was performed on the filtered, aggregated count matrix using DESeq2 (design = ~ sex) with alpha = 0.1. The

BNSTp_Cplx3 cluster was excluded, as none of the replicates in this cluster contained more than 20 nuclei. Clusters containing $\geq 25\%$ nuclei with ≥ 1 *Esr1* counts in the main Seurat object were classified as *Esr1+* (i1:Nfix, i2:Tac2, i3:Esr2, i4:Bnc2, i5:Haus4, i6:Epsti1, i7:Nxph2, i8:Zeb2, i9:Th, i10:Synpo2, i11:C1ql3, i12:Esr1, i13:Avp, i14:Gli3). To identify TFs that correlate with sex DEG number per cluster (Fig. 2g), a linear regression model with percentage of TF expression as the predictor variable and sex DEG number per cluster as the response variable was generated using the lm function in R stats (formula = percentage of TF expression ~ DEG number). This model was tested for all TFs in the SCENIC⁸⁶ mm10 database. All TFs were then ranked by R^2 to identify those most predictive of sex DEG number, and the ranked R^2 values are shown in Fig. 2g.

To visualize BNSTp *Esr1+* snRNA-seq data (Fig. 2a), BNSTp *Esr1+* clusters were subsetted from the main Seurat object. Gene counts were normalized and log transformed (LogNormalize), and the top 2,000 variable features were identified using FindVariableFeatures (selection.method = vst). Gene counts were scaled, and linear dimensionality reduction was performed by principal component analysis (runPCA, ncs = 10). BNSTp *Esr1+* clusters were visualized with UMAP (runUMAP, dims = 10). To generate the heatmaps in Extended Data Fig. 7a, pseudo-bulk counts for each biological replicate included in the analysis were normalized and transformed with variance-stabilizing transformation (DESeq2 vst), subsetted for sex-biased genes in each cluster, and z-scaled across pseudo-bulk replicates.

To examine differential abundance of BNSTp *Esr1+* clusters between sexes (Fig. 2b), the proportion of total nuclei in each BNSTp *Esr1+* cluster was calculated for each biological replicate. After calculating the proportions of nuclei, sample MALE6 was excluded as an outlier for having no detection (0 nuclei) of i1:Nfix and i2:Tac2 clusters and overrepresentation of the i5:Haus4 cluster. The one-sided Wilcoxon rank-sum test (wilcox.test in R stats) was used to test for male-biased abundance of nuclei across biological replicates in each cluster. P values were adjusted for multiple hypothesis testing using the Benjamini–Hochberg procedure (method = fdr).

To identify marker genes enriched in the i1:Nfix cluster relative to the remaining six BNSTp *Esr1+* clusters (Extended Data Fig. 6b), differential gene expression analysis was performed using DESeq2 with design = ~

cluster_id (betaPrior = TRUE), alpha = 0.01, lfcThreshold = 2, altHypothesis = greater.

To identify the enrichment of *Lamp5*+ subclass markers in BNSTp and MPOA *Esr1*+ clusters (Extended Data Fig. 6e), a Seurat object was created from the Allen Brain Atlas Cell Types dataset. Gene counts per cell were normalized and log transformed (LogNormalize), and subclass-level marker genes were calculated with the Wilcoxon rank-sum test (FindAllMarkers, test.use = wilcox, min.diff.pct = 0.2). The mean expression of *Lamp5*+ subclass markers ($\text{avg_log[FC]} > 0.75$, $P_{\text{adj}} < 0.05$, <40% in non-*Lamp5*+ subclasses) was calculated in BNSTp and MPOA *Esr1*+ clusters and visualized using pheatmap.

To generate the UMAP plots shown in Extended Data Fig. 6g, BNSTp *Esr1*+ clusters were integrated with MPOA/BNST *Esr1*-expressing clusters (e3: Cartpt_Isl1, i18: Gal_Tac2, i20: Gal_Moxd1, i28: Gaba_Six6, i29: Gaba_Igfsf1, i38: Kiss1_Th) using Seurat. Anchors were identified between cells from the two datasets, using FindIntegrationAnchors. An integrated expression matrix was generated using IntegrateData (dims = 1:10). The resulting integrated matrix was used for downstream PCA and UMAP visualization (dims = 1:10).

MetaNeighbor analysis

MetaNeighbor²⁸ was used to quantify the degree of similarity between BNSTp *Esr1*+ clusters and MPOA *Esr1*+ clusters and between BNSTp *Esr1*+ clusters and cortical/hippocampal GABAergic neuron subclasses from the Allen Brain Atlas Cell Types database²⁹. Briefly, the BNST and MPOA Seurat objects were subsetted for *Esr1*+ clusters, and then transformed and merged into one SingleCellExperiment object. For the BNSTp and cortex comparison, BNSTp *Esr1*+ clusters were merged into a SingleCellExperiment with cortical/hippocampal GABAergic cortical clusters. Unsupervised MetaNeighbor analysis was performed between BNST and MPOA clusters, and between BNST and cortical/hippocampal clusters, using highly variable genes identified across datasets (called with the variableGenes function). The median AUROC value per

cortical/hippocampal GABAergic subclass across Allen Brain Atlas datasets for each BNSTp *Esr1*⁺ cluster is shown in Fig. 2d.

Neonatal bulk ATAC–seq analysis

Differential peak calling on the neonatal bulk ATAC–seq experiment was performed with DiffBind v2.10.0 and edgeR. A count matrix was created from individual replicate BAM and MACS2 narrowpeak files ($n = 3$ per condition). Consensus peaks were recentred to ± 250 bp around the point of highest read density (summits = 250), and the consensus peakset count matrix was subsequently used as input to edgeR. Differential peaks across the three treatment groups (NV female, NV male, NE female) were calculated by specifying multiple coefficients in glmQLFTTest (coefficient = 4:5). To identify accessibility patterns across differential peaks ($P_{\text{adj}} < 0.05$), a matrix of normalized counts in differential peaks was hierarchically clustered using pheatmap, and the resulting dendrogram tree was cut with $k = 6$ to achieve 6 peak clusters (Extended Data Fig. 8a). The two largest clusters were identified as having higher accessibility in NV males and NE females compared to NV females (cluster 3, labelled as NE open), or lower accessibility in NV male and NE female compared to NV females (cluster 5, labelled as NE close). Motif enrichment analysis of NE-open peaks was performed with AME using the 2020 JASPAR core non-redundant vertebrate database. GO biological process, DO and HGNC gene family enrichment analyses were performed, as described above for adult GDX treatment ATAC–seq data analysis.

Neonatal single-nucleus multiome data processing and analysis

Raw sequencing data were processed using the Cell Ranger ARC pipeline (v2.0.0) with the cellranger-arc mm10 reference. Default parameters were used to align reads, count unique fragments or transcripts, and filter high-quality nuclei. Individual HDF5 files for each sample containing RNA counts and ATAC fragments per cell barcode were loaded into Seurat (Read10X_h5). Nuclei with lower-end ATAC and RNA QC metrics (<1,000 ATAC fragments, <500 counts, nucleosomal signal > 3, TSS enrichment < 2) were removed. DoubletFinder⁸⁷ was then used to remove predicted doublets from each sample (nExp = 9% of nuclei per sample). Following doublet

removal, nuclei surpassing upper-end ATAC and RNA QC metrics (>60,000 ATAC fragments, >20,000 RNA counts, >6,000 genes detected) were removed. After filtering, Seurat objects for each sample were subsetted for the RNA assay and merged. Gene counts were normalized and log transformed (LogNormalize), and the top 2,000 variable features were identified using FindVariableFeatures (selection.method = 'vst'). Gene counts were scaled, regressing out the following variables: number of RNA counts, number of RNA genes, percentage of mitochondrial counts and biological sex. Linear dimensionality reduction was performed by principal component analysis (runPCA, n pcs = 25). A k -nearest-neighbours graph was constructed on the basis of Euclidean distance in PCA space and refined (FindNeighbors, n pcs = 25), and then the nuclei were clustered using the Louvain algorithm (FindClusters, resolution = 0.8). snRNA clusters were visualized with UMAP (runUMAP, dims = 25). To reduce the granularity of clustering, a phylogenetic tree of cluster identities was generated from a distance matrix constructed in PCA space (BuildClusterTree) and visualized as a dendrogram (PlotClusterTree). DEGs between clusters in terminal nodes of the phylogenetic tree were calculated (FindMarkers, test.use = 'wilcox', $P_{adj} < 0.05$), and clusters were merged if they had fewer than 10 DEGs with the following parameters: >0.5 avg_log[FC], <10% expression in negative nuclei, and >25% expression in positive nuclei. The final de novo snRNA-seq clusters are shown in Extended Data Fig. [10c](#).

Inhibitory neuron clusters (*Slc32a1/Gad2+*) from the neonatal multiome dataset were subsequently assigned to adult BNST *Esr1*+ cluster labels using Seurat. Adult BNST *Esr1*+ clusters (as defined above) were subsetted from the adult snRNA-seq object and randomly downsampled to 5,000 nuclei. Normalization, data scaling and linear dimensionality reduction were performed with the same parameters as for neonatal and adult *Esr1*+ inhibitory neuron clusters. Anchor cells between adult (reference) and neonatal (query) datasets were first identified using FindTransferAnchors. Reference cluster labels, as well as the corresponding UMAP structure, were subsequently transferred to the neonatal dataset using MapQuery. Prediction scores, which measure anchor consistency across the neighbourhood structure of reference and query datasets as previously described⁸⁵, were used to quantify the confidence of label transfer from adult to neonatal nuclei. Extended Data Fig. [10d](#) shows the prediction scores per reference

cluster and time point of nuclei mapped onto adult reference cluster labels as well as the percentage of nuclei from each de novo cluster mapped onto each adult reference cluster (prediction score > 0.5). To further validate the quality of label transfer between adult and neonatal datasets, we computed DEGs between neonatal clusters post label transfer (FindMarkers, test.use = 'wilcox', $P_{adj} < 0.05$, min.diff.pct = 0.1, avg_log[FC] > 0.5) and calculated their background-subtracted, average expression (AddModuleScore) in neonatal and adult BNST *Esr1*⁺ nuclei (visualized in Extended Data Fig. 10e).

To generate pseudo-bulk, normalized ATAC bigwig tracks for each snATAC cluster, we first re-processed the cellranger ARC output BAM file for each sample using SAMtools (-q 30 -f 2) and removed duplicate reads per cell barcode using picard MarkDuplicates (BARCODE_TAG=CB REMOVE_DUPLICATES = true). Sinto (<https://timoast.github.io/sinto/>) was used to split ATAC alignments for each cluster into individual BAM files using cell barcodes extracted from the Seurat object. CPM-normalized bigwig files were computed for each pseudo-bulk BAM file using DeepTools bamCoverage (--binSize 1--normalizeUsing CPM).

To analyse the neonatal multiome snATAC data, we used ArchR⁸⁸. Separate Arrow files were created for each multiome sample, and then merged into a single ArchR project. Gene activity scores per nucleus were calculated at the time of Arrow file creation (addGeneScoreMat = TRUE). Metadata (cluster label, sex, time and QC metrics) were transferred from the previously generated Seurat object to the ArchR project by cell barcode-matching. Dimensionality reduction was performed on the snATAC data using ArchR's iterative Latent Semantic Indexing approach (addIterativeLSI). Per-nucleus imputation weights were added using MAGIC⁸⁹ in ArchR (addImputeWeights) to denoise sparse ATAC data for UMAP visualization. Cluster-aware ATAC peak calling was performed using ArchR's iterative overlap peak merging approach (addReproduciblePeaks, groupBy = 'cluster'). Following peak calling, CISBP human motif annotations were added for each peak (addPeakAnnotation), and chromVAR deviation scores (addDeviationsMatrix) were calculated for each motif. In addition, chromVAR was used to calculate per-nucleus deviation scores for consensus BNSTp Nfix CUT&RUN peaks. To perform neuron identity regulator

analysis (Extended Data Fig. 10g), the correlation between TF RNA expression and motif deviation score was calculated for all TFs in the CISBP motif database (correlateMatrices). TFs with a correlation coefficient >0.5 and a maximum TF RNA $\log_2[FC]$ value between each cluster in the top 50% were classified as neuron identity regulators (coloured pink in Extended Data Fig. 10g).

For visualization of gene activity and CISBP motif deviation scores (Fig. 3c and Extended Data Fig. 10g), scores were imputed (imputeMatrix), transferred to the original Seurat object by cell barcode matching, and visualized using FeaturePlot. Signac⁹⁰ was used to generate and store peak-by-cell count matrices for each sample. snATAC markers for each cluster were calculated (FindAllMarkers, test.use = 'LR', vars.to.regress = 'nCount_ATAC', min.pct = 0.1, min.diff.pct = 0.05, logfc.threshold = 0.15). Pseudo-bulk snATAC cluster CPM was computed for each marker peak using DeepTools multiBigwigSummary and visualized with pheatmap (Extended Data Fig. 10f). Motif enrichment analysis of snATAC marker peaks for each cluster was performed using FindMotifs. The top three enriched motifs per snATAC cluster are shown in Extended Data Fig. 10f.

To identify sex-biased enrichment of NE-open loci across P4 snATAC clusters (Fig. 3d), we first filtered out low-abundance P4 snATAC clusters (<400 nuclei), and then computed the difference in ATAC CPM between males and females at NE-open loci in each cluster. Differential ATAC CPM values were scaled across clusters, then grouped using k -means clustering ($k = 12$, iter.max = 50) and visualized with pheatmap (Fig. 3d). To call sex DEGs ($P_{adj} < 0.05$) in each cluster and time point, we used MAST⁹¹ in Seurat (FindMarkers, test.use = 'MAST', min.pct = 0.05, logfc.threshold = 0.2, latent.vars = 'nFeature_RNA', 'nCount_RNA').

To link NE-regulated loci to sex DEGs at P4 and P14 (Fig. 3e and Extended Data Fig. 11h), we computed the Pearson correlation coefficient between sex DEG expression and NE-regulated peak accessibility for each cluster (LinkPeaks, min.distance = 2,000, distance = 1,000,000, min.cells = 2% of cluster size). Sex DEG $\log_2[FC]$ values and NE-regulated ATAC site correlation coefficients were hierarchically clustered and visualized using ComplexHeatmap⁹².

P14 snRNA-seq data processing and analysis

Raw sequencing data were processed using the Cell Ranger pipeline (v6.0.0) with the refdata-gex-mm10-2020-A reference. Default parameters were used to align reads, count unique transcripts and filter high-quality nuclei.

Individual HDF5 files for each sample were loaded into Seurat. Nuclei with lower-end RNA QC metrics (<1,000 counts) were removed.

DoubletFinder⁸⁷ was then used to remove predicted doublets from each sample ($n_{Exp} = 9\%$ of nuclei per sample). Following doublet removal, nuclei surpassing upper-end RNA QC metrics (>20,000 counts, >6,000 genes detected) were removed. After filtering, Seurat objects were merged. Gene counts were normalized and scaled, as described for the single-nucleus multiome data processing.

The P14 snRNA-seq dataset was assigned to adult BNST inhibitory cluster labels using Seurat. Adult BNST inhibitory clusters were subsetted from the adult snRNA-seq object and randomly downsampled to 10,000 nuclei. Normalization, data scaling and linear dimensionality reduction were performed with the same parameters for P14 and adult inhibitory neuron clusters. Label transfer was then performed as described for the single-nucleus multiome data processing. Extended Data Fig. [12b](#) shows the prediction scores of P14 nuclei mapped onto adult reference cluster labels. To validate the quality of label transfer between adult and P14 datasets, we computed DEGs between P14 clusters post label transfer, as described above, and calculated their background-subtracted, average expression (AddModuleScore) in P14 and adult BNST inhibitory clusters (shown in Extended Data Fig. [12c](#)). Sex DEGs between control females and control or conditional ERα KO males were calculated for each P14 cluster, as described above for the multiome analysis. Cluster abundance for each group was computed and is plotted in Extended Data Fig. [12d](#).

Neonatal bulk nuclear RNA-seq data processing and analysis

Reads were trimmed to remove Illumina adapters and low-quality basecalls (cutadapt -q 30), and then mapped to the mm10 reference genome using STAR. Technical duplicate reads (identical start and end positions with the same strand orientation and identical molecular identifiers) were removed

using the nudup.py python package (<https://github.com/tecangenomics/nudup>). The number of reads mapping to each gene (including introns) on each strand (-s 1) was calculated with featureCounts⁸², using the mm10.refGene.gtf file. Differential gene expression analysis was performed using DESeq2 (design = ~ treatment) after prefiltering genes by expression (rowMeans ≥ 5).

Reporting summary

Further information on research design is available in the [Nature Research Reporting Summary](#) linked to this paper.

Data availability

All sequencing data generated in this study have been deposited in GEO ([GSE144718](#)). The following publicly available datasets were also analysed: MCF7 ER α ChIP-seq ([GSE59530](#)), mouse liver ER α ChIP-seq ([GSE49993](#)), mouse liver ER α ChIP-seq ([GSE52351](#)), mouse uterus ER α ChIP-seq ([GSE36455](#)), mouse uterus ER α ChIP-seq dataset ([GSE49993](#)), mouse aorta ER α ChIP-seq ([GSE52351](#)), mouse mammary gland ER α ChIP-seq ([GSE130032](#)), BNST snRNA-seq ([GSE126836](#)), MPOA single-cell RNA-seq ([GSE113576](#)) and the Allen Brain Institute Cell Type Database (<https://portal.brain-map.org/atlas-and-data/rnaseq/mouse-whole-cortex-and-hippocampus-10x>). Source data are provided with this paper.

Code availability

Custom scripts can be found at
https://github.com/gegenhu/estrogen_gene_reg.

References

1. MacLusky, N. J. & Naftolin, F. Sexual differentiation of the central nervous system. *Science* **211**, 1294–1303 (1981).

2. McEwen, B. S. Neural gonadal steroid actions. *Science* **211**, 1303–1311 (1981).
3. McCarthy, M. M. Estradiol and the developing brain. *Physiol. Rev.* **88**, 91–124 (2008).
4. Wharton, W., Gleason, C. E., Olson, S. R. M. S., Carlsson, C. M. & Asthana, S. Neurobiological underpinnings of the estrogen - mood relationship. *Curr. Psychiatry Rev.* **8**, 247–256 (2012).
5. Mauvais-Jarvis, F., Clegg, D. J. & Hevener, A. L. The role of estrogens in control of energy balance and glucose homeostasis. *Endocr. Rev.* **34**, 309–338 (2013).
6. Galea, L. A. M., Frick, K. M., Hampson, E., Sohrabji, F. & Choleris, E. Why estrogens matter for behavior and brain health. *Neurosci. Biobehav. Rev.* **76**, 363–379 (2017).
7. Becker, J. B. & Chartoff, E. Sex differences in neural mechanisms mediating reward and addiction. *Neuropsychopharmacology* **44**, 166–183 (2019).
8. Krause, W. C. et al. Oestrogen engages brain MC4R signalling to drive physical activity in female mice. *Nature* **599**, 131–135 (2021).
9. Kumar, V. et al. Functional domains of the human estrogen receptor. *Cell* **51**, 941–951 (1987).
10. Clarkson, J. & Herbison, A. E. Hypothalamic control of the male neonatal testosterone surge. *Philos. Trans. R. Soc. B* **371**, 20150115 (2016).
11. Simerly, R. B. Wired for reproduction: organization and development of sexually dimorphic circuits in the mammalian forebrain. *Annu. Rev. Neurosci.* **25**, 507–536 (2002).
12. Li, Y. & Dulac, C. Neural coding of sex-specific social information in the mouse brain. *Curr. Opin. Neurobiol.* **53**, 120–130 (2018).

13. Wei, D., Talwar, V. & Lin, D. Neural circuits of social behaviors: innate yet flexible. *Neuron* **109**, 1600–1620 (2021).
14. Skene, P. J., Henikoff, J. G. & Henikoff, S. Targeted in situ genome-wide profiling with high efficiency for low cell numbers. *Nat. Protoc.* **13**, 1006–1019 (2018).
15. Hurtado, A., Holmes, K. A., Ross-Innes, C. S., Schmidt, D. & Carroll, J. S. FOXA1 is a key determinant of estrogen receptor function and endocrine response. *Nat. Genet.* **43**, 27–33 (2011).
16. Wu, M. V. & Tollkuhn, J. Estrogen receptor alpha is required in GABAergic, but not glutamatergic, neurons to masculinize behavior. *Horm. Behav.* **95**, 3–12 (2017).
17. Flanigan, M. E. & Kash, T. L. Coordination of social behaviors by the bed nucleus of the stria terminalis. *Eur. J. Neurosci.* <https://doi.org/10.1111/ejn.14991> (2020).
18. Gegenhuber, B. & Tollkuhn, J. Signatures of sex: sex differences in gene expression in the vertebrate brain. *Wiley Interdiscip. Rev. Dev. Biol.* **9**, e348 (2020).
19. Srivastava, D. P., Woolfrey, K. M. & Penzes, P. Insights into rapid modulation of neuroplasticity by brain estrogens. *Pharmacol. Rev.* **65**, 1318–1350 (2013).
20. Guertin, M. J., Zhang, X., Coonrod, S. A. & Hager, G. L. Transient estrogen receptor binding and p300 redistribution support a squelching mechanism for estradiol-repressed genes. *Mol. Endocrinol.* **28**, 1522–1533 (2014).
21. Xu, Y. et al. ER α is an RNA-binding protein sustaining tumor cell survival and drug resistance. *Cell* **184**, 5215–5229 (2021).
22. Allen, L. S. & Gorski, R. A. Sex difference in the bed nucleus of the stria terminalis of the human brain. *J. Comp. Neurol.* **302**, 697–706 (1990).

23. Hines, M., Allen, L. S. & Gorski, R. A. Sex differences in subregions of the medial nucleus of the amygdala and the bed nucleus of the stria terminalis of the rat. *Brain Res.* **579**, 321–326 (1992).
24. Wu, M. V. et al. Estrogen masculinizes neural pathways and sex-specific behaviors. *Cell* **139**, 61–72 (2009).
25. Tsukahara, S. et al. Effects of aromatase or estrogen receptor gene deletion on masculinization of the principal nucleus of the bed nucleus of the stria terminalis of mice. *Neuroendocrinology* **94**, 137–147 (2011).
26. Welch, J. D. et al. Single-cell multi-omic integration compares and contrasts features of brain cell identity. *Cell* **177**, 1873–1887 (2019).
27. Zuloaga, D. G., Zuloaga, K. L., Hinds, L. R., Carbone, D. L. & Handa, R. J. Estrogen receptor β expression in the mouse forebrain: age and sex differences. *J. Comp. Neurol.* **522**, 358–371 (2014).
28. Crow, M., Paul, A., Ballouz, S., Huang, Z. J. & Gillis, J. Characterizing the replicability of cell types defined by single cell RNA-sequencing data using MetaNeighbor. *Nat. Commun.* **9**, 884 (2018).
29. Yao, Z. et al. A taxonomy of transcriptomic cell types across the isocortex and hippocampal formation. *Cell* **184**, 3222–3241 (2021).
30. Paul, A. et al. Transcriptional architecture of synaptic communication delineates GABAergic neuron identity. *Cell* **171**, 522–539 (2017).
31. Fishell, G. & Kepcs, A. Interneuron types as attractors and controllers. *Annu. Rev. Neurosci.* **43**, 1–30 (2020).
32. Moffitt, J. R. et al. Molecular, spatial, and functional single-cell profiling of the hypothalamic preoptic region. *Science* **362**, eaau5324 (2018).
33. Cooke, B. M. & Simerly, R. B. Ontogeny of bidirectional connections between the medial nucleus of the amygdala and the principal bed

- nucleus of the stria terminalis in the rat. *J. Comp. Neurol.* **489**, 42–58 (2005).
34. Gotsiridze, T., Kang, N., Jacob, D. & Forger, N. G. Development of sex differences in the principal nucleus of the bed nucleus of the stria terminalis of mice: role of Bax-dependent cell death. *Dev. Neurobiol.* **67**, 355–362 (2007).
 35. McCarthy, M. M. et al. The epigenetics of sex differences in the brain. *J. Neurosci.* **29**, 12815–12823 (2009).
 36. Di Bella, D. J. et al. Molecular logic of cellular diversification in the mouse cerebral cortex. *Nature* **595**, 554–559 (2021).
 37. Ma, S. et al. Chromatin potential identified by shared single-cell profiling of RNA and chromatin. *Cell* **183**, 1103–1116 (2020).
 38. Satterstrom, F. K. et al. Large-scale exome sequencing study implicates both developmental and functional changes in the neurobiology of autism. *Cell* **180**, 568–584 (2020).
 39. Overstreet-Wadiche, L. & McBain, C. J. Neurogliaform cells in cortical circuits. *Nat. Rev. Neurosci.* **16**, 458–468 (2015).
 40. Karigo, T. et al. Distinct hypothalamic control of same- and opposite-sex mounting behaviour in mice. *Nature* **589**, 258–263 (2020).
 41. Clowney, E. J., Iguchi, S., Bussell, J. J., Scheer, E. & Ruta, V. Multimodal chemosensory circuits controlling male courtship in *Drosophila*. *Neuron* **87**, 1036–1049 (2015).
 42. Kallman, B. R., Kim, H. & Scott, K. Excitation and inhibition onto central courtship neurons biases *Drosophila* mate choice. *Elife* **4**, e11188 (2015).
 43. Koganezawa, M., Kimura, K.-I. & Yamamoto, D. The neural circuitry that functions as a switch for courtship versus aggression in *Drosophila* males. *Curr. Biol.* **26**, 1395–1403 (2016).

44. Chiu, H., Hoopfer, E. D., Coughlan, M. L. & Anderson, D. J. A circuit logic for sexually shared and dimorphic aggressive behaviors in *Drosophila*. *Cell* **184**, 507–520 (2020).
45. Brovkina, M. V., Duffié, R., Burtis, A. E. C. & Clowney, E. J. Fruitless decommissions regulatory elements to implement cell-type-specific neuronal masculinization. *PLoS Genet.* **17**, e1009338 (2021).
46. Edwards, D. A. & Burge, K. G. Early androgen treatment and male and female sexual behavior in mice. *Horm. Behav.* **2**, 49–58 (1971).
47. Kimchi, T., Xu, J. & Dulac, C. A functional circuit underlying male sexual behaviour in the female mouse brain. *Nature* **448**, 1009–1014 (2007).
48. Hashikawa, K. et al. Esr1+ cells in the ventromedial hypothalamus control female aggression. *Nat. Neurosci.* **20**, 1580–1590 (2017).
49. Wei, Y.-C. et al. Medial preoptic area in mice is capable of mediating sexually dimorphic behaviors regardless of gender. *Nat. Commun.* **9**, 279 (2018).
50. Lee, H. et al. Scalable control of mounting and attack by Esr1+ neurons in the ventromedial hypothalamus. *Nature* **509**, 627–632 (2014).
51. Sanz, E. et al. Cell-type-specific isolation of ribosome-associated mRNA from complex tissues. *Proc. Natl Acad. Sci. USA* **106**, 13939–13944 (2009).
52. Mo, A. et al. Epigenomic signatures of neuronal diversity in the mammalian brain. *Neuron* **86**, 1369–1384 (2015).
53. Vong, L. et al. Leptin action on GABAergic neurons prevents obesity and reduces inhibitory tone to POMC neurons. *Neuron* **71**, 142–154 (2011).
54. Feng, Y., Manka, D., Wagner, K.-U. & Khan, S. A. Estrogen receptor-alpha expression in the mammary epithelium is required for ductal and

- alveolar morphogenesis in mice. *Proc. Natl Acad. Sci. USA* **104**, 14718–14723 (2007).
55. Ahrens, S. et al. A central extended amygdala circuit that modulates anxiety. *J. Neurosci.* **38**, 5567–5583 (2018).
 56. Corces, M. R. et al. An improved ATAC-seq protocol reduces background and enables interrogation of frozen tissues. *Nat. Methods* **14**, 959–962 (2017).
 57. Paxinos, G. & Franklin, K. B. J. *Paxinos and Franklin's the Mouse Brain in Stereotaxic Coordinates* (Academic, 2019).
 58. Martin, M. Cutadapt removes adapter sequences from high-throughput sequencing reads. *EMBnet J.* **17**, 10–12 (2011).
 59. Langmead, B. & Salzberg, S. L. Fast gapped-read alignment with Bowtie 2. *Nat. Methods* **9**, 357–359 (2012).
 60. Li, H. et al. The Sequence Alignment/Map format and SAMtools. *Bioinformatics* **25**, 2078–2079 (2009).
 61. Ramírez, F. et al. deepTools2: a next generation web server for deep-sequencing data analysis. *Nucleic Acids Res.* **44**, W160–W165 (2016).
 62. Zhang, Y. et al. Model-based analysis of ChIP-Seq (MACS). *Genome Biol.* **9**, R137 (2008).
 63. Quinlan, A. R. & Hall, I. M. BEDTools: a flexible suite of utilities for comparing genomic features. *Bioinformatics* **26**, 841–842 (2010).
 64. Stark, R. & Brown, G. DiffBind: Differential binding analysis of ChIP-Seq peak data. *R package version* **100**, 4–3 (2011).
 65. Robinson, M. D., McCarthy, D. J. & Smyth, G. K. edgeR: a Bioconductor package for differential expression analysis of digital gene expression data. *Bioinformatics* **26**, 139–140 (2010).

66. Yu, G., Wang, L.-G. & He, Q.-Y. ChIPseeker: an R/Bioconductor package for ChIP peak annotation, comparison and visualization. *Bioinformatics* **31**, 2382–2383 (2015).
67. Zhu, Q., Liu, N., Orkin, S. H. & Yuan, G.-C. CUT&RUNTools: a flexible pipeline for CUT&RUN processing and footprint analysis. *Genome Biol.* **20**, 192 (2019).
68. Wang, S. et al. Target analysis by integration of transcriptome and ChIP-seq data with BETA. *Nat. Protoc.* **8**, 2502–2515 (2013).
69. Bailey, T. L. et al. MEME SUITE: tools for motif discovery and searching. *Nucleic Acids Res.* **37**, W202–W208 (2009).
70. Hewitt, S. C. et al. Research resource: whole-genome estrogen receptor α binding in mouse uterine tissue revealed by ChIP-seq. *Mol. Endocrinol.* **26**, 887–898 (2012).
71. Gertz, J. et al. Distinct properties of cell-type-specific and shared transcription factor binding sites. *Mol. Cell* **52**, 25–36 (2013).
72. Gordon, F. K. et al. Research resource: aorta- and liver-specific ER α -binding patterns and gene regulation by estrogen. *Mol. Endocrinol.* **28**, 1337–1351 (2014).
73. Yao, G. et al. Genome-wide mapping of in vivo ER α -binding sites in male mouse efferent ductules. *Endocrinology* **158**, 3724–3737 (2017).
74. Palaniappan, M. et al. The genomic landscape of estrogen receptor α binding sites in mouse mammary gland. *PLoS ONE* **14**, e0220311 (2019).
75. Yu, G., Wang, L.-G., Han, Y. & He, Q.-Y. clusterProfiler: an R package for comparing biological themes among gene clusters. *OMICS* **16**, 284–287 (2012).
76. Durinck, S., Spellman, P. T., Birney, E. & Huber, W. Mapping identifiers for the integration of genomic datasets with the R/Bioconductor package biomaRt. *Nat. Protoc.* **4**, 1184–1191 (2009).

77. Yu, G., Wang, L.-G., Yan, G.-R. & He, Q.-Y. DOSE: an R/Bioconductor package for disease ontology semantic and enrichment analysis. *Bioinformatics* **31**, 608–609 (2015).
78. Grant, C. E., Bailey, T. L. & Noble, W. S. FIMO: scanning for occurrences of a given motif. *Bioinformatics* **27**, 1017–1018 (2011).
79. Franco, H. L., Nagari, A. & Kraus, W. L. TNF α signaling exposes latent estrogen receptor binding sites to alter the breast cancer cell transcriptome. *Mol. Cell* **58**, 21–34 (2015).
80. Bailey, T. L. DREME: motif discovery in transcription factor ChIP-seq data. *Bioinformatics* **27**, 1653–1659 (2011).
81. Dobin, A. et al. STAR: ultrafast universal RNA-seq aligner. *Bioinformatics* **29**, 15–21 (2013).
82. Liao, Y., Smyth, G. K. & Shi, W. FeatureCounts: an efficient general purpose program for assigning sequence reads to genomic features. *Bioinformatics* **30**, 923–930 (2014).
83. Love, M. I., Huber, W. & Anders, S. Moderated estimation of fold change and dispersion for RNA-seq data with DESeq2. *Genome Biol.* **15**, 550 (2014).
84. Schep, A. N., Wu, B., Buenrostro, J. D. & Greenleaf, W. J. chromVAR: inferring transcription-factor-associated accessibility from single-cell epigenomic data. *Nat. Methods* **14**, 975–978 (2017).
85. Stuart, T. et al. Comprehensive integration of single-cell data. *Cell* **177**, 1888–1902 (2019).
86. Aibar, S. et al. SCENIC: single-cell regulatory network inference and clustering. *Nat. Methods* **14**, 1083–1086 (2017).
87. McGinnis, C. S., Murrow, L. M. & Gartner, Z. J. DoubletFinder: doublet detection in single-cell RNA sequencing data using artificial nearest neighbors. *Cell Syst.* **8**, 329–337 (2019).

88. Granja, J. M. et al. ArchR is a scalable software package for integrative single-cell chromatin accessibility analysis. *Nat. Genet.* **53**, 403–411 (2021).
89. van Dijk, D. et al. Recovering gene interactions from single-cell data using data diffusion. *Cell* **174**, 716–729 (2018).
90. Stuart, T., Srivastava, A., Madad, S., Lareau, C. A. & Satija, R. Single-cell chromatin state analysis with Signac. *Nat. Methods* **18**, 1333–1341 (2021).
91. Finak, G. et al. MAST: a flexible statistical framework for assessing transcriptional changes and characterizing heterogeneity in single-cell RNA sequencing data. *Genome Biol.* **16**, 278 (2015).
92. Gu, Z., Eils, R. & Schlesner, M. Complex heatmaps reveal patterns and correlations in multidimensional genomic data. *Bioinformatics* **32**, 2847–2849 (2016).

Acknowledgements

We thank E. J. Clowney and H. A. Ingraham for comments and discussions, and C. Regan and J. Preall for assistance with single-cell sequencing. This work was performed with assistance from Cold Spring Harbor Laboratory Shared Resources, including the Animal, Next Generation Genomics, Flow Cytometry, Microscopy and Single Cell Core Facilities, which are supported by the National Institutes of Health Cancer Center Support Grant 5P30CA045508. National Institutes of Health grant S10OD028632-01 supports the graphical processing units and large-memory nodes at Cold Spring Harbor Laboratory. This work was supported by funding to J.T. (Stanley Family Foundation, R01 MH113628 and SFARI600568) and B.G. (2T32GM065094 and F31MH124365).

Author information

Authors and Affiliations

1. Cold Spring Harbor Laboratory, Cold Spring Harbor, NY, USA
B. Gegenhuber, M. V. Wu, R. Bronstein & J. Tollkuhn
2. Cold Spring Harbor Laboratory School of Biological Sciences, Cold Spring Harbor, NY, USA
B. Gegenhuber

Contributions

performed the Nfix CUT&RUN. B.G. and J.T. conceived the study, designed the experiments and wrote the manuscript.

Corresponding author

Correspondence to [J. Tollkuhn](#).

Ethics declarations

Competing interests

The authors declare no competing interests.

Peer review

Peer review information

Nature thanks Margaret McCarthy and the other, anonymous, reviewer(s) for their contribution to the peer review of this work. [Peer reviewer reports](#) are available.

Additional information

Publisher's note Springer Nature remains neutral with regard to jurisdictional claims in published maps and institutional affiliations.

Extended data figures and tables

Extended Data Fig. 1 Validation of ER α CUT&RUN in MCF-7 cells.

a, Heatmap of mean MCF-7 ER α CUT&RUN CPM \pm 1Kb around 12,995 17 β -estradiol (E2)-induced MCF-7 ER α ChIP-seq peaks (DiffBind, DESeq2, padj < 0.01) for individual replicates (n = 2 per condition and antibody). **b**, pA-MNase-cut footprint (CUT&RUNTools) around ESR1 motif sites (FIMO) detected in ER α ChIP-seq peaks. **c**, MA plots of differential ER α CUT&RUN peaks (DiffBind, DESeq2, padj < 0.1) for ER α antibody #1 (Santa Cruz sc-8002) and ER α antibody #2 (EMD Millipore Sigma 06-935). **d**, Pearson correlation coefficient of CPM-normalized CUT&RUN signal within the consensus peak matrix across ER α CUT&RUN samples. Red text indicates E2 treatment group. **e**, ER α CUT&RUN (both antibodies) and ChIP-seq tracks at canonical MCF-7 ER α target genes (*TFF1*, *GREB1*). **f**, (left) Top enriched motifs (AME) and (right) top *de novo* motifs (DREME) within ER α ChIP-seq peaks, Ab #1 ER α CUT&RUN peaks, and Ab #2 ER α CUT&RUN peaks. % TP = % of peaks called as positive for the indicated motif. *De novo* motifs were classified into motif families using TomTom.

Extended Data Fig. 2 Additional analysis of adult brain ER α CUT&RUN dataset.

a, MA plot of differential ER α CUT&RUN peaks (DiffBind, edgeR, padj < 0.1) in adult mouse brain. red dots=E2-induced peaks, grey dots=E2-down peaks. **b**, Heatmap of mean brain ER α CUT&RUN CPM \pm 1Kb around 1930 E2-induced ER α CUT&RUN peaks (see also Fig. 1b) for individual replicates (n = 2 per condition). **c**, ESR1 motif footprint in ER α peaks

(CUT&RUNTools). **d**, Top enriched motifs (AME) in (left) E2-induced ER α peaks and (right) E2-down ER α peaks. **e**, Heatmap of mean brain IgG and ER α CUT&RUN CPM \pm 1Kb around 185 E2-down ER α peaks. **f**, Number of overlaps between E2-induced ER α peaks and 7 external ER α ChIP-seq peaksets: intersected peaks of uterus 1 and uterus 2, intersected peaks of liver 1 and liver 2, aorta, efferent ductules, and mammary gland. Red indicates brain-specific ER α peaks. **g**, Log-odds motif scores (FIMO) for the ESR1 motif (MA0112.3, left) and ESR2 motif (MA0258.2, right) in brain-specific (red) and shared (pink) ER α peaks. Boxplot center=median, box boundaries=1st and 3rd quartile, whiskers=1.5*IQR from boundaries. n = 1304 brain-specific ESR1, 139 shared ESR1, 1276 brain-specific ESR2, 157 shared ESR2. p-values from two-sided, Wilcoxon rank-sum test. **h**, Top Hugo Gene Nomenclature Committee (HGNC) gene families (clusterProfiler, padj < 0.1) enriched within brain-specific ER α peak-associated genes. **i**, Top Disease Ontology terms associated with genes nearest to brain-specific ER α peaks (DOSE, padj < 0.1). **j**, Brain-specific ER α peak-associated genes within each enriched Disease Ontology (DO) term (clusterProfiler, padj < 0.1), colored by term **k**, Example brain-specific (*Cntnap2*, *Ntrk2*), shared (*Rybp*, *Myrip*), and disease-associated (*Drd3*, *Htr1a*, *Grin2b*) ER α peaks.

Extended Data Fig. 3 Additional BNSTp ISH validation.

In situ hybridization (ISH) validation of additional BNSTp E2-regulated genes identified by RNA-seq (see also Fig. [1e, f](#)). Boxplot center=median, box boundaries=1st and 3rd quartile, whiskers=1.5*IQR from boundaries. p-value from 2-way ANOVA test, n = 4, scale = 200 um.

Extended Data Fig. 4 Additional analysis of adult BNSTp ATAC-seq.

a, GFP immunofluorescence staining in an adult male *Esr1*^{Cre/+}; *Sun-GFP*^{lx/+} mouse, scale = 1mm. Inset shows Sun1-GFP signal at nuclear membrane, scale = 10um. **b**, Fluorescence-activated cell sorting (FACS) gating strategy for isolating BNSTp GFP+ nuclei for ATAC-seq. **c**, Proportion of E2-open ATAC peaks (red), total E2 ATAC peaks (black), and

total Veh ATAC peaks (black) annotated to promoters ($\pm 1\text{Kb}$ around TSS), exons, introns, and intergenic regions. E2-open ATAC peaks have a significantly lower proportion of peaks annotated to gene promoters than total vehicle (11% vs 1%, Fisher's Exact Test, $p = 4.6 \times 10^{-260}$) and total E2 (11% vs 1%, Fisher's Exact Test, $p = 4.3 \times 10^{-267}$) peaks. *** $p < 0.001$. **d**, Heatmap of mean BNSTp *Esr1*+ ATAC CPM $\pm 1\text{Kb}$ around 7293 E2-open ATAC peaks for individual female and male replicates ($n = 3$ per condition) (see also Fig. 1g). **e–g**, Top Gene Ontology (GO) Biological Process terms (**e**), HGNC gene families (**f**), and DO terms (**g**) enriched within E2-open ATAC peak-associated genes (clusterProfiler, $\text{padj} < 0.1$). **h**, Top motifs enriched in E2-open ATAC-seq peaks (AME). % of peaks containing motifs determined with FIMO. **i**, Overlap in E2-open ATAC peaks containing the ESR1 motif (blue) and the ESR2 motif (red), identified using FIMO. The majority of peaks (4434/6479) containing either motif are the same. **j**, (left) Overlap between brain ER α CUT&RUN peaks and E2-open ATAC peaks ($\log_2\text{FC} > 1$). (right) Overlap between remaining 777 brain ER α CUT&RUN peaks and $\log_2\text{FC} > 0$ E2-open ATAC peaks.

Extended Data Fig. 5 Integration of adult RNA-seq, ATAC-seq, and CUT&RUN datasets.

a–b, BETA enrichment of E2-open ATAC peaks (**a**) and brain ER α CUT&RUN peaks (**b**) at E2-induced and E2-down genes identified by RNA-seq (DESeq2, $p < 0.01$) relative to a background of non-differential, expressed genes. **c**, Top enriched motifs (AME) in E2-open ATAC peaks $\pm 350\text{Kb}$ around E2-down genes (identified with BETA). **d**, Example E2-open ATAC peaks/ER α peaks at E2-repressed genes, *Nr2f1* and *Astn2*. **e**, Normalized counts for example genes (*Ccdc134*, *Zfp804b*) with a sex-dependent response to E2 treatment. Boxplot center=median, box boundaries=1st and 3rd quartile, whiskers=1.5*IQR from boundaries. $n = 4$. **f**, (Left) Volcano plot of sex-dependent, E2-responsive genes; light blue and red dots (DESeq2, $\text{padj} < 0.1$), dark blue and red dots (DESeq2, $\text{padj} < 0.1$). (Right) Mean, normalized expression of sex-dependent, E2-responsive genes (DESeq2, $\text{padj} < 0.1$), grouped by k-means clustering. **g**, Lack of significant enrichment of E2-open ATAC peaks (top) and ER α peaks (bottom) at sex-dependent, E2-responsive genes relative to a background of non-differential, expressed genes (BETA). **h**, Volcano plots of sex-

dependent, E2-responsive ER α CUT&RUN peaks (edgeR, padj < 0.1) (left) and ATAC peaks (edgeR, padj < 0.1). **i**, MA plot of male E2 vs. female E2 ER α CUT&RUN peaks (DiffBind, edgeR, padj < 0.1); red dots=male E2-biased peaks, grey dots=female E2-biased peaks. **j**, Heatmap of mean ATAC CPM, split by sex and treatment, \pm 1Kb around E2-induced ER α peaks.

Extended Data Fig. 6 Characterization of a shared BNSTp/MPOA transcriptomic cluster.

a, Dotplot of top marker genes for each adult BNSTp *Esr1*+ GABAergic cluster (Wilcoxon rank-sum test, padj < 0.05). **b**, Differentially-expressed genes between the i1:Nfix cluster and the other six BNSTp *Esr1*+ inhibitory neuron clusters (DESeq2, log2FC > 2, padj < 0.01). **c**, ISH of adult gonadectomized, Veh-treated male (*Esr1*) and adult male (*Nfix*) mouse. Arrows denote *Nfix* ISH staining in BNSTp (dorsal) and POA (ventral). Scale = 1 mm. **d**, Co-expression of top i1:Nfix marker genes (*St18*, *Moxd1*, *Nfix*, *Cplx3*) in individual BICCN cortical and hippocampal scRNA-seq GABAergic clusters, colored by subclass. Co-expression defined as % of cells per cluster with non-zero counts for all 4 marker genes. **e**, Mean expression of *Lamp5*+ subclass marker genes (Wilcoxon rank-sum test, avg_log_FC > 0.75, <40% expression in non-*Lamp5*+ neurons, padj < 0.05) in BNSTp (left) and MPOA (right) *Esr1*+ clusters, scaled across clusters within each brain region. **f**, Normalized expression of top marker genes (*Moxd1*, *St18*, *Nfix*, *Cplx3*, *Gpd1*, *Prox1*) shared between i1:Nfix and i20:Gal.Moxd1 (labeled in red). Boxplot center=median, box boundaries=1st and 3rd quartile, whiskers=1.5*IQR from boundaries. n = 297 i20:Gal.Moxd1 cells, 2459 i1:Nfix cells. **g**, UMAP visualization of integrated BNSTp and MPOA *Esr1*+ clusters, demonstrating shared *Nfix* expression across datasets (see also Fig. 2e). **h**, GFP (left) and Nfix (middle) immunofluorescence staining in an adult male *Esr1*^{Cre/+}; *Sun-GFP*^{lx/+} mouse. Solid white circle indicates BNSTp; dotted white circle indicates SDN-POA. Scale = 100 um.

Extended Data Fig. 7 Additional analysis of BNSTp sex DEGs and gonadally intact ATAC-seq.

a, Normalized, pseudo-bulk expression of sex DEGs identified within each BNSTp *Esrl*+ cluster (DESeq2, $p_{adj} < 0.1$). Each heatmap column corresponds to a pseudo-bulk sample (gene counts aggregated across cells in sample). **b**, Hierarchical clustering of log2FC values for sex DEGs called as significant in at least one BNSTp *Esrl*+ cluster. Sex DEGs with non-significant differential expression colored in white. **c**, Example sex DEGs with significant differential expression in a single *Esrl*+ cluster (*Dlg2*, *Kctd16*) and in multiple *Esrl*+ clusters (*Tiparp*, *Socs2*). Boxplot center=median, box boundaries=1st and 3rd quartile, whiskers=1.5*IQR from boundaries. $n = 4\text{-}7$ female pseudo-bulk replicates, 6-8 male pseudo-bulk replicates. **d**, Top HGNC gene families (clusterProfiler, $p_{adj} < 0.1$) enriched within female-biased DEGs (left) and male-biased DEGs (right) relative to non-differential, expressed genes. **e**, Number of sex DEGs per cluster in *Esrl*+ clusters annotated to the BNST posterior (BNSTp, $n = 7$ clusters) and anterior (BNSTA, $n = 7$ clusters) subregions. Boxplot center=median, box boundaries=1st and 3rd quartile, whiskers=1.5*IQR from boundaries. p-value from two-sided, Wilcoxon rank-sum test. **f**, Dotplot of sex hormone receptor (HR) expression across BNSTp *Esrl*+ clusters. **g**, Barplots of (top) male-biased DEGs ranked by male-biased ATAC peak regulatory potential score and (bottom) female-biased DEGs ranked by female-biased ATAC peak regulatory potential score. Higher score indicates higher density of sex-biased ATAC peaks around the TSS of sex DEGs. **h**, Example sex DEGs (*Fkbp5*, *Ephab6*) with high density of sex-biased ATAC peaks. *sex-biased ATAC peak. **i**, Principal component analysis (PCA) of gonadally intact and gonadectomized (GDX), Veh-treated ATAC CPM values within the consensus peak matrix. **j**, Heatmap of ATAC CPM for gonadally intact ($n = 2$ per condition) and GDX, Veh-treated ATAC samples ($n = 3$ per condition) at differential peaks (edgeR, glmQLFTest, $p_{adj} < 0.01$), grouped by k-means clustering (see also Fig. 2*i*). **k**, Example differential ATAC peaks in k-means clusters c3 (left) and c4 (right).

Extended Data Fig. 8 P4 ATAC-seq and P0 ERα CUT&RUN analysis.

a, Heatmap of mean ATAC CPM for P4 NV male, NV female, and NE female individual replicates ($n = 3$ per condition) at differential peaks

(edgeR, glmQLFTest, $padj < 0.1$), grouped by hierarchical clustering (cutree, $k = 6$). Clusters c3 and c5 correspond to NE-open and NE-close sites, respectively, shown in Fig. 4a. b, Top enriched motifs (AME) in NE-open ATAC peaks. c, (left) Overlap between P4 NE-open ATAC peaks and adult E2-open ATAC peaks ($\log_2 FC > 1$). (right) Overlap between remaining 509 P4 NE-open ATAC peaks and $\log_2 FC > 0$ E2-open ATAC peaks. d, Example P4 NE-open ATAC peaks not detected as E2-induced in adult E2-open ATAC peakset. e, MA plot of P0 female E2 vs. female Veh ER α CUT&RUN peaks (DiffBind, DESeq2, $padj < 0.01$); red dots=E2-induced peaks, grey dots=E2-down peaks. f, Top enriched motifs (AME) in P0 E2-induced ER α peaks. g, Heatmap of mean P0 ER α CUT&RUN CPM $\pm 1\text{Kb}$ around 8102 E2-induced ER α peaks for individual replicates ($n = 2$ per condition). h, (left) Overlap between P4 NE-open ATAC peaks and P0 E2-induced ER α peaks. (right) Overlap between P4 NE-close ATAC peaks and P0 E2-induced ER α peaks. i, (top) Top GO Biological Process terms (clusterProfiler, $padj < 0.1$), (middle) DO terms (clusterProfiler, $padj < 0.1$), and (bottom) HGNC gene families (clusterProfiler, $padj < 0.1$) enriched within P4 NE-open peak-associated genes. j, Example P0 ER α peaks overlapping P4 NE-open peaks at high-confidence ASD candidate genes, *Scn2al* and *Slc6al*.

Extended Data Fig. 9 Comparison of P4 and adult *Esr1*+ ATAC-seq.

a, (left) Overlap between P4 NE-open ATAC peaks and gonadally intact adult male-biased ATAC peaks. (right) Overlap between P4 NE-close ATAC peaks and gonadally intact adult female-biased ATAC peaks. b, Dotplot of BETA enrichment p-values for P4 NE-open ATAC peaks (top) and NE-close ATAC peaks (bottom) at adult BNST snRNA-seq sex DEGs relative to a background of non-differential, expressed genes (see also Fig. 2h). c, Histogram of mean distance between P4 NE-open peaks and nearest gonadally intact adult male-biased ATAC peak (red line) vs. nearest chromosome-matched, non-differential adult ATAC peak ($n = 1000$ permutations) (blue histogram). Mean distance between P4 NE-open peaks and adult male-biased peaks is significantly smaller than the expected distribution (Permutation test, $p = 0.007$). d, Example adult male-biased DEGs (*Prlr*, *Cckar*, *Pdzrn4*, *Tiparp*) with neighboring P4 NE-open

(highlighted in yellow) and adult male-biased ATAC peaks (highlighted in purple).

Extended Data Fig. 10 Additional analysis of neonatal BNST *Esr1*+ single-nucleus multiome dataset.

a–b, RNA (**a**) and ATAC (**b**) quality control (QC) metrics for neonatal (P4, P14) single-nucleus multiome experiments, split by timepoint and sex. Boxplot center=median, box boundaries=1st and 3rd quartile, whiskers=minimum and maximum values. n = 4265 P14_male, 3148 P14_female, 3128 P4_male, 4295 P4_female. **c**, UMAPs of *de novo* clustering of neonatal multiome snRNA data, colored by cluster identity (top left), sex (top right), timepoint (bottom left), and *Esr1* expression (bottom right). **d**, (left) Prediction scores of adult-to-neonatal label transfer for each adult BNST *Esr1*+ reference cluster, split by timepoint. Boxplot center=median, box boundaries=1st and 3rd quartile, whiskers=minimum and maximum values. n = 14836 cells. (right) % of nuclei in each neonatal *de novo* cluster that mapped to each adult BNST *Esr1*+ cluster. **e**, UMAPs of neonatal marker gene module expression in neonatal dataset (left) and adult dataset (right). **f**, (left) Heatmap of pseudo-bulk ATAC CPM at 18783 marker peaks for neonatal multiome clusters. (right) Top three motifs enriched in marker peaks for each multiome cluster. **g**, (left) Correlation analysis of TF expression and motif accessibility across cells. Putative identity regulator TFs colored in pink. (right) TF RNA expression, activity score, and motif deviation UMAPs of example putative BNST *Esr1*+ neuron identity regulators, *Nr4a2* and *Zfhx3* (see also Fig. 3c, d). **h**, Heatmap of mean cortical IgG and BNSTp Nfix CUT&RUN CPM $\pm 1\text{Kb}$ around 32,578 consensus Nfix peaks. **i**, Top motifs enriched (AME) in (top) 30,825 mHypoA cell Nfix CUT&RUN peaks (MACS2, q < 0.01) and in (bottom) 32,578 consensus BNSTp Nfix CUT&RUN peaks (MACS2, q < 0.01; peaks intersected across treatment and sex). %TP=% of peaks called as positive for the indicated motif.

Extended Data Fig. 11 Sex differences in single-nucleus multiome dataset.

a, Hierarchical clustering of log2FC values for P4 sex DEGs detected in *Esr1*+ inhibitory neuron clusters (see also Fig. 3e). Sex DEGs with non-significant differential expression colored in white. **b**, Neonatal E2 (NE) vs. neonatal vehicle (NV) female nuclear RNA-seq on P4 BNST *Esr1*+ cells; grey, red dots (DESeq2, padj < 0.1). **c**, (top) Overlap between NE-induced genes and P4 multiome male-biased genes. (bottom) Overlap between NE-downregulated genes and female-biased genes. **d**, (left) Pearson's correlation coefficient values for non-differential (grey) and NE-regulated (gold) ATAC peaks that correlate with P4 sex DEG expression. Boxplot center=median, box boundaries=1st and 3rd quartile, whiskers=1.5*IQR from boundaries. n = 5169 non-differential, 244 NE-regulated. p-value from two-sided, Wilcoxon rank-sum test. (right) Distance between non-differential (grey) and NE-regulated (gold) ATAC peaks to P4 sex DEG transcription start sites (TSS). p-value from Kolmogorov-Smirnov test. **e**, Example P4 sex-biased genes that are also NE-regulated, *Htr4* (top) and *Csgalnact1* (bottom). (left) n = 3, (right) n = 887 i1:Nfix female cells, 676 i1:Nfix male cells, 404 i3:Esr2 female cells, 550 i3:Esr2 male cells. **f**, Tracks for NE-open ATAC peaks that correlate with NE-regulated, sex-biased targets, *Htr4* and *Csgalnact1*. **g**, Different NE-open ATAC peaks across i1:Nfix, i3:Esr2, and i4:Bnc2 neurons correlated with a common male-biased target, *Arid1b*. **h**, Heatmaps indicating (left) RNA log2FC of P14 sex DEGs and (right) Pearson's correlation coefficient of NE-open (red) and -close (blue) ATAC peaks linked to sex DEGs within each cluster. Non-significant genes and correlation values colored in white.

Extended Data Fig. 12 Additional analysis of P14 BNST *Vgat*+ snRNA-seq dataset.

a, RNA QC metrics for P14 BNST *Vgat*+ snRNA-seq experiment, split by sample. a and b refer to technical replicates. Boxplot center=median, box boundaries=1st and 3rd quartile, whiskers=minimum and maximum values. n = 6355 ko_male_a, 5614 ko_male_b, 7184 wt_female_a, 6367 wt_female_b, 6881 wt_male_a, 6561 wt_male_b. **b**, Prediction scores of adult-to-P14 label transfer for each adult BNST *Vgat*+ reference cluster, split by group. Boxplot center=median, box boundaries=1st and 3rd quartile, whiskers=minimum and maximum values. n = 38962 cells. **c**, Heatmap of P14 marker gene mean module score in P14 BNST *Vgat*+

clusters (left) and adult BNST *Vgat*⁺ clusters (right). **d**, Proportion of total P14 *Vgat*⁺ nuclei in each *Vgat*⁺ cluster, separated by group. Adult male-biased *Esr1*⁺ clusters i1:Nfix and i3:Esr2 are indicated in grey. **e**, Heatmap of mean expression of sex DEGs in (left) i3:Esr2 and (right) i4:Bnc2 clusters, scaled across experimental groups (see also Fig. 4b). **f**, % of sex DEGs in P14 *Vgat*⁺/*Esr1*⁺ clusters with that are also detected as sex-biased on P4 in corresponding multiome clusters.

Extended Data Table 1 Riboprobe sequences used for *in situ* hybridization

Supplementary information

[Reporting Summary](#)

[Peer Review File](#)

[41586_2022_4686_MOESM3_ESM.xlsx](#)

Supplementary Table 1 **Differential peaks for adult brain ER α CUT&RUN**. DiffBind output for ER α CUT&RUN experiment from ER α -expressing brain regions, along with ChIPSeeker gene annotations. Includes lists of genes annotated to brain-specific ER α and tissue-shared peaks.

[Supplementary Table 2 Differential gene list for BNSTp ER \$\alpha\$ + neuron RNA-seq, DESeq2 comparisons and HT counts for RNA-seq experiments from adult BNSTp ER \$\alpha\$ + neurons.](#)

[41586_2022_4686_MOESM5_ESM.xlsx](#)

Supplementary Table 3 **Differential peaks for BNSTp ER α + neuron ATAC-seq**. DiffBind output for ATAC-seq experiment from BNSTp of gonadectomized animals treated with oestradiol or vehicle, along with ChIPSeeker gene annotations.

41586_2022_4686_MOESM6_ESM.xlsx

Supplementary Table 4 Sex-biased genes in each adult BNSTp ER α + snRNA-seq cluster. DESeq2 output for differential expression analysis between female and male pseudo-bulk replicates in each adult BNSTp ER α + snRNA-seq cluster.

41586_2022_4686_MOESM7_ESM.xlsx

Supplementary Table 5 Differential peaks for adult BNSTp ER α + neuron ATAC-seq. edgeR output for sex differences in gonadectomized, vehicle-treated and gonadally intact BNSTp ER α + ATAC-seq datasets, along with ChIPSeeker gene annotations. edgeR ANOVA output for differences across sex and gonadal hormone status; differential peaks grouped using k -means clustering.

41586_2022_4686_MOESM8_ESM.xlsx

Supplementary Table 6 Differential peaks for P4 BNST ER α + neuron ATAC-seq. edgeR ANOVA output for differences across sex and neonatal hormone treatment status; differential peaks grouped using hierarchical clustering.

41586_2022_4686_MOESM9_ESM.xlsx

Supplementary Table 7 Differential peaks for P0 brain ER α CUT&RUN. DiffBind output for P0 ER α CUT&RUN experiment from ER α -expressing brain regions, along with ChIPSeeker gene annotations.

41586_2022_4686_MOESM10_ESM.xlsx

Supplementary Table 8 Total and differential peaks for BNSTp Nfix CUT&RUN. DiffBind output for Nfix CUT&RUN experiment from adult BNSTp, along with ChIPSeeker gene annotations.

41586_2022_4686_MOESM11_ESM.xlsx

Supplementary Table 9 Sex-biased genes in each neonatal BNST ER α + snRNA-seq cluster in multiome dataset. MAST output for differential expression analysis between females and males in each BNST ER α + snRNA-seq cluster on P4 and P14.

[41586_2022_4686_MOESM12_ESM.xlsx](#)

Supplementary Table 10 Differential gene list for P4 BNST ER α + nuclear RNA-seq. DESeq2 output for bulk nuclear RNA-seq experiment from BNST ER α + neurons of P4 females treated at birth with oestradiol or vehicle.

[41586_2022_4686_MOESM13_ESM.xlsx](#)

Supplementary Table 11 Sex-biased genes in each P14 BNST vGAT+ snRNA-seq cluster. MAST output for differential expression analysis between control females and males, and between control females and conditional ER α -mutant males, in each P14 BNST vGAT+/ER α + snRNA-seq cluster.

Source data

[Source Data Fig. 1](#)

[Source Data Fig. 2](#)

Rights and permissions

Open Access This article is licensed under a Creative Commons Attribution 4.0 International License, which permits use, sharing, adaptation, distribution and reproduction in any medium or format, as long as you give appropriate credit to the original author(s) and the source, provide a link to the Creative Commons license, and indicate if changes were made. The images or other third party material in this article are included in the article's Creative Commons license, unless indicated otherwise in a credit line to the material. If material is not included in the

article's Creative Commons license and your intended use is not permitted by statutory regulation or exceeds the permitted use, you will need to obtain permission directly from the copyright holder. To view a copy of this license, visit <http://creativecommons.org/licenses/by/4.0/>.

Reprints and Permissions

About this article

Cite this article

Gegenhuber, B., Wu, M.V., Bronstein, R. *et al.* Gene regulation by gonadal hormone receptors underlies brain sex differences. *Nature* **606**, 153–159 (2022). <https://doi.org/10.1038/s41586-022-04686-1>

- Received: 05 January 2021
- Accepted: 24 March 2022
- Published: 04 May 2022
- Issue Date: 02 June 2022
- DOI: <https://doi.org/10.1038/s41586-022-04686-1>

Share this article

Anyone you share the following link with will be able to read this content:

[Get shareable link](#)

Sorry, a shareable link is not currently available for this article.

[Copy to clipboard](#)

Provided by the Springer Nature SharedIt content-sharing initiative

Further reading

- [**Sex differences of oestradiol-mediated gene expression**](#)

- Katharine H. Wrighton

Nature Reviews Genetics (2022)

This article was downloaded by **calibre** from <https://www.nature.com/articles/s41586-022-04686-1>

| [Section menu](#) | [Main menu](#) |

[Download PDF](#)

- Article
- Open Access
- [Published: 25 May 2022](#)

Developmental dynamics of two bipotent thymic epithelial progenitor types

- [Anja Nusser](#) [ORCID: orcid.org/0000-0002-8157-0560^{1 na1}](#),
- [Sagar^{2,3 na1}](#),
- [Jeremy B. Swann](#) [ORCID: orcid.org/0000-0003-2168-8994^{1 na1}](#),
- [Brigitte Krauth¹](#),
- [Dagmar Diekhoff¹](#),
- [Lesly Calderon^{1 nAff7}](#),
- [Christiane Happe¹](#),
- [Dominic Grün](#) [ORCID: orcid.org/0000-0002-3364-5898^{2,4,5}](#) &
- [Thomas Boehm](#) [ORCID: orcid.org/0000-0001-5172-7478^{1,6}](#)

[Nature](#) volume 606, pages 165–171 (2022)

- 6423 Accesses
- 202 Altmetric
- [Metrics details](#)

Subjects

- [Cell biology](#)
- [Immunology](#)

Abstract

T cell development in the thymus is essential for cellular immunity and depends on the organotypic thymic epithelial microenvironment. In comparison with other organs, the size and cellular composition of the thymus are unusually dynamic, as exemplified by rapid growth and high T cell output during early stages of development, followed by a gradual loss of functional thymic epithelial cells and diminished naive T cell production with age^{1,2,3,4,5,6,7,8,9,10}. Single-cell RNA sequencing (scRNA-seq) has uncovered an unexpected heterogeneity of cell types in the thymic epithelium of young and aged adult mice^{11,12,13,14,15,16,17,18}; however, the identities and developmental dynamics of putative pre- and postnatal epithelial progenitors have remained unresolved^{1,12,16,17,19,20,21,22,23,24,25,26,27}. Here we combine scRNA-seq and a new CRISPR–Cas9-based cellular barcoding system in mice to determine qualitative and quantitative changes in the thymic epithelium over time. This dual approach enabled us to identify two principal progenitor populations: an early bipotent progenitor type biased towards cortical epithelium and a postnatal bipotent progenitor population biased towards medullary epithelium. We further demonstrate that continuous autocrine provision of Fgf7 leads to sustained expansion of thymic microenvironments without exhausting the epithelial progenitor pools, suggesting a strategy to modulate the extent of thymopoietic activity.

Main

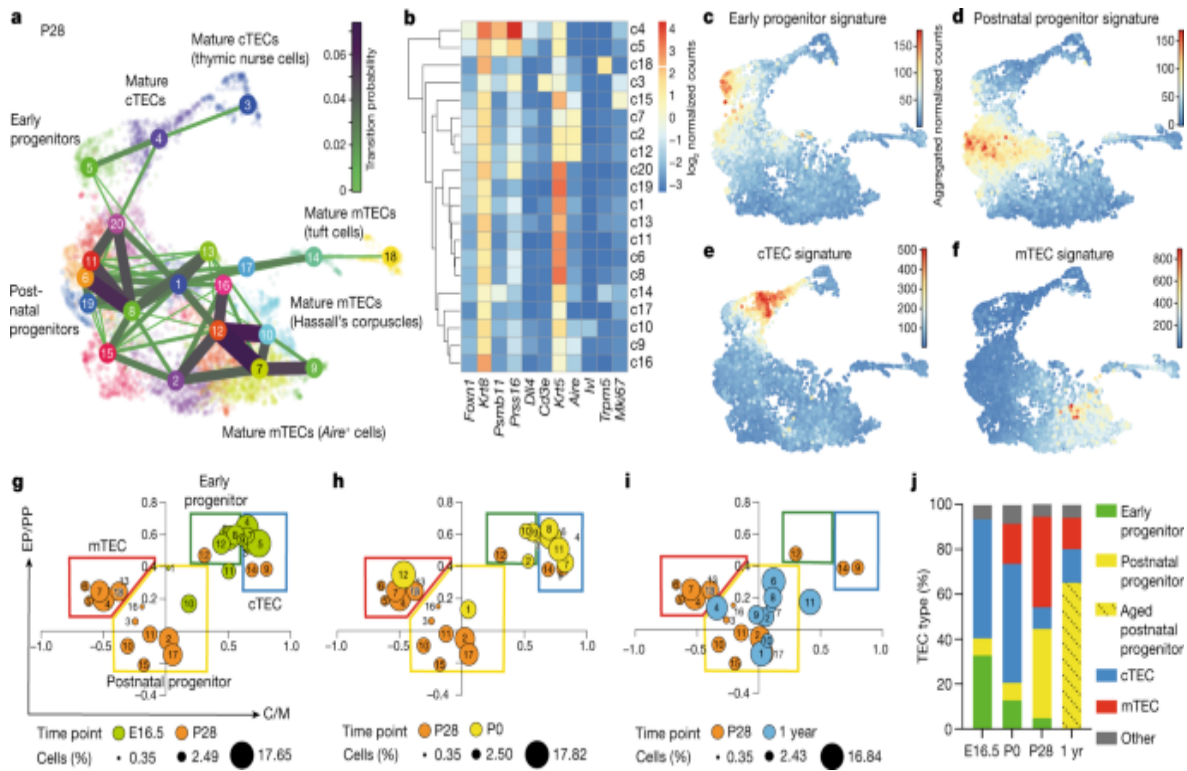
Differentiation of thymic epithelial cells (TECs) is dependent on the Foxn1 transcription factor^{28,29,30,31,32,33,34,35}, and defects in epithelial specification and development are known to block T cell development, resulting in profound immunodeficiency and/or autoimmunity^{36,37}. Because the thymic epithelium occupies such a central role in the formation and maintenance of cellular immunity, it has become an attractive target for immunomodulatory and regenerative therapies^{38,39,40,41,42,43} designed to correct congenital lack or iatrogenic loss of thymic tissue or to modify failing central tolerance. However, despite the immunological importance of TECs, central aspects of the biology of these cells remain unresolved. Progenitor activity in the

embryonic thymus is associated with cells expressing *Psmbl1*, encoding a thymus-specific component of the immunoproteasome^{1,24,25}; however, the presence of a bipotent epithelial progenitor (or multiple bipotent progenitors)^{22,23} capable of giving rise to the cortical and medullary regions of the adult thymus, as well as the many different specialized epithelial subtypes^{11,12,13,14,15,16,17,18}, has not yet been demonstrated. Here a high-resolution CRISPR–Cas9-based barcoding scheme combined with single-cell RNA sequencing (scRNA-seq) identifies bipotent progenitors in embryonic and adult TEC populations and shows their developmental relationship. Notably, we also demonstrate that continuous signalling via Fgfr2b causes a massive and sustained quantitative increase in TEC numbers, without altering the dynamic qualitative changes associated with the ageing thymic microenvironment.

Cellular heterogeneity among TECs

We used scRNA-seq by CEL-Seq2 (refs. [44,45](#)) to examine the cellular heterogeneity of CD45[−]EpCAM⁺ TECs from 4-week-old (postnatal day (P) 28) mice (Extended Data Fig. [1a,b](#)). Cells with similar transcriptional profiles were identified by Louvain clustering using VarID⁴⁶, and their predicted relationships were quantified by VarID transition probabilities. In agreement with previous studies^{1,11,12,13,14,15,16,17,18}, the resulting Uniform Manifold Approximation and Projection (UMAP) plot (Fig. [1a](#)) illustrates the complexity of the epithelial compartment in terms of gene expression profiles and cluster sizes (Fig. [1b](#) and Extended Data Fig. [1c–f](#)). At this age, few sex-related differences were apparent (Extended Data Fig. [1a,b](#)).

Fig. 1: Heterogeneity of TECs.



a, UMAP representation of transcriptome similarities among 6,959 individual TECs derived from 4-week-old wild-type male ($n = 2$) and female ($n = 2$) mice. Cell clusters and transition probabilities were inferred with VarID⁴⁴; connections with probability $P > 0.001$ are shown, with transition probabilities indicated by line thickness and colour. The positions of clusters containing early and postnatal bipotent progenitors and mature cTEC and mTEC clusters are indicated. Colours mark cells in the identified cell clusters. **b**, Expression profiles of signature genes in individual TEC clusters. **c–f**, UMAP plots highlighting the aggregated expression profiles of gene groups distinguishing early (**c**) and postnatal (**d**) progenitors and cTECs (**e**) and mTECs (**f**). **g–i**, Age-dependent changes in the TEC compartment. Transcriptome features of TEC clusters are shown at various time points expressed as ratios of progenitor and mature TEC gene set transcript counts; the P28 time point was used as a reference. Assignment of clusters to the four main populations in the coordinate system is indicated in **g**; the sizes of dots correspond to the relative fraction in the TEC population. **j**, Summary of dynamic changes in the composition of the TEC compartment. yr, year.

[Source data](#)

Identification of putative progenitors

We next sought to identify candidate progenitor populations within the epithelial compartment. Cells in several of the transcriptionally defined clusters expressed genes associated with mature TECs, including medullary TECs (mTECs; *Aire* and *Ivl*), tuft cells (*Trpm5*), cortical TECs (cTECs; *Prss16*) and nurse cells (*Prss16* and *Cd3e* co-expression, indicative of cTECs with enclosed thymocytes⁴⁷), and were therefore excluded from our search, as mature TECs are unlikely to possess progenitor potential.

Furthermore, we excluded highly proliferative cells (expressing *Mki67*) and those lacking expression of *Foxn1*, which is known to be expressed in TEC progenitor cells^{22,34} (Fig. 1b and Extended Data Fig. 1c–e). We then considered the transition probabilities (links) between the eight remaining candidate progenitor clusters (c1, c5, c6, c8, c11, c13, c19 and c20). Cluster c5 had links to mature cTECs (c3 and c4) and to c1 and c20, of which the latter two expressed *Krt5*, a marker of the mTEC lineage. Except for mature cTECs in c4, c5 exhibited the highest level of *Psmb11* expression, which is indicative of mature cTECs⁴⁸ but also cells possessing progenitor potential, at least during embryogenesis^{1,24,25} and in the early postnatal period⁴⁹. Hence, c5 exhibited features consistent with a bipotent progenitor. The transcriptomes of c6, c11 and c19 were very similar and had affinity for c1, which itself was connected to c5, c8 and c13 (Fig. 1b and Extended Data Fig. 1d). Cells in c6, c8, c11, c13 and c19 expressed *Krt5* but only low levels of *Psmb11*, in line with the view that, in contrast to the situation in the embryo²⁴, adult mTECs do not directly originate from a *Psmb11*-expressing TEC compartment^{1,25}. Collectively, these analyses suggest the presence of at least two potential bipotent progenitor cell types: one progenitor population exhibiting a bias towards cTEC development (represented by c5; henceforth referred to as ‘early progenitors’) and another more heterogeneous progenitor population exhibiting a distinct mTEC bias (represented by c1 and c6; henceforth referred to as ‘postnatal progenitors’).

Age-dependent dynamics of TEC populations

Given the presumed developmental dynamics of TEC progenitors, we tested the hypothesis that the early progenitor population dominates in the

embryonic and perinatal stages of development, whereas the postnatal progenitor population is more prevalent in adolescent and adult stages. To do this, we assigned four largely non-overlapping gene sets to mark the two progenitor populations (Supplementary Tables 1 and 2, and Extended Data Fig. 2a, b) and the mature cTEC and mTEC populations (Supplementary Tables 3 and 4). Population-specific scores were calculated by summation of transcript counts in the four separate gene lists. Notably, although the genes in these sets showed different temporal dynamics, the aggregated scores were not dominated by individual highly expressed genes (for example, see Extended Data Fig. 2c, d); pathway analysis associated regulation of cell growth with the two progenitor populations and immune-related processes with the two mature TEC populations (Extended Data Fig. 2e). The aggregated expression levels of progenitor and mature TEC gene sets mark four distinct domains in the UMAP plot of 4-week-old (P28) mice (Fig. 1c–f). At embryonic day (E) 16.5, the transcriptional landscape of TECs was dominated by the cTEC signature and early progenitor cells (Extended Data Figs. 3a, e and 4a). In new-born mice (P0), the number of postnatal progenitors and mTECs began to increase (Extended Data Figs. 3b, f and 4b). At P28, cells with the postnatal progenitor signature were more numerous than those with the early progenitor signature; moreover, the cTEC compartment was much smaller than at earlier stages, with mTEC-like cells dominating the TEC population (Extended Data Figs. 3c, g and 4c). At 1 year of age, the TEC compartment exhibited signs of functional deterioration. At this time, mature cTECs and mTECs made up only a small fraction of the thymic epithelia; by contrast, an unusually large number of cells simultaneously exhibited signatures of both progenitor types. These features suggest that, in aged mice, expanded progenitor-like cells may have lost their defining characteristics and that this indistinct phenotype is associated with low differentiation potential of these aged progenitors (Extended Data Figs. 3d, h and 4d). In a previous study, a putative progenitor population was identified with a distinct mTEC bias¹; on the basis of gene expression profiles, the ‘intertypical’ TECs described in the study are closely related to the postnatal progenitor population defined here (Extended Data Fig. 5).

To visualize dynamic age-related changes in the TEC compartment, we calculated the ratios of transcript scores for early and postnatal progenitors

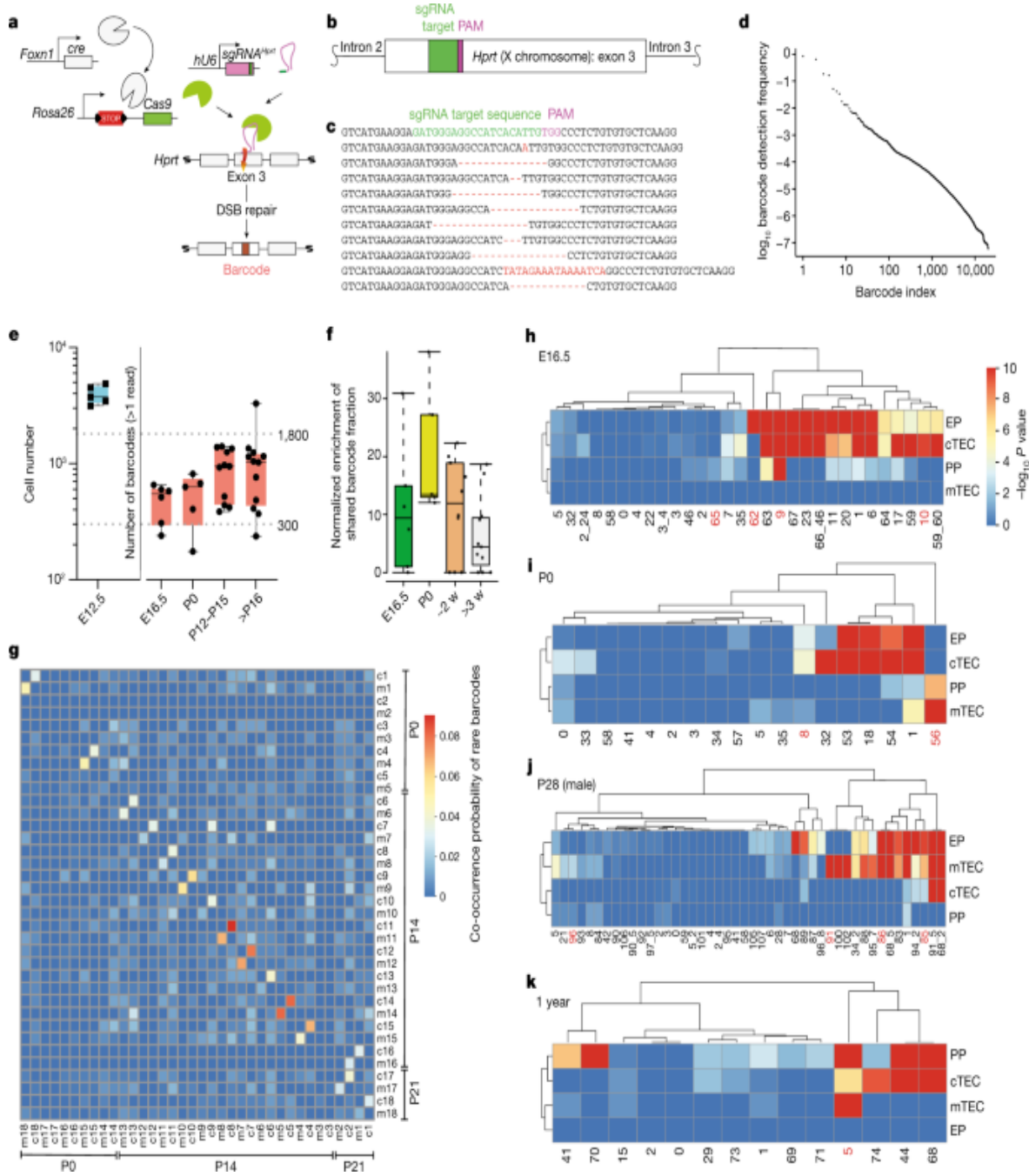
(EP/PP) and for mature cTEC and mTEC populations (C/M) for each cell cluster and plotted them with reference to the P28 time point (Fig. 1g–i). Whereas the E16.5 TEC compartment was dominated by cells closely resembling early progenitors and mature cTECs (Fig. 1g), the P0 time point reflected the transition from an embryonic to an adult TEC compartment, as exemplified by the composition at P28 (Fig. 1h). The 1-year time point was characterized by few mature TECs (Fig. 1i). At this stage, most cell clusters populating the postnatal progenitor compartment (c2, c6, c7, c8 and c9) exhibited increased EP/PP ratios when compared with the corresponding P28 cell clusters, as a result of increased expression levels of genes that are associated with early progenitors; we refer to TECs with this indistinct phenotype as ‘aged progenitors’ (Fig. 1i,j). Our results support the notion that progenitor compartment(s) increase with age¹. The age-dependent differences in TEC composition are summarized in Fig. 1j.

Shared ancestry of Ly51⁺ and UEA-1⁺ TECs

To further explore potential progenitor–progeny relationships in the TEC compartment, we developed a high-resolution lineage tracing method based on CRISPR–Cas9-mediated scarring in exon 3 of the *Hprt* gene (Fig. 2a,b and Extended Data Fig. 6a,b). In the *hU6-sgRNA^{Hprt}; Foxn1-cre; Rosa26-flox-STOP-flox-Cas9* triple-transgenic mice used here, TECs are marked in early embryogenesis as soon as *Foxn1* expression begins at around E11.5 (ref. 50). Because essentially all embryonic and adult TECs have a history of *Foxn1* expression³⁴, the scars (Fig. 2c) introduced in individual epithelial cells of the thymic rudiment in early embryogenesis indelibly mark their subsequent progeny. As is the case with other barcoding schemes^{51,52}, individual scars, referred to as barcodes below, are generated at different frequencies (Fig. 2d); the most frequent sequences were shared by different mice (Extended Data Fig. 6c–e). The total number of different barcodes per thymus was on the order of 500–1,000 (Fig. 2e), close to the number of medullary islets observed in adult mice (300–1,800)²⁶. We found a significant enrichment (Extended Data Fig. 6f) of barcodes that were shared by the EpCAM⁺CD45[−]Ly51⁺UEA-1[−] cTEC and EpCAM⁺CD45[−]Ly51[−] UEA-1⁺ mTEC subsets (Extended Data Fig. 7a–f) of male mice, at several pre- and postnatal time points (Fig. 2f), suggesting a common origin for

these subsets. We then identified barcodes that were represented only twice in the purified TEC populations of all mice, referred to as rare barcodes for the purpose of this experiment, and determined the probabilities of their co-occurrence in cTECs and mTECs of the same mouse versus any other mouse. On average, the corresponding mTEC and cTEC samples from the same mouse shared 3.5% of rare barcodes, whereas samples from different mice shared only 0.27% of rare barcodes. Without prefiltering based on barcode frequency, the fraction of barcodes shared by mTEC and cTEC populations was >50%. The significant degree of co-occurrence of such rare barcodes in mTEC and cTEC samples from the same mouse (Fig. 2g) suggests that cTECs and mTECs have a shared ancestor.

Fig. 2: Barcoding shows the differentiation capacity of progenitor populations.



a, Schematic of the CRISPR–Cas9-based barcoding system. DSB, double-strand break. **b**, Location of the target site in exon 3 of the mouse *Hprt* gene. **c**, Examples of barcodes; the germline sequence is shown with the sgRNA target and protospacer adjacent motif (PAM) sequences indicated at top. Nucleotide additions and deletions (dashes) are indicated in red. **d**, Frequencies of individual barcodes in decreasing order. **e**, Number of *Foxn1*-expressing TECs in the thymic rudiment of E12.5 embryos⁹ (left; $n = 5$) and P0, P12, P15, and >P16 mice (right). **f**, Normalized enrichment of shared barcode fraction. **g**, Heatmap of co-occurrence probability of rare barcodes. **h**, Hierarchical clustering of E16.5, P0, and P28 (male) samples. **i**, Hierarchical clustering of P0 samples. **j**, Hierarchical clustering of P28 (male) samples. **k**, Hierarchical clustering of 1-year-old samples.

numbers of different barcodes in the thymi of mice of different ages (right): E16.5, $n = 6$; P0, $n = 5$; P12–P15, $n = 11$; >P16, $n = 12$. The dotted lines indicate the range of the numbers of progenitors previously inferred from medullary islet counts in adult mice²⁶. **f**, Enrichment of shared barcodes in the Ly51⁻UEA-1⁺ mTEC and Ly51⁺UEA-1⁻ cTEC fractions of mice of different ages. Enrichment values were significantly different in the comparison of mice at P0 and >3 weeks (w) ($P = 0.009$, one-sided Wilcoxon test). E16.5, $n = 6$; P0, $n = 5$; ~2 weeks, $n = 11$; >3 weeks, $n = 11$. For **e** and **f**, boxes extend from the 25th to 75th percentile; whiskers extend to the largest and smallest values; and the median is indicated. See the [Methods](#) for a definition of the enrichment value E_m . **g**, Co-occurrence probability of rare barcodes across pairs of samples highlighting enhanced co-occurrence in mTEC (m) and cTEC (c) fractions of the same mouse; individual mice are identified by number. Data are shown for $n = 18$ mice. **h–k**, P values ($-\log_{10}$) of barcode frequencies indicating co-occurrence of individual barcodes in progenitor and mature TEC fractions (as defined in Fig. [1c–f](#)) at different time points. For **g–k**, P values were calculated as described in the [Methods](#) and corrected for multiple testing by the Benjamini–Hochberg method. The red numbers refer to clones discussed in the text.

[Source data](#)

Combining scRNA-seq and barcode tracing

Next, we applied simultaneous scRNA-seq and barcode tracing to dissect progenitor–progeny relationships within the TEC compartments of mice of different ages (Fig. [2h–k](#)). To gain insight into the distribution of individual barcodes, we compared the barcode frequencies in each compartment to the expected barcode frequencies obtained from the bulk samples of 33 mice (Fig. [2d](#) and Extended Data Fig. [6g](#)). At E16.5, about two-thirds of the barcode sequences were found in early progenitors; the majority of barcodes enriched in early progenitors were also over-represented in cTECs (for example, barcode 10) (Fig. [2h](#)), confirming the notion^{19,21} that the early progenitor population has a distinct bias towards differentiation into cTECs. The presence of shared barcodes (for example, barcode 9) also indicated a developmental relationship between early and postnatal progenitor

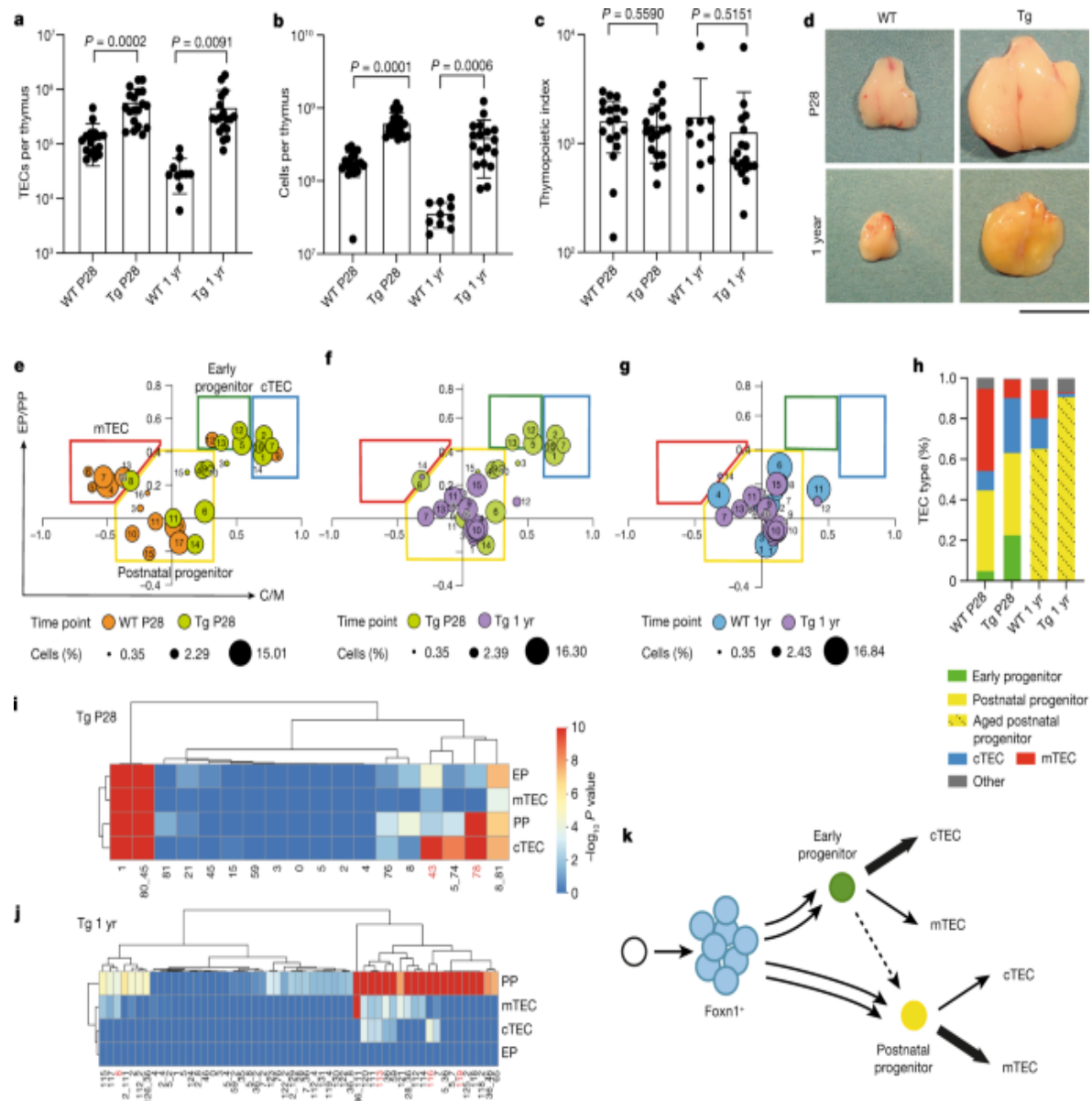
populations. Some early and postnatal progenitor cells had not yet contributed to cTECs or mTECs by this time in development (barcodes 62 and 65, respectively). At P0, the most notable additions to lineage relationships (Fig. 2*i*) concerned the presence of a postnatal progenitor giving rise predominantly to mTECs (barcode 56) and the presence of an embryonic progenitor giving rise to both cTECs and mTECs (barcode 8). At P28, cells with the transcriptional signature of early progenitors predominantly gave rise to mTECs (barcode 86) rather than both mTECs and cTECs (barcode 85); the number of postnatal progenitors biased towards mTEC differentiation (barcode 96) increased (Fig. 2*j*), a pattern that was independent of the sex of the animal (Extended Data Fig. 7*g, h*). Interestingly, several barcodes uniquely over-represented in mTECs were also observed (for example, barcode 91), suggesting the existence of compartment-specific progenitor activity (Extended Data Fig. 8); the corresponding barcodes may no longer be detectable in the bipotent progenitor populations either because the particular progenitor clones have ceased to exist or because they have too low a frequency to be reliably sampled. Finally, although the TEC compartment of aged mice lacked evidence of productive early progenitor cell types, bipotent progenitors were present (barcode 5) (Fig. 2*k*); however, most barcodes in aged postnatal progenitors were linked to cells with the cTEC signature, in line with the notion that cTEC-like cells increase in frequency in aged mice^{2,9}. Collectively, our results illustrate the advantage gained from using a barcoding scheme in the identification and characterization of progenitor populations and their progeny when this approach is combined with transcriptome data at single-cell resolution.

Fgf signalling does not exhaust bipotent progenitors

Next, we combined scRNA-seq and lineage analysis to examine the cellular composition of the TEC compartment under conditions of continuous fibroblast growth factor (Fgf) signalling, which is known to regulate the size of the TEC compartment. For instance, whereas functionally mature TECs are generated in the absence of *Fgfr2b*, the overall size of the TEC compartment is small, resulting in a hypoplastic thymus⁵³; by contrast, mice

treated with pharmacological doses of the Fgfr2b ligand KGF, the human homologue of Fgf7, exhibit an increase in the number of TECs^{54,55}. However, it is not known whether Fgf stimulation targets progenitors, mature TECs or both. To examine this question, we generated several mouse models for continuous autocrine provision of an Fgfr2b ligand in the thymus. We established that, under physiological conditions, the extent of Fgf signalling in TECs (Extended Data Fig. 9) is determined by limiting levels of ligand(s), rather than the receptor (Extended Data Fig. 10); notably, we found that pharmacological supplementation of the Fgfr2b ligand Fgf7 could be mimicked in vivo by ectopic expression of Fgf7 in the TECs of *Foxn1-Fgf7* transgenic mice (Extended Data Fig. 11). Continuous autocrine provision of Fgf7 within the epithelial compartment in this transgenic model increased the number of TECs and thymocytes (Fig. 3a–c) and resulted in a massive and sustained increase in thymus size (Fig. 3d). Except for an increase in the number of Ly51⁺ TECs at P28 (Extended Data Fig. 12a–d) and a small reduction in the CD4/CD8 double-positive thymocyte compartment in old age (Extended Data Fig. 12e–h), thymopoiesis occurred normally in transgenic mice. Age-related diminution of thymopoiesis still occurred under conditions of chronic Fgf stimulation; however, the thymus of aged transgenic mice remained much larger than that of P28 wild-type mice (Fig. 3d). It appears therefore that reduced provision of Fgfr2b ligands contributes to the age-related progressive diminution of TEC numbers. Of note, expression levels of the *Fgfr2* genes in the different TEC populations were highest in early progenitors and cTECs at all time points (Extended Data Fig. 13a).

Fig. 3: Autocrine Fgf stimulation results in sustained thymic hyperplasia.



a–c, Quantitative assessment of thymopoiesis in wild-type (WT) and *Foxn1-Fgf7* transgenic (Tg) mice at 4 weeks and 1 year of age. **a**, WT P28, $n=18$; Tg P28, $n=19$; WT 1 yr, $n=10$; Tg 1 yr, $n=18$. **b**, WT P28, $n=19$; Tg P28, $n=21$; WT 1 yr, $n=10$; Tg 1 yr, $n=18$. **c**, WT P28, $n=18$; Tg P28, $n=19$; WT 1 yr, $n=10$; Tg 1 yr, $n=18$. Data are shown as the mean \pm s.d. *P* values are indicated from two-sided *t* tests. **d**, Representative photographs of thymi from the mice analysed in **a**; scale bar, 10 mm. **e–g**, Transcriptome features of TEC clusters expressed as ratios of progenitor and mature TEC gene set transcript counts. Assignment of clusters to the four main populations in the coordinate system is indicated in **e**; the sizes of dots

correspond to the relative fraction in the TEC population. **h**, Summary of dynamic changes in the composition of the TEC compartment. **i, j**, *P* values ($-\log_{10}$) of barcode frequencies indicating co-occurrence of individual barcodes in progenitor and mature TEC fractions (as defined in Fig. [1c–f](#)) at two time points. *P* values were calculated as described in the [Methods](#) and corrected for multiple testing by the Benjamini–Hochberg method. The red numbers correspond to clones discussed in the text. **k**, Schematic indicating the divergent developmental trajectories of embryonic and postnatal epithelial progenitors. Line thickness corresponds to lineage bias; the dashed line indicates the presumptive lineage relationship of the two progenitor populations.

[Source data](#)

At the P28 and 1-year time points, the Fgf-stimulated thymic microenvironment also exhibited considerable heterogeneity, in terms of both transcriptional diversity and cluster size (Extended Data Fig. [13b–g](#)). As indicated by the changes in flow cytometry profiles (Extended Data Fig. [12a](#)), the proportion of cells exhibiting the cTEC signature was increased at P28, as was the proportion of early progenitors (Extended Data Fig. [12i](#)). In aged transgenic mice, the TEC compartment exhibited the indistinct phenotype of aged postnatal progenitors (Extended Data Fig. [12j](#)) that was observed in their wild-type siblings (Fig. [1j](#)). The relative shifts in populations under conditions of continuous Fgf stimulation away from mTECs at P28 and away from mature cell types at 1 year of age (Extended Data Fig. [12j](#)) were also apparent from the representation of cell clusters in the coordinate system discriminating the transcriptional signatures of progenitor cells and mature TECs (Fig. [3e–g](#)), a feature summarized in Fig. [3h](#).

The lineage relationships of Fgf-stimulated TECs at P28 (Fig. [3i](#)) showed the presence of barcodes that were shared by both types of progenitors and mature cTECs and mTECs (for example, barcode 43) and of barcodes that connected both progenitor types and cTECs (for example, barcode 78). The lineage structure in 1-year-old mice (Fig. [3j](#)) showed a large number of progenitors that did not give rise to differentiated progeny (barcode 119). Other postnatal progenitors gave rise to either cTECs (barcode 116) or mTECs (barcode 8). In contrast to the dominance of lineage-biased

progenitors, bipotent progenitors were rare (barcode 113). Collectively, our data indicate that TEC progenitors are not depleted by autocrine Fgf stimulation and actively contribute to the microenvironment in aged mice.

Conclusions

Our study provides firm evidence for the contribution of early and postnatal bipotent progenitors to the formation and maintenance of the thymic epithelial microenvironment and reveals several new aspects of TEC biology. First, the two progenitor populations, an early cTEC-biased progenitor type and a postnatal mTEC-biased progenitor type, are already born during embryonic development and co-exist at E16.5, suggesting that some bipotent postnatal progenitors may be descendants of the early progenitor population (Fig. 3k). Second, the identification of private barcodes in both progenitor populations suggests that not all TEC progenitors are active at the same time, a phenomenon that is referred to as dormancy and known from other stem cell systems⁵⁶. Third, the presence of private barcodes in mature cTECs and mTECs suggests the possibility that their corresponding progenitor(s) have been lost, in line with the notion that not all progenitor cells are long-lived^{24,25}. Our current barcoding scheme does not allow us to determine whether these mature TECs can self-renew; resolution of this question awaits the use of an inducible version of the current marking scheme. Fourth, because the half-life of TECs is measured in weeks⁷, we conclude that long-term maintenance of the TEC compartment is associated with the activity of the postnatal progenitors identified here. Fifth, although continuous stimulation of thymic epithelia via autocrine secretion of an Fgfr2b ligand greatly increases the number of TECs, the qualitative characteristics of the thymic epithelium remain the same. However, the identification of progenitor populations provides new opportunities for focused pharmacological interventions to modulate the activity of the thymic microenvironment.

Methods

Mice

C57BL/6 mice were maintained in the Max Planck Institute of Immunobiology and Epigenetics. *Foxn1-eGFP*⁵⁷, *Foxn1-cre*⁵⁸, *Rosa26-LSL-EYFP*⁵⁹, *Foxn1-s-Fgfr2IIIb*⁶⁰, *pLck-cre*⁶¹, *Rosa26-LSL-Cas9-EYFP*⁶² and *Foxn1-mCardinal*⁹ transgenic mice have been described previously. The *Foxn1-Fgf7* transgene was created by inserting a cDNA fragment corresponding to nucleotides 347–934 in GenBank accession number [NM_008008](#) as a NotI fragment into pAHB14 (ref. [63](#)); in some aged female *Foxn1-Fgf7* transgenic mice (FVB/N-tg(*Foxn1-Fgf7*)1^{Tbo}/Mpie), the two thymic lobes were asymmetric in size and shape; these mice were not included in our analysis. The *Foxn1-Fgfr2IIIb* transgene was created by inserting a cDNA fragment corresponding to nucleotides 1214–3366 in GenBank accession number [NM_201601.2](#) as a NotI fragment into pAHB14 (ref. [63](#)) and used to generate transgenic mice (FVB/N-tg(*Foxn1-Fgfr2*)1^{Tbo}/Mpie). The *hU6-sgRNA^{Hprt}* transgene was cloned as a NotI fragment into the Bluescript vector and consists of the human *U6* promotor (nucleotides 1–264 in GenBank accession number [JN255693](#)) followed by the mouse *Hprt* target sequence (5'-GATGGGAGGCCATCACATTGG-3'; nucleotides 255–274 in GenBank accession number [J00423](#)), the sgRNA backbone (nucleotides 218–139 (reverse complement) in Addgene plasmid 42250) and a short 3' sequence (TTTTTTGGAA); for injection into fertilized eggs, the construct was linearized with SacI. Transgenic mice were generated on an FVB/N background (FVB/N-tg(*hU6-sgRNA-Hprt*)1^{Tbo}/Mpie) and subsequently backcrossed to a C57BL/6J background. For timed matings, the day of plug detection was designated as E0.5. Genotyping information is summarized in Supplementary Table [15](#). Mice were kept in the animal facility of the Max Planck Institute of Immunobiology and Epigenetics under specific pathogen-free conditions. All animal experiments were performed in accordance with the relevant guidelines and regulations, approved by the review committee of the Max Planck Institute of Immunobiology and Epigenetics and Regierungspräsidium Freiburg, Germany (licences 35-9185.81/G-12/85; 35-9185.81/G-16/67).

KGF treatment

At the age of 4 weeks, male mice received nine intraperitoneal injections of KGF (Kepivance, Biovitrum, lot D120961G; 5 mg kg⁻¹ body mass) at days

1, 2, 3, 8, 9, 10, 15, 16 and 17; the mice were killed on day 21.

Histology

Embryos for RNA in situ hybridization (ISH) were fixed in 4% paraformaldehyde (PFA) and subsequently embedded in paraffin using standard techniques.

qPCR

The Applied Biosystems 7500 Fast system was used to detect the signal generated with gene-specific primers combined with 5'-FAM (6-carboxyfluorescein)-labelled hydrolysis probes from Universal Probe Library (Roche). Primer sequences were as follows: *Fgf7*, 5'-TGGCTGACACCATGACTAGC-3' and 5'-GGCTACAGGCTGTCGTTTT-3' (probe 42); *Fgf10*, 5'-CGGGACCAAGAACATGAAGACT-3' and 5'-GCAACAACTCCGATTCCAC-3' (probe 80); *CD31* (*Pecam*), 5'-CGGTGTTCAGCGAGATCC-3' and 5'-ACTCGACAGGATGGAAATCAC-3' (probe 45); *Ly51* (*Enpep*), 5'-TGGACTCCAAGCTGATCCT-3' and 5'-TCAGCCCCTGACTGGAAT-3' (probe 83). Expression levels were normalized to those of *Hprt*, using primers 5'-TCCTCCTCAGACCGCTTT-3' and 5'-CCTGGTTCATCATCGCTAATC-3' (probe 95).

RNA ISH

RNA ISH on paraffin sections was performed using DIG-labelled probes as described⁶⁴. Sequence coordinates in GenBank accession numbers were as follows: *Foxn1*, nucleotides 2181–3584 in [XM_006532266.3](#); *Fgf7*, nucleotides 153–877 in [NM_008008.3](#); *Fgf10*, nucleotides 859–1570 in [NM_008002.3](#); *Fgfr1*, nucleotides 761–1614 in [NM_001079909.2](#); *Fgfr2*, nucleotides 328–800 in [EF143340](#); *Fgfr2_exon3b*, nucleotides 1819–1964 in [NM_201601.2](#); *Fgfr2_exon3c*, nucleotides 2169–2306 in [NM_010207.2](#); *Hspb1*, nucleotides 224–632 in [NM_013560.2](#); *Trpm5*, nucleotides 499–962 in [NM_020277.2](#).

Immunohistochemistry

Thymi were fixed in 4% PFA, washed in PBS, incubated in 20% sucrose overnight and embedded in OCT. Sections of 8–10 µm were dried overnight at room temperature and before staining were moistened in PBS followed by a 30-min blocking step (PBS with 0.5% BSA, 0.2% Tween and anti-mouse IgG (1:50)). Antibody staining was performed at room temperature in staining buffer (PBS with 0.5% BSA, 0.2% Tween and 3% serum). Sections were stained for 2 h with primary antibodies (Supplementary Table 6) and then for 45 min with secondary antibodies and streptavidin. Sections were washed with PBS between incubations. After staining, sections were mounted in Fluoromount G.

Image analysis

Images were acquired on Zeiss microscopes (Axioplan 2 or Imager Z1 with ApoTome attachment) equipped with AxioCam MRc 5 cameras.

Flow cytometry

To generate single-cell suspensions for analytical and preparative flow cytometry of TECs, the procedures described in refs. 18,65 were followed. Relevant staining reagents are listed in Supplementary Table 16. The enzymatic cocktail required to liberate TECs destroys the extracellular domains of the CD4 and CD8 surface markers (but not that of the CD45 molecule); hence, when analysis of thymocyte subsets was desired, thymocyte suspensions were prepared in parallel by mechanical liberation, achieved by gently pressing thymic lobes through 40-µm sieves. To isolate thymic mesenchymal and endothelial cells, the cell suspension of total thymocytes was depleted of CD45⁺ cells; the EpCAM[−]CD45[−] cell population was stained for Ly51 and CD31 to purify EpCAM[−]CD31[−]Ly51⁺ mesenchymal and EpCAM[−]CD31⁺Ly51[−] endothelial cells. Cell sorting and analytical flow cytometry were carried out using MoFlow and Fortessa instruments, respectively (both from Dako Cytomation-Beckman Coulter); flow cytometry experiments were carried out using FACSDiva and FlowJo software. The fraction of *Foxn1*-expressing cells was determined by eGFP fluorescence emanating from the *Foxn1*-eGFP transgene⁵⁷, which faithfully

recapitulates acute levels of *Foxn1* expression^{18,34}. The thymopoietic index was calculated by dividing the total number of thymocytes by the number of TECs.

Single-cell RNA amplification and library preparation

scRNA-seq was performed using the CEL-Seq2 method⁴⁵ with several modifications⁴⁴. A fivefold volume reduction was achieved using a nanolitre-scale pipetting robot (Mosquito HTS, TTP Labtech)⁶⁶.

EpCAM⁺CD45⁻ TECs were sorted into 384-well plates containing 240 nl of primer mix⁶⁷ and 1.2 µl of mineral oil (Sigma-Aldrich) replacing Vapor-lock. Sorted plates were centrifuged at 2,200g for 3 min at 4 °C, snap-frozen in liquid nitrogen and stored at –80 °C before further processing. To convert RNA into cDNA, 160 nl of reverse-transcription reaction mix including 0.4 µM template-switch oligonucleotide (5'-AAGCAGTGGTATCAACGCAGAGTGAATrGrGrG-3'; adapted from ref. 68) and 2.2 µl of second-strand reaction mix were added.

For the purpose of simultaneous transcriptome and barcode analysis, the volume of each well was equally split in half; that is, 1.1 µl per well was transferred to a new 384-well plate. The original plate (including the mineral oil) was used for barcode analysis, while the copy of the plate was used for analysis of individual cell transcriptomes.

For barcode analysis, all transcripts in each well were amplified by template-switch PCR (5'-AAGCAGTGGTATCAACGCAGAGT-3' (template-switch oligonucleotide primer) and 5'-CAGAGTTCTACAGTCCGA-3' (short P5 primer)), followed by amplification of the scar region of *Hprt* transcripts (5'-GCCGGTAATACGACTCACTATAGGGAGTTCTACAGTCCGACGATC-6bp UMI-6bp cell barcode-CCAGTTAAAGTTGAGAGATCATCTCC-3' (*Hprt* barcoding primer), 5'-GCCTTGGCACCCGAGAATTCCATAGCGATGATGAACCAGGTTATGA CC-3' (*Hprt* short P7 primer)) using the PrimeSTAR GXL system (Takara Bio). Libraries were completed by addition of full-length adaptors by PCR (RP1, RPI1-48 TruSeq Small RNA Illumina adaptor sequences). Libraries from 96 cells were pooled before clean-up. In total, 32 libraries (E16.5 time point), 32 libraries (P0 time point), 28, 40 and 80 libraries (three P28 time

points), 32 libraries (1-year time point), 44 libraries (*Foxn1-Fgf7* transgenic mice, P28 time point) and 60 libraries (*Foxn1-Fgf7* transgenic mice, 1-year time point) were sequenced on the MiSeq sequencing system (2×300 bp) at a depth of $\geq 4,000$ reads per cell.

Transcriptomes were generated as described previously⁶⁶; for the P28 wild-type dataset from a non-barcoded mouse, the whole sample volume was used for transcriptome generation. cDNAs from 96 cells were pooled before clean-up and in vitro transcription, generating four libraries from one 384-well plate. For all purification steps, $0.8 \mu\text{l}$ of AMPure/RNA Clean XP beads (Beckman Coulter) was used per $1 \mu\text{l}$ of sample, including in library clean-up.

In total, 32 libraries (E16.5 time point), 32 libraries (P0 time point), 28, 40 and 80 libraries (three P28 time points), 28 libraries (non-barcoded dataset of P28 time point), 32 libraries (1-year time point), 44 libraries (*Foxn1-Fgf7* transgenic mice at P28 time point) and 60 libraries (*Foxn1-Fgf7* transgenic mice at 1-year time point) (each library was generated by pooling 96 cells) were sequenced on the Illumina HiSeq 2500 or NovaSeq 6000 sequencing system (paired-end multiplexing run, high-output mode) at a depth of $\sim 170,000$ reads per cell.

Quantification of transcript abundance

Paired-end reads were aligned to the transcriptome using bwa (version 0.6.2-r126) with default parameters⁶⁹. The transcriptome contained all gene models based on the mouse ENCODE VM9 release downloaded from the UCSC genome browser, comprising 57,207 isoforms, with 57,114 isoforms mapping to fully annotated chromosomes (1 to 19, X, Y, mitochondria). All isoforms of the same gene were merged to a single gene locus. Furthermore, gene loci overlapping by $>75\%$ were merged to larger gene groups. This procedure resulted in 34,111 gene groups. The right mate of each read pair was mapped to the ensemble of all gene loci and to the set of 92 ERCC spike-ins in the sense direction⁷⁰. Reads mapping to multiple loci were discarded. The left read contained the barcode information: the first six bases corresponded to the cell-specific barcode followed by six bases representing the unique molecular identifier (UMI). The remainder of the

left read contained a poly(T) stretch. The left read was not used for quantification. For each cell barcode, the number of UMIs per transcript was counted and aggregated across all transcripts derived from the same gene locus. On the basis of binomial statistics, the number of observed UMIs was converted into transcript counts⁷¹.

scRNA-seq data analysis

Clustering analysis and visualization of all datasets were performed with the VarID algorithm⁴⁶. Cells with a total number of transcripts of <1,000 (1-year wild-type dataset), <1,500 (wild-type and *Foxn1-Fgf7* transgenic P28 datasets) and <3,000 (wild-type E16.5, wild-type P0 and *Foxn1-Fgf7* transgenic 1-year datasets) were discarded, and the count data of the remaining cells were normalized by downscaling. Notably, before normalization, cells yielding transcriptomes containing >2% *Kcnq1ot1* transcripts, a previously identified marker of low-quality cells, were removed from the analysis⁷². Moreover, transcripts correlating to *Kcnq1ot1* with a Pearson's correlation coefficient of >0.65 were also removed. Furthermore, mitochondrial genes as well as *Hprt* were excluded. The following genes and correlating gene groups were removed from the analysis using the CGenes parameter (all datasets): *Jun*, *Fos* and predicted genes with *Gm* identifiers. For the wild-type P28 datasets, *Malat1*, *Xist* and *Neat1* were excluded using the FGenes parameter. A pruned *k* nearest neighbour (kNN) matrix was inferred using the pruneKnn function of VarID with default parameters except alpha (set to 1) and no_cores (set to 10). The UMAP representation was used for cell cluster visualization⁷³. Transition probabilities between clusters were computed using the transitionProbs function of VarID with the *P* value set to 0.001. Differentially expressed genes between two subgroups of cells were identified similarly to in a previously published method⁷⁴. First, negative binomial distributions reflecting the gene expression variability within each subgroup were inferred on the basis of the background model for the expected transcript count variability computed by the RaceID3 algorithm⁴⁴. Using these distributions, a *P* value for the observed difference in transcript counts between the two subgroups was calculated and corrected for multiple testing with the Benjamini–Hochberg method.

High-resolution lineage tracing

The lineage tracing method developed here was based on CRISPR–Cas9-mediated scarring in exon 3 of the *Hprt* gene (Fig. 2a). Repair of Cas9-induced double-strand breaks results in a number of different sequence outcomes, which we refer to here as barcodes because they indelibly mark all cell progeny. Most barcodes carry deletions (Fig. 2b), preventing secondary modifications of their sequence; however, in rare instances, we recorded cells with two barcodes of similar sequence, presumably originating from ongoing modifications of the target sequence or from relaxed X-chromosome inactivation. In bulk and single-cell analyses of male mice, barcodes can be unambiguously read out on both the DNA and transcript level from the single X chromosome. In female mice, which carry two X chromosomes, DNA analysis at the level of cell populations yields ambiguous results; however, for single-cell analysis, the phenomenon of dosage compensation enables unambiguous barcode analysis at the RNA level. For the bulk analyses described here, we therefore used only male mice, whereas single-cell transcriptome analyses were conducted in both male and female mice. In the *hU6-sgRNA^{Hprt}; Foxn1-cre; Rosa26-LSL-Cas9-EYFP* triple-transgenic mice used here, TECs are marked in early embryogenesis, as soon as *Foxn1* expression begins; our previous analysis indicated that, at the onset of *Foxn1* expression, the thymic rudiment harbours ~4,000 epithelial cells⁹, thus placing an upper limit on the number of barcodes that can be observed in TECs at later developmental stages. However, the observed number of barcodes was three- to fourfold lower, presumably because the outcome of the repair process is not random; hence, some barcodes, although independently generated, are identical in sequence. The different frequencies of barcode generation must be taken into account when reconstructing lineage relationships; rare barcode sequences are more informative than frequently generated barcodes. On the basis of previous experiments using our *Foxn1-cre* transgenic line and the accessibility of the *Rosa26* locus in TECs³⁴, we assume that the overwhelming majority of TECs (>95%) are barcoded early in embryogenesis. However, we cannot exclude the possibility that some cells in the thymic rudiment are recruited into the *Foxn1*-positive lineage at later stages of development. If so, this would however only lessen the ability to identify clonal relationships across all time points.

Single-cell barcoding analysis

Paired-end fastq files were used for the identification of scar sequences in single cells. The first six bases of the left read contained the UMI information, followed by six bases representing the cell barcode. The remainder of the left read contained the *Hprt* scar sequence. The right mate of the paired-end reads also contained the overlapping *Hprt* scar sequence; that is, both reads contained the full scar sequences. Primers (forward, 5'-GCTCGAGATGTCATGAAGG-3'; reverse, 5'-GGGGGGCTATAAGTTCTT-3') were used to extract the targeted region of the *Hprt* gene containing the edited sequence. Because both the left and right mates of the paired-end reads contain the full scar sequences, only sequences that appeared in both paired-end reads were used for further analysis. Moreover, only cells yielding ≥ 200 reads were included in the analysis; cells were excluded from further analysis if more than one scar sequence was detected in male cells (the threshold for the second sequence was set at $\geq 10\%$ of the major sequence) and if more than two scar sequences were detected in female cells (the threshold for the third sequence was set at $\geq 10\%$ of the second sequence).

Barcodes shared by cTECs and mTECs

DNA was isolated from sorted EpCAM $^+$ CD45 $^-$ Ly51 $^+$ UEA-1 $^-$ (cTEC) and EpCAM $^+$ CD45 $^-$ Ly51 $^-$ UEA-1 $^+$ (mTEC) populations from each mouse, and the region of exon 3 of the *Hprt* gene was amplified using the following primers: 5'-ACACTCTTCCCTACACGACGCTCTCCGATCTTCATAGAGACAA GGAATGTGTCC-3' (forward, P5-DD302) and 5'-GTGACTGGAGTTCAGACGTGTGCTCTCCGATCTAGTTGATTATGT AGCAAtAGTTGACAAG-3' (reverse, P7-DD305). Libraries were sequenced at a depth of $\sim 250,000$ reads per sample on the MiSeq sequencing system (2×300 bp).

Next, a table containing the counts of all barcodes across cTECs and mTECs for each mouse ($n = 33$ mice) was constructed, and the frequency distribution of barcodes was determined (Fig. 2d). To quantify enrichment of shared barcodes between the cTEC and mTEC samples for a given mouse,

we first extracted the set of all barcodes B_i for sample i that were observed no more than twice in all animal samples; then, we determined the number of barcodes within set B_i co-occurring in another sample j and divided this by the number of barcodes in B_i to compute the co-occurrence probability of rare barcodes, termed P_{ij} :

$$\text{\$}\$\{P\}_{ij}=\frac{\sum_{k \in B_i} \chi_{\{B_j\} \cap \{B_k\}}}{\sum_{k \in B_i} \chi_{\{B_k\}}} \text{\$}$$

Here $\chi_T(x)$ denotes the indicator function; that is, $\chi_T(x) = 1$ if $x \in T$, $\chi_T(x) = 0$ otherwise.

If i and j denote mTEC and cTEC samples from the same mouse, we would like to test whether P_{ij} is relatively increased compared with cases where i and j denote samples from different mice.

An increased co-occurrence probability in corresponding samples compared with all other mice is indicative of a common barcode repertoire and is interpreted to mean that cTEC and mTEC populations in a mouse arise from common progenitors marked by particular barcodes; conversely, a similar ratio across all animals suggests the random occurrence of rare barcodes and argues against a common origin. The observation that some of the rare barcodes are not shared by cTEC and mTEC populations from the same mouse can be explained by the low frequency of these rare barcodes, resulting in sampling dropouts, but may also have a biological explanation, for example, if either mTEC or cTEC progeny derived from the same progenitor have died out. In this context, it is worth noting that, without prefiltering based on barcode frequency, the fraction of barcodes shared by mTEC and cTEC populations was >50%.

To quantify a single enrichment value E_m for a given animal m , the ratios calculated for a corresponding pair of cTEC and mTEC samples, m_{cTEC} and m_{mTEC} , from the same mouse were divided (with cTECs or mTECs as a reference) by the average of the ratios for pairings involving either the respective cTEC or mTEC sample and a sample from any other animal, excluding the samples from animal m . The enrichment value E_m is then

calculated as the maximum of these ratios with mTECs or cTECs from the same animal as a reference:

```

$${\begin{array}{ccc}E_m &=& \max \\(\frac{P_m(\rm{cTEC})}{m(\rm{mTEC})}) & & \frac{1}{N-2}\sum_{j \neq m}(\rm{cTEC}_j) \\&& &\& \frac{P_m(\rm{mTEC})}{m(\rm{cTEC})}) \\&& &\& \frac{1}{N-2}\sum_{j \neq m}(\rm{mTEC}_j)\end{array}}$$

```

Here N is the total number of samples and \wedge indicates logical conjunction. In the summation of the denominators, we exclude pairings involving the mTEC or cTEC samples for animal m .

The enrichment values of shared rare barcodes for each mouse were then plotted for each individual mouse grouped by age bin in Fig. 2f. Note that the analysis of bulk populations is most robust with respect to sampling when the numbers of cTECs and mTECs are approximately equal, as is the case for the P14 time point⁹. In situations where only a small number of barcodes are recovered, a diminished degree of co-occurrence is probably the result of sampling dropouts and the associated reduced statistical power.

Lineage analysis

To quantify the enrichment of shared barcodes between different populations within the TEC compartment at single-cell resolution, we first identified the cell clusters representing early progenitors, postnatal progenitors, and mature cTECs and mTECs in the scRNA-seq analysis of the individual mice. For a given mouse, we determined the barcode repertoire and counted the number of cells for each barcode; in the rare instances where a pair of barcodes was observed, we used the combination of barcodes for quantification. Cells with more than two barcodes were discarded, as this situation is the result of cell doublets and/or sequencing errors. For each barcode (or pair of quantified barcodes), we next determined its frequency for each TEC population in a given sample. These frequencies were compared with background barcode frequencies derived from the barcode distribution quantified from the bulk DNA sequencing data ($n = 33$; Fig. 2d).

averaging across all samples. We considered sampling dropouts as a reference background model for technical variability and, therefore, assessed significant over-representation of barcodes on the basis of the estimated probability mass of a binomial distribution with a probability parameter informed by the barcode frequency derived from the bulk sequencing experiments. It is well known that UMI-based abundance derived from scRNA-seq data can be modelled by a negative binomial distribution without explicitly modelling zero inflation and that variability in genes (or barcodes) with low expression is described well by the binomial noise component⁷¹.

If $n_{b,i}$ is the number of times barcode b was observed in bulk DNA sequencing sample i , the background frequency of barcode f_b was calculated as

$$\text{\$}\{f\}_{\{b\}}=\frac{1}{N}\sum_{i \in S} \frac{n_{b,i}}{\sum_{k \in B} n_{k,i}}$$

Here B denotes the set of all barcodes, S denotes the set of all samples and N is the size of S .

Assuming binomial sampling statistics, we then calculated the P value $P_{b,i}$ for the observed number of cells $c_{b,i}$ with barcode b among all barcode-carrying cells in sample i obtained by scRNA-seq as the right tail probability of the binomial distribution with background probability f_b and the total number of barcode-carrying cells as parameters:

$$\text{\$}\{P\}_{\{b,i\}}=\mathop{\sum}_{j=c_{b,i}}^{\infty} \binom{C_i}{j} B^{(j)} f_{\{b\}}, \{C_i\}, \{w\}, \{i\}, \{t\}, \{h\}, \{C_i\}) = \sum_{k \in B} c_{k,i}$$

These P values were further corrected for multiple testing by the Benjamini-Hochberg method, considering all P values for all detected barcodes in a given dataset. For cells with two barcodes, we calculated P values accordingly after multiplying the background frequencies of the co-occurring barcodes. Barcodes were considered informative if their P value indicated a significant deviation from the expected frequency ($P_{b,i} < 0.001$).

Gene set analysis

Population-specific gene sets were derived by performing differential gene expression analysis of clusters representing early progenitors (c5), postnatal progenitors (c1 and c6), cTECs (c4) and mTECs (c12, c2, c7, c9, c10 and c18) versus all other clusters from data for 4-week-old (P28) mice using the diffexpnb function of the RaceID3 package⁴⁴. Genes with adjusted $P < 0.01$ and $\log_2(\text{fold change}) > 1$ were included in gene sets, from which genes with *Gm* and *Rik* identifiers were excluded. Overlapping genes between early progenitor and cTEC gene sets were excluded from the early progenitor gene set. Genes included in the gene sets of each of the four populations are listed in Supplementary Tables 1–4.

Although the transcriptional profiles of the progenitor clusters differed from those of the mature TEC subsets by the expression of heat shock protein genes, these genes were not included in the final lists, as they did not distinguish between the early and postnatal progenitors. The final gene sets were analysed for enriched biological processes using the Database for Annotation, Visualization and Integrated Discovery (DAVID) version 6.8 Analysis Wizard annotation tool^{75,76}. In the representation of gene set ratios, clusters expressing T cell progenitor-related genes (representing thymic nurse cells) and parathyroid-associated genes (representing ectopic parathyroid tissue) were excluded.

scRNA-seq data comparisons

The present data were compared with publicly available scRNA-seq data for TECs isolated from mice of different ages¹. To do this, the raw count matrices and metadata describing the nine subtypes of TECs were obtained through the Bioconductor data package MouseThymusAgeing (<https://bioconductor.org>; <https://doi.org/10.18129/B9.bioc.MouseThymusAgeing>). Data normalization, dimensionality reduction and visualization with UMAP were then performed using the default parameters of the scRNA-seq data analysis CRAN package Seurat version 3 (ref. ⁷⁷).

Statistical analysis and reproducibility

Two-tailed *t* tests were used to determine the significance levels of differences between the means of two independent samples, considering equal or unequal variance as determined by the *F* test. For multiple tests, the conservative Bonferroni correction was applied. For all analyses, several biological replicas were studied; numbers of replicas are indicated in the figures and/or figure legends. No statistical methods were used to predetermine sample sizes; blinding and randomization were not used.

Reporting summary

Further information on research design is available in the [Nature Research Reporting Summary](#) linked to this paper.

Data availability

The primary read files as well as expression count files for the scRNA-seq datasets reported in this paper are available to download from GEO (accession number [GSE106856](#)). [Source data](#) are provided with this paper.

References

1. Baran-Gale, J. et al. Ageing compromises mouse thymus function and remodels epithelial cell differentiation. *eLife* **9**, e56221 (2020).
2. Venables, T., Griffith, A. V., DeAraujo, A. & Petrie, H. T. Dynamic changes in epithelial cell morphology control thymic organ size during atrophy and regeneration. *Nat. Commun.* **10**, 4402 (2019).
3. George, A. J. T. & Ritter, M. A. Thymic involution with ageing: obsolescence or good housekeeping? *Immunol. Today* **17**, 267–272 (1996).
4. Boehm, T. & Swann, J. B. Thymus involution and regeneration: two sides of the same coin? *Nat. Rev. Immunol.* **13**, 831–838 (2013).
5. Steinmann, G. G., Klaus, B. & Müller-Hermelink, H.-K. The involution of the ageing human thymic epithelium is independent of puberty. A

- morphometric study. *Scand. J. Immunol.* **22**, 563–575 (1985).
6. Nikolich-Žugich, J. Ageing and life-long maintenance of T-cell subsets in the face of latent persistent infections. *Nat. Rev. Immunol.* **8**, 512–522 (2008).
 7. Gray, D. H. D. et al. Developmental kinetics, turnover, and stimulatory capacity of thymic epithelial cells. *Blood* **108**, 3777–3785 (2006).
 8. Griffith, A. V., Fallahi, M., Venables, T. & Petrie, H. T. Persistent degenerative changes in thymic organ function revealed by an inducible model of organ regrowth. *Aging Cell* **11**, 169–177 (2012).
 9. Hirakawa, M. et al. Fundamental parameters of the developing thymic epithelium in the mouse. *Sci. Rep.* **8**, 11095 (2018).
 10. Gray, D., Abramson, J., Benoist, C. & Mathis, D. Proliferative arrest and rapid turnover of thymic epithelial cells expressing Aire. *J. Exp. Med.* **204**, 2521–2528 (2007).
 11. Bautista, J. L. et al. Single-cell transcriptional profiling of human thymic stroma uncovers novel cellular heterogeneity in the thymic medulla. *Nat. Commun.* **12**, 1096 (2021).
 12. Wells, K. L. et al. Combined transient ablation and single-cell RNA-sequencing reveals the development of medullary thymic epithelial cells. *eLife* **9**, e60188 (2020).
 13. Miller, C. N. et al. Thymic tuft cells promote an IL-4-enriched medulla and shape thymocyte development. *Nature* **559**, 627–631 (2018).
 14. Kadouri, N., Nevo, S., Goldfarb, Y. & Abramson, J. Thymic epithelial cell heterogeneity: TEC by TEC. *Nat. Rev. Immunol.* **20**, 239–253 (2020).
 15. Bornstein, C. et al. Single-cell mapping of the thymic stroma identifies IL-25-producing tuft epithelial cells. *Nature* **559**, 622–626 (2018).

16. Abramson, J. & Anderson, G. Thymic epithelial cells. *Annu. Rev. Immunol.* **35**, 85–118 (2017).
17. Takahama, Y., Ohigashi, I., Baik, S. & Anderson, G. Generation of diversity in thymic epithelial cells. *Nat. Rev. Immunol.* **17**, 295–305 (2017).
18. Rode, I. et al. Foxn1 protein expression in the developing, aging, and regenerating thymus. *J. Immunol.* **195**, 5678–5687 (2015).
19. Li, J. et al. NOTCH1 signaling establishes the medullary thymic epithelial cell progenitor pool during mouse fetal development. *Development* **147**, dev178988 (2020).
20. Ishikawa, T., Akiyama, N. & Akiyama, T. In pursuit of adult progenitors of thymic epithelial cells. *Front. Immunol.* **12**, 621824 (2021).
21. Liu, D. et al. Canonical Notch signaling controls the early thymic epithelial progenitor cell state and emergence of the medullary epithelial lineage in fetal thymus development. *Development* **147**, dev178582 (2020).
22. Bleul, C. C. et al. Formation of a functional thymus initiated by a postnatal epithelial progenitor cell. *Nature* **441**, 992–996 (2006).
23. Wong, K. et al. Multilineage potential and self-renewal define an epithelial progenitor cell population in the adult thymus. *Cell Rep.* **8**, 1198–1209 (2014).
24. Ohigashi, I. et al. Aire-expressing thymic medullary epithelial cells originate from β 5t-expressing progenitor cells. *Proc. Natl Acad. Sci. USA* **110**, 9885–9890 (2013).
25. Mayer, C. E. et al. Dynamic spatio-temporal contribution of single β 5t⁺ cortical epithelial precursors to the thymus medulla. *Eur. J. Immunol.* **46**, 846–856 (2016).

26. Rodewald, H.-R., Paul, S., Haller, C., Bluethmann, H. & Blum, C. Thymus medulla consisting of epithelial islets each derived from a single progenitor. *Nature* **414**, 763–768 (2001).
27. Ulyanchenko, S. et al. Identification of a bipotent epithelial progenitor population in the adult thymus. *Cell Rep.* **14**, 2819–2832 (2016).
28. Bosticardo, M. et al. Heterozygous *FOXN1* variants cause low TRECs and severe T cell lymphopenia, revealing a crucial role of FOXN1 in supporting early thymopoiesis. *Am. J. Hum. Genet.* **105**, 549–561 (2019).
29. Nehls, M., Pfeifer, D., Schorpp, M., Hedrich, H. & Boehm, T. New member of the winged-helix protein family disrupted in mouse and rat nude mutations. *Nature* **372**, 103–107 (1994).
30. Blackburn, C. C. et al. The *nu* gene acts cell-autonomously and is required for differentiation of thymic epithelial progenitors. *Proc. Natl Acad. Sci. USA* **93**, 5742–5746 (1996).
31. Nehls, M. et al. Two genetically separable steps in the differentiation of thymic epithelium. *Science* **272**, 886–889 (1996).
32. Chen, L., Xiao, S. & Manley, N. R. Foxn1 is required to maintain the postnatal thymic microenvironment in a dosage-sensitive manner. *Blood* **113**, 567–574 (2009).
33. O'Neill, K. E. et al. *Foxn1* is dynamically regulated in thymic epithelial cells during embryogenesis and at the onset of thymic involution. *PLoS ONE* **11**, e0151666 (2016).
34. Corbeaux, T. et al. Thymopoiesis in mice depends on a *Foxn1*-positive thymic epithelial cell lineage. *Proc. Natl Acad. Sci. USA* **107**, 16613–16618 (2010).
35. Nowell, C. S. et al. Foxn1 regulates lineage progression in cortical and medullary thymic epithelial cells but is dispensable for medullary sublineage divergence. *PLoS Genet.* **7**, e1002348 (2011).

36. Kreins, A. Y., Maio, S. & Dhalla, F. Inborn errors of thymic stromal cell development and function. *Semin. Immunopathol.* **43**, 85–100 (2021).
37. Fletcher, A. L., Calder, A., Hince, R. M. N., Boyd, L. & Chidgey, A. P. The contribution of thymic stromal abnormalities to autoimmune disease. *Crit. Rev. Immunol.* **31**, 171–187 (2011).
38. Campinoti, S. et al. Reconstitution of a functional human thymus by postnatal stromal progenitor cells and natural whole-organ scaffolds. *Nat. Commun.* **11**, 6372 (2020).
39. Alawam, A. S., Anderson, G. & Lucas, B. Generation and regeneration of thymic epithelial cells. *Front. Immunol.* **11**, 858 (2020).
40. Oh, J., Wang, W., Thomas, R. & Su, D. M. Thymic rejuvenation via FOXN1-reprogrammed embryonic fibroblasts (FREFs) to counteract age-related inflammation. *JCI Insight* **5**, e140313 (2020).
41. Parent, A. V. et al. Generation of functional thymic epithelium from human embryonic stem cells that supports host T cell development. *Cell Stem Cell* **13**, 219–229 (2013).
42. Sun, X. et al. Directed differentiation of human embryonic stem cells into thymic epithelial progenitor-like cells reconstitutes the thymic microenvironment in vivo. *Cell Stem Cell* **13**, 230–236 (2013).
43. Bredenkamp, N. et al. An organized and functional thymus generated from FOXN1-reprogrammed fibroblasts. *Nat. Cell Biol.* **16**, 902–908 (2014).
44. Herman, J. S., Sagar, & Grün, D. FateID infers cell fate bias in multipotent progenitors from single-cell RNA-seq data. *Nat. Methods* **15**, 379–386 (2018).
45. Hashimshony, T. et al. CEL-Seq2: sensitive highly-multiplexed single-cell RNA-Seq. *Genome Biol.* **17**, 77 (2016).

46. Grün, D. Revealing dynamics of gene expression variability in cell state space. *Nat. Methods* **17**, 45–49 (2020).
47. Nakagawa, Y. et al. Thymic nurse cells provide microenvironment for secondary T cell receptor α rearrangement in cortical thymocytes. *Proc. Natl Acad. Sci. USA* **109**, 20572–20577 (2012).
48. Murata, S. et al. Regulation of CD8 $^{+}$ T cell development by thymus-specific proteasomes. *Science* **316**, 1349–1353 (2007).
49. Yamazaki, Y. et al. PAX1 is essential for development and function of the human thymus. *Sci. Immunol.* **5**, eaax1036 (2020).
50. Gordon, J., Bennett, A. R., Blackburn, C. C. & Manley, N. R. Gcm2 and Foxn1 mark early parathyroid- and thymus-specific domains in the developing third pharyngeal pouch. *Mech. Dev.* **103**, 141–143 (2001).
51. Pei, W. et al. Polylox barcoding reveals haematopoietic stem cell fates realized in vivo. *Nature* **548**, 456–460 (2017).
52. Alemany, A., Florescu, M., Baron, C. S., Peterson-Maduro, J. & van Oudenaarden, A. Whole-organism clone tracing using single-cell sequencing. *Nature* **556**, 108–112 (2018).
53. Revest, J. M., Suniara, R. K., Kerr, K., Owen, J. J. T. & Dickson, C. Development of the thymus requires signaling through the fibroblast growth factor receptor R2-IIIb. *J. Immunol.* **167**, 1954–1961 (2001).
54. Min, D. et al. Sustained thymopoiesis and improvement in functional immunity induced by exogenous KGF administration in murine models of aging. *Blood* **109**, 2529–2537 (2007).
55. Rossi, S. W. et al. Keratinocyte growth factor (KGF) enhances postnatal T-cell development via enhancements in proliferation and function of thymic epithelial cells. *Blood* **109**, 3803–3811 (2007).
56. Pei, W. et al. Resolving fates and single-cell transcriptomes of hematopoietic stem cell clones by PolyloxExpress barcoding. *Cell Stem Cell* **27**, 383–395 (2020).

57. Terszowski, G. et al. Evidence for a functional second thymus in mice. *Science* **312**, 284–287 (2006).
58. Soza-Ried, C., Bleul, C. C., Schorpp, M. & Boehm, T. Maintenance of thymic epithelial phenotype requires extrinsic signals in mouse and zebrafish. *J. Immunol.* **181**, 5272–5277 (2008).
59. Srinivas, S. et al. Cre reporter strains produced by targeted insertion of *EYFP* and *ECFP* into the *ROSA26* locus. *BMC Dev. Biol.* **1**, 4 (2001).
60. Schlake, T. FGF signals specifically regulate the structure of hair shaft medulla via IGF-binding protein 5. *Development* **132**, 2981–2990 (2005).
61. Orban, P. C., Chui, D. & Marth, J. D. Tissue- and site-specific DNA recombination in transgenic mice. *Proc. Natl Acad. Sci. USA* **89**, 6861–6865 (1992).
62. Platt, R. J. et al. CRISPR–Cas9 knockin mice for genome editing and cancer modeling. *Cell* **159**, 440–455 (2014).
63. Bleul, C. C. & Boehm, T. BMP signaling is required for normal thymus development. *J. Immunol.* **175**, 5213–5221 (2005).
64. Swann, J. B., Happe, C. & Boehm, T. Elevated levels of Wnt signaling disrupt thymus morphogenesis and function. *Sci. Rep.* **7**, 785 (2017).
65. Nagakubo, D., Krauth, B. & Boehm, T. Genetic and non-genetic determinants of thymic epithelial cell number and function. *Sci. Rep.* **7**, 10314 (2017).
66. Sagar, J. S. H., Pospisilik, J. A. & Grün, D. High-throughput single-cell RNA sequencing and data analysis. *Methods Mol. Biol.* **1766**, 257–283 (2018).
67. Herrtwich, L. et al. DNA damage signaling instructs polyploid macrophage fate in granulomas. *Cell* **167**, 1264–1280 (2016).

68. Ranskold, D. et al. Full-length mRNA-Seq from single-cell levels of RNA and individual circulating tumor cells. *Nat. Biotechnol.* **30**, 777–782 (2012).
69. Li, H. & Durbin, R. Fast and accurate long-read alignment with Burrows–Wheeler transform. *Bioinformatics* **26**, 589–595 (2010).
70. Baker, S. C. et al. The External RNA Controls Consortium: a progress report. *Nat. Methods* **2**, 731–734 (2005).
71. Grün, D., Kester, L. & van Oudenaarden, A. Validation of noise models for single-cell transcriptomics. *Nat. Methods* **11**, 637–640 (2014).
72. Grün, D. et al. De novo prediction of stem cell identity using single-cell transcriptome data. *Cell Stem Cell* **19**, 266–277 (2016).
73. Becht, E. et al. Dimensionality reduction for visualizing single-cell data using UMAP. *Nat. Biotechnol.* **37**, 38–44 (2018).
74. Anders, S. & Huber, W. Differential expression analysis for sequence count data. *Genome Biol.* **11**, R106 (2010).
75. Huang da, W., Sherman, B. T. & Lempicki, R. A. Systematic and integrative analysis of large gene lists using DAVID bioinformatics resources. *Nat. Protoc.* **4**, 44–57 (2009).
76. Huang da, W., Sherman, B. T. & Lempicki, R. A. Bioinformatics enrichment tools: paths toward the comprehensive functional analysis of large gene lists. *Nucleic Acids Res.* **37**, 1–13 (2009).
77. Stuart, T. et al. Comprehensive integration of single-cell data. *Cell* **177**, 1888–1902 (2019).
78. van den Brink, S. C. et al. Single-cell sequencing reveals dissociation-induced gene expression in tissue subpopulations. *Nat. Methods* **14**, 935–936 (2017).
79. Yeh, B. K. et al. Structural basis by which alternative splicing confers specificity in fibroblast growth factor receptors. *Proc. Natl Acad. Sci.*

USA **100**, 2266–2271 (2003).

80. Ohuchi, H. et al. FGF10 acts as a major ligand for FGF receptor 2 IIIb in mouse multi-organ development. *Biochem. Biophys. Res. Commun.* **277**, 643–649 (2000).
81. Celli, G., LaRochelle, W. J., Mackem, S., Sharp, R. & Merlini, G. Soluble dominant-negative receptor uncovers essential roles for fibroblast growth factors in multi-organ induction and patterning. *EMBO J.* **17**, 1642–1655 (1998).

Acknowledgements

We thank the late M. Kijima for her contribution to the initial implementation of the barcoding system, B. Kanzler for help with the generation of transgenic mouse lines, K. Schuldes and A. Würch for help with cell sorting, and U. Bönisch for assistance with high-throughput sequencing. This work was supported by the Max Planck Society, the European Research Council under the European Union’s Seventh Framework Programme (FP7/2007-2013; ERC grant agreement no. 323126 to T.B.) and the Deutsche Forschungsgemeinschaft (grant GR4980/3-1 to D.G.).

Funding

Open access funding provided by Max Planck Society.

Author information

Author notes

1. Lesly Calderon

Present address: Institute of Molecular Pathology, Vienna, Austria

2. These authors contributed equally: Anja Nusser, Sagar, Jeremy B. Swann

Authors and Affiliations

1. Department of Developmental Immunology, Max Planck Institute of Immunobiology and Epigenetics, Freiburg, Germany

Anja Nusser, Jeremy B. Swann, Brigitte Krauth, Dagmar Diekhoff, Lesly Calderon, Christiane Happe & Thomas Boehm

2. Quantitative Single Cell Biology Group, Max Planck Institute of Immunobiology and Epigenetics, Freiburg, Germany

Sagar & Dominic Grün

3. Department of Medicine II, University Hospital Freiburg, Freiburg, Germany

Sagar

4. Würzburg Institute of Systems Immunology, Max Planck Research Group at the Julius-Maximilians-Universität Würzburg, Würzburg, Germany

Dominic Grün

5. Helmholtz Institute for RNA-Based Infection Research (HIRI), Helmholtz Centre for Infection Research (HZI), Würzburg, Germany

Dominic Grün

6. Faculty of Medicine, University of Freiburg, Freiburg, Germany

Thomas Boehm

Contributions

All authors designed experiments and analysed data. A.N., S., J.B.S., B.K., D.D., L.C. and C.H. performed experiments; A.N., S., B.K. and D.D. carried out scRNA-seq experiments; A.N., S., D.G. and T.B. analysed scRNA-seq data; A.N., J.B.S., B.K., D.D., L.C. and T.B. generated and analysed

transgenic mice; D.G. devised the computational analysis of barcode data; T.B. and D.G. co-directed the study. T.B. conceived the study and wrote the paper with input from all authors.

Corresponding authors

Correspondence to [Dominic Grün](#) or [Thomas Boehm](#).

Ethics declarations

Competing interests

The authors declare no competing interests.

Peer review

Peer review information

Nature thanks Hans-Reimer Rodewald, Sarah Teichmann and the other, anonymous, reviewer(s) for their contribution to the peer review of this work.

Additional information

Publisher's note Springer Nature remains neutral with regard to jurisdictional claims in published maps and institutional affiliations.

Extended data figures and tables

[Extended Data Fig. 1 Characterization of TECs isolated from 4 week-old mice.](#)

a, UMAP representation highlighting the 20 clusters identified by VarID. **b**, Distribution of male and female TECs (colour-coded) in the UMAP map. **c**, Expression levels of cell cycle-related genes (see Supplementary Table 5).

Cluster 3 corresponds to thymic nurse cells, which have a mixed phenotype of cTECs and thymocytes, the latter likely contributing to the proliferative signature; cluster 15 has affinities to the postnatal progenitor cluster but already expresses significant levels of *Aire*, a marker of mature mTECs, suggesting that this cluster harbours transit amplifying cells feeding into the mature mTEC populations. The first and third quartiles are marked by the box, the median is denoted by a horizontal line, the boundaries of the whiskers are set at 1.5 times the interquartile range, outliers are indicated as dots outside the boundary of the whiskers. Numbers of cells are as follows: Cluster 1, n = 516; cluster 2, n = 697; cluster 3, n = 288; cluster 4, n = 449; cluster 5, n = 296; cluster 6, n = 420; cluster 7, n = 773; cluster 8, n = 443; cluster 9, n = 136; cluster 10, n = 418; cluster 11, n = 306; cluster 12, n = 670; cluster 13, n = 81; cluster 14, n = 222; cluster 15, n = 401; cluster 16, n = 61; cluster 17, n = 21; cluster 18, n = 203; cluster 19, n = 189; cluster 20, n = 369. **d**, Expression profiles of the indicated signature genes. **e**, RNA *in situ* hybridization depicting *Hspb1* expression patterns in the thymus of 4-week-old mice; cortex (c) and medulla (m) are indicated, dashed lines highlight the cortico-medullary junction. *Hspb1*, as well as other genes not shown here, are often referred to as stress-related genes that may become upregulated during tissue dissociation and single-cell isolation, causing artefactual associations in the transcriptome analysis⁷⁸. However, when assayed by RNA *in situ* hybridization in the intact thymic lobe of 4-week-old mice, *Hspb1* marks a subset of medullary cells, indicating that its expression is an intrinsic characteristic of TECs and confirming that its expression profile deduced from scRNA-seq (see panel d) is not affected by the isolation procedure. Scale bar, 0.5 mm. **f**, Number of cells in individual TEC clusters. Cluster 17 represents cells derived from ectopic parathyroid tissue

[Source data](#)

Extended Data Fig. 2 Characterization of gene sets defining embryonic and postnatal progenitors.

a, b, Five transcriptional trajectories each define the gene sets characterizing embryonic (**a**) and postnatal (**b**) progenitors. Gene lists are given in Supplementary Tables [1](#) and [2](#). The P28 time point is used as the reference

point for expression levels. **c, d**, Expression values of individual genes in the sets characterizing embryonic (**c**) and postnatal (**d**) progenitors. Most genes exhibit low expression values. **e**, Pathway analysis of unique gene sets (Supplementary Tables 1–4) characterizing early and postnatal progenitors and mature cTECs and mTECs. The three most enriched biological processes each as defined by the database for annotation, visualization and integrated discovery (DAVID) annotation tool^{75,76} are shown; the genes driving the enrichment for the GO categories are listed in Supplementary Table 6. Both progenitor populations express a number of heat shock protein genes, which are not considered here

Source data

Extended Data Fig. 3 Age-dependent changes in the TEC compartment.

a–d, UMAP representation of transcriptome similarities between individual TECs isolated from thymi at various time points. Note that for P28, a combined analysis of three mice (2 females, 1 male) is shown, as they were subsequently used for the barcoding analysis; in Fig. 1, data from an additional non-barcoded mouse is included. Left panels in a-d indicate the cluster designation deduced by VarID. The right panels indicate the transcriptional relationships in terms of VarID-derived transition probabilities; connections with probabilities $P > 0.001$ are shown and the transition probabilities are indicated by line thickness and colouring. For orientation purposes, the major cell populations are also indicated. Cells derived from ectopic parathyroid tissue were detected at P28 (**c**, cluster 8), and 1 year (**d**, clusters 3 and 5). **e–h**, Expression profiles of TEC clusters for the indicated signature genes and the four time points. The fractions of each cluster expressing a particular gene and their respective expression levels are depicted according to the scales shown on the right. Dot colour represents the z-score of the mean expression levels of the gene in the respective cluster, and dot size represents the fraction of cells in the cluster expressing the gene; gene names are coloured according to shared expression patterns (EP: green; PP: orange; cTEC, blue; mTEC, red; other genes of interest, black). z-scores above 1 and below -2 are replaced by 1 and -1 respectively.

Extended Data Fig. 4 Age-dependent changes in the TEC compartment.

a–d, UMAP maps of progenitor and mature TEC populations at 4 different time points; embryonic day 16.5 (E16.5), newborn (P0), 4-week-old (P28), and 1-year-old (1 yr). The UMAP maps for P28 mice were generated by inclusion of only barcoded mice.

Extended Data Fig. 5 Comparative analysis of scRNA-seq data.

a–d, Projection of aggregated read-counts for gene sets defining early and postnatal progenitors and mature cTEC and mTEC (Supplementary Tables 1–4) onto the 9 major TEC subsets defined by Baran-Gale *et al.* (1).

Whereas the early progenitor signature cannot be unequivocally assigned, the postnatal progenitor signature maps to the intertypical TEC subset; the cTEC and mTEC signatures match the description of Baran-Gale *et al.* (1). **e**, Analysis of scRNA-seq data of Baran-Gale *et al.* (1) visualized using UMAP. Their 9 different TEC subtypes are distinguished by different colours, matching the code in a-d. **f**, Projection of aggregated read-counts for the early progenitor gene set onto the UMAP, indicating partial overlap with cells referred to as mature and perinatal cTECs. **g**, Projection of aggregated read-counts for the postnatal progenitor gene set onto the UMAP indicating good correspondence with the majority of intertypical TECs.

Extended Data Fig. 6 Characterization of the *sgRNA^{Hprt}* cassette.

a, Schematic of the components of the *hU6:sgRNA^{Hprt}* transgene; key features are indicated by name and are colour-coded; the bar representing the hU6 promotor sequence was truncated. **b**, Nucleotide sequence of the *hU6:sgRNA^{Hprt}* transgene construct (colour code as in a). **c–e**, Frequencies of individual barcodes in decreasing order from left to right grouped by the degree of occurrence in the cohort of mice analysed here ($n = 33$); colours indicate those barcodes that satisfy the criterion indicated at the top right of each plot. **f**, Scatter plots of barcode frequencies for mTECs and cTECs from the same mouse versus barcode frequencies in cTECs isolated from

two different mice. **g**, Fraction of informative barcodes observed in the TEC compartment of individual mice; informative barcodes are those whose P values indicate a significant deviation ($P_{b,i} < 0.001$ for barcode b in sample i) from the barcode frequencies expected from the background model. Since these values represent singular data points, statistical comparisons were not done. Barcode data are listed in Supplementary Tables [7–14](#)

[Source data](#)

Extended Data Fig. 7 Characterization of wild-type TEC subsets at P28.

a, Flow cytometric analysis of EpCAM $^+$ CD45 $^-$ TECs after co-staining with anti-Ly51 antibody and UEA-1 lectin. The cTEC gate is indicated on the upper left (2.64% of TECs), the mTEC gate is indicated on the lower right (75.7% of TECs). **b**, UMAP representation of transcriptome similarities resulting from the combined analysis of three types of wild-type TECs; EpCAM $^+$ TECs without further purification, and TECs purified according to positive Ly51 and UEA-1 staining characteristics, with origins of TECs indicated by colours (EpCAM $^+$ TECs without further purification, grey; Ly51 $^+$, blue; UEA-1 $^+$, red). **c–f**, Gene expression profiles of *Foxn1* (c), *Psmb11* (d), *Prss16* (e), and *Aire* (f), depicted as normalized absolute counts. **g, h**, Reproducibility of lineage relationships in barcoded TEC populations of female mice; see Fig. [2j](#) for the pattern of the male mouse. P values were calculated as described in the Methods section and multiple-testing corrected by the Benjamini-Hochberg method.

Extended Data Fig. 8 Characterization of clonal relationships in the mTEC compartment.

a, Co-occurrence of individual barcodes in individual TEC clusters (as defined in Extended Data Fig. [3c](#); [4c](#)) at P28; the $-\log_{10} P$ values of barcode frequencies are indicated. *Aire*-positive cells share several barcodes with the postnatal progenitor population but also exhibit private barcodes (barcodes 91 and 102); this observation may be explained by the fact that a certain

progenitor originally giving rise to the *Aire*-expressing cells has ceased to exist; alternatively, sublineage-restricted progenitors and their descendants that appear with developmental time may at some point outnumber the original bipotent ancestor, resulting in a lower sampling probability of the latter. *Trmp5*-expressing tuft cells^{13,15} (cluster18) share barcodes 1 and 68_5 with the postnatal progenitor population and the *Aire*⁺ mTEC compartment, suggesting that they belong to the mTEC lineage. *P* values were calculated as described in the Methods section and multiple-testing corrected by the Benjamini-Hochberg method. **b, c**, Expression of *Foxn1* (left panel) and *Trmp5* (middle and right panels) genes was detected by RNA *in situ* hybridization using thymus sections of a 4- week-old wild-type mouse; the cortico-medullary junction is indicated by the dashed line; part of the medullary area (boxed) is shown as higher power view. Note that *Foxn1*-positive cells are present in both cortex and medulla, whereas *Trmp5*-expressing cells are found in the medulla only. *Trmp5*-positive cells express Krt8, but neither *Ivl* nor *Foxn1*; *Ivl*-expressing cells are Krt8 negative (Fig. 1b). **d**, Identification of scattered Krt18-positive cells in the medulla; most medullary cells express Krt5 (blue) and cortical cells express Krt18 (green). **e**, Active *Foxn1* expression as revealed by the activity of the *Foxn1:mCardinal* transgene using an anti-RFP antibody (red). **f**, *Foxn1* expression (as in e) in cortical and medullary TECs relative to Krt8 expressing TECs (anti-Krt8 antibody, blue); note that Krt8 typically identifies cTEC (as does Krt18). The rare Krt8 expressing cells in the medulla do not express *Foxn1* (arrows). **g**, Identification of *Foxn1*-expressing cells (as in e), post-*Foxn1* cells. *Foxn1* expression is recorded via the *Foxn1:mCardinal* transgenic construct (anti-RFP antibody; red). Post-*Foxn1* cells are identified by *Foxn1*-activated indelible EYFP expression in the *Foxn1:Cre; Rosa26-LSL-EYFP* reporter background (anti-GFP antibody, green); note the presence of purely green cells (arrows), indicating that such cells have lost *Foxn1* expression. **h**, Combined analysis of all three cell states; Krt8-positive cells are post-*Foxn1* cells (arrows); a magnification of the indicated area is shown on the left. Collectively, these data suggest that the Krt8-positive post-*Foxn1* cells in the medulla are tuft cells. Scale bars, 0.1 mm. Panels in b and c are representative of 3 mice; panels in d-h are representative of 2 mice.

Extended Data Fig. 9 Characterization of the Fgfr2-signalling pathway in mouse embryos.

a–f, RNA *in situ* hybridization (ISH) analysis of mouse embryos. **a–e**, ISH performed on E13.5 embryos indicates that *Fgfr2IIIb* (but neither *Fgfr2IIIC* nor *Fgfr1*) expression is a common feature of pharyngeal epithelia. **a**, No detectable expression of the *Fgfr1* gene in the thymic epithelium (higher magnification in inset). **b**, The *Fgfr2* gene is expressed in epithelia of pharyngeal organs, including the thymus (inset). **c**, Low levels of expression of *Fgfr2IIIC* in the thymus. **d**, Moderate levels of expression of *Fgfr2IIIb* in the thymus; anatomical structures are indicated. **e**, Expression of *Fgfr2IIIb* is present in E13.5 *Foxn1*-deficient thymic epithelial rudiment and thus independent of *Foxn1* activity. **f**, Expression of *Fgf7* (E15.5, middle panel) and *Fgf10* (E13.5, bottom panel) genes in the mesenchymal capsule of the thymus (indicated by arrows), but not in the epithelium that is marked by *Foxn1* expression (E15.5, upper panel). The capsular zone is indicated with dashed red lines in the inset of each panel. **g**, qPCR analysis of gene expression patterns in purified thymic mesenchyme (isolated as CD45[−]EpCAM[−]CD31[−]Ly51⁺ cells) and endothelium (isolated as CD45[−]EpCAM[−]CD31⁺Ly51[−] cells) of 4-week-old mice; data are shown as mean±s.e.m. n = 3 for all experiments. *Enpep* encodes the mesenchymal Ly51 marker (note that *Enpep* is also expressed on cTECs, which unlike mesenchymal cells also express the epithelial marker EpCAM); *Cd31* expression marks endothelial cells. This analysis indicates that of the many ligands of Fgfr2b^{79,80}, *Fgf7* and *Fgf10* are expressed by thymic mesenchyme, but not endothelial cells. Embryo genotypes for **a–d**, *Foxn1*^{+/-}, for **e**, *Foxn1*^{-/-}; for **f** and **g** *Foxn1*^{+/+}. Panels in a-f are representative of 3 mice. Scale bars, 0.1 mm for main panels; 0.05 mm for insets.

Source data

Extended Data Fig. 10 Strategy of transgenic interference targeting the Fgfr2-signalling pathway.

a, Schematic illustration of the Fgf signalling pathway in the thymus. The mesenchyme (green) produces Fgf7 (and other Fgfr2 ligands) that bind to

the Fgfr2IIIb variant of the receptor expressed by thymic epithelial cells (top row, left panel). In the present study, this pathway is genetically modulated in several ways to explore whether, under physiological conditions, the receptor or the ligand are in excess. We used the *Foxn1* promotor⁶³ to direct expression of various components of the Fgf signalling cascade in thymic epithelial cells, either singly or in combination. (i) Overexpression of the Fgfr2b receptor (top row, middle panel). The *Foxn1:Fgfr2IIIb* transgenic is designed to increase the sensitivity of epithelial cells to Fgf ligands. This transgenic constellation should result in a stimulatory effect if the ligand is in excess, because more receptor/ligand complexes can form at the cell surface of the target cell. However, if the ligand rather than the receptor is limiting, providing more receptors should have no effect on the target cell. (ii) Expression of a soluble decoy receptor (top row, right panel). The *Foxn:s-Fgfr2IIIb* transgenic line expresses a soluble dominant-negative form of the Fgfr2IIIb receptor^{60,81} and is expected to disrupt productive Fgfr2IIIb receptor signalling. In this experiment, a decrease in the concentration of free ligand in the extracellular space should reduce engagement of receptors and thus diminish signalling activity. (iii) Autocrine provision of Fgf7 (bottom row, left panel). In the *Foxn1:Fgf7* transgenic line, an autocrine loop is generated in the thymic microenvironment by expression of Fgf7 in TECs, resulting in an increase in the concentration of free ligand in the extracellular space. If, in the wild-type situation, receptor molecules are in excess and hence mostly free of ligand, signalling activity should increase; conversely, if under normal circumstances the ligand is in excess over the receptor, no effect should be seen. (iv) Simultaneous overexpression of both Fgf7 ligand and Fgfr2IIIb receptor (bottom row, right panel). This constellation is designed to test if the effect of excess Fgf7 ligand can be further increased by provision of additional receptors; if so, it would indicate that endogenous receptors are fully occupied by excess free ligand. **b**, Overexpression of *Fgf7* (middle panel) and *Fgfr2IIIb* (bottom panel) in the thymic epithelium of *Foxn1:Fgf7*-transgenic and *Foxn1:Fgfr2IIIb*-transgenic mice respectively, as demonstrated by RNA *in situ* hybridization performed on sections from E15.5 embryos with the indicated probes. Scale bars, 0.1 mm. Panels are representative of 3 mice. **c**, Thymopoietic activities in 4-week-old mice of the indicated genotypes; the number of mice per genotype is indicated below each column; data are shown as mean±s.e.m. From multiple comparisons, only the statistically

significant differences are indicated. No significant differences between male and female mice were observed; hence, data from animals of both sexes were pooled for the analysis. The variable extents of thymopoietic activity in the seven transgenic mouse lines studied herein indicate that, under physiological conditions, limiting levels of ligand(s) rather than those of the receptor determine the extent of Fgf signalling in TECs; note, for instance, that expression of a soluble Fgfr2IIIb decoy receptor impaired thymopoiesis in a wild-type background and even partially neutralized the autocrine effects of the *Foxn1*:*Fgf7* transgene. t-test; two-sided; multiple-testing corrected by Benjamini-Hochberg method. P values for significant differences (i. e., $P < 0.05$) are indicated. **d**, Immunohistochemical analysis of wild-type and *Foxn1*:*Fgf7* transgenic 4-week-old thymi; CD45-positive haematopoietic cells, red; Krt5-positive TECs, blue; Krt18-positive TECs, green. Scale bars, 0.1 mm. Panels are representative of 3 mice.

[Source data](#)

Extended Data Fig. 11 Response of the thymic epithelium to KGF-treatment and autocrine stimulation.

These experiments are designed to test the hypothesis that acute provision of an Fgfr2b ligand increases the number of cells expressing the Fgfr2b receptor. **a**, Flow cytometric analysis of dissociated thymic tissue; the percentage of EpCAM⁺CD45⁻ TECs is indicated in the left panels. The cell surface pattern of TECs is resolved after co-staining with anti-Ly51 antibody and UEA-1 lectin (right panels). The control is from a 2-week-old wild-type thymus; representative profiles for *Foxn1*:*Fgfr2b* transgenic cohorts of male mice treated with PBS or KGF (human Fgf7) are shown in the middle and bottom rows, respectively. As shown in Extended Data Fig. 10, the presence of the transgene as such has no influence on the magnitude of the endogenous Fgf7 response. Unlike the response to continuous Fgf stimulation (c.f., Fig. 3), short-term treatment of adult mice with exogenous human Fgf7 (KGF) causes a disproportional increase in Ly51⁺ cells at the expense of UEA-1⁺ TECs. **b**, Numerical assessment of TEC subsets ($n = 3$ per condition; data are shown as mean \pm s.e.m.). At the age of four weeks, male mice received 9 intra-peritoneal injections of KGF at days 1, 2, 3, 8, 9, 10, 15, 16, 17 and were sacrificed on day 21; note the large increase of

Ly51+ TECs after KGF treatment. The lack of a significant increase in thymocyte numbers indicates that the Fgf-responsive TEC compartment initially gives rise to functionally immature Ly51⁺ progeny¹⁸; this observation supports the notion that the Ly51⁺ TEC compartment is functionally heterogeneous and indicates that Ly51 expression as such does not unequivocally identify mature cTECs. t-test; two-sided; P values are indicated. **c**, Age-related down-regulation of *Foxn1*-expression in Fgf-stimulated TECs revealed by flow cytometry. Representative flow cytometric profiles of EpCAM⁺CD45[−] TECs of 7 to 8 week-old female and male mice with the indicated genotypes; the non-transgenic wild-type cells serve as a negative control for reporter expression levels arising from the *Foxn1:EGFP* transgene⁵⁷. Note that Fgf7 stimulation does not prevent the age-dependent physiological down-regulation of the *Foxn1* gene. **d**, *Foxn1*-negative TECs once expressed *Foxn1*, as indicated by the presence of indelible lineage marks in TECs of 4 to 6 week-old female mice (males show the same pattern) as revealed by the *Rosa26-LSL-EYFP*; *Foxn1:Cre* reporter line⁵⁸. For **c** and **d**, the profiles are representative of at least 4 biological replicates. **e**, Fgf7 stimulation fails to increase the number of TECs in *Foxn1*-deficient mice. The numbers of mice in the two cohorts are shown below the histogram; data are shown as mean±s.e.m. Since *Foxn1*-deficient epithelia do not proliferate in response to Fgf stimulation, all changes in the TEC compartment described here are likely to originate from *Foxn1*-expressing cells.

Source data

Extended Data Fig. 12 Changes in the thymic microenvironment upon autocrine Fgf stimulation.

a, Representative flow cytometric profiles of Epcam⁺CD45[−] TECs from wild-type (left panel) and *Foxn1:Fgf7* transgenic (right panel) mice at either 4-weeks (P28) or 1-year (1 yr) of age (top and bottom rows respectively); the percentages of individual TEC subpopulations are indicated in the respective gates. **b–d**, Numerical analysis of TEC subpopulations based on flow cytometry. For b-d, Wt P28, n = 11; Fgf7 tg P28, n = 12; Wt 1 yr, n = 10; Fgf7 tg 1 yr, n = 18. Data are shown as mean±s.e.m. **e–h**, Flow cytometric analyses of CD45⁺ thymocyte populations; DN, CD4[−]CD8[−]; DP,

$CD4^+CD8^+$; $CD4SP$, $CD4^+CD8^-$; $CD8SP$, $CD4^-CD8^+$. For e-h, Wt P28, n = 11; Fgf7 tg P28, n = 12; Wt 1 yr, n = 10; Fgf7 tg 1 yr, n = 18. Data are shown as mean \pm s.e.m. t-test; two-sided; P values are indicated. **i, j**, UMAP representation of progenitor and mature TEC populations in *Foxn1:Fgf7* transgenic mice at (**i**) P28 and (**j**) 1 year of age.

Source data

Extended Data Fig. 13 Effect of continuous Fgf7 signalling on the TEC compartment in young and old mice.

a, Expression of the *Fgfr2* gene in cells of different TEC subsets of mice at different time points (E16.5 EP, n = 721 cells; E16.5 PP, n = 166 cells; E16.5 cTECs, n = 1,159 cells; E16.5 others, n = 141 cells; P0 EP, n = 136 cells; P0 PP, n = 226 cells; P0 cTECs, n = 924 cells; P0 mTECs, n = 311 cells; P0 others, n = 148 cells; P28 EP, n = 292 cells; P28 PP, n = 2,302 cells; P28 cTECs, n = 554 cells; P28 mTECs, n = 2,338 cells; P28 others, n = 303 cells; 1yr PP, n = 981 cells; 1yr cTECs, n = 225 cells; 1yr mTECs, n = 209 cells; 1 yr others, n = 87 cells). Data are presented as violin plots; the red dots indicate median expression levels. Negative cells are given a pseudo-count of 0.1. scRNA-seq datasets of barcoding mice across different time points were merged and normalized by downscaling to 1,500 transcript counts in order to calculate the log₂-normalized transcript counts for *Fgfr2*. **b, d**, UMAP representation of transcriptome similarities between individual TECs isolated from thymi of P28 (**b**), or 1 year-old (**d**) *Foxn1:Fgf7* transgenic mice. **c, e**, Cluster designations deduced by VarID indicating the transcriptional relationships in terms of VarID-derived transition probabilities; connections with probabilities P > 0.001 are shown and the transition probabilities are indicated by line thickness and colouring. For orientation purposes, the major cell populations are also indicated. In panel (e), cluster 5 represents cells derived from ectopic parathyroid tissue. **f, g**, Expression profiles of TEC clusters for the indicated signature genes and the two time points. The fractions of each cluster expressing a particular gene and their respective expression levels are depicted according to the scales shown on the right. Dot colour represents the z-score of the mean expression levels of the gene in the respective cluster and dot size represents the fraction of cells in the cluster expressing the gene; gene names are coloured

according to shared expression patterns (EP: green; PP: orange; cTEC, blue; mTEC, red; other genes of interest, black). z-scores above 1 and below -1 are replaced by 1 and -1 respectively. **h**, Immunohistochemical analysis of thymic lobes of wild-type (wt) and *Foxn1:Fgf7* transgenic mice at two different time points. Sections were stained with anti-Keratin 5 (green) and anti-Keratin 18 (red) antibodies, marking medullary and cortical compartments. Scale bars are indicated; panels are representative of 4 mice.

Supplementary information

Supplementary Tables

This file contains Supplementary Tables 1–16.

Reporting Summary

Source data

Source Data Fig. 1

Source Data Fig. 2

Source Data Fig. 3

Source Data Extended Data Fig. 1

Source Data Extended Data Fig. 2

Source Data Extended Data Fig. 6

Source Data Extended Data Fig. 9

Source Data Extended Data Fig. 10

Source Data Extended Data Fig. 11

Source Data Extended Data Fig. 12

Rights and permissions

Open Access This article is licensed under a Creative Commons Attribution 4.0 International License, which permits use, sharing, adaptation, distribution and reproduction in any medium or format, as long as you give appropriate credit to the original author(s) and the source, provide a link to the Creative Commons license, and indicate if changes were made. The images or other third party material in this article are included in the article's Creative Commons license, unless indicated otherwise in a credit line to the material. If material is not included in the article's Creative Commons license and your intended use is not permitted by statutory regulation or exceeds the permitted use, you will need to obtain permission directly from the copyright holder. To view a copy of this license, visit <http://creativecommons.org/licenses/by/4.0/>.

Reprints and Permissions

About this article

Cite this article

Nusser, A., Sagar, Swann, J.B. *et al.* Developmental dynamics of two bipotent thymic epithelial progenitor types. *Nature* **606**, 165–171 (2022). <https://doi.org/10.1038/s41586-022-04752-8>

- Received: 22 December 2017
- Accepted: 11 April 2022
- Published: 25 May 2022
- Issue Date: 02 June 2022
- DOI: <https://doi.org/10.1038/s41586-022-04752-8>

Share this article

Anyone you share the following link with will be able to read this content:

[Get shareable link](#)

Sorry, a shareable link is not currently available for this article.

[Copy to clipboard](#)

Provided by the Springer Nature SharedIt content-sharing initiative

This article was downloaded by **calibre** from <https://www.nature.com/articles/s41586-022-04752-8>

| [Section menu](#) | [Main menu](#) |

[Download PDF](#)

- Article
- Open Access
- [Published: 11 May 2022](#)

Fundamental immune–oncogenicity trade-offs define driver mutation fitness

- [David Hoyos¹](#)^{na1},
- [Roberta Zappasodi](#) ^{2,3,4,5}^{na1},
- [Isabell Schulze^{2,4}](#),
- [Zachary Sethna^{1,6,7}](#),
- [Kelvin César de Andrade⁸](#),
- [Dean F. Bajorin](#) [ORCID: orcid.org/0000-0003-4001-7088^{3,7}](#),
- [Chaitanya Bandlamudi^{9,10}](#),
- [Margaret K. Callahan](#) [ORCID: orcid.org/0000-0002-9087-0012^{3,7}](#),
- [Samuel A. Funt^{3,7}](#),
- [Sine R. Hadrup](#) [ORCID: orcid.org/0000-0002-5937-4344¹¹](#),
- [Jeppe S. Holm¹¹](#),
- [Jonathan E. Rosenberg^{3,7}](#),
- [Sohrab P. Shah](#) [ORCID: orcid.org/0000-0001-6402-523X^{1,12}](#),
- [Ignacio Vázquez-García](#) [ORCID: orcid.org/0000-0003-0427-2639¹](#),
- [Britta Weigelt](#) [ORCID: orcid.org/0000-0001-9927-1270⁹](#),
- [Michelle Wu](#) [ORCID: orcid.org/0000-0001-6889-8345¹³](#),
- [Dmitriy Zamarin](#) [ORCID: orcid.org/0000-0002-0094-0161^{2,3,7}](#),
- [Laura F. Campitelli¹⁴](#),
- [Edward J. Osborne¹⁴](#),
- [Mark Klinger¹⁴](#),
- [Harlan S. Robins¹⁴](#),

- [Payal P. Khincha](#)⁸,
- [Sharon A. Savage](#) ORCID: orcid.org/0000-0001-6006-0740⁸,
- [Vinod P. Balachandran](#) ORCID: orcid.org/0000-0002-2956-223X^{3,4,6,7,15},
- [Jedd D. Wolchok](#) ORCID: orcid.org/0000-0001-6718-2222^{2,3,4,16},
- [Matthew D. Hellmann](#) ORCID: orcid.org/0000-0002-2670-9777^{3,4,17},
- [Taha Merghoub](#) ORCID: orcid.org/0000-0002-1518-5111^{2,3,4,16 na2},
- [Arnold J. Levine](#) ORCID: orcid.org/0000-0002-1871-6387^{18 na2},
- [Marta Łuksza](#)^{19 na2} &
- [Benjamin D. Greenbaum](#) ORCID: orcid.org/0000-0001-6153-8793^{1,12 na2}

[Nature](#) volume **606**, pages 172–179 (2022)

- 14k Accesses
- 185 Altmetric
- [Metrics details](#)

Subjects

- [Computational models](#)
- [Evolutionary theory](#)
- [Tumour immunology](#)
- [Tumour-suppressor proteins](#)

An [Author Correction](#) to this article was published on 31 May 2022

This article has been [updated](#)

Abstract

Missense driver mutations in cancer are concentrated in a few hotspots¹. Various mechanisms have been proposed to explain this skew, including biased mutational processes², phenotypic differences^{3,4,5,6} and immunoediting of neoantigens^{7,8}; however, to our knowledge, no existing model weighs the relative contribution of these features to tumour evolution. We propose a unified theoretical ‘free fitness’ framework that parsimoniously integrates multimodal genomic, epigenetic, transcriptomic and proteomic data into a biophysical model of the rate-limiting processes underlying the fitness advantage conferred on cancer cells by driver gene mutations. Focusing on *TP53*, the most mutated gene in cancer¹, we present an inference of mutant p53 concentration and demonstrate that *TP53* hotspot mutations optimally solve an evolutionary trade-off between oncogenic potential and neoantigen immunogenicity. Our model anticipates patient survival in The Cancer Genome Atlas and patients with lung cancer treated with immunotherapy as well as the age of tumour onset in germline carriers of *TP53* variants. The predicted differential immunogenicity between hotspot mutations was validated experimentally in patients with cancer and in a unique large dataset of healthy individuals. Our data indicate that immune selective pressure on *TP53* mutations has a smaller role in non-cancerous lesions than in tumours, suggesting that targeted immunotherapy may offer an early prophylactic opportunity for the former. Determining the relative contribution of immunogenicity and oncogenic function to the selective advantage of hotspot mutations thus has important implications for both precision immunotherapies and our understanding of tumour evolution.

Main

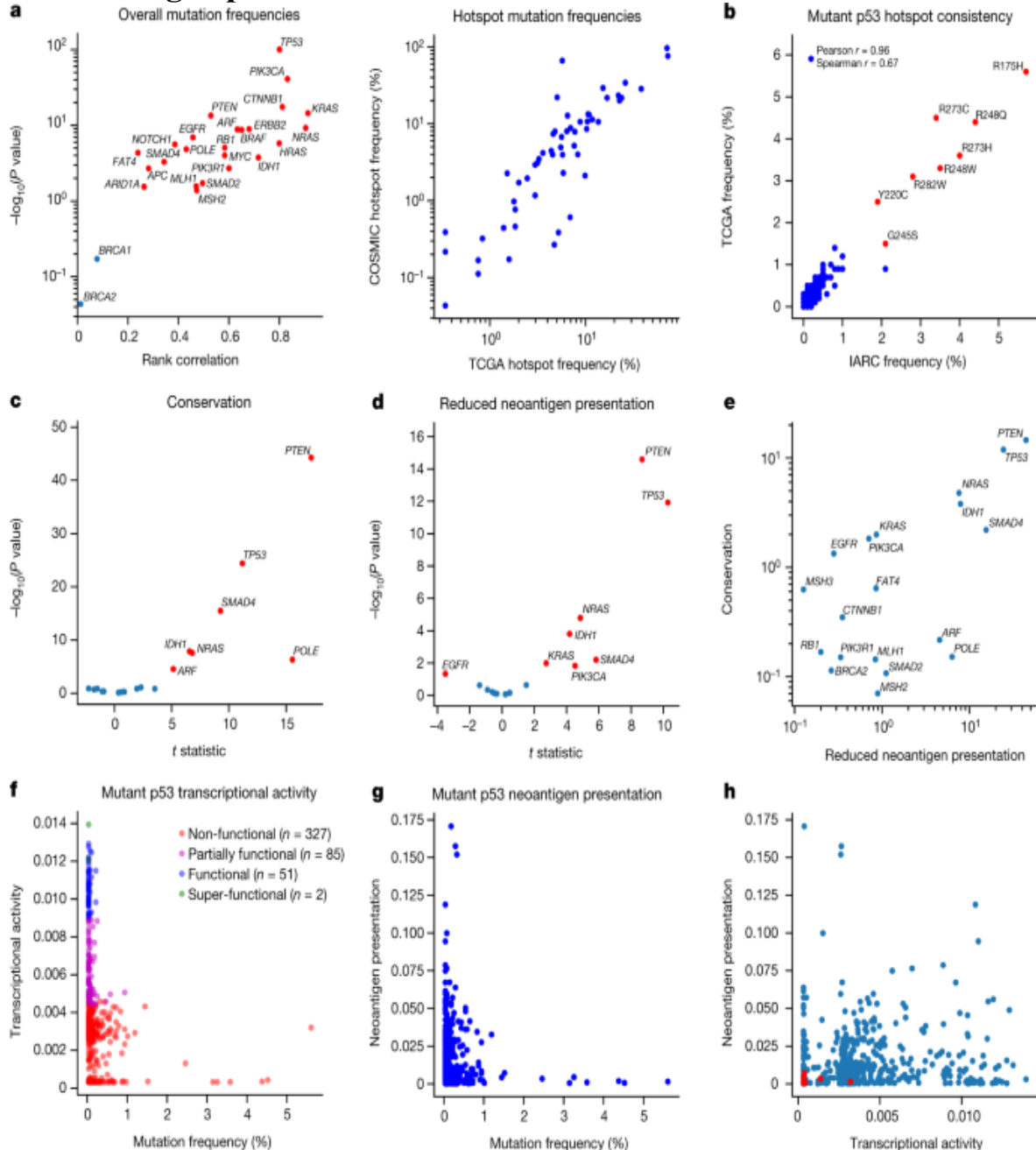
The distribution of mutations in cancer is highly non-uniform. Mutations in oncogenes and tumour suppressors are enriched across cancers, and specific sites known as hotspots are more frequently mutated, leading to the hypothesis that hotspot mutations offer a selective advantage¹. A paradigmatic example is the tumour suppressor p53. Although *TP53* is mutated in more than 50% of cancers, only eight hotspot mutations make up approximately one-third of all missense *TP53* mutations³. Several hypotheses have been offered to explain the mechanisms behind this skewed distribution, including biased generative mutational processes during tumour

evolution^{2,3}, degree of functional alteration^{3,4,5}, structural stability^{3,6} and immune editing^{7,8}. However, these hypotheses are not mutually exclusive. Mutations and subsequent selection can lead to substantial alterations in the concentration of oncogenic proteins^{9,10,11}, a factor that has not been quantified as a contributor to the predominance of hotspot mutations. Generally, mutant p53 is present at a higher concentration than wild-type protein, depending on the tissue, copy-number alteration and mutation^{12,13,14}. Yet, divergence from self and overexpression can contribute to mutant p53 neoantigen immunogenicity, constraining the ability of mutant p53 to avoid immune surveillance. Because neoantigens from mutations in tumour driver genes that are shared across patients and tumour types represent attractive immunotherapeutic targets^{15,16}, understanding this issue is of critical importance. Here we examine the relationship between oncogenicity and immunogenicity for tumour driver mutations, using p53 as a primary example, to develop a model for predicting therapeutic targeting strategies, such as for neoantigen-based immune therapies.

We found that mutation frequency distributions for commonly mutated driver genes were conserved across multiple cancer mutation databases (Fig. 1a, b) and that innate mutation rates based on trinucleotide context significantly correlated with mutation frequencies for several genes (Supplementary Information). We next quantified amino acid conservation over homologous proteins, a proxy for functional phenotype (Fig. 1c), and in silico-predicted reduced neoantigen presentation by major histocompatibility complex class I (MHC-I) molecules (Fig. 1d) across driver genes⁷. Several genes have hotspots at conserved sites and are poorly presented (Fig. 1e), implying that the fitness advantages the mutations confer may be driven by both features. We focused on *TP53* because it is widely mutated in tumours, with well-established, order-conserved pan-cancer hotspots (Fig. 1b and Supplementary Table 1) and broadly available functional phenotypic data⁵. We quantified the altered transcription factor function of mutant p53 across eight principal transcriptional targets with a quantitative yeast assay⁵ (Fig. 1f and Extended Data Fig. 1). We found that, although loss of transactivation was present for hotspot mutations, many non-hotspot mutations had comparatively low transactivation capacity. Moreover, we predicted MHC-I molecule presentation for the set of nonamer neopeptides surrounding p53 hotspot mutations to be worse than for non-hotspot peptides in The Cancer

Genome Atlas (TCGA; $P = 4.748 \times 10^{-7}$, two-sided Welch's t -test; Fig. 1g). Mutant p53 loss of transcriptional activity and neoantigen presentation of derived neopeptides showed only weak rank correlation (Fig. 1h), leading us to conclude that all of the mechanisms proposed to underlie mutant p53 fitness are likely to provide some predictive information.

Fig. 1: Driver gene hotspots are highly conserved and have relatively poor neoantigen presentation.

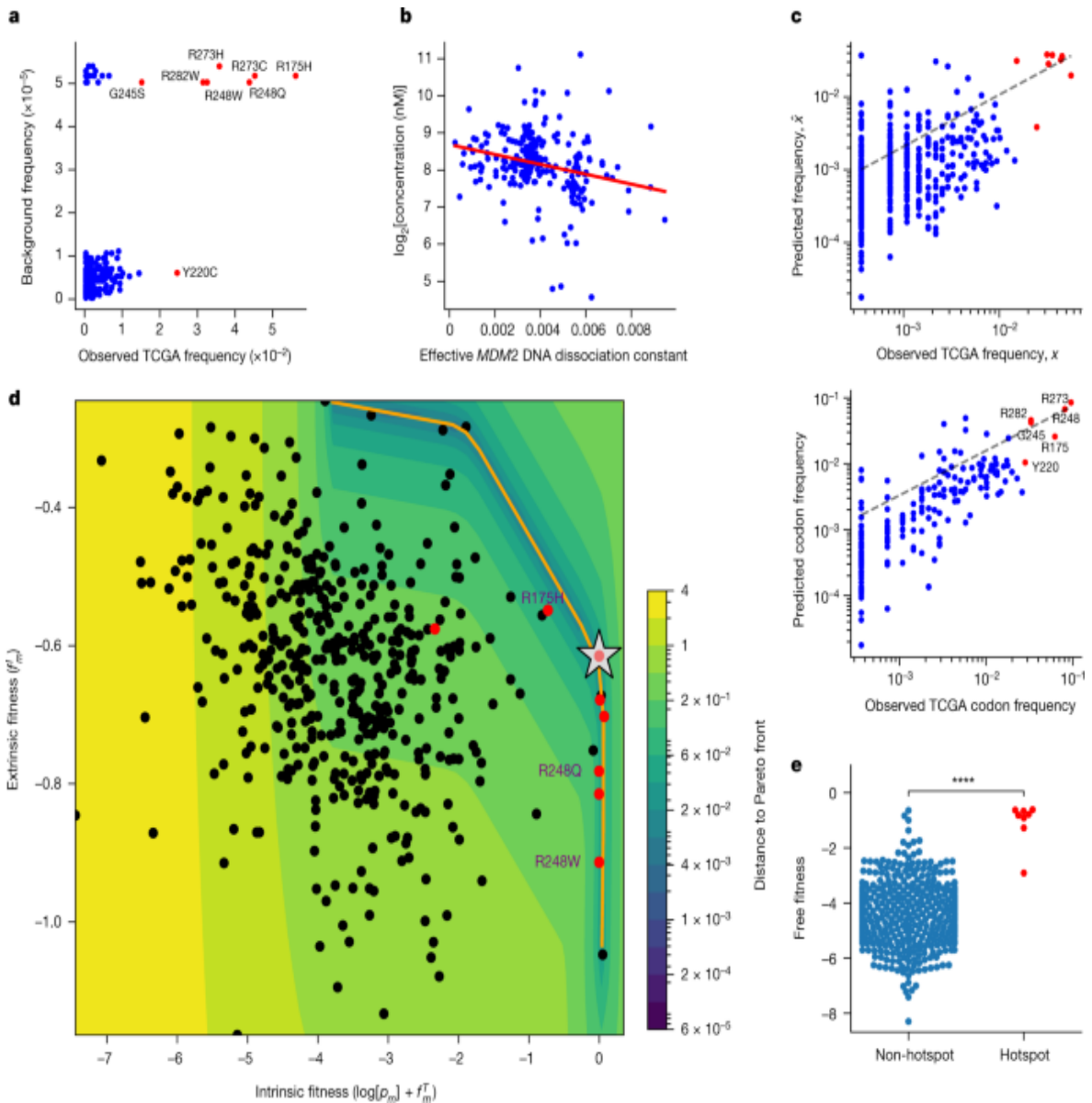


a, Left, rank correlation between shared mutation frequencies in TCGA and the Catalogue of Somatic Mutations in Cancer (COSMIC) database for commonly mutated tumour suppressors and oncogenes plotted against the $-\log_{10}$ -transformed rank correlation P value. Points corresponding to $P < 0.05$ are coloured red. Right, correlation of individual hotspot mutation frequencies in TCGA and the COSMIC database, excluding TCGA samples (Pearson $r = 0.860$, $P < 0.0001$; Spearman $r = 0.851$, $P < 0.0001$). **b**, Comparison of *TP53* mutation distributions in the TCGA ($n = 2,764$) and IARC ($n = 21,170$) databases (Pearson $r = 0.963$, $P < 0.0001$; Spearman $r = 0.672$, $P < 0.0001$; labelled hotspots coloured in red). **c**, Comparison of conservation in hotspots and other mutations in the same gene (Welch's t -test P value, $P < 0.05$ annotated in red). **d**, Comparison of reduced neoantigen presentation between hotspots and other mutations in the same gene (Welch's t -test P value, $P < 0.05$ annotated in red). **e**, $-\log_{10} P$ values from **c** and **d** plotted against each other. **f**, Mutant p53 transcriptional activity defined as the median of the inferred association constant for transcription factor affinity across eight transcriptional targets (*WAF1*, *MDM2*, *BAX*, *h1433s*, *AIP1*, *GADD45*, *NOXA* and *P53R2*) plotted against the frequency of *TP53* mutations in TCGA (Pearson $r = -0.204$, $P < 0.0001$; Spearman $r = -0.404$, $P < 0.0001$). **g**, Neoantigen presentation defined as effective mutant peptide affinity versus mutation frequency in TCGA (Pearson $r = -0.079$, $P = 0.088$; Spearman $r = -0.053$, $P = 0.256$; hotspots coloured in red). **h**, Mutant p53 transcriptional activity plotted against neoantigen presentation shows weak dependence between the two features (Pearson $r = 0.073$, $P = 0.117$; Spearman $r = 0.144$, $P = 0.002$; hotspots coloured in red).

We therefore sought to harmonize this proposed feature set within a mechanistic mathematical model of mutant p53 fitness^{17,18,19,20,21}. A model based on background mutation rates alone was insufficient to separate the hotspots from other mutations (Fig. 2a). We further looked to capture variation in mutant p53 concentration, which affects both the transcription factor function and neoantigen presentation. We assigned TCGA samples a normalized p53 protein concentration and effective *MDM2* promoter affinity to infer typical per-allele mutant-specific concentrations^{22,23}. We consistently found a significant inverse relationship between these two variables across tumour types (Fig. 2b and Extended Data Fig. 2a) and a significant correlation between our concentration estimates and

immunohistochemistry data (Extended Data Fig. 2b,c). We constructed a nonlinear, two-parameter model that separates mutant p53 fitness onto a positive pro-oncogenic probability and a negative immunogenic probability ([Supplementary Methods](#)) coupled to mutant p53 concentration. Each component is given an appropriate weight by maximum-likelihood fitting with respect to TCGA mutation frequencies. Our fitness model successfully predicts the distribution of mutation frequencies, both per mutation and per codon (Fig. 2c and [Supplementary Information](#)), and accurately predicts the increase or decrease in each mutant frequency with respect to background frequency (Extended Data Fig. 3a,b). We found that predicting the distribution of *TP53* mutations requires both functional and immune components through determining the relative likelihoods of the models ([Supplementary Table 2](#) and [Supplementary Methods](#)). Model optimization depended strongly on the sampled MHC-I haplotype and all mutant phenotypes (Extended Data Fig. 3c,d and [Supplementary Information](#)). We optimized and applied similar models to other driver genes, with conservation used as a proxy for function (Extended Data Fig. 4a and [Supplementary Methods](#)). Combined models were more predictive for mutation distributions with larger frequency variance across all database mutations, which implies that increased mutation frequency variance relates to increased selection, as expected from Fisher's theorem²⁴ (Extended Data Fig. 4b), such as for *PTEN* (Extended Data Fig. 4c). To build a predictive model for *KRAS*, we were able to include measured binding affinities to the downstream Raf effector protein for a limited set of hotspot mutations²⁵ ([Supplementary Methods](#)), in addition to inferences in conservation and immunogenicity (Extended Data Fig. 4d).

Fig. 2: Mutant p53 fitness model quantifies the trade-off between oncogenicity and immunogenicity.



a, Model with only background intrinsic mutational frequencies (Kullback–Leibler divergence, 1.222; Pearson $r = 0.324, P < 0.0001$; Spearman $r = 0.2, P < 0.0001$; hotspots coloured in red). **b**, Relationship between mutant p53 concentration (\log_2 transformed) and the predicted effective p53 association constant for the *MDM2* promoter across TCGA ($n = 219$; Pearson $r = -0.25, P < 0.001$; Spearman $r = -0.29, P < 0.0001$). **c**, Correlation of predicted *TP53* mutation frequencies to observed frequencies on a per-mutation basis (top; Kullback–Leibler divergence, 0.599; Pearson $r = 0.671, P < 0.0001$; Spearman $r = 0.39, P < 0.0001$) and per-protein position basis (bottom; Kullback–Leibler divergence, 0.337; Pearson $r = 0.794, P < 0.0001$;

Spearman $r = 0.782$, $P < 0.0001$). **d**, Sum of the log-transformed background frequency $\log[p_m]$ and positive functional fitness $(\{f\}_m^T)$, denoted intrinsic fitness, plotted against negative immune fitness ($(\{f\}_m^I)$, extrinsic fitness) (Pearson $r = -0.31$, $P < 0.0001$; Spearman $r = -0.33$, $P < 0.0001$). The orange line corresponds to the Pareto front; the silver star indicates optimal free fitness constrained by the Pareto front; and the heat map corresponds to the distance to the Pareto front. The hotspot mutations are coloured red and the R175H and R248Q/W mutations are shown. **e**, Comparison of the free fitness distributions of non-hotspot and hotspot mutations ($P < 0.0001$, Welch's t -test).

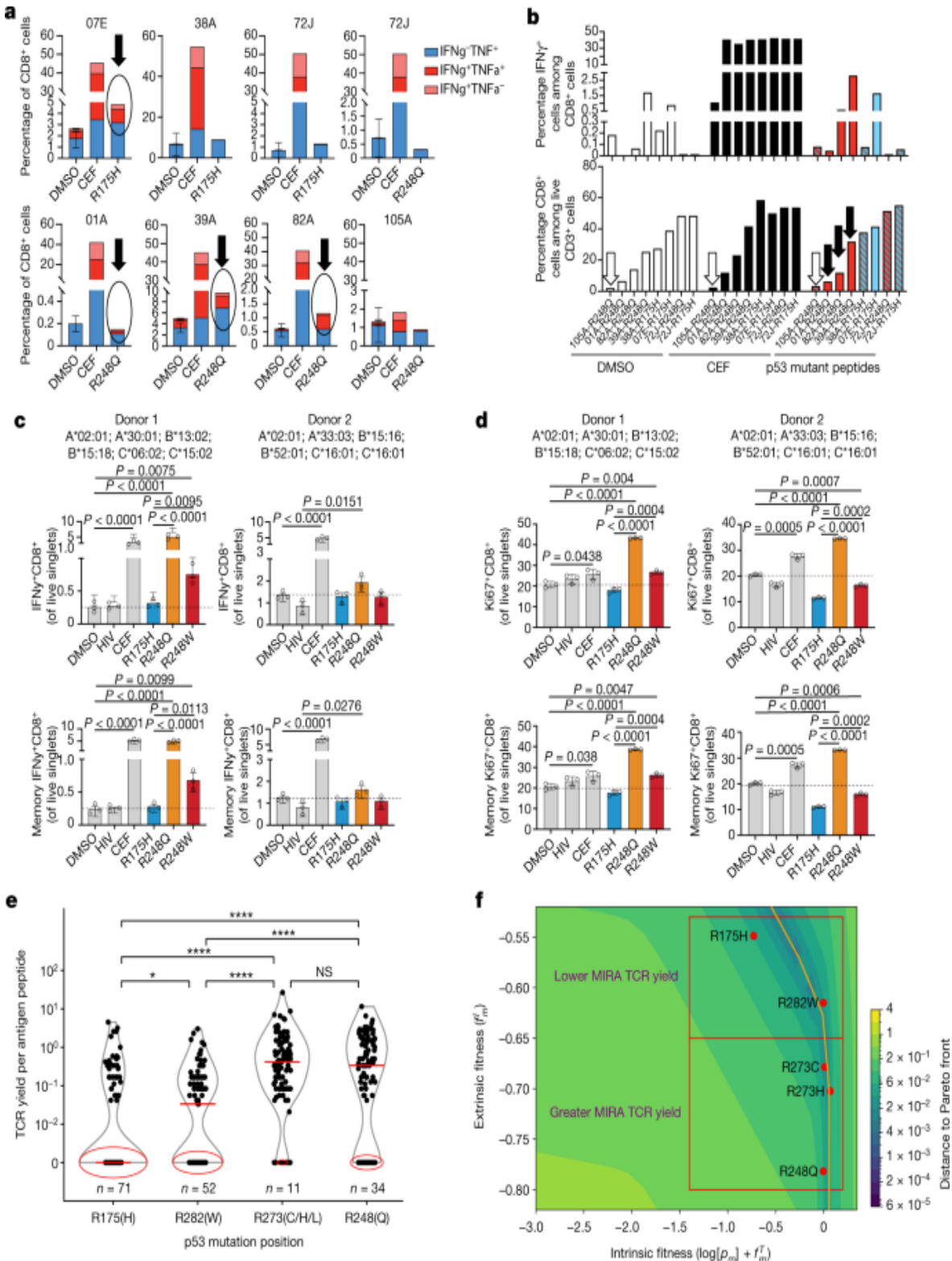
To represent the landscape of mutant p53 fitness, we defined a ‘free fitness’ function of each mutation as the sum of the positive functional fitness, the negative immune fitness and the logarithm of the background frequency ([Supplementary Methods](#)), analogous to a free energy in statistical physics with the multiplicity of states derived from the background mutation rate. We plotted the free fitness landscape (Fig. [2d](#)) and observed a general trade-off between intrinsic fitness (logarithm of the background frequency and functional fitness; [Supplementary Methods](#)) and extrinsic immune fitness. The trade-off observed in *TP53* is reminiscent of other evolutionary trade-offs, and we theorized that *TP53* hotspots were Pareto optimal^{[26,27](#)}. We computed the Pareto front and identified the optimal fitness coordinate constrained by the front when using our model (Fig. [2d](#) and [Supplementary Methods](#)). We found that hotspots had statistically higher free fitness (Fig. [2e](#)) and occupied an optimal regime in which they successfully trade off between the pro-tumorigenic benefit of functional loss and the cost of presenting immunogenic neoantigens. However, there was substantial variation among the hotspot mutations. For instance, R175H is functionally the most wild-type-like hotspot but typically has the poorest MHC-I binding capacity. By contrast, the R248Q and R248W (R248Q/W) mutations have nearly complete loss of transcriptional function and therefore can more often afford to generate potentially immunogenic neoantigens, because the proliferative competitive advantage induced by mutation would offset the cost of immunogenicity. For *KRAS*, under more restrictive assumptions, we observed evidence for a trade-off between functional and immune fitness for hotspot mutations in pancreatic adenocarcinoma, where *KRAS* is typically mutated (Extended Data Fig. [4e](#) and [Supplementary Methods](#)).

One possible explanation for the inverse relationship is that mutations that alter protein function are generally more likely to generate differentially immunogenic peptides. We therefore compared non-pathogenic and pathogenic mutations in a curated set of non-cancerous disease driver genes and found that both types of mutation generated comparably predicted immunogenic peptides (Extended Data Fig. 5), implying that the trade-off observed is not to be expected a priori. Moreover, because our functional predictions for mutant *TP53* are based on precision yeast assays, we checked for evidence of an oncogenic–immunogenic trade-off using independent TCGA assay for transposase-accessible chromatin with sequencing (ATAC-seq) and RNA sequencing assay to develop a score for the lack of mutant p53 binding site occupancy ([Supplementary Methods](#)). We found that the functional component of our fitness model correlated significantly with lack of binding (Extended Data Fig. 6a) and that samples with increased lack of p53 binding consistently showed decreases in p53 target gene RNA expression (Extended Data Fig. 6b). We independently re-derived the oncogenicity–immunogenicity trade-off by comparing the inferred immunogenicity to our scores for lack of binding (Extended Data Fig. 6c). Finally, as a further control, we found a correlation between the yeast assay-derived probability of DNA binding and median target gene RNA expression conditioned on chromatin accessibility (Extended Data Fig. 6d).

We tested our immunogenicity predictions for mutant p53 using peptides from hotspot mutations predicted to be presented on human leukocyte antigen (HLA)-A*02:01 ([Supplementary Table 3](#) and [Supplementary Methods](#)), which is the most frequent MHC-I allele in TCGA. First, we asked whether these peptides had differential ability to bind and stabilize HLA on the cell surface, using the TAP2-deficient human lymphoblastoid T2 cell line ([Supplementary Methods](#)). We found that R248Q/W peptides but not R175H peptide could significantly stabilize HLA-A*02:01 expression on T2 cells in a dose-dependent manner in comparison with the respective wild-type peptide sequence (Extended Data Fig. 7a and [Supplementary Table 3](#)). We next asked whether R175H and R248Q/W *TP53* hotspot mutations elicit differential immune responses *in vivo* in patients with cancer. We identified seven HLA-A*02:01-positive patients with either bladder or ovarian tumours with these mutations and available peripheral blood mononuclear cell (PBMC) samples at Memorial Sloan Kettering Cancer Center (MSKCC). In total, three samples were from

patients with R175H-mutant tumours (07E, 38A and 72J) and five samples were from patients with R248Q-mutant tumours (72J, 01A, 39A, 82A and 105A) (Supplementary Table 4). One patient's tumour (72J) had both mutations, although the R175H clonal fraction was far lower (Supplementary Table 4). All but two patients (72J and 07E) were immunotherapy naive at the time of sample collection. Patient 72J, who had a tumour with both hotspot mutations, had an ongoing complete response to nivolumab (anti-programmed death (PD)-1) treatment with no disease detectable at the time of PBMC collection. Patient 07E, who harboured the R175H mutation, was on atezolizumab (anti-PD-L1) treatment at the time of PBMC collection. All other samples were collected before treatment initiation. We stimulated the PBMCs with peptides harbouring the R175H or R248Q mutations or with a CEF (cytomegalovirus, Epstein–Barr virus, and influenza virus) peptide pool or DMSO as positive and negative controls, respectively (Supplementary Table 3). We then measured the interferon- γ (IFN γ) and tumour necrosis factor- α (TNF α) production in CD8 $^{+}$ T cells by flow cytometry (Fig. 3a, b and Extended Data Fig. 7b). We found responses in three of the five R248Q samples, with the response proportional to the size of the CD8 $^{+}$ T cell population (Fig. 3a, b and Extended Data Fig. 7c, d). This indicates responses might correlate with the frequency of CD8 $^{+}$ T cell precursors recognizing the neopeptides. By contrast, only one of the three patients with R175H-mutant tumours had neopeptide reactivity; this patient (07E) had one of the largest expansions for the mutant *TP53* allele and a concomitant increase in protein abundance as well as a positive response to anti-PD-L1 treatment (Fig. 3a and Extended Data Fig. 7e). This finding in combination with the lack of T cell reactivity in the immunotherapy-naive patient (38A) with four mutant R175H alleles indicates despite expansion of the mutant allele, R175H tends to be less immunogenic than R248Q/W, but anti-R175H T cell responses may be unleashed by immune checkpoint blockade therapy. Consistent with this, we found no reactivity in patient 72J, who harboured both hotspot mutations at lower abundance (Extended Data Fig. 7e) and had a complete response to immune checkpoint blockade therapy. This indicates that, in cancer, expansion and/or persistence of cognate T cell pools depends on the levels of the mutant protein.

Fig. 3: Validation of differential reactivity to mutant p53 neoepitopes in healthy donors and patients with cancer.



a, b, PBMCs from patients with R175H and/or R248Q p53-mutant tumours were cultured with the indicated p53 neopeptides or with CEF or DMSO as

positive and negative controls, respectively. **a**, Flow cytometry quantification of cells expressing $\text{IFN}\gamma \pm \text{TNF}\alpha$ among $\text{CD8}^+ \text{CD3}^+$ live T cells in the indicated samples. DMSO data are the mean \pm s.d. of two to three technical replicates. **b**, Assessment of $\text{IFN}\gamma$ responses ($\text{IFN}\gamma^+$ cells among CD8^+ T cells) in the same samples as in **a** in association with the frequencies of total CD8^+ T cells in those cultures. Black arrows indicate reacting samples; a white arrow indicates low-input CD8^+ T cells. **c–f**, Reactivity of PBMCs from healthy donors to the indicated p53 neoantigens by an optimized ex vivo priming assay (**c**, **d**) and MIRA assay using TCR sequencing to quantify specific T cell clonal expansion (**e–f**). $\text{IFN}\gamma$ (**c**) and Ki67 (**d**) expression was assessed in the total CD8^+ T cell fraction (top) or the non-naive memory CD8^+ T cell fraction (bottom). Frequencies are shown for two individual healthy donors as the percentage of live single cells in culture after 2 weeks of in vitro stimulation with the indicated p53 neopeptides compared with CEF and DMSO or an HIV peptide pool as positive and negative controls, respectively. **e**, Quantification of reactive TCRs in 107 healthy donors in 222 MIRA assay experiments, with an average of two experiments per donor. Median values are denoted by red horizontal line; zero values are circled in red with the number of zero values annotated in blue. **f**, *TP53* hotspots tested in **e** along the Pareto front yielding fewer or more TCRs grouped in red squares. Statistical significance was assessed by unpaired two-sided *t*-tests (**c**, **d**) or Mann–Whitney *U*-test (**e**). * $P \leq 0.05$, ** $P \leq 0.01$, *** $P \leq 0.001$, **** $P \leq 0.0001$.

We next asked whether differential immunogenicity of *TP53* hotspots was a broad phenomenon in the healthy population and therefore potentially linked to the frequency of T cell precursors recognizing a mutant peptide. We compared the capacity of R175H and R248Q/W peptides when loaded onto autologous antigen-presenting cells to prime and expand specific T cells in two healthy donors with the HLA-A*02:01 allele (Extended Data Fig. 7b, Supplementary Table 3 and [Supplementary Methods](#)). We consistently noted greater $\text{IFN}\gamma$ and Ki67 expression in T cells stimulated with R248Q/W peptides than in those stimulated with R175H peptides in both donors (Fig. 3c, d and Extended Data Fig. 7f). Furthermore, we assessed the yield of *TP53* hotspot-specific T cell clones by multiplex identification of T cell receptor (TCR) antigen specificity (MIRA) assay (Adaptive Biotechnologies) in PBMC samples from 107 healthy donors representing a

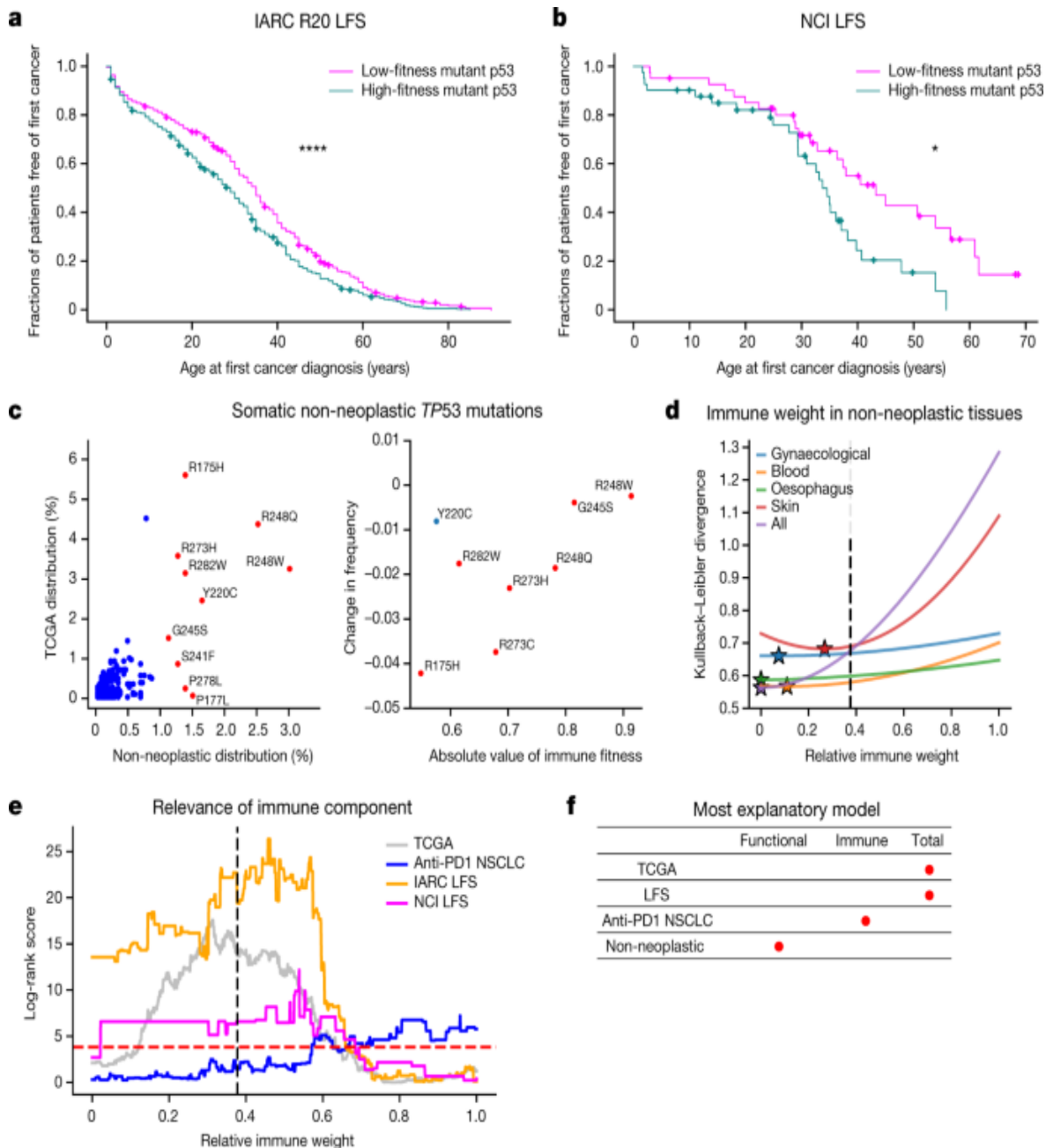
set of distinct HLA alleles, including 25 *HLA-A*, 46 *HLA-B* and 20 *HLA-C* alleles ([Supplementary Methods](#)). Forty mutant epitopes from R175, R282, R273 and R248 loci covering the top six p53 hotspots were screened for multiple peptide lengths. The distribution of normalized TCR yield per antigen peptide per donor, indicative of specific clonal expansion, was plotted for each hotspot position (Fig. [3e](#)). Notably, we found that the R175 hotspot yielded statistically lower TCR reactivity per peptide as compared with all other hotspots, having a median value of zero reacting TCRs per peptide. Moreover, we found that hotspot reactivity corresponded to fitness model predictions (Fig. [3f](#)). These results indicate that the MHC-I haplotype and TCR repertoire distributions of the healthy population may be more likely to react to the R248 locus than the R175 locus.

Validating the link between increased immunogenicity and immune response to mutant p53, we found that the protein abundance of the CTLA-4, PD-1 and PD-L1 immune checkpoint proteins was higher in TCGA samples with *TP53* mutations that were predicted to be more immunogenic (Extended Data Fig. [8](#)). Our results suggest increased immune activation and concurrent establishment of adaptive immune resistance. When we segregated survival on the basis of functional, immune and combined fitness in TCGA and a cohort of patients with non-small-cell lung cancer (NSCLC) treated with anti-PD-1 at MSKCC (Extended Data Fig. [9](#)), we found that functional and immune fitness components were required to achieve significant survival separation in TCGA, whereas immune fitness on its own significantly separated immunotherapy-treated patients with NSCLC by survival. For robustness, we retrained our models across a range of relative weights between functional and immune fitness ([Supplementary Methods](#)). We demonstrated that both components contributed to a model optimized for survival separation across TCGA, with the functional component carrying greater weight, whereas the immune component was the main determinant for an equivalent model in the immunotherapy-treated NSCLC cohort (Fig. [4e](#)).

Because germline *TP53* mutations are the primary cause of Li–Fraumeni syndrome (LFS), which is a highly cancer-prone autosomal dominant disorder²⁸, we theorized that mutant p53 fitness relates to the time to first tumour formation in patients with LFS. We plotted Kaplan–Meier curves showing the age of tumour onset for persons with germline missense *TP53*

mutations in the International Agency for Research on Cancer (IARC) R20 germline dataset and for an independent LFS cohort coordinated by the National Cancer Institute (NCI)²⁹, stratified on the basis of mutant p53 fitness ([Supplementary Methods](#)). We found that functional and immune components were required for significant separation of patients based on time to onset, with the immune component required across a range of relative weights (Fig. [4a, b](#) and Extended Data Fig. [10](#)). These results may seem counterintuitive in that mutant p53 may be interpreted as ‘self’ by the adaptive immune system in patients with LFS. However, increased mutant p53 abundance, compounded by additional somatic mutations, may increase tumour immune surveillance and mutant p53 antigenicity during tumorigenesis. These findings suggest a possible role for immune surveillance and the potential for immune intervention in germline *TP53*-mutant tumours.

Fig. 4: Mutant p53 fitness informs LFS age of tumour onset and non-neoplastic *TP53* mutation distribution.



a, b, Kaplan–Meier curves split on median mutant p53 fitness from the combined model for age of tumour onset in the IARC R20 germline dataset ($n = 998$) (a) and the NCI LFS dataset ($n = 82$) (b). **c,** Left, comparison of *TP53* mutation frequencies in non-neoplastic tissues (3,451 mutation occurrences) and the frequencies in TCGA (2,764 mutation occurrences; Pearson $r = 0.732$, $P < 0.0001$; Spearman $r = 0.544$, $P < 0.0001$; top 10 non-neoplastic mutations coloured in red and annotated). Right, positive relationship between hotspot frequency difference in non-cancerous and

cancerous cells and magnitude of immune fitness. CpG-associated hotspots are coloured in red; Y220C is coloured in blue (overall: Pearson $r = 0.594$, $P = 0.120$; Spearman $r = 0.619$, $P = 0.102$; CpG-associated hotspots only: Pearson $r = 0.827$, $P = 0.022$; Spearman $r = 0.786$, $P = 0.036$). **d**, Kullback–Leibler divergence plotted as a function of relative immune weight for the largest tissue-specific mutation distributions across collected non-neoplastic somatic p53 mutations. Optimal immune weights are denoted as stars, and the optimal relative immune weight derived independently to best represent the observed mutation frequency in TCGA is denoted as a black dotted line. **e**, Log-rank scores of the TCGA ($n = 1,941$), NSCLC ($n = 289$) and LFS (IARC, $n = 946$; NCI, $n = 82$) cohorts as a function of the relative immune weight. The dashed red line corresponds to the log-rank score for $P = 0.05$; the dashed black line marks the choice of parameters trained independently to best represent the observed mutation frequency in TCGA. **f**, The most explanatory models across mutant *TP53* datasets, as indicated by red dots.

Finally, non-cancerous cells in diverse tissues harbour somatic *TP53* mutations that confer a competitive advantage, predisposing the clones containing such mutations to develop into cancer³⁰. We collated mutation data from multiple published works across many mutated tissues ([Supplementary Information](#)) and found the same cancer hotspots in non-neoplastic cells (Fig. [4c](#)). Unexpectedly, however, the frequency of the hotspot mutations was different. R175H was markedly under-represented in non-neoplastic cells compared with tumours ($P < 0.0001$, two-sided binomial test), whereas the potentially more immunogenic R248Q/W mutations were among the most frequent. The addition of an immune component in the non-neoplastic setting improved predictions to a substantially lower degree than in the neoplastic setting (Fig. [4d](#) and Supplementary Table [5](#)), supporting the hypothesis that the difference in hotspot frequency between non-cancerous and cancerous datasets is driven by the hotspot mutation’s immune fitness. We then split the non-neoplastic *TP53* mutation dataset into the largest tissue-specific subgroups and found that immune weight depended on the tissue type (Fig. [4d](#)), although the weight was always weaker than the optimal value for fitting the TCGA mutation distribution. Overall, these findings suggest that more functionally fit mutations probably predominate in non-cancerous and precancerous

lesions owing to their selective replicative advantage; for cancer to form, however, immune escape becomes critical (Fig. 4f).

We present a general mathematical framework for predicting the fitness of tumour driver mutations. For p53, we used a free fitness model that integrates the background mutation rate, protein concentration, functional fitness advantage and immune fitness cost. Hotspots were predicted to fall on a near-optimal Pareto front, with trade-offs constraining driver mutations from completely evading immune selection, as has been shown for specific hotspot mutations^{31,32,33}. Immune fitness has less of a role in predicting the distribution of non-cancerous *TP53* mutations, which is consistent with recent observations that immune editing is less relevant in precancerous lesions³⁴. Our insights therefore help define a window of opportunity for prophylactic immune intervention against mutant p53. Additionally, our model shows that mutant p53 fitness may have a role in determining the age of tumour onset in LFS, implying a benefit in targeting germline *TP53* mutations immunotherapeutically. Inducing prophylactic immunity against mutant p53 seems to be possible according to our in vitro data showing the possibility of inducing anti-mutant p53 T cell responses in healthy individuals and even against poorly immunogenic mutations when sufficient antigen concentration and proper immune co-stimulation are delivered. Our approach captures critical mechanistic determinants of mutant p53 fitness and is amenable to extensions as data become available. For instance, although we considered only functional alterations for a set of canonical p53-regulated genes in this study, future models can include additional new measures for describing mutant gain of function, such as novel binding interactions between mutant p53 and other molecules due to changes in protein conformation or concentration. Similarly, other functions reflecting the vital role of p53 as a central transcription factor may be incorporated with additional data, such as induction of apoptosis at the mitochondria, immune regulation and surveillance of transposons and other genome parasites. The latter evolutionary role of p53 in preserving genome integrity may be responsible for p53's centrality as a bottleneck across transcriptional networks^{35,36,37}. Finally, our free fitness framework lends itself naturally to interpretable, free energy-based machine learning models³⁸, which broadens the applicability of our approach to additional topics and modalities. By quantifying the underlying mechanisms of driver mutation fitness, we can

therefore uncover both fundamental knowledge about tumour evolution and new opportunities for precision therapies.

Methods

All research involving human participants was approved by the authors' institutional review board (MSKCC IRB), and all clinical investigation was conducted according to the principles expressed in the Declaration of Helsinki. Written informed consent was obtained from the participants.

Reporting summary

Further information on research design is available in the [Nature Research Reporting Summary](#) linked to this paper.

Data availability

Original data required for running the fitness model are available at https://github.com/dfhoyosg/p53_fitness_tradeoff.

Code availability

Original code required for running the fitness model is available at https://github.com/dfhoyosg/p53_fitness_tradeoff.

Change history

- [31 May 2022](#)

A Correction to this paper has been published:
<https://doi.org/10.1038/s41586-022-04879-8>

References

1. Martínez-Jiménez, F. et al. A compendium of mutational cancer driver genes. *Nat. Rev. Cancer* **20**, 555–572 (2020).
2. Giacomelli, A. O. et al. Mutational processes shape the landscape of *TP53* mutations in human cancer. *Nat. Genet.* **50**, 1381–1387 (2018).
3. Baugh, E. H., Ke, H., Levine, A. J., Bonneau, R. A. & Chan, C. S. Why are there hotspot mutations in the *TP53* gene in human cancers? *Cell Death Differ.* **25**, 154–160 (2018).
4. Petitjean, A. et al. Impact of mutant p53 functional properties on *TP53* mutation patterns and tumor phenotype: lessons from recent developments in the IARC *TP53* database. *Hum. Mutat.* **28**, 622–629 (2007).
5. Kato, S. et al. Understanding the function–structure and function–mutation relationships of p53 tumor suppressor protein by high-resolution missense mutation analysis. *Proc. Natl Acad. Sci. USA* **100**, 8424–8429 (2003).
6. Kotler, E. et al. A systematic p53 mutation library links differential functional impact to cancer mutation pattern and evolutionary conservation. *Mol. Cell* **71**, 178–190 (2018).
7. Marty, R. et al. MHC-I genotype restricts the oncogenic mutational landscape. *Cell* **171**, 1272–1283 (2017).
8. Pyke, R. M. et al. Evolutionary pressure against MHC class II binding cancer mutations. *Cell* **175**, 416–428 (2018).
9. Ding, J. et al. Systematic analysis of somatic mutations impacting gene expression in 12 tumour types. *Nat. Commun.* **6**, 8554 (2015).
10. Huang, N., Shah, P. K. & Li, C. Lessons from a decade of integrating cancer copy number alterations with gene expression profiles. *Brief. Bioinform.* **13**, 305–316 (2012).
11. Fehrman, R. S. et al. Gene expression analysis identifies global gene dosage sensitivity in cancer. *Nat. Genet.* **47**, 115–125 (2015).

12. Köbel, M. et al. Optimized p53 immunohistochemistry is an accurate predictor of *TP53* mutation in ovarian carcinoma. *J. Pathol. Clin. Res.* **2**, 247–258 (2016).
13. Murnyák, B. & Hortobágyi, T. Immunohistochemical correlates of *TP53* somatic mutations in cancer. *Oncotarget* **7**, 64910 (2016).
14. Cole, A. J. et al. Assessing mutant p53 in primary high-grade serous ovarian cancer using immunohistochemistry and massively parallel sequencing. *Sci. Rep.* **6**, 26191 (2016).
15. Tran, E. et al. T-cell transfer therapy targeting mutant *KRAS* in cancer. *N. Engl. J. Med.* **375**, 2255–2262 (2016).
16. Hsiue, E. H. et al. Targeting a neoantigen derived from a common *TP53* mutation. *Science* **371**, eabc8697 (2021).
17. Eigen, M. Selforganization of matter and the evolution of biological macromolecules. *Naturwissenschaften* **58**, 465–523 (1971).
18. Gerland, U. & Hwa, T. On the selection and evolution of regulatory DNA motifs. *J. Mol. Evol.* **55**, 386–400 (2002).
19. Łuksza, M. & Lässig, M. A predictive fitness model for influenza. *Nature* **507**, 57–61 (2014).
20. Balachandran, V. P. et al. Identification of unique neoantigen qualities in long-term survivors of pancreatic cancer. *Nature* **551**, 512–516 (2017).
21. Łuksza, M. et al. A neoantigen fitness model predicts tumour response to checkpoint blockade immunotherapy. *Nature* **551**, 517–520 (2017).
22. Ma, L. et al. A plausible model for the digital response of p53 to DNA damage. *Proc. Natl Acad. Sci. USA* **102**, 14266–14271 (2005).
23. Gaglia, G., Guan, Y., Shah, J. V. & Lahav, G. Activation and control of p53 tetramerization in individual living cells. *Proc. Natl Acad. Sci. USA* **110**, 15497–15501 (2013).

24. Price, G. R. Fisher's 'fundamental theorem' made clear. *Ann. Hum. Genet.* **36**, 129–140 (1972).
25. Hunter, J. C. et al. Biochemical and structural analysis of common cancer-associated KRAS mutations. *Mol. Cancer Res.* **13**, 1325–1335 (2015).
26. Shoval, O. et al. Evolutionary trade-offs, pareto optimality, and the geometry of phenotype space. *Science* **336**, 1157–1160 (2012).
27. Pinheiro, F., Warsi, O., Andersson, D. I. & Lässig, M. Metabolic fitness landscapes predict the evolution of antibiotic resistance. *Nat. Ecol. Evol.* **5**, 677–687 (2021).
28. Kratz, C. P. et al. Analysis of the Li–Fraumeni spectrum based on an international germline TP53 variant data set: an International Agency for Research on Cancer TP53 database analysis. *JAMA Oncol.* **7**, 1800–1805 (2021).
29. De Andrade, K. C. et al. Cancer incidence, patterns, and genotype–phenotype associations in individuals with pathogenic or likely pathogenic germline TP53 variants: an observational cohort study. *Lancet Oncol.* **22**, 1787–1798 (2021).
30. Martincorena, I. & Campbell, P. J. Somatic mutation in cancer and normal cells. *Science* **349**, 1483–1489 (2015).
31. Caushi, J. X. et al. Transcriptional programs of neoantigen-specific TIL in anti-PD-1-treated lung cancers. *Nature* **596**, 126–132 (2021).
32. Bear, A. S. et al. Biochemical and functional characterization of mutant KRAS epitopes validates this oncoprotein for immunological targeting. *Nat. Commun.* **12**, 4365 (2021).
33. Malekzadeh, P. et al. Antigen experienced T cells from peripheral blood recognize p53 neoantigens. *Clin. Cancer Res.* **26**, 1267–1276 (2020).
34. Colom, B. et al. Mutant clones in normal epithelium outcompete and eliminate emerging tumours. *Nature* **598**, 510–514 (2021).

35. Wylie, A. et al. *p53* genes function to restrain mobile elements. *Genes Dev.* **30**, 64–77 (2016).
36. Levine, A. J., Ting, D. T. & Greenbaum, B. D. *p53* and the defenses against genome instability caused by transposons and repetitive elements. *Bioessays* **38**, 508–513 (2016).
37. McKerrow, W. et al. LINE-1 expression in cancer correlates with *p53* mutation, copy number alteration, and S phase checkpoint. *Proc. Natl Acad. Sci. USA* **119**, e2115999119 (2022).
38. Dayan, P., Hinton, G. E., Neal, R. M. & Zemel, R. S. The Helmholtz machine. *Neural Comput.* **7**, 889–904 (1995).

Acknowledgements

We thank U. Alon, C. Chan, N. Copeland, P. Hainaut, N. Jenkins, S. Lowe, D. Pardoll, A. Snyder, D. Ting and the staff of the Balachandran, Greenbaum, Savage and Wolchok laboratories for offering conversations. We also thank N. Rusk for comments and editing. This research was funded in part through National Institutes of Health (NIH)/NCI Cancer Center Support Grant P30CA008748, Swim Across America, the Ludwig Institute for Cancer Research, the Ludwig Center for Cancer Immunotherapy at Memorial Sloan Kettering, the Cancer Research Institute, the Parker Institute for Cancer Immunotherapy, NIH grants R01AI081848, U01CA224175, R01CA240924 and U01CA228963, a collaboration of Stand Up To Cancer, the Society for Immunotherapy of Cancer and the Lustgarten Foundation, the V Foundation for Cancer Research, Sephora and the Pershing Square Sohn Foundation. C.B. was supported by NIH grant R01CA227534-03. D.F.B., S.A.F. and J.E.R. were supported by NIH grant P50CA221745 and the Ludwig Institute for Cancer Research. S.A.F. is supported by NIH grant K12CA184746-01A1. B.D.G. was supported by the Pershing Square Sohn Prize–Mark Foundation Fellowship supported by funding from the Mark Foundation for Cancer Research. M.L. is a Pew Biomedical Scholar. The work of K.C.A., P.P.K. and S.A.S. is supported by the Intramural Research Program of the Division of Cancer Epidemiology and Genetics, NCI. S.P.S. was supported by the LesLois Shaw Foundation

and holds the Nicholls-Biondi Chair in Computational Oncology at MSKCC. B.W. is funded in part by Breast Cancer Research Foundation and Cycle for Survival grants. R.Z. was supported by the Parker Bridge Fellow Award. D.Z. is supported by the Ovarian Cancer Research Foundation Liz Tilberis Award and the Department of Defense Ovarian Cancer Research Academy (OC150111).

Author information

Author notes

1. These authors contributed equally: David Hoyos, Roberta Zappasodi
2. These authors jointly supervised this work: Taha Merghoub, Arnold J. Levine, Marta Łuksza, Benjamin D. Greenbaum

Authors and Affiliations

1. Computational Oncology, Department of Epidemiology & Biostatistics, Memorial Sloan Kettering Cancer Center, New York, NY, USA

David Hoyos, Zachary Sethna, Sohrab P. Shah, Ignacio Vázquez-García & Benjamin D. Greenbaum

2. Swim Across America Laboratory and Ludwig Collaborative, Immunology Program, Parker Institute for Cancer Immunotherapy, Memorial Sloan Kettering Cancer Center, New York, NY, USA

Roberta Zappasodi, Isabell Schulze, Dmitriy Zamarin, Jedd D. Wolchok & Taha Merghoub

3. Department of Medicine, Weill Cornell Medical College, New York, NY, USA

Roberta Zappasodi, Dean F. Bajorin, Margaret K. Callahan, Samuel A. Funt, Jonathan E. Rosenberg, Dmitriy Zamarin, Vinod P. Balachandran, Jedd D. Wolchok, Matthew D. Hellmann & Taha Merghoub

4. Parker Institute for Cancer Immunotherapy, Memorial Sloan Kettering Cancer Center, New York, NY, USA

Roberta Zappasodi, Isabell Schulze, Vinod P. Balachandran, Jedd D. Wolchok, Matthew D. Hellmann & Taha Merghoub

5. Immunology and Microbial Pathogenesis Program, Weill Cornell Graduate School of Medical Sciences, New York, NY, USA

Roberta Zappasodi

6. Hepatopancreatobiliary Service, Department of Surgery, Memorial Sloan Kettering Cancer Center, New York, NY, USA

Zachary Sethna & Vinod P. Balachandran

7. Department of Medicine, Memorial Sloan Kettering Cancer Center, New York, NY, USA

Zachary Sethna, Dean F. Bajorin, Margaret K. Callahan, Samuel A. Funt, Jonathan E. Rosenberg, Dmitriy Zamarin & Vinod P. Balachandran

8. Division of Cancer Epidemiology and Genetics, Clinical Genetics Branch, National Cancer Institute, National Institutes of Health, Rockville, MD, USA

Kelvin César de Andrade, Payal P. Khincha & Sharon A. Savage

9. Department of Pathology and Laboratory Medicine, Memorial Sloan Kettering Cancer Center, New York, NY, USA

Chaitanya Bandlamudi & Britta Weigelt

10. Kravis Center for Molecular Oncology, Memorial Sloan Kettering Cancer Center, New York, NY, USA

Chaitanya Bandlamudi

11. Experimental and Translational Immunology, Health Technology,
Technical University of Denmark, Lyngby, Denmark

Sine R. Hadrup & Jeppe S. Holm
12. Physiology, Biophysics & Systems Biology, Weill Cornell Medicine,
Weill Cornell Medical College, New York, NY, USA

Sohrab P. Shah & Benjamin D. Greenbaum
13. Department of Surgery, Memorial Sloan Kettering Cancer Center, New
York, NY, USA

Michelle Wu
14. Adaptive Biotechnologies, Seattle, WA, USA

Laura F. Campitelli, Edward J. Osborne, Mark Klinger & Harlan S.
Robins
15. David M. Rubenstein Center for Pancreatic Cancer Research, Memorial
Sloan Kettering Cancer Center, New York, NY, USA

Vinod P. Balachandran
16. Human Oncology and Pathogenesis Program, Memorial Sloan
Kettering Cancer Center, New York, NY, USA

Jedd D. Wolchok & Taha Merghoub
17. Thoracic Oncology Service, Memorial Sloan Kettering Cancer Center,
New York, NY, USA

Matthew D. Hellmann
18. Simons Center for Systems Biology, Institute for Advanced Study,
Princeton, NJ, USA

Arnold J. Levine

19. Department of Oncological Sciences, Tisch Cancer Institute, Icahn School of Medicine at Mount Sinai, New York, NY, USA

Marta Łuksza

Contributions

B.D.G. conceptualized the study. T.M., A.J.L., M.Ł. and B.D.G. developed the research plan. D.H., Z.S., M.Ł. and B.D.G. developed the computational methodology. R.Z., I.S., A.J.L. and T.M. developed the experimental methodology. D.H., Z.S. and K.C.A. performed the computational analysis. R.Z. and I.S. performed the experimental analysis. P.P.K. and S.A.S. performed the LFS data collection and analysis. S.A.F., J.S.H., J.D.W., M.D.H. and T.M. collected and analysed the human samples. C.B., D.F.B., M.K.C., S.A.F., J.S.H., S.R.H., J.E.R., S.P.S., I.V.-G., B.W., M.W. and D.Z. collected samples from patients with cancer. L.F.C., E.J.O., M.K. and H.S.R. conducted MIRA assays and analysis. D.H., R.Z., I.S., Z.S. T.M., M.Ł. and B.D.G. wrote the manuscript. K.C.A., V.P.B., M.D.H., P.P.K., S.A.S., S.P.S., B.W. and J.D.W. reviewed and edited the manuscript. T.M., A.J.L., M.Ł. and B.D.G. are credited with senior authorship.

Corresponding authors

Correspondence to [Roberta Zappasodi](#), [Taha Merghoub](#) or [Benjamin D. Greenbaum](#).

Ethics declarations

Competing interests

D.F.B. is a consultant for Bristol Myers Squibb, Merck, Genentech–Roche, AstraZeneca and Pfizer and has received research support from Merck, Genentech–Roche, AstraZeneca, Novartis and Bristol Myers Squibb.

M.K.C. has received consulting fees for Bristol Meyers Squibb, Merck, Incyte, Moderna, Immunocore and AstraZeneca and research funding from Bristol Meyers Squibb. L.F.C., E.J.O., M.K. and H.S.R. are employees of Adaptive Biotechnologies. S.A.F. has received research support from

AstraZeneca and Genentech–Roche; is a consultant and advisory board member for Merck; and owns stock in UroGen, Allogene Therapeutics, Neogene Therapeutics, Kronos Bio and IconOVir. B.D.G. has received honoraria for speaking engagements from Merck, Bristol Meyers Squibb and Chugai Pharmaceutical; has received research funding from Bristol Meyers Squibb; has been a compensated consultant for PMV Pharma, DarwinHealth and ROME Therapeutics; and is a cofounder of ROME Therapeutics. M.D.H. reports personal fees from Achilles, Adagene, Adicet, Arcus, AstraZeneca, Blueprint, Bristol Myers Squibb, Da Volterra, Eli Lilly, Genentech–Roche, Genzyme–Sanofi, Janssen, Immunai, Instil Bio, Mana Therapeutics, Merck, Mirati, Natera, PACT Pharma, Shattuck Labs and Regeneron and has equity options with Factorial, Immunai, Shattuck Labs and Arcus. M.D.H. also reports that a patent filed by Memorial Sloan Kettering related to the use of tumour mutational burden to predict response to immunotherapy (PCT/US2015/062208) is pending and licensed by Personal Genome Diagnostics and that, subsequent to completing this work, he became an employee of AstraZeneca. A.J.L. is a founder, director and shareholder of PMV Pharma and is the chair of the Janssen scientific advisory board. T.M. is a cofounder and holds equity in Imvaq Therapeutics; is a consultant for ImmunOs Therapeutics, ImmunoGenesis and Pfizer; has received research support from Bristol Myers Squibb, Surface Oncology, Kyn Therapeutics, Infinity Pharmaceuticals, Peregrine Pharmaceuticals, Adaptive Biotechnologies, Leap Therapeutics and Aprea; and has patent applications related to work on oncolytic viral therapy, alpha virus-based vaccines, neoantigen modelling, CD40, GITR, OX40, PD-1 and CTLA-4. I.S. is an inventor on a patent application related to work on CD40. J.E.R. has received consulting fees and trial funding from Bayer, Seagen, AstraZeneca, Roche, Astellas Pharma and QED Therapeutics; consulting fees from Bristol Myers Squibb, Merck, Pfizer, Pharmacyclics, Boehringer Ingelheim, GlaxoSmithKline, Infinity, Janssen, Mirati, EMD Serono, Gilead, BioClin, Eli Lilly and Company, Tyra Biosciences and Pharmacyclics; honoraria for continuing medical education from Research to Practice, MJH Life Sciences, Medscape, Clinical Care Options, OncLive and EMD Serono; royalties from UpToDate. B.W. reports ad hoc membership of the scientific advisory board of Repare Therapeutics, outside the submitted work. J.D.W. is a consultant for Adaptive Biotechnologies, Amgen, Apricity, Ascentage Pharma, ArsenalBio, Astellas, AstraZeneca, Bayer, BeiGene, Boehringer

Ingelheim, Bristol Myers Squibb, Celgene, Chugai, Eli Lilly, Elucida, F-
Star, Georgiamune, Imvaq, Kyowa Kirin, Linneaus, Merck, Neon
Therapeutics, Polynoma, PsiOxus, Recepta, Takara Bio, Trieza, Truvax,
SELLAS, Serametrix, Surface Oncology, Syndax, Syntalogic and Werewolf
Therapeutics; receives grant and research support from Bristol Myers
Squibb and Sephora; and has equity in Tizona Pharmaceuticals, Adaptive
Biotechnologies, Imvaq, BeiGene, Linneaus, Apricity, ArsenalBio and
Georgiamune. R.Z. is an inventor on patent applications related to work on
GITR, PD-1 and CTLA-4; is a scientific advisory board member of iTEOS
Therapeutics; has consulted for Leap Therapeutics; and receives grant
support from AstraZeneca and Bristol Myers Squibb. D.Z. is a consultant for
Merck, Agenus, Hookipa Biotech, AstraZeneca, Western Oncolytics,
Synthekine, MANA Therapeutics, Xencor, Memgen and Takeda; receives
grant and research support from AstraZeneca, Roche and Plexxikon; holds
stock options with ImmunOs Therapeutics, Calidi Biotherapeutics and
Accurius; and has a patent related to use of Newcastle disease virus for
cancer therapy with royalties paid by Merck.

Peer review

Peer review information

Nature thanks Alexander Anderson, Paul Thomas and the other, anonymous, reviewer(s) for their contribution to the peer review of this work.

Additional information

Publisher's note Springer Nature remains neutral with regard to jurisdictional claims in published maps and institutional affiliations.

Extended data figures and tables

[Extended Data Fig. 1 Inferred relationships between relative transactivation and apparent dimer dissociation constant.](#)

Relationship between the relative transactivation and the inferred apparent dimer dissociation constant for mutant homodimer p53. Blue dotted lines correspond to wild-type p53, which has a relative transactivation of 1 (Methods). The hotspots' inferred values are annotated in red.

Extended Data Fig. 2 Relationship between mutant p53 concentration and predicted MDM2 binding affinities.

a, Variation in normalized concentration across mutant p53 versus predicted affinity to *MDM2* DNA in common *TP53*-mutated tissues within TCGA. Protein concentration is expressed as log₂ of inferred protein concentration in nanomolar (nM) units. **b**, Fraction positive immunohistochemistry (IHC) assay from the IARC R20 dataset plotted against predicted per-allele mutant p53 concentration averaged across tissues. Correlations are for mutations with at least 10 IHC data entries (Pearson p-value 0.00848, Spearman p-value 0.00967). **c**, Fraction positive IHC assay plotted against predicted per-allele mutant p53 concentration averaged across tissues only for mutant *TP53* hotspots (Pearson p-value 0.0207, Spearman p-value 0.00503).

Extended Data Fig. 3 Fitness model prediction analysis.

a, Predicted ratio from combined fitness model plotted against posterior ratio for each *TP53* mutation. Mutations are colored by their observed frequency. Ratios > 1 are predicted to be fixed in the cancer population. Diagonal line corresponds to ratios being equal. **b**, Prediction accuracy plotted as the proportion of observed mutation frequency for true positive (TP), false positive (FP), true negative (TN) and false negative (FN) model predictions. **c**, Kullback-Leiber divergence versus number of simulated HLA-I haplotypes shows improved model predictions according to the haplotype sample size. **d**, Internal validation by shuffling background mutation frequencies, functional phenotypes and immune phenotypes of *TP53* mutations for 1,000 iterations and computing the Kullback-Leibler divergence for each iteration. The histogram is of the distribution of Kullback-Leibler divergences from all iterations. Permutation-mean Kullback-Leibler divergence is plotted as a vertical black dotted line and the true Kullback-Leibler divergence is plotted as a vertical red dotted line.

Extended Data Fig. 4 Fitness model predicts mutation frequencies in commonly mutated cancer driver genes.

a, Degree to which models of varying complexity account for mutation distributions from TCGA and COSMIC, excluding TCGA samples, across 27 commonly mutated cancer driver genes. Models are ranked by Bayesian Information Criterion (BIC) in descending order (models with the lowest BIC value are deemed the most explanatory). **b**, Boxplots of observed mutation frequency variances of driver genes best explained by a particular model, ranked by complexity in ascending order. **c**, Fitness model results for *PTEN* per protein position in TCGA, using both conservation and immunogenicity over background mutation rates. The full model is justified by the BIC value (KL divergence = 0.269; Pearson r = 0.701, p-value = 2.013e-24; Spearman r = 0.701, p-value = 2.386e-24). **d**, Fitness model results for *KRAS* per protein position in TCGA, using a full model with conservation, function and immunogenicity over background mutation rates with functional information available for seven frequent *KRAS* cancer mutations (G12A/C/D/R/V, G13D and Q61L). All components are justified by the BIC value (KL divergence = 0.256; Pearson r = 0.981, p-value = 2.095e-24; Spearman r = 0.616, p-value = 0.000104). **e**, Trade-off between gain-of-function and avoidance of neoantigen presentation, defined as $\sqrt{1 - \{I\}_{m} \text{left}(H \text{right})}$, in TCGA pancreatic cancer for *KRAS* hotspots (Pearson r = -0.750, p-value = 2.599e-23; Spearman r = -0.774, p-value = 1.507e-25). Each point corresponds to an individual pancreatic cancer sample with a hotspot *KRAS* mutation.

Extended Data Fig. 5 Inferred mutant immunogenicity is not related to pathogenicity in non-cancer driver genes.

a–f, Comparison of inferred immunogenicity across not-pathogenic and pathogenic missense mutations in nine non-cancerous disease driver genes (*HBA*, *HBB*, *HBD*, *HG1*, *HG2*, *F8*, *PAH*, *PHEX* and *POGZ*) using the Mann-Whitney U-test. Six out of nine genes had sufficient data for comparison between not-pathogenic and pathogenic mutations (*HBA*, *HBB*, *F8*, *PAH*, *PHEX* and *POGZ*). **g**, Data corresponding to all hemoglobin subunits (*HBA*, *HBB*, *HBD*, *HG1* and *HG2*) were combined and compared (Hemoglobin). Mutations and their “Not-pathogenic” and “Pathogenic”

status were determined using the NCBI's dbSNP and ClinVar systems, respectively.

Extended Data Fig. 6 Fitness trade-offs inferred from ATAC-and RNA-seq.

a, Lack of binding score plotted versus predicted functional fitness. Most TCGA ATAC-seq samples were breast cancers (BRCA), therefore we only plot matched BRCA samples to normalize on tissue-specific protein abundance (Pearson $r = 0.46$, p-value = 0.063, Spearman $r = 0.55$, p-value 0.023, N = 17). **b**, \log_2 of median TCGA RNA expression (TPM) of eight p53 target genes utilized in fitness model split on median TCGA ATAC-seq lack of DNA binding score (Mann-Whitney p-value = 0.006). **c**, Immune fitness plotted versus ATAC-seq-based lack of DNA binding footprinting score for each TCGA sample (Pearson $r = -0.45$, p-value < 0.0001; Spearman $r = -0.49$, p-value < 0.0001). **d**, Median TCGA RNA expression (TPM) of the target genes with available ATAC-seq data (*WAF1*, *BAX*, *h1433s*, *AIP1*, *GADD45* and *NOXA*) plotted versus median probability of mutant p53 binding DNA, conditioned on target DNA chromatin accessibility (Pearson $r = 0.25$, p-value 0.0459; Spearman $r = 0.088$, p-value 0.480).

Extended Data Fig. 7 Differential T-cell reactivity to p53 neopeptides.

a, Flow cytometry quantification of HLA-A*02:01 expression on the surface of live T2 cells as a measure of peptide:MHC stabilization via binding to specific peptides. T2 cells were incubated overnight in serum-free media with recombinant human B2M and the indicated peptides at the indicated concentrations, or DMSO as vehicle control. Blue, negative controls (DMSO and unrelated HLA-B*35-restricted NY-ESO-1-derived peptide); red, positive controls (HLA-A*02:01-restricted peptides from flu and HIV viral antigens and Mart1/Melan-A melanoma-associated antigen); gray, experimental peptides containing the indicated mutation in comparison with the corresponding wild-type (wt) sequence. Data are mean \pm SD of 2-3 replicates. P values are calculated with a two-sided unpaired t-test. **b**, Model illustrating the molecular basis of the T-cell stimulation assay and

stimulation conditions (APC, antigen presenting cell; TCR, T-cell receptor). **c**, Representative plots of IFN- γ ± TNF-a expressing cells among CD8+CD3+ live T cells in PBMCs from patients with mutant p53 tumors as in Fig. 3a. **d**, Correlation analyses between indicated parameters in PBMC samples from R248Q mutant patients with presence of disease (N = 4) at the time of PBMC collection as in Fig. 3b. **e**, Estimate of mutant p53 amount per tumor cell before treatment in the same patients. Samples with R175H mutations are colored in blue. The sample which reacted, corresponding to the patient who received immune checkpoint blockade (ICB) therapy, is in solid blue, and the sample which did not react, and did not receive ICB, has filled-in lines. **f**, Flow cytometry gating strategy for total CD8 and non-naïve memory CD8 T-cells analyzed in Fig. 3c,d. TN: naïve T-cells, TCM: central memory T-cells, TEM, effector memory T-cells, TEMRA: effector memory T-cells re-expressing CD45RA.

Extended Data Fig. 8 Relationships between immune fitness and immune checkpoint protein expression in TCGA.

a, b, Continuous and categorical relationships between CTLA-4 (**a**) and PD-1 (**b**) protein expression available from TCGA RPPA proteomics assay and immune fitness. For the CTLA-4 scatterplot, Pearson p-value < 0.0001, Spearman p-value < 0.0001. For the PD-1 scatterplot, Pearson p-value = 0.00153, Spearman p-value < 0.0001. Categorical differences measured with the Welch's t-test. **c**, Continuous and categorical relationships between PD-L1 protein expression available from TCGA RPPA proteomics assay and immune fitness in commonly *TP53*-mutated tissues. Correlation p-values: Ovarian - Pearson p-value = 0.2, Spearman p-value = 0.0829; Colorectal - Pearson p-value = 0.157, Spearman p-value 0.003; NSCLC - Pearson p-value = 0.0812, Spearman p-value = 0.00793; Breast - Pearson p-value = 0.00671, Spearman p-value = 0.000140. Categorical differences measured with the Welch's t-test.

Extended Data Fig. 9 p53 fitness predicts survival and immune relevance in diverse p53-mutated groups.

Kaplan-Meier curves separated by median functional, immune and total fitness in TCGA and MSKCC non-small cell lung cancer (NSCLC) ICB-

treated samples. For NSCLC samples, matched HLA-*TP53* mutation pairs with lung-specific and allele-specific concentrations were used to determine functional, immune and combined fitness. *ns* p > 0.05, * p ≤ 0.05, ** p ≤ 0.01, *** p ≤ 0.001, **** p ≤ 0.0001.

Extended Data Fig. 10 Relationships of germline mutant p53 fitness and age of tumour onset.

Kaplan-Meier curves separated by median functional and immune mutant p53 fitness for first-cancer age of onset in the LFS IARC R20 germline dataset (N = 998) and the NCI LFS cohort (N = 82). Mutant p53 fitness was determined using TCGA-derived tissue-specific mutant p53 concentrations for both datasets, with individual HLA-I types for the NCI cohort and averages taken over TCGA haplotypes for the IARC dataset, which lacked individual HLA-I types.

Supplementary information

Supplementary Information

This file contains Table 1, Supplementary Figs. 1–5 and Supplementary References.

Reporting Summary

Supplementary Methods

Supplementary Table 1

Supplementary Table 2

Supplementary Table 3

Supplementary Table 4

Supplementary Table 5

Supplementary Table 6

Supplementary Table 7

Rights and permissions

Open Access This article is licensed under a Creative Commons Attribution 4.0 International License, which permits use, sharing, adaptation, distribution and reproduction in any medium or format, as long as you give appropriate credit to the original author(s) and the source, provide a link to the Creative Commons license, and indicate if changes were made. The images or other third party material in this article are included in the article's Creative Commons license, unless indicated otherwise in a credit line to the material. If material is not included in the article's Creative Commons license and your intended use is not permitted by statutory regulation or exceeds the permitted use, you will need to obtain permission directly from the copyright holder. To view a copy of this license, visit <http://creativecommons.org/licenses/by/4.0/>.

Reprints and Permissions

About this article

Cite this article

Hoyos, D., Zappasodi, R., Schulze, I. *et al.* Fundamental immune–oncogenicity trade-offs define driver mutation fitness. *Nature* **606**, 172–179 (2022). <https://doi.org/10.1038/s41586-022-04696-z>

- Received: 23 January 2021
- Accepted: 28 March 2022
- Published: 11 May 2022

- Issue Date: 02 June 2022
- DOI: <https://doi.org/10.1038/s41586-022-04696-z>

Share this article

Anyone you share the following link with will be able to read this content:

[Get shareable link](#)

Sorry, a shareable link is not currently available for this article.

[Copy to clipboard](#)

Provided by the Springer Nature SharedIt content-sharing initiative

[Tumour driver mutations compromise between cancer growth and immune responses](#)

Nature Research Briefing 11 May 2022

This article was downloaded by **calibre** from <https://www.nature.com/articles/s41586-022-04696-z>

| [Section menu](#) | [Main menu](#) |

[Download PDF](#)

- Article
- Open Access
- [Published: 18 May 2022](#)

MCM complexes are barriers that restrict cohesin-mediated loop extrusion

- [Bart J. H. Dequeker](#) ORCID: orcid.org/0000-0001-7975-2245^{1 na1},
- [Matthias J. Scherr](#) ORCID: orcid.org/0000-0003-0110-3709^{2 na1},
- [Hugo B. Brandão](#) ORCID: orcid.org/0000-0001-5496-0638^{3 nAff9},
- [Johanna Gassler](#) ORCID: orcid.org/0000-0002-4408-6577^{1,4},
- [Sean Powell](#)¹,
- [Imre Gaspar](#)⁴,
- [Ilya M. Flyamer](#)⁵,
- [Aleksandar Lalic](#) ORCID: orcid.org/0000-0001-5250-3556⁴,
- [Wen Tang](#)⁶,
- [Roman Stocsits](#) ORCID: orcid.org/0000-0002-9478-3928⁶,
- [Iain F. Davidson](#) ORCID: orcid.org/0000-0003-4945-6415⁶,
- [Jan-Michael Peters](#) ORCID: orcid.org/0000-0003-2820-3195⁶,
- [Karl E. Duderstadt](#) ORCID: orcid.org/0000-0002-1279-7841^{2,7},
- [Leonid A. Mirny](#) ORCID: orcid.org/0000-0002-0785-5410⁸ &
- [Kikuë Tachibana](#) ORCID: orcid.org/0000-0002-6564-7484^{1,4}

Nature volume **606**, pages 197–203 (2022)

- 8919 Accesses
- 137 Altmetric

- [Metrics details](#)

Subjects

- [Chromosomes](#)
- [Computational biology and bioinformatics](#)
- [Nuclear organization](#)

Abstract

Eukaryotic genomes are compacted into loops and topologically associating domains (TADs)^{1,2,3}, which contribute to transcription, recombination and genomic stability^{4,5}. Cohesin extrudes DNA into loops that are thought to lengthen until CTCF boundaries are encountered^{6,7,8,9,10,11,12}. Little is known about whether loop extrusion is impeded by DNA-bound machines. Here we show that the minichromosome maintenance (MCM) complex is a barrier that restricts loop extrusion in G1 phase. Single-nucleus Hi-C (high-resolution chromosome conformation capture) of mouse zygotes reveals that MCM loading reduces CTCF-anchored loops and decreases TAD boundary insulation, which suggests that loop extrusion is impeded before reaching CTCF. This effect extends to HCT116 cells, in which MCMs affect the number of CTCF-anchored loops and gene expression. Simulations suggest that MCMs are abundant, randomly positioned and partially permeable barriers. Single-molecule imaging shows that MCMs are physical barriers that frequently constrain cohesin translocation in vitro. Notably, chimeric yeast MCMs that contain a cohesin-interaction motif from human MCM3 induce cohesin pausing, indicating that MCMs are ‘active’ barriers with binding sites. These findings raise the possibility that cohesin can arrive by loop extrusion at MCMs, which determine the genomic sites at which sister chromatid cohesion is established. On the basis of in vivo, in silico and in vitro data, we conclude that distinct loop extrusion barriers shape the three-dimensional genome.

Main

Eukaryotic genomes are folded into loops that are generated by structural maintenance of chromosomes (SMC) proteins, including cohesin and condensin complexes (reviewed previously¹³). Structures that emerge through loop extrusion are detected by Hi-C experiments. The extrusion process is hypothesized to form progressively larger loops until cohesin encounters a barrier and/or is released by Wapl (refs. ^{9,10,11}). The predominant barrier to loop extrusion in vertebrates is CTCF (ref. ¹²), which has an instructive role in establishing extrusion-mediated structures that are visible in Hi-C¹⁴. However, the loop extrusion machinery encounters other obstacles on chromatin, such as nucleosomes and other protein complexes. Although RNA polymerases are moving barriers for condensin translocation in bacteria¹⁵ and affect cohesin translocation in eukaryotes^{16,17}, it remains unknown how SMCs can extrude loops on ‘busy’ eukaryotic chromosomes that are bound by a myriad of proteins. Whether other DNA-bound proteins can influence three-dimensional genome architecture in eukaryotes is not known, and could be critical for understanding their function.

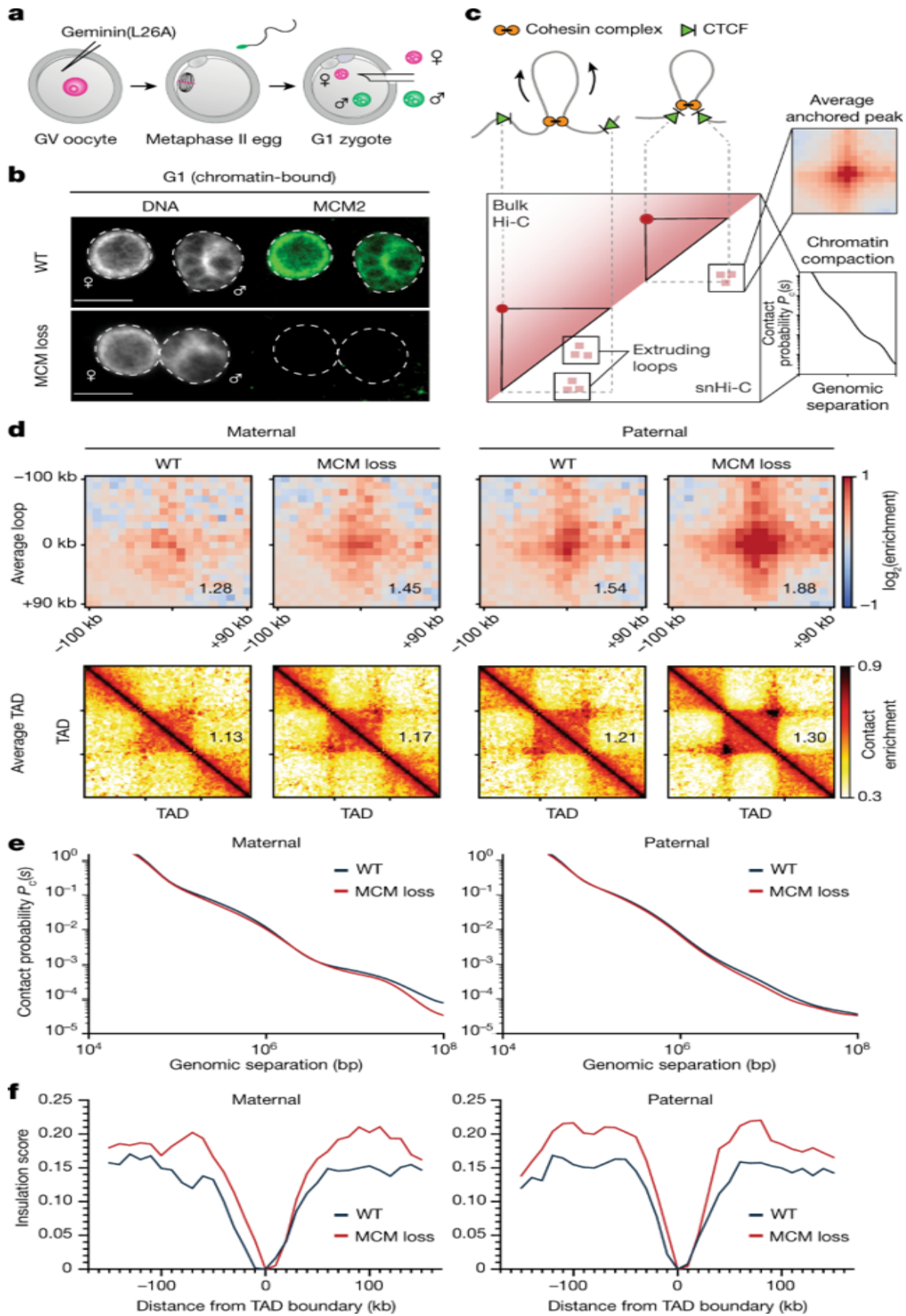
The minichromosome maintenance (MCM) complex is an abundant macromolecular machine that is essential for DNA replication in eukaryotes and archaea¹⁸. MCM2–MCM7 complexes (hereafter MCM) are loaded at replication origins by the origin recognition complex (ORC), Cdc6 and Cdt1 to form the pre-replication complex during mitosis and G1 phase¹⁹. The head-to-head double MCM hexamer topologically entraps double-stranded DNA and is catalytically inactive as a helicase until the initiation of DNA replication²⁰. Notably, 10–100-fold more MCMs are loaded onto chromatin than are needed for S-phase progression. This is referred to as the ‘MCM paradox’²¹. One hypothesis to explain this phenomenon is that surplus complexes mark dormant origins that fire under conditions such as DNA damage checkpoint activation²². Surplus MCMs have been shown to protect against DNA breaks by reducing replication fork speed²³. Whether they have any functional consequences in G1 phase remains unclear. Given the abundance of MCMs, their long residence time on chromatin²⁴ (more than 6 h) and their comparable size²⁵ (13 nm) to the FtsK helicase (12.5 nm) (Extended Data Fig. 1) that can push cohesin on DNA in vitro²⁶, we asked whether MCMs are obstacles to cohesin-mediated loop extrusion and in this way influence genome architecture.

MCMs impede CTCF-anchored loops

To test this hypothesis, we used the oocyte-to-zygote transition to investigate whether MCM loss affects loop extrusion. Oocytes are female germ cells that divide meiotically and, after fertilization, generate one-cell embryos (zygotes). These contain maternal and paternal pronuclei, the chromatin of which is organized into cohesin-dependent loops and TADs^{27,28}. Although zygotes are limited by paucity of material, they offer advantages for: (1) studying MCM loading on newly assembled paternal chromatin; (2) deciphering haplotype-resolved chromatin organization; (3) manipulating the assembly of the pre-replication complex without interfering with cell-cycle progression, as there is no DNA replication between meiosis I and II; and (4) disentangling direct from indirect effects because of transcriptional inactivity²⁹.

To generate zygotes that are deficient in chromatin-bound MCMs, we interfered with the Cdt1-mediated loading pathway. Cdt1 deposits MCMs onto chromatin, and this reaction is inhibited by geminin, a target of the anaphase-promoting complex/cyclosome (APC/C)³⁰ (Extended Data Fig. 2a). Mutation of geminin's destruction box generates a non-degradable version (geminin(L26A)) that inhibits the Cdt1-mediated loading of MCMs in G1 phase³¹ (Extended Data Fig. 2a). To achieve this, mouse oocytes were microinjected with mRNA encoding an injection marker GFP with or without geminin(L26A) (Fig. 1a). Metaphase II eggs were fertilized in vitro and zygotes were analysed in G1 phase (Extended Data Fig. 2c). Geminin(L26A) expression did not grossly affect the abundance of Scc1 and CTCF (Extended Data Fig. 2e,f). By contrast, few or no chromatin-bound MCMs were detected and EdU was not incorporated in zygotes expressing geminin(L26A) (referred to as 'MCM loss') (Fig. 1b, Extended Data Fig. 2b, d), demonstrating the efficient inhibition of MCM loading.

Fig. 1: Chromatin-bound MCMs impede loop and TAD formation in G1-phase zygotes.



a, Germinal vesicle (GV)-stage oocytes were injected with geminin(L26A) mRNA and metaphase II eggs were fertilized in vitro. Maternal and paternal pronuclei were extracted for snHi-C. **b**, Representative images of immunofluorescence staining of chromatin-bound MCM2 in wild-type (WT) and MCM-loss G1-phase zygotes. DNA is stained with DAPI. Scale bars, 10 μ m. **c**, Comparison of contacts detected in snHi-C versus bulk Hi-C. Contact probability curves, $P_c(s)$, provide insights into chromatin compaction. **d**, Average loops and TADs for wild-type and MCM-loss chromatin in G1 phase. The data shown are based on n (WT, maternal) = 13, n (WT, paternal) = 16, n (MCM loss, maternal) = 16, n (MCM loss, paternal) = 15, from 4 independent experiments using 4–6 females for each experiment. Heat maps were normalized to an equal number of *cis* contacts. **e**, $P_c(s)$ curves for wild-type and MCM-loss conditions. **f**, Insulation scores at TAD borders.

Using this approach, we generated MCM-loss and control zygotes, isolated maternal and paternal pronuclei in G1 phase and performed single-nucleus Hi-C (snHi-C) (Fig. 1a). The sparsity of snHi-C data precluded de novo calling of loops (referred to as ‘peaks’), which represent contacts between CTCF-bound loci. Instead, we used 12,000 loop coordinates from mouse embryonic fibroblast Hi-C data that report on cohesin-dependent contacts in zygotes³² (Fig. 1c). Notably, MCM loss resulted in an increase in aggregate peaks and aggregate TADs (referred to as ‘peaks’ and ‘TADs’) in maternal chromatin and an even stronger increase in paternal chromatin (Fig. 1d, Extended Data Fig. 3a–c), which will be focused on hereafter. The increase in peak strengths after MCM loss could reflect higher CTCF occupancy, but this could not explain the barrier effect seen in vitro (see Fig. 4d).

Alternatively, it could reflect increased access of cohesin to CTCF sites, owing to changes in either loop extrusion (potentially caused by barrier loss) or transcription. There were few transcriptomic differences between control and MCM-loss zygotes (Extended Data Fig. 4a, b). We conclude that MCMs hinder the formation of CTCF-anchored loops and TADs largely independently of changes in gene expression.

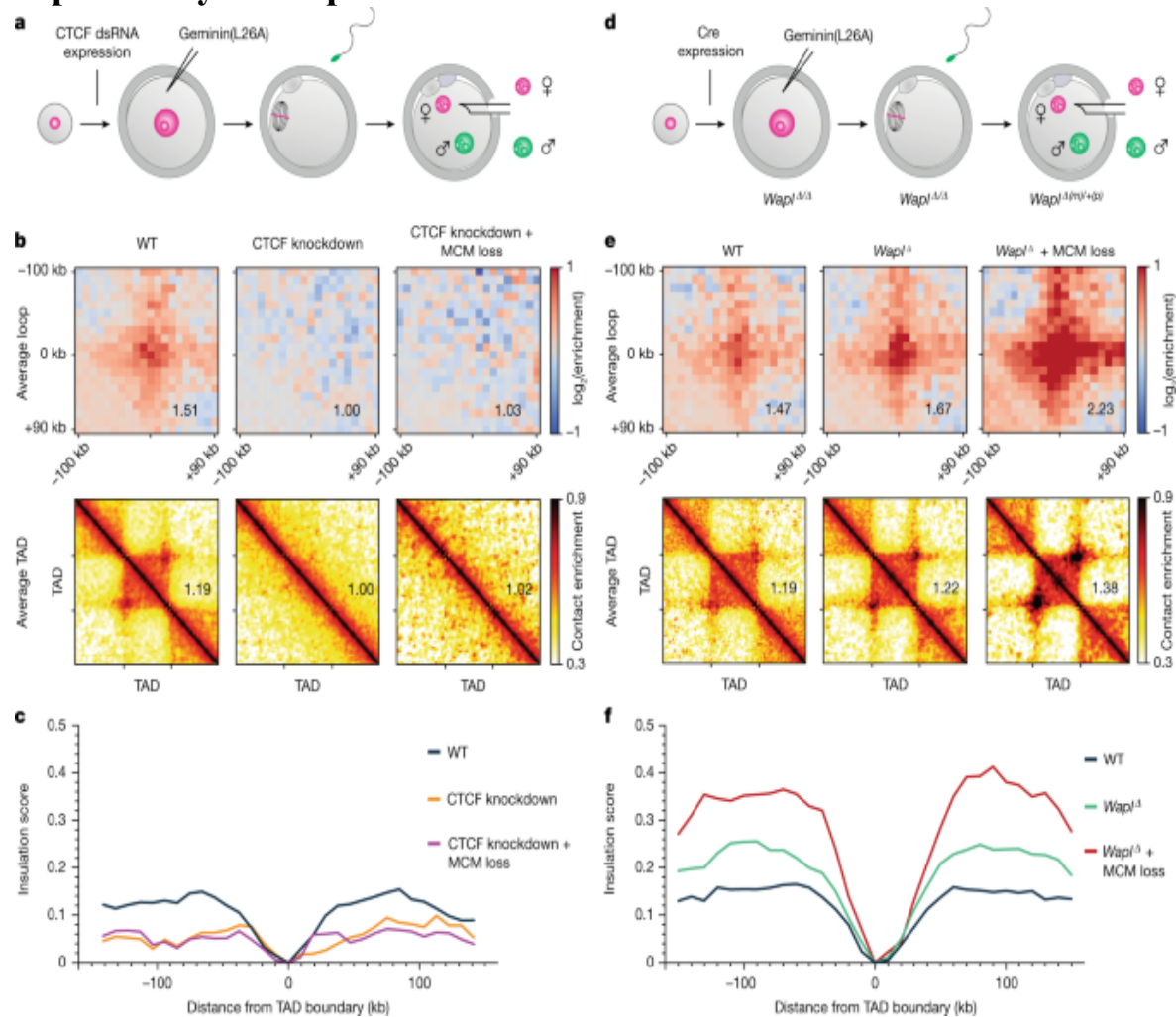
To find out whether cohesin is responsible for the increase in snHi-C peak strength caused by MCM loss, we used a conditional genetic knockout approach based on Cre recombinase under control of the *Zp3* promoter to

delete floxed alleles of the cohesin subunit *Scc1* in oocytes^{27,33}. We expressed geminin(L26A) in *Scc1*^{Δ/Δ} oocytes isolated from *Scc1*^{f/f} (*Tg*)*Zp3*-Cre females and generated maternal *Scc1* knockout zygotes (*Scc1*^{Δ(m)/+(p)}) (Extended Data Fig. 4c). Loops and TADs were undetectable in *Scc1*^{Δ(m)/+(p)} zygotes, as reported previously²⁷, and remained undetectable if MCM loading was prevented (Extended Data Fig. 4d). We conclude that MCMs interfere with cohesin-dependent chromatin structures.

To determine how MCMs affect chromatin organization, we examined the contact probability $P_c(s)$ as a function of genomic distance (s) (Fig. 1e, Extended Data Fig. 3d,e). The position of the ‘shoulder’ on the $P_c(s)$ curve is informative of the mean size of extruded loops²⁷ (Extended Data Fig. 3f). Of note, MCM loss has little effect on the $P_c(s)$ curve below 1 Mb (Fig. 1e); this is reminiscent of CTCF loss^{14,34}, and suggests that the mean size of extruded loops is largely unaffected. However, the effect of CTCF loss on ‘peaks’ is opposite to that of MCM loss. We reasoned that if MCMs impede formation of CTCF-mediated structures, then MCM loss should lead to increased CTCF peaks and increased insulation of TAD boundaries, as observed (Fig. 1f). These effects on chromatin organization are consistent with a mechanism in which MCMs impede loop extrusion by altering loop positioning without considerably changing their sizes.

We tested whether CTCF and MCM together determine the strengths of peaks and TAD boundary insulation. We expressed geminin(L26A) in CTCF-knockdown oocytes isolated from (*Tg*)*Zp3-CTCFdsRNA* females and generated maternal CTCF-knockdown zygotes³⁵ (Fig. 2a, Extended Data Fig. 5a). CTCF knockdown without or with MCM perturbation resulted in a loss of loops and TADs (Fig. 2b, Extended Data Fig. 5b); this shows that CTCF is essential for these structures in zygotes. Knockdown of CTCF caused a weakening of TAD boundary insulation and did not grossly change $P_c(s)$ curves below 1 Mb (Fig. 2c, Extended Data Fig. 5c–e). The lack of TAD organization after knockdown of CTCF, irrespective of MCMs, suggests that MCMs have no instructive function for establishing position-specific boundaries. This is consistent with MCMs being largely located in different positions in different cells³⁶.

Fig. 2: MCMs impede CTCF-anchored loops and function independently of Wapl.



a, CTCF-knockdown oocytes from *(Tg)Zp3-dsCTCF* females were injected with geminin(L26A) mRNA and eggs were fertilized to generate zygotes for snHi-C analysis in G1 phase. **b**, Average loops and TADs for wild-type, CTCF-knockdown and CTCF-knockdown + MCM loss for paternal chromatin in G1. Data are based on n (WT, paternal) = 12, n (CTCF knockdown, paternal) = 8 and n (CTCF knockdown + MCM loss, paternal) = 8 nuclei, from 4 independent experiments using 4–6 females for each genotype. Heat maps were normalized to an equal number of *cis* contacts. **c**, Insulation scores at TAD borders for paternal chromatin. **d**, *Wapl^{Δ/Δ}* oocytes from *Wapl^{f/f} (Tg)Zp3-Cre* females were injected with geminin(L26A) mRNA and eggs were fertilized to generate zygotes for snHi-C analysis in G1 phase. **e**, Average loops and TADs for control (wild type), *Wapl^{Δ/Δ}*, and *Wapl^{Δ/Δ}* + MCM loss genotypes.

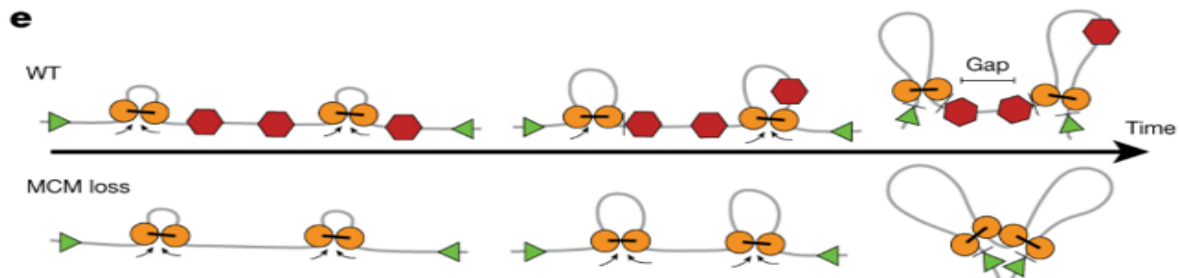
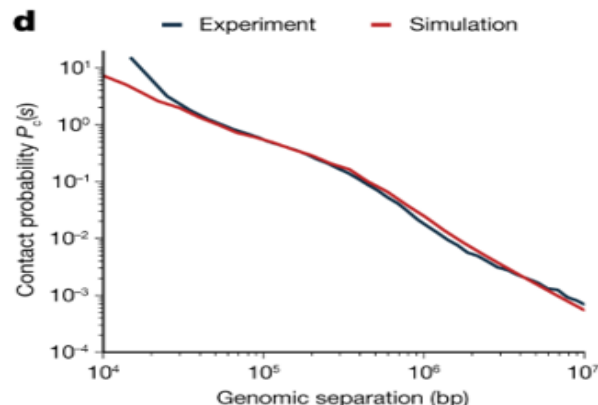
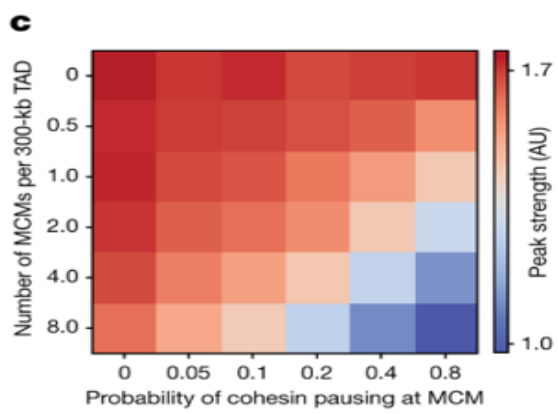
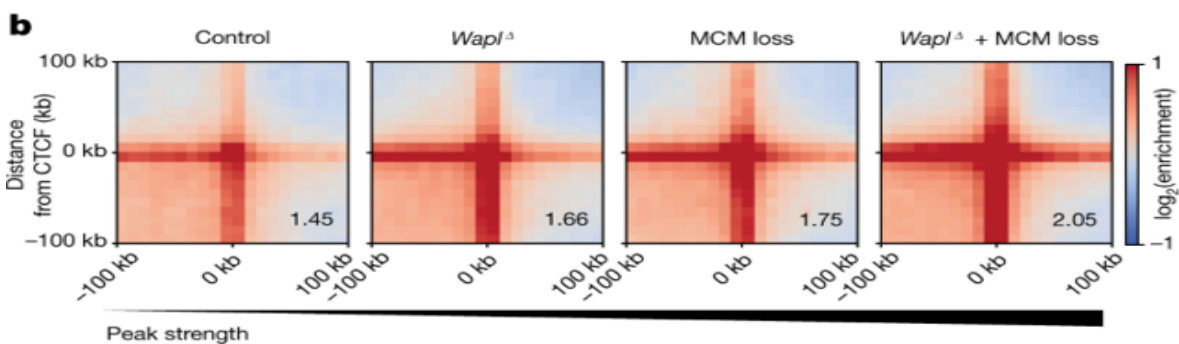
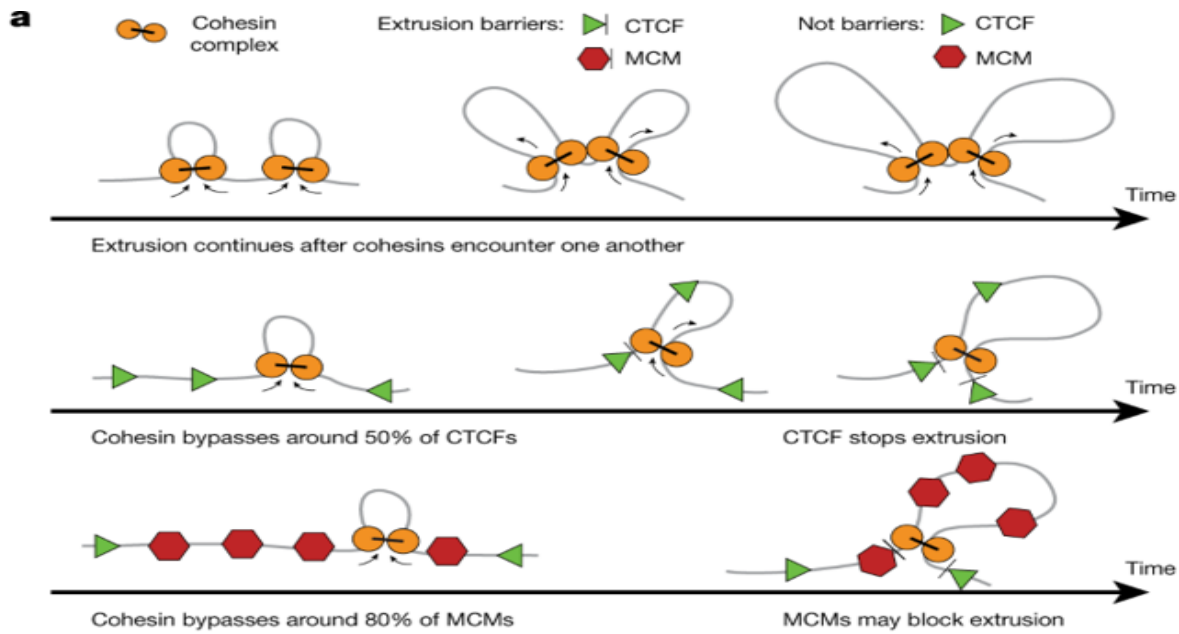
type), *Wapl*^Δ and *Wapl*^Δ + MCM loss for paternal chromatin in G1. Data shown are based on n (WT, paternal) = 20, n (*Wapl*^Δ, paternal) = 11, n (*Wapl*^Δ + MCM loss, paternal) = 9 nuclei, from 4 independent experiments using 4–6 females for each genotype. Control samples are wild type (this study) pooled with *Wapl*^{fl} samples (published previously²⁷). Heat maps were normalized to an equal number of *cis* contacts. **f**, Insulation scores at TAD borders for paternal chromatin.

We considered an alternative possibility that MCMs affect loops by functioning with Wapl in releasing cohesin from chromatin. This is based on the similar effects on Hi-C peak and TAD strengths after *Wapl* knockout and MCM loss^{27,34,37} (Fig. 2e). If Wapl and MCMs function together, then their co-depletion would be expected to resemble individual depletions. If they function independently, then co-depletion could have synergistic effects. To distinguish between these, we expressed geminin(L26A) in *Wapl*^{Δ/Δ} oocytes isolated from *Wapl*^{fl/fl} (*Tg*)*Zp3*-Cre females and generated maternal *Wapl* knockout zygotes³² (*Wapl*^{Δ(m)/+(p)}) (Fig. 2d). Combined MCM loss and *Wapl* knockout strongly increased peak and TAD strengths over the individual conditions (Fig. 2e, Extended Data Fig. 6a–d), suggesting that they function through separate mechanisms. The combined loss increased TAD boundary insulation, suggesting that MCMs restrict loop extrusion also when cohesin residence time is increased (Fig. 2f, Extended Data Fig. 6b).

MCMs are semi-permeable barriers

We introduced MCMs as randomly located permeable extrusion barriers into polymer models of loop extrusion (Fig. 3a). Polymer simulations identified parameters, including the permeability of MCMs, such that the peak strengths and $P_c(s)$ curves of paternal chromatin can be quantitatively reproduced (Fig. 3b, d, Extended Data Fig. 6e–h, Supplementary Figs. 2–5). In the model, cohesin extrudes loops and is stopped at CTCF sites (around 50% of encounters)³⁸ and MCMs (around 20% of encounters, for an estimated density of 1 MCM per 75 kb) (Fig. 3a). If MCM density is lower in zygotes, then blocking will occur more frequently (more than 20%) (Fig. 3c). The predicted semi-permeability of MCMs could explain how CTCF-anchored loops are generated in the presence of MCMs in G1 phase.

Fig. 3: Simulation model of MCMs as a random barrier to cohesin loop extrusion.



a, A quantitative model for loop extrusion by cohesin and interactions with CTCF and MCMs. Cohesin (yellow) extrudes loops. On encountering barriers such as CTCF sites (green triangles), MCMs (red hexagons) or other cohesins, extrusion can be blocked. Cohesins may bypass some CTCFs and MCMs, but not others; the choice to bypass an MCM or CTCF site is stochastic and varies in time. **b–d**, For paternal chromatin simulations, we assume that CTCF stalls cohesin around 45% of the time, as measured in mouse embryonic stem cells¹², and that MCMs stall cohesin 20% of the time. **b**, Peak strengths for simulated paternal chromatin under various perturbations for TADs of 300 kb average length. **c**, Matrix of peak strengths in the wild type, showing a linear trade-off between MCM density and its ability to pause cohesin. AU, arbitrary units. **d**, The simulated contact probability decay curve $P_c(s)$ for the MCM-loss condition is well matched with experimental data. **e**, Model summarizing the finding that chromatin-bound MCMs can function as barriers for loop extrusion in G1 phase.

Our model provides a rationale for the seemingly contradictory ability of MCM to reduce CTCF–CTCF peak strength without strongly affecting the mean size of extruded loops. A peak emerges if cohesin extrudes all chromatin between a pair of CTCFs into loops. A random barrier prevents cohesin from extruding all chromatin between CTCFs, leaving an unextruded gap³⁹ (Fig. 3e). The effect of random barriers on the average loop size is, however, marginal (less than 15%) if barriers are sufficiently permeable or sparse (one per TAD of around 300 kb). This is an unexpected effect of random barriers on features of chromosome organization.

MCMs affect transcription and loops

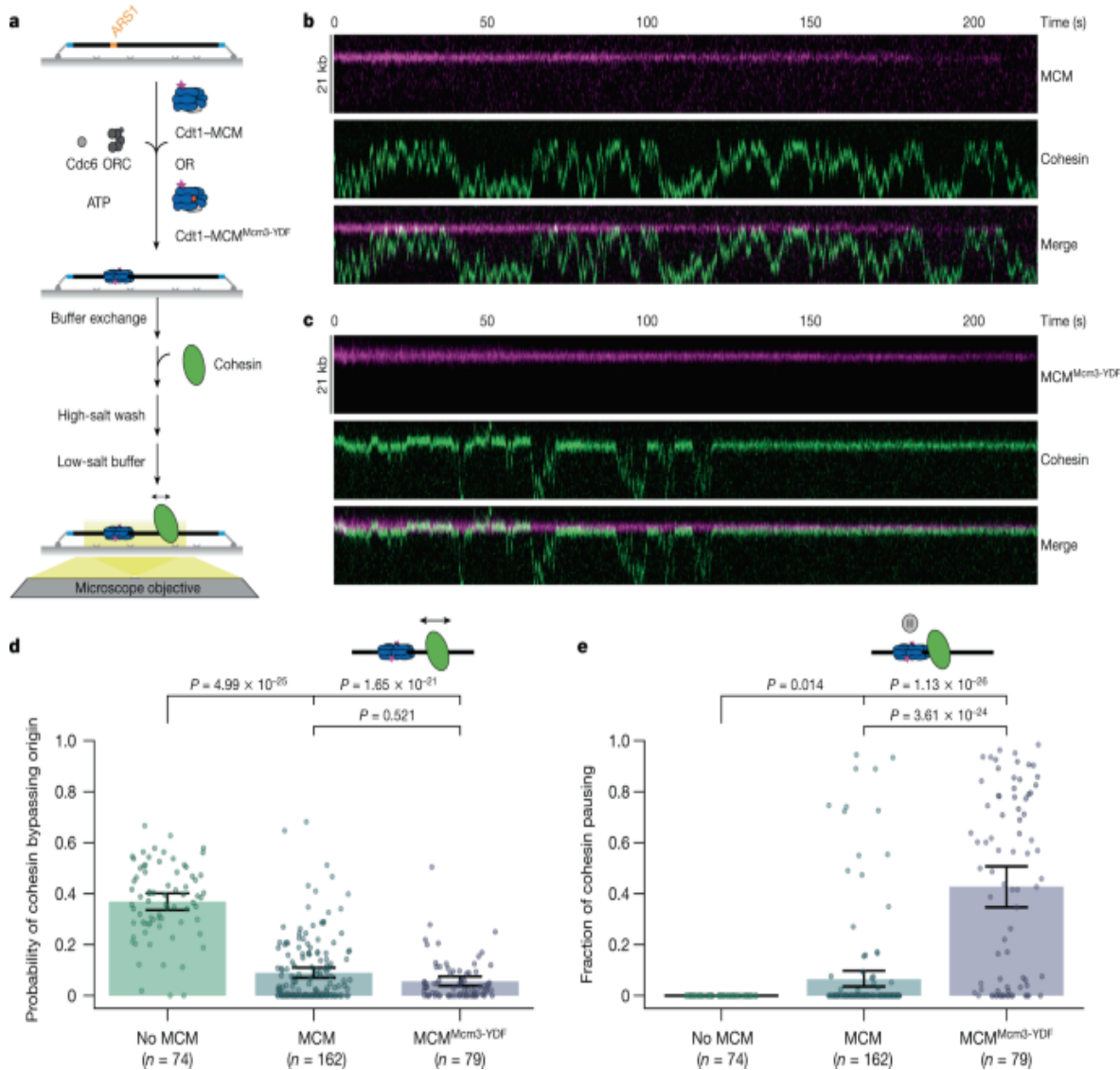
As these findings were obtained in zygotes, we tested whether MCMs also impede loop extrusion in somatic cells. To directly degrade MCMs, we treated G1-synchronized HCT116 cells carrying auxin-inducible degron MCM2-mAID alleles with dimethyl sulfoxide (DMSO) or auxin⁴⁰ (Extended Data Figs. 7a–g, 8a–f). Treatment with auxin reduced chromatin-bound MCM2 and MCM4 without grossly affecting the abundance of CTCF and cohesin (Extended Data Figs. 7c, 8c). Acute MCM degradation resulted in the differential expression of 229 genes (Extended Data Fig. 8l, m), which is comparable to the effects of acute CTCF degradation¹⁴. Hi-C data showed

a moderate increase in aggregate peak strengths in MCM-depleted versus control cells (Extended Data Fig. 7d,e). To confirm this result using another method, we performed Micro-C and found that MCM depletion results in a moderate but genome-wide and significant ($P = 1.87 \times 10^{-70}$) increase in the peak strength (Extended Data Fig. 8d,g–i). Notably, de novo peak calling identified a greater number of loops in MCM-depleted cells, consistent with loop extrusion reaching CTCF sites more frequently (Extended Data Fig. 8j,k). The effects show the same directionality but are much more subtle than in zygotes and cannot be explained solely by RNA polymerase in somatic cells (Extended Data Fig. 8n,o). On the basis of the consistent increases in loop strengths and numbers after MCM degradation, we conclude that MCMs impede the formation of CTCF-anchored loops in somatic cells.

MCMs block cohesin translocation

The most parsimonious interpretation of the effects of MCM loss on genome architecture is that MCMs interfere with loop extrusion by forming randomly located barriers. To directly test this, we established an MCM ‘roadblock assay’ for passive translocation of cohesin using total internal reflection fluorescence microscopy that detects real-time cohesin–MCM interactions at the single-molecule level. Origin licensing was reconstituted from purified components in a stepwise manner on origin-containing DNA molecules⁴³ (Fig. 4a). Loading of yeast MCM and double-hexamer formation—a hallmark of proper origin licensing—was observed in the presence of ORC, Cdc6 and Cdt1 (ref. 41) (Extended Data Fig. 9a). Cohesin was introduced in low-salt conditions, followed by a high-salt wash to select for fully loaded MCMs^{41,42,43}. To mimic intracellular conditions, experiments were imaged in physiological salt conditions, promoting cohesin translocation on fast timescales³⁸ (Extended Data Fig. 9b, Supplementary Video 1). The cohesin diffusion coefficient remained unchanged in the presence of MCMs (Extended Data Fig. 9c).

Fig. 4: MCMs are barriers for cohesin translocation in vitro.



a, Principle of a single-molecule cohesin translocation assay on licensed DNA. MCM is loaded onto DNA by the licensing factors ORC, Cdc6 and Cdt1, followed by cohesin. A high-salt wash removes licensing factors and intermediates from DNA. Cohesin translocation is visualized at physiological salt conditions (0.15 M NaCl) without free protein and buffer flow. **b, c**, Representative kymographs of translocating cohesin on licensed DNA. Origin-bound MCM (**b**) and MCM^{Mcm3-YDF} (**c**) are efficient barriers for cohesin translocation. **d**, Probability of translocating cohesin bypassing the origin in the absence or in the presence of MCM or MCM^{Mcm3-YDF}, calculated from 74, 162 or 79 molecules with 12,175, 15,348 or 9,455 visualized encounters, respectively. **e**, Cohesin translocation pauses at MCM in a YDF-disordered-region-dependent manner. Fraction of cohesin pausing

of the total observation time in the absence or in the presence of MCM or MCM^{Mcm3-YDF}. Data in **d**, **e** are depicted as mean within a 95% confidence interval (generated by bootstrapping). *P* values were determined by Kruskal–Wallis test followed by Dunn’s post-hoc test.

Direct visualization of cohesin encounters with MCMs revealed constrained cohesin translocation with a fourfold reduction in origin passage (Fig. [4b, d](#), Extended Data Fig. [9d–g](#), Supplementary Videos [2, 3](#)). Similar results were obtained at higher salt concentrations (Extended Data Figs. [9c, 10a–f](#), Supplementary Videos [4–6](#)). A subpopulation of cohesin molecules were unable to pass origins even once during the 220-s imaging window (67/162; Fig. [4b](#), Extended Data Fig. [9d](#)). By contrast, origin passage was unimpeded in the absence of MCMs (72/74; Extended Data Fig. [9b](#)). The observed permeability of MCMs is lower than that predicted by simulations, which could be a result of different conditions from loop extrusion *in vivo*. It will be important in future studies to test whether MCMs halt loop extrusion, which requires a combined assay that has thus far not been established owing to different reaction conditions *in vitro*. We conclude that MCMs are physical barriers to cohesin translocation and may occasionally be bypassed.

Finally, we tested whether mammalian MCMs are stronger barriers than yeast MCMs to cohesin translocation. Unlike yeast Mcm3, human MCM3 contains a 19-amino-acid disordered region containing a YDF motif that is sufficient to bind STAG2–SCC1 cohesin *in vitro*^{[44](#)}. The same motif mediates an interaction between CTCF and STAG2–SCC1 (ref. [44](#)). As there is no established human origin licensing assay, we modified the yeast assay to load a chimeric MCM complex containing a ‘humanized’ MCM3 subunit (MCM-YDF). We found that cohesin bypasses MCM-YDF slightly less frequently compared to MCM, suggesting that its barrier strength is comparable to that of yeast MCMs (Fig. [4d](#)). Notably, we observed frequent pausing of cohesin upon encountering MCM-YDF (Fig. [4c](#), Extended Data Fig. [9h, i](#)), with pauses accounting for 43% of the total observation time on average (Fig. [4e](#)). These pauses were much less frequent (6.4%) in the presence of MCMs lacking YDF, which suggests that pausing reflects a molecular docking of cohesin to the YDF region.

Discussion

We have identified MCM complexes as barriers for loop extrusion on the basis of in vivo, in silico and in vitro data. MCMs are members of a new class of randomly positioned and cell-cycle-phase-specific barriers that impede the formation of CTCF-anchored loops and TADs. A key question is which features determine whether a protein impedes loop extrusion.

Nanoparticles larger than the diameter of SMC complexes can be bypassed by extruding SMC complexes⁴⁵, suggesting that size is not the sole determinant. Unlike those permeable roadblocks, MCMs have two distinguishing features that can promote barrier function. MCMs bind DNA in a topological manner. Although the mechanism of bypassing obstacles is not known, it is conceivable that a topological engagement of proteins around DNA could interfere with cohesin binding to DNA to ‘swing over’ a protein⁴⁶. Consistent with this, cohesin that topologically entraps sister chromatids restricts loop extrusion mediated by other cohesin complexes in oocytes^{32,47}. In addition, the YDF disordered region alters the outcome of cohesin–MCM collisions from blocking to pausing, which suggests that MCMs are active chemical barriers with binding sites rather than passive physical barriers.

The finding that MCMs are barriers to loop extrusion provides a different perspective on the body of knowledge on MCMs and cohesin loading. MCMs recruit cohesin to pre-replication complexes in *Xenopus* extracts^{48,49} and promote cohesin loading during DNA replication in human cells⁵⁰. These studies proposed that MCMs have a role in loading cohesin; that is, capturing cohesin from nucleoplasm and converting it from a freely diffusive into a DNA-bound state. Our work raises the possibility that cohesin could arrive at an MCM site by loop extrusion, where it is either blocked, passes by or pauses. Extruding cohesin pausing at MCMs could potentially be converted into a topologically binding complex that establishes cohesion after passage of the DNA replication fork (Extended Data Fig. 10g). A similar conversion of DNA binding mode has recently been proposed at CTCF sites⁵¹. Our idea distinguishes cohesin loading by MCMs from the arrival of cohesin at MCM sites by loop extrusion.

Given the evolutionary conservation of MCMs, it is possible that replicative helicases might be ancestral barriers in species that lack CTCF-anchored loops, such as *Drosophila*, in which the establishment of TADs during

embryonic development coincides with a switch in replication origin usage⁵². Finally, our data suggest that the ‘MCM paradox’ has consequences for chromatin organization and gene expression, which might have relevance for human pathologies such as Meier–Gorlin syndrome that are linked to mutations in the MCM loading pathway⁵³.

Methods

Animals

The mice used in this work were bred and maintained in agreement with the authorizing committee according to the Austrian Animal Welfare law and the guidelines of the International Guiding Principles for Biomedical Research Involving Animals (CIOMS, the Council for International Organizations of Medical Sciences). Mice were housed in individually ventilated cages under a 14-h light–10-h dark cycle at an ambient temperature of $22\text{ }^{\circ}\text{C} \pm 1\text{ }^{\circ}\text{C}$ and humidity of $55\% \pm 5\%$ with continuous access to food and water. Mice were housed in groups (maximum four males per cage and maximum five females per cage). All mice were bred in the IMBA animal facility. Wild-type, *Scc1*^{f/f} and *Scc1*^{Myc/+} mice were bred on a mixed background (B6, 129, Sv). *Wapl*^{f/f} and *Zp3-dsCTCF* mice were bred on a primarily C57BL/6J background. *Zp3-dsCTCF* mice were maintained by breeding *Zp3-dsCTCF* males with C57BL/6J females. Experimental *Scc1*^{f/f} and *Wapl*^{f/f} mice were obtained by mating of homozygous floxed females with homozygous floxed males carrying *Tg(Zp3Cre)*⁵⁴. Experimental *Scc1*^{Myc/+} mice were obtained by intercrossing heterozygous *Scc1*^{Myc/+} mice. Experimental *Zp3-dsCTCF* mice were maintained by breeding *Zp3-dsCTCF* males with C57BL/6J females.

Collection and in vitro culture of mouse oocytes

Ovaries were dissected from sexually mature female mice, which were euthanized by cervical dislocation. Fully grown germinal vesicle (GV) oocytes from 2–5-month-old females were isolated by physical disaggregation of ovaries with hypodermic needles. GV oocytes were cultured in M2 medium supplemented with 0.2 mM of the phosphodiesterase

inhibitor 3-isobutyl-1-methylxanthine (IBMX, Sigma-Aldrich) at 37 °C. Mature oocytes were selected according to appearance (size, central nucleus, smooth zona pellucida) and cultured in M16 medium supplemented with IBMX in an incubator at 37 °C and 5% CO₂. Oocytes were cultivated in approximately 40-μl drops covered with paraffin oil (NidOil).

Microinjection

GV oocytes were microinjected with in-vitro-transcribed mRNA dissolved in RNase-free water (mMessage mMachine T3 kit, Ambion). The following mRNA concentrations were injected: 2.3 pmol hGeminin(L26A) and 0.2 pmol GFP. Microinjection was performed in approximately 20-μl drops of M2 (0.2 mM IBMX) covered with mineral oil (Sigma-Aldrich) using a Pneumatic PicoPump (World Precision Instruments) and hydraulic micromanipulator (Narishige) mounted onto a Zeiss Axiovert 200 microscope equipped with a 10×/0.3 EC plan-neofluar and 40×/0.6 LD Apochromat objective. Injected oocytes were cultured for 2 h and then released from IBMX inhibition by washing in M16 to resume meiosis.

In vitro maturation and in vitro fertilization

Oocyte collection and culturing was performed as described above but M2 and M16 media were supplemented with 20% FBS (Gibco) and 6 mg ml⁻¹ fetuin (Sigma-Aldrich). After microinjection and IBMX release as described above, GV oocytes were subsequently incubated at 37 °C and in low-oxygen conditions (5% CO₂, 5% O₂, 90% N₂) to initiate in vitro maturation to metaphase II (MII) eggs. Next, MII eggs were in vitro fertilized 10.5–12 h after release of IBMX. Sperm was isolated from the cauda epididymis and vas deferens of stud males (2–5 months old) and capacitated in fertilization medium (Cook Austria GmbH) in a tilted cell culture dish for at least 30 min before incubation with MII eggs. For in vitro fertilization of wild-type, *Scc1^{f/f}* (*Tg*)Zp3-Cre and Zp3-dsCTCF oocytes, sperm was obtained from B6CBAF1 males, whereas sperm of C57BL/6J males was used for in vitro fertilization of *Wapl^{f/f}* (*Tg*)Zp3-Cre oocytes. Zygotes were scored by the formation of visible pronuclei at 5 h after fertilization.

In situ fixation, immunofluorescence staining and imaging

Zygotes were pulsed with 1 mM 5-ethynyl-2'-deoxyuridine (EdU) (Invitrogen) before in situ fixation to check the time frame of G1 phase. To check for DNA replication, zygotes were fixed in G2 after continuous incubation in the presence of EdU. Oocytes and zygotes were stripped from their zona pellucida by using acidic Tyrode's solution (Sigma-Aldrich) before in situ fixation in 4% paraformaldehyde (PFA) (in phosphate-buffered saline (PBS)) for 30 min at room temperature, followed by permeabilization in 0.2% Triton X-100 in PBS (PBSTX) for 30 min at room temperature. EdU-pulsed cells were processed according to the manual of the Click-iT EdU Alexa Fluor 647 imaging kit (Invitrogen). Blocking was performed using 10% goat serum (Dako) in PBSTX for 1 h at room temperature or at 4 °C overnight. Cells were incubated with primary antibodies for 2.5 h at room temperature or at 4 °C overnight. The following primary antibodies were used: anti-MCM2 (1:500; BD Transduction Laboratories, 610701), anti-CTCF (1:250, Peters Laboratory, A992), anti-MYC (1:500, Millipore, 05-724). After washing in blocking solution three times for at least 20 min, cells were incubated with goat anti-mouse Alexa Fluor 488 (1:500, Invitrogen, A11029), donkey anti-rabbit Alexa Fluor 568 (1:500, Invitrogen, A10042) or goat anti-mouse Alexa Fluor 647 (1:500, Invitrogen, A-21235) secondary antibodies for 1 h at room temperature. The excess of secondary antibody was removed by washing three times in 0.2% PBSTX for at least 20 min, which was followed by a short PBS wash and submerging for 20 min in Vectashield with DAPI (Vector Labs). Cells were mounted in Vectashield with DAPI using imaging spacers (Sigma-Aldrich) to preserve three-dimensional integrity. Detection of chromatin-bound MCM2 required pre-extraction before fixation and was performed as described previously³³. In short, the zona pellucida was not removed and zygotes were incubated in ice-cold extraction buffer (50 mM NaCl, 3 mM MgCl₂, 300 mM sucrose, 25 mM HEPES, 0.5% Triton X-100) for 7 min on ice, followed by three short washes in ice-cold extraction buffer without Triton X-100. In situ fixation and immunofluorescence was performed as described above. To avoid zona pellucida collapse, cells were submerged in increasing Vectashield concentrations before final mounting. Image acquisition was performed on a Zeiss LSM780 or LSM880 confocal microscope using a plan-apochromat 63×/1.4 oil immersion objective. Image analysis was performed in

Fiji/ImageJ. Mean intensity was measured within a defined nuclear area of each zygote. To measure nuclear signal over background, images were first deconvoluted by Huygens Professional (SVI) followed by segmentation into nuclei and surrounding cytoplasm using a custom ImageJ macro.

Cell culture and synchronization

HCT116 cells were cultured as previously described⁴⁰. In brief, cells were cultured in McCoy's 5A medium (Thermo Fisher Scientific) supplemented with 10% FBS (Gibco), 2 mM l-glutamine (Invitrogen) and 10% penicillin–streptomycin solution (Sigma-Aldrich). Cells were grown in an incubator at 37 °C with 5% CO₂. MCM2–mAID degradation was induced by addition of 500 µM 3-indoleacetic acid (Sigma-Aldrich) for 6 h. To synchronize cells in G1 for Hi-C analysis, a 2 mM thymidine arrest was followed by release into fresh medium for 6 h. Subsequently, nocodazole was added for 5 h, followed by shake-off of prometaphase cells and release in fresh medium for 4 h. Cells were fixed for Hi-C, microscopy and fluorescence-activated cell sorting (FACS). Cell-cycle profiling was performed using propidium iodide staining. For G1 FACS, cells were synchronized with a double-thymidine arrest–release followed by release into fresh medium for 12 h. Four hours before sorting, Hoechst 33342 (Sigma) was added to the medium at a concentration of 0.2 µg ml⁻¹. For the triptolide (Trp) experiment, 4 h before sorting, triptolide (Sigma) at 1 µM was added. Live-cell sorting was performed with the BD FACS Aria II flow cytometry instrument. The following gating strategy was used: gating for cells with SSC-A versus FSC-A, excluding doublets with FSC-H versus FSC-A, selecting Hoechst 33342-stained cells with HOECHST-W versus HOECHST-A gating and Count versus HOECHST-A to select to select the G1 population. To avoid S-phase cell contamination, only cells in the left part of the G1 peak were collected (red dashed box in Extended Data Fig. 8) (see [Supplementary Fig. 6](#) for the gating strategy).

Chromatin fractionation and protein detection

Fractionation was performed as previous described³⁴. In brief, cells were extracted in a buffer consisting of 20 mM Tris–HCl (pH 7.5), 100 mM NaCl, 5 mM MgCl₂, 2 mM NaF, 10% glycerol, 0.2% NP40, 20 mM β-

glycerophosphate, 0.5 mM DTT and protease inhibitor cocktail (Complete EDTA-free, Roche). Chromatin pellets and supernatant were separated and collected by centrifugation at 1,700g for 5 min. The chromatin pellets were washed three times with the same buffer. Protein concentration was measured using a Bradford assay. Proteins were separated through SDS-PAGE on a Bolt 4–12% Bis-Tris Plus Gel (Invitrogen) and transferred to a nitrocellulose membrane. After overnight blocking with 5% skimmed milk in TBS-T at 4 °C, the membrane was incubated with primary antibodies for 2.5 h at room temperature. The following antibodies were used: anti-MCM2 (1:5,000; BD Transduction Laboratories, 610701), anti-MCM4 (1:5,000; Abcam, ab4459), anti-H3 (1:2,000; Cell Signaling, 97155), anti-GAPDH(1:2,500; Millipore, MAB374), anti-CTCF (1:1,000, Peters Laboratory, A992), anti-PCNA (1:500, Santa Cruz, PC10), anti-SCC1 (1:1,000, Millipore, 05-908) and anti-Pol II 8WG16 (1:500, Santa Cruz, sc-56767). Goat anti-mouse immunoglobulins–HRP (1:500, Dako, P0447) and goat anti-rabbit immunoglobulins–HRP (1:500, Dako, P0448) secondary antibodies were used to detect primary antibodies. Detection was performed using Immobilon Forte Western HRP Substrate (Merck) with a ChemiDoc imaging system (Bio-Rad).

snHi-C

snHi-C was carried out as previously described^{27,28,32,47}. Pronuclei of wild-type, *Sccl^{Δ/Δ}*, *Wapl^{Δ/Δ}* and *Zp3-dsCTCF* zygotes were fixed around 1.5 h after visualization of pronuclei (corresponding to 6–6.5 h after fertilization) and therefore are expected to be in G1 phase of the cell cycle. No blinding or randomization was used for handling of the cells. In brief, isolated pronuclei were fixed in 2% PFA for 15 min, transferred to microwell plates (Sigma, M0815) and then lysed on ice in lysis buffer (10 mM Tris-HCl pH 8.0, 10 mM NaCl, 0.5% (v/v) NP-40 substitute (Sigma), 1% (v/v) Triton X-100 (Sigma), 1× Halt Protease Inhibitor Cocktail (Thermo Fisher Scientific)) for at least 30 min. After a brief PBS wash, the pronuclei were incubated in 1× NEB3 buffer (New England Biolabs) with 0.6% SDS at 37 °C for 2 h with shaking in a humidified atmosphere. The pronuclei were then washed once in 1× DpnII buffer (New England Biolabs) with 1× bovine serum albumin (BSA) (New England Biolabs) and further digested overnight with 5 U DpnII (New England Biolabs) at 37 °C in a humidified atmosphere. After a

brief PBS wash and a wash through 1× ligation buffer (Thermo Fisher Scientific), the pronuclei were then ligated with 5 U T4 ligase (Thermo Fisher Scientific) at 16 °C for 4.5 h with rotation (50 rpm), followed by 30 min ligation at room temperature. Next, whole-genome amplification was performed using the illustra GenomiPhi V2 DNA amplification kit (GE Healthcare). In brief, the pronuclei were transferred to 0.2-ml PCR tubes in 3 µl sample buffer covered with mineral oil (Sigma-Aldrich) and were de-cross-linked at 65 °C overnight. Then, the pronuclei were lysed by adding 1.5 µl lysis solution (600 mM KOH, 10 mM EDTA, 100 mM DTT) and incubated for 10 min at 30 °C, followed by neutralization with the addition of 1.5 µl neutralization solution (4 vol 1 M Tris HCl, pH 8.0; 1 vol 3 M HCl). Whole-genome amplification was carried out by addition of 4 µl sample buffer, 9 µl reaction buffer and 1 µl enzyme mixture and incubation at 30 °C for 4 h followed by heat activation at 65 °C for 10 min. High-molecular-weight DNA was purified using AMPure XP beads (Beckman Coulter, 1.8:1.0 beads:DNA ratio) and 1 µg DNA was sonicated to approximately 300–1,300-bp fragments using the E220 Focused-Ultrasonicator (Covaris). The sonicated DNA was purified with a PCR purification kit (Qiagen) and used to prepare Illumina libraries with the NEB Next Ultra Library Prep kit (Illumina). Libraries were sequenced on the HiSeq 2500 v4 with 125-bp paired-end reads (at the VBCF NGS unit) or on the NextSeq high-output lane with 75-bp paired-end reads (at the MPIB NGS core facility).

snHi-C data analysis

snHi-C data were processed and analysed similarly to a previous report²⁸ and as previously described in^{27,32,47}. In brief, the reads of each sample were mapped to the mm9 genome with bwa and processed by the pairtools framework (<https://pairtools.readthedocs.io/en/latest/>) into pairs files. These data were subsequently converted into COOL files by the cooler package and used a container for Hi-C contact maps.

Loops were analysed by summing up snHi-C contact frequencies for loop coordinates of over 12,000 loops identified using the Hi-C data from wild-type mouse embryonic fibroblasts published previously³². We removed the effect of distance dependence by averaging 20 × 20 matrices surrounding the

loops and dividing the final result by similarly averaged control matrices. Control matrices were obtained by averaging 20×20 matrices centred on the locations of randomly shifted positions of known loops (shifts ranged from 100 to 1,100 kb with 100 shifts for each loop). For display and visual consistency with the loop strength quantification, we set the backgrounds levels of interaction to 1. The background is defined as the top left 6×6 and the bottom right 6×6 submatrices. To quantify the loop strength, the average signal in the middle 6×6 submatrix is divided by the average signal in the top left and bottom right (at the same distance from the main diagonal) 6×6 submatrices. Weighted statistics were calculated using the weights package in R (<https://CRAN.R-project.org/package=weights>).

For average TAD analysis, we used published TAD coordinates for the CH12-LX mouse cell line³. We averaged Hi-C maps of all TADs and their neighbouring regions, chosen to be of the same length as the TAD, after rescaling each TAD to a 90×90 matrix. For visualization, the contact probability of these matrices was rescaled to follow a shallow power law with distance (-0.25 scaling). TAD strength was quantified using contact probability normalized snHi-C data. In Python notation, if M is the 90×90 TAD numpy array (where numpy is np) and $L = 90$ is the length of the matrix, then $\text{TAD_strength} = \text{box1}/\text{box2}$, where $\text{box1} = 0.5 * \text{np.sum}(M[0:L//3, L//3:2*L//3]) + 0.5 * \text{np.sum}(M[L//3:2*L//3, 2*L//3:L])$; and $\text{box2} = \text{np.sum}(M[L//3:2*L//3, L//3:2*L//3])$.

To calculate the insulation score, we computed the sum of read counts within a sliding 40-kb-by-40-kb diamond. The diamond was positioned such that the ‘tip’ touched the main axis of the snHi-C map corresponding to a ‘self-interaction’. As snHi-C maps are not iteratively corrected, we normalized all insulation profiles by the score of the minimum insulation and then subtracted 1. This way, the insulation/domain boundary is at 0 and has a minimum of 0.

Contact probability $P_c(s)$ curves were computed from 10-kb binned snHi-C data. We divided the linear genomic separations into logarithmic bins with a factor of 1.3. Data within these log-spaced bins (at distance, s) were averaged to produce the value of $P_c(s)$. Both $P_c(s)$ curves and their log-space slopes are shown following a Gaussian smoothing (using the

`scipy.ndimage.filters.gaussian_smoothing1d` function with radius 0.8). Both the y axis (that is, $\log(P_c(s))$) and the x axis (that is, $\log[s]$) were smoothed. The average loop size was determined by studying the derivative of the $P_c(s)$ curve in log–log space; that is, the slope of $\log(P_c(s))$. The location of the maximum of the derivative curve (that is, the position of the smallest slope) closely matches the average length of extruded loops.

Hi-C library preparation and sequencing

Hi-C was performed largely as described previously³ with minor modifications. In brief, around 5×10^6 HCT116 cells were cross-linked in 1% formaldehyde for 10 min at room temperature, snap-frozen and stored at -80°C . After permeabilization in lysis buffer (0.2% Igepal, 10 mM Tris-HCl pH 8.0, 10 mM NaCl, 1× Halt Protease inhibitor cocktail) nuclei were isolated in 0.3% SDS in NEBuffer 3 at 62°C for 10 min. SDS was quenched with 1% Triton X-100 at 37°C for 1 h, then the nuclei were pelleted and resuspended in 250 μl DpnII buffer with 600 U DpnII (New England Biolabs) at 37°C . After overnight digestion, 200 U DpnII was added followed by 2 h more incubation. Then, nuclei were spun down and resuspended in fill-in mix (biotin-14-dATP (Thermo Fisher Scientific), dCTP, dGTP and dTTP (Thermo Fisher Scientific), Klenow Polymerase (NEB), 1× NEB 2 buffer) for 1.5 h at 37°C with rotation. After ligation at room temperature for 4 h with T4 ligase (NEB), the nuclei were pelleted, resuspended in 200 μl H_2O and digested with proteinase K for 30 min at 55°C in the presence of 1% SDS. NaCl was added to a final concentration of 1.85 M before cross-links were reversed at 65°C overnight. After ethanol precipitation and a 70%–80% ethanol wash, DNA was resuspended in 10 mM Tris EDTA, transferred to a Covaris microtube (Covaris) and sheared to approximately 300–1,300-bp fragments on the E220 Focused-Ultrasonicator (Covaris). DNA was then bound to Dynabeads MyOne Streptavidin C1 beads (Thermo Fisher Scientific) for biotin pull-down. Beads were resuspended in H_2O used for library preparation with the NEBNext Ultra II Library Prep kit for Illumina (NEB). Beads were then washed four times using Tween wash buffer (5 mM Tris-HCl, 1 M NaCl, 0.5 mM EDTA, 0.05% Tween20) and DNA was eluted using 95% formamide, 10 mM EDTA at 65°C for 2 min. After precipitation, DNA was washed with 70–80% ethanol

and resuspended in H₂O. The finished libraries were sequenced on the NovaSeq 6000 system (Illumina) with 100-bp paired-end reads (at the VBCF NGS unit) or on the NextSeq high-output lane (Illumina) with 75-bp paired-end reads (at the MPIB NGS core facility).

Micro-C library preparation and sequencing

The Micro-C libraries were prepared using the Dovetail Micro-C Kit following the manufacturer's protocol. In brief, the chromatin was fixed with disuccinimidyl glutarate (DSG) and formaldehyde in the nucleus. The cross-linked chromatin was then digested *in situ* using micrococcal nuclease (MNase). After digestion, the cells were lysed with SDS to extract the chromatin fragments and the chromatin fragments were bound to chromatin capture beads. Next, the chromatin ends were repaired and ligated to a biotinylated bridge adapter followed by proximity ligation of adapter-containing ends. After proximity ligation, the cross-links were reversed, the associated proteins were degraded and the purified DNA was converted into a sequencing library using Illumina-compatible adaptors. Biotinylated molecules were pulled down on streptavidin beads before PCR amplification. The library was sequenced on the NextSeq high-output lane (Illumina) with 75-bp paired-end reads (at the MPIB NGS core facility).

Hi-C and Micro-C data analysis

Hi-C and Micro-C data processing was performed using distiller—a nextflow-based pipeline (<https://github.com/open2c/distiller-nf>)⁵⁵. Reads were mapped to the hg38 reference genome with default settings except dedup/max_mismatch_bp=0. Multiresolution cooler files⁵⁶ generated by distiller were used for visualization in HiGlass⁵⁷ and in the downstream analyses.

For downstream analysis, we used quaich (<https://github.com/open2c/quaich>), a new snakemake pipeline for Hi-C postprocessing. It uses cooltools (<https://github.com/open2c/cooltools>)⁵⁸, chromosight⁵⁹ and coolpup.py⁶⁰ to perform compartment and insulation analysis, peak annotation and pileups, respectively. The config file we used

is available here:

<https://gist.github.com/Phlya/5c2d0688610ebc5236d5aa7d0fd58adb>.

We annotated peaks of enriched contact frequency in untreated HCT116 cells from a previous report⁶¹ using chromosight at 5 kb resolution with default parameters. Then we used this annotation to quantify the strength of Hi-C peaks in our datasets using pileups at 5 kb resolution. Similarly, valleys of insulation score at 10 kb resolution with a window of 500 kb (and prominence over 0.1) were identified in the same published dataset and filtered to remove those that don't disappear after cohesin depletion (or don't become at least fivefold weaker) to identify cohesin-dependent domain boundaries. These were used to quantify changes in insulation in our datasets. Neighbouring insulation valleys were joined together to form TADs; regions longer than 1.5 Mb were ignored. TAD coordinates were used for rescaled pileup analysis²⁸ to quantify their strength in our datasets. De novo peaks were called using Mustache⁶².

To investigate whether the increase in loop strength occurs genome wide, we split all loop calls into 1 Mb bins, using the coordinate of the centre of the loops. Then for each bin, we created pileups normalized to the global chromosome arm-wide expected level of interactions, using coolpuppy at 5 kb resolution with 100 kb flanks. In addition, each pileup (105×105 kb) was normalized to the mean value of the top left and bottom right 3×3 pixels, to remove variability in local background between different regions of the genome. Then the mean of the central 3×3 square of the pileup was used as the measure of normalized loop strength for this bin. Having done this for both MCM2-depleted and control cells, we plotted the result as a histogram of \log_2 ratio between the two, to investigate whether the overall distribution of scores is shifted between the two conditions.

RNA sequencing (RNA-seq) of G1 zygotes

For each replicate, a pool of 10 G1 zygotes were lysed, total RNA was extracted and cDNA was synthesized using the SMART-Seq v4 Ultra Low Input RNA Kit (Takara Bio Europe). Sequencing libraries were prepared with the Nextera XT DNA Library Preparation Kit for Illumina. Libraries

were sequenced on the HiSeq 2500 v4 (Illumina) with 50-bp single-end reads at the VBCF NGS unit.

RNA-seq of tissue culture cells

Total RNA from HCT116 cells was isolated using a lysis step based on guanidine thiocyanate (adapted from a previous study⁶³ and using magnetic beads (GE Healthcare, 65152105050450). mRNA sequencing libraries were prepared from 1 µg total RNA using NEBNext Poly(A) mRNA Magnetic Isolation Module (E7490) and NEBNext Ultra II Directional RNA Library Prep Kit for Illumina (E7760). Paired-end sequencing was performed on Illumina NextSeq 500 (2×43 -bp reads). A total of six samples were multiplexed and sequenced on a NextSeq 500/550 High Output Kit v2.5 (75 Cycles) at the MPIB NGS core facility. BCL raw data were converted to FASTQ data and demultiplexed by bcl2fastq.

RNA-seq analysis

FASTQ files from sequencing mouse G1 zygotes or the human HCT116 cell line were pseudoaligned to the mm10 or hg38 releases of the *Mus musculus* or *Homo sapiens* genomes, respectively, using Kallisto with 100 bootstraps⁶⁴. The resulting abundance measures were analysed in R to generate PCA plots⁶⁵ (factoextra) and a heat map of the correlation matrix (heatmap.2)⁶⁶. To find differentially expressed transcripts we used the Wald test for Sleuth model (sleuth) in R. Gene ontology (GO) term enrichment of molecular functions of up- and downregulated genes were carried out using ShinyGO (<http://bioinformatics.sdsstate.edu/go/>).

The changes in the chromatin contact frequencies that occurred upon MCM depletion around the TSS of differentially expressed (DE), non-differentially expressed (non-DE) and non-expressed genes were analysed by aggregating the number of contacts as determined in Micro-C experiments with 5 kb resolution. The number of contacts was normalized with LOESS using HICcompare in R, and ensemble analysis of the four expression categories (upregulated, $n = 164$; downregulated, $n = 65$; non-DE, $n = 916$; non-expressed, $n = 1,000$) was carried out in distance bins of 0–5 kb, 5–25 kb, 25–250 kb, 250–1,000 kb and over 1,000 kb up- and downstream of the TSS.

The mean change of contact frequencies in each bin for every category was calculated by averaging the auxin versus DMSO treatment ratios of the normalized sum of contacts. All of the mean contact frequency changes were tested against the non-DE TSS control using the non-parametric Kruskal–Wallis test followed by pairwise Wilcoxon (Mann–Whitney U) test.

All plots were compiled with ggplot2 in R.

Protein expression and purification

Cohesin

Human recombinant cohesin^{STAG1, SCC1-Halo} was purified and fluorescently labelled with Janelia Fluor 549 HaloTag (Promega) as previously described⁶.

ORC and Cdc6

Saccharomyces cerevisiae recombinant ORC and Cdc6 were purified as previously described⁶⁷.

SFP synthase

SFP synthase was purified essentially as previously described⁶⁸.

Cdt1–MCM and Cdt1–MCM^{Mcm3-YDF}

To generate fluorescently labelled *S. cerevisiae* recombinant Cdt1–MCM, the *S. cerevisiae* strain ySA4 was generated. In brief, a ybbR and 3×Flag tag were fused to the N and C terminus of Mcm6, respectively, generating Cdt1–MCM^{ybbR-Mcm6}. The chimeric MCM complex containing a humanized Mcm3 subunit (Cdt1–MCM^{Mcm3-YDF}, ybbR-Mcm6) was expressed in strain yMS1, which was generated by further modification of ySA4. For this, the corresponding region in *S. cerevisiae* Mcm3 was replaced by the 19-amino-acid disordered region that contains a YDF motif present in human MCM3⁴⁴, using CRISPR–Cas9-based genome editing essentially as

previously described⁶⁹. To target *S. cerevisiae* Mcm3, the following guide sequence was used: 5'-TATAATGTCACCGCTTCCTG-3'. The homologous repair template (synthesized by Eurofins Genomics) encoding the 19-amino-acid disordered region containing the YDF motif (underlined) was: 5'-ACTCCAAGAAGGTCAACGGCATCTTCCGTTAACGCCACGCCATCG TCAGCACGCAGAATATTACGTTTCAAGATGACGAACAGAACGCT GGTGAAGACGATGGGGATTCATACGACCCCTATGACTTCAGTGAC ACAGAGGAGGAAATGCCTCAAAGGCTCAACTGGGGTTGAGAGT GTCTCCAAGACGTAGAGAACATCTCACGCACCTGAGGAAGGTTG GTCGGGACCTCTTACCGAGGTGGTACTCCA-3'. Notably, this strategy allowed the modification of all Mcm3 alleles (confirmed by sequencing) and thus ensured the complete absence of wild-type Mcm3 in the subsequent preparation. Strain yMS1 grew comparably to the parental strain ySA4, confirming that the YDF motif did not alter the MCM function.

Cells were grown in 6 l YP medium supplemented with 2% (v/v) raffinose at 30 °C. At an optical density at 600 nm ($OD_{600\text{ nm}}$) of 1.2, cells were arrested at G1 by adding α-factor to a final concentration of 150 ng ml⁻¹ for 3 h. Subsequently, protein expression was induced by the addition of 2 % (v/v) galactose. After 4 h, cells were collected and washed once with cold MilliQ water + 0.3 mM PMSF and once with buffer A (100 mM HEPES-KOH, pH 7.6, 0.8 M sorbitol, 10 mM Mg(OAc)₂, 0.75 M potassium glutamate (KGlu)). Finally, cells were resuspended in 1 packed cell volume of buffer A + 1 mM DTT supplemented with a protease inhibitor cocktail (2 μM pepstatin, 2 μM leupeptin, 1 mM PMSF, 1 mM benzamidine, 1 μg ml⁻¹ aprotinin) and frozen dropwise in liquid N₂. Frozen cells were lysed in a freezer mill (SPEX) and lysed cell powder was resuspended in 1 packed cell volume buffer B (45 mM HEPES-KOH, pH 7.6, 0.02 % (v/v) Nonidet P40 Substitute, 5 mM Mg(OAc)₂, 10 % (v/v) glycerol, 1 mM ATP, 1 mM DTT) + 300 mM KGlu. All subsequent purification steps were performed at 4 °C unless stated otherwise. The lysate was cleared by ultracentrifugation at 235,000g for 60 min. Soluble lysate was incubated with 0.5 ml bed volume (BV) Anti-Flag M2 affinity gel (Sigma) equilibrated with buffer B + 300 mM KGlu for 3 h. The resin was washed twice with 20 BV buffer B + 300 mM KGlu and twice with 20 BV buffer B + 100 mM KGlu. Protein was eluted with buffer B + 100 mM KGlu + 0.5 mg ml⁻¹ 3×Flag peptide.

For site-specific labelling, Cdt1-MCM^{ybbR-Mcm6} or Cdt1-MCM^{Mcm3-YDF, ybbR-Mcm6} was incubated with SFP-Synthase and LD655-CoA (Lumidyne Technologies) at a 1:3:6 molar ratio for 2 h at 30 °C in buffer B + 100 mM KGlu, 10 mM MgCl₂. Labelled protein was further purified on a Superdex 200 increase 10/300 gel filtration column (GE Healthcare) equilibrated in buffer B + 100 mM potassium acetate (KOAc). Protein-containing fractions were pooled, concentrated with a MWCO 50000 Amicon Ultra Centrifugal Filter unit (Merck) and stored in aliquots at –80 °C. The labelling efficiency was estimated to be around 90% from the extinction coefficients of Cdt1-MCM and LD655.

Single-molecule imaging

Single-molecule assays were performed using an RM21 micromirror TIRF microscope (Mad City Labs) built in a similar manner to that previously described⁷⁰ with an Apo N TIRF 60× oil-immersion TIRF objective (NA 1.49, Olympus). Janelia Fluor 532 and LD655 were excited with a 532 nm and 637 nm laser (OBIS 532 nm LS 120 mW and OBIS 637 nm LX 100 mW, Coherent), respectively at a frame rate of around 6 fps. Residual scattered light from excitation was removed with a ZET532/640m emission filter (Chroma). Emission light was split at 635 nm (T635lpxr, Chroma) and recorded as dual-view with an iXon Ultra 888 EMCCD camera (Andor). All microscope parts were controlled using Micromanager v1.4 (ref. ⁷¹) and custom Beanshell scripts.

Preparation of PEG–biotin microscope slides

Glass coverslips (22 × 22 mm, Marienfeld) were cleaned in a plasma cleaner (Zepto, Diener Electronic) and subsequently incubated in 2% (v/v) 3-aminopropyltriethoxysilane (Roth) in acetone for 5 min. Silanized coverslips were washed with ddH₂O, dried and incubated at 110 °C for 30 min. Slides were covered with a fresh solution of 0.1 M NaHCO₃ containing 0.4% (w/v) biotin–PEG-SC-5000 and 15% (w/v) mPEG-SC-5000 (Laysan Bio) and incubated overnight. Functionalized slides were washed with ddH₂O, dried and incubated again overnight in a fresh biotin–PEG/mPEG solution. Slides were finally washed, dried and stored under vacuum.

DNA substrate for single-molecule imaging

To generate pMSuperCos-ARS1, first, a 21 kb genomic DNA fragment of bacteriophage lambda (NEB) was flanked by a unique XbaI (position 0) and NotI restriction site on either end and cloned into a pSuperCos1 backbone (Stratagene). Second, the yeast origin ARS1 was inserted at a BamHI site around position 5.3 kb within the 21 kb genomic DNA fragment.

To produce the DNA substrate for single-molecule imaging, pMSuperCos-ARS1 was isolated from DH5 α using a Plasmid Maxi Kit (Qiagen). One hundred micrograms of plasmid was digested with 100 U NotI-HF and XbaI (NEB) for 7 h at 37 °C. The resulting 21,202 bp ARS1-DNA fragment was separated from the SuperCos1 backbone on a 10–40 % sucrose gradient. DNA handles were prepared by annealing oligonucleotides MS_200/201 MS202/203 (see [Supplementary Table 2](#) for oligonucleotide sequences) in equimolar amounts in 30 mM HEPES, pH 7.5, 100 mM KOAc by heating to 95 °C for 5 min and cooling to 4 °C at –1 °C per min. Annealed handles were mixed with the purified 21 kb ARS1-DNA at a molar ratio of 15:1 and ligated with T4 DNA Ligase in 1× T4 ligase buffer (both NEB) at 16 °C overnight. Free handles were removed on a Sephadex S-1000 SF Tricorn 10/300 gel filtration column (GE Healthcare) equilibrated in 10 mM Tris, pH 8, 300 mM NaCl, 1 mM EDTA. Peak fractions were pooled, ethanol precipitated and reconstituted in TE buffer. Final DNA was stored in aliquots at –80 °C. Note that the final linear DNA is functionalized with biotin at a NotI site and an 18-bp single-stranded DNA overhang at an XbaI site that is used for orientation specific doubly tethering.

Flow cell preparation

A functionalized PEG–biotin slide was incubated with blocking buffer (20 mM Tris-HCl, pH 7.5, 50 mM NaCl, 2 mM EDTA, 0.2 mg ml $^{-1}$ BSA, 0.025 % (v/v) Tween20) + 0.2 mg ml $^{-1}$ streptavidin (Sigma) for 30 min. A flow cell was assembled by placing a polydimethylsiloxane block on top to generate a 0.5 mm wide and 0.1 mm high flow channel and a polyethylene tube (inner diameter 0.58 mm) was inserted at either end.

DNA was introduced to the flow cell at 5 pM in blocking buffer and incubated for 15 min in the absence of buffer flow to allow binding to the slide surface. To doubly tether DNA, the flow lane was flushed with 100 μ M oligonucleotide MS_204 (see [Supplementary Table 2](#) for oligonucleotide sequences) in blocking buffer at 100 μ l per min.

Single-molecule sliding assay

Helicase loading was achieved by introducing 0.25 nM ORC, 4 nM Cdc6 and 10 nM Cdt1–MCM^{ybbR-LD655-Mcm⁶} or Cdt1–MCM^{Mcm3-YDF, ybbR-LD655-Mcm⁶} in licensing buffer (30 mM HEPES-KOH, pH 7.6, 8 mM Mg(OAc)₂, 0.1 mg ml⁻¹ BSA, 0.05 % (v/v) Tween20) + 200 mM KOAc, 5 mM DTT, 3 mM ATP to a prepared flow cell and incubating for 25 min. Cohesin loading and sliding was essentially performed as previously described⁷².

Cohesin^{STAG1, SCC1-Halo-JF546} (0.7 nM) was incubated with licensed DNA in cohesin binding buffer (35 mM Tris, pH 7.5, 25 mM NaCl, 25 mM KCl, 1 mM MgCl₂, 10% (v/v) glycerol, 0.1 mg ml⁻¹ BSA, 0.003 (v/v) Tween20, 1 mM DTT, 0.2 mM ATP) for 10 min. To remove free protein, DNA-bound licensing factors and MCM loading intermediates, the flow cell was washed with licensing buffer + 500 mM NaCl, 1 mM DTT, 0.6 mM ATP supplemented with an oxygen scavenging system (1 mM Trolox, 2.5 mM PCA, 0.21 U ml⁻¹ PCD (all Sigma))⁷³. Imaging was either started directly (high-salt condition) or after lowering the salt concentration to 150 mM NaCl (physiological salt condition) in an otherwise identical buffer to that described for the high-salt condition. DNA was post-stained with 50 nM SYTOX Orange (Thermo Fisher Scientific) in the same buffer that was used during imaging.

Single-molecule data analysis

Single-molecule data were analysed in Fiji using the Molecule Archive Suite (Mars) plug-in (<https://github.com/duderstadt-lab/>)⁷⁴ and custom Python scripts. In brief, all doubly tethered DNA molecules containing cohesin were chosen for analysis. Cohesin and MCM were tracked individually and merged with DNA to determine their position on the same DNA molecule. Pauses during cohesin translocation were determined by fitting cohesin

trajectories (position on DNA versus time) with the kinetic change point algorithm⁷⁵ with the following settings: confidence value 0.6; global sigma 300 base pairs (bps)/s. Subsequently, resulting segments with rates lower than 200 bps per s, standard deviations of less than 30 bps per s and length greater than 1 s were classified as pause segments. If two adjacent segments were classified as pauses and the end and start position on DNA of the first and second pause segment, respectively, were within 1 kb, these segments were merged to one pause segment. The fraction of cohesin pausing reported was determined by calculating the cumulative time of all pause segments divided by the total observation time. These pauses were excluded when calculating cohesin–MCM passing probabilities and diffusion coefficients (see below).

The probability of cohesin passing MCM was addressed as follows: Frames in which cohesin colocalized with MCM (median position) within less than thresh1 were classified as encounter. Upon an encounter, if cohesin passed MCM in the consecutive frame by at least thresh2, the encounter was determined as successful bypassing. All remaining frames (distance > thresh1 to MCM) were further evaluated for MCM passing as described above, and in addition counted as an encounter with successful bypassing. DNA molecules with cohesin only were analysed the same way using the theoretical ARS1 position on DNA. All frames within the cohesin trajectory that were part of a translocation pause were excluded from this analysis and instead classified as one encounter with failed bypassing. To account for different resolution at different extensions, two dynamic thresholds, thresh1 and thresh2, were set to 1.5 kb and 0.5 kb at the mean DNA extension of all DNA molecules and adjusted for the individual length of the DNA molecule (Extended Data Fig. 9g).

MCM photobleaching steps were defined as abrupt drops in fluorescence intensity and detected using the kinetic change point algorithm⁷⁵.

Diffusion coefficients (D) were calculated with:

$$D = \frac{\langle x^2 \rangle - \langle x \rangle^2}{2t}$$

in which $\langle x^2 \rangle$ is the mean square displacement in kb^2 and t is the time in s.

All kymographs were generated using Fiji. For this, individual DNA ends were fitted with subpixel localization and the kymograph was generated along the connecting line. Individual DNA molecules doubly tethered with different extension to the slide surface and as a consequence, kymographs differ in pixel heights. These length differences were accounted for throughout all of the analysis steps described above.

Loop extrusion simulations and contact map generation

Simulations overview

We introduced MCMs into polymer models of loop extrusion¹¹ (Fig. 3a), as randomly located extrusion barriers. Both CTCF and MCM barriers stall cohesin with some probability (CTCF 50%; ref. ³⁸) but allow bypassing, consistent with single-molecule experiments (Fig. 4d). By sweep parameters (processivity and linear density of cohesin, and density and permeability of MCM; Supplementary Figs. 2–5), we found a narrow range of values for each condition such that the peak strengths and paternal $P_c(s)$ curves can be simultaneously reproduced (Fig. 3b, d, Extended Data Fig. 6e–h, Supplementary Figs. 2–5). The simulations suggest that in wild-type conditions, cohesins extrude 110–130-kb loops and have a density of around 1 per 300 kb. MCM permeability was essential to achieve the increase in peak strength without strongly affecting the average loop size after MCM loss; in this regime, there is a linear trade-off between the MCM density and permeability (Fig. 3c). Using MCM densities (one per 30–150 kb) experimentally measured in other cell types (see below), cohesins should bypass MCMs in around 60–90% of encounters.

Time steps and lattice set-up

We use a fixed-time-step Monte Carlo algorithm as in previous work³⁹. We define the chromosome as a lattice of $L = 10,000$ sites, in which each lattice site corresponds to 2 kb of DNA. Loop extruding factors (LEFs) are represented as two motor subunits, which move bidirectionally away from one another one lattice site at a time. When LEFs encounter one another, we assume that they cannot bypass each other as is typical for cohesin

simulations⁷⁶. The ends of the chromosome (that is, the first and last lattice sites) are considered boundaries to LEF translocation; this way, LEFs cannot ‘walk off’ the chromosome.

CTCF and MCM boundary elements

To simulate TADs, we specify that every 150th lattice site is a CTCF site. In this way, our simulated 20 Mb chromosome segment is composed of 66 TADs each of size 300 kb. CTCF sites may stall the translocation of a LEF subunit with a probability of 0.45. This stalling probability is chosen within the experimental estimates of 15%–50% fractional occupancy of CTCF sites via ChIP-seq and microscopy³⁸. For simulations mimicking the ‘control’ and ‘Wapl’ depletion conditions (that is, where MCM is present on the genome), we also add random extrusion barriers to our lattice to mimic the presence of MCMs. For our parameter sweep, we add 33, 66, 132, 264, 528 barriers (that is, representing MCMs) randomly dispersed in the 20 Mb chromosome segment; this corresponds to a density of 1 MCM complex per 600 kb, 300 kb, 150 kb, 75 kb, 37.5 kb, respectively. The MCM barriers are fixed in place for the duration of a simulation. Like the CTCFs, the MCM barriers can also stall LEF translocation. A randomly translocating LEF subunit will be stalled at an MCM site with a probability of 0.0001, 0.05, 0.2, 0.4 or 0.8 (meaning that LEFs can bypass between around 20–100% of MCM sites). For both CTCF and MCM lattice sites, ‘stalling’ a LEF subunit is a permanent event that prevents further movement of that subunit. Stalling events are only resolved after dissociation of the LEF from the lattice. For simulations in which there is ‘MCM loss’, we set the total number of random MCM barriers to zero but keep the CTCF lattice sites the same. All results presented in this paper are from an average over 25 different random distributions of MCMs (that is, 25 simulation runs were performed for each condition).

LEF separations and processivity

For our simulations of ‘control’ and ‘MCM-loss’ conditions, the default LEF processivity was 90 kb, and the default LEF separation was 300 kb. For our simulations of the ‘*Wapl*^A’ and ‘*Wapl*^A + MCM loss’ conditions, the LEF processivity was 130 kb, and the separations were 180 kb. The

approximately 50% increase in density after Wapl depletion is supported by quantitative immunofluorescence data indicating there is a modest enrichment of cohesin after removal of Wapl^{[37](#)}.

Association and dissociation rates

All simulations are performed with fixed numbers of extruders. The dissociation rate is ultimately tied to the ‘processivity’ of the LEF, which is the average distance in kb (or lattice sites) that the LEF travels before dissociating. We allow LEFs to randomly associate to at any lattice position after a dissociation event.

Loop extrusion equilibration steps

We compute 10,000 initialization steps for each simulation before creating any contact maps. This ensures that the loop statistics have reached a steady-state. Subsequent loop configurations were sampled every 100 simulation steps to generate contact maps. We sampled from at least 2,500 different LEF configurations (that is, 100 configurations from 25 different simulations) to generate contact probability decay curves and perform aggregate peak analysis (see below).

Contact maps

We generated contact maps semi-analytically, which uses a Gaussian approximation to calculate contact probability maps directly from the positions of LEFs. This approach was developed previously^{[39](#)} and used to simulate bacterial Hi-C maps. We note that as the density of cohesins is sufficiently low in the zygotes (that is, the processivity and separation ratio is close to or less than 1), and as the contact probability scaling exponent up to 10 Mb is close to -1.5 in the absence of cohesins^{[27](#)}, we are justified in using the Gaussian approximation to generate contact maps. To generate the $P_c(s)$ curves, we use at least 9,000,000 random samples of the contact probability; these samples were taken from varying genomic positions and relative separations within the simulated 20 Mb of chromosome and averaged using logarithmically spaced bins (factor of 1.3). To generate the

equivalent of the aggregate peak analysis for contact enrichments at CTCF sites, we used at least 144,000,000 random samples of the contact probability from a 100 kb by 100 kb window centred on the CTCF sites. These 144,000,000 samples were distributed evenly between 64 TADs (there are 66 TADs, but we excluded the 2 TADs closest to the chromosome ends) and at least 2,500 LEF conformations. Control matrices for normalization were obtained as described above, but using a shifted window shifted by 150 kb from the TAD boundaries. Aggregate peak analysis plots are shown coarse-grained to 20×20 bins.

Comparing simulated and experimental data

The criteria for comparing the experimental data and the simulated data were two-fold. First, we computed from snHi-C the corner peak strength above background; this was usually a number between 1 and 3 depending on the condition. Second, we computed the $P(s)$ curves from experiments genome wide. However, we knew from previous studies^{27,34}, that the effect of cohesin on $P(s)$ typically only extends up to around 1 Mb under normal conditions. Moreover, above 1 Mb, the semi-analytical approach to generating contact maps becomes less reliable as non-equilibrium effects, chain topology, and chain swelling may start to have a role in the $P(s)$ curve, which are not accounted for in our model³⁹. Below 30 kb, Hi-C data have been shown to contain artefacts and can vary significantly between different protocols. Thus, we restricted our comparisons to the range 30 kb–1 Mb.

The criteria then for evaluating the goodness of a simulation, were to (1) obtain quantitative values for the corner peak strengths as close as possible to the experiments, preserving the correct relative ordering between various conditions (for example, in paternal zygotes, the corner peak strength from weakest to highest was: wild type, Wapl depletion, MCM depletion, MCM + Wapl depletion). We directly scored the goodness of the simulation by minimizing the absolute error between the simulated and experimental corner peak strengths. (2) Simultaneously, we evaluated the absolute values and shapes of the $P(s)$ curves between 30 kb–1 Mb. The goodness of $P(s)$ fit was evaluated by visual agreement. Therefore, we used a combined approach to evaluate the match between experiments and simulations, in which the dot strength and $P(s)$ curves were evaluated together.

Estimation of chromatin-bound MCM density in mammalian cells

Using mass-spectrometry analysis, the copy number of each MCM subunit is estimated at around 670,000 in HeLa cells⁷⁷, and quantitative immunoblotting shows that in late G1 phase around 45% of MCM2 is bound to chromatin⁷⁸. This leads to the estimate that around 301,500 MCMs are bound to the chromatin in late G1. Knowing that MCMs form double hexamers on chromatin and that the average genome size of HeLa cells is around 7.9×10^9 (ref. ⁷⁹), we estimate a density of 1 MCM double hexamer every approximately 52 kb ($7.9 \times 10^9 / (301,500/2)$) (assuming a random distribution of MCMs).

Reporting summary

Further information on research design is available in the [Nature Research Reporting Summary](#) linked to this paper.

Data availability

All sequencing data in support of the findings of this study have been deposited in the Gene Expression Omnibus (GEO) under the series accession numbers [GSE196497](#) (snHi-C and RNA-seq) and [GSE155971](#) (Hi-C and Micro-C). The single-molecule video datasets supporting the findings in this study have been deposited at Zenodo with the following: <https://doi.org/10.5281/zenodo.5911106> (high-salt experiments), <https://doi.org/10.5281/zenodo.5911210> (physiological salt experiments) and <https://doi.org/10.5281/zenodo.5911284> (YDF experiments). All data are also available from the authors upon request.

Code availability

The snHi-C and single-molecule processing scripts are deposited at Zenodo under <https://doi.org/10.5281/zenodo.5906351> and <https://doi.org/10.5281/zenodo.5911644>, respectively. The simulation codes are available at <https://github.com/mirnylab/MCMs-as-random-barriers-to-loop-extrusion-paper>.

References

1. Nora, E. P. et al. Spatial partitioning of the regulatory landscape of the X-inactivation centre. *Nature* **485**, 381–385 (2012).
2. Dixon, J. R. et al. Topological domains in mammalian genomes identified by analysis of chromatin interactions. *Nature* **485**, 376–380 (2012).
3. Rao, S. S. P. et al. A 3D map of the human genome at kilobase resolution reveals principles of chromatin looping. *Cell* **159**, 1665–1680 (2014).
4. Cuartero, S. et al. Control of inducible gene expression links cohesin to hematopoietic progenitor self-renewal and differentiation. *Nat. Immunol.* **19**, 932–941 (2018).
5. Zhang, Y. et al. The fundamental role of chromatin loop extrusion in physiological V(D)J recombination. *Nature* **573**, 600–604 (2019).
6. Davidson, I. F. et al. DNA loop extrusion by human cohesin. *Science* **366**, 1338–1345 (2019).
7. Kim, Y., Shi, Z., Zhang, H., Finkelstein, I. J. & Yu, H. Human cohesin compacts DNA by loop extrusion. *Science* **366**, 1345–1349 (2019).
8. Golfier, S., Quail, T., Kimura, H. & Brugués, J. Cohesin and condensin extrude DNA loops in a cell cycle-dependent manner. *eLife* **9**, e53885 (2020).
9. Alipour, E. & Marko, J. F. Self-organization of domain structures by DNA-loop-extruding enzymes. *Nucleic Acids Res.* **40**, 11202–11212 (2012).
10. Sanborn, A. L. et al. Chromatin extrusion explains key features of loop and domain formation in wild-type and engineered genomes. *Proc. Natl Acad. Sci. USA* **112**, E6456–E6465 (2015).

11. Fudenberg, G. et al. Formation of chromosomal domains by loop extrusion. *Cell Rep.* **15**, 2038–2049 (2016).
12. Hansen, A. S. CTCF as a boundary factor for cohesin-mediated loop extrusion: evidence for a multi-step mechanism. *Nucleus* **11**, 132–148 (2020).
13. Davidson, I. F. & Peters, J.-M. Genome folding through loop extrusion by SMC complexes. *Nat. Rev. Mol. Cell Biol.* **22**, 445–464 (2021).
14. Nora, E. P. et al. Targeted degradation of CTCF decouples local insulation of chromosome domains from genomic compartmentalization. *Cell* **169**, 930–944 (2017).
15. Brandão, H. B. et al. RNA polymerases as moving barriers to condensin loop extrusion. *Proc. Natl Acad. Sci. USA* **116**, 20489–20499 (2019).
16. Heinz, S. et al. Transcription elongation can affect genome 3D structure. *Cell* **174**, 1522–1536 (2018).
17. Busslinger, G. A. et al. Cohesin is positioned in mammalian genomes by transcription, CTCF and Wapl. *Nature* **460**, 410 (2017).
18. Deegan, T. D. & Diffley, J. F. X. MCM: one ring to rule them all. *Curr. Opin. Struct. Biol.* **37**, 145–151 (2016).
19. Hyrien, O. How MCM loading and spreading specify eukaryotic DNA replication initiation sites. *F1000Res.* **5**, 2063 (2016).
20. Remus, D. & Diffley, J. F. X. Eukaryotic DNA replication control: lock and load, then fire. *Curr. Opin. Cell Biol.* **21**, 771–777 (2009).
21. Das, M., Singh, S., Pradhan, S. & Narayan, G. MCM paradox: abundance of eukaryotic replicative helicases and genomic integrity. *Mol. Biol. Int.* **2014**, 574850 (2014).
22. Ibarra, A., Schwob, E. & Méndez, J. Excess MCM proteins protect human cells from replicative stress by licensing backup origins of

- replication. *Proc. Natl Acad. Sci. USA* **105**, 8956–8961 (2008).
23. Sedlackova, H. et al. Equilibrium between nascent and parental MCM proteins protects replicating genomes. *Nature* **587**, 297–302 (2020).
 24. Kuipers, M. A. et al. Highly stable loading of Mcm proteins onto chromatin in living cells requires replication to unload. *J. Cell Biol.* **192**, 29–41 (2011).
 25. Li, N. et al. Structure of the eukaryotic MCM complex at 3.8 Å. *Nature* **524**, 186–191 (2015).
 26. Stigler, J., Çamdere, G. Ö., Koshland, D. E. & Greene, E. C. Single-molecule imaging reveals a collapsed conformational state for DNA-bound cohesin. *Cell Rep.* **15**, 988–998 (2016).
 27. Gassler, J. et al. A mechanism of cohesin-dependent loop extrusion organizes zygotic genome architecture. *EMBO J.* **36**, 3600–3618 (2017).
 28. Flyamer, I. M. et al. Single-nucleus Hi-C reveals unique chromatin reorganization at oocyte-to-zygote transition. *Nature* **544**, 110–114 (2017).
 29. Aoki, F., Worrad, D. M. & Schultz, R. M. Regulation of transcriptional activity during the first and second cell cycles in the preimplantation mouse embryo. *Dev. Biol.* **181**, 296–307 (1997).
 30. McGarry, T. J. & Kirschner, M. W. Geminin, an inhibitor of DNA replication, is degraded during mitosis. *Cell* **93**, 1043–1053 (1998).
 31. Wohlschlegel, J. A. et al. Inhibition of eukaryotic DNA replication by geminin binding to Cdt1. *Science* **290**, 2309–2312 (2000).
 32. Silva, M. C. C. et al. Wapl releases Scc1-cohesin and regulates chromosome structure and segregation in mouse oocytes. *J. Cell Biol.* **219**, e201906100 (2020).

33. Ladstätter, S. & Tachibana-Konwalski, K. A surveillance mechanism ensures repair of DNA lesions during zygotic reprogramming. *Cell* **167**, 1774–1787 (2016).
34. Wutz, G. et al. Topologically associating domains and chromatin loops depend on cohesin and are regulated by CTCF, WAPL, and PDS5 proteins. *EMBO J.* **36**, 3573–3599 (2017).
35. Wan, L.-B. et al. Maternal depletion of CTCF reveals multiple functions during oocyte and preimplantation embryo development. *Development* **135**, 2729–2738 (2008).
36. Wang, W. et al. Genome-wide mapping of human DNA replication by optical replication mapping supports a stochastic model of eukaryotic replication. *Mol. Cell* **81**, 2975–2988 (2021).
37. Haarhuis, J. H. I. et al. The cohesin release factor WAPL restricts chromatin loop extension. *Cell* **169**, 693–707 (2017).
38. Hansen, A. S., Pustova, I., Cattoglio, C., Tjian, R. & Darzacq, X. CTCF and cohesin regulate chromatin loop stability with distinct dynamics. *eLife* **6**, 2848 (2017).
39. Banigan, E. J., van den Berg, A. A., Brandão, H. B., Marko, J. F. & Mirny, L. A. Chromosome organization by one-sided and two-sided loop extrusion. *eLife* **9**, e53558 (2020).
40. Natsume, T. et al. Acute inactivation of the replicative helicase in human cells triggers MCM8-9-dependent DNA synthesis. *Genes Dev.* **31**, 816–829 (2017).
41. Remus, D. et al. Concerted loading of MCM2–7 double hexamers around DNA during DNA replication origin licensing. *Cell* **139**, 719–730 (2009).
42. Evrin, C. et al. A double-hexameric MCM2–7 complex is loaded onto origin DNA during licensing of eukaryotic DNA replication. *Proc. Natl Acad. Sci. USA* **106**, 20240–20245 (2009).

43. Scherr, M. J., Abd Wahab, S., Remus, D. & Duderstadt, K. E. Mobile origin-licensing factors confer resistance to conflicts with RNA polymerase. *Cell Rep.* **38**, 110531 (2022).
44. Li, Y. et al. The structural basis for cohesin–CTCF-anchored loops. *Nature* **578**, 472–476 (2020).
45. Pradhan, B. et al. SMC complexes can traverse physical roadblocks bigger than their ring size. Preprint at *bioRxiv* <https://doi.org/10.1101/2021.07.15.452501> (2021).
46. Bauer, B. W. et al. Cohesin mediates DNA loop extrusion by a “swing and clamp” mechanism. *Cell* **184**, 5448–5464 (2021).
47. Chatzidaki, E. E. et al. Ovulation suppression protects against chromosomal abnormalities in mouse eggs at advanced maternal age. *Curr. Biol.* **31**, 4038–4051 (2021).
48. Takahashi, T. S., Yiu, P., Chou, M. F., Gygi, S. & Walter, J. C. Recruitment of *Xenopus* Scc2 and cohesin to chromatin requires the pre-replication complex. *Nat. Cell Biol.* **6**, 991–996 (2004).
49. Gillespie, P. J. & Hirano, T. Scc2 couples replication licensing to sister chromatid cohesion in *Xenopus* egg extracts. *Curr. Biol.* **14**, 1598–1603 (2004).
50. Zheng, G., Kanchwala, M., Xing, C. & Yu, H. MCM2–7-dependent cohesin loading during S phase promotes sister-chromatid cohesion. *eLife* **7**, 9906 (2018).
51. Liu, Y. & Dekker, J. Biochemically distinct cohesin complexes mediate positioned loops between CTCF sites and dynamic loops within chromatin domains. Preprint at *bioRxiv* <https://doi.org/10.1101/2021.08.24.457555> (2021).
52. Hug, C. B., Grimaldi, A. G., Kruse, K. & Vaquerizas, J. M. Chromatin architecture emerges during zygotic genome activation independent of transcription. *Cell* **169**, 216–2289 (2017).

53. de Munnik, S. A. et al. Meier–Gorlin syndrome genotype–phenotype studies: 35 individuals with pre-replication complex gene mutations and 10 without molecular diagnosis. *Eur. J. Hum. Genet.* **20**, 598–606 (2012).
54. Lewandoski, M., Wassarman, K. M. & Martin, G. R. *Zp3-cre*, a transgenic mouse line for the activation or inactivation of loxP-flanked target genes specifically in the female germ line. *Curr. Biol.* **7**, 148–151 (1997).
55. Goloborodko, A. et al. mirnylab/distiller-nf: v0.3.3
<https://doi.org/10.5281/zenodo.3350937> (Zenodo, 2019).
56. Abdennur, N. & Mirny, L. A. Cooler: scalable storage for Hi-C data and other genomically labeled arrays. *Bioinformatics* **36**, 311–316 (2020).
57. Kerpedjiev, P. et al. HiGlass: web-based visual exploration and analysis of genome interaction maps. *Genome Biol.* **19**, 125 (2018).
58. Venev, S. et al. mirnylab/cooltools: v0.3.2
<https://doi.org/10.5281/zenodo.3787004> (Zenodo, 2020).
59. Matthey-Doret, C. et al. Computer vision for pattern detection in chromosome contact maps. *Nat. Commun.* **11**, 5795 (2020).
60. Flyamer, I. M., Illingworth, R. S. & Bickmore, W. A. Coolpup.py: versatile pile-up analysis of Hi-C data. *Bioinformatics* **36**, 2980–2985 (2020).
61. Rao, S. S. P. et al. Cohesin loss eliminates all loop domains. *Cell* **171**, 305–320 (2017).
62. Roayaei Ardakany, A., Gezer, H. T., Lonardi, S. & Ay, F. Mustache: multi-scale detection of chromatin loops from Hi-C and Micro-C maps using scale-space representation. *Genome Biol.* **21**, 256 (2020).
63. Boom, R. et al. Rapid and simple method for purification of nucleic acids. *J. Clin. Microbiol.* **28**, 495–503 (1990).

64. Bray, N. L., Pimentel, H., Melsted, P. & Pachter, L. Near-optimal probabilistic RNA-seq quantification. *Nat. Biotechnol.* **34**, 525–527 (2016).
65. Lê, S., Josse, J. & Husson, F. FactoMineR: an R package for multivariate analysis. *J. Stat. Soft.* **25**, 1–18 (2008).
66. Warnes, G. R. et al. gplots: various R programming tools for plotting data. R version 3.0. 1 <https://CRAN.R-project.org/package=gplots> (2016).
67. Frigola, J., Remus, D., Mehanna, A. & Diffley, J. F. X. ATPase-dependent quality control of DNA replication origin licensing. *Nature* **495**, 339–343 (2013).
68. Yin, J., Lin, A. J., Golan, D. E. & Walsh, C. T. Site-specific protein labeling by Sfp phosphopantetheinyl transferase. *Nat. Protoc.* **1**, 280–285 (2006).
69. Laughery, M. F. et al. New vectors for simple and streamlined CRISPR–Cas9 genome editing in *Saccharomyces cerevisiae*: vectors for simple CRISPR–Cas9 genome editing in yeast. *Yeast* **32**, 711–720 (2015).
70. Larson, J. et al. Design and construction of a multiwavelength, micromirror total internal reflectance fluorescence microscope. *Nat. Protoc.* **9**, 2317–2328 (2014).
71. Edelstein, A., Amodaj, N., Hoover, K., Vale, R. & Stuurman, N. Computer control of microscopes using µManager. *Curr. Protoc. Mol. Biol.* **92**, 14.20.1–14.20.17 (2010).
72. Davidson, I. F. et al. Rapid movement and transcriptional re-localization of human cohesin on DNA. *EMBO J.* **35**, 2671–2685 (2016).
73. Aitken, C. E., Marshall, R. A. & Puglisi, J. D. An oxygen scavenging system for improvement of dye stability in single-molecule fluorescence experiments. *Biophys. J.* **94**, 1826–1835 (2008).

74. Huisjes, N. M. et al. Mars, a molecule archive suite for reproducible analysis and reporting of single molecule properties from bioimages. Preprint at *bioRxiv* <https://doi.org/10.1101/2021.11.26.470105> (2021).
75. Hill, F. R., van Oijen, A. M. & Duderstadt, K. E. Detection of kinetic change points in piece-wise linear single molecule motion. *J. Chem. Phys.* **148**, 123317 (2018).
76. Banigan, E. J. & Mirny, L. A. Loop extrusion: theory meets single-molecule experiments. *Curr. Opin. Cell Biol.* **64**, 124–138 (2020).
77. Kulak, N. A., Pichler, G., Paron, I., Nagaraj, N. & Mann, M. Minimal, encapsulated proteomic-sample processing applied to copy-number estimation in eukaryotic cells. *Nat. Meth.* **11**, 319–324 (2014).
78. Dimitrova, D. S., Todorov, I. T., Melendy, T. & Gilbert, D. M. Mcm2, but not Rpa, is a component of the mammalian early G1-phase prereplication complex. *J. Cell Biol.* **146**, 709–722 (1999).
79. Landry, J. J. M. et al. The genomic and transcriptomic landscape of a HeLa cell line. *G3* **3**, 1213–1224 (2013).

Acknowledgements

We thank M. S. Bartolomei for the (*Tg*)*Zp3-dsCTCF* mouse strain; M. T. Kanemaki for the *MCM2-mAID* HCT116 cell line; the D. Remus laboratory for generating the ySA4 MCM strain that was used in vitro single-molecule assays; Z. Lygerou for sharing the geminin(L26A)-GFP plasmid; U. Cramer and R. Hornberger for technical assistance in generating the MCM3–YDF yeast strains; and H. C. Theußl and J. R. Wojciechowski for reviving (*Tg*)*Zp3-dsCTCF* embryos. Illumina sequencing was performed at the VBCF NGS unit and the MPIB NGS core facility (<http://www.vbcf.ac.at> and <https://www.biochem.mpg.de/7076201/NGS>). B.J.H.D. is funded by the PhD program (DK) Chromosome Dynamics (W1238-B20), supported by the Austrian Science Fund (FWF). L.A.M. and H.B.B. acknowledge support from the National Institutes of Health Common Fund 4D Nucleome Program (DK107980) and the Human Frontier Science Program (HFSP RGP0057/2018). I.M.F. is supported by a Medical Research Council UK

University Unit grant (MC_UU_00007/2). Research in the K.E.D. laboratory is supported by the European Research Council (ERC; ERC-StG-804098 ReplisomeBypass), the German Research Foundation (DFG, SFB863-111166240) and the Max Planck Society. Research in the J.-M.P. laboratory is supported by Boehringer Ingelheim, the Austrian Research Promotion Agency (Headquarter grant FFG-878286), the ERC (grant agreement no. 693949 and 101020558), HFSP (RGP0057/2018) and the Vienna Science and Technology Fund (grant LS19-029). Research in the K.T. laboratory is supported by the ERC (ERC-CoG-818556 TotipotentZygoteChrom), HFSP (RGP0057/2018), the Herzfelder Foundation and FWF (P30613-B21), the Austrian Academy of Sciences and the Max Planck Society.

Funding

Open access funding provided by Max Planck Society.

Author information

Author notes

1. Hugo B. Brandão

Present address: Illumina Inc., San Diego, CA, USA

2. These authors contributed equally: Bart J. H. Dequeker, Matthias J. Scherr

Authors and Affiliations

1. Institute of Molecular Biotechnology of the Austrian Academy of Sciences (IMBA), Vienna BioCenter (VBC), Vienna, Austria

Bart J. H. Dequeker, Johanna Gassler, Sean Powell & Kikuë Tachibana

2. Structure and Dynamics of Molecular Machines, Max Planck Institute of Biochemistry (MPIB), Martinsried, Germany

Matthias J. Scherr & Karl E. Duderstadt

3. Harvard Program in Biophysics, Harvard University, Cambridge, MA, USA

Hugo B. Brandão

4. Department of Totipotency, Max Planck Institute of Biochemistry (MPIB), Martinsried, Germany

Johanna Gassler, Imre Gaspar, Aleksandar Lalic & Kikuë Tachibana

5. MRC Human Genetics Unit, Institute of Genetics and Molecular Medicine (IGMM), University of Edinburgh, Edinburgh, UK

Ilya M. Flyamer

6. Research Institute of Molecular Pathology (IMP), Vienna BioCenter (VBC), Vienna, Austria

Wen Tang, Roman Stocsits, Iain F. Davidson & Jan-Michael Peters

7. Department of Physics, Technical University of Munich, Garching, Germany

Karl E. Duderstadt

8. Department of Physics, Massachusetts Institute of Technology (MIT), Cambridge, MA, USA

Leonid A. Mirny

Contributions

K.T. conceived the project. B.J.H.D. supervised by K.T. performed snHi-C, Hi-C, Micro-C, RNA-seq and imaging experiments. H.B.B. developed and performed snHi-C data analysis and polymer simulations with L.A.M. M.J.S. supervised by K.E.D. performed single-molecule imaging and analysis. J.G. performed snHi-C and imaging experiments. S.P. performed

snHi-C data analysis and RNA-seq analysis. I.G. performed RNA-seq analysis and contributed to imaging analysis. A.L. performed Micro-C experiments. J.G., S.P., I.G. and A.L. were supervised by K.T. I.M.F. performed Hi-C and Micro-C analysis. I.F.D. purified recombinant cohesin^{STAG1, SCC1-Halo}. W.T. contributed to development of cell lines and R.S. to bioinformatic analyses. I.F.D., W.T. and R.S. were supervised by J.-M.P. B.J.H.D., H.B.B., M.J.S., I.M.F. and I.G. prepared the figures. B.J.H.D., H.B.B., M.J.S., I.G., K.E.D., L.A.M. and K.T. wrote the manuscript with input from all authors.

Corresponding authors

Correspondence to [Karl E. Duderstadt](#), [Leonid A. Mirny](#) or [Kikuë Tachibana](#).

Ethics declarations

Competing interests

The authors declare no competing interests.

Peer review

Peer review information

Nature thanks the anonymous reviewers for their contribution to the peer review of this work. [Peer reviewer reports](#) are available.

Additional information

Publisher's note Springer Nature remains neutral with regard to jurisdictional claims in published maps and institutional affiliations.

Extended data figures and tables

Extended Data Fig. 1 Dimensions of cohesin compared to the estimated size of the MCM2–7 complex and the FtsK roadblock.

Size comparison between a schematic representation of the ring-shaped heterotrimeric cohesin (SMC1-SMC3-SCC1) with the MCM2–7 double hexamer and the FtsK monohexamer. The size estimation of MCM2–7 and FtsK was based on their crystal structure. PDB accessions codes for each protein are shown in parentheses.

Extended Data Fig. 2 Prevention of MCM loading in G1-synchronized zygotes.

a, Expression of geminin(L26A), a non-degradable variant of geminin, prevents the recruitment of MCMs to chromatin in G1 phase by inhibiting the Cdt1-mediated loading pathway. **b**, Quantification of mean chromatin-bound MCM2 intensity in maternal and paternal pronuclei from wild type (WT, n = 7) and MCM-loading inhibited (MCM loss, n = 7) G1-phase zygotes from 1 experiment using 4 females. Representative image is shown in Fig. [1b](#). **c**, 5-ethynyl-2'-deoxyuridine (EdU)-cultured zygotes collected at 6.5h post-fertilization do not incorporate EdU (0/12) and therefore have not yet entered S phase. Zygotes without EdU in the medium (no EdU) also don't incorporate EdU (0/6), while zygotes fixed at 12h post-fertilization show EdU-incorporation (7/7). Quantification of EdU intensity as signal over background shown for both maternal and paternal pronuclei from G1/no Edu (n = 6), G1/EdU (n = 12) and S/EdU (n = 7) zygotes examined in 1 experiment using 6 females. **d**, Immunofluorescence analysis of WT (n = 9) and MCM loss (n = 11) zygotes from 1 experiment using 6 females that were cultured in continuous presence of EdU and collected at 14h post-fertilization (G2 phase). Top, representative image. Bottom, quantification of EdU signal over background in maternal and paternal pronuclei. **e, f**, Immunofluorescence analysis of chromatin-bound CTCF (**e**) and SCC1-MYC (**f**) in WT (n = 7 for CTCF, n = 5 for SCC1-MYC) and MCM loss (n = 8 for CTCF, n = 7 for SCC1-MYC) G1-phase zygotes from 1 experiment for each staining using 5 females each. Left, representative image. Right, Quantification of CTCF and SCC1-MYC intensity as signal over background in maternal and paternal pronuclei. *P* values were determined by two-sided unpaired *t*-test (**b, c, e, f**) or by two-sided Mann-Whitney *U* test

(d). Quantifications in panels b-f are depicted as mean \pm s.d.; *, sperm head. †, degraded polar body. DNA is stained with DAPI. Scale bars, 10 μ m.

Extended Data Fig. 3 MCMs impede loops in G1 zygotes while having little effect on the $P_c(s)$ curve in the range of cohesin-dependent contacts up to 1 Mb.

a, Peak strength of individual samples for wild type (WT) and MCM-loading inhibited (MCM loss) conditions, shown for maternal and paternal pronuclei. Size of the bullets corresponds to the number of cis 1kb+ contacts per sample (weights). Data are based on n(WT, maternal) = 13, n(WT, paternal) = 16, n(MCM loss, maternal) = 16, n(MCM loss, paternal) = 15, from 4 independent experiments using 4-6 females for each experiment (same samples as in Fig. 1d). Data presented as weighted mean \pm s.d.; P values were calculated using weighted statistics (Methods). **b**, Aggregate peak analysis for intermediate (100-250kb) and long loops (>250 kb) in WT and MCM loss conditions for maternal and paternal pronuclei. Data are based on the same samples as in (a) and Fig. 1d. **c**, Aggregate peak analysis for WT and MCM loss conditions from a subset of 4, 8 and 12 samples, shown for maternal and paternal pronuclei. **d**, Contact probability $P_c(s)$ curve as a function of genomic distance (s). Cohesin is directly involved in shaping the $P_c(s)$ in the range up to 1 Mb. The contact frequency in this region is decreased after cohesin depletion (*Scc1*^Δ) and is increased after enrichment of chromatin-bound cohesin (*Wapl*^Δ). **e**, Contact probability $P_c(s)$ curves from individual maternal and paternal pronuclei with average $P_c(s)$ (same as in Fig. 1e) in bold overlaid. **f**, Slopes of the $P_c(s)$ curves (depicted in Fig. 1e) as an indication for the average size of cohesin-extruded loops in WT and MCM loss conditions.

Extended Data Fig. 4 MCMs impede cohesin-dependent loops and TADs largely independently of transcriptional changes.

a, Principal component analysis (PCA) of the transcriptomes of G1 wild type (G1_WT), G1 MCM-loading inhibited (G1_MCM loss) and G2 wild type (G2_WT) zygotes. **b**, Volcano plot showing statistical significance –

\log_{10} (FDR) versus fold change (\log_2 fold change) for RNA-Seq data between WT and MCM loss conditions in G1 zygotes. Numbers indicate the number of transcripts significantly up- (right) or downregulated (left) after MCM loss at FDR = 0.1. Dashed vertical lines indicate -0.585 and $+0.585$ \log_2 fold change in expression (1.5-fold decrease and increase in expression), respectively. **c**, $Scc1^{\Delta/\Delta}$ oocytes from $Scc1^{fl/fl}$ (*Tg*)*Zp3-Cre* females were injected with geminin(L26A) mRNA and eggs were fertilized to generate maternal knockout $Scc1^{\Delta(m)/+(p)}$ zygotes for snHi-C analysis in G1 phase. Because most proteins are provided by the oocyte and the G1-phase zygote is practically transcriptionally inactive, these maternal knockout zygotes are depleted for $Scc1$ ³³. **d**, Aggregate peak and TAD analysis for $Scc1^{fl}$ (WT), $Scc1^{\Delta}$ and $Scc1^{\Delta} +$ MCM loss. Maternal and paternal data are shown pooled together. Data are based on $n(Scc1^{fl}) = 26$, $n(Scc1^{\Delta}) = 42$, and $n(Scc1^{\Delta} + \text{MCM loss}) = 10$ nuclei. Heat maps were normalized to an equal number of *cis* contacts. Control ($Scc1^{fl}$) samples and 38 $Scc1$ -depleted samples ($Scc1^{\Delta}$) were previously published²⁷.

Extended Data Fig. 5 CTCF is required for loop and TAD formation in G1 zygotes.

a, Immunofluorescence analysis of CTCF in wild type ($n = 5$) and CTCF-depleted ($n = 12$) surrounded nucleolus (SN) oocytes from 1 experiment using 2 females for each genotype. Left, representative images, DNA is stained with DAPI. Scale bars: 20 μm . Right, Quantification of CTCF intensity as signal over background. Data are presented as mean \pm s.d.; P value was determined by two-sided unpaired *t*-test. **b**, Aggregate peak and TAD analysis for wild type (WT), CTCF-depleted (CTCF knockdown) and CTCF-depleted combined with prevention of MCM loading (CTCF knockdown + MCM loss) maternal chromatin in G1 zygotes. Data shown are based on $n(\text{WT, maternal}) = 12$, $n(\text{CTCF knockdown, maternal}) = 12$, $n(\text{CTCF knockdown + MCM loss, maternal}) = 10$ nuclei, from 4 independent experiments using 4-6 females for each genotype. Heat maps were normalized to an equal number of *cis* contacts. **c**, Insulation scores at TAD borders for maternal nuclei. **d**, Average contact probability $P_c(s)$ curves for WT and CTCF knockdown conditions, shown separately for maternal

and paternal nuclei. **e**, $P_c(s)$ curves for individual samples (maternal and paternal pronuclei) with average $P_c(s)$ (same as in **d**) in bold overlaid.

Extended Data Fig. 6 MCM restricts loop and TAD formation in maternal chromatin independently of Wapl-mediated cohesin release.

a, Aggregate peak and TAD analysis for control (WT), *Wapl^A* and *Wapl^A* + MCM loss for maternal chromatin in G1 zygotes. Data shown are based on n(WT, maternal) = 17, n(*Wapl^A*, maternal) = 10, n(*Wapl^A* + MCM loss, maternal) = 10, from 4 independent experiments using 4-6 females for each genotype. Control samples are WT (this study) pooled with *Wapl^{fl}* samples (published in²⁷). **b**, Insulation scores at TAD borders for maternal nuclei. **c**, Average contact probability $P_c(s)$ curves for control (WT), *Wapl^A* and *Wapl^A* + MCM loss, shown separately for maternal and paternal nuclei. **d**, $P_c(s)$ curves for individual samples (maternal and paternal pronuclei) with average $P_c(s)$ (same as in panel c) in bold overlaid. **e**, Matrix of peak strengths, generated by polymer simulations, showing a linear trade-off between the MCM density and its ability to pause cohesins in *Wapl^A*. **f–g**, Simulated contact probability decay curve $P_c(s)$ for WT (**f**), *Wapl^A* (**g**) and *Wapl^A* + MCM loss (**h**). The simulated $P_c(s)$ curve is well matched with the experimental data.

Extended Data Fig. 7 Moderate increase in aggregate peak strength after acute depletion of MCM in HCT116 cells using Hi-C.

a, Schematic for G1 synchronization of HCT116 MCM2-mAID cells. **b**, Cell cycle profiles of asynchronous and G1-synchronized (Control/MCM depletion) HCT116 MCM2-mAID cells. **c**, Immunoblotting analysis of whole-cell lysate (W), supernatant (S) and chromatin (C) fraction for MCM2, MCM4, GAPDH and H3 from G1-synchronized HCT116 MCM2-mAID cells treated with DMSO (Control) or auxin (MCM depletion). GAPDH and H3 are used as loading controls for supernatant and chromatin

fraction, respectively. Uncropped blots are displayed in [Supplementary Fig. 1](#). This experiment was repeated independently three more times with similar results. **d**, Hi-C contact matrices for control and MCM depletion conditions for the region 112,5-117,6 Mb on chromosome 12 at 10 kb resolution. Increased corner peaks are denoted with an arrow. CTCF sites are depicted above the contact matrices. **e**, Average of total contact frequency for loops and TADs in aggregate peak and TAD analysis for control and MCM-depleted cells. **f**, Contact probability $P_c(s)$ curves for control and MCM depletion conditions. **g**, Insulation scores at TAD borders for control and MCM-depleted cells. Read statistics for Hi-C replicates can be found in [Supplementary Table 1](#).

Extended Data Fig. 8 Micro-C reveals a genome-wide increase in peak strength and in de novo loop number after acute depletion of MCM2 in HCT116 cells.

a, Schematic for G1 synchronization of HCT116 MCM2-mAID cells before G1 FACS sorting. **b**, FACS-analysis of synchronized HCT116 MCM2-mAID cells. Only cells in the left part of the G1 peak were sorted and collected for Micro-C and RNA-seq to avoid contamination of S-phase cells (red dashed box). **c**, Immunoblotting analysis of whole-cell lysate (W), supernatant (S) and chromatin fraction (C) for MCM2, MCM4, CTCF, SCC1, PCNA, GAPDH and H3 from asynchronous and G1-sorted HCT116 MCM2-mAID cells treated with DMSO (Control) or auxin (MCM depletion). GAPDH and H3 are used as loading controls for the supernatant and chromatin fraction, respectively. Uncropped blots are displayed in [Supplementary Fig. 1](#). This experiment was repeated independently one more time with similar results. **d**, Micro-C contact matrices for the region 57 - 58.5 Mb on chromosome 15 at 10 kb resolution in control vs MCM-depleted cells. **e**, $P_c(s)$ curves for control and MCM depletion conditions. **f**, Insulation scores at TAD borders for control and MCM-depleted cells. **g**, Average of the total contact frequency of loops in an aggregate peak analysis for two independent Micro-C replicates (middle and lower panel) and pooled dataset (upper panel) in control and MCM-depleted cells. **h**, Peak strengths for control and MCM-depleted cells over a range of genomic distances. **i**, Histogram showing the distribution of \log_2 ratio of peak strengths in MCM-depleted and control

cells within 1 Mb bins across the whole genome, normalized to global and local background of interactions. Higher values indicate increase of peak strength after MCM depletion. Mean of the distribution is highly significantly different from 0 (one sample *t*-test), $P = 1.87 \times 10^{-70}$. **j**, de novo called loops using Mustache over a range of genomic distances in control and MCM-depleted cells. **k**, Number of de novo loops (called with Mustache) in independent Hi-C and Micro-C experiments. All replicates were downsampled to 300 million total contacts. **l**, Volcano plot showing statistical significance $-\log_{10}$ (FDR) versus fold change (\log_2 fold change) for RNA-seq data between MCM2-mAID expressing HCT116 cells treated with DMSO (Control) or auxin (MCM depletion). Numbers indicate the number of transcripts significantly up- (right) or downregulated (left) after MCM depletion at FDR = 0.1. Dashed vertical lines indicate -0.585 and $+0.585 \log_2$ fold change in expression (1.5-fold decrease and increase in expression), respectively. RNA-seq libraries were generated in triplicate (independent replicates). **m**, Correlation between gene expression changes and relative change in chromatin contact frequencies around the transcriptional start sites (TSSs) after MCM loss. All mean contact frequency changes were tested against the non-DE TSS control using the non-parametric Kruskal-Wallis test followed by pairwise Wilcoxon (Mann-Whitney *U*) test. **n**, Immunoblotting analysis of whole-cell lysate (W), supernatant (S) and chromatin fraction (C) from asynchronous and G1-sorted HCT116 MCM2-mAID cells treated with triptolide (chromatin-bound RNA PolII degradation) and either DMSO (Control) or auxin (MCM depletion). H3 is used as loading control for the chromatin fraction. Uncropped blots are displayed in [Supplementary Fig. 1](#). This experiment was repeated independently one more time with similar results. **o**, Peak strengths for control, MCM-depleted, triptolide-treated (DMSO/trp) and triptolide-treated/MCM-depleted (MCM depletion/trp) cells over a range of genomic distances. Notes: Micro-C datasets (control/MCM depletion) are pooled replicates from two biologically independent Micro-C experiments, unless otherwise stated. Read statistics for Hi-C and Micro-C replicates can be found in [Supplementary Table 1](#).

Extended Data Fig. 9 Translocating cohesin can bypass MCM with reduced efficiency.

a, MCM loads as double-hexamers at origins. Time traces of origin-bound MCM fluorescence intensity (purple) show two-step bleaching but less frequent also one and multi-step (black, fits by kinetic change point analysis) **b**, Representative kymograph of translocating cohesin in the absence of MCM at the origin. **c**, MCM does not alter observed cohesin translocation velocity. Box plots of cohesin diffusion coefficients in the absence (green) or presence (blue) of MCM at 150 or 500 mM NaCl. The centre line displays median, box edges show quartiles 1–3, and whiskers span quartiles $1–3 \pm 1.5 \times$ interquartile range. P values were determined by two-sided Mann-Whitney U test. **d**, **e**, Representative kymographs of translocating cohesin in the presence of MCM at the origin. MCM is a strong barrier for cohesin translocation (**d**) with MCM passage observed infrequently (**e**) during a 220 s interval. **f**, Multiple loaded MCMs do not increase the barrier strength for cohesin translocation. Photobleaching analysis confirm loaded MCM double-hexamers as main species. Data are depicted as mean within a 95 % confidence interval (generated by bootstrapping). P values were determined by Kruskal-Wallis test. **g**, Length distribution of doubly tethered DNA in pixels (px). The line represents a Gaussian fit. **h**, Cohesin translocation pauses at origins bound by MCM. Distribution of cohesin pause (green) and corresponding MCM (blue) positions on DNA. **i**, Representative kymographs of translocating cohesin showing frequent pausing after encountering MCM^{Mcm3-YDF} at the origin. All data displayed (except in **e** and where specified in **c**) were imaged under physiological salt conditions (0.15 M NaCl).

Extended Data Fig. 10 MCM is a barrier for cohesin translocation at a high salt concentration.

a, Schematic principle of a single-molecule cohesin translocation assay on licensed DNA. MCM is loaded onto DNA in the presence of the licensing factors ORC and Cdc6, followed by cohesin as described in Fig. [4a](#). Subsequently, cohesin translocation is visualized at high salt concentration (0.5 M NaCl) in the absence of free protein and buffer flow. **b–d**, Representative kymographs of translocating cohesin on DNA in the absence (**b**) or presence of MCM at the origin (**c**, **d**). Origin-bound MCM is a strong barrier to cohesin translocation (**c**) with passage events occurring infrequently (**d**) during a 220 s observation interval. **e**, MCM is a barrier for

cohesin translocation at high salt concentration. Probability of translocating cohesin bypassing the origin in the absence or presence of MCM calculated from 40 or 64 molecules with 7802 or 9829 visualized encounters, respectively. **f**, Multiple loaded MCMs do not increase the barrier strength for cohesin translocation. Data in **e**, **f** are depicted as mean within a 95 % confidence interval (generated by bootstrapping). *P values* were determined by Kruskal-Wallis followed by Dunn's post-hoc test. All data displayed were imaged in the presence of 0.5 M NaCl. **g**, Model showing that pausing of extruding cohesin at MCMs could promote sister-chromatid cohesion.

Supplementary information

Supplementary Information

This file contains Supplementary Figures 1-6.

Reporting Summary

Peer Review File

Supplementary Table 1

Read statistics of Hi-C and micro-C replicates.

Supplementary Table 2

Oligonucleotide sequences used for the DNA substrate for single-molecule imaging.

Supplementary Video 1

Video showing translocating cohesin (green) on doubly tethered DNA (blue) in the absence of MCM at 0.15 M NaCl (corresponds to kymograph in Extended Data Fig. 9b).

Supplementary Video 2

Video showing origin-bound MCM (magenta) as an efficient barrier for cohesin translocation (green) on doubly tethered DNA (blue) at 0.15 M NaCl (corresponds to kymograph in Fig. 4b).

Supplementary Video 3

Video showing translocating cohesin (green) on doubly tethered DNA (blue) that occasionally can bypass origin-bound MCM (magenta) at 0.15 M NaCl (corresponds to kymograph in Extended Data Fig. 9e).

Supplementary Video 4

Video showing translocating cohesin (green) on doubly tethered DNA (blue) in the absence of MCM at 0.5 M NaCl (corresponds to kymograph in Extended Data Fig. 10b).

Supplementary Video 5

Video showing origin-bound MCM (magenta) as an efficient barrier for cohesin translocation (green) on doubly tethered DNA (blue) at 0.5 M NaCl (corresponds to kymograph in Extended Data Fig. 10c, left).

Supplementary Video 6

Video showing translocating cohesin (green) on doubly tethered DNA (blue) that occasionally can bypass origin-bound MCM (magenta) at 0.5 M NaCl (corresponds to kymograph in Extended Data Fig. 10d, left).

Rights and permissions

Open Access This article is licensed under a Creative Commons Attribution 4.0 International License, which permits use, sharing, adaptation, distribution and reproduction in any medium or format, as long as you give appropriate credit to the original author(s) and the source, provide a link to the Creative Commons license, and indicate if changes were made. The images or other third party material in this article are included in the article's

Creative Commons license, unless indicated otherwise in a credit line to the material. If material is not included in the article's Creative Commons license and your intended use is not permitted by statutory regulation or exceeds the permitted use, you will need to obtain permission directly from the copyright holder. To view a copy of this license, visit <http://creativecommons.org/licenses/by/4.0/>.

Reprints and Permissions

About this article

Cite this article

Dequeker, B.J.H., Scherr, M.J., Brandão, H.B. *et al.* MCM complexes are barriers that restrict cohesin-mediated loop extrusion. *Nature* **606**, 197–203 (2022). <https://doi.org/10.1038/s41586-022-04730-0>

- Received: 23 October 2020
- Accepted: 06 April 2022
- Published: 18 May 2022
- Issue Date: 02 June 2022
- DOI: <https://doi.org/10.1038/s41586-022-04730-0>

Share this article

Anyone you share the following link with will be able to read this content:

[Get shareable link](#)

Sorry, a shareable link is not currently available for this article.

[Copy to clipboard](#)

Provided by the Springer Nature SharedIt content-sharing initiative

This article was downloaded by **calibre** from <https://www.nature.com/articles/s41586-022-04730-0>

| [Section menu](#) | [Main menu](#) |